Multiscale Modeling and Simulation of Turbulent Geophysical Flows

Omer San

Dissertation submitted to the Faculty of the
Virginia Polytechnic Institute and State University
in partial fulfillment of the requirements for the degree of

Doctor of Philosophy
in
Engineering Mechanics

Anne E. Staples, Chair
Raffaella De Vita
Traian Iliescu
Saad A. Ragab
Mark A. Stremler

June 11, 2012
Blacksburg, Virginia

Keywords: Geophysical Flows, Physical Oceanography, Multiscale Modeling, Multigrid, Large Eddy Simulation, Computational Fluid Dynamics

Multiscale Modeling and Simulation of Turbulent Geophysical Flows

Omer San

ABSTRACT

The accurate and efficient numerical simulation of geophysical flows is of great interest in numerical weather prediction and climate modeling as well as in numerous critical areas and industries, such as agriculture, construction, tourism, transportation, weather-related disaster management, and sustainable energy technologies. Oceanic and atmospheric flows display an enormous range of temporal and spatial scales, from seconds to decades and from centimeters to thousands of kilometers, respectively. Scale interactions, both spatial and temporal, are the dominant feature of all aspects of general circulation models in geophysical fluid dynamics. In this thesis, to decrease the cost for these geophysical flow computations, several types of multiscale methods were systematically developed and tested for a variety of physical settings including barotropic and stratified wind-driven large scale ocean circulation models, decaying and forced two-dimensional turbulence simulations, as well as several benchmark incompressible flow problems in two and three dimensions. The new models proposed here are based on two classes of modern multiscale methods: (i) interpolation based approaches in the context of the multigrid/multiresolution methodologies, and (ii) deconvolution based spatial filtering approaches in the context of large eddy simulation techniques. In the first case, we developed a *coarse-grid projection* method that uses simple interpolation schemes to go between the two components of the problem, in which the solution algorithms have different levels of complexity. In the second case, the use of *approximate deconvolution* closure modeling strategies was implemented for large eddy simulations of large-scale turbulent geophysical flows. The numerical assessment of these approaches showed that both the coarse-grid projection and approximate deconvolution methods could represent viable tools for computing more realistic turbulent geophysical flows that provide significant increases in accuracy and computational efficiency over conventional methods.

Dedication

Dedicated to my family:

Sevgili annem, babam ve kardeşlerime...

biricik eşim Sümeyra'ya...

ve şimdilerde heyecanla beklediğimiz kızımıza...

Acknowledgments

I would like to first express my gratitude toward my advisor, Prof. Annie Staples, for her invaluable guidance, continued support and encouragement during my research. Her vision on multiscale modeling has lead me to explore many horizons of this evolving branch of computational science and engineering. She has given me the opportunity to work on several research projects other than the subject of this dissertation and, more importantly, she has helped me a lot to start developing my own academic style. She did make me feel like her colleague, more than a graduate student, throughout my entire graduate study in Virginia Tech. Besides, she has been very considerate, tolerant and accommodating all along.

This work received support from the Institute for Critical Technology and Applied Science (ICTAS) via grant number 118709. Partial funding for this research was also provided by the Department of Engineering Science and Mechanics. The author gratefully acknowledges this financial support from Virginia Tech.

Many thanks go to my committee members: Profs. Raffaella De Vita, Traian Iliescu, Saad Ragab, and Mark Stremler. Their interest and input into my research has been very insightful. I would like to address special thanks to Prof. Traian Iliescu who has been a great source of advice and inspiration throughout the development of this research on geophysical fluid dynamics. Special thanks are also due to Prof. Saad Ragab and Prof. Danesh Tafti for their advice and excellent instruction in computational fluid dynamics. Being familiar with those materials has been crucial for the progress of this research. I also thank Prof. Jeff Borggaard for his helpful communications and discussions.

I would like to acknowledge all my professors, past and present, for teaching me the fundamentals and inspiring me with their knowledge and character. Three persons deserve special mention, Prof. Adil Yukselen of Istanbul Technical University, Prof. Osama Kandil of Old Dominion University, and Prof. Hassan Aref of Virginia Tech, because my present understanding of fluid dynamics embodies so many of their ideas.

This list would be incomplete without a big thank to friends in Turkey and in the USA for their moral support, and for putting up with me during the more difficult times. Extra special thanks must go to my friends all over campus for making life more enjoyable and valuable here in Blacksburg. I also would like to thank my labmates Leila and Yasser for their friendship and for all those good times we shared together.

I am most grateful to my parents. Their unconditional love and support made me achieve many things that otherwise would be impossible. I want to extend to them my heartfelt thanks for all they have done and gone through for me. I owe it all to them. A very special thanks also goes to my sister, Zeynep, who is in a category of her own and has surprisingly made the last year of my PhD program that much nicer.

Last but not least, I would like to express my deepest gratitude to my wife, Sumeyra, for her endless love, encouragement and understanding over the years. Her love and her support mean more to me than I can ever put into words. I'm quite sure I wouldn't have made it through without her. Thanks!

Contents

List of Figures

List of Tables

Chapter 1

Introduction

It must be admitted that the principal result of the fifty years of turbulence research is the recognition of the profound difficulties of the subject.

S. A. Orszag (1970)

1.1 Motivation

Geophysical flows in the atmosphere and oceans exhibit complex patterns of fluid motion over a vast range of space and time scales that may vary from planetary scales to microscales and from years to seconds. Scale interactions, both spatial and temporal, are the dominant feature of all aspects of general circulation models in geophysical fluid dynamics (Lynch, 2008; Washington et al., 2009; Klein, 2010). Global planetary-scale circulations appear in many different form such as waves, jets, gyres, boundary layers and turbulence. It is not an exaggeration to say that almost all problems in geophysical systems have multiple spatial or temporal scales. The key to solving these problems is to understand scale-specific flow phenomena where turbulence, convection, waves, vortices, and jet streams can all interact in a complex manner across a wide range of temporal and spatial scales.

Turbulent fluctuations occur over a wide range of excited length and time scales leading to broadband energy spectra in wave number space. In his book, Hinze (1975) suggests that it is necessary to introduce the notion of the scale of turbulence: a certain scale in time and a certain scale in space in order to describe a turbulent motion quantitatively. Turbulence is a multiscale problem with highly nonlinear coupling between scales. This picture illustrates why the accurate prediction of turbulent flows is such a difficult problem. Indeed, most fluid flows occurring in nature as well as in engineering applications are turbulent. Fluid motion becomes turbulent when the Reynolds number exceeds a specific threshold, below which frictional (viscous) forces prevent chaotic behavior. Thus, the difficulty of understanding turbulence in fluids is one of the most legendarily challenging topics in fluid dynamics. For example, a famous quotation is variously attributed to Albert Einstein, Werner Heisenberg, Richard Feynman, or Arnold Sommerfeld: "Turbulence is the last great unsolved problem of classical physics." Whether any of those prominent scientists actually uttered those words is beside the point here, everyone in the field would probably agree with the main idea in the statement. Consequently, it does not take any further comment to emphasize that computational studies of turbulent flows are of outstanding importance for the scientific community.

An important feature of turbulent flows is that they are composed of fluctuating eddies or vortices of many sizes, which are constantly interacting with each other. The phenomenology of turbulence was described by Richardson (1920) and quantified in a scaling theory by Kolmogorov (1941). Two-dimensional (2D) turbulence, to the first approximation, is a reduced dimensional version of "real" three-dimensional (3D) turbulence, where the flow is constrained to two dimensions. Although in reality 2D turbulence is never realized in nature or in the laboratory, both of which have always some degree of three-dimensionality, many aspects of idealized 2D turbulence appear to be relevant for physical systems in geophysics, astronomy and plasma physics (Boffetta and Ecke, 2012). One of the most important reasons for studying 2D turbulence is to improve our understanding of geophysical flows in the atmosphere and ocean (Lilly, 1971; Charney, 1971; McWilliams, 1984; Maltrud and Vallis,

1991; Ferziger et al., 2002), in which stratification and rotation suppress vertical motions in the thin layers of fluid.

From a theoretical perspective, 2D turbulence is not simply a reduced dimensional version of 3D turbulence because a completely different phenomenology arises from new conservation laws in two dimensions. In fact, two-dimensional turbulence behaves in a profoundly different way from 3D turbulence due to different energy cascade behavior, and follows the Kraichnan-Batchelor-Leith (KBL) theory (Kraichnan, 1967; Batchelor, 1969; Leith, 1971). In 3D turbulence, energy is transferred forward, from large scales to smaller scales, via the vortex stretching and tilting mechanism. This cascade mechanism has been summarized by Richardson (1920) in the following ditty:

Big whorls have little whorls, that feed on their velocity;
And little whorls have lesser whorls, and so on to viscosity

In two dimensions that mechanism is absent, and it turns out that under most forcing and dissipation conditions energy will be transferred from smaller scales to larger scales. Inverting nicely the above ditty, the upscale cascade in two-dimensional turbulence has been described by Vallis (2006):

Smaller whorls beget bigger whorls, that feed upon their energy;
And bigger whorls beget larger whorls, and so on, with much synergy

Despite the apparent simplicity of dealing with two rather than three spatial dimensions, two-dimensional turbulence is possibly richer in its dynamics due to its conservation properties (Davidson, 2004), such as its inverse energy and forward enstrophy cascading mechanisms, which three-dimensional turbulence do not possess.

The most important features that distinguish fluid flow in the atmosphere and ocean are the effects of rotation and stratification (Majda, 2003). However, flow patterns in the atmosphere and oceans are generated by vastly different physical mechanisms. In general, the

atmosphere is thermodynamically driven, that is, the solar radiation is the primary source of energy. In contrast, the oceans are forced by a variety of mechanisms. In addition to gravitational forces that generate the tides, the upper ocean surface is subjected to wind stresses that drive most ocean currents. Local differences between air and sea temperatures generate heat fluxes, evaporation, and precipitation, which in turn act as thermodynamical forcings of producing additional currents (Cushman-Roisin, 1994). Ocean modeling is closely related in method and spirit to atmospheric modeling, but atmospheric modeling was developed earlier, driven by the need for operational weather prediction (Miller, 2007). The development of general circulation models of the atmosphere and ocean have brought primarily two great advantages: (i) weather prediction for several days with a high degree of confidence; (ii) long range climate prediction. The present day climate models are composites of the major dynamic models of the Earth's climate system (Bryan, 1987; Satoh, 2004; Staniforth and Wood, 2008).

Numerical modeling has become an essential component of most research in geophysical flows for simulating the complex, multiscale interactions intrinsic to atmospheric and oceanic fluid motions (Shuman, 1957; Smagorinsky, 1963; Lilly, 1965; McWilliams, 1996; Hourdin and Armengaud, 1999; Steppeler et al., 2003; Miller, 2007; Durran, 2010; Cushman-Roisin and Beckers, 2011; Lauritzen et al., 2011). The accurate and efficient numerical simulation of geophysical flows is of great interest in numerous critical areas and industries, such as agriculture, construction, tourism, transportation, weather-related disaster management (tsunami and hurricane prediction), sustainable energy technologies such as wind turbine farms, biofuel production, solar energy arrays, ocean power extraction, and watershed management. Correctly predicting the long-term behavior of Earth's climate and seas, the effect of increased carbon emissions on the atmosphere, and changing weather pattern phenomena, which are issues of current interest to the scientific community, also require accurate and efficient computations.

To decrease the computational cost required for an accurate representation of the numerous interconnected physical atmospheric and oceanic flows, significant advancements

were made during the past decades in developing simplified models for geophysical fluid dynamics (GFD), including (i) the Boussinesq equations, (ii) the primitive equations, (iii) the shallow-water equations, and (iv) the quasi-geostrophic equations (Gill, 1982; Pedlosky, 1987; Cushman-Roisin, 1994; Holton, 2004; Vallis, 2006; McWilliams, 2006; Miller, 2007), which have been instrumental in providing relatively accurate numerical results at a reasonable computational price. Although these GFD models have continued to produce increasingly accurate results and therefore improved weather forecasting, their use in long time integrations such as those required by climate modeling remains challenging (Ghil et al., 2008; Lynch, 2008; Staniforth and Wood, 2008; Washington et al., 2009). The reason is that when used for time intervals of 100 years or more, the spatial and temporal resolutions in the GFD models must remain modest, and consequently the accuracy is decreased. There is a need for computational strategies that can significantly decrease the computational cost of GFD models without compromising their physical accuracy.

Multiscale modeling and simulation (MMS) is a rapidly evolving branch in applied science and engineering that will probably result in a fundamental impact on computing oceanic and atmospheric flows, which display an enormous range of spatial and temporal scales. The accurate and efficient computation of these geophysical flows is of foremost importance in weather and climate models and could perhaps benefit from a dedicated investigation of the application of classes of modern MMS methods (Brandt, 2002; Barth et al., 2002; Fish, 2009; E, 2011), which exploit vastly different temporal and spatial scales in problems in order to speed up their computations. Similar to the parallel developments in engineering and applied mathematics, interest in the development and testing of the MMS methods in geophysical flow settings has increased in recent years (Iskandarani et al., 2002; Majda and Klein, 2003; Khairoutdinov et al., 2008; Alam, 2011; Campin et al., 2011; Ringler et al., 2011), leading to several successful applications and research efforts at numerous weather and climate centers. The MMS framework could provide a significant increase in the accuracy and computational efficiency of numerous interconnected geophysical flow models for advanced numerical weather prediction, data assimilation and climate modeling strategies.

1.2 Contributions

In this thesis several modern MMS approaches have been utilized for geophysical flow settings. The motivation is mainly to apply these state-of-the-art modeling strategies to the important problems of geostrophic turbulence and large-scale ocean circulation. The development and testing of these methods is a crucial step for not only enhancing our understanding of characteristics of geophysical flows but also is of paramount importance in numerous critical areas and industries related to weather and climate systems. The new models proposed here are based on two classes of modern MMS methods: (i) interpolation based approaches in the context of the multigrid/multiresolution methodologies, and (ii) deconvolution based spatial filtering approaches in the context of large eddy simulation techniques.

In the first approach, a coarse-grid projection (CGP) method is first developed for incompressible flow solvers and then applied to the large-scale quasigeostrophic (QG) ocean circulation problems. In this approach, we separate the problem into two parts based on the nature of the QG models: (i) the elliptic sub-problem and (ii) the potential vorticity evolution equation. Most of the demand on computational resources by QG models comes in the solution of the elliptic inversion sub-problem which states the relationship between the potential vorticity and stream function. In the CGP method, the cost of the flow computations is reduced by coarsening the resolution of the numerical grid on which the elliptic sub-problem is solved by factors of two in each direction. This first step in the numerical assessment of the proposed ocean circulation models shows that CGP methodology could represent a viable tool for QG models of more realistic turbulent geophysical flows.

In the second approach, an approximate deconvolution large eddy simulation (LES) technique is first proposed for a one-layer barotropic quasigeostrophic large-scale ocean circulation model, and then extended to two-layer stratified ocean models considering baroclinic effects. The idea of spatial filtering is central in LES: the large, spatially filtered flow variables are approximated, whereas the effect of the small scales is modeled. Therefore, the characteristics of different filtering strategies are also systematically analyzed in this study.

The approximate deconvolution closure model is purely mathematical and employs repeated filtering of the filtered variables to obtain an approximation of the unfiltered variables. It has been shown here that the approximate deconvolution model provides an accurate approximation for under-resolved subfilter-scale effects.

The development and testing of these MMS strategies can be seen throughout this dissertation in applications to benchmark problems in incompressible flows, barotropic and stratified wind-driven ocean circulation models, and two-dimensional turbulence simulations. This thesis is organized in a manuscript format and each of the following chapters includes an up-to-date literature review, mathematical formulations, developed numerical methods, computed results, and discussion sections.

1.3 Research outline

The research conducted here investigates the development and use of some modern MMS methods to reduce the spatial and temporal complexity of geophysical flow computations, while retaining a high level of accuracy compared to current GFD computations. Two approaches are proposed: (i) interpolation based coarse-grid projection method, and (ii) approximate deconvolution based large eddy simulation technique. To demonstrate the potential applicability of these methods to the longstanding problems of computing and modeling geophysical fluid flows, we have organized our research in the following chapters:

Chapter 2 provides the development of a coarse-grid projection method (CGP) for accelerating incompressible flow computations for various forms of the Navier-Stokes equations. The performance of the CGP method for seven different benchmark problems is investigated.

The application of the coarse-grid projection method to the large-scale wind-driven ocean circulation problems is presented in Chapter 3 where the quasigeostrophic system of equations is also introduced. The applicability of the method to both barotropic and stratified ocean models is analyzed for mid-latitude oceanic basins.

Chapter 4 examines the characteristics of several high-order numerical schemes for the two-dimensional decaying turbulence problem. In addition to testing the behavior of various numerical schemes, one of the most important reasons for studying two-dimensional turbulence is to improve our understanding of geophysical flows in the atmosphere and ocean, in which stratification and rotation suppress vertical motions in the thin layers of fluid.

A Markovian forcing scheme is presented in Chapter 5 in which the effects of various forcing and dissipation mechanisms are investigated for two-dimensional isotropic homogenous stationary turbulence. The universality of turbulence statistics are discussed by showing the scaling exponents of structure functions and energy spectra.

Chapter 6 puts forth a new large eddy simulation closure modeling strategy for two-dimensional large-scale turbulent geophysical flows. The performance of this approximate deconvolution (AD) model is investigated by solving the barotropic vorticity equations in mid-latitude forced-dissipative ocean settings where the rotational effects account for using the beta plane approximation.

The approximate deconvolution method is extended in Chapter 7 to study stratified geophysical flows by using a baroclinic two-layer quasigeostrophic ocean circulation model. This chapter also investigates the effect of different filtering procedures and provides an insightful approach to eddy viscosity parametrization.

Chapter 8 provides a posteriori analysis of spatial filters for approximate deconvolution large eddy simulations of homogeneous incompressible flows by solving the three-dimensional Taylor-Green vortex flow problem, which is perhaps the simplest system in which to study the generation of increasingly smaller scale motions and the resulting turbulence.

Each of the chapters contains a review of the current literature and novel aspects of the presented research, followed by details of the mathematical and numerical methodology, and finally a discussion of the results, which includes comparisons with earlier theoretical or experimental studies where applicable. Finally, a summary of our findings and suggestions for future work are presented in Chapter 9.

Chapter 2

A Coarse-Grid Projection Method for Accelerating Incompressible Flow Computations

We present a coarse-grid projection (CGP) method for accelerating incompressible flow computations, which is applicable to methods involving Poisson equations as incompressibility constraints. The CGP methodology is a modular approach that facilitates data transfer with simple interpolations and uses black-box solvers for the Poisson and advection-diffusion equations in the flow solver. After solving the Poisson equation on a coarsened grid, an interpolation scheme is used to obtain the fine data for subsequent time stepping on the full grid. A particular version of the method is applied here to the vorticity-stream function, primitive variable, and vorticity-velocity formulations of incompressible Navier-Stokes equations. We compute several benchmark flow problems on two-dimensional Cartesian and non-Cartesian grids, as well as a three-dimensional flow problem. The method is found to accelerate these computations while retaining a level of accuracy close to that of the fine resolution field,

O. San and A. E. Staples, "A coarse-grid projection method for accelerating incompressible flow computations," submitted to *Journal of Computational Physics*.

which is significantly better than the accuracy obtained for a similar computation performed solely using a coarse grid. A linear acceleration rate is obtained for all the cases we consider due to the linear-cost elliptic Poisson solver used, with reduction factors in computational time between 2 and 42. The computational savings are larger when a suboptimal Possion solver is used. We also find that the computational savings increase with increasing distortion ratio on non-Cartesian grids, making the CGP method a useful tool for accelerating generalized curvilinear incompressible flow solvers.

2.1 Introduction

Computational studies of incompressible flow problems are important in basic scientific research, and for a multitude of engineering applications. In the decades since the first incompressible flow computations were performed, many successful algorithms have been proposed for computing these flows (Kwak and Kiris, 2010; Hafez and Kwak, 2003; Temam, 2001; Ferziger et al., 1999; Moin and Mahesh, 1998; Quartapelle, 1993). Incompressible flows are fluid flows in which the flow speed is small compared to the speed of sound. Interestingly, this simple condition introduces some computational difficulties. One basic approach to solving incompressible flow problems is to retain the full compressible form of the Navier-Stokes and continuity equations (e.g., artificial compressibility methods (Chorin, 1967; Choi and Merkle, 1985; Soh and Goodrich, 1988; Rogers and Kwak, 1991; Mateescu et al., 1994; Tang and Sotiropoulos, 2007)). The other basic approach is to use pressure-based methods in which the Navier-Stokes equations are simplified by treating the fluid density as constant. In this approach a different difficulty arises: the continuity equation no longer involves the time derivative of the density, which was previously used to calculate the pressure field from an equation of state, so there is no longer an independent equation for the pressure (Kwak et al., 2005). The solution, then, is to construct the pressure field to guarantee that the continuity equation is satisfied (e.g., the vorticity-stream function formulation (Arakawa, 1966; Tezduyar et al., 1990), the marker and cell method (Harlow and Welch, 1965), or projection

algorithms for the primitive variable formulation of the problem (Chorin, 1968; Kim and Moin, 1985; Brown et al., 2001)). This is accomplished by solving a Poisson equation to find the pressure field (Chorin, 1968; Kim and Moin, 1985; Bell et al., 1989; Choi and Moin, 1994; Zang et al., 1994; Jordan and Ragab, 1996a; Blasco et al., 1998; Strikwerda and Lee, 1999; Yanwen et al., 1999; Brown et al., 2001; Kiris and Kwak, 2001; Liu, 2001; Guermond et al., 2006; Matsumoto, 2006).

This latter approach has been given much attention in the literature (Kwak et al., 2005), and is the approach we focus on here. The computational cost per time step of the pressure-based methods is that of solving a vector-valued parabolic-type advection-diffusion equation and a scalar-valued elliptic-type Poisson equation. The number of Poisson equations that must be solved at each time step varies with the method and the problem dimensions, but for all the pressure-based methods, solving the Poisson equation takes considerably more computational resources than solving the advection-diffusion time dependent equations, especially for large scale problems and high Reynolds number flows (Guermond et al., 2006).

One straightforward way to accelerate incompressible flow simulations is to reduce the number of grid points for the most time consuming part of the problem, the elliptic solver. The coarse-grid projection (CGP) framework was first proposed by Lentine et al. (2010) and successfully applied to three-dimensional flow simulations for computer games using finite volume methods on unstructured grids. Here, we apply the CGP method to the primitive variable fractional step, the vorticity-stream function, and the vorticity-velocity formulations for incompressible flow problems using finite differences on structured grids to analyze the accuracy and efficiency of the CGP framework for several benchmark flows in two and three dimensions. We also solve flow problems on distorted grids, and on generalized curvilinear grids. The cost of the flow computations is reduced by coarsening the resolution of the numerical grid on which the Poisson equation is solved by factors of two in each direction according to $M = 2^{-\ell}N$, where N is the fine resolution of the numerical grid on which the advection-diffusion part of the problem is solved, and M is the coarse resolution for the solution of the Poisson equation. When $\ell = 0$ no coarsening is applied and the CGP

method reduces to the underlying incompressible flow solver method. For just one level of coarsening, in which $\ell = 1$, and $M = N/2$, we have found that, remarkably, there is no significant resulting loss of accuracy in the fine resolution field data. For each subsequent level of coarsening investigated ($\ell = 2$ and $\ell = 3$) there is a further gain in computational speed-up, and an associated reduction in the accuracy of the fine resolution field data. However, the results obtained by the CGP method are more accurate than those of the standard coarse simulations for all the cases. In the current study, the third-order Runge-Kutta (Gottlieb and Shu, 1998; Shu, 2003) and the second-order central difference schemes are used for temporal and spatial discretizations, respectively. The method is general in nature and can be applied to any Poisson equation-based incompressible Navier-Stokes solver. The results demonstrate that it is possible to obtain high-accuracy fine resolution data at the price of a mostly coarse computation. The method can easily be applied to high Reynolds number turbulence simulations in three dimensions, where we expect the saving in computational time to be significant.

One of the important aspects of the proposed method is its flexibility and its ease of use with existing incompressible flow solvers. The method is independent of the choice of Poisson solver and the choice of solver used for the advection-diffusion part of the governing equations. Linear- or quadratic-rate acceleration can be obtained, depending on the choice of Poisson solver. In this study we use two types of efficient linear-cost Poisson solvers, the V-cycle multigrid iterative solver and the fast Fourier transform (FFT) based direct solver, as our black-box Poisson solvers. The computational savings reported in this study are greater for flow solvers that use suboptimal, quadratic-cost Poisson solvers, as is demonstrated in one of the benchmark problem in this study.

This paper is organized as follows: the mathematical models including the primitive variable formulation, the vorticity-stream function formulation, and the vorticity-velocity formulation of Navier-Stokes equations are presented in Section 2.2. In Section 2.3, the CGP method is developed and the joint flow solver algorithms are presented. In Section 2.4, the CGP flow solver algorithms are applied to several different two-dimensional benchmark

flow problems: the Taylor-Green decaying vortex problem, the evaluation of a double shear layer, the merging of a pair of co-rotating vortices, two-dimensional decaying turbulence, the Taylor-Green vortex problem on a distorted grid, and laminar flow over a circular cylinder. This section also includes the application of the CGP method to three-dimensional Taylor-Green vortex flows, in which vortex stretching and tilting occurs. The results are compared to results obtained by performing the calculations using the basic flows solvers alone to test the validity of the CGP framework. Speed-ups in computational time ranging from 2 to 42 are found. Final conclusions and some comments about the effectiveness and applicability of the CGP method are presented in Section 2.5.

2.2 Governing equations

2.2.1 Primitive variable (PV) formulation

The primitive variable formulation of the governing equations for incompressible viscous flows in dimensionless form with index notation is:

$$\frac{\partial u_i}{\partial t} + \frac{\partial u_i u_j}{\partial x_j} = -\frac{\partial p}{\partial x_i} + \frac{1}{Re}\frac{\partial^2 u_i}{\partial x_j \partial x_j} \tag{2.1}$$

$$\frac{\partial u_j}{\partial x_j} = 0 \tag{2.2}$$

where Re is the Reynolds number, u_i is the velocity component in the ith direction, and p is the pressure. We use the fractional step procedure (Chorin, 1968; Kim and Moin, 1985; Brown et al., 2001), in which the first (predictor) step is to solve the advection-diffusion equation to obtain an estimate of the velocity field that does not satisfy the incompressibility condition. Next, the pressure (or pressure-like quantities in other formulations) is computed by solving a Poisson equation for which the estimated velocity field supplies the source term. Finally, a pressure correction is applied, and the resulting velocity field is a divergence-free solution of Navier-Stokes equations. In the predictor step, the pressure is neglected, and the

intermediate velocities are computed by integrating the momentum equations as follows:

$$\frac{\partial \tilde{u}_i}{\partial t} + \frac{\partial \tilde{u}_i \tilde{u}_j}{\partial x_j} = \frac{1}{Re} \frac{\partial^2 \tilde{u}_i}{\partial x_j \partial x_j}. \tag{2.3}$$

The Poisson equation for the pressure becomes:

$$\frac{\partial^2 p}{\partial x_i \partial x_i} = f(\tilde{u}_i) \tag{2.4}$$

where f is a function of the intermediate velocity field. Finally, the corrected velocity field is calculated via:

$$u_i = g(\tilde{u}_i, p) \tag{2.5}$$

where g is another function of the computed pressure and the intermediate velocity field. There are several variations of the procedure given above. Here, we use a formulation based on the third-order Runge-Kutta algorithm, which we present in detail in Section 2.3.2.

2.2.2 Vorticity-stream function (VS) formulation

An alternative to the fractional step procedure in the primitive variable formulation is the vorticity-stream function formulation, which is obtained by taking the curl of the momentum equations (Quartapelle, 1993; Majda and Bertozzi, 2002). Specifically, for two-dimensional incompressible flows, the dimensionless form of vorticity-stream function formulation is:

$$\frac{\partial \omega}{\partial t} + \frac{\partial \psi}{\partial y}\frac{\partial \omega}{\partial x} - \frac{\partial \psi}{\partial x}\frac{\partial \omega}{\partial y} = \frac{1}{Re}\left(\frac{\partial^2 \omega}{\partial x^2} + \frac{\partial^2 \omega}{\partial y^2}\right). \tag{2.6}$$

This equation is used in conjunction with the kinematic relationship between the vorticity and the stream function, which has the form of a Poisson equation:

$$\frac{\partial^2 \psi}{\partial x^2} + \frac{\partial^2 \psi}{\partial y^2} = -\omega \tag{2.7}$$

where ω is the vorticity (defined in Eq. (2.9) as ω_z), and ψ is the stream function. There are several advantages to the vorticity-stream function formulation for two-dimensional flows. Not only has the pressure been removed from the system of equations, and continuity implicity satisfied by the definition of stream function, but also it eliminates the possible projection inaccuracies of the fractional step formulations. The vorticity-stream function formulation also allows one to reduce the number of equations to be solved.

2.2.3 Vorticity-velocity (VV) formulation

The Navier-Stokes equations can also be written in the vorticity-velocity formulation (Fasel et al., 1990; Fasel, 2002). It consists of three equations, one for each of the three components of vorticity:

$$\frac{\partial \boldsymbol{\omega}}{\partial t} + \boldsymbol{u} \cdot \nabla \boldsymbol{\omega} = \boldsymbol{\omega} \cdot \nabla \boldsymbol{u} + \frac{1}{Re} \nabla^2 \boldsymbol{\omega} \tag{2.8}$$

where the vorticity field is defined as the curl of velocity field, $\boldsymbol{\omega} = \nabla \times \boldsymbol{u}$. The components of the vorticity vector are:

$$\omega_x = \frac{\partial w}{\partial y} - \frac{\partial v}{\partial z}, \quad \omega_y = \frac{\partial u}{\partial z} - \frac{\partial w}{\partial x}, \quad \omega_z = \frac{\partial v}{\partial x} - \frac{\partial u}{\partial y} \tag{2.9}$$

where u, v, and w are the Cartesian velocity components. In addition, there are three Poisson equations to compute these velocity components:

$$\frac{\partial^2 v}{\partial x^2} + \frac{\partial^2 v}{\partial y^2} + \frac{\partial^2 v}{\partial z^2} = \frac{\partial \omega_z}{\partial x} - \frac{\partial \omega_x}{\partial z} \tag{2.10}$$

$$\frac{\partial^2 u}{\partial x^2} + \frac{\partial^2 u}{\partial z^2} = \frac{\partial \omega_y}{\partial z} - \frac{\partial^2 v}{\partial x \partial y} \tag{2.11}$$

$$\frac{\partial^2 w}{\partial x^2} + \frac{\partial^2 w}{\partial z^2} = -\frac{\partial \omega_y}{\partial x} - \frac{\partial^2 v}{\partial y \partial z}. \tag{2.12}$$

In the context of the current study, the fractional step primitive variable formulation, the vorticity-stream function formulation, and the vorticity-velocity formulation have in common

an elliptic inversion sub-problem that needs to be solved at every time step that takes most of the computational effort within that step.

2.3 Coarse-grid projection (CGP) methodology

In almost all Poisson equation-based incompressible flow solvers, solving the Poisson equation takes considerably more computational time than solving the advective-diffusive time dependent part of the problem. Within each time step, solving the advective-diffusive part of the problem is usually of $O(N_t)$ where "N_t" is the number of degrees of freedom (total grid points, N^2 for two-dimensional problems and N^3 for three-dimensional problems) of the problem. In general, the alternating direction implicit (ADI), Gauss-Seidel (GS) or successive over relaxation (SOR) types of iterative algorithms for solving the Poisson equation are of $O(N_t^2)$ (Saad, 2003). The practical consequence is that it is not feasible to use these types of iterative Poisson solvers for high resolution (and therefore high Reynolds number) computations along with long time integration. In order to accelerate these solvers, very successful multigrid algorithms have been developed that reduce the computational effort to close to $O(C_{MG}N_t)$ where C_{MG} is a proportionality constant (Saad, 2003; Wesseling, 2004; Gupta et al., 1997; Zhang, 1998). And for certain ideal problems on equally-spaced grids, fast Fourier transform (FFT)-based fast Poisson solvers (FPS) can be used that are $O(C_{FFT}N_t log(N_t))$, and are presently the fastest algorithms ($C_{FFT}log(N_t) < C_{MG}$ in the relevant resolutions) for solving Poisson equations (Moin, 2001). Since we design our CGP framework for structured grid problems on either Cartesian or curvilinear grids, iterative elliptic solvers based on Krylov subspace methods such as the GMRES method used in Lentine et al. (2010) have been not included in our analysis.

The computational efficiencies of different Poisson solvers are tabulated in Table 2.1 for a square domain with equidistant grid spacing. The computational time for solving just one Poisson equation is also illustrated in Figure 2.1. This preliminary comparison shows

Table 2.1: Computational efficiency of Poisson solvers. CPU times (seconds) for solving one Poisson equation.

Poisson Solver	32^2	64^2	128^2	256^2	512^2	1024^2	2048^2
Gauss-Seidel	0.093	1.582	26.15				
ADI	0.085	1.339	22.11				
SOR	0.009	0.182	3.131				
V-Multigrid	0.002	0.01	0.041	0.175	0.869	3.979	14.71
FFT-FPS	0.001	0.003	0.009	0.037	0.149	0.659	2.781

that FFT-FPS is the most efficient solver for most of our test problems. Therefore, we use FFT-FPS for all cases except the distorted grid Taylor-Green vortex problem where mixed derivatives occur in the elliptic equations in the transformed generalized coordinates. The V-cycle multigrid Poisson solver is used instead for the distorted grid computations. In the multigrid solver, the Poisson equation is solved in such a way that the error in the residual is linearly smoothed. Therefore, it is an optimal linear-cost iterative solution technique for the elliptic sub-problem. Similar to the multigrid approach, in our CGP approach, we use prolongation and restriction operators between the data for the advection-diffusion part and the elliptic part of the problem. This seems to be effectively a low-pass filter on the solution to the Poisson equation. In addition to different prolongation and restriction operators, the approach presented in this study differs from Lentine et al. (2010), in which the restrictions and prolongations operate on velocities, whereas in our implementation they operate on pressures.

The basic idea behind coarse-grid projection (CGP) is to use a smaller number of grid points for solving the elliptic sub-problem. The CGP approach we propose here is modular and independent of the Poisson solver that is used. Usually fast Poisson solvers are optimal for rectangular domain problems because they are fast and have minimal storage requirements. They are preferred because of their efficiency when using orthogonal coordinate systems in which there are no mixed derivatives. The general domains treated with

body-fitted coordinates are out of bounds for fast Poisson solvers due to the presence of mixed derivatives in the transformed generalized curvilinear coordinates. In that case, the V-cycle multigrid solver becomes the optimal Poisson solver to use, and we use it for our benchmark problems on distorted grids. On the other hand, for the test case of flow over a circular cylinder, due to the O-grid system, we use a fast Poisson solver in which we utilize FFTs in the circumferential direction and the Thomas algorithm in radial direction, and the result is a linear-cost fast Poisson solver (Moin, 2001).

Fast Poisson solvers can be implemented in our computations in two different ways. One way is to perform FFTs on the equation directly which results in a spectral accuracy for the Poisson equation, and the other is to discretize the Poisson equation first and then apply FFTs, which results in the same spatial order of accuracy as the underlying finite difference scheme (second-order, in this case). According to our preliminary computations for incompressible flows, both strategies give the same results. For example, to invert a two-dimensional Poisson equation, $\nabla^2 u = f$, in a uniform rectangular domain, the second-order scheme is:

$$\frac{u_{i-1,j} - 2u_{i,j} + u_{i+1,j}}{\Delta x^2} + \frac{u_{i,j-1} - 2u_{i,j} + u_{i,j+1}}{\Delta y^2} = f_{i,j} \tag{2.13}$$

where the subscripts represent the grid indices, and Δx and Δy are the grid spacing in x and y directions, respectively. The three-step procedure for the FPS is Press et al. (1992):

(i) Apply an inverse FFT to find the Fourier coefficients $\hat{f}_{i,j}$ from the grid values $f_{i,j}$

(ii) Solve for the Fourier coefficients $\hat{u}_{i,j}$ according to:

$$\hat{u}_{i,j} = \frac{\hat{f}_{i,j}}{\frac{2}{\Delta x^2}\left[\cos(\frac{2\pi i}{N_x}) + \lambda^2 \cos(\frac{2\pi j}{N_y}) - (1+\lambda^2)\right]} \tag{2.14}$$

where $\lambda = \Delta x/\Delta y$, and N_x and N_y are the number of grid points in the x and y directions, respectively

(iii) Apply a forward FFT to find the grid values $u_{i,j}$ from the Fourier coefficients $\hat{u}_{i,j}$

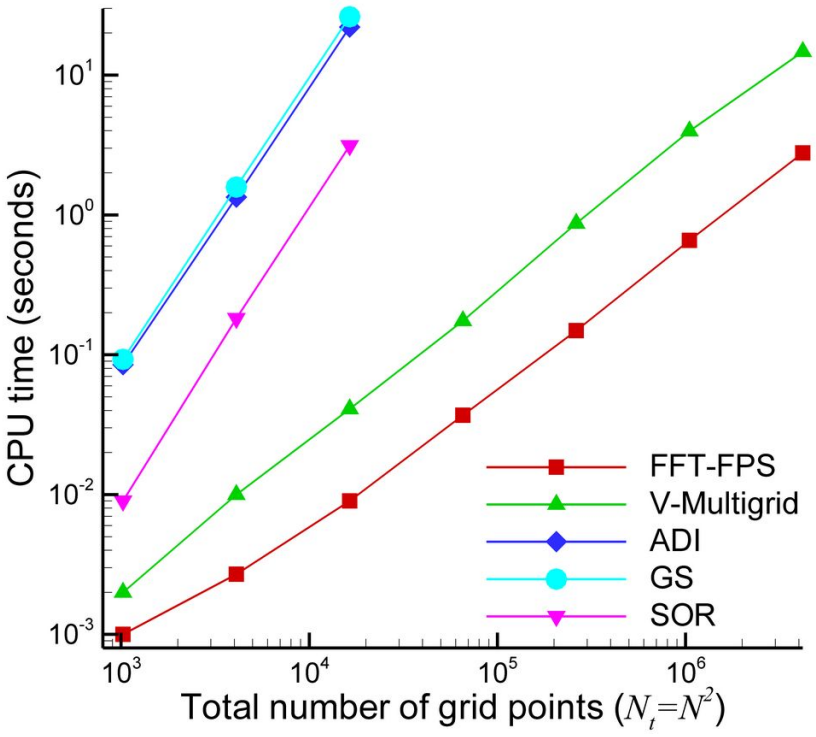

Figure 2.1: Efficiency of Poisson solvers. ADI, GS, and SOR are classical iterative solvers that scale as N_t^2. FFT-FPS is the fast Fourier transform based direct solver, and V-Multigrid is the V-cycle iterative multigrid solver, which both scale as N_t.

Even though we use the fastest Poisson solver available for our computations, the most time consuming part of the computations is still the Poisson equation constraint to the velocity field (e.g., see Table 2.4). With this in mind, we propose a new multiresolution approach that reduces the number of degrees of freedom for the Poisson solver part of the problem to accelerate the computation. The procedure is as follows: first, we solve the advection-diffusion part of the problem using a fine resolution, N (the resolution in one direction). Next, we restrict these data to a coarser grid with resolution $M = 2^{-\ell}N$, where ℓ is an integer that determines the level of coarsening ($\ell = 0$ corresponds to no grid coarsening). After solving the Poisson equation on this coarser grid, we then perform a prolongation of the coarse data to the fine resolution grid for subsequent time stepping. In the primitive variable formulation of fractional step method, the procedure is:

(i) Compute intermediate velocities on fine grid using fractional step method

(ii) Map intermediate velocity field data from fine grid to coarse grid to obtain source term for Poisson equation

(iii) Solve pressure Poisson equation and correct velocity field so that continuity equation is satisfied on coarse grid

(iv) Remap pressure field data from coarse grid to fine grid

(v) Update velocities on fine grid, continue to (i) for next time step

The procedures for the vorticity-stream function formulation and the vorticity-velocity formulation are similar to the primitive variable formulation, except that the underlying elliptic and advection-diffusion parts of the formulations are different as outlined in the preceding sections.

2.3.1 Mapping operators

The only modifications to the standard flow solver computational procedures are the mapping procedures from fine to coarse data and vice versa. In the current study, the full weighting averaging operation is used for data coarsening (restriction), which is given for a two-dimensional equally spaced data array as (Moin, 2001):

$$\begin{aligned}\bar{\phi}_{i,j} = \frac{1}{16}[4\phi_{2i,2j} + 2(\phi_{2i,2j-1} + \phi_{2i,2j+1} + \phi_{2i-1,2j} + \phi_{2i+1,2j}) \\ +\phi_{2i+1,2j+1} + \phi_{2i+1,2j-1} + \phi_{2i-1,2j+1} + \phi_{2i-1,2j-1}]\end{aligned} \tag{2.15}$$

where $\bar{\phi}_{i,j}$ and $\phi_{i,j}$ are the coarse and fine data arrays, and i, j are the coarse grid indices. The extension to three dimensions is relatively straightforward. The full weighting operator for mapping from the fine scale to the coarse scale for three-dimensional data arrays is constructed by using weighting factors of eight, four, two, and one, depending of the location

of the fine data (Zhang, 1998). For almost all multiscale computations, the mapping from the coarse data to the fine data is a critical issue (E et al., 2007; Kevrekidis and Samaey, 2009). The bilinear interpolation procedure that we use is given for two-dimensional equally spaced grid as (Moin, 2001):

$$\begin{aligned}
\phi_{2i,2j} &= \bar{\phi}_{i,j} \\
\phi_{2i+1,2j} &= \frac{1}{2}(\bar{\phi}_{i,j} + \bar{\phi}_{i+1,j}) \\
\phi_{2i,2j+1} &= \frac{1}{2}(\bar{\phi}_{i,j} + \bar{\phi}_{i,j+1}) \\
\phi_{2i+1,2j+1} &= \frac{1}{4}(\bar{\phi}_{i,j} + \bar{\phi}_{i+1,j} + \bar{\phi}_{i,j+1} + \bar{\phi}_{i+1,j+1}).
\end{aligned} \tag{2.16}$$

The half mapping procedures given by Eq. (2.15) for restriction and Eq. (2.16) for prolongation can be performed multiple times to obtain different levels of coarsening. The mapping procedure does not take significant computational time compared to the Poisson solver. The mapping procedures used in this study could potentially be improved by introducing higher-order spline formulas. Since we are using a second-order spatial discretization scheme, however, bilinear interpolation is suitable for this study. For three-dimensional grids, depending on the location, values of fine grid points are obtained by injection wherein the values of common points of the fine and coarse grid are directly transferred, and the values of the nearest two, four, or eight points on the coarse grid. The detailed formulas can be found in Wesseling (2004).

2.3.2 CGP algorithm for the primitive variable formulation

The coarse-grid projection (CGP) method is independent from the time integration method used. It can be implemented using any time stepping algorithm, for example, the backward difference method, or a method from the Adams-Bashforth or Adams-Moulton families (Schäfer, 2006). Here, the CGP method is used in conjunction with the third-order Runge-

Kutta method for the fractional step primitive variable formulation of the problem. The joint CGPRK3-PV algorithm is presented below. Starting with velocity field data, u_i^n, the velocity field is computed for the next time step according to the following sequence of computations:

$$\tilde{u}_i^{(1)} = u_i^n + \Delta t H_i^n \tag{2.17}$$

$$\tilde{u}_i^{(1)} \Rightarrow \bar{\tilde{u}}_i^{(1)} \tag{2.18}$$

$$\frac{\partial^2 \bar{p}}{\partial x_i \partial x_i} = \frac{1}{\Delta t} \frac{\partial \bar{\tilde{u}}_i^{(1)}}{\partial x_i} \tag{2.19}$$

$$p \Leftarrow \bar{p} \tag{2.20}$$

$$u_i^{(1)} = \tilde{u}_i^{(1)} - \Delta t \frac{\partial p}{\partial x_i} \tag{2.21}$$

$$\tilde{u}_i^{(2)} = \frac{3}{4} u_i^n + \frac{1}{4} u_i^{(1)} + \frac{1}{4} \Delta t H_i^{(1)} \tag{2.22}$$

$$\tilde{u}_i^{(2)} \Rightarrow \bar{\tilde{u}}_i^{(2)} \tag{2.23}$$

$$\frac{\partial^2 \bar{p}}{\partial x_i \partial x_i} = \frac{1}{(\frac{1}{4}\Delta t)} \frac{\partial \bar{\tilde{u}}_i^{(2)}}{\partial x_i} \tag{2.24}$$

$$p \Leftarrow \bar{p} \tag{2.25}$$

$$u_i^{(2)} = \tilde{u}_i^{(2)} - \frac{1}{4} \Delta t \frac{\partial p}{\partial x_i} \tag{2.26}$$

$$\tilde{u}_i^{(3)} = \frac{1}{3} u_i^n + \frac{2}{3} u_i^{(2)} + \frac{2}{3} \Delta t H_i^{(2)} \tag{2.27}$$

$$\tilde{u}_i^{(3)} \Rightarrow \bar{\tilde{u}}_i^{(3)} \tag{2.28}$$

$$\frac{\partial^2 \bar{p}}{\partial x_i \partial x_i} = \frac{1}{(\frac{2}{3}\Delta t)} \frac{\partial \bar{\tilde{u}}_i^{(3)}}{\partial x_i} \tag{2.29}$$

$$p \Leftarrow \bar{p} \tag{2.30}$$

$$u_i^{n+1} = \tilde{u}_i^{(3)} - \frac{2}{3} \Delta t \frac{\partial p}{\partial x_i} \tag{2.31}$$

where H_i is the combination of the convection and viscous diffusion terms:

$$H_i = -\frac{\partial u_i u_j}{\partial x_j} + \frac{1}{Re} \frac{\partial^2 u_i}{\partial x_j \partial x_j}. \tag{2.32}$$

The CGP procedure for coarsening the grid on which the pressure Poisson equation is solved reduces the accuracy of the pressure field, as is to be expected. Any accuracy loss in the pressure field, however, does not propagate forward in time, and so a higher accuracy pressure field can be obtained at any time step by simply solving the Poisson equation on a fine grid according to:

$$\frac{\partial^2 p}{\partial x_j \partial x_j} = -\frac{\partial^2 u_i u_j}{\partial x_i \partial x_j} \tag{2.33}$$

which is obtained directly by taking the divergence of the momentum equation.

2.3.3 CGP algorithm for the vorticity-stream function formulation

Similar to the algorithm for the fractional step primitive variable formulation presented in the previous section, we present here the CGP method used in conjunction with the third-order Runge-Kutta method for the vorticity-stream function formulation of the governing equations of incompressible fluid flows. Starting with the value of the vorticity, ω^n, at the current time step, the joint CGPRK3-VS algorithm for computing the vorticity at the next time step, ω^{n+1}, consists of the following steps:

$$\omega^n \Rightarrow \bar{\omega}^n \tag{2.34}$$

$$\frac{\partial^2 \bar{\psi}^n}{\partial x^2} + \frac{\partial^2 \bar{\psi}^n}{\partial y^2} = -\bar{\omega}^n \tag{2.35}$$

$$\psi^n \Leftarrow \bar{\psi}^n \tag{2.36}$$

$$\omega^{(1)} = \omega^n + \Delta t G^n \tag{2.37}$$

$$\omega^{(1)} \Rightarrow \bar{\omega}^{(1)} \tag{2.38}$$

$$\frac{\partial^2 \bar{\psi}^{(1)}}{\partial x^2} + \frac{\partial^2 \bar{\psi}^{(1)}}{\partial y^2} = -\bar{\omega}^{(1)} \tag{2.39}$$

$$\psi^{(1)} \Leftarrow \bar{\psi}^{(1)} \tag{2.40}$$

$$\omega^{(2)} = \frac{3}{4}\omega^n + \frac{1}{4}\omega^{(1)} + \frac{1}{4}\Delta t G^{(1)} \tag{2.41}$$

$$\omega^{(2)} \Rightarrow \bar{\omega}^{(2)} \tag{2.42}$$

$$\frac{\partial^2 \bar{\psi}^{(2)}}{\partial x^2} + \frac{\partial^2 \bar{\psi}^{(2)}}{\partial y^2} = -\bar{\omega}^{(2)} \tag{2.43}$$

$$\psi^{(2)} \Leftarrow \bar{\psi}^{(2)} \tag{2.44}$$

$$\omega^{n+1} = \frac{1}{3}\omega^n + \frac{2}{3}\omega^{(2)} + \frac{2}{3}\Delta t G^{(2)} \tag{2.45}$$

where

$$G = -\frac{\partial \psi}{\partial y}\frac{\partial \omega}{\partial x} + \frac{\partial \psi}{\partial x}\frac{\partial \omega}{\partial y} + \frac{1}{Re}\left(\frac{\partial^2 \omega}{\partial x^2} + \frac{\partial^2 \omega}{\partial y^2}\right). \tag{2.46}$$

We favor the vorticity-stream function formulation for two-dimensional problems, especially for those having periodic boundary conditions. This particular formulation is an excellent model for testing the proposed CGP framework because of the absence of projection inaccuracies and errors due to boundary conditions.

2.4 Results

To investigate the performance of the CGP method seven different flow problems are computed. First, four flow problems in periodic domains are computed: the Taylor-Green decay-

ing vortex problem, the evaluation of a double shear layer, the merging of a pair of co-rotating vortices, and two-dimensional decaying turbulence. Problems with periodic boundary conditions are chosen both to eliminate any possible error arising from boundary condition implementations, and to be able to use fast Poisson solvers. Next, the Taylor-Green vortex problem is solved on a distorted grid, and the benchmark test problem of flow over a circular cylinder is studied to demonstrate the efficiency of CGP for non-Cartesian grid applications. Finally, the behavior of the method is tested for a three-dimensional problem, the Taylor-Green vortex problem, demonstrating the applicability of the method in three-dimensions, in the presence of vortex stretching and tilting.

2.4.1 Taylor-Green vortex

In this section, the CGPRK3 algorithms in the vorticity-stream function formulation and primitive variable formulation are validated by solving the Taylor-Green decaying vortex problem in a two-dimensional square domain. The problem describes the two-dimensional, unsteady flow of a decaying vortex (or set of vortex arrays), and is an exact analytic solution of the unsteady, incompressible Navier-Stokes equations in Cartesian coordinates. The analytic solution in $[0, 2\pi] \times [0, 2\pi]$ domain with periodic boundary conditions is given for the velocity field by:

$$u^e(x, y, t) = -\cos(qx)\sin(qy)\exp(-2q^2t/Re) \tag{2.47}$$

$$v^e(x, y, t) = \sin(qx)\cos(qy)\exp(-2q^2t/Re) \tag{2.48}$$

and for vorticity field it is given by:

$$\omega^e(x, y, t) = 2q\cos(qx)\cos(qy)\exp(-2q^2t/Re) \tag{2.49}$$

where q is an integer. We performed numerical simulations for $Re = 10$ with both the CGPRK3-PV and CGPRK3-VS algorithms introduced earlier with $\Delta t = 2.5 \times 10^{-4}$ and the

Taylor array number, $q = 1$. For the primitive variable formulation, the difference between the exact and computed solutions is:

$$e_{i,j} = |u^e_{i,j} - u_{i,j}| \tag{2.50}$$

where u is the x-component of the velocity. Similarly, for the vorticity-stream function formulation, the error in vorticity field is defined as:

$$e_{i,j} = |\omega^e_{i,j} - \omega_{i,j}|. \tag{2.51}$$

In order to quantify the accuracy of the CGP method, we computed two different norms, the root mean squared L_2 norm:

$$L_2 = \sqrt{\frac{1}{N_x N_y} \sum_{i=1}^{N_x} \sum_{j=1}^{N_y} e^2_{i,j}} \tag{2.52}$$

and the L_∞ norm:

$$L_\infty = \text{Max}(e_{i,j}). \tag{2.53}$$

The computed L_2 and L_∞ norms at time $t = 1$ are tabulated in Table 2.2 and Table 2.3 for the vorticity-stream function and the primitive variable formulation solutions, respectively. Results obtained using the coarse-grid projection algorithm (CGPRK3) and the standard flow solver (RK3) without the CGP procedure are compared for different levels of coarsening. In these tables, the first resolution listed is for the fine grid on which the advection-diffusion part of the problem is solved, and the second value is the resolution of the coarse grid on which the Poisson equation is solved to constrain the fine scale field data: the vorticity field in the vorticity-stream function formulation, or the velocity field in primitive variable formulation. When these resolutions are the same, the standard method is recovered.

Three different levels of coarsening: half-coarsening ($\ell = 1$, $M = N/2$), 1/4-coarsening ($\ell = 2$, $M = N/4$) and 1/8-coarsening ($\ell = 3$, $M = N/8$), were performed to investigate

Table 2.2: The computed error norms for the vorticity-stream function formulation algorithm (RK3/CGPRK3-VS) for $Re = 10$, $\Delta t = 2.5 \times 10^{-4}$ at time $t = 1$. The first resolution number represents the number of grid points used for solving the advection-diffusion equation (vorticity-transport equation), and the second resolution number is the number of grid points used for solving the Poisson equation (kinematic relationship between vorticity and stream function). The speed-up ratio is defined as the ratio of the CPU times for the computations performed without using the CGP procedure (using the standard method) and with the CGP procedure. Results obtained using the SOR scheme for the Poisson equation are also included for comparison.

Method	Resolution	$\|\|\omega\|\|_\infty$	$\|\|\omega\|\|_{L_2}$	CPU (s)	Speed-up
FFT-FPS					
RK3 ($\ell = 0$)	$512^2 : 512^2$	4.1099E-6	2.0589E-6	2500.03	1.00
CGPRK3 ($\ell = 1$)	$512^2 : 256^2$	4.1099E-6	2.0590E-6	976.94	2.56
CGPRK3 ($\ell = 2$)	$512^2 : 128^2$	1.1188E-5	3.3678E-6	510.24	4.90
CGPRK3 ($\ell = 3$)	$512^2 : 64^2$	6.6467E-5	2.2245E-5	406.31	6.15
RK3 ($\ell = 0$)	$256^2 : 256^2$	1.6439E-5	8.2518E-6	522.67	1.00
CGPRK3 ($\ell = 1$)	$256^2 : 128^2$	1.6439E-5	8.2525E-6	218.85	2.39
CGPRK3 ($\ell = 2$)	$256^2 : 64^2$	7.6177E-5	2.2801E-5	132.42	3.95
CGPRK3 ($\ell = 3$)	$256^2 : 32^2$	5.1640E-4	1.7568E-4	114.09	4.58
RK3 ($\ell = 0$)	$128^2 : 128^2$	6.5755E-5	3.3132E-5	112.29	1.00
CGPRK3 ($\ell = 1$)	$128^2 : 64^2$	6.5755E-5	3.3176E-5	47.15	2.29
RK3 ($\ell = 0$)	$64^2 : 64^2$	2.6297E-4	1.3351E-4	27.10	1.00
CGPRK3 ($\ell = 1$)	$64^2 : 32^2$	2.6335E-4	1.3624E-4	12.16	2.23
RK3 ($\ell = 0$)	$32^2 : 32^2$	1.0511E-3	5.4149E-4	6.19	1.00
SOR					
RK3 ($\ell = 0$)	$128^2 : 128^2$	6.5756E-5	3.3133E-5	90334.46	1.00
CGPRK3 ($\ell = 1$)	$128^2 : 64^2$	6.5757E-5	3.3176E-5	7131.36	12.67
RK3 ($\ell = 0$)	$64^2 : 64^2$	2.6298E-4	1.3351E-4	7113.46	1.00
CGPRK3 ($\ell = 1$)	$64^2 : 32^2$	2.6346E-4	1.3626E-4	442.71	16.07
RK3 ($\ell = 0$)	$32^2 : 32^2$	1.0511E-3	5.4150E-4	431.58	1.00

Table 2.3: The computed error norms for the primitive variable fractional step algorithm (RK3/CGPRK3-PV) for $Re = 10$, $\Delta t = 2.5 \times 10^{-4}$ at time $t = 1$. The first resolution number is the number of grid points used for solving the advection-diffusion equations (auxiliary momentum equations in both directions), and the second resolution number is the number of grid points used for solving the pressure Poisson equation. The speed-up ratio is defined as the ratio of CPU times for the computations performed without using the CGP procedure (using standard methods) and with the CGP procedure.

Method	Resolution	$\|\|u\|\|_\infty$	$\|\|u\|\|_{L_2}$	CPU (s)	Speed-up
RK3 ($\ell = 0$)	$512^2 : 512^2$	2.0550E-6	1.0247E-6	2915.10	1.00
CGPRK3 ($\ell = 1$)	$512^2 : 256^2$	2.0504E-6	1.0364E-6	1291.46	2.26
CGPRK3 ($\ell = 2$)	$512^2 : 128^2$	8.9268E-6	3.2635E-6	846.53	3.44
CGPRK3 ($\ell = 3$)	$512^2 : 64^2$	7.1230E-5	2.6292E-5	708.61	4.12
RK3 ($\ell = 0$)	$256^2 : 256^2$	8.2200E-6	4.0987E-6	661.86	1.00
CGPRK3 ($\ell = 1$)	$256^2 : 128^2$	8.6218E-6	4.0625E-6	314.74	2.10
CGPRK3 ($\ell = 2$)	$256^2 : 64^2$	6.7819E-5	2.5271E-5	227.65	2.91
CGPRK3 ($\ell = 3$)	$256^2 : 32^2$	6.4426E-4	2.1464E-4	196.49	3.68
RK3 ($\ell = 0$)	$128^2 : 128^2$	3.2878E-5	1.6393E-5	141.63	1.00
CGPRK3 ($\ell = 1$)	$128^2 : 64^2$	3.5194E-5	1.6566E-5	69.78	2.03
RK3 ($\ell = 0$)	$64^2 : 64^2$	1.3148E-4	6.5554E-5	33.35	1.00
CGPRK3 ($\ell = 1$)	$64^2 : 32^2$	1.9054E-4	8.5045E-5	16.72	2.00
RK3 ($\ell = 0$)	$32^2 : 32^2$	5.2546E-4	2.6192E-4	7.74	1.00

the behavior of the CGP method. The optimal results from the point of view of accuracy were obtained using the half-coarsening CGP method. For this level of coarsening, there is a significant reduction in computational time (by a factor of about 2.2) and no corresponding reduction in the accuracy of the flow field variables. Although it is fairly small, there is actually an increase in error from the 64^2:64^2 resolution to the 64^2:32^2 resolution case. For higher resolution, the pressure field is well resolved because the exact solution consists of two low frequencies. This contributes to the same level accuracy for one level of coarsening for higher resolution computations. For further levels of coarsening, there are increased savings in computational time, but also associated reductions in the accuracy of the flow

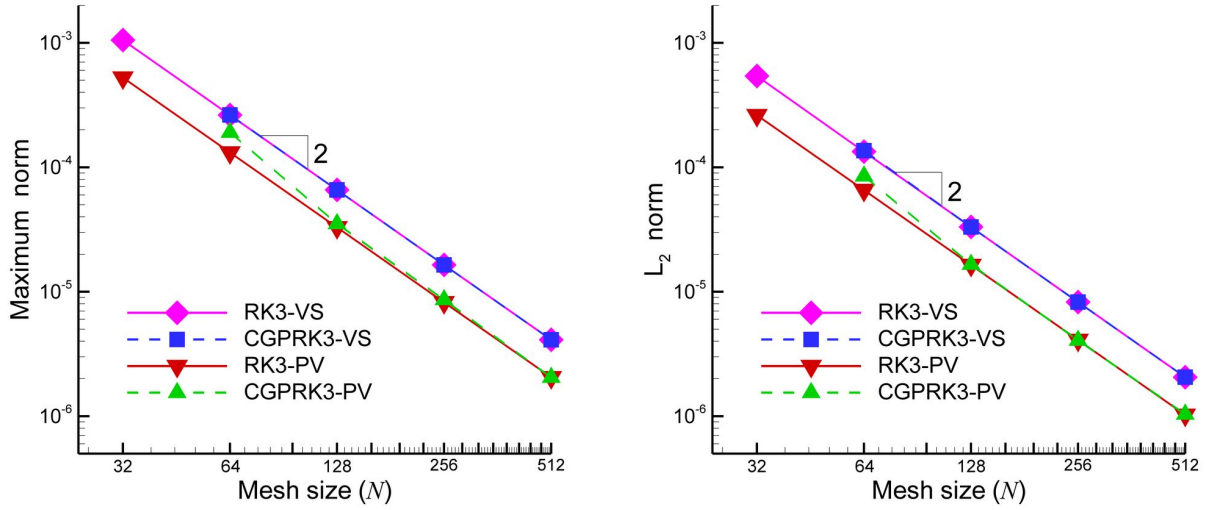

Figure 2.2: Convergence in the exact errors for the Taylor-Green decaying vortex problem using both standard and CGP methods: (left) L_∞ norms, and (right) L_2 norms.

field variables. The computational speed-up rate obtained using the CGP methodology was found to increase with the increasing resolution. These results are also tabulated in Table 2.2 and Table 2.3. Since we are using one of the fastest available Poisson solver routines, it is reasonable to expect that the speed-up will become much more pronounced when different Poisson solvers are implemented, as will be required for general flow problems that cannot be solved on a regular grid. Table 2.2 also includes the results obtained using a sub-optimal SOR-type iterative Poisson solver, showing that the computational speed-up in the CGP framework depends highly on the choice of Poisson solver. We can also see that the accuracy of the results are independent of the choice of Poisson solver. For the rest of our analysis, we will use an optimal FFT-FPS except for in the distorted grid problem, where there are mixed derivatives in the corresponding Poisson equation in curvilinear coordinates. In that case, we use a V-cycle multigrid solver.

It can be seen from the results presented in Table 2.2 and Table 2.3 that second-order accurate results are obtained in practice for both of the CGP formulations. For example,

from Table 2.2, the slope of the maximum infinity norm and the averaged L_2 norm are:

$$n_\infty = \frac{ln\left(\frac{||\omega||_\infty^{512^2}}{||\omega||_\infty^{256^2}}\right)}{ln(\frac{h}{2h})} = 1.9999, \quad n_{L_2} = \frac{ln\left(\frac{||\omega||_{L_2}^{512^2}}{||\omega||_{L_2}^{256^2}}\right)}{ln(\frac{h}{2h})} = 2.0028. \tag{2.54}$$

The spatial convergence properties of the standard RK3 methods and the CGPRK3 methods for both the vorticity-stream function and primitive variable formulations are also illustrated in Figure 2.2 by showing that a single level of coarsening strategy produces a similar convergence rate. A linear reduction rate is obtained with the slope of all curves being 2, verifying the second-order spatial scheme. It can be seen that there is a slight increase in the error norms for the low resolution computations in the fractional step primitive variable formulation. This can be attributed to a small projection error in the fractional step procedure, showing that the CGP is also somewhat solver dependent. We demonstrate, however, that there is a significant benefit to using the CGP method in both formulations.

The Taylor-Green vortex problem is one of the simplest incompressible flow test cases, having a smooth decaying field. We solve it to be able to perform an exact error analysis by comparing our results to the analytical solution of the problem. In the following sections, the CGP method is applied to more challenging flow problems.

2.4.2 Double shear layer

The double shear layer problem was introduced by Bell et al. (1989) to test the performance of a projection method, and studied later by Minion and Brown (1997) using various schemes to determine the effects of the grid resolution on solutions of the unsteady, incompressible Navier-Stokes equations. It is a benchmark problem for testing the accuracy and resolution of a time dependent numerical method. The double shear layer problem with periodic boundary conditions in a square domain $[0, 2\pi] \times [0, 2\pi]$ is subjected to the following initial conditions

Yanwen et al. (1999):

$$u(x,y,0) = \begin{cases} \tanh[\sigma(y-\frac{\pi}{2})] & \text{if} \quad y \leq \pi \\ \tanh[\sigma(\frac{3\pi}{2}-y)] & \text{if} \quad y > \pi \end{cases} \tag{2.55}$$

$$v(x,y,0) = \delta \sin(x) \tag{2.56}$$

where the constants σ and δ determine the thickness of the shear layer and the amplitude of the initial perturbation, respectively. The initial vorticity field to be evolved using the vorticity-stream function formulation algorithm can easily be obtained analytically from the expressions above:

$$\omega(x,y,0) = \begin{cases} \delta \cos(x) - \sigma \cosh^{-2}[\sigma(y-\frac{\pi}{2})] & \text{if} \quad y \leq \pi \\ \delta \cos(x) + \sigma \cosh^{-2}[\sigma(\frac{3\pi}{2}-y)] & \text{if} \quad y > \pi \end{cases} \tag{2.57}$$

In our computations, the thickness parameter is $\sigma = 15/\pi$, the perturbation amplitude is $\delta = 0.05$, the Reynolds number is $Re = 10^4$, and the time step is $\Delta t = 10^{-3}$. The perturbed shear layer rolls up into a single vortex and the shear layers become thinner and thinner as the flow evolves in time as shown in Figure 2.3.

Vorticity contours at $t = 10$ obtained using the vorticity-stream function formulation with and without the CGP method are shown in Figure 2.4 for different spatial resolutions. These results demonstrate that high fidelity numerical simulations can be obtained using the CGP method. For example, if we consider two numerical experiments with 512^2:512^2 and 512^2:256^2 resolutions, they have almost the same resulting vorticity field, but the latter results (with a half-coarsened grid for the Poisson equation) were obtained almost 3 times faster than the former results (without CGP), and more importantly, the resulting field obtained using the CGP method with the 512^2:256^2 resolution are better than those obtained on the 256^2:256^2 grid without the CGP method. These results demonstrate that the CGP methodology can provide an accelerated method for solving flow problems with strong shear components.

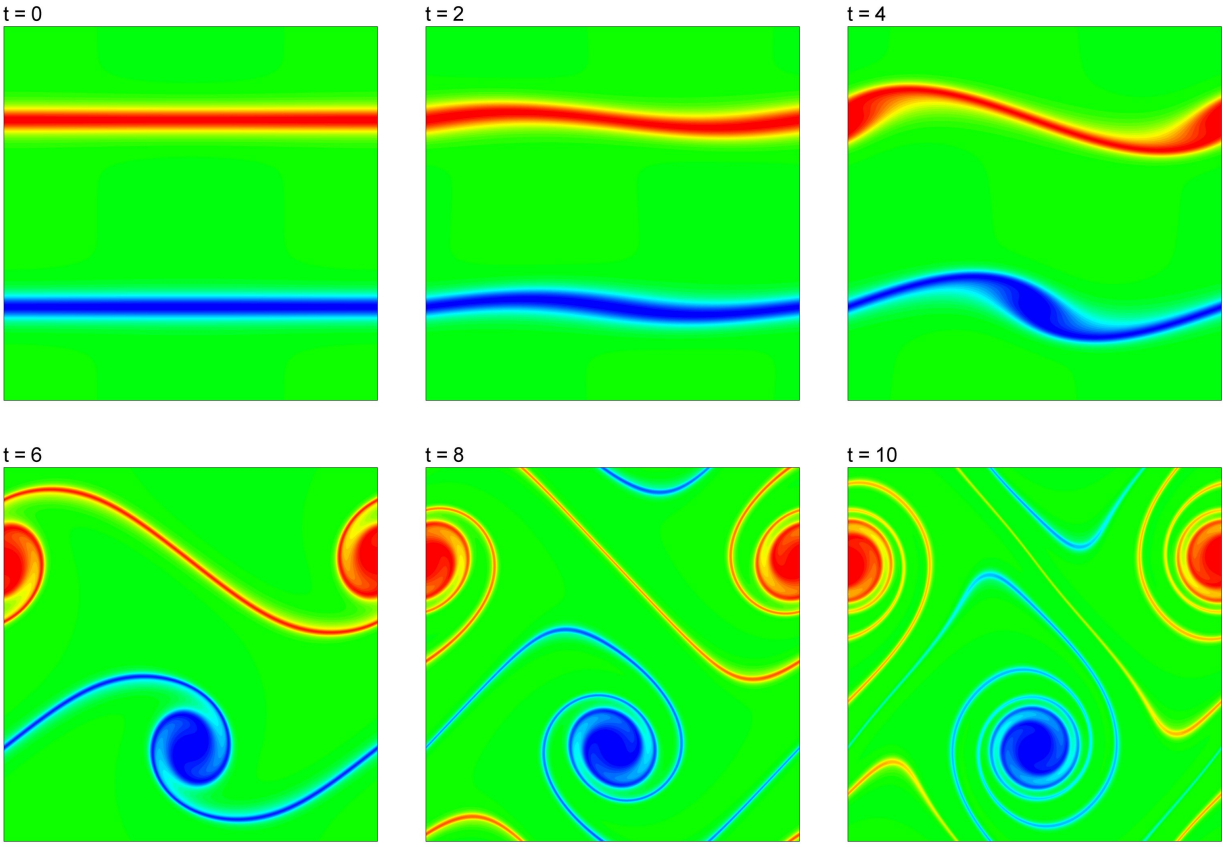

Figure 2.3: The vorticity field at different times obtained by the CGPRK3 method on $1024^2 : 512^2$ resolution grids.

The CPU times and the relative percentages for the main operational subroutines are tabulated in Table 2.4. Although we use one of the fastest (linear-cost) Poisson solver in our computations, these statistics clearly show that the computational cost of the elliptic part of the problem is significantly more expensive than that of the advection-diffusion part. The data presented in Table 2.4 also demonstrates that the computational speed-up increases with increasing spatial resolution. One consequence of this is that the CGP method should be a good candidate for accelerating complex three-dimensional turbulent flow simulations. And it should be able to accelerate direct numerical simulations (DNS) of turbulence by coarsening the number of grid points for the Poisson solver without affecting the well resolved DNS data, a topic we intend to investigate in a future study.

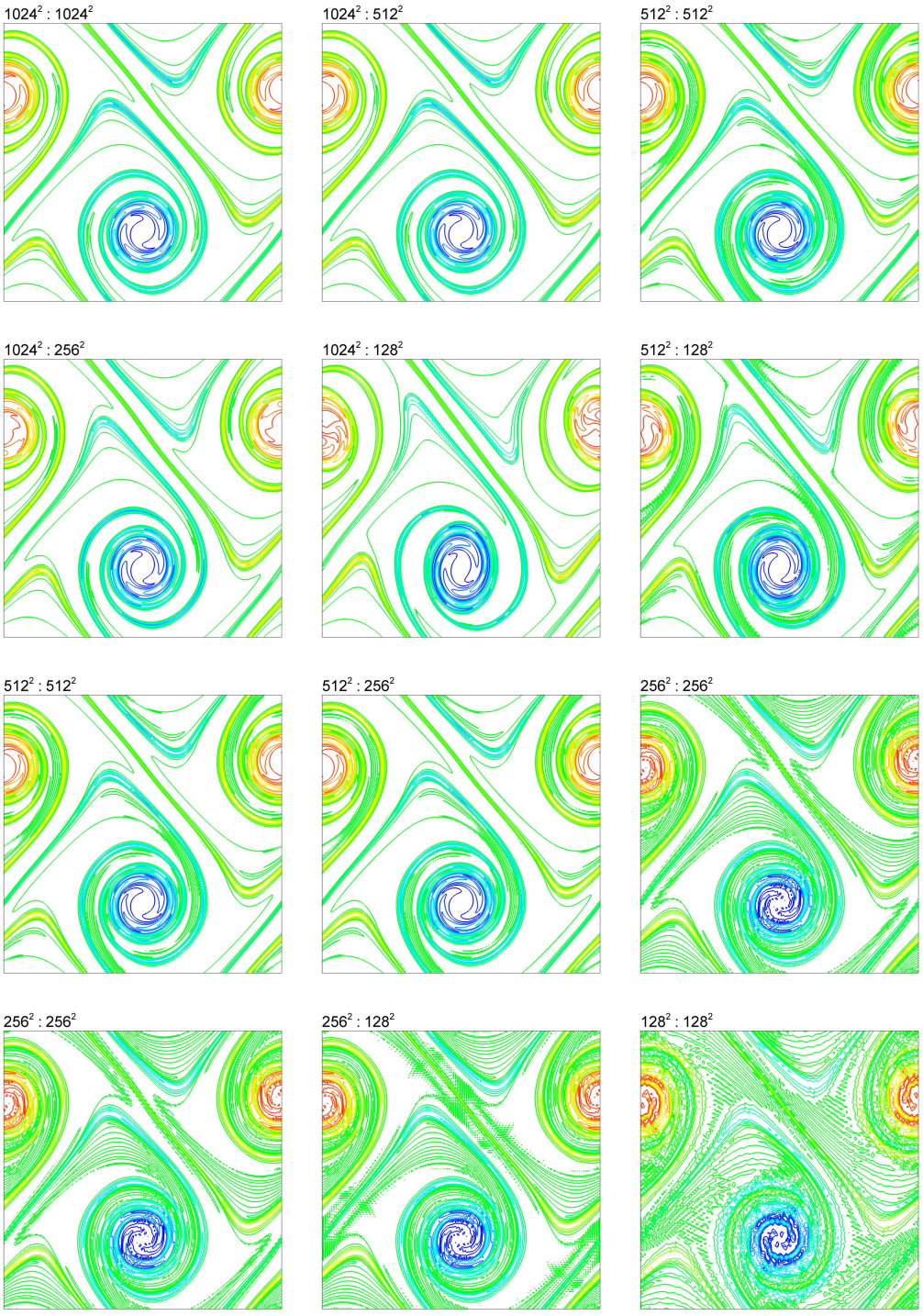

Figure 2.4: The vorticity fields for the double shear layer problem at $t = 10$ obtained using the vorticity-stream function formulation. Labels shows the resolutions for both parts of the solver in the form $N^2 : M^2$, where N^2 is the resolution for the vorticity-transport equation, and M^2 is the resolution for the Poisson equation.

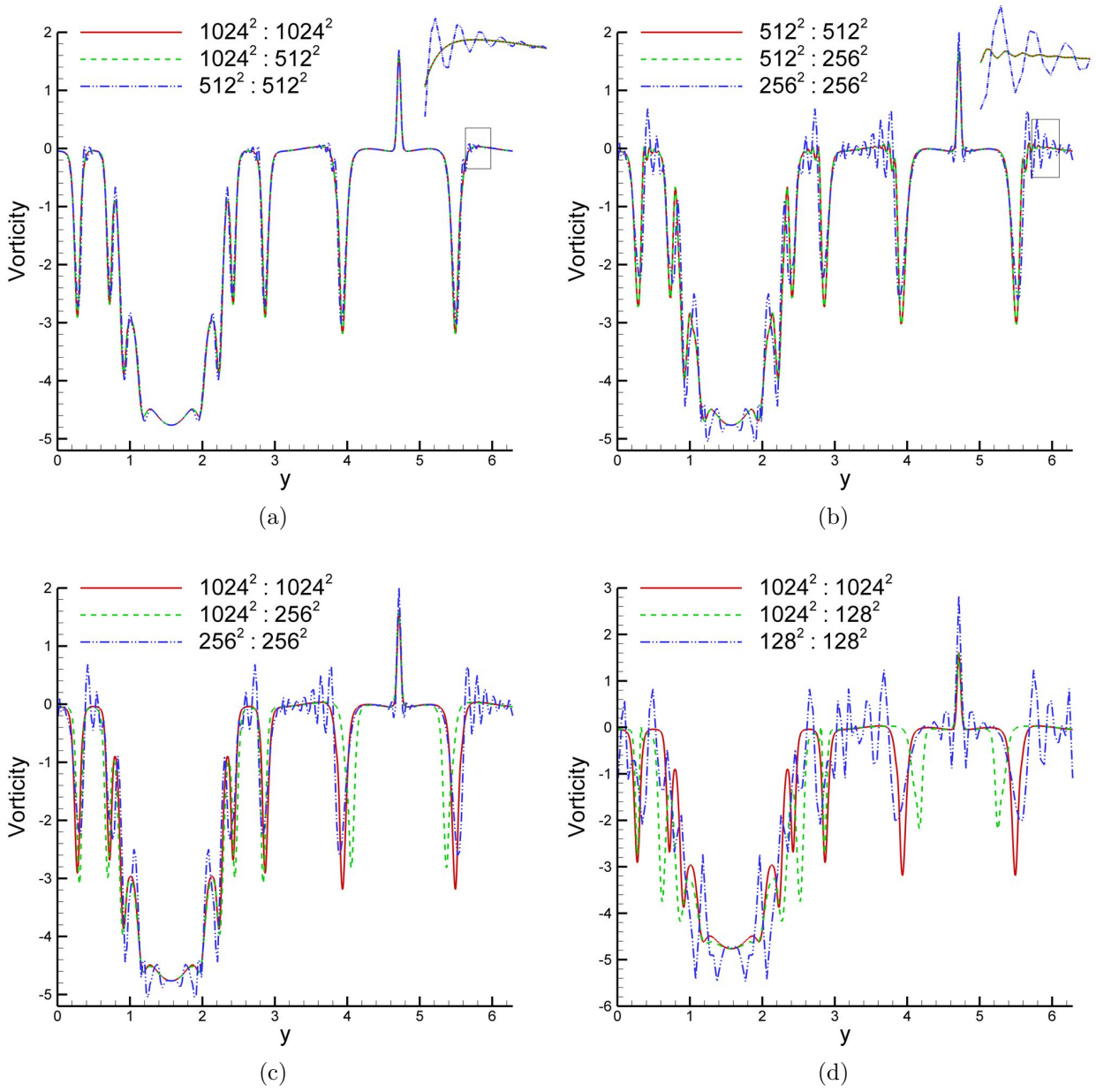

Figure 2.5: Centerline vorticity distributions for the double shear layer problem at $t = 10$ obtained using the vorticity-stream function formulation; (a) comparison for one level coarsening including the standard computation (RK3) on $1024^2 : 1024^2$ resolution grids, the CGPRK3 method on $1024^2 : 512^2$ resolution grids, and the standard computation (RK3) on $512^2 : 512^2$ resolution grids, (b) comparison for one level coarsening including the standard computation (RK3) on $512^2 : 512^2$ resolution grids, the CGPRK3 method on $512^2 : 256^2$ resolution grids, and the standard computation (RK3) on $256^2 : 256^2$ resolution grids, (c) comparison for two levels of coarsening, and (d) comparison for three levels of coarsening.

Table 2.4: Total CPU times for the double shear layer problem and their component percentages (i.e., percent CPU times for the advection-diffusion part, the Poisson part, and the mappings between these two parts) for the CGP and standard algorithms for various resolutions.

Method	Resolutions	% Adv-Dif	% Poisson	% Map	CPU (hr)
RK3 ($\ell = 0$)	$1024^2 : 1024^2$	6.8	93.2	-	10.24
CGPRK3 ($\ell = 1$)	$1024^2 : 512^2$	29.9	64.2	5.9	2.40
CGPRK3 ($\ell = 2$)	$1024^2 : 256^2$	26.0	59.5	14.6	1.26
CGPRK3 ($\ell = 3$)	$1024^2 : 128^2$	74.1	6.8	19.1	1.02
RK3 ($\ell = 0$)	$512^2 : 512^2$	10.1	89.9	-	1.74
CGPRK3 ($\ell = 1$)	$512^2 : 256^2$	33.8	59.6	6.6	0.53
CGPRK3 ($\ell = 2$)	$512^2 : 128^2$	61.9	22.8	15.3	0.29
RK3 ($\ell = 0$)	$256^2 : 256^2$	12.5	87.5	-	0.36

The centerline vorticity distributions along the y-axis at $t = 10$ obtained using the vorticity-stream function formulation with and without the CGP method are shown in Figure 2.5 for different resolutions. It can be seen clearly from the figure that we obtain the fine resolution data at a reduced computational cost using the CGP coarsening strategy, and that this data is significantly better than that obtained via the wholly coarse computation. Both Figure 2.5(a) and Figure 2.5(b) demonstrate that the one level of coarsening CGP method obtains the fine resolution computational results, but uses less computational time. This is especially true for well resolved computations. In fact, data from less well resolved simulations, as shown in Figure 2.4, for example, demonstrate that one level of coarsening does increase the error, although there is still a significant benefit to using the CGP approach in that case. This shear layer problem is particularly important in that the presence of the thinner and thinner shear layers as the flow field evolves in time is not captured by low grid resolution representations.

The Gibbs phenomenon, numerical oscillations occurring near sharp vorticity gradients, occurs for under-resolved simulations in which the grid size is larger than the shear layer

thickness. For example, if we look at the results obtained with a 512^2 resolution (at a relatively high Reynolds number), it can clearly be seen that this resolution is not high enough to capture the correct physics without numerical oscillations. To be able to obtain all the small-scale physical layers, a resolution of at least 1024^2 needs to be used (using a spatially second-order accurate scheme for the underlying equations). Here, we demonstrate that we can obtain the properly-resolved physical behavior at the computational price of under-resolved simulations. Interestingly, however, coarsening the Poisson equation using the CGP method appears to eliminate the Gibbs phenomenon, and produces a similar accuracy to the finest resolved scale simulation for one level of coarsening, while accelerating the simulation with a linear reduction in computational cost. The savings are linear because a fast Poisson solver is used in the algorithm. As shown in the previous problem, the savings would be greater if a suboptimal Poisson solver were used. It should also be noted that no Gibbs phenomenon appears for further levels of coarsening, as is shown in Figure 2.5(c) for two levels of coarsening, and in Figure 2.5(d) for three levels of coarsening. This can be understood by considering the spatial and temporal discretization of the advection-diffusion part as a low-pass filter over the grid, and the Poisson solver as a pre-filtering process. It is possible that the real-frequency limit of the advection-diffusion part is lower than the grid resolution and that the CGP method is acting as a low-pass pre-filter. Accordingly, this study demonstrates that the numerical oscillations that occur in under-resolved simulations with strong shear layers can be eliminated efficiently by using the CGP method.

Similarly, Figure 2.6 shows the vorticity field data obtained using the primitive variable fractional step method. The corresponding centerline vorticity distributions are plotted in Figure 2.7. The vorticity field data is obtained via a postprocessing procedure at the desired times. Similar speed-up is observed upon performing the CGP strategy as for the primitive variable formulation case. The results also illustrate that the CGP method provides very similar data to the full fine scale simulations for the case of primitive variable fractional step formulation. If we compare the vorticity-stream function formulation and the primitive variable formulation by looking at Figure 2.4 and Figure 2.6 for vorticity field plots and

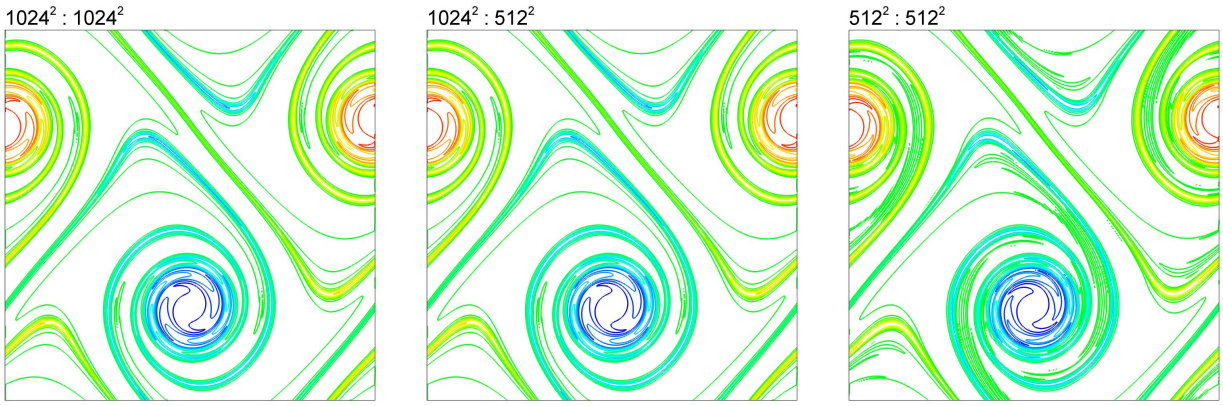

Figure 2.6: The double shear layer problem vorticity fields at $t = 10$ obtained using the primitive variable fractional step formulation (CGPRK3-PV) showing the standard computation on $1024^2 : 1024^2$ resolution grids, the CGP method on $1024^2 : 512^2$ resolution grids, and the standard computation on $512^2 : 512^2$ resolution grids.

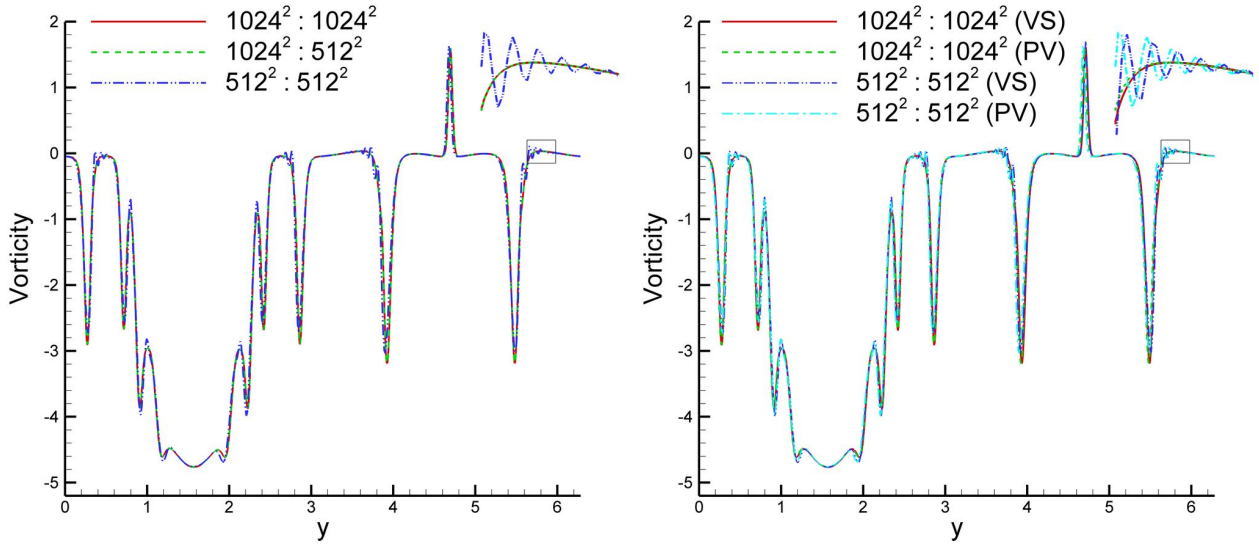

(a) (b)

Figure 2.7: Centerline vorticity distributions at $t = 10$ for the double shear layer problem: (a) Results obtained using the primitive variable fractional step formulation (CGPRK3-PV) showing a comparison of the standard computation on $1024^2 : 1024^2$ resolution grids, the CGP method on $1024^2 : 512^2$ resolution grids, and the standard computation on $512^2 : 512^2$ resolution grids. (b) Comparison of the primitive variable (PV) formulation and the vorticity-stream function (VS) formulation.

by looking at Figure 2.7 for centerline vorticity comparisons, we see that the vorticity-stream function formulation provides slightly more accurate data than the primitive variable formulation, mainly because of a small projection error in the fractional step procedure.

2.4.3 Co-rotating vortex pair

In this section, the CGP method is applied to the problem of a merging, co-rotating vortex pair (Buntine and Pullin, 1989; Von Hardenberg et al., 2000). The superposition of two Gaussian-distributed vortices gives the following initial vorticity field:

$$\omega(x, y, 0) = \Gamma_1 e^{-\rho[(x-x_1)^2+(y-y_1)^2]} + \Gamma_2 e^{-\rho[(x-x_2)^2+(y-y_2)^2]} \tag{2.58}$$

where, for our computations, the vortices have the same circulation $\Gamma_1 = \Gamma_2 = 1$, the interacting constant is set to $\rho = \pi$, and the vortex centers are initially located near each other with coordinates $(x_1, y_1) = (3\pi/4, \pi)$ and $(x_2, y_2) = (5\pi/4, \pi)$. A box of side length 2π is used as the computational domain, and computations are carried out for a Reynolds number of $Re = 10^4$ and a time step of $\Delta t = 10^{-3}$, with periodic boundary conditions. As is illustrated in Figure 2.8, as time evolves, the exterior strain field from each vortex deforms the vorticity field of the other vortex so that the vorticity fields wrap around each other.

Vorticity field contours at time $t = 50$ obtained using the CGP method are plotted in Figure 2.9 along with the regular fine and coarse computations. As in the double shear layer problem, the labels show the resolutions in the form of $N^2 : M^2$, where N^2 is the resolution for the vorticity-transport equation, and M^2 is the resolution for the Poisson equation. The computed results with one level of coarsening are identically to those from the fine scale computations. Furthermore, results with two and three levels of coarsening also agree well with the fine scale computations. A comparison of accuracy and efficiency is also summarized in Table 2.5. The absolute values of maximum amplitude of the vorticity field and corresponding L_2 norms are given in this table showing the applicability of the

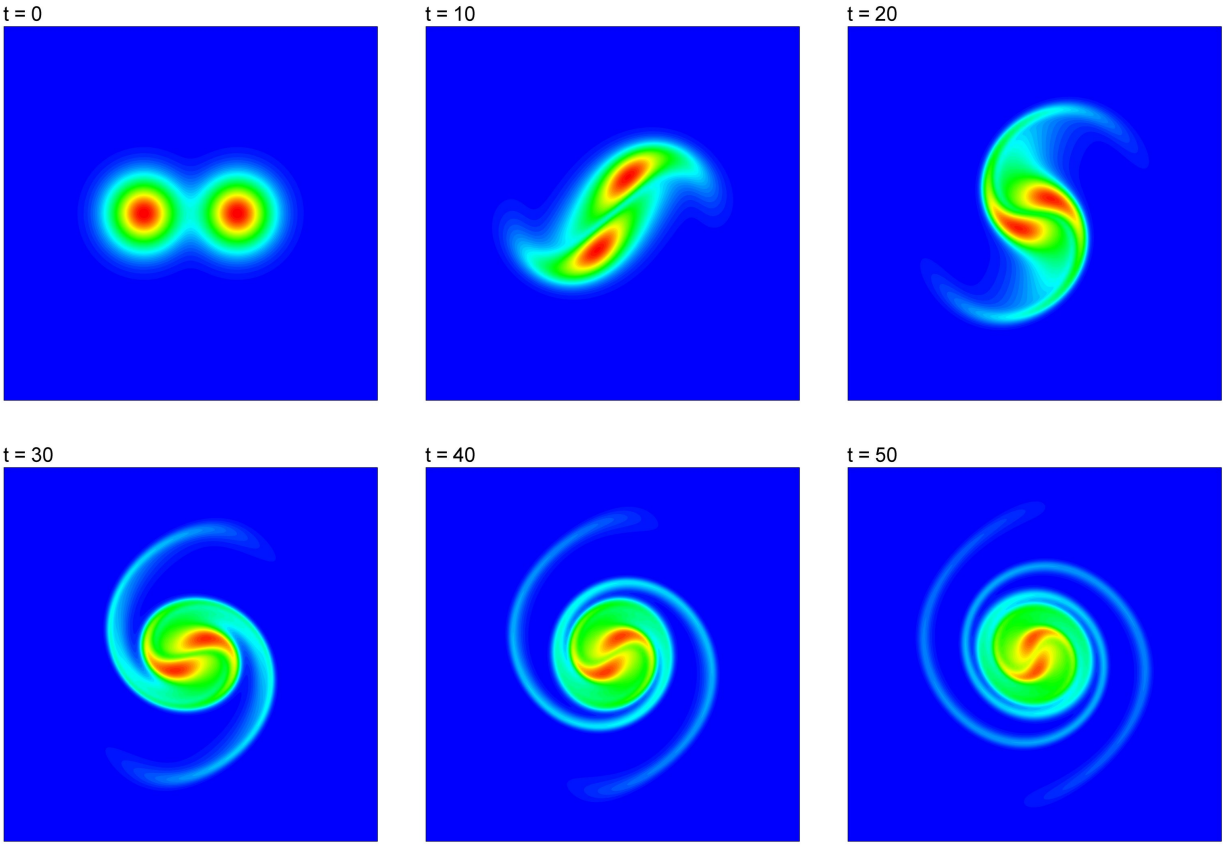

Figure 2.8: Vorticity field at different times obtained using CGPRK3 on $1024^2 : 512^2$ resolution grids.

CGP method. The centerline vorticity distribution along the y-axis at time $t = 50$ is shown in Figure 2.10. These results further demonstrate that both the fine scale simulation and the CGP simulations (including one level, two levels, and three levels of coarsening) provide very similar field data with negligible accuracy loss, but at a reduced computational cost.

2.4.4 Two-dimensional decaying turbulence

Two-dimensional homogenous decaying turbulence is an incompressible flow setting in which energy decays with time and can be thought of as the process of many random vortices merging (Kraichnan, 1967; Batchelor, 1969; Leith, 1971; Brachet et al., 1988). One of the most

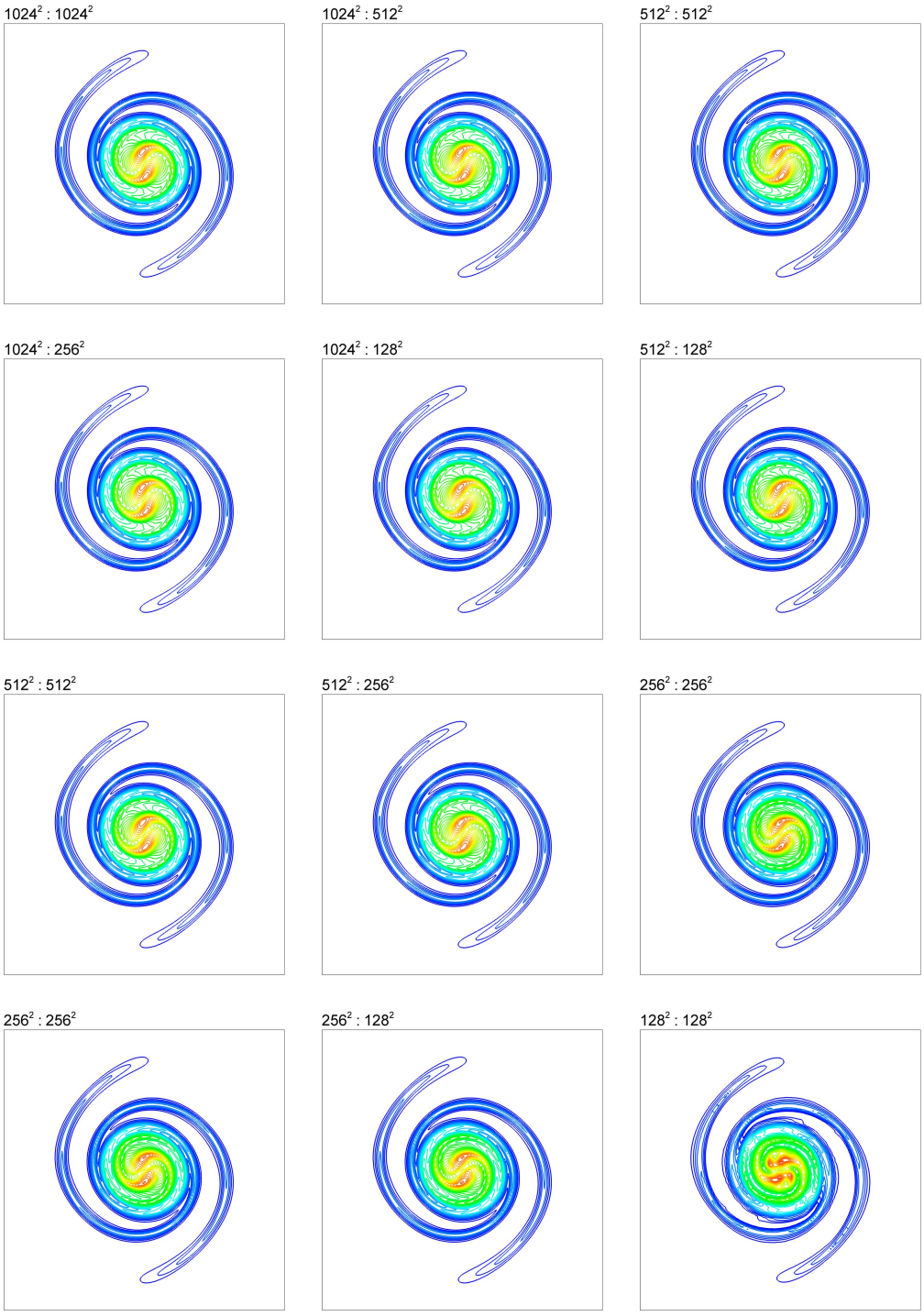

Figure 2.9: The vorticity fields for the merging co-rotating vortex pair problem at $t = 50$ obtained using the vorticity-stream function formulation. Labels show the resolutions for both parts of the solver in the form $N^2 : M^2$, where N^2 is the resolution for the vorticity-transport equation, and M^2 is the resolution for the Poisson equation.

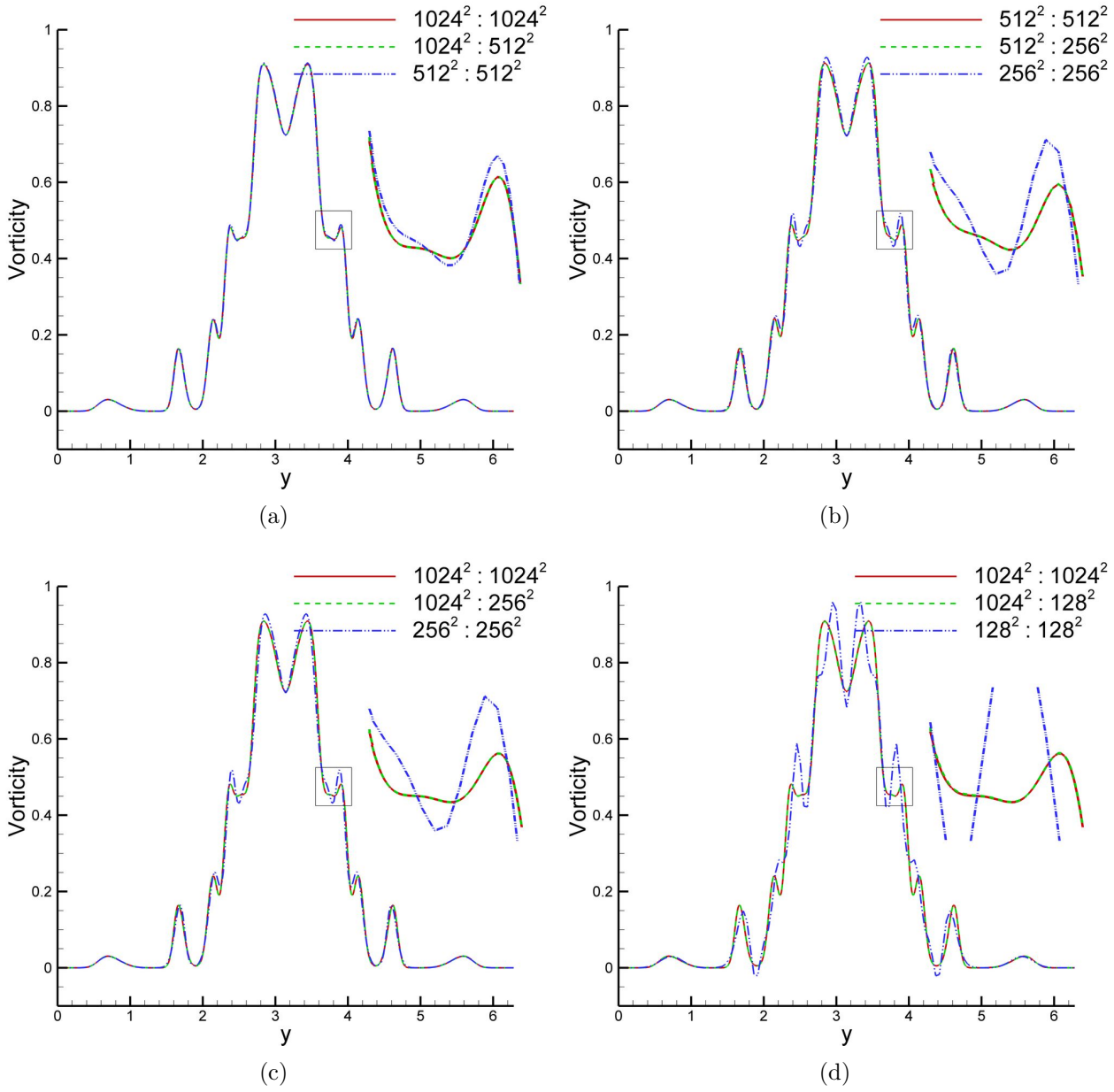

Figure 2.10: Centerline vorticity distributions for the merging co-rotating vortex pair problem at $t = 50$ obtained using the vorticity-stream function formulation; (a) comparison for one level of coarsening including the standard computation (RK3) on $1024^2 : 1024^2$ resolution grids, the CGPRK3 method on $1024^2 : 512^2$ resolution grids, and the standard computation (RK3) on $512^2 : 512^2$ resolution grids, (b) comparison for one level of coarsening including the standard computation (RK3) on $512^2 : 512^2$ resolution grids, the CGPRK3 method on $512^2 : 256^2$ resolution grids, and the standard computation (RK3) on $256^2 : 256^2$ resolution grids, (c) comparison for two levels of coarsening, and (d) comparison for three levels of coarsening.

Table 2.5: Comparison of methods for the co-rotating vortex pair merging problem for $Re = 10^4$ at $t = 50$. L_2 norms are computed with reference to the values obtained on the finest resolution grid.

Method	Resolutions	$\|\omega\|_{max}$	$\|\|\omega\|\|_{L_2}$	CPU (hr)	Speed-up
RK3 ($\ell = 0$)	$1024^2 : 1024^2$	0.9133	-	81.61	1.00
CGPRK3 ($\ell = 1$)	$1024^2 : 512^2$	0.9133	6.7173E-7	18.82	4.34
CGPRK3 ($\ell = 2$)	$1024^2 : 256^2$	0.9132	3.0447E-5	9.68	8.43
CGPRK3 ($\ell = 3$)	$1024^2 : 128^2$	0.9117	1.9605E-4	7.93	10.29
RK3 ($\ell = 0$)	$512^2 : 512^2$	0.9159	1.9975E-3	15.18	1.00
CGPRK3 ($\ell = 1$)	$512^2 : 256^2$	0.9159	1.9993E-3	4.13	3.68
CGPRK3 ($\ell = 2$)	$512^2 : 128^2$	0.9145	2.0611E-3	2.42	6.27
RK3 ($\ell = 0$)	$256^2 : 256^2$	0.9292	9.4755E-3	2.82	1.00
CGPRK3 ($\ell = 1$)	$256^2 : 128^2$	0.9291	9.4997E-3	0.95	2.97
RK3 ($\ell = 0$)	$128^2 : 128^2$	0.9588	2.8086E-2	0.61	1.00

important reasons for studying two-dimensional turbulence is to improve our understanding of geophysical flows in the atmosphere and ocean (Herring et al., 1974; Boer and Shepherd, 1983; McWilliams, 1984; San et al., 2011). Recent reviews on two-dimensional turbulence have been provided by Tabeling (2002) and Boffetta and Ecke (2012). This system has an inertial (intermediate wave number) range in the energy spectrum that is proportional to k^α, where $\alpha = 3$ and k is the wave number, in the inviscid limit according to Kraichnan's theory of two-dimensional turbulence (Kraichnan, 1967). The computational domain we use to solve this problem is a square box whose edge has a length of 2π. Periodic boundary conditions are used. The initial energy spectrum in Fourier space is given by Ishiko et al. (2009):

$$E(k) = \frac{a_s}{2}\frac{1}{k_p}\left(\frac{k}{k_p}\right)^{2s+1} \exp\left[-\left(s+\frac{1}{2}\right)\left(\frac{k}{k_p}\right)^2\right] \tag{2.59}$$

where $k = |\mathbf{k}| = \sqrt{k_x^2 + k_y^2}$. The maximum value of the initial energy spectrum occurs at a wavenumber of k_p. We use $k_p = 12$ in this study. The coefficient a_s normalizes the initial

kinetic energy and is given by:

$$a_s = \frac{(2s+1)^{s+1}}{2^s s!} \tag{2.60}$$

where s is a shape parameter. In this study, we take $s = 3$. The magnitude of the vorticity Fourier coefficients related to the assumed energy spectrum becomes:

$$|\tilde{\omega}(\mathbf{k})| = \sqrt{\frac{k}{\pi} E(k)} \tag{2.61}$$

and the initial vorticity distribution in Fourier space is then obtained by introducing a random phase:

$$\tilde{\omega}(\mathbf{k}) = \sqrt{\frac{k}{\pi} E(k)} \;\; e^{i\zeta(\mathbf{k})} \tag{2.62}$$

where the phase function is given by $\zeta(\mathbf{k}) = \xi(\mathbf{k}) + \eta(\mathbf{k})$, where $\xi(\mathbf{k})$ and $\eta(\mathbf{k})$ are independent random values chosen in $[0, 2\pi]$ at each coordinate point in the first quadrant of the k_x-k_y plane. Following Ishiko et al. (2009), the conjugate relations for other quadrants are:

$$\begin{aligned}
\xi(-k_x, k_y) &= -\xi(k_x, k_y) \\
\xi(-k_x, -k_y) &= -\xi(k_x, k_y) \\
\xi(k_x, -k_y) &= \xi(k_x, k_y) \\
\eta(-k_x, k_y) &= \eta(k_x, k_y) \\
\eta(-k_x, -k_y) &= -\eta(k_x, k_y) \\
\eta(k_x, -k_y) &= -\eta(k_x, k_y).
\end{aligned} \tag{2.63}$$

After the randomization process described above for the phases, the initial vorticity field in physical space is obtained by performing an inverse FFT. The resulting initial vorticity field contour plot is illustrated in Figure 2.11(a).

In this section, first, two different flow field with Reynolds numbers $Re = 250$ and $Re = 500$ are computed using the CGP method and compared to results using the standard

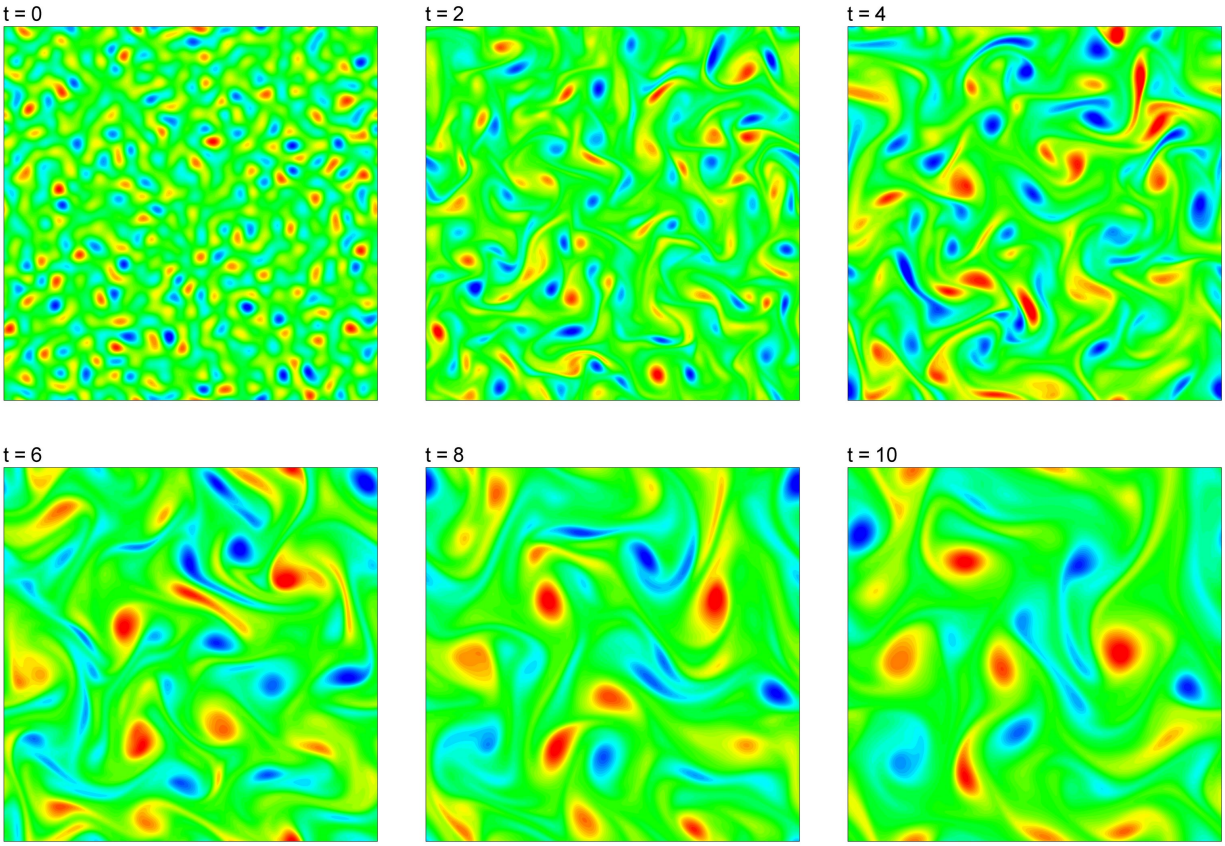

Figure 2.11: The vorticity field at different times for two-dimensional decaying turbulence obtained using the CGP method on $1024^2 : 512^2$ resolution grids for $Re = 500$.

method without the CGP methodology. The time step is chosen to be $\Delta t = 2 \times 10^{-4}$, which leads to a solution that is well resolved in time. The numerical experiments are performed until a final time of $t = 10$, and the resulting vorticity contour plots are shown in Figure 2.11 for $Re = 500$.

Figure 2.12 shows vorticity contours obtained using the CGP method as well as standard fine and coarse scale computations for $Re = 250$. The first resolution number in the legend corresponds to the grid resolution for computing the advection-diffusion part of the problem, and the second one corresponds to the grid resolution for the Poisson equation. We chose this Reynolds number in particular to show the effect of the cell Reynolds number, defined

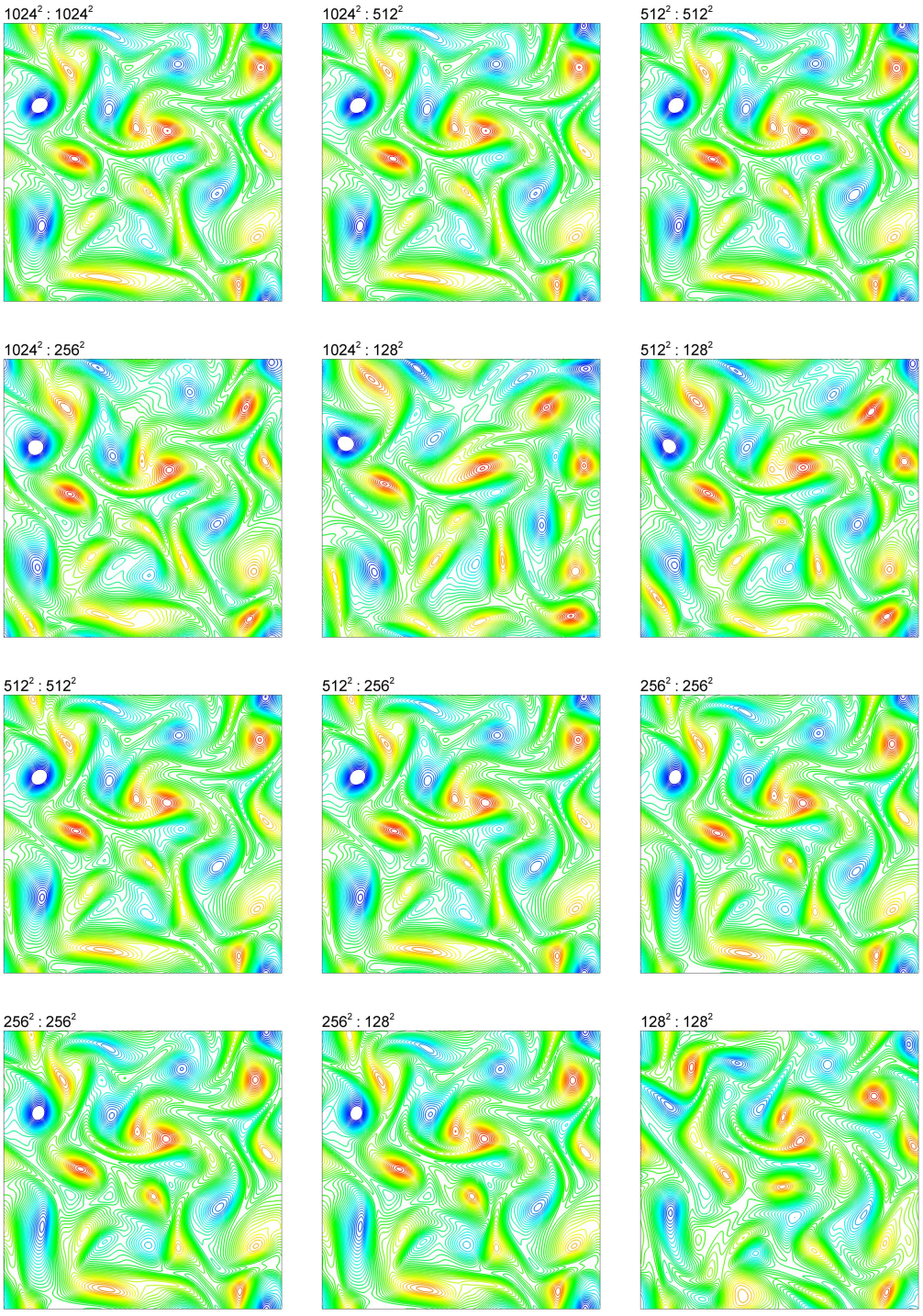

Figure 2.12: Vorticity fields for the decaying turbulence problem at $t = 10$ obtained using the vorticity-stream function formulation for $Re = 250$. Labels show the resolutions for both parts of the solver in the form $N^2 : M^2$, where N^2 is the resolution for the vorticity-transport equation, and M^2 is the resolution for the Poisson equation. The same equidistant contour levels are used in all cases.

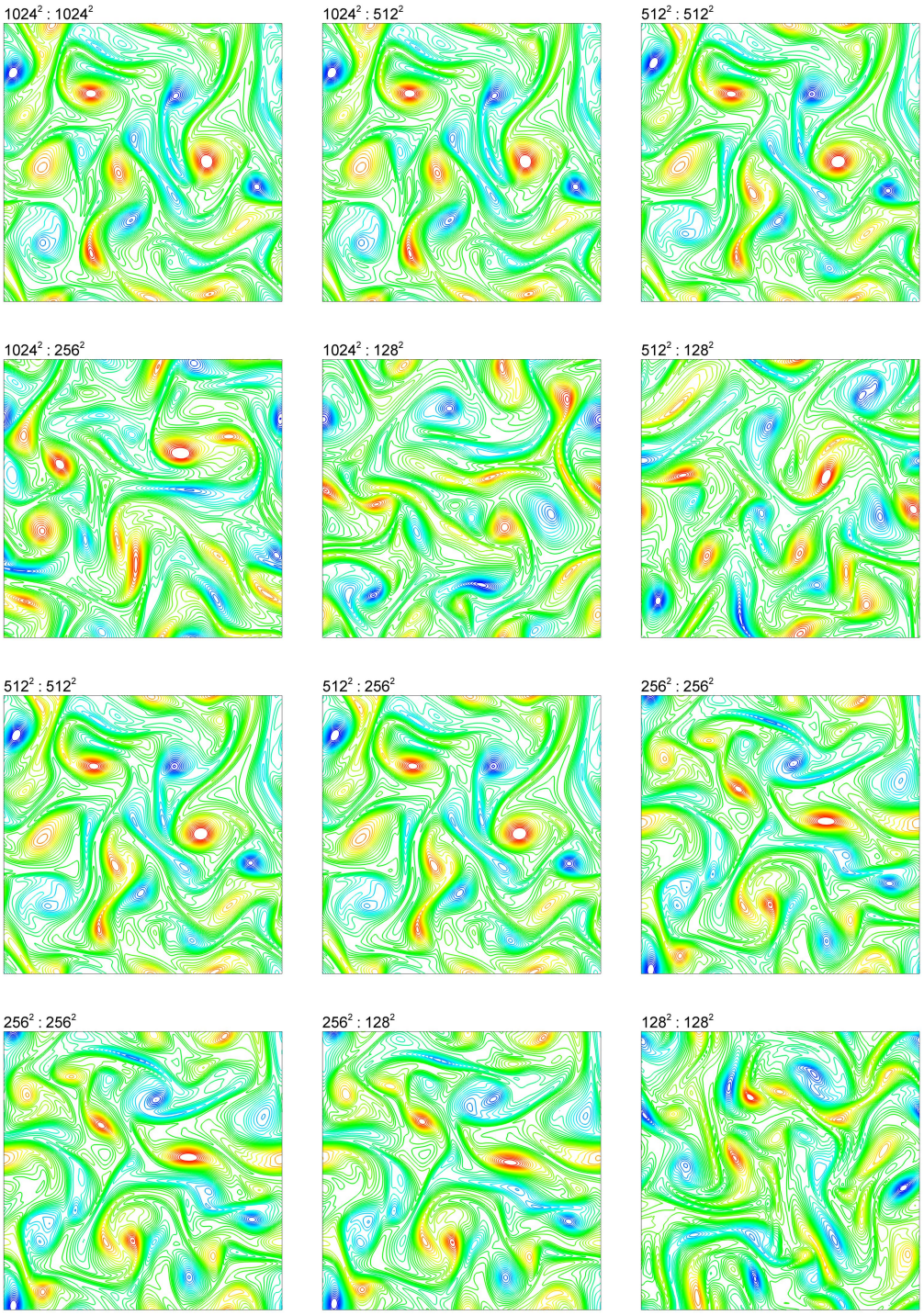

Figure 2.13: Vorticity fields for the decaying turbulence problem at $t = 10$ obtained using the vorticity-stream function formulation for $Re = 500$. Labels show the resolutions for both parts of the solver in the form $N^2 : M^2$, where N^2 is the resolution for the vorticity-transport equation, and M^2 is the resolution for the Poisson equation. The same equidistant contour levels are used in all cases.

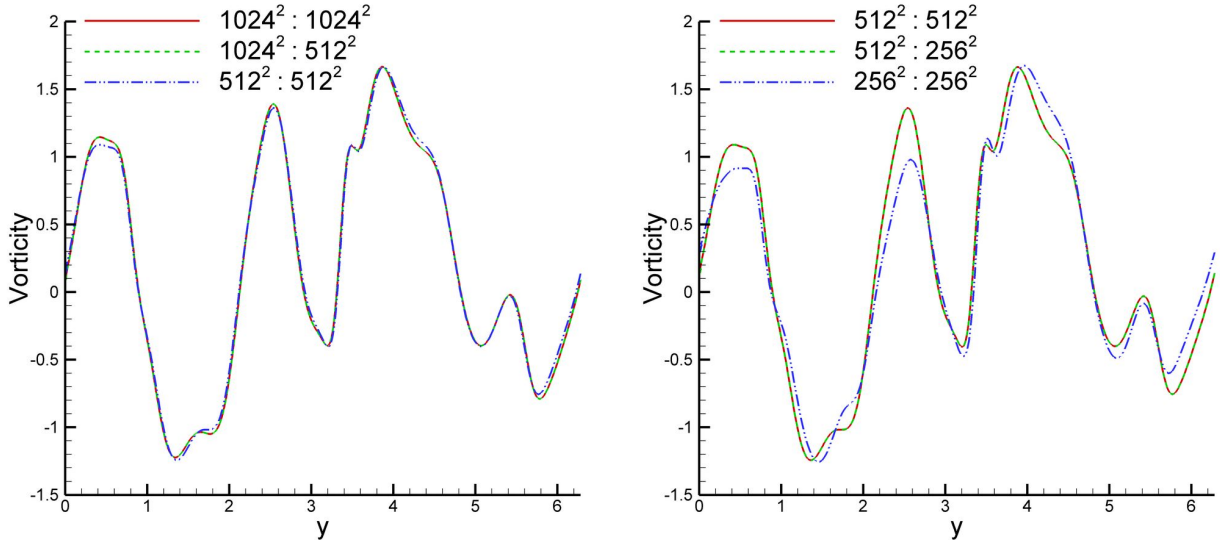

(a) (b)

Figure 2.14: Centerline vorticity distributions for the two-dimensional decaying turbulence problem at $t = 10$ for $Re = 250$; (a) comparison for the standard computation (RK3) on $1024^2 : 1024^2$ resolution grids, the CGPRK3 method on $1024^2 : 512^2$ resolution grids, and the standard computation (RK3) on $512^2 : 512^2$ resolution grids, (b) comparison for the standard computation (RK3) on $512^2 : 512^2$ resolution grids, the CGPRK3 method on $512^2 : 256^2$ resolution grids, and the standard computation (RK3) on $256^2 : 256^2$ resolution grids.

as:

$$Re_{cell} = Re\frac{2\pi}{N_x} \tag{2.64}$$

where $N_x = N_y$ is the grid resolution along one direction. Re_{cell} should be smaller than 2 in order to accurately capture viscous effects for a particular resolution. For $Re = 250$, the cell Reynolds numbers are 1.53 and 3.07 for resolutions of 1024^2 and 512^2, respectively. Since the cell Reynolds numbers are smaller than 2, both the fine and coarse simulations produce similar results (i.e., grid independent solutions). The CGP method provides data identical with that of the pure fine scale simulations.

Similar comparisons are made for $Re = 500$ in Figure 2.13. The cell Reynolds numbers are now 3.07 and 6.14 for resolutions of 1024^2 and 512^2, respectively. The results of the CGP and the fine resolution computations are very close and highly superior to those from the

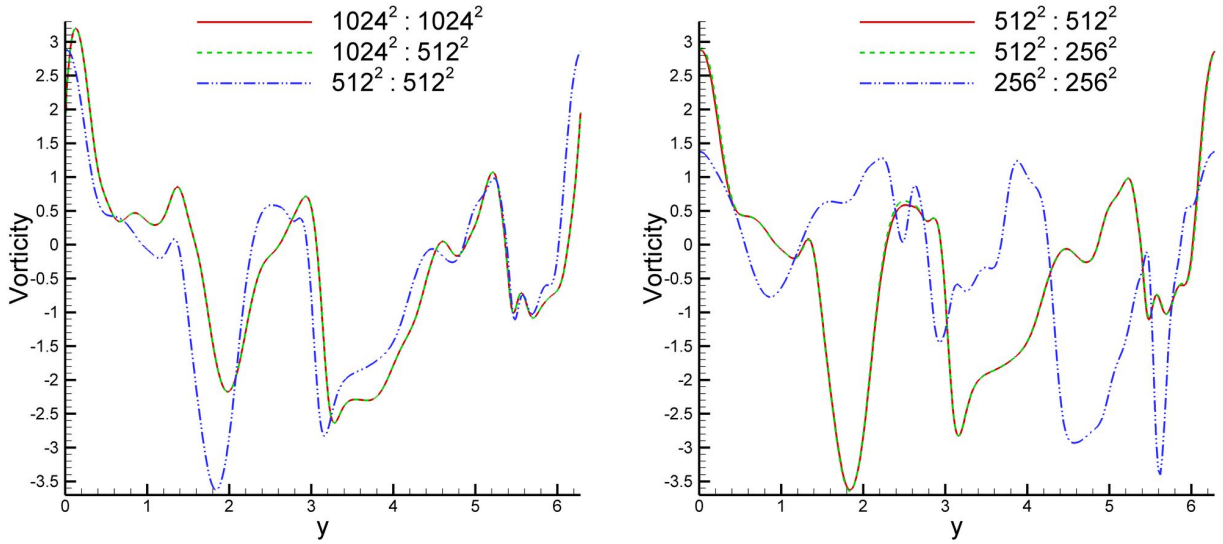

(a) (b)

Figure 2.15: Centerline vorticity distributions for the two-dimensional decaying turbulence problem at $t = 10$ for $Re = 500$; (a) comparison for the standard computation (RK3) on $1024^2 : 1024^2$ resolution grids, the CGPRK3 method on $1024^2 : 512^2$ resolution grids, and the standard computation (RK3) on $512^2 : 512^2$ resolution grids, (b) comparison for the standard computation (RK3) on $512^2 : 512^2$ resolution grids, the CGPRK3 method on $512^2 : 256^2$ resolution grids, and the standard computation (RK3) on $256^2 : 256^2$ resolution grids.

coarse resolution computation. The CGP method captures the same flow details as the fine scale simulation at a lower computational price when we use one level of coarsening. We see that the accuracy of the CGP method also depends on the resolution. For well resolved cases, the difference between the standard fine resolution computation and the coarse-grid projection computation is negligible, although the error is not that small for lower resolution cases. However, there is still strong benefit to using the coarse-grid projection approach due to the significant improvement of the accuracy of the results compared to the standard low resolution computations. The total computational times for these simulations are: 87.4 hr for the standard computation on a fine resolution ($1024^2 : 1024^2$) grid, 22.9 hr for the computation using the CGP method on a $1024^2 : 512^2$ resolution grid, and 13.1 hr for the standard computation on a grid of resolution $512^2 : 512^2$. Vorticity distributions along the vertical centerline at time $t = 10$ for $Re = 250$ and $Re = 500$ are shown in Figure 2.14 and

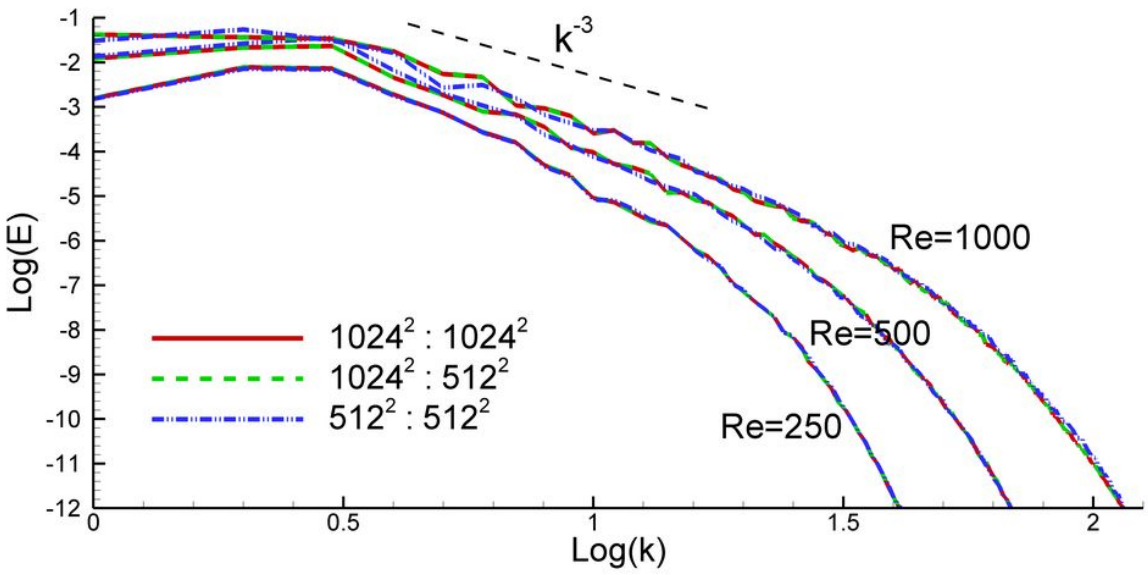

Figure 2.16: Comparisons of the angle averaged energy spectra at time $t = 10$ for different Reynolds numbers obtained by standard computations (RK3) on $1024^2 : 1024^2$ resolution grids, the CGPRK3 method on $1024^2 : 512^2$ resolution grids, and standard computations (RK3) on $512^2 : 512^2$ resolution grids. Angle averaged energy spectra asymptotically approach k^{-3} scaling in the inertial range with increasing Re.

Figure 2.15, respectively. As discussed earlier, the speed up in computations would be even greater if we used a suboptimal Poisson solver in the computations.

Finally, we perform a comparison of turbulence statistics. Figure 2.16 demonstrates the angle averaged energy spectrum for different Reynolds numbers. The energy spectrum is defined as:

$$\hat{E}(\mathbf{k}, t) = \frac{1}{2} k^2 |\tilde{\psi}(\mathbf{k}, t)|^2 \tag{2.65}$$

and the angle averaged energy spectrum is:

$$E(k, t) = \sum_{k \leq |\acute{k}| \leq k+1} \hat{E}(\acute{\mathbf{k}}, t). \tag{2.66}$$

The angle averaged energy spectra obtained by CGP and standard methods are shown in Figure 2.16, and demonstrate that the energy spectra converge to k^{-3} scaling in the inertial

range for increasing Re. Our primary goal in this study is to investigate the behavior of the CGP method in long time integration turbulence simulations. Therefore, we do not perform any further computations at larger Reynolds numbers. This decaying turbulence test case primarily shows that the CGP method can be used to obtain highly accurate simulations of complex flow fields at greatly accelerated rates, with a speed-up factor of 3 obtained for this particular Poisson solver. Again, we expect this gain to be even more pronounced with the choice any other suboptimal Poisson solver.

2.4.5 Taylor-Green vortex on a distorted grid

All the previous test cases were computed on Cartesian grids. Since the method is intended to be generally applicable, we analyze here the performance of the CGP method on a non-Cartesian, randomly distorted grid. Specifically, we perform quantitative error analyzes for the Taylor-Green vortex problem on the distorted grid. The grid distortion is accomplished using a random number generator returning a real number between zero and a defined distortion parameter, τ, at each query. For $\tau = 0$, we obtain a regular Cartesian grid. Figure 2.17 shows the distorted grids with $\tau = 0.1$ and $\tau = 0.2$, that are used in our computations. First we transform the vorticity-stream function formulation of the governing equations to generalized curvilinear coordinates. The metrics and Jacobian are computed again via finite differences (Tannehill et al., 1997). Here, we apply the CGP method to the vorticity-stream function formulation in curvilinear coordinates. We apply the previous full weighting restriction and bilinear prolongation operators before and after solving the elliptic constraint equation to reduce the computational time. Since we transformed our equations to generalized coordinates, it is not at all straightforward to use FFT-based elliptic Poisson solvers for this case. For that reason, we use another linear-cost efficient Poisson solver, the V-cycle multigrid method (Gupta et al., 1997). Both the L_∞ and L_2 norms, are computed according to the exact analytical solution given in Eq. (2.49).

A comparison of the efficiency and accuracy of the CGP method and the other methods

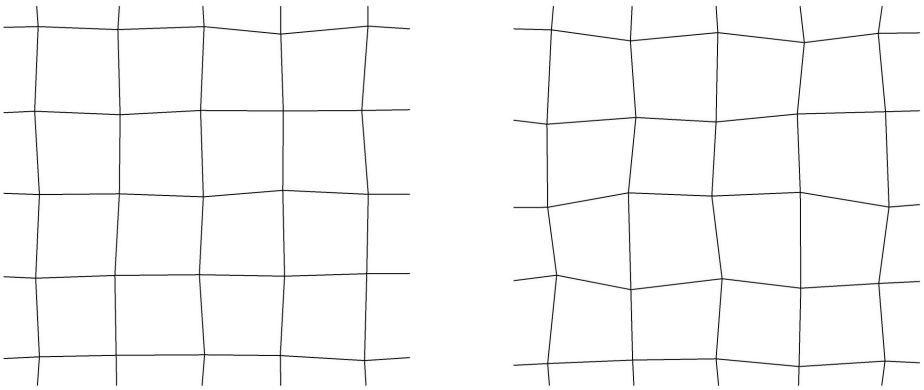

Figure 2.17: Distorted grids for the Taylor-Green vortex problem for distortion parameters $\tau = 0.1$ (left), and $\tau = 0.2$ (right).

is shown in Table 2.6, with three different grid distortion ratios used. These results clearly demonstrate the applicability of the CGP method to problems solved on generalized non-Cartesian grids. As we expect, for no distortion ($\tau = 0$) the results are nearly the same as those found in Table 2.2 and verify that the method is independent of the choice of Poisson solver. The measured CPU times are different due to the different Poisson solver as well as the curvilinear transform, but the speed-up ratios are identical. It can be seen that the errors due to using coarser grids is due mainly due to the restriction and prolongation operators rather than solution of the Poisson equation. Increasing the distortion ratio results an increased CPU times for the simulation. We compare the CPU times obtained by the CGPRK3 algorithm with the results obtained with the regular solver (RK3) for the same resolutions. We find that increasing the distortion ratio results in more and more computational efficiency when using the CGP method. For $\tau = 0.2$ the simulation was 42 times faster when performed with the CGP method, without an accompanying degeneracy in the accuracy of the results.

Table 2.6: Computed error norms for the Taylor-Green vortex problem on distorted grids for $Re = 10$ and $\Delta t = 2.5 \times 10^{-4}$ at time $t = 1$. The first resolution number is the number of grid points used to solve the advection-diffusion equation (vorticity-transport equation), and the second resolution number is that used to solve the Poisson equation (the V-cycle multigrid Poisson solver is used). The speed-up ratio is defined as the ratio of the CPU times for the computations performed without using the CGP procedure (using standard methods) and with the CGP procedure.

Method	Resolutions	$\|\|\omega\|\|_\infty$	$\|\|\omega\|\|_{L_2}$	CPU (s)	Speed-up
RK3 ($\tau = 0$)	$256^2 : 256^2$	1.6439E-5	8.1561E-6	3171.09	1.00
CGPRK3 ($\tau = 0$)	$256^2 : 128^2$	1.6439E-5	8.1568E-6	1234.72	2.56
RK3 ($\tau = 0$)	$128^2 : 128^2$	6.5756E-5	3.3133E-5	1076.88	1.00
CGPRK3 ($\tau = 0$)	$128^2 : 64^2$	6.5757E-5	3.3176E-5	550.73	1.96
RK3 ($\tau = 0.1$)	$256^2 : 256^2$	6.3111E-4	1.1422E-4	9566.87	1.00
CGPRK3 ($\tau = 0.1$)	$256^2 : 128^2$	6.3253E-4	1.2802E-4	1137.14	8.41
RK3 ($\tau = 0.1$)	$128^2 : 128^2$	1.0933E-3	1.8148E-4	1886.91	1.00
CGPRK3 ($\tau = 0.1$)	$128^2 : 64^2$	1.0946E-3	1.9874E-4	482.37	3.91
RK3 ($\tau = 0.2$)	$256^2 : 256^2$	1.4867E-3	3.0031E-4	88109.04	1.00
CGPRK3 ($\tau = 0.2$)	$256^2 : 128^2$	1.4836E-3	3.4331E-4	2080.43	42.35
RK3 ($\tau = 0.2$)	$128^2 : 128^2$	2.4964E-3	4.2399E-4	5642.90	1.00
CGPRK3 ($\tau = 0.2$)	$128^2 : 64^2$	2.4696E-3	5.0689E-4	969.37	5.82

2.4.6 Laminar flow over a circular cylinder

The laminar flow over a cylinder was computed to demonstrate that the coarse-grid projection method also is applicable to external flows. Flow over a cylinder is a fundamental fluid mechanics problem of practical importance. The cylinder is represented in two dimensions by a circle, and a flow domain surrounds the circle, for which we set the outer diameter to be 30 times bigger than the cylinder diameter. The flow field over the cylinder is symmetric at low values of the Reynolds number. As the Reynolds number increases, the flow begins to separate behind the cylinder causing vortex shedding, an unsteady phenomenon. Since we present our results for $Re = 40$ based on the free stream velocity and cylinder diameter, a

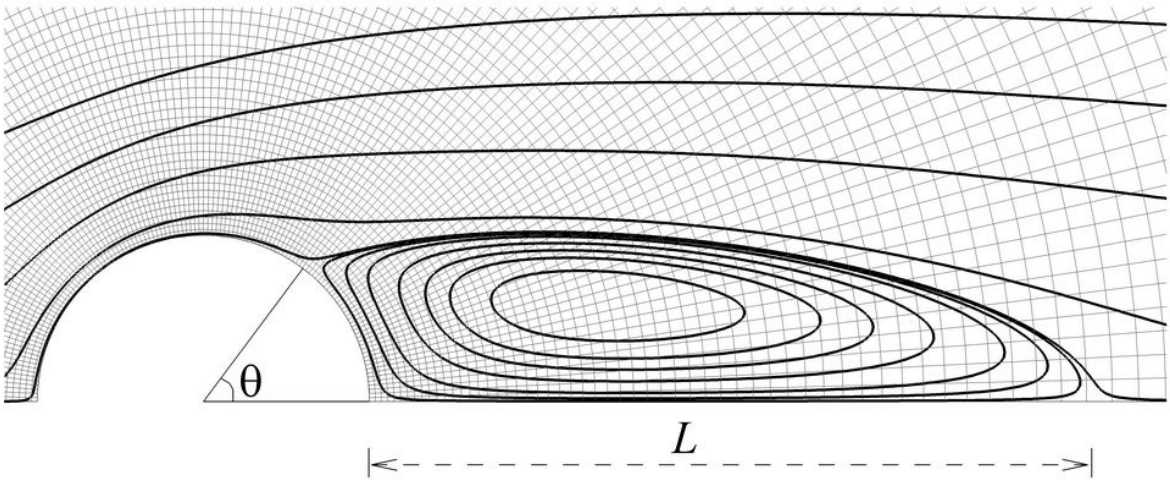

Figure 2.18: Computational mesh for a cylinder with 128 radial and 128 circumferential nodes using the stretching parameter $\beta = 1.04$ with the definitions of separation angle, θ, and separation bubble length, L.

relatively low Reynolds number, we only compute the flow in the upper half of the domain. In this case, a stationary separation bubble forms behind the cylinder and the flow field is symmetric about the x-axis. In order to compare the results with those available in the literature, we have computed the separation bubble length (reattachment length), L, and separation angle, θ, as shown in Figure 2.18. This canonical flow problem has been used as a benchmark case in many computational studies (Choi et al., 2007; Dennis and Chang, 1970; Galbraith and Abdallah, 2011; Linnick and Fasel, 2005; Russell and Wang, 2003).

We used the vorticity-stream function formulation in generalized curvilinear coordinates. The metrics and Jacobian of the transformation were computed analytically according to the following transformation:

$$x = \left(\frac{D-1}{2}\kappa(\eta) + \frac{1}{2}\right)\cos\left(\pi(1-\xi)\right) \tag{2.67}$$

$$y = \left(\frac{D-1}{2}\kappa(\eta) + \frac{1}{2}\right)\sin\left(\pi(1-\xi)\right) \tag{2.68}$$

where D is the outer diameter, and $\kappa(\eta)$ is the logarithmic stretching function, which is given

as (Hoffmann and Chiang, 2000):

$$\kappa(\eta) = \frac{(\beta+1) - (\beta-1)\left(\frac{\beta+1}{\beta-1}\right)^{1-\eta}}{1 + \left(\frac{\beta+1}{\beta-1}\right)^{1-\eta}} \tag{2.69}$$

where β is the stretching parameter. Here, we set $\beta = 1.04$ and $D = 30$. The computational mesh shown in Figure 2.18 consists of an O-grid with 128 radial and 128 circumferential nodes.

As in the Taylor-Green problem on a distorted grid, transforming the physical space (x-y) to a Cartesian computational space (ξ-η) allows one to utilize the coarse-grid projection methodology for the flow around a circular cylinder. The full weighting restriction operator and bilinear interpolation are used for data transfer between the vorticity-transport equation and the elliptic equation in transformed coordinates. Here, we utilize a fast sine transform linear-cost elliptic solver (FFTs in the circumfrential direction and the Thomas algorithm in the radial direction (Moin, 2001)), and obtain a speed up of about 2, as was obtained in the previous cases for one level of coarsening. As in the previous cases, the speed up would be greater if we used other, suboptimal elliptic solvers. Starting with zero initial conditions, we integrated until the flow field reached stationarity and recirculating eddies were obtained. Stream function and vorticity field contours are shown in Figure 2.19 and Figure 2.20, respectively. The various resolutions used in the computations are written in the labels of the subfigures. The labels include the resolution for the advection-diffusion part and the resolution for the elliptic part, as described in the captions. As was the case in previous sections, we compare the CGPRK3 computations with standard RK3 computations. For example, the flow field obtained by a standard computation with $128^2 : 128^2$ agrees well with that obtained by the CGP method with $128^2 : 64^2$, and better than that of the standard computation with $64^2 : 64^2$. Similar observations holds for higher and lower resolution computations as well. It can clearly be seen that the CGP approach provides results at the same level of accuracy, but at a reduced computational cost compared to the

Table 2.7: Separation angle and separation bubble length for a cylinder at $Re = 40$.

Study	θ°	L
Coutanceau and Bouard (1977)	53.5	2.13
Choi et al. (2007)	53.6	2.21
Dennis and Chang (1970)	53.8	2.35
Galbraith and Abdallah (2011)	54.0	2.23
Linnick and Fasel (2005)	53.6	2.28
Russell and Wang (2003)	53.1	2.29
CGPRK3	53.8	2.20

standard, fine resolution simulations, by reducing the resolution of the elliptic sub-problem. According to our findings, as shown in Table 2.7, the separation bubble recirculation length is $L = 2.2$ and the separation angle is $\theta = 53.8$ which agree well with the experimental results of Coutanceau and Bouard (1977), as well as the computational studies presented in Choi et al. (2007); Dennis and Chang (1970); Galbraith and Abdallah (2011); Linnick and Fasel (2005); Russell and Wang (2003).

2.4.7 Three-dimensional Taylor-Green vortex

Here, the coarse-grid projection method is applied to the three-dimensional Taylor-Green vortex flow problem (Taylor and Green, 1937; Brachet et al., 1983), which is perhaps the simplest system in which to study the generation of increasingly smaller scale motions and the resulting turbulence. The fundamental mechanism involved in homogeneous three-dimensional turbulent flows is the enhancement of vorticity by vortex stretching and consequent production of small eddies. Energy is transferred forward in spectral space, from large scales to smaller scales, via the vortex stretching mechanism. This process controls the turbulent energy dynamics and hence the global structure of the evolution of the turbulent flow. A prototype of this process is given by the generalized Taylor-Green vortex problem (Brachet

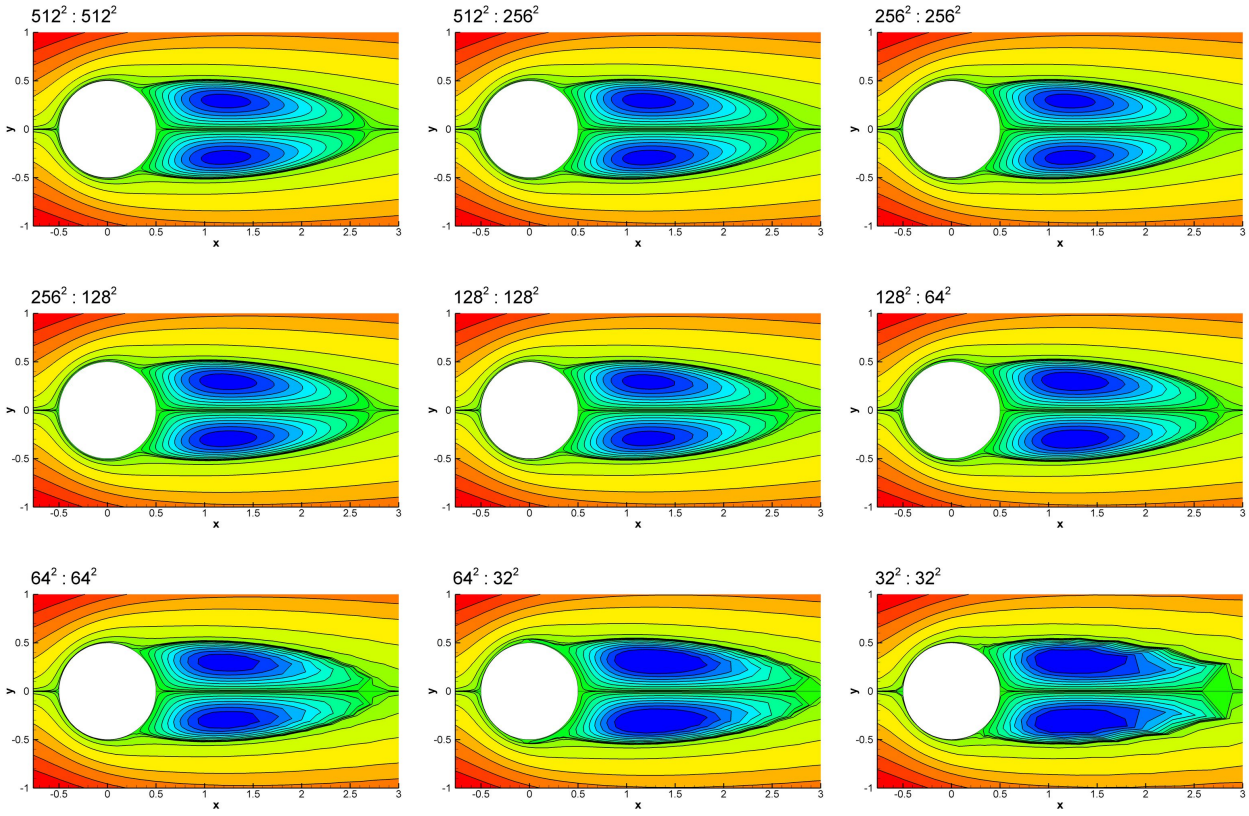

Figure 2.19: Stream function contours for laminar flow over a cylinder at $Re = 40$. Labels include the resolutions for both parts of the solver in the form $N^2 : M^2$, where N^2 is the resolution for the vorticity-transport equation, and M^2 is the resolution for the Poisson equation. The contour interval layouts are identical in all cases.

et al., 1983), which is a three-dimensional flow that develops from the single mode initial condition:

$$u(x, y, z, t = 0) = \frac{2}{\sqrt{3}} \sin\left(\theta + \frac{2\pi}{3}\right) \sin(x)\cos(y)\cos(z) \tag{2.70}$$

$$v(x, y, z, t = 0) = \frac{2}{\sqrt{3}} \sin\left(\theta - \frac{2\pi}{3}\right) \cos(x)\sin(y)\cos(z) \tag{2.71}$$

$$w(x, y, z, t = 0) = \frac{2}{\sqrt{3}} \sin\left(\theta\right) \cos(x)\cos(y)\sin(z) \tag{2.72}$$

where u, v, and w are the Cartesian velocity components. The computational domain used is a cubic box whose edge has a length of 2π. Periodic boundary conditions are used in all

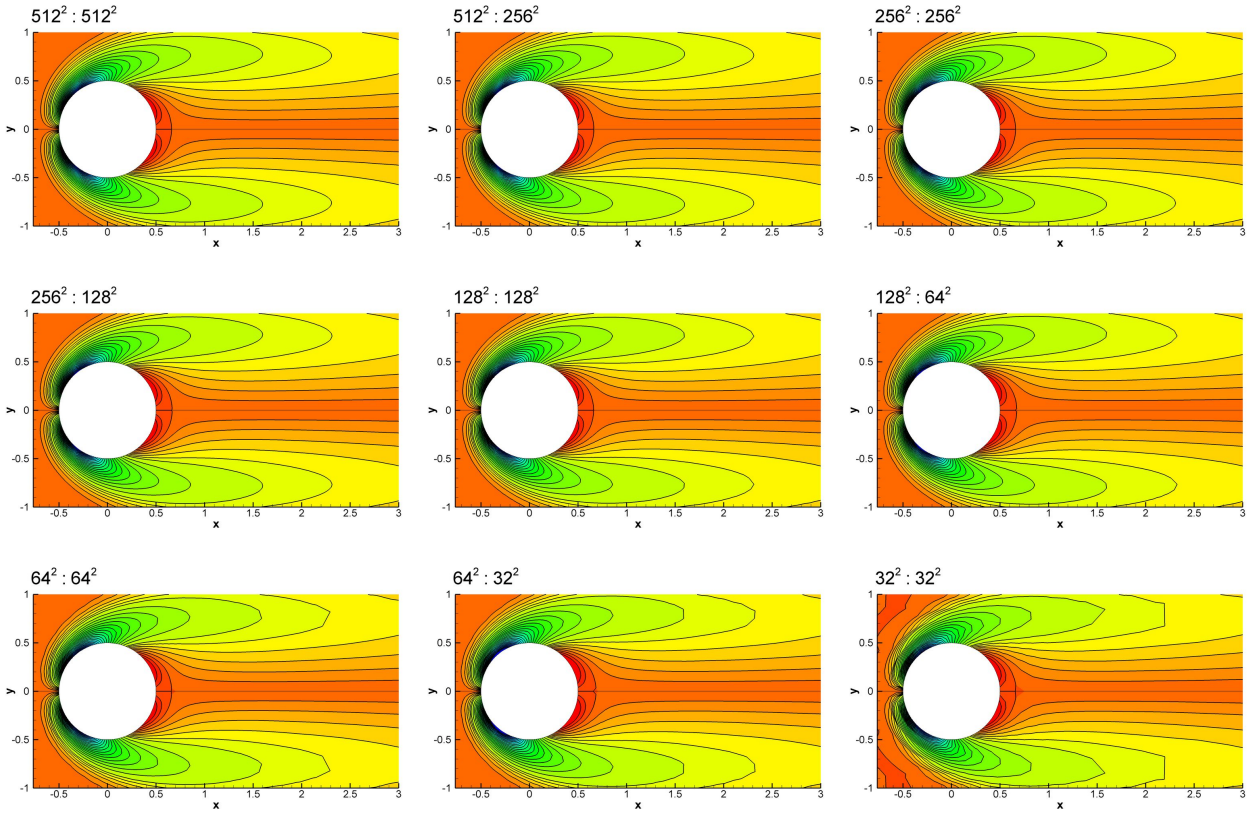

Figure 2.20: Vorticity contours for laminar flow over a cylinder at $Re = 40$. Labels include the resolutions for both parts of the solver in the form $N^2 : M^2$, where N^2 is the resolution for the vorticity-transport equation, and M^2 is the resolution for the Poisson equation. The contour interval layouts are identical in all cases.

directions and we set $\theta = 0$. In this case, the initial flow has two-dimensional streamlines, but the flow is three-dimensional for all $t > 0$. We performed numerical simulations for $Re = 200$ using the vorticity-velocity formulation of the governing equations given in Section 2.2.3 with $\Delta t = 4 \times 10^{-3}$.

The evolution of flow field is shown in Figure 2.21 in terms of the x-component of vorticity vector. Instantaneous vorticity isosurfaces colored blue for $\omega_x = -0.5$ and red for $\omega_x = 0.5$ are illustrated in this figure showing the generation of small scale structures by vortex stretching. Comparisons of the CGP method with the standard method are shown in Figures 2.22-2.24 for components of the vorticity field at time $t = 10$. In order to visualize

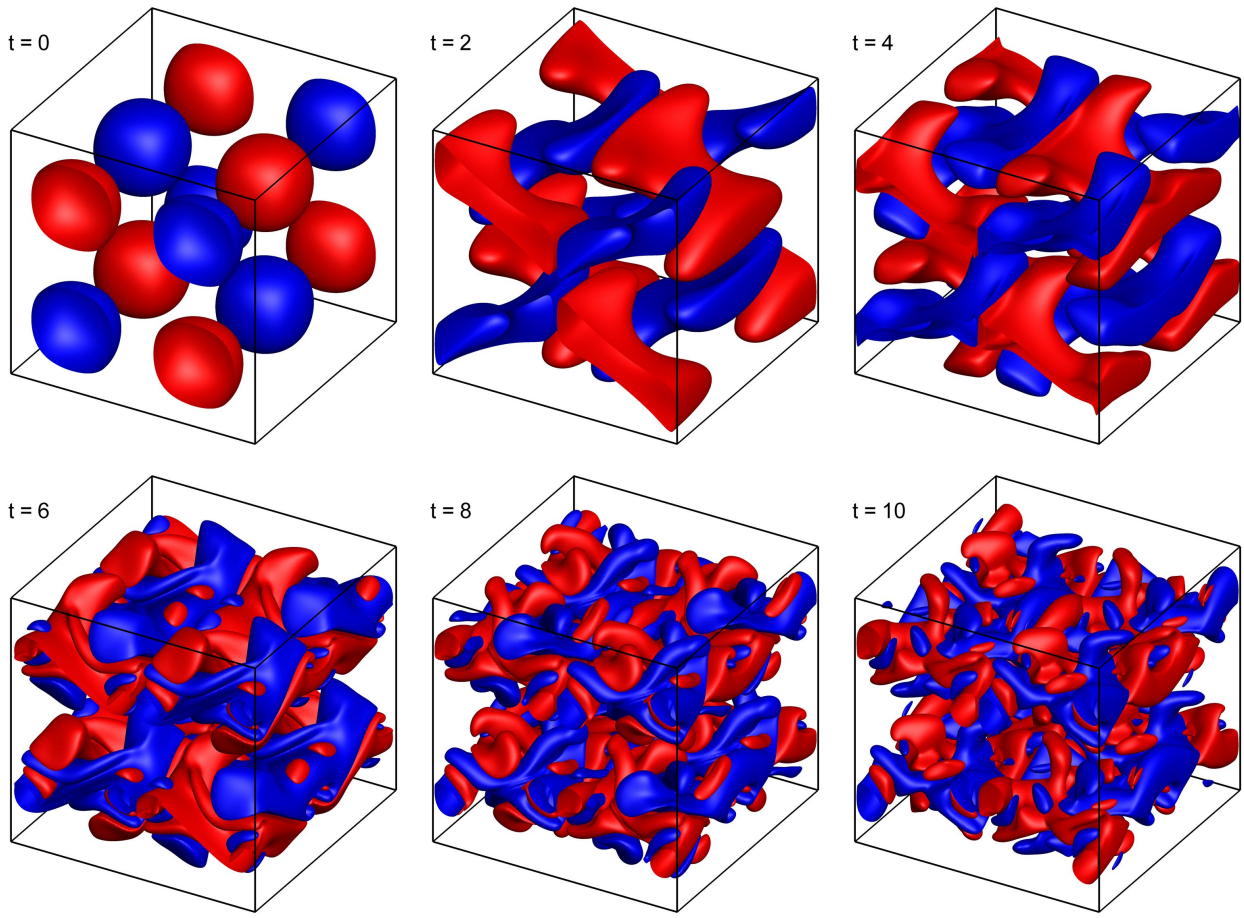

Figure 2.21: Evolution of the x-component of the vorticity obtained using the CGP method on a $256^3 : 128^3$ resolution grid for $Re = 200$. Isosurfaces of $\omega_x = -0.5$ (blue) and $\omega_x = 0.5$ (red) are shown.

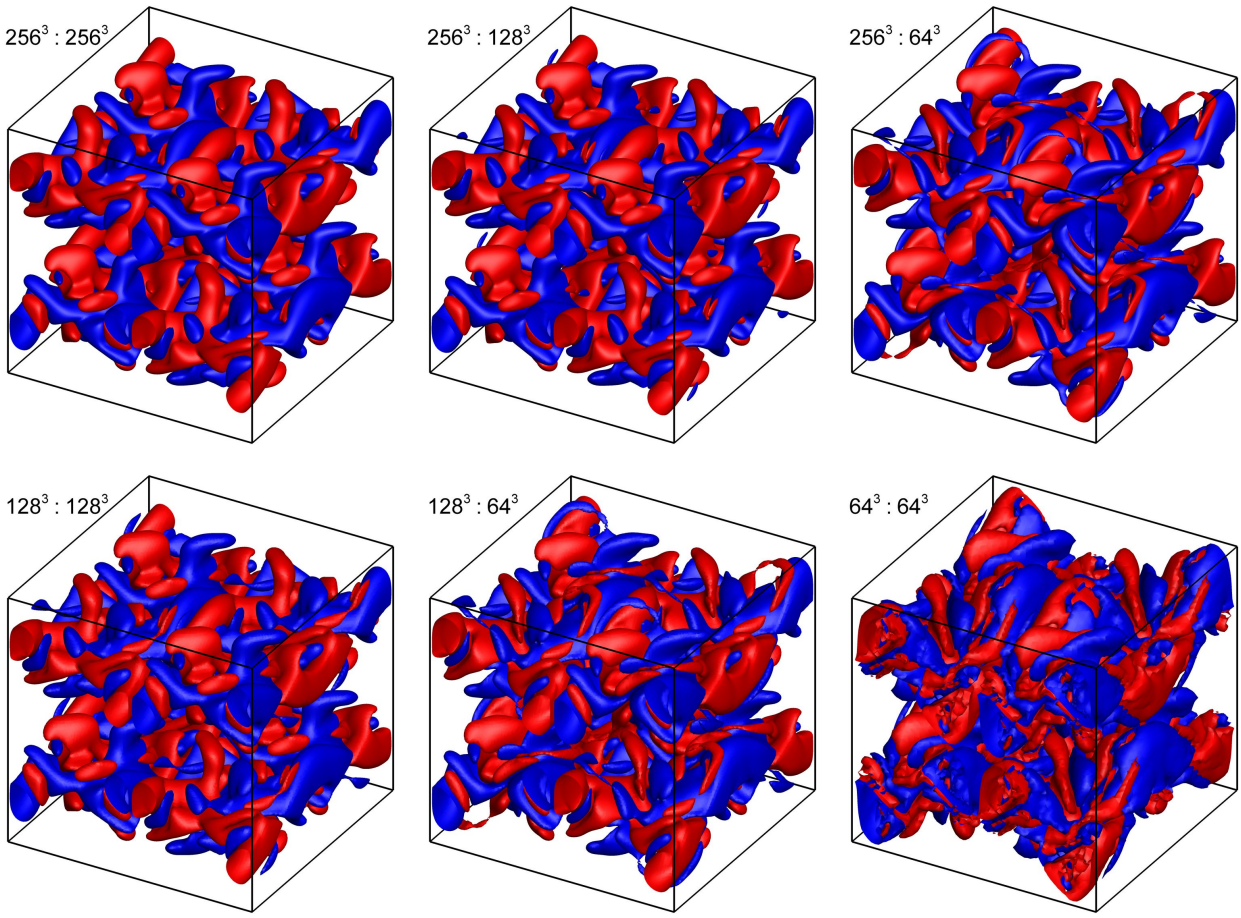

Figure 2.22: Comparison of the x-component of the vorticity at $t = 10$ for $Re = 200$. Isosurfaces of $\omega_x = -0.5$ (blue) and $\omega_x = 0.5$ (red) are shown. Labels include the resolutions for both parts of the solver in the form $N^3 : M^3$, where N^3 is the resolution for the vorticity-transport equations, and M^3 is the resolution for the elliptic sub-problems.

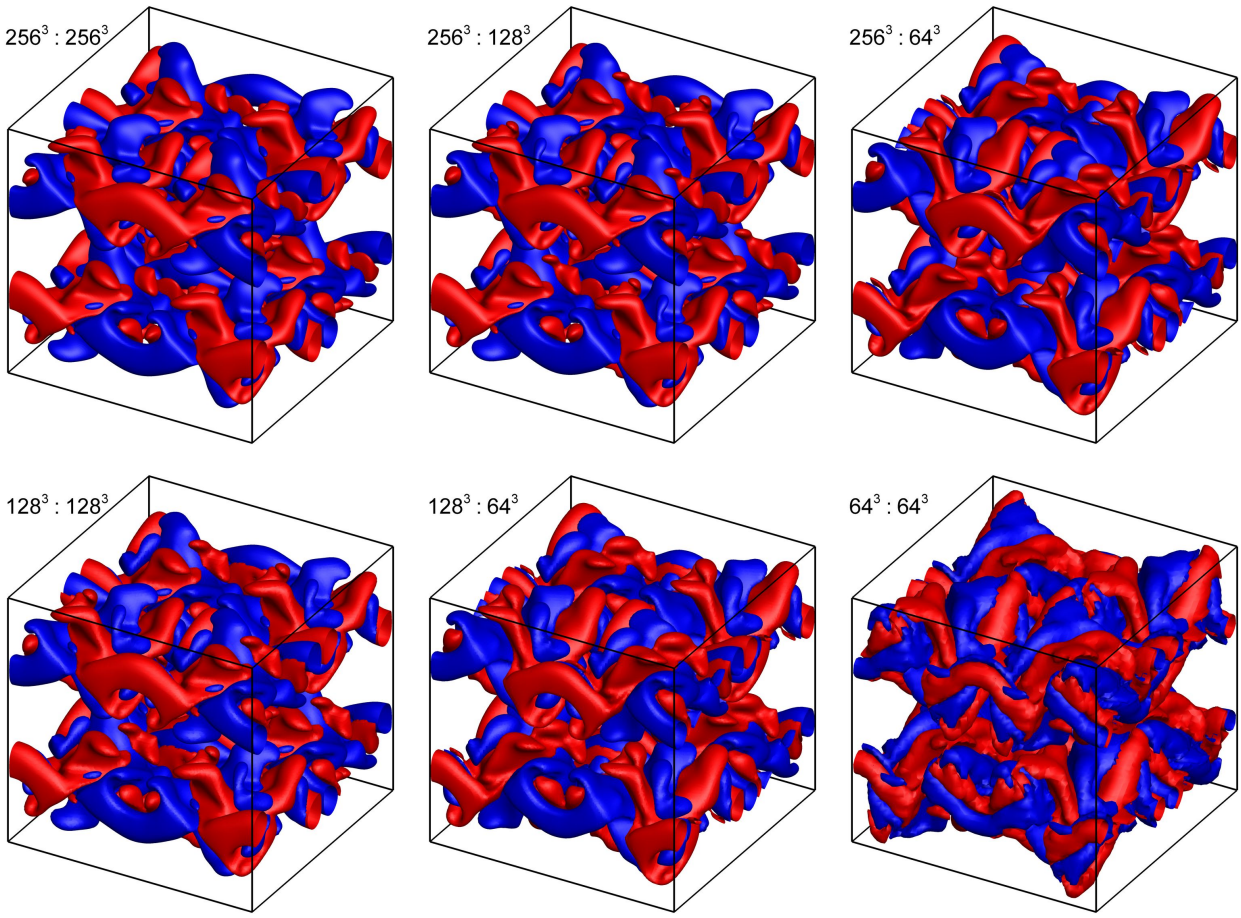

Figure 2.23: Comparison of the y-component of the vorticity at $t = 10$ for $Re = 200$. Isosurfaces of $\omega_y = -0.5$ (blue) and $\omega_y = 0.5$ (red) are shown. Labels include the resolutions for both parts of the solver in the form $N^3 : M^3$, where N^3 is the resolution for the vorticity-transport equations, and M^3 is the resolution for the elliptic sub-problems.

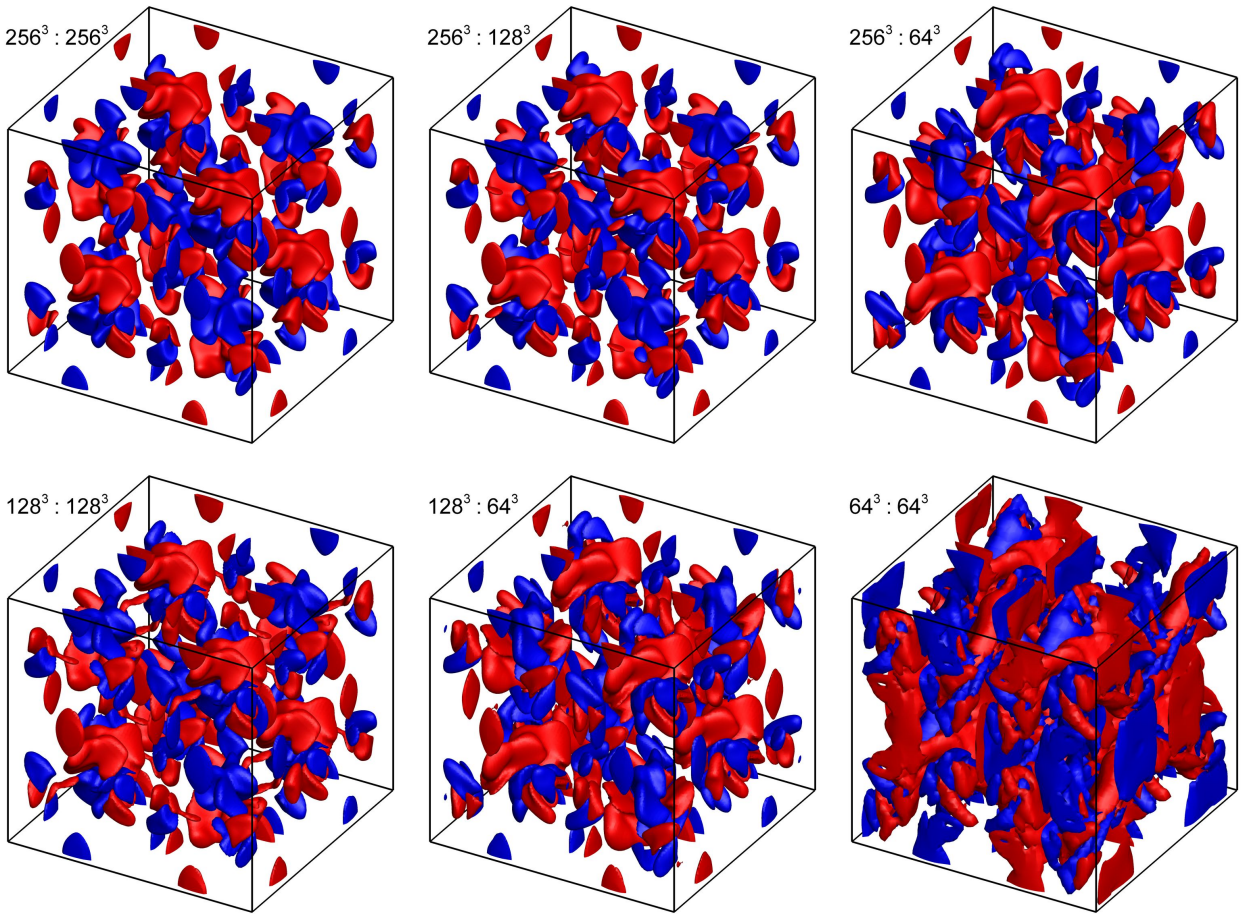

Figure 2.24: Comparison of the z-component of the vorticity at $t = 10$ for $Re = 200$. Isosurfaces of $\omega_z = -1.0$ (blue) and $\omega_z = 1.0$ (red) are shown. Labels include the resolutions for both parts of the solver in the form $N^3 : M^3$, where N^3 is the resolution for the vorticity-transport equations, and M^3 is the resolution for the elliptic sub-problems.

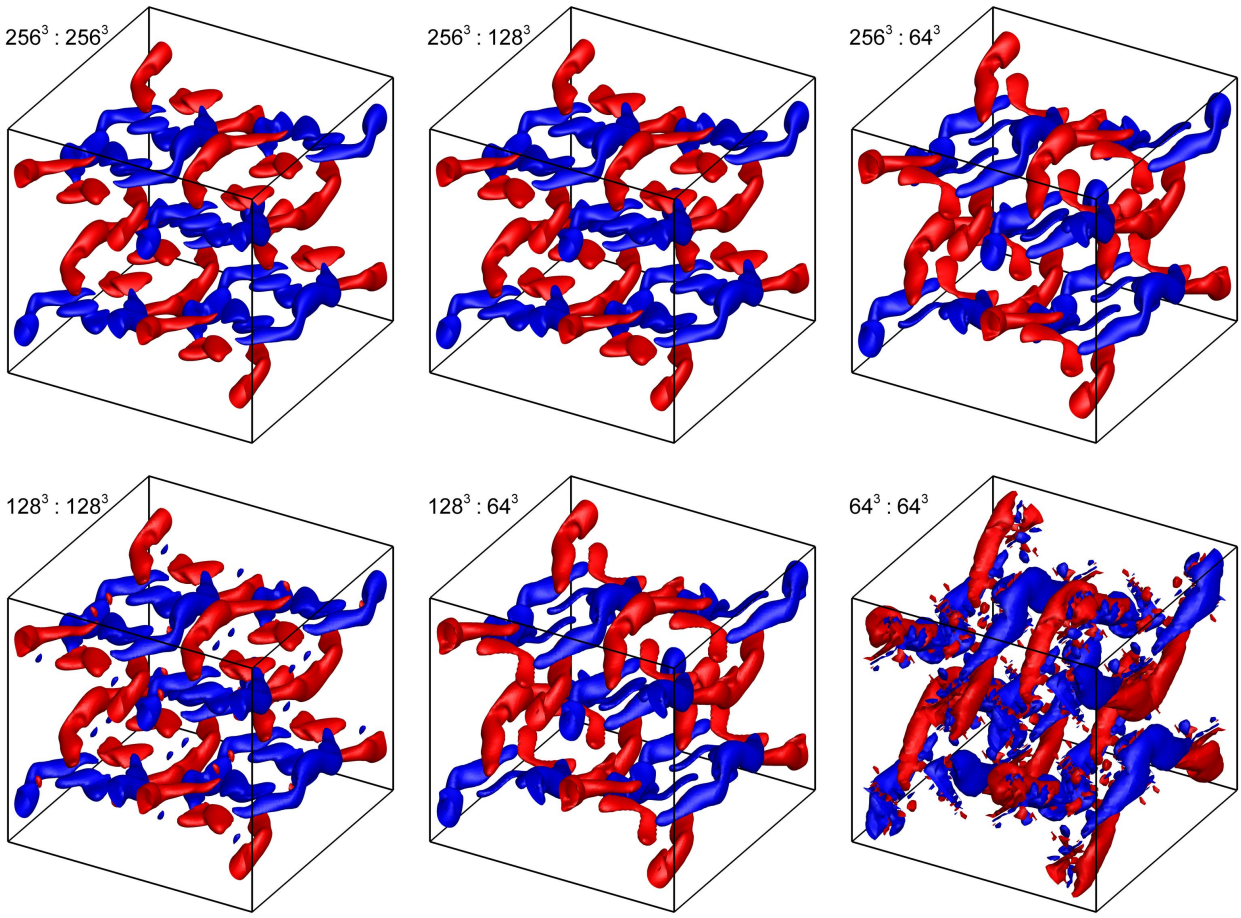

Figure 2.25: Comparison of the x-component of the vorticity at $t = 10$ for $Re = 200$. Isosurfaces of $\omega_x = -2.0$ (blue) and $\omega_x = 2.0$ (red) are shown. Labels include the resolutions for both parts of the solver in the form $N^3 : M^3$, where N^3 is the resolution for the vorticity-transport equations, and M^3 is the resolution for the elliptic sub-problems.

Table 2.8: Comparison of methods for the three-dimensional Taylor-Green vortex problem for $Re = 200$ at $t = 10$. Percent errors are computed with respect to the values computed at the finest resolution.

Method	Resolutions	$\|\omega_x\|_{max}$	% Error	CPU (hr)	Speed-up
RK3 ($\ell = 0$)	$256^3 : 256^3$	4.6039	-	206.84	1.00
CGPRK3 ($\ell = 1$)	$256^3 : 128^3$	4.8667	5.70	37.91	5.46
CGPRK3 ($\ell = 2$)	$256^3 : 64^3$	5.1513	11.89	26.41	7.83
RK3 ($\ell = 0$)	$128^3 : 128^3$	5.2037	13.03	21.29	1.00
CGPRK3 ($\ell = 1$)	$128^3 : 64^3$	5.6668	23.08	4.61	4.62
RK3 ($\ell = 0$)	$64^3 : 64^3$	8.5696	86.14	1.56	1.00

fine details of the flow field better, we also plot the vorticity isosurfaces for higher values of vorticity in Figure 2.25. In these figures, labels include the resolutions for both parts of the solver in the form $N^3 : M^3$, where N^3 is the resolution for the vorticity-transport equations, and M^3 is the resolution for the elliptic sub-problems. It is clear from these figures that the results using the CGP method agree well with the results of the fine scale computations using the standard method with a considerable reduction in computational cost as reported in Table 2.8. In this table, we also report the maximum values of ω_x in the simulation box and the corresponding percent errors computed according to the finest resolution. In these computations we use a linear-cost fast Poisson solver, and the CGP method yields a 5-8 fold reduction in computational cost. As discussed earlier, the speed ups would be greater if we used a quadratic-cost sub-optimal Poisson solver.

2.5 Conclusions

In the coarse-grid projection (CGP) methodology the cost of incompressible flow computations is reduced by coarsening the number of grid points used for the solution of the Poisson equation in the governing equations of incompressible fluid flows. The CGP framework is

applicable to incompressible flow solvers that require solving a Poisson equation at every time step to enforce the divergence-free constraint on the velocity or vorticity field, which requires the bulk of the computational effort. The CGP approach is general and in fact constitutes a family of methods, since in addition to choosing the coarsening and prolongation operators and the time integration scheme, the Poisson solver used in the approach can vary.

In this work, we investigated the performance of a particular CGP method that uses an optimal Poisson solver, the full weighting operation for the coarsening operator, and bilinear interpolation for the prolongation operator in the structured grid framework. We tested the proposed approach for the vorticity-stream function, primitive variable fractional step, and vorticity-velocity formulations of the governing equations using finite differences for spatial derivatives and the third-order Runge-Kutta scheme for temporal integration. Seven different benchmark flow problems were solved to investigate the performance of the method. We first tested the CGP approach for four problems with periodic boundary conditions: the Taylor-Green decaying vortex problem, for which error norms were calculated via exact solutions, a double shear layer, the merging of a pair of co-rotating vortices, and two-dimensional decaying turbulence. We then used CGP for two problems on non-Cartesian grids, the Taylor-Green vortex problem on a distorted grid and the laminar flow over a circular cylinder, to investigate the performance of the CGP method in generalized curvilinear coordinates. Finally, we performed computations for the three-dimensional Taylor-Green vortex problem, which is perhaps the simplest test case in which to study the generation of small scale motions and turbulence, to test the applicability of the CGP method in the presence of vortex stretching and tilting.

Using the CGP method, very similar fine resolution field data were obtained at reduced computational costs for one level of coarsening. If $2N$:N (advection:Poisson) is the CGP resolution, $2N$:$2N$ is the fine grid resolution, and N:N is the coarse grid resolution, there is a significant benefit to using $2N$:N grid-based computations in terms of decreasing computational cost and obtaining accuracies close to $2N$:$2N$ computations and significantly better than N:N computations. Strong benefits to using $2N$:N simulations are demonstrated

throughout the manuscript, in the selected problems. In some cases, which are problem and resolution dependent, there is very little loss of accuracy for the $2N$:N case compared to the $2N$:$2N$ case with a significant reduction in computational time. This is particulary true for well resolved cases in which the coarsening in the Poisson equation behaves as a low-pass filter and does not reduce the accuracy of the advection-diffusion part as much as pure coarsening does due to the corresponding prolongation operator. For two further levels of grid coarsening (reducing the number of grid points in each direction by factors of 4 and 8, respectively), increased reductions in computational time were found, but the accuracy of the fine resolution field data was reduced at each level of coarsening. Speed up factors between 2 and 42 were found using the CGP method, and the speed-up obtained was found to increase with increasing resolution of the fine level field data, as is to be expected. We also found that the acceleration rate of the computations due to CGP increases with the grid distortion ratio in curvilinear grid settings.

The proposed CGP approach works independently of the choice of Poisson solver and the choice of algorithm for the advection-diffusion part. It uses them as black-box solvers and uses simple interpolations between them. In this work we used optimal Poisson solvers with linear computational cost in all cases, either a FFT-based fast Poisson solver or a V-cycle multigrid Poisson solver, as our black-box solver. We expect the speed-up of the CGP method to increase dramatically for versions of the method that use other, suboptimal, Poisson solvers (which are generally $O(N^2)$). The results of these computations demonstrate that this version of the CGP approach is well suited for accelerating incompressible flow solvers that require the solution of a Poisson equation as a constraint to produce a divergence-free field. This suggests that the method may provide a useful tool for computing incompressible flows both in Cartesian and non-Cartesian domains. The current study yields promising results for structured Cartesian and curvilinear grids. The three-dimensional computations also suggest that the CGP method can be used to accelerate the DNS of turbulence by coarsening the number of grid points for the Poisson solver without affecting the well resolved DNS data, a topic we intend to investigate further in a future study.

Chapter 3

An Efficient Coarse-Grid Projection Method for Quasigeostrophic Models of Large-Scale Ocean Circulation

This paper puts forth a coarse-grid projection (CGP) multiscale method to accelerate computations of quasigeostrophic (QG) models for large scale ocean circulation. These models require solving an elliptic sub-problem at each time step, which takes the bulk of the computational time. The method we propose here is a modular approach that facilitates data transfer with simple interpolations and uses black-box solvers for solving the elliptic sub-problem and potential vorticity equations in the QG flow solvers. After solving the elliptic sub-problem on a coarsened grid, an interpolation scheme is used to obtain the fine data for subsequent time stepping on the full grid. The potential vorticity field is then updated on the fine grid with savings in computational time due to the reduced number of grid points for the elliptic solver. The method is applied to both single layer barotropic and two-layer stratified QG ocean models for mid-latitude oceanic basins in the beta plane, which are stan-

O. San and A. E. Staples, "An efficient coarse-grid projection method for quasigeostrophic models of large-scale ocean circulation," accepted to appear in *International Journal for Multiscale Computational Engineering* (2012).

dard prototypes of more realistic ocean dynamics. The method is found to accelerate these computations while retaining the same level of accuracy in the fine-resolution field. A linear acceleration rate is obtained for all the cases we consider due to the efficient linear-cost fast Fourier transform based elliptic solver used. We expect the speed-up of the CGP method to increase dramatically for versions of the method that use other, suboptimal, elliptic solvers, which are generally quadratic cost. It is also demonstrated that numerical oscillations due to lower grid resolutions, in which the Munk scales are not resolved adequately, are effectively eliminated with CGP method.

3.1 Introduction

Oceanic and atmospheric flows display an enormous range of spatial and temporal scales, from seconds to decades and from centimeters to thousands of kilometers. Scale interactions, both spatial and temporal, are the dominant feature of all aspects of general circulation models in geophysical fluid dynamics (Klein, 2010; Hurrell et al., 2009) and bridging the scales in geophysical systems is of paramount importance in numerous critical areas and industries. Atmospheric and oceanic flows have intrinsic complex multiscale interactions. The accurate and efficient numerical simulation of these geophysical flows is of great importance in weather and climate models and could perhaps benefit from a dedicated investigation of the application of classes of modern *multiscale modeling and simulation (MMS)* methods (Brandt, 2002; Barth et al., 2002; Fish, 2009; E, 2011), which exploit vastly different temporal and spatial scales in problems in order to speed up their computations. Similar to the parallel developments in applied mathematics and engineering science, interest in the development and testing of the MMS methods in geophysical flow settings has increased in recent years (Iskandarani et al., 2002; Majda and Klein, 2003; Khairoutdinov et al., 2008; Alam, 2011; Campin et al., 2011; Ringler et al., 2011), leading to several successful applications and research efforts at numerous weather and climate centers. The MMS framework could provide a significant increase in the accuracy and computational efficiency of numerous in-

terconnected physical oceanic and atmospheric flow models for advanced numerical weather prediction, data assimilation and climate modeling strategies.

The ocean is a forced-dissipative fluid system, with forcing largely at the boundaries and dissipation at the molecular scale. The investigation of characteristics of the forced-dissipative ocean circulation models is of primary importance in developing our understanding of the complex large-scale nonlinear motions of large-scale oceanic flows that move in great circular sweeps (called "gyres"). As one of the main circulation sources, most of the surface currents in the ocean are shaped by wind, which drives the general circulation associated with the subtropical and subpolar gyres, which can be identified with the strong, persistent, sub-tropical and sub-polar western boundary currents in the North Atlantic Ocean (the Gulf Stream and the Labrador Current) and North Pacific Ocean (the Kuroshio and the Oyashio Currents) and sub-tropical counterparts in the southern hemisphere (Stommel, 1972; Kelly et al., 2010). One of the major similarities between the various ocean basins is the asymmetry of the gyres: strong western boundary currents and weaker flow in the interior; weak and shallow eastern boundary currents. The most obvious motivation for being interested in forced-dissipative wind-driven ocean circulation is the connection between ocean currents and climate dynamics (Ghil et al., 2008; Lynch, 2008; Stocker, 2011).

Ocean eddies have a horizontal scale of typically several hundred kilometers and are often much stronger than the mean flow, leading to a highly turbulent, chaotic flow. The mean pattern of currents only emerges after averaging over many years. The wind-driven circulation in an enclosed, midlatitude rectangular or square oceanic basin is a classical problem in physical oceanography, studied extensively by modelers (Allen, 1980; Holland and Rhines, 1980; Griffa and Salmon, 1989; Vallis, 2006; Miller, 2007). To decrease the computational cost required for an accurate representation of large-scale oceanic flows, several class of simplified models are derived from the full-fledged equations of geophysical flows, Boussinesq equations (BEs) or the primitive equations (PEs), to guide the theoretical studies on boundary currents, alternating zonal flows, or jet formations, as well as to identify some key issues related to the robustness of the model dynamics to the changes of parameters that is closely

linked to a dynamical system point of view (Speich et al., 1995; Meacham, 2000; Chang et al., 2001; Nauw et al., 2004; Dijkstra, 2005; Dijkstra and Ghil, 2005). The quasigeostrophic (QG) model is a simplification of the primitive equation model that retains many of the essential features of geophysical fluid flows. Details of the mathematical and physical approximations may be found in standard textbooks on geophysical fluid dynamics, such as Pedlosky (1987), Vallis (2006), and McWilliams (2006). The main assumptions that go into the QG models are: the hydrostatic balance, the β-plane approximation (i.e., the variation of the Coriolis parameter with latitude), the geostrophic balance, and the eddy viscosity parameterization. Despite the fact that the QG models are a simplified version of the full-fledged equations of geophysical flows, their numerical simulation is still computationally challenging when long-time integration is required, as is the case in climate modeling.

The *barotropic vorticity equation (BVE)* represents one of the most commonly used mathematical models for this type of geostrophic flows with various dissipative and forcing terms (Majda and Wang, 2006). In reality, the ocean is a stratified fluid on a rotating Earth driven from its upper surface by patterns of momentum and buoyancy fluxes (Marshall et al., 1997). While the barotropic model is not stratified, it exhibits many of the features that are observed in the stratified case. To explore some of the effects of the stratification, the one-layer barotropic equation can be extended to the 1.5-layer model, also called the reduced gravity QG model (Özgökmen et al., 2001). There are two layers in this model, but the second layer is infinitely deep and at rest (passive), and the dynamics are effectively barotropic. The two-layer model takes the next step in increasing the complexity of stratification by adding a second dynamically active layer (Holland, 1978; Özgökmen and Chassignet, 1998; Berloff and McWilliams, 1999; DiBattista and Majda, 2001; Berloff et al., 2009). The dynamics in this model include the first baroclinic modes. The complexity of the models could be increased by adding more active layers, resulting in the N-layer models (Siegel et al., 2001), which, in turn, yield the three dimensional primitive equations when N goes to infinity (McWilliams, 2006). In this study, we use both the *one-layer quasigeostrophic (QG1)* and *two-layer quasigeostrophic (QG2)* models.

Although large-scale ocean dynamics are well represented by QG ocean models, primitive equation models have been used in state of art weather prediction softwares. Several reasons have been addressed for the recent lack of popularity in of these quasigeostrophic models (Miller, 2007). One is the ready availability of full-fledged primitive equation codes on the web, but that is not the only reason. There is a need for computational strategies that can significantly decrease the computational cost of the geophysical models without compromising their physical accuracy. Large eddy simulation (LES) approaches appear as a natural choice to accelerate the simulation on coarser grid in which the subgrid scale terms are modeled to capture the under-resolved flow, i.e., the flow in the regions where the grid size becomes greater than the specified Munk scale. San et al. (2011) proposed an approximate deconvolution large eddy simulation technique for one-layer barotropic quasiqeostropic large-scale ocean model. It was shown that the approximate deconvolution model provides an accurate approximation for under-resolved subfilter-scale effects.

Here, we approach to the problem from a different point of view. Instead of filtering the governing equations and modeling under-resolved quantities on a coarser grid, we separate the problem to two parts based on the nature of the QG models: (i) the elliptic sub-problem and (ii) the potential vorticity evolution. Most of the demand on computational resources by QG models comes in the solution of the elliptic inversion sub-problem which states the relationship between the potential vorticity and stream function. The natural advantages of QG models may well lead to increased application when efficient methods available for elliptic sub-problem. One straightforward way to accelerate QG simulations is to reduce the number of grid points for the most time consuming part of the problem, the elliptic sub-problem. Previous studies have demonstrated that scale dependant computational slowness can be overcome by multiscale and multiresolution algorithms (Brandt, 2005). Along this direction, the coarse-grid projection (CGP) framework was proposed by Lentine et al. (2010) and successfully applied to three-dimensional incompressible flow simulations by coarsening the number of grid points for the Poisson equation. A systematic error analysis on the coarse-grid projection method has been provided in Chapter 2 for Navier-Stokes equations.

The main goal of this report is to extend the CGP approach to the QG large scale ocean circulation models. The cost of the flow computations is reduced by coarsening the resolution of the numerical grid on which the elliptic sub-problem is solved by factors of two in each direction according to $M = 2^{-\ell}N$, where N is the fine resolution of the numerical grid on which the potential vorticity equation is solved, and M is the coarse resolution for the solution of the elliptic sub-problem. When $\ell = 0$ no coarsening is applied and the CGP method reduces to the underlying standard QG solver. In our numerical investigations, we serendipitously discovered that the CGP procedure can actually predict the fine level simulation details without loss of accuracy for a reduced computational cost.

The coarse-grid projection methodology is a modular approach that facilitates data transfer with simple restriction and prolongation interpolations and uses black-box solvers for the advection-diffusion and elliptic parts of the QG models. A particular version of the method is applied here using a third-order Runge-Kutta method for advection-diffusion part and a fast Fourier transform based direct solver for the elliptic part. The full weighting operation for mapping from the fine to coarse grids is used to obtain the data for the elliptic sub problem. After solving the elliptic part on a coarsened grid, bilinear interpolation is used to obtain the fine data for consequent time stepping on the full grid. Similar mapping operators have been used in multigrid algorithms (Brandt, 1977; Hackbusch, 1985; Briggs et al., 2000; Trottenberg et al., 2001). The efficiency of the interpolation based methods highly depends on the interpolation scheme (Fish and Chen, 2004), and has been substantially investigated in the multigrid literature. Since we are using a second-order spatial discretization scheme, however, the full weighting operator for the restriction and bilinear interpolation for the prolongation are consistent and efficient for our study. The mapping procedures used in this study could potentially be improved by introducing higher-order spline formulas, or more advanced methods for deriving interpolations (Lee et al., 1997; Höllig et al., 2002; Brezina et al., 2005; Brandt, 2010). The coarse-grid projection approach proposed here can be classified within the systematic upscaling methodologies that have been used in the context of the multigrid/multiresolution branch of multiscale methods.

The rest of the paper is organized as follows: Both barotropic one-layer BVE and two-layer stratified QG models, the mathematical models used in this report, are presented in Section 3.2. Section 3.3 presents the coarse-grid projection methodology for these QG models. The numerical methods used in our simulations are briefly discussed in Section 3.4. The results for the new CGP method for the large-scale ocean models are presented in Section 3.5. Finally, the conclusions are summarized in Section 3.6.

3.2 Mathematical models

In this section, we present the quasigeostrophic models used in the numerical investigation of the proposed coarse-grid projection method for large scale ocean circulation. We first present the BVE which is one of the most used mathematical models for geostrophic flows with various dissipative and forcing terms (Majda and Wang, 2006). Next, we present the two-layer QG model which is the simple extension of single-layer barotropic model to the stratified ocean by including another active layer.

3.2.1 One-layer barotropic model

In this section, we present the BVE, one of the most used mathematical models for forced-dissipative large scale ocean circulation problem. Studies of wind-driven circulation using an idealized double-gyre wind forcing have played an important role in understanding various aspects of ocean dynamics, including the role of mesoscale eddies and their effect on mean circulation. Following Greatbatch and Nadiga (2000), we briefly describe the BVE. For more details on the physical mechanism and various formulations utilized, the reader is referred to Greatbatch and Nadiga (2000); Munk and Wunsch (1982); Cummins (1992); Nadiga and Margolin (2001); Fox-Kemper (2005).

The barotropic vorticity equation for one-layer quasigeostrophic forced-dissipative ocean

model can be written as

$$\frac{\partial q}{\partial t} + J(\psi, q) = D + F. \tag{3.1}$$

where D and F represent the dissipation and forcing terms, respectively. In Eq. (3.1), q is the potential vorticity, defined as

$$q = \omega + \beta y, \tag{3.2}$$

where β is the gradient of the Coriolis parameter at the basin center ($y = 0$). Here, ω is the local vorticity, the curl of the velocity field, and the kinematic relationship between the vorticity and the stream function yields the following definition

$$\omega = \nabla^2 \psi = \frac{\partial^2 \psi}{\partial x^2} + \frac{\partial^2 \psi}{\partial y^2}. \tag{3.3}$$

in which ∇^2 is the Laplacian operator, and ψ symbolizes the velocity stream function. Flow velocity components can be found from the stream function:

$$u = -\frac{\partial \psi}{\partial y}; \quad v = \frac{\partial \psi}{\partial x} \tag{3.4}$$

The nonlinear convection term in Eq. (3.1), called the Jacobian, is defined as

$$J(\psi, q) = \frac{\partial \psi}{\partial x}\frac{\partial q}{\partial y} - \frac{\partial \psi}{\partial y}\frac{\partial q}{\partial x}. \tag{3.5}$$

The viscous dissipation in Eq. (3.1) has the form

$$D = \nu \left(\frac{\partial^2 \omega}{\partial x^2} + \frac{\partial^2 \omega}{\partial y^2} \right), \tag{3.6}$$

where ν is the uniform eddy viscosity coefficient. Viscous term can be written in terms of stream function in the following form

$$D = \nu \nabla^4 \psi \tag{3.7}$$

The double-gyre wind forcing is given by

$$F = \frac{\pi \tau_0}{\rho H} \sin(\pi y), \tag{3.8}$$

where τ_0 is the maximum amplitude of double-gyre wind stress, ρ is the mean density, and H is the mean depth of the ocean basin. In order to nondimensionalize the BVE equation we use the following definitions

$$x = \frac{\tilde{x}}{L},\ y = \frac{\tilde{y}}{L},\ t = \frac{\tilde{t}}{L/V},\ q = \frac{\tilde{q}}{\beta L},\ \psi = \frac{\tilde{\psi}}{VL}, \tag{3.9}$$

where the tilde denotes the corresponding dimensional variables. In the nondimensionalization, L represents the characteristic horizontal length scale (i.e., in our study L is the basin dimension in x direction), and V represents the characteristic velocity scale. The Sverdrup velocity scale used for nondimensionalization can be written in the follwing form:

$$V = \frac{\pi\ \tau_0}{\rho H \beta L}. \tag{3.10}$$

Finally, the governing equations for two-dimensional incompressible barotropic flows can be written in dimensionless form of the potential vorticity formulation in the beta plane as the BVE:

$$\frac{\partial \tilde{q}}{\partial \tilde{t}} + J(\tilde{\psi}, \tilde{q}) = \left(\frac{\delta_M}{L}\right)^3 \tilde{\nabla}^4 \tilde{\psi} + sin(\pi \tilde{y}). \tag{3.11}$$

where δ_M is the Munk scale. The elliptic sub-problem which relates the potential vorticity and stream function becomes

$$\tilde{q} = \left(\frac{\delta_I}{L}\right)^2 \tilde{\nabla}^2 \tilde{\psi} + \tilde{y}, \tag{3.12}$$

where δ_I is defined as Rhines scale. In dimensionless form, there are only two physical parameters, the Rhines scale and the Munk scale, which are related to the physical parameters

in the following way:

$$\frac{\delta_I}{L} = \left(\frac{V}{\beta L^2}\right)^{1/2}; \qquad \frac{\delta_M}{L} = \left(\frac{\nu}{\beta L^3}\right)^{1/3}. \tag{3.13}$$

The physical parameters in the BVE given by Eq. (3.11), the Rhines scale δ_I and the Munk scale δ_M, are related to the Reynolds and Rossby numbers through the following formulas:

$$\frac{\delta_I}{L} = (\mathrm{Ro})^{1/2}, \tag{3.14}$$

$$\frac{\delta_M}{L} = (\mathrm{Re}^{-1}\mathrm{Ro})^{1/3}, \tag{3.15}$$

where Ro is the Rossby number and Re is the Reynolds number based on the basin dimension, L. We note that some authors use a boundary layer Reynolds number, which is written as

$$\mathrm{Re}_B = \mathrm{Re}\frac{\delta_I}{L} = \frac{\delta_I^3}{\delta_M^3}, \tag{3.16}$$

where $\mathrm{Re}_B \sim O(10) - O(10^3)$ for oceanic flows Fox-Kemper (2005). Finally, in order to completely specify the mathematical model, boundary and initial conditions need to be prescribed. In many theoretical studies of large scale ocean circulation, slip or no-slip boundary conditions are used. Following these studies Greatbatch and Nadiga (2000); Nadiga and Margolin (2001); Holm and Nadiga (2003); Cummins (1992); Munk (1950); Bryan (1963), we use slip boundary conditions for the velocity, which translate into homogenous Dirichlet boundary conditions for the vorticity: $\omega|_\Omega = 0$. The impermeability boundary condition is imposed as $\psi|_\Omega = 0$. For the initial condition, we start our computations from a quiescent state and integrate Eq. (3.11) until a statistically steady state is obtained in which the wind forcing, dissipation, and Jacobian balance each other.

3.2.2 The two-layer quasigeostrophic equations

The two-layer quasigeostrophic model used in this study is one of the simplified forced-dissipative oceanic models that considers baroclinic effects. The stratified ocean is partitioned into two isopycnal layers, each of constant depth, density and temperature. The governing quasigeostrophic potential vorticity equations for the two dynamically active layers are (Pedlosky, 1987; Salmon, 1998; McWilliams, 2006)

$$\frac{\partial q_1}{\partial t} + J(\psi_1, q_1) = D_1 + F_1, \tag{3.17}$$

$$\frac{\partial q_2}{\partial t} + J(\psi_2, q_2) = D_2 + F_2, \tag{3.18}$$

where the layer index starts from top, q_i represents potential vorticities, and ψ_i denotes for stream functions. The dissipation and forcing (Ekman pumping) terms are represented by D_i, and F_i, respectively. The potential vorticities for each layer are related to the velocity stream functions through the following elliptic coupled system of equations:

$$q_1 = \nabla^2\psi_1 + \beta y + \frac{f_0^2}{g'H_1}(\psi_2 - \psi_1), \tag{3.19}$$

$$q_2 = \nabla^2\psi_2 + \beta y + \frac{f_0^2}{g'H_2}(\psi_1 - \psi_2). \tag{3.20}$$

The isopycnal flow velocity components can be found from the velocity stream functions:

$$u_i = -\frac{\partial \psi_i}{\partial y}; \quad v_i = \frac{\partial \psi_i}{\partial x}. \tag{3.21}$$

The two symbols β and f_0 are parts of the linearized β-plane approximation to the Coriolis parameter $f = f_0 + \beta y$. Here $f_0 = 2\,\Omega \sin(\phi_0)$ is the local rotation rate at $y = 0$, where Ω is the rotational speed of the earth and ϕ_0 is the latitude at $y = 0$. This is equivalent to approximating the spherical Earth with a tangent plane at $y = 0$. Stratification is represented by two stacked isopycnal layers with thicknesses H_1 and H_2, starting from the top, and $g' = g\frac{\Delta\rho}{\rho_1}$ is reduced gravity associated with the density jump between the two

layers in which $\Delta\rho$ is the density difference between the two layers, ρ_1 is the reference (upper layer) density, and g is the gravitational acceleration. The inertial radius of deformation between layers, a measure of stratification strength, is defined as the Rossby deformation radius $R_d = \sqrt{\frac{g' H_1 H_2}{f_0^2 H}}$, where $H = H_1 + H_2$. In this study, the top and bottom layers of the ocean are forced by an Ekman pumping of the form

$$F_1 = \frac{1}{\rho_1 H_1} \hat{k} \cdot \nabla \times \vec{\tau}, \tag{3.22}$$

$$F_2 = -\gamma \nabla^2 \psi_2, \tag{3.23}$$

where $\vec{\tau} = (\tau^{(x)}, \tau^{(y)})$ is the stress vector for surface wind forcing, and $\hat{k}$ is unit vector in vertical direction. In the present model, we use a double-gyre wind forcing only for zonal direction: $\tau^{(x)} = \tau_0 \cos\left(\frac{2\pi}{L} y\right)$, where L is the meridional length of the ocean basin centered at $y = 0$, and τ_0 is the maximum amplitude of the wind stress. This form of wind stress represents the meridional profile of easterly trade winds, mid-latitude westerlies, and polar easterlies from South to North. The bottom Ekman layer is parameterized by a linear bottom friction with coefficient γ. In the equations above, ∇ and ∇^2 are the gradient and Laplacian operators, respectively. For the dissipation terms, the following EV parameterizations are used:

$$D_1 = \nu \nabla^4 \psi_1, \tag{3.24}$$

$$D_2 = \nu \nabla^4 \psi_2, \tag{3.25}$$

where ν is eddy viscosity coefficient. Similar to the previous analysis, the governing equations can be written in dimensionless form by using the Sverdrup balance to set the velocity scale of the form

$$V = \frac{2\pi\tau_0}{\rho_1 H_1 \beta L}. \tag{3.26}$$

Then the two-layer quasigeostrophic equations in dimensionless form become

$$\frac{\partial \tilde{q}_1}{\partial \tilde{t}} + J(\tilde{\psi}_1, \tilde{q}_1) = A\tilde{\nabla}^4\tilde{\psi}_1 + \sin(2\pi\tilde{y}), \tag{3.27}$$

$$\frac{\partial \tilde{q}_2}{\partial \tilde{t}} + J(\tilde{\psi}_2, \tilde{q}_2) = A\tilde{\nabla}^4\tilde{\psi}_2 - \sigma\tilde{\nabla}^2\tilde{\psi}_2. \tag{3.28}$$

In dimensionless form, the kinematic relationships between potential vorticities and stream functions yield the following elliptic sub-problem:

$$\tilde{q}_1 = \mathrm{Ro}\tilde{\nabla}^2\tilde{\psi}_1 + \tilde{y} + \frac{\mathrm{Fr}}{\delta}(\tilde{\psi}_2 - \tilde{\psi}_1), \tag{3.29}$$

$$\tilde{q}_2 = \mathrm{Ro}\tilde{\nabla}^2\tilde{\psi}_2 + \tilde{y} + \frac{\mathrm{Fr}}{1-\delta}(\tilde{\psi}_1 - \tilde{\psi}_2). \tag{3.30}$$

For clarity of exposition, in the remainder of the paper we will drop the tilde symbol used for the dimensionless variables. In the two-layer QG model, $\delta = \frac{H_1}{H}$ is the aspect ratio of vertical layer thicknesses, Ro is the Rossby number, Fr is the Froude number, A is the lateral eddy viscosity coefficient, and σ is the Ekman bottom later friction coefficient. The definitions of these dimensionless parameters are:

$$\mathrm{Ro} = \frac{V}{\beta L^2};\ \mathrm{Fr} = \frac{f_0^2 V}{g'\beta H};\ A = \frac{\nu}{\beta L^3};\ \sigma = \frac{\gamma}{\beta L}. \tag{3.31}$$

The following three length scales are useful for setting the two-layer problem parameters: (i) the Munk scale, $\delta_M = \left(\frac{\nu}{\beta}\right)^{1/3}$, for the viscous boundary layer; this is related to the smaller scale dissipation; (ii) the Stommel scale, $\delta_S = \frac{\gamma}{\beta}$, for the bottom boundary layer thickness; this is accounting for larger scale damping; and (iii) the Rhines scale, $\delta_I = \left(\frac{V}{\beta}\right)^{1/2}$, for the inertial boundary layer; this is measuring the strength of the nonlinearity.

In order to complete the mathematical model, boundary and initial conditions should be prescribed. In many theoretical studies of ocean circulation, the modelers either use free-slip boundary conditions or no-slip boundary conditions. Following Cummins (1992); Özgökmen and Chassignet (1998), we use free-slip boundary conditions for the velocity for

both isopycnal layers, which translates into homogenous Dirichlet boundary conditions for the vorticity (Laplacian of stream function): $\nabla^2\psi|_\Omega = 0$. The impermeability boundary condition is imposed as $\psi|_\Omega = 0$. Similar to the one-layer problem, we start from a rest state, integrate the model until a statistically steady state is obtained, and continue for several decades to compute time-averaged results.

3.3 Coarse-grid projection

In QG models solving the elliptic sub-problem takes considerably more computational time than solving the time dependent part (i.e., potential vorticity evolution equation) of the problem. Within each time step, solving the time dependant part of the problem is usually of $O(N_p)$ where "N_p" is the number of degrees of freedom (total grid points, $N_x \times N_y$ for one-layer setting and $2N_x \times 2N_y$ for two-layer setting) of the problem. In general, the alternating direction implicit (ADI), Gauss-Seidel (GS) or successive over relaxation (SOR) types of iterative algorithms for solving the elliptic equation are of $O(N_p^2)$ (Saad, 2003). The practical consequence is that it is not feasible to use these types of iterative elliptic solvers for high resolution (and therefore high Reynolds number) computations along with long time integration. In order to accelerate these solvers, very successful multigrid algorithms have been developed that reduce the computational effort to close to $O(C_{MG}N_p)$ where C_{MG} is a proportionality constant (Wesseling, 2004; Gupta et al., 1997; Zhang, 1998). On the other hand, for certain ideal problems on equally-spaced grids, fast Fourier transform (FFT) based fast Poisson solvers can be used that are $O(C_{FFT}N_p log(N_p))$, and are presently the fastest algorithms ($C_{FFT}log(N_p) < C_{MG}$ in the relevant resolutions) for solving Poisson equations (Moin, 2001). The computational efficiencies of different elliptic solvers are shown in Figure 3.1 for solving a standard Poisson equation on a square domain with equidistant grid spacing. This preliminary comparison shows that FFT based elliptic solver is the most efficient solver for our sub-problems in the QG models. The computational gains in the CGP method are directly related to selection of the elliptic solver. We have intentionally

selected most efficient linear-cost elliptic solver to show the concept. We highlight that any computational gain obtained with this optimal linear-cost FFT based elliptic solver would be more immense if we used some other sub-optimal iterative type elliptic solver.

The basic idea behind coarse-grid projection (CGP) is to use a smaller number of grid points for solving the elliptic sub-problem. The CGP approach we propose here is modular and independent of the elliptic solver that is used. As shown by our preliminary analysis for solving Poisson equation, usually FFT based elliptic solvers are optimal for rectangular domain problems because they are fast and have minimal storage requirements. They are preferred because of their efficiency when using orthogonal coordinate systems in which there are no mixed derivatives. The general domains treated with body-fitted coordinates are out of bounds for FFT solvers due to the presence of mixed derivatives in the transformed generalized curvilinear coordinates. In that case, the V-cycle multigrid solver becomes the optimal elliptic solver to use. Since we used Drichlet type boundary conditions (i.e., free-slip

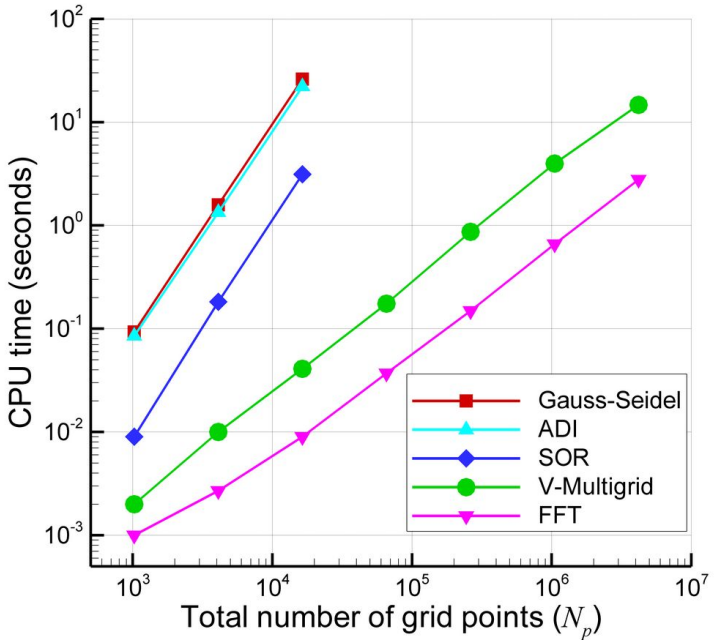

Figure 3.1: Computational efficiency of Poisson solvers. ADI, GS, and SOR are classical iterative solvers that scale as N_p^2. FFT is the fast Fourier transform based direct solver, and V-Multigrid is the V-cycle iterative multigrid solver, which both scale as N_p.

boundary contions) for our oceanic basins, a fast sine transform are utilized which we will briefly address on the following section where we present the numerical methods.

Even though we use the fastest elliptic solver available for our computations, the most time consuming part of the computations is still solving the elliptic sub-problem. With this in mind, we propose a new multiresolution approach that reduces the number of degrees of freedom for the elliptic solver part of the problem to accelerate the computation. The procedure is as follows: first, we solve the potential vorticity part of the problem using a fine resolution, N (the resolution in one direction). Next, we restrict these data to a coarser grid with resolution $M = 2^{-\ell}N$, where ℓ is an integer that determines the level of coarsening ($\ell = 0$ corresponds to no grid coarsening). After solving the Poisson equation on this coarser grid, we then perform a prolongation of the coarse data to the fine-resolution grid for subsequent time stepping. The procedure can be summarized in the following form:

(i) Compute potential vorticity equation on fine grid

(ii) Map potential vorticity data from fine grid to coarse grid to provide source term for elliptic sub-problem

(iii) Solve elliptic sub-problem for stream function on coarse grid

(iv) Remap stream function data from coarse grid to fine grid, continue to (i) for subsequent time step

We use prolongation and restriction operators between the data for the potential vorticity part and the elliptic sub-problem part of the problem. This seems to be effectively a low-pass filter on the solution to the elliptic sub-problem, similar to the large eddy simulation (LES) methods. However, the concept in CGP is fundamentally different than LES approaches. The philosophy of the LES concept is based on decomposition of the flow variables into resolved and unresolved scales by applying a filter to Navier-Stokes equations (Sagaut, 2006; Berselli et al., 2006). The idea of spatial filtering is central in LES: the large, spatially filtered flow

variables are approximated, whereas the effect of the small scales is modeled. This allows for much coarser spatial meshes and thus a computational cost that is significantly lower than that of a direct numerical simulation (DNS). To achieve the same order of physical accuracy as fine resolved DNS, however, LES needs to correctly treat the closure problem: the effect of the small scales on the large ones needs to be modeled. Since the inception of the LES for numerical solution of turbulent flows, substantial effort has been devoted to the turbulence models. These closure models have been suggested to relate the effects of subfilter scales into resolved scales.

On the other hand, the CGP method requires the reduction of degree of freedom just for the most time consuming part of the problem. Although the CGP method can be classified in multigrid methods, the underpinning idea behind CCM is different than the classical multigrid methods. In CGP method we use a smaller number of grid points for solving the most time consuming part of the mathematical model (i.e., elliptic sub-problems in QG models). We demonstrate that it is possible to accelerate simulations without a loss of accuracy by utilizing simple averaging and interpolations between the time dependant part of the solver and the elliptic part. We do this by reducing the size of the problem (via a restriction operation) before we solve the elliptic sub-problem, and solving a smaller sized elliptic system (using any Poisson solver), and then prolongating the results for the consequent time step. We add the costs of the restriction and prolongation operations to the solver, but we save much more computational time in solving the elliptic system because the Poisson equation is solved on a coarser grid. In the classical multigrid approach, the elliptic equation is solved iteratively in such a way that the error in the residual is linearly smoothed. Therefore, it is an optimal linear-cost iterative solution technique for elliptic equations. It doesn't require changing anything in the existing black-box elliptic solver. The same is true for the algorithm for the time dependant part of mathematical model. Therefore, the multigrid type of elliptic solver can be used in CGP framework. As shown in our preliminary computations for a simple elliptic Possion equation on Cartesian domain, FFT based direct elliptic solver is the most efficient. Since we had chosen only standard oceanic basins on

regular Cartesian grids, the FFT-based direct solver became the optimal one for our study. If, instead of using the FFT-based direct solver, we used a multigrid solver, we would see the same speed-up ratios but longer CPU times in the reported results. The speed-up would become larger if we would use a sub-optimal classical solver for the elliptic sub-problem.

3.3.1 Mapping operators

The only modifications to the standard flow solver computational procedures are the mapping procedures from fine to coarse data and vice versa. In the current study, the full weighting averaging operation is used for data coarsening (restriction), which is given for a two-dimensional equally spaced data array as (Moin, 2001):

$$\begin{aligned}\bar{\phi}_{i,j} = \frac{1}{16}[4\phi_{2i,2j} + 2(\phi_{2i,2j-1} + \phi_{2i,2j+1} + \phi_{2i-1,2j} + \phi_{2i+1,2j}) \\ +\phi_{2i+1,2j+1} + \phi_{2i+1,2j-1} + \phi_{2i-1,2j+1} + \phi_{2i-1,2j-1}]\end{aligned} \tag{3.32}$$

where $\bar{\phi}_{i,j}$ and $\phi_{i,j}$ are the coarse and fine data arrays, and i, j are the coarse grid indices. For almost all multiscale computations, the mapping from the coarse data to the fine data is a critical issue (E et al., 2007; Kevrekidis and Samaey, 2009; Fish, 2009; Wagner et al., 2010). The bilinear interpolation procedure that we use is given for two-dimensional equally spaced grid as:

$$\begin{aligned}\phi_{2i,2j} &= \bar{\phi}_{i,j} \\ \phi_{2i+1,2j} &= \frac{1}{2}(\bar{\phi}_{i,j} + \bar{\phi}_{i+1,j}) \\ \phi_{2i,2j+1} &= \frac{1}{2}(\bar{\phi}_{i,j} + \bar{\phi}_{i,j+1}) \\ \phi_{2i+1,2j+1} &= \frac{1}{4}(\bar{\phi}_{i,j} + \bar{\phi}_{i+1,j} + \bar{\phi}_{i,j+1} + \bar{\phi}_{i+1,j+1}).\end{aligned} \tag{3.33}$$

The half mapping procedures given by Eq. (3.32) for restriction and Eq. (3.33) for prolongation can be performed multiple times to obtain different levels of coarsening. The

mapping procedure does not take significant computational time compared to the elliptic solver. The mapping procedures used in this study could potentially be improved by introducing higher-order spline formulas. Since we are using a second-order spatial discretization scheme, however, bilinear interpolation is suitable for this study.

3.3.2 CGP algorithm

The coarse-grid projection (CGP) method is independent from the time integration method used. It can be implemented using any time stepping algorithm, for example, the backward difference method, or a method from the Adams-Bashforth or Adams-Moulton families (Schäfer, 2006). Here, the CGP method is used in conjunction with the third-order Runge-Kutta method for the QG models. The joint CGPRK3 algorithm for one-layer barotropic model is presented below. Starting with the value of the potential vorticity, q^n, at the current time step, the CGPRK3 algorithm for computing the potential vorticity at the next time

step, q^{n+1}, consists of the following steps:

$$q^n \Rightarrow \bar{q}^n \tag{3.34}$$

$$\frac{\partial^2 \bar{\psi}^n}{\partial x^2} + \frac{\partial^2 \bar{\psi}^n}{\partial y^2} = \left(\frac{\delta_I}{L}\right)^{-2} (\bar{q}^n - y) \tag{3.35}$$

$$\psi^n \Leftarrow \bar{\psi}^n \tag{3.36}$$

$$q^{(1)} = q^n + \Delta t G^n \tag{3.37}$$

$$q^{(1)} \Rightarrow \bar{q}^{(1)} \tag{3.38}$$

$$\frac{\partial^2 \bar{\psi}^{(1)}}{\partial x^2} + \frac{\partial^2 \bar{\psi}^{(1)}}{\partial y^2} = \left(\frac{\delta_I}{L}\right)^{-2} (\bar{q}^{(1)} - y) \tag{3.39}$$

$$\psi^{(1)} \Leftarrow \bar{\psi}^{(1)} \tag{3.40}$$

$$q^{(2)} = \frac{3}{4} q^n + \frac{1}{4} q^{(1)} + \frac{1}{4} \Delta t G^{(1)} \tag{3.41}$$

$$q^{(2)} \Rightarrow \bar{q}^{(2)} \tag{3.42}$$

$$\frac{\partial^2 \bar{\psi}^{(2)}}{\partial x^2} + \frac{\partial^2 \bar{\psi}^{(2)}}{\partial y^2} = \left(\frac{\delta_I}{L}\right)^{-2} (\bar{q}^{(2)} - y) \tag{3.43}$$

$$\psi^{(2)} \Leftarrow \bar{\psi}^{(2)} \tag{3.44}$$

$$q^{n+1} = \frac{1}{3} q^n + \frac{2}{3} q^{(2)} + \frac{2}{3} \Delta t G^{(2)} \tag{3.45}$$

where

$$G = -J(\psi, q) + D + F. \tag{3.46}$$

The arrows in the algorithm represent the mapping operators. The procedure for the two-layer QG model for stratified flow computations is similar to the one-layer algorithm except that two potential vorticity equations for each isopycnal layer along with a coupled system for elliptic sub-problem are be solved. We will address the solution procedure for the elliptic sub-problem in the following section.

3.4 Numerical methods

In many physically relevant situations, where the Munk and Rhines scales being close to each other, the solutions to oceanic models, such as the QG models, do not converge to a steady state as time goes to infinity (Medjo, 2000). Rather they remain time dependent by producing statistically steady state with one or multiple equilibria. Therefore, numerical schemes designed for numerical integration of such phenomena should be suited for such behavior of the solutions and for the long-time integration. In this study, the governing equations are solved by a fully conservative finite difference scheme along with a third-order Runge-Kutta adaptive time stepping algorithm. An efficient, linear-cost, fast sine transform method is utilized for solving the elliptic subproblems.

3.4.1 Arakawa scheme for the Jacobian

Arakawa (1966) suggested that the conservation of energy, enstrophy, and skew-symmetry is sufficient to avoid computational instabilities stemming from nonlinear interactions. The second-order Arakawa scheme for the Jacobian (i.e., the nonlinear term in the governing equations) is

$$J(\psi,q)=\frac{1}{3}\big(J_1(\psi,q)+J_2(\psi,q)+J_3(\psi,q)\big), \tag{3.47}$$

where the discrete Jacobians have the following forms:

$$\begin{aligned} J_1(\psi,q)=\frac{1}{4\,\Delta_x\,\Delta_y}\big[&-(q_{i+1,j}-q_{i-1,j})(\psi_{i,j+1}-\psi_{i,j-1})\\ &+(q_{i,j+1}-q_{i,j-1})(\psi_{i+1,j}-\psi_{i-1,j})\big], \end{aligned} \tag{3.48}$$

$$\begin{aligned} J_2(\psi,q)=\frac{1}{4\,\Delta_x\,\Delta_y}\big[&-q_{i+1,j}(\psi_{i+1,j+1}-\psi_{i+1,j-1})+q_{i-1,j}(\psi_{i-1,j+1}-\psi_{i-1,j-1})\\ &+q_{i,j+1}(\psi_{i+1,j+1}-\psi_{i-1,j+1})-q_{i,j-1}(\psi_{i+1,j-1}-\psi_{i-1,j-1})\big], \end{aligned} \tag{3.49}$$

$$\begin{aligned} J_3(\psi,q)=\frac{1}{4\,\Delta_x\,\Delta_y}\big[&-q_{i+1,j+1}(\psi_{i,j+1}-\psi_{i+1,j})+q_{i-1,j-1}(\psi_{i-1,j}-\psi_{i,j-1})\\ &+q_{i-1,j+1}(\psi_{i,j+1}-\psi_{i-1,j})-q_{i+1,j-1}(\psi_{i+1,j}-\psi_{i,j-1})\big]. \end{aligned} \tag{3.50}$$

Note that J_1, which corresponds to the central second-order difference scheme, is not sufficient for the conservation of energy, enstrophy, and skew-symmetry by the numerical discretization. Arakawa (1966) showed that the judicious combination of J_1, J_2, and J_3 in Eq. (3.47) achieves the above discrete conservation properties.

3.4.2 Time integration scheme

For the time discretization, as illustrated in the CGP algorithm, we employ an optimal third-order total variation diminishing Runge-Kutta (TVDRK3) scheme (Gottlieb and Shu, 1998). For clarity of notation, we rewrite the governing equations in the following form:

$$\frac{dq_i}{dt} = R_i, \tag{3.51}$$

where subscript i represents the layer index and R_i denotes the discrete spatial derivative operator, including the nonlinear Jacobian of the convective term, the linear biharmonic diffusive term, and the forcing term. For each layer, the TVDRK3 scheme then becomes:

$$\begin{aligned} q_i^{(1)} &= q^n + \Delta t R_i^{(n)}, \\ q_i^{(2)} &= \frac{3}{4} q_i^n + \frac{1}{4} q_i^{(1)} + \frac{1}{4} \Delta t R_i^{(1)}, \\ q_i^{n+1} &= \frac{1}{3} q_i^n + \frac{2}{3} q_i^{(2)} + \frac{2}{3} \Delta t R_i^{(2)}, \end{aligned} \tag{3.52}$$

where Δt is the adaptive time step size, which can be computed at the end of each time step by:

$$\Delta t = c \frac{\min(\Delta_x, \Delta_y)}{\max\left\{ |\frac{\partial \psi_i}{\partial x}|, |\frac{\partial \psi_i}{\partial y}| \right\}}, \tag{3.53}$$

where c is known as Courant-Friedrichs-Lewy (CFL) number which is restricted to $c \leq 1$ due to numerical stability of the TVDRK3 scheme.

3.4.3 Elliptic sub-problems

Most of the demand on computing resources posed by QG models comes in the solution of the elliptic inversion subproblem (Miller, 2007). This is also true for our study. However, we take advantage of the simple square shape of our domain and utilize one of the fastest available techniques, which is the FFT based direct inversion to solve the elliptic sub-problems. For example, the linear coupled elliptic sub-problem for the two-layer QG model can be written in the following form:

$$Q_1 = \mathrm{Ro}\nabla^2\psi_1 + \frac{\mathrm{Fr}}{\delta}(\psi_2 - \psi_1), \tag{3.54}$$

$$Q_2 = \mathrm{Ro}\nabla^2\psi_2 + \frac{\mathrm{Fr}}{1-\delta}(\psi_1 - \psi_2), \tag{3.55}$$

where $Q_1 = q_1 - y$ and $Q_2 = q_2 - y$. The impermeability boundary condition imposed as $\psi|_\Omega = 0$ suggests the use of a fast sine transform (an inverse transform) for each layer:

$$\hat{Q}_{1_{k,l}} = \frac{2}{N_x}\frac{2}{N_y}\sum_{i=1}^{N_x-1}\sum_{j=1}^{N_y-1} Q_{1_{i,j}} \sin\left(\frac{\pi k i}{N_x}\right)\sin\left(\frac{\pi l j}{N_y}\right), \tag{3.56}$$

$$\hat{Q}_{2_{k,l}} = \frac{2}{N_x}\frac{2}{N_y}\sum_{i=1}^{N_x-1}\sum_{j=1}^{N_y-1} Q_{2_{i,j}} \sin\left(\frac{\pi k i}{N_x}\right)\sin\left(\frac{\pi l j}{N_y}\right), \tag{3.57}$$

where N_x and N_y are the total number of grid points in x and y directions. Here the symbol hat is used to represent the corresponding Fourier coefficient of the physical grid data with a subscript pair i, j, where $i = 0, 1, ...N_x$ and $j = 0, 1, ...N_y$. As a second step, we directly solve the subproblem in Fourier space:

$$\hat{\psi}_{1_{k,l}} = \frac{\alpha_{k,l}\hat{Q}_{1_{k,l}} - \frac{\mathrm{Fr}}{1-\delta}\hat{Q}_{1_{k,l}} - \frac{\mathrm{Fr}}{\delta}\hat{Q}_{2_{k,l}}}{\alpha_{k,l}\left(\alpha_{k,l} - \frac{\mathrm{Fr}}{\delta} - \frac{\mathrm{Fr}}{1-\delta}\right)}, \tag{3.58}$$

$$\hat{\psi}_{2_{k,l}} = \frac{\alpha_{k,l}\hat{Q}_{2_{k,l}} - \frac{\mathrm{Fr}}{1-\delta}\hat{Q}_{1_{k,l}} - \frac{\mathrm{Fr}}{\delta}\hat{Q}_{2_{k,l}}}{\alpha_{k,l}\left(\alpha_{k,l} - \frac{\mathrm{Fr}}{\delta} - \frac{\mathrm{Fr}}{1-\delta}\right)}, \tag{3.59}$$

where

$$\alpha_{k,l} = \frac{\mathrm{Ro}}{\Delta_x^2}\left[2\cos\left(\frac{\pi k}{N_x}\right) - 2\right] + \frac{\mathrm{Ro}}{\Delta_y^2}\left[2\cos\left(\frac{\pi l}{N_y}\right) - 2\right]. \tag{3.60}$$

Finally, the stream function arrays for each layer are found by performing a forward sine transform:

$$\psi_{1_{i,j}} = \sum_{k=1}^{N_x-1}\sum_{l=1}^{N_y-1} \hat{\psi}_{1_{k,l}} \sin\left(\frac{\pi k i}{N_x}\right)\sin\left(\frac{\pi l j}{N_y}\right), \tag{3.61}$$

$$\psi_{2_{i,j}} = \sum_{k=1}^{N_x-1}\sum_{l=1}^{N_y-1} \hat{\psi}_{2_{k,l}} \sin\left(\frac{\pi k i}{N_x}\right)\sin\left(\frac{\pi l j}{N_y}\right), \tag{3.62}$$

The computational cost of this elliptic solver is $\mathcal{O}\left(N_x\, N_y\, \log(N_x)\, \log(N_y)\right)$. The FFT algorithm given by Press et al. (1992) is used for forward and inverse sine transforms. The elliptic sub-problem for the one-layer barotropic model can be easily inverted by using similar approach.

3.5 Results

To investigate the performance of the CGP method we consider two different large-scale QG ocean circulation models, one with one-layer barotropic ocean basin, one with two-layer stratified ocean basin. For each model we present several numerical experiments having different physical setting to evaluate the characteristics of the CGP multiscale method.

3.5.1 CGP experiments for one-layer QG model

The main goal of this section is to test the proposed CGP method in the numerical simulation of the wind-driven circulation in a barotropic shallow ocean basin, a standard prototype

of more realistic ocean dynamics. The model employs the BVE driven by a symmetric double-gyre wind forcing, which yields a four-gyre circulation in the time mean. This test problem has been used in numerous studies (Cummins, 1992; Greatbatch and Nadiga, 2000; Nadiga and Margolin, 2001; Holm and Nadiga, 2003; Fox-Kemper, 2005; San et al., 2011). This problem represents an ideal test for the one-layer QG models. Indeed, as showed in Greatbatch and Nadiga (2000), although a double gyre wind forcing is used, the long time average yields a four gyre pattern, which is challenging to capture on coarse spatial resolutions. Thus, we will investigate numerically whether our CGP model can reproduce the four gyre time average on a coarse mesh.

The mathematical model used in the four gyre problem is the BVE given by Eq. (3.11). We utilize two different parameter sets, corresponding to two physical oceanic settings: Experiment I with a Rhines scale of $\delta_I/L = 0.04$ and a Munk scale of $\delta_M/L = 0.02$, which corresponds to a Reynolds number of $Re = 200$ (or a boundary layer based Reynolds number of $Re_B = 8$) and a Rossby number of $Ro = 0.0016$; and Experiment II with a Rhines scale of $\delta_I/L = 0.05$ and a Munk scale of $\delta_M/L = 0.02$, which corresponds to a Reynolds number of $Re = 312.5$ (or a boundary layer based Reynolds number of $Re_B = 15.625$) and a Rossby number of $Ro = 0.0025$. Since we set the Munk scale to $\delta_M/L = 0.02$ in our study, the uniform eddy viscosity coefficient embedded in the model can be calculated from Eq. (3.13). For example, if we set the mid-latitude ocean basin length to $L = 2000$ km and the gradient of the Coriolis parameter to $\beta = 1.75 \times 10^{-11}$ m^{-1}s^{-1}, then our model uses $\nu = 1120$ m^{2}s^{-1} as its eddy viscosity parametrization. Table 3.1 summarizes the physical variables associated with the one-layer QG experiments considered in this study. All numerical experiments conducted here are solved for a maximum dimensionless time of $T_{max} = 50$. This value corresponds to the dimensional times of 28.3 and 18.1 years for Experiment I and Experiment II, respectively, which are long enough to capture statistically steady states.

We start by performing a DNS computation on a fine mesh with a spatial resolution of 256×512. As shown in Figure 3.2, for both experiments, after a transient period, a statistically steady state solution is obtained at a time of around $t = 5$. However, the behavior of

Table 3.1: Physical parameter sets used in the numerical experiments for the one-layer QG model.

Variable (unit)	Experiment I	Experiment II
$L_x = L\ (km)$	2000	2000
$L_y\ (km)$	4000	4000
$\beta\ (m^{-1}s^{-1})$	1.75×10^{-11}	1.75×10^{-11}
$\nu\ (m^2s^{-1})$	1120	1120
$V\ (ms^{-1})$	0.112	0.175
$L/V\ (year)$	0.566	0.362
δ_M/L	0.02	0.02
δ_I/L	0.04	0.05
Ro	0.0016	0.0025
Re	200	312.5

the system in statistically steady state is quite different due to regime transition. In the classification of Berloff and McWilliams (1999), Experiment I lie in the chaotic regime, whereas in the Experiment II the flow regime showed a quasi-periodic variability. Instantaneous con-

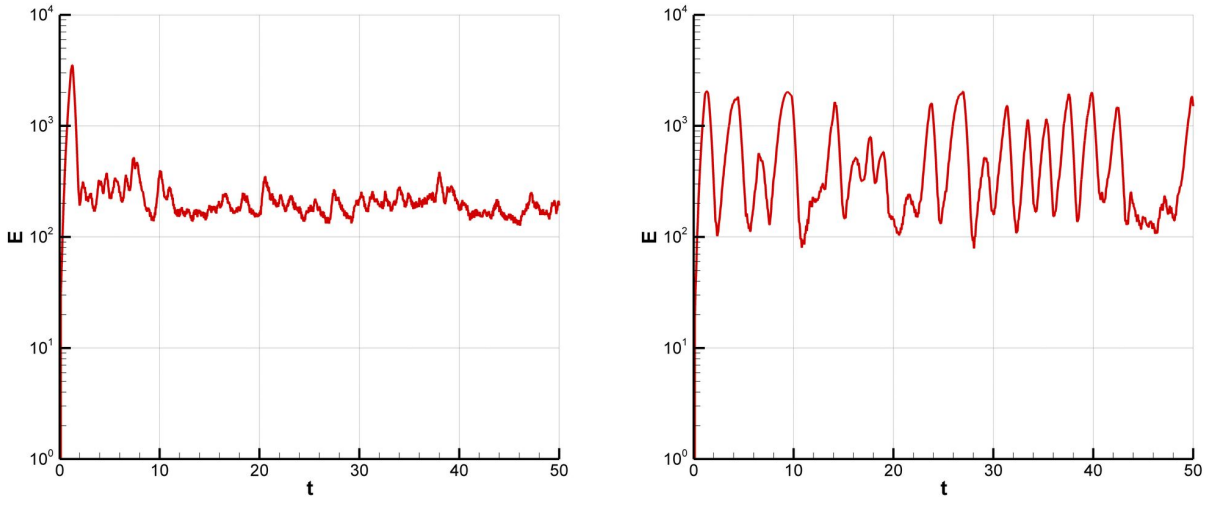

(a) Experiment I

(b) Experiment II

Figure 3.2: Time histories of basin integrated total kinetic energy.

tour plots at the final time $t = 50$ for the potential vorticity are shown in Figure 3.3 for both experiments. In all the one-layer experiments presented in this study, the time average of the data is taken between time $t = 10$ and $t = 50$ using 20 thousands snapshots in order to quantify the statistically steady state. The DNS results are included as a reference value in the following analysis when we present the results with the CGP method.

Three different levels of coarsening: half-coarsening ($\ell = 1$, $M = N/2$), 1/4-coarsening ($\ell = 2$, $M = N/4$) and 1/8-coarsening ($\ell = 3$, $M = N/8$), are performed to investigate the behavior of the CGP method. Mean stream function and potential vorticity field contours obtained using the CGP method are plotted in Figure 3.4 and Figure 3.5 along with the

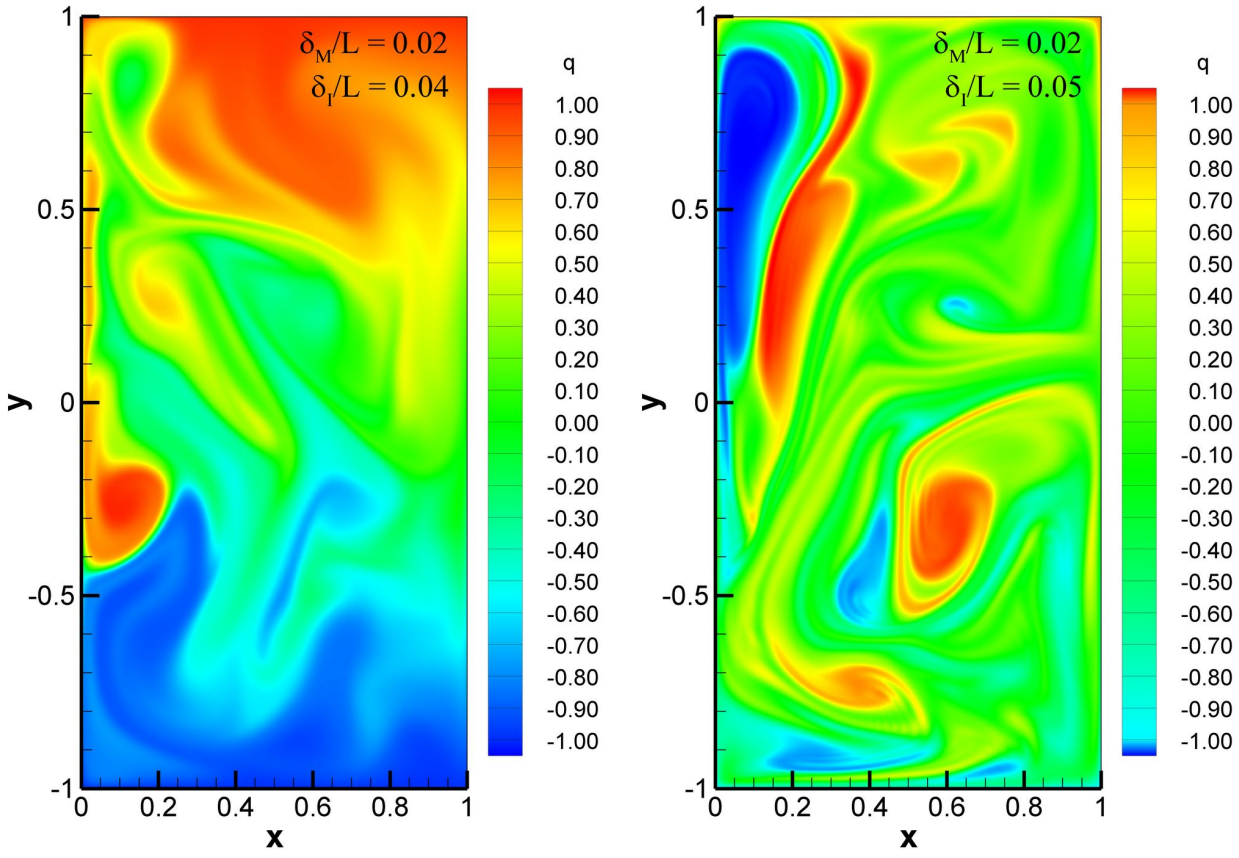

(a) Experiment I

(b) Experiment II

Figure 3.3: Instantaneous potential vorticity contour plots at time $t = 50$.

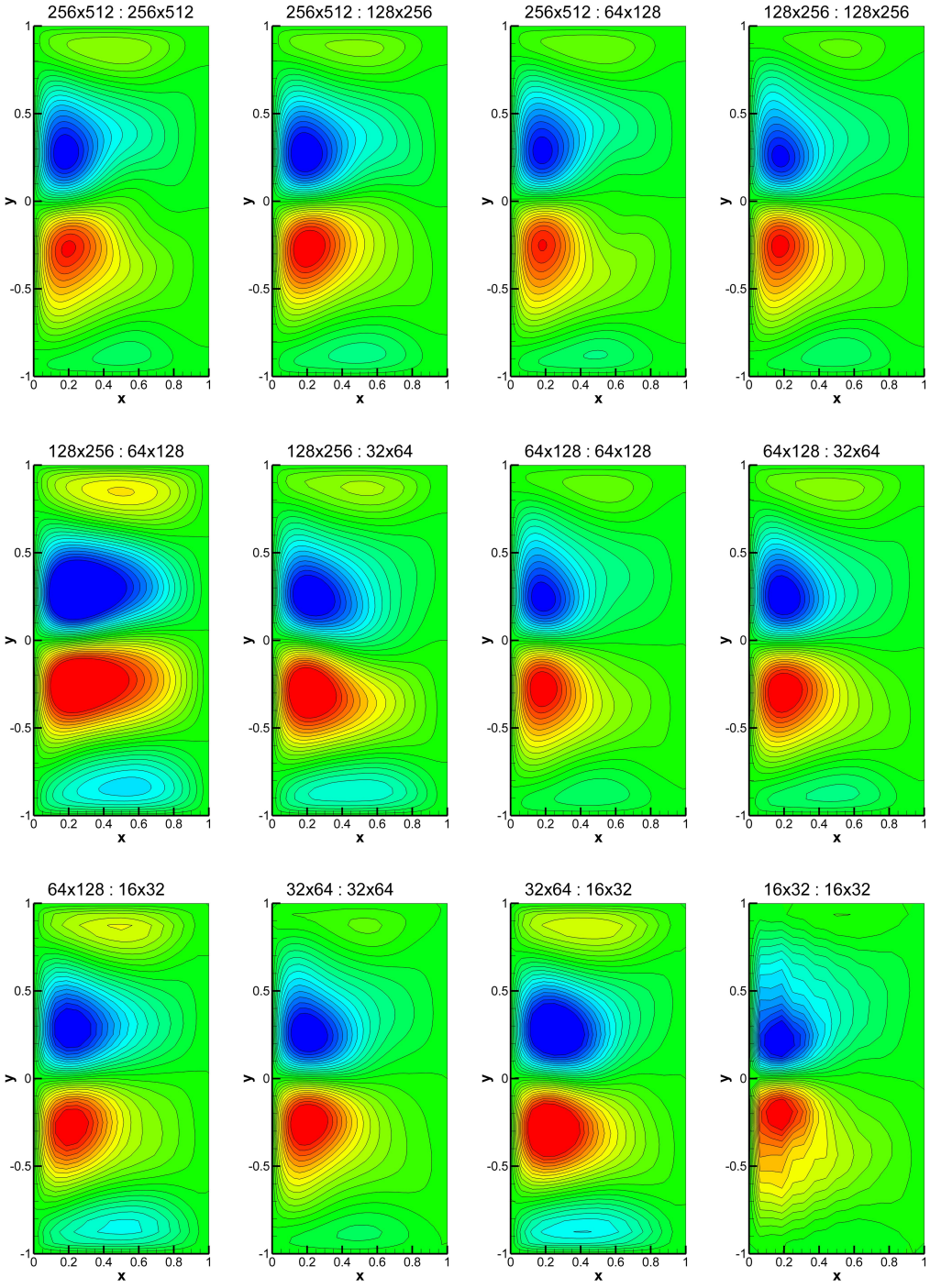

Figure 3.4: Experiment I: Comparison of mean stream functions for $Re = 200$ and $Ro = 0.0016$ (i.e., $\delta_M/L = 0.02$, and $\delta_I/L = 0.04$). Labels include the resolutions for both parts of the solver in the form $N_x \times N_y : M_x \times M_y$, where $N_x \times N_y$ is the resolution for the barotropic vorticity transport equation, and $M_x \times M_y$ is the resolution for the elliptic sub-problems.

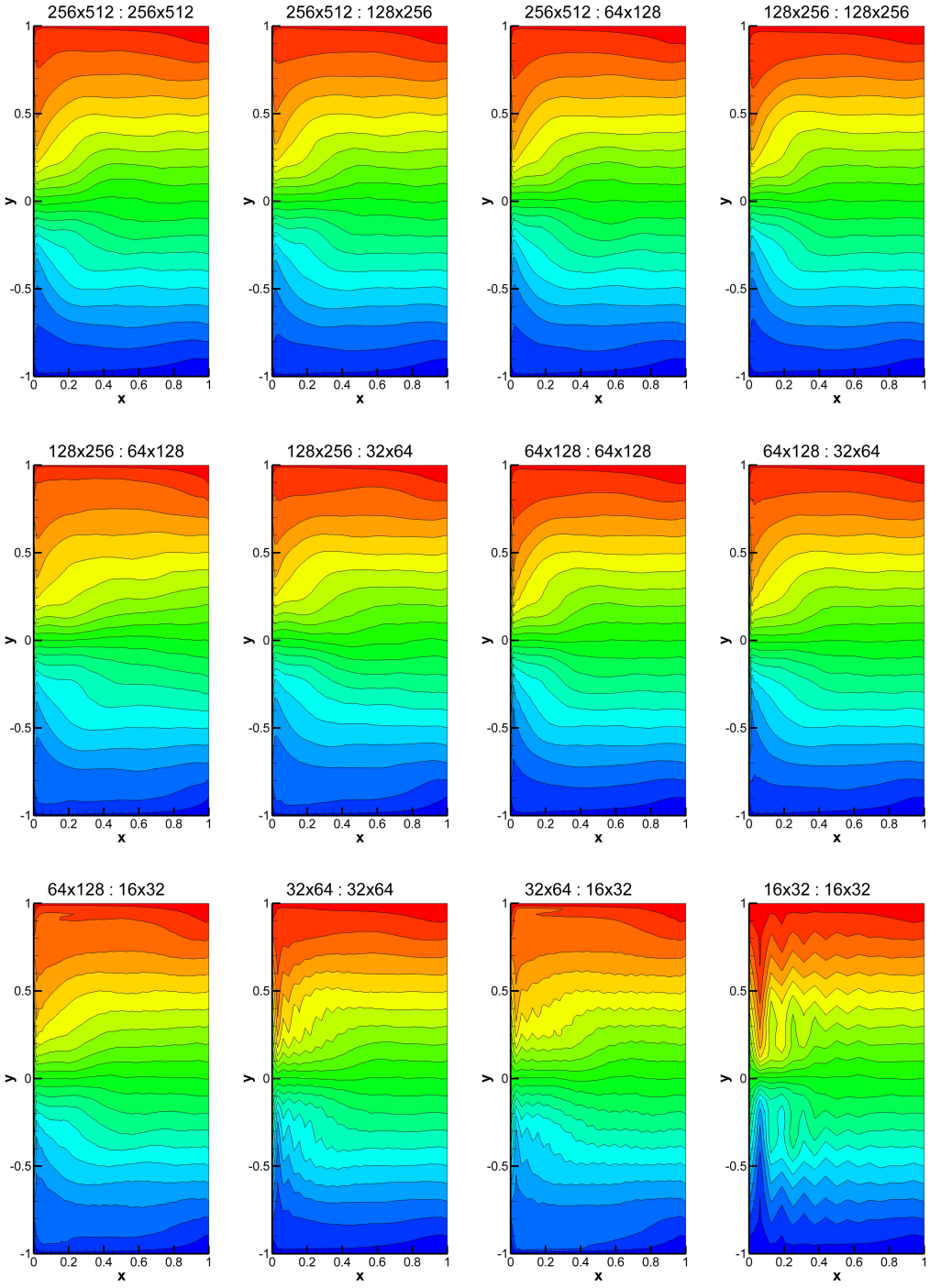

Figure 3.5: Experiment I: Comparison of mean potential vorticity for $Re = 200$ and $Ro = 0.0016$ (i.e., $\delta_M/L = 0.02$, and $\delta_I/L = 0.04$). Labels include the resolutions for both parts of the solver in the form $N_x \times N_y : M_x \times M_y$, where $N_x \times N_y$ is the resolution for the barotropic vorticity transport equation, and $M_x \times M_y$ is the resolution for the elliptic sub-problems.

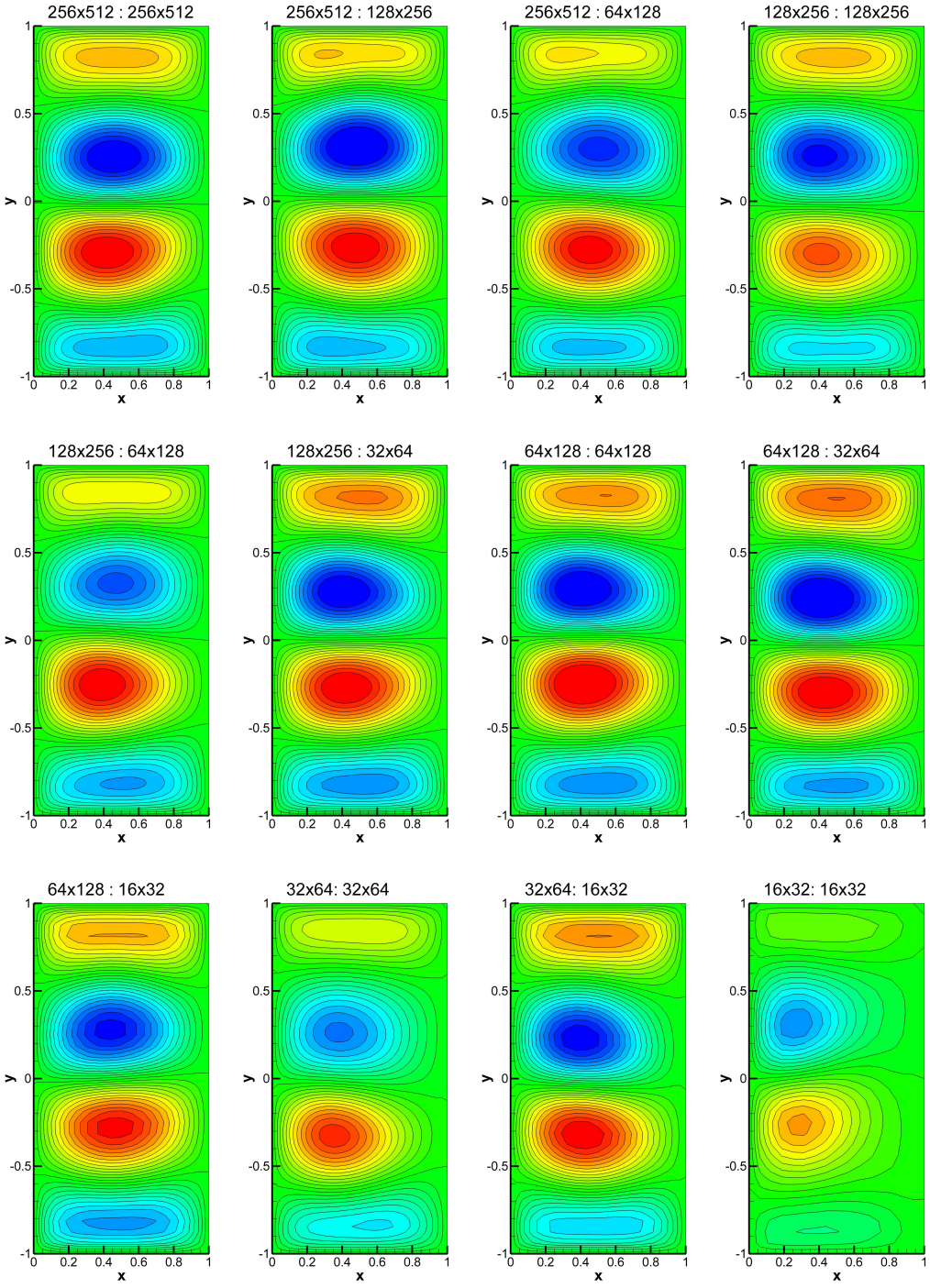

Figure 3.6: Experiment II: Comparison of mean stream functions for $Re = 312.5$ and $Ro = 0.0025$ (i.e., $\delta_M/L = 0.02$, and $\delta_I/L = 0.05$). Labels include the resolutions for both parts of the solver in the form $N_x \times N_y : M_x \times M_y$, where $N_x \times N_y$ is the resolution for the barotropic vorticity transport equation, and $M_x \times M_y$ is the resolution for the elliptic sub-problems.

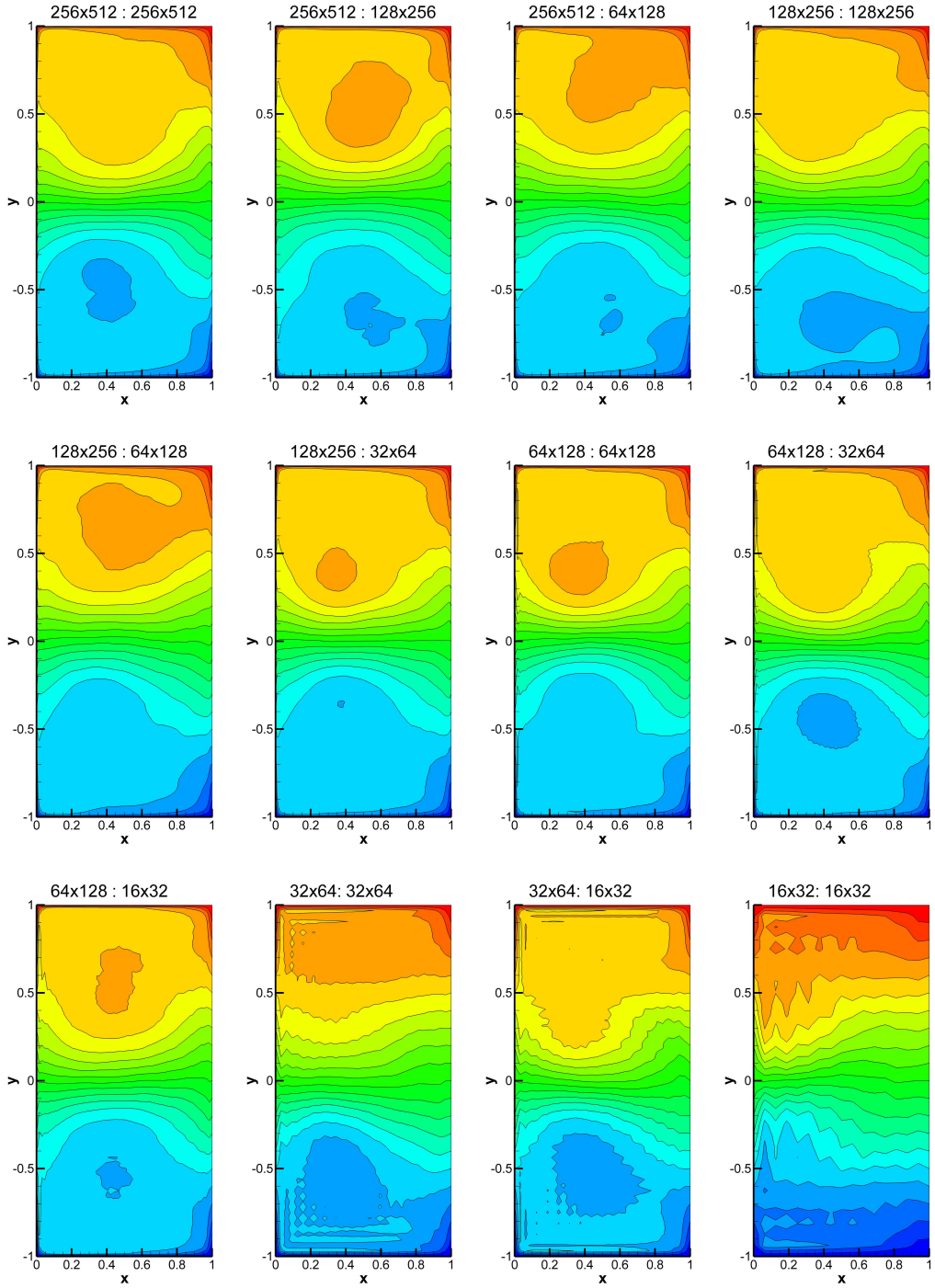

Figure 3.7: Experiment II: Comparison of mean potential vorticity for $Re = 312.5$ and $Ro = 0.0025$ (i.e., $\delta_M/L = 0.02$, and $\delta_I/L = 0.05$). Labels include the resolutions for both parts of the solver in the form $N_x \times N_y : M_x \times M_y$, where $N_x \times N_y$ is the resolution for the barotropic vorticity transport equation, and $M_x \times M_y$ is the resolution for the elliptic sub-problems.

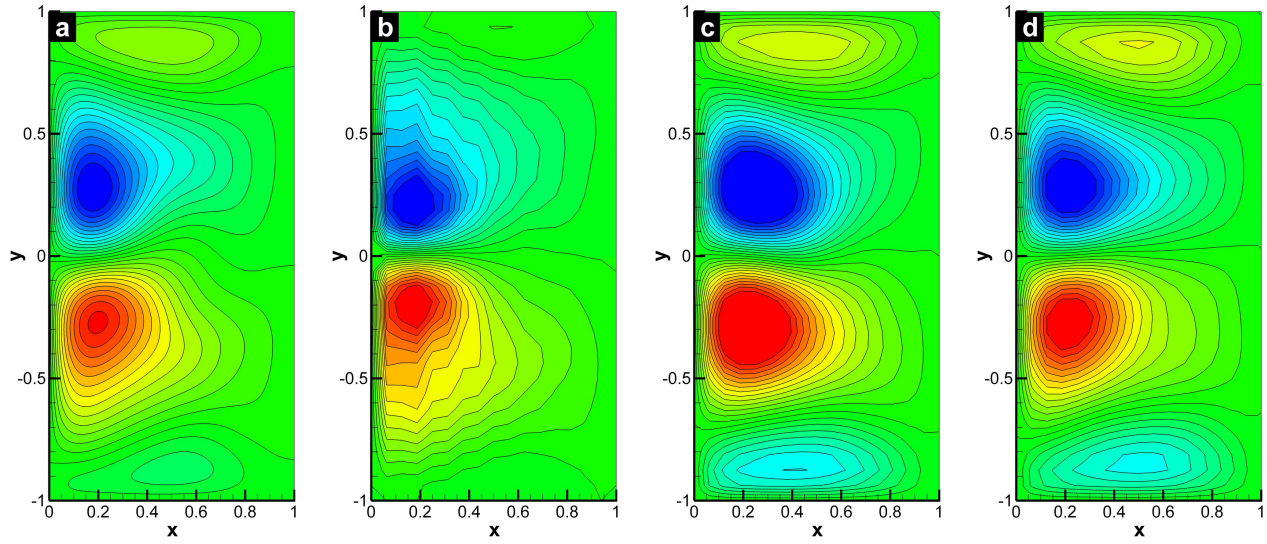

Figure 3.8: Experiment I: Comparison of mean stream function for $Re = 200$ and $Ro = 0.0016$ (i.e., $\delta_M/L = 0.02$, and $\delta_I/L = 0.04$). (a) DNS result ($256 \times 512 : 256 \times 512$), (b) standard coarse simulation without CGP ($16 \times 32 : 16 \times 32$), (c) CGP with one-level coarsening ($32 \times 64 : 16 \times 32$), and (d) CGP with two-level coarsening ($64 \times 128 : 16 \times 32$). The contour interval layouts are identical in all cases. Cases (b)-(d) have the same resolutions for the elliptic part of the problem.

regular fine and coarse computations. In these figures, the labels show the resolutions in the form of $N_x \times N_y : M_x \times M_y$, where $N_x \times N_y$ is the resolution for the time dependant potential vorticity equation, and $M_x \times M_y$ is the resolution for the elliptic sub-problem. The computed results with one level of coarsening are very close to those from the fine scale computations. Furthermore, results with two and three levels of coarsening also agree well with the fine scale computations. These results demonstrate that high fidelity numerical simulations can be obtained using the CGP method. For example, if we consider two numerical experiments with $32 \times 64 : 32 \times 64$ and $32 \times 64 : 16 \times 32$ resolutions, they have almost the same resulting flow field, but the latter results (with a half-coarsened grid for the elliptic sub-problem) were obtained almost 3 times faster than the former results (without CGP), and more importantly, the resulting field obtained using the CGP method with the $32 \times 64 : 16 \times 32$ resolution are better than those obtained on the $16 \times 32 : 16 \times 32$ grid without the CGP method.

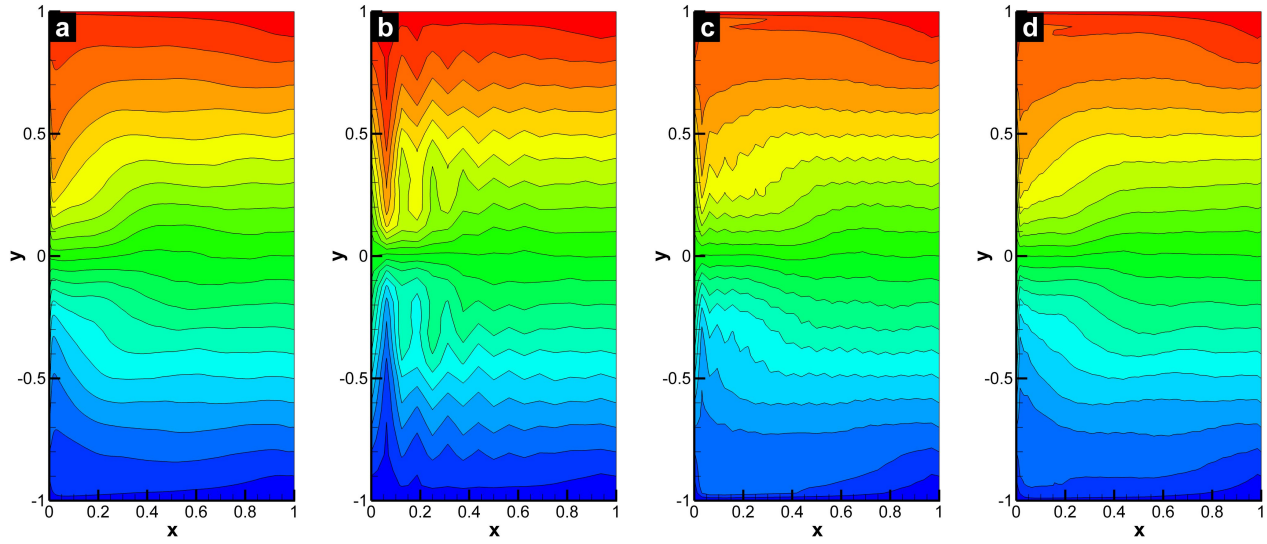

Figure 3.9: Experiment I: Comparison of mean potential vorticity for $Re = 200$ and $Ro = 0.0016$ (i.e., $\delta_M/L = 0.02$, and $\delta_I/L = 0.04$). (a) DNS result ($256 \times 512 : 256 \times 512$), (b) standard coarse simulation without CGP ($16 \times 32 : 16 \times 32$), (c) CGP with one-level coarsening ($32 \times 64 : 16 \times 32$), and (d) CGP with two-level coarsening ($64 \times 128 : 16 \times 32$). The contour interval layouts are identical in all cases. Cases (b)-(d) have the same resolutions for the elliptic part of the problem.

Similar analysis is performed for the physical setting for Experiment II which shows a quasi-periodic flow regime. Comparisons of mean stream function and potential vorticity fields are plotted in Figure 3.6 and Figure 3.7, respectively. Similar to previous analysis, it is clear from these figures that the results using the CGP method agree well with the results of the fine scale computations using the standard method with a considerable reduction in computational cost. We emphasize that, for both parameter sets, *four gyres* are clearly visible in the stream function plots. It is more clear in Experiment II due to higher variability in quasi statistically steady state. These results demonstrate that the CGP methodology can provide an accelerated method for solving large scale QG models for ocean circulation problem.

In order to elucidate the fidelity of the CGP method for coarser resolutions, for Experiment I, we plot the time-averaged stream function and potential vorticity contours in

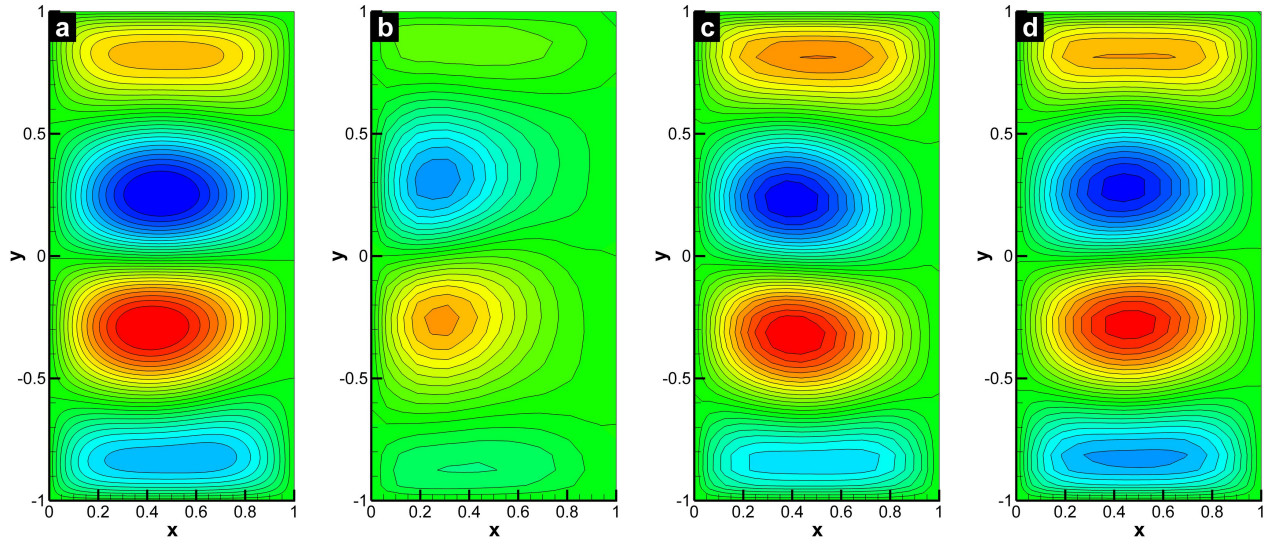

Figure 3.10: Experiment II: Comparison of mean stream function for $Re = 312.5$ and $Ro = 0.0025$ (i.e., $\delta_M/L = 0.02$, and $\delta_I/L = 0.05$). (a) DNS result ($256 \times 512 : 256 \times 512$), (b) standard coarse simulation without CGP ($16 \times 32 : 16 \times 32$), (c) CGP with one-level coarsening ($32 \times 64 : 16 \times 32$), and (d) CGP with two-level coarsening ($64 \times 128 : 16 \times 32$). The contour interval layouts are identical in all cases. Cases (b)-(d) have the same resolutions for the elliptic part of the problem.

Figure 3.8 and Figure 3.9, respectively. We include the high-resolution DNS results as well. In these figures, all results except the DNS are obtained with a constant resolution of 16×32 for the elliptic sub-problem. One and two level coarsening methods are compared with non-coarsening standard procedure. We note that the new CGP models with both one-level and two-level coarsening yield improved results by smoothing out the numerical oscillations present in the results obtained by under-resolved standard computations without CGP method. This improvement is more clearly displayed in the potential vorticity contour plot in Figure 3.9. Similar observations can be drawn from Figure 3.10 and Figure 3.11 for Experiment II. The CGP model yields results that are significantly better than those corresponding to the under-resolved BVE simulations having the same resolution for the elliptic sub-problem. In computational point of view, the price of CCM simulations are close to the price of the coarse grid simulation (i.e., the price of mapping operators and explicit time integration procedure is smaller than the price of solving elliptic sub-problem), while

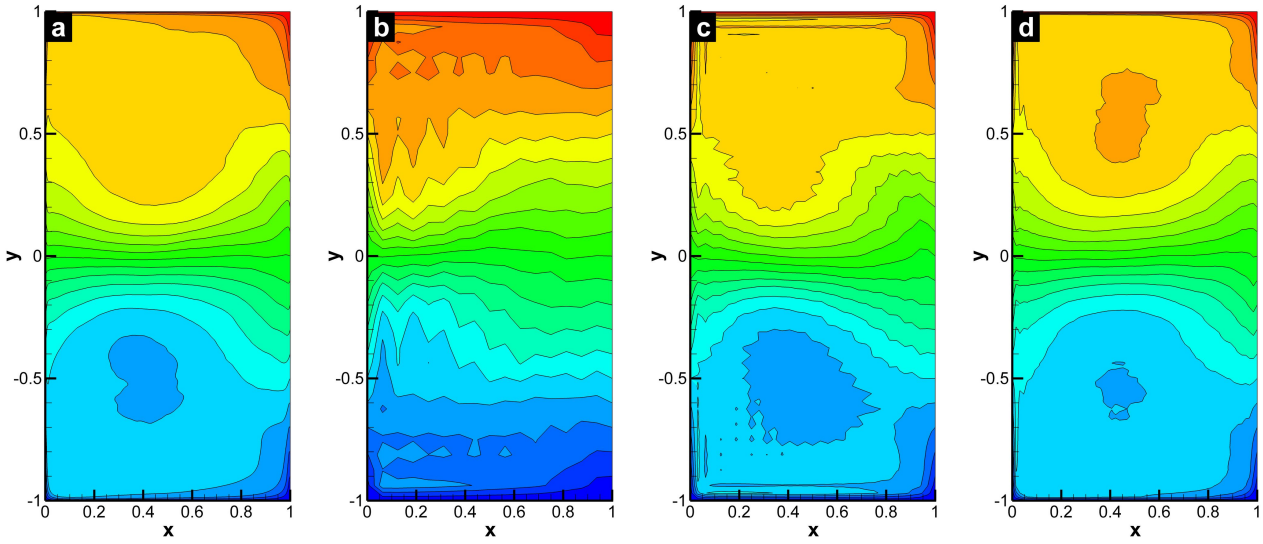

Figure 3.11: Experiment II: Comparison of mean potential vorticity for $Re = 312.5$ and $Ro = 0.0025$ (i.e., $\delta_M/L = 0.02$, and $\delta_I/L = 0.05$). (a) DNS result ($256 \times 512 : 256 \times 512$), (b) standard coarse simulation without CGP ($16 \times 32 : 16 \times 32$), (c) CGP with one-level coarsening ($32 \times 64 : 16 \times 32$), and (d) CGP with two-level coarsening ($64 \times 128 : 16 \times 32$). The contour interval layouts are identical in all cases. Cases (b)-(d) have the same resolutions for the elliptic part of the problem.

giving the same results as the high-resolution computations. In these computations we use a linear-cost fast Poisson solver, which is indeed one of the fastest elliptic solvers, and the CGP method yields a 3-8 fold reduction in computational cost. As discussed earlier, we highlight that the speed ups would be greater if we used a quadratic-cost sub-optimal elliptic solver.

3.5.2 CGP experiments for two-layer QG model

The main goal of this section is to test the CGP method in the numerical simulation of the two-layer QG model, which is a standard prototype representing many characteristics of more realistic ocean dynamics including stratification and baroclinic effects. To evaluate the performance of CGP method, we utilize two different parameter sets, corresponding to two physical oceanic settings: (i) Experiment 1 represents a moderate ocean basin with the physical parameters used by Özgökmen and Chassignet (1998), (ii) Experiment 2 represents

Table 3.2: Physical parameter sets used in the numerical experiments.

Variable (unit)	Experiment 1	Experiment 2
L (km)	2000	5000
H_1 (km)	1.0	0.6
H_2 (km)	4.0	3.4
f_0 (s^{-1})	9.35×10^{-5}	9.35×10^{-5}
β $(m^{-1}s^{-1})$	1.75×10^{-11}	1.75×10^{-11}
ρ_1 (kgm^{-3})	1030	1030
g' (ms^{-2})	0.02	0.02
τ_0 (Nm^{-2})	0.1	0.1
γ (s^{-1})	5×10^{-8}	4×10^{-7}
ν (m^2s^{-1})	50	100
δ_M (km)	14.19	17.88
δ_S (km)	2.86	22.86
δ_I (km)	31.56	25.77
R_d (km)	42.79	31.16
V (ms^{-1})	0.0174	0.0116
L/V $(year)$	3.64	13.64
Ro	2.49×10^{-4}	2.66×10^{-5}
Fr	0.087	0.073
σ	1.43×10^{-3}	4.57×10^{-3}
A	3.57×10^{-7}	4.57×10^{-8}
δ	0.2	0.15
Re	697.16	580.97

a large ocean basin with the physical parameters used by Tanaka and Akitomo (2010). In terms of the classification given by Berloff and McWilliams (1999), both sets of experiments lie under the chaotic regime. The physical parameters and corresponding dimensionless parameters are summarized in Table 3.2.

We start by performing a DNS on a fine mesh of 512^2 spatial resolution. Similar to the one-layer analysis, we emphasize that the term DNS in this study is not meant to indicate

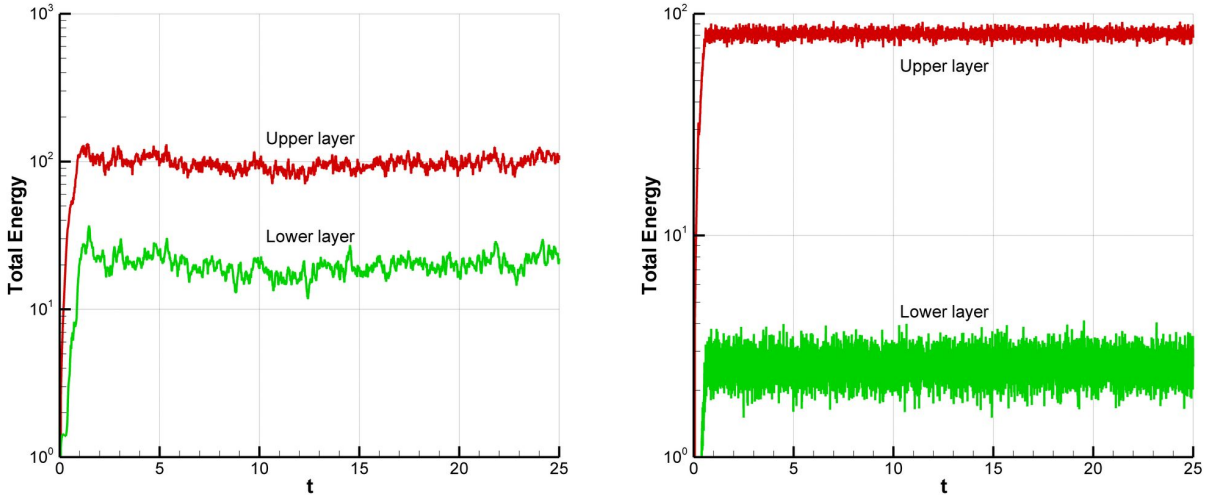

(a) Experiment 1

(b) Experiment 2

Figure 3.12: Time histories of basin integrated total kinetic energy for upper and lower layers.

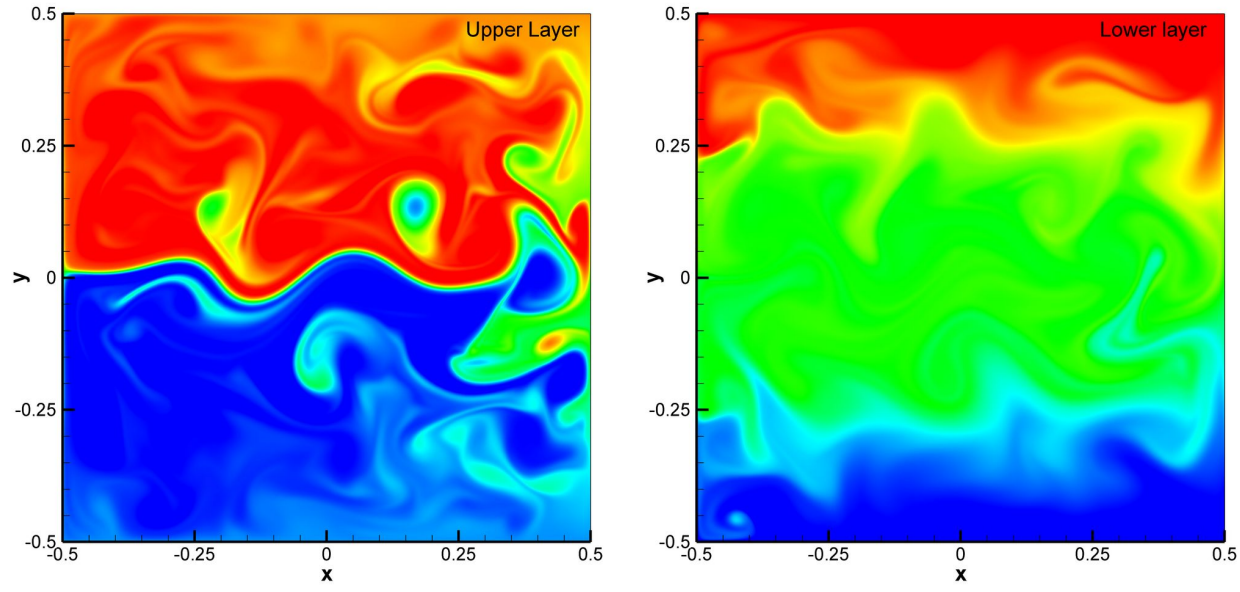

Figure 3.13: Instantaneous potential vorticity contour plots at time $t = 25$ for Experiment 1.

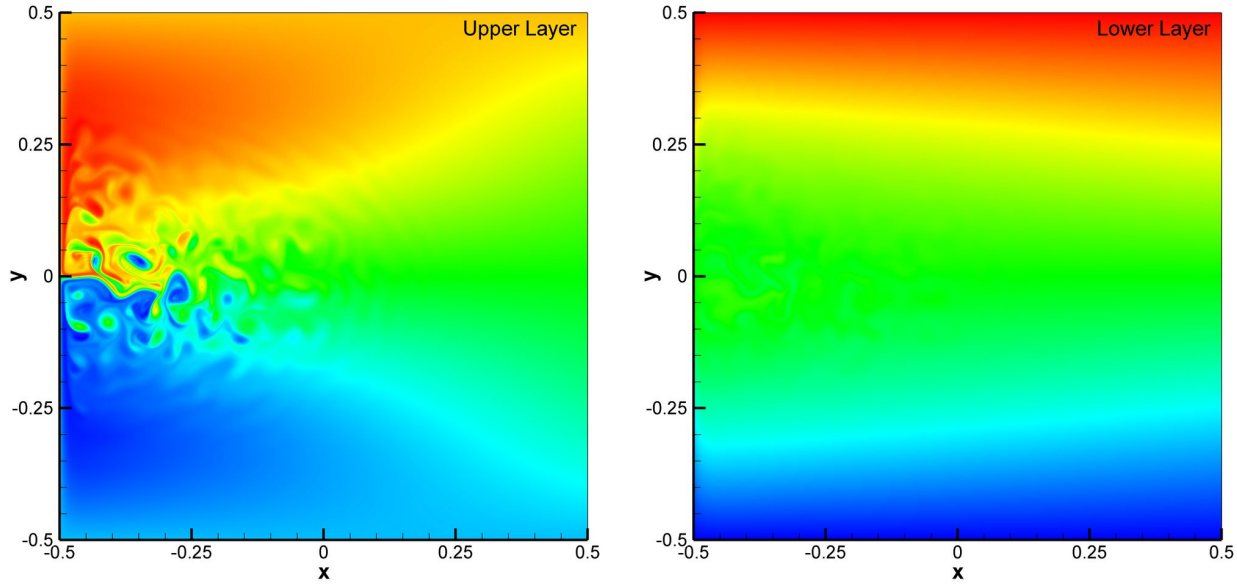

Figure 3.14: Instantaneous potential vorticity contour plots at time $t = 25$ for Experiment 2.

that a fully detailed solution is being computed on the molecular viscosity scale, but instead refers to resolving the simulation down to the Munk scale via the specified lateral eddy viscosity parameterization. A statistically steady state solution is obtained after an initial transient spin-up process. The basin integrated total kinetic energy is

$$E_i(t) = \frac{1}{2} \iint \left(\frac{\partial \psi_i}{\partial x} \right)^2 + \left(\frac{\partial \psi_i}{\partial y} \right)^2 dx\, dy, \tag{3.63}$$

where the subscript i represents the layer index. Figure 3.12 shows the time history of the basin integrated kinetic energy for the upper and lower layers for both of the oceanic settings. As shown in this figure, the system reaches the statistically steady state after the dimensionless time $t = 1$. As expected, the total energy of the upper layer is much larger than that in the lower layer. It is important to emphasize that, second layer in Experiment 1 is more active than that of Experiment 2. Instantaneous contour plots for the potential vorticities in the upper and lower layers are shown in Figure 3.13 and Figure 3.14 for Experiment 1 and Experiment 2, respectively. The length scales in these two experiments are

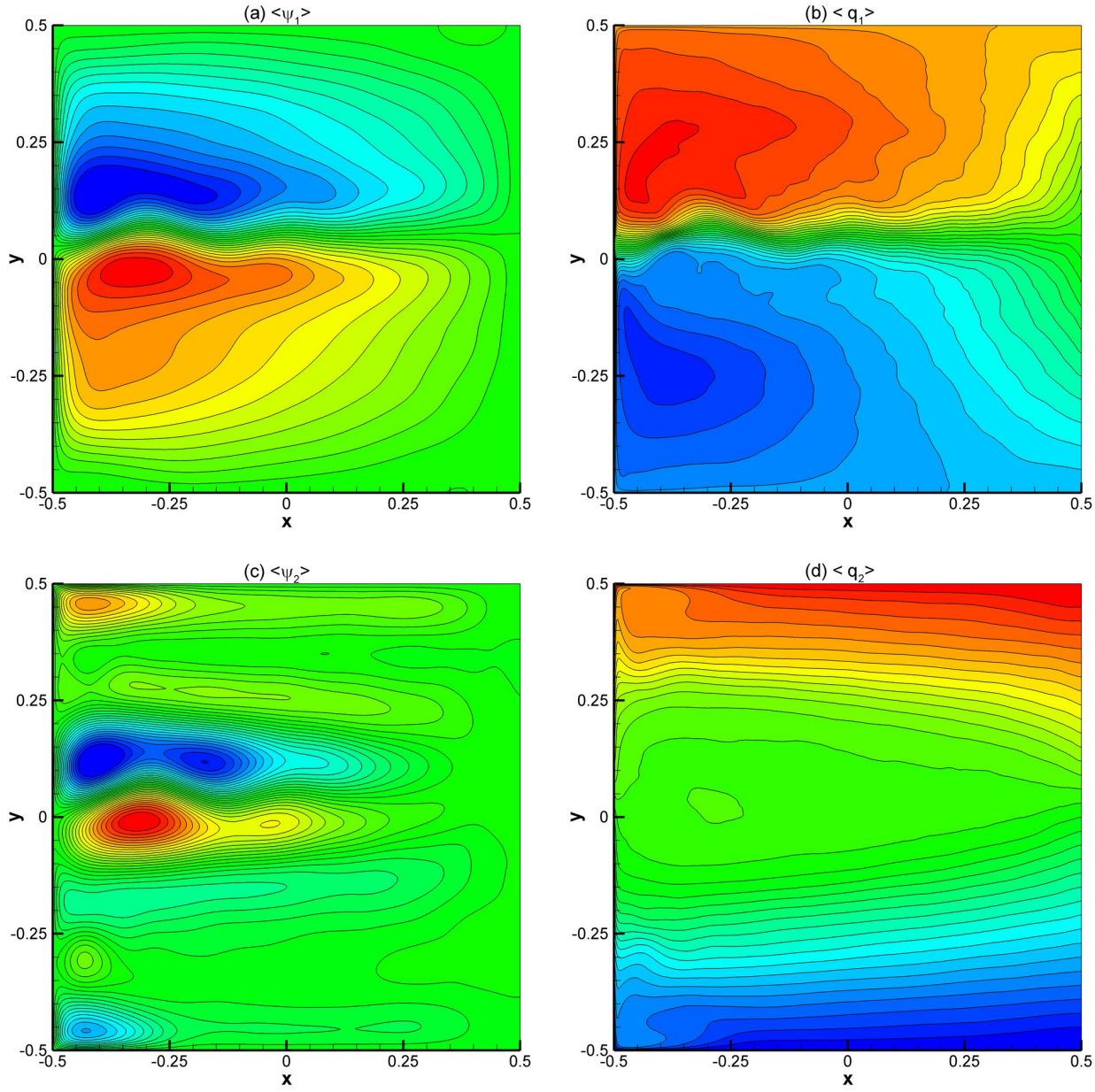

Figure 3.15: Experiment 1: DNS results for (a) mean stream function contours for the upper layer, (b) mean potential vorticity contours for the upper layer, (c) mean stream function contours for the lower layer, and (d) mean potential vorticity contours for the lower layer.

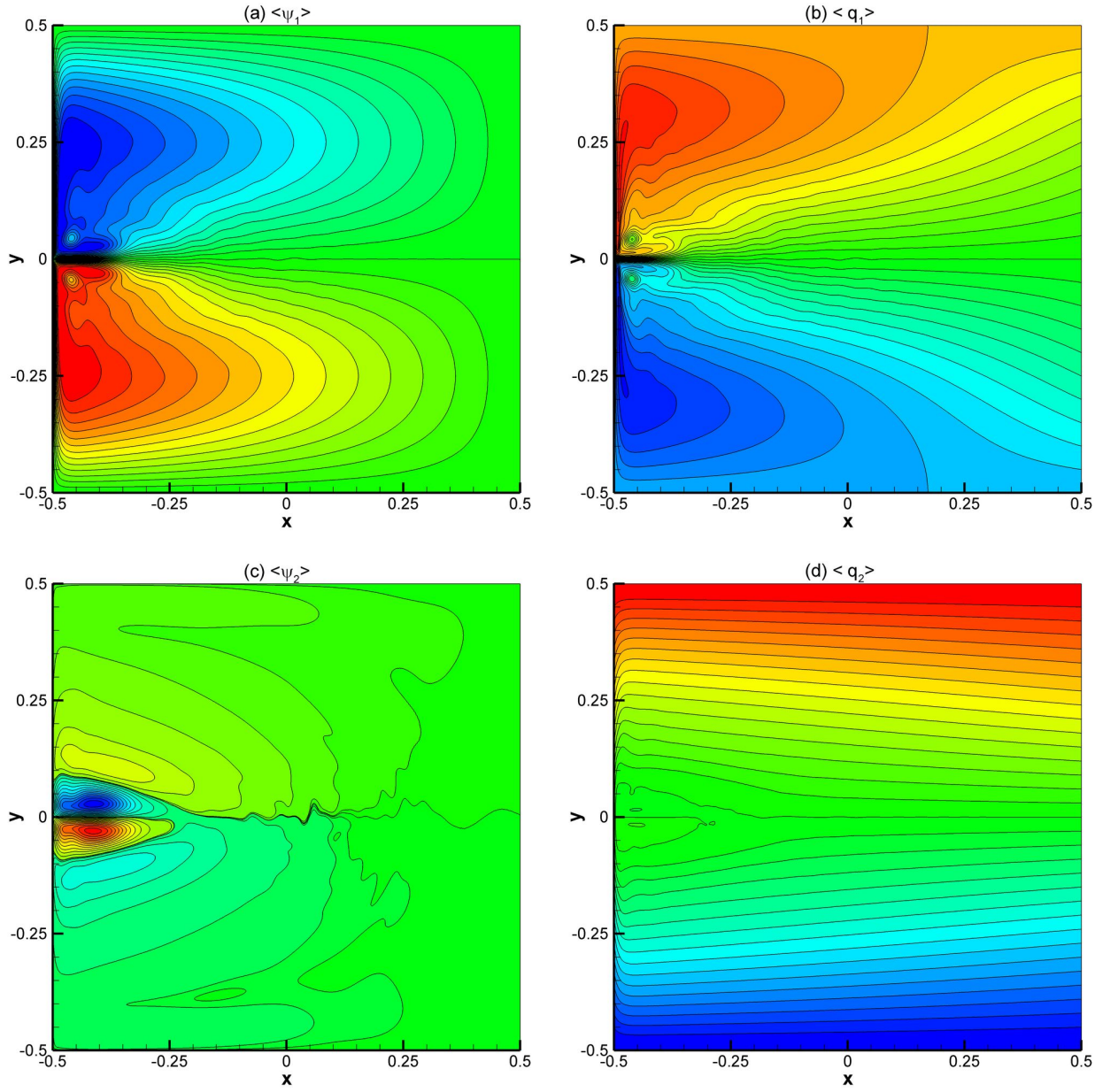

Figure 3.16: Experiment 2: DNS results for (a) mean stream function contours for the upper layer, (b) mean potential vorticity contours for the upper layer, (c) mean stream function contours for the lower layer, and (d) mean potential vorticity contours for the lower layer.

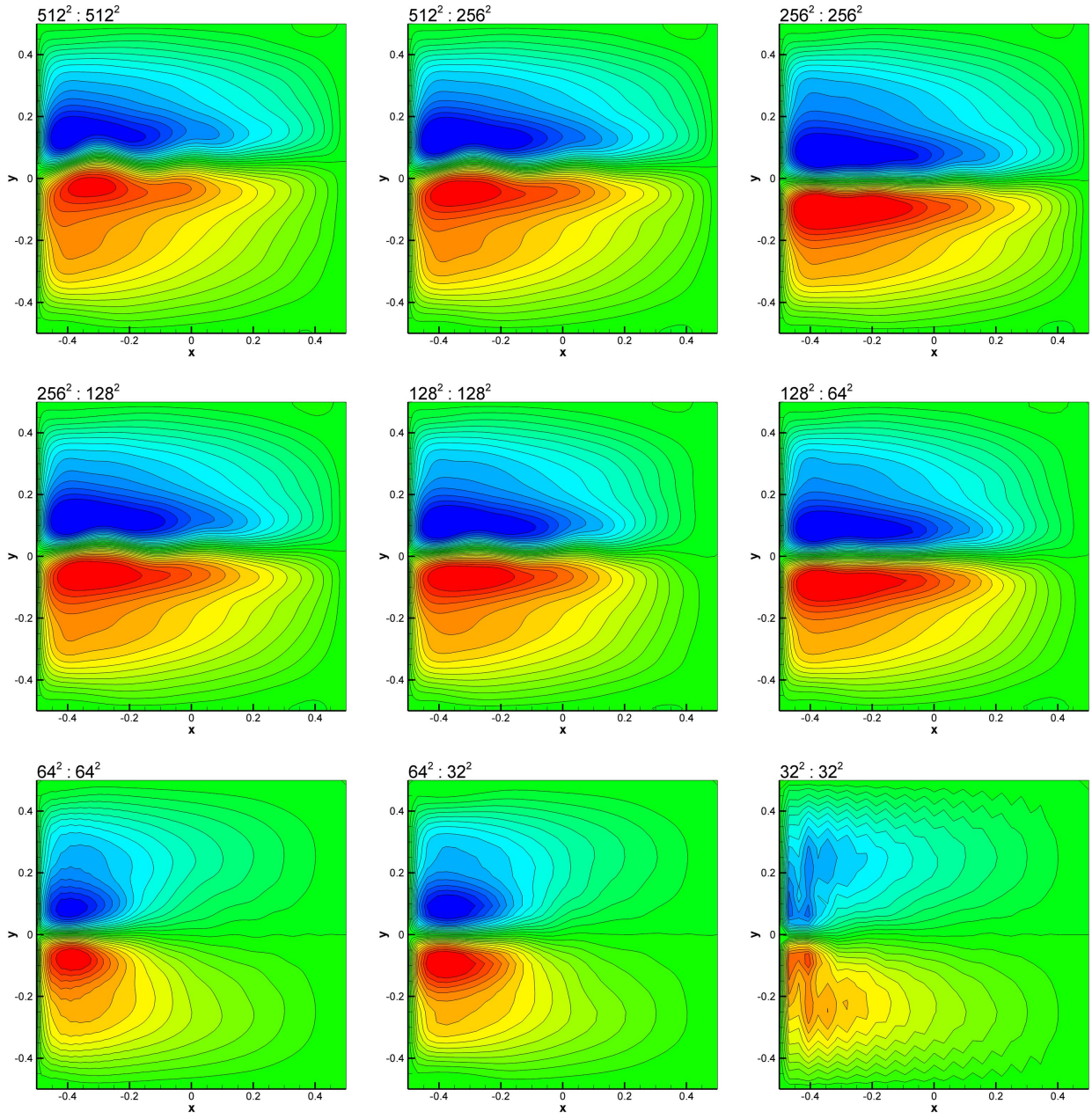

Figure 3.17: Comparison of mean stream function for the upper layer for the Experiment 1. Labels include the resolutions for both parts of the solver in the form $N^2 : M^2$, where N^2 is the resolution for the vorticity transport equations, and M^2 is the resolution for the elliptic sub-problems.

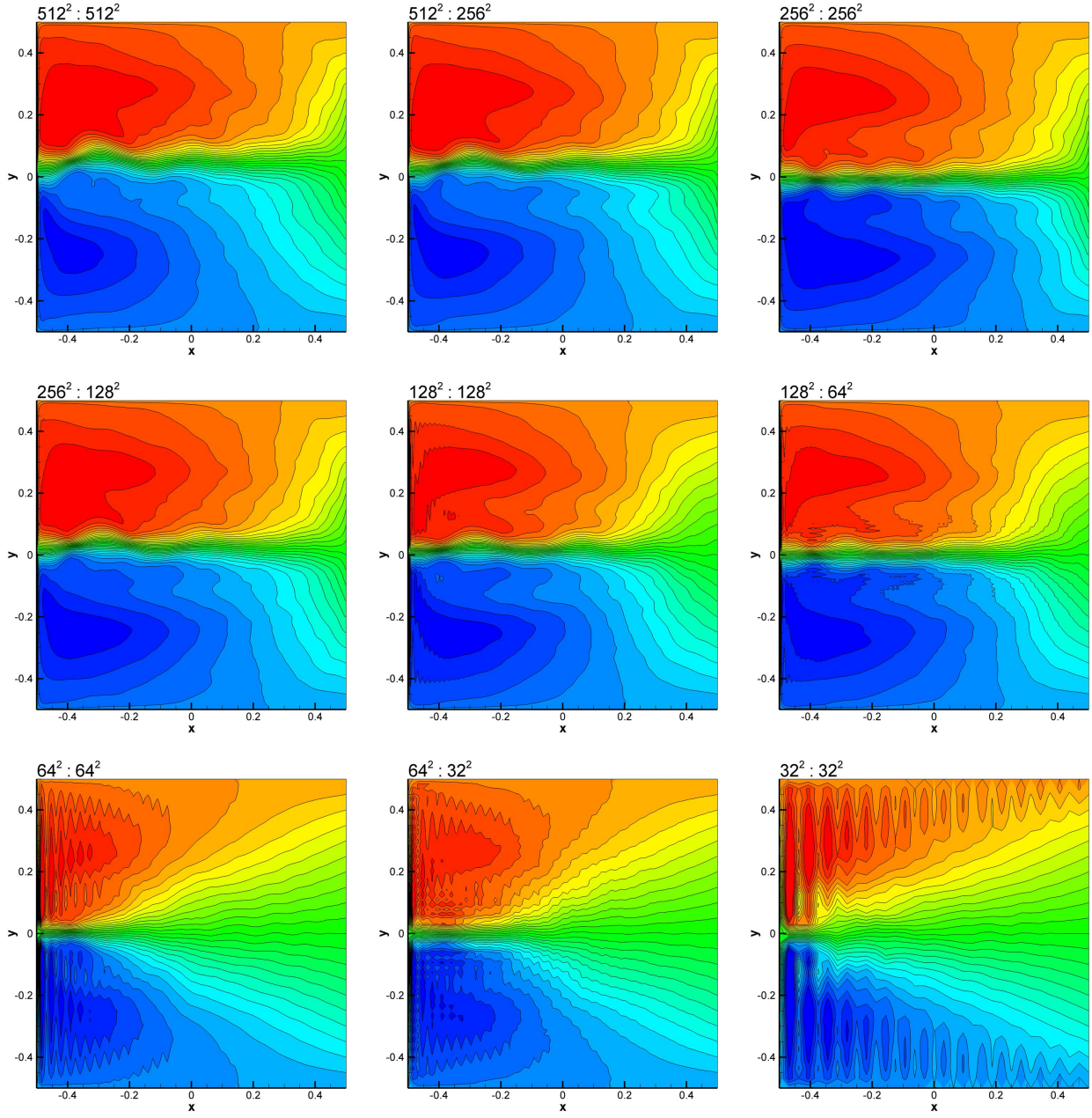

Figure 3.18: Comparison of mean potential vorticity for the upper layer for the Experiment 1. Labels include the resolutions for both parts of the solver in the form $N^2 : M^2$, where N^2 is the resolution for the vorticity transport equations, and M^2 is the resolution for the elliptic sub-problems.

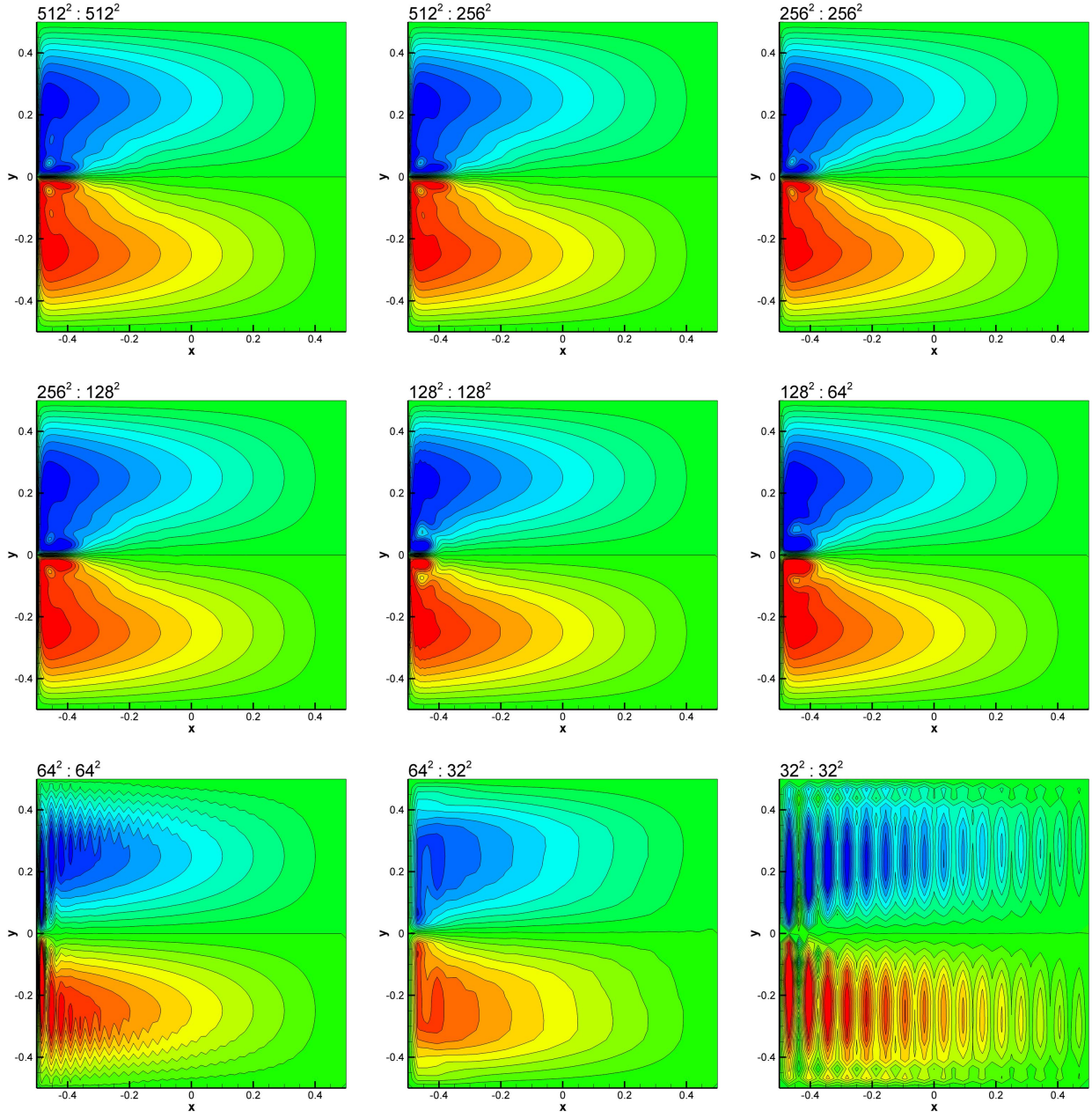

Figure 3.19: Comparison of mean stream function for the upper layer for the Experiment 2. Labels include the resolutions for both parts of the solver in the form $N^2 : M^2$, where N^2 is the resolution for the vorticity transport equations, and M^2 is the resolution for the elliptic sub-problems.

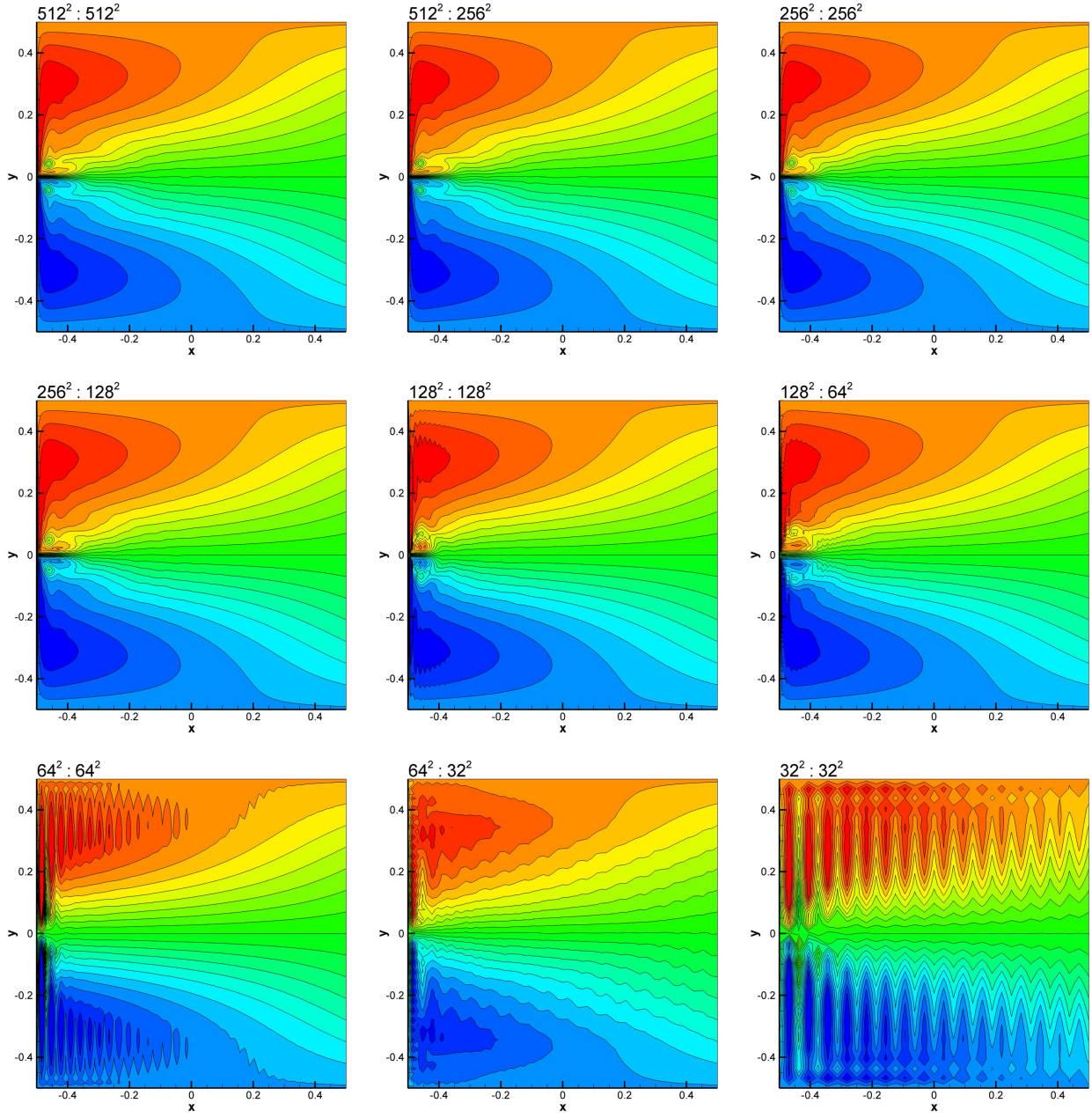

Figure 3.20: Comparison of mean potential vorticity for the upper layer for the Experiment 2. Labels include the resolutions for both parts of the solver in the form $N^2 : M^2$, where N^2 is the resolution for the vorticity transport equations, and M^2 is the resolution for the elliptic sub-problems.

quite different. For example, the ratio of the basin length scale L to the Rossby deformation radius R_d is $L/R_d = 46.74$ for Experiment 1 and $L/R_d = 160.5$ for Experiment 2. Therefore, the structure of the eastward jet formation on the western boundary for Experiment 1 is different from that of Experiment 2. This difference becomes more obvious in the mean flow field. The results for time-averaged mean field data obtained from 75 thousands snapshots between time $t = 10$ and $t = 25$ in the statistically steady state are given in Figure 3.15 and Figure 3.16. The results show strong western boundary currents with cyclonic (counter-clockwise rotating) subpolar gyres and anticyclonic (clockwise rotating) subtropical gyres producing a strong eastward jet in both experiments. However, the produced eastward jet formation in Experiment 1 shows swirling structure and almost reaches the eastern boundary of the basin. Compared to Experiment 2, the bottom layer is more active in Experiment 1. Since in Experiment 1 we used the same parameters and boundary conditions as in Özgökmen and Chassignet (1998), the plot in Figure 3.16 is similar to Figure 2 in Özgökmen and Chassignet (1998). Although in Experiment 2 we have used the same parameters as those used in Tanaka and Akitomo (2010), the boundary conditions we used are different from their boundary conditions: we used the slip boundary conditions, whereas they used the no-slip boundary conditions. Thus, the plot in Figure 3.15 is different from the corresponding one in Tanaka and Akitomo (2010).

To test the CGP method, we employ the standard coarsening methodology. The criterion used in assessing the success of the new CGP model is its ability to produce more accurate (i.e., closer to the DNS) results than those for standard method without CGP having the same resolution for elliptic sub-problem, without a significant increase in computational time. For Experiment 1, we plot the mean stream function and potential vorticity contours in Figure 3.17 and Figure 3.18, respectively. The various resolutions used in the computations are written in the labels of the subfigures. The labels include the resolution for the time dependant part and the resolution for the elliptic part, as described in the captions. As was the case in previous analysis for one-layer model, we compare the CGP computations with standard computations without CGP. For example, the flow field obtained by a standard

computation with $128^2 : 128^2$ agrees well with that obtained by the CGP method with $128^2 : 64^2$, and better than that of the standard computation with $64^2 : 64^2$. Similar observations holds for higher and lower resolution computations as well. It can clearly be seen that the CGP approach provides results at the same level of accuracy, but at a reduced computational cost compared to the standard, fine-resolution simulations, by reducing the resolution of the elliptic sub-problem.

Similarly, we plot the mean stream function and potential vorticity contours in Figure 3.19 and Figure 3.20 for Experiment 2. We note that the proposed CGP model yields again improved results by smoothing out the numerical oscillations present in the under-resolved standard simulations without CGP. The numerical results for both experiments clearly suggest that the the CGP model can provide relatively accurate results for stratified geophysical flows at a low computational cost.

3.6 Conclusions

A new coarse-grid projection (CGP) multiscale method was introduced for large-scale ocean circulation models. The CGP method was tested in the numerical simulation of the wind-driven circulation in both one-layer and two-layer ocean basins, standard prototypes of more realistic ocean dynamics. The first mathematical model employed was the barotropic vorticity equation (BVE) for the one-layer quasigeostrophic model, which is driven by a symmetric double-gyre wind forcing that yielded a four-gyre circulation in the time mean. The second mathematical model used was the two-layer quasigeostrophic equations for a stratified ocean model accounting for baroclinic effects.

In the CGP methodology the cost of large-scale ocean dynamics computations is reduced by coarsening the number of grid points used for the solution of the elliptic sub-problem in quasigeostrophic (QG) ocean models. The CGP approach is general and in fact constitutes a family of methods, since in addition to choosing the coarsening and prolongation operators

and the time integration scheme, the elliptic solver used in the approach can vary. In this work, we investigated the performance of a particular CGP method that uses an optimal FFT based elliptic solver, the full weighting operation for the coarsening operator, and bilinear interpolation for the prolongation operator. We used the spatially second-order accurate fully conservative Arakawa scheme along with the third-order TVD Runge-Kutta time integration scheme. The CGP method was tested on meshes that were coarser than those used for the direct numerical simulation (DNS) computations. The CGP method yielded numerical results that were in close agreement with those of the DNS for both barotropic and stratified ocean circulation models. In particular, we found that the new CGP models with both one-level and multiple-level coarsening yield improved results by smoothing out the numerical oscillations present in the results obtained by under-resolved standard computations without the CGP procedure. This first step in the numerical assessment of the proposed ocean circulation models shows that CGP methodology could represent a viable tool for QG models of more realistic turbulent geophysical flows.

Chapter 4

High-Order Methods for Decaying Two-Dimensional Homogeneous Isotropic Turbulence

Numerical schemes used for the integration of complex flow simulations should provide accurate solutions for the long time integrations these flows require. To this end, the performance of various high-order accurate numerical schemes is investigated for direct numerical simulations (DNS) of homogeneous isotropic two-dimensional decaying turbulent flows. The numerical accuracy of compact difference, explicit central difference, Arakawa, and dispersion-relation-preserving schemes are analyzed and compared with the Fourier-Galerkin pseudospectral scheme. In addition, several explicit Runge-Kutta schemes for time integration are investigated. We demonstrate that the centered schemes suffer from spurious Nyquist signals that are generated almost instantaneously and propagate into much of the field when the numerical resolution is insufficient. We further show that the order of the scheme becomes increasingly important for increasing cell Reynolds number. Surpris-

O. San and A. E. Staples, "High-order methods for decaying two-dimensional homogeneous isotropic turbulence," *Computers & Fluids*, vol. 63, pp. 105–127, 2012. Reprinted with permission from Computers & Fluids, Elsevier.

ingly, the sixth-order schemes are found to be in perfect agreement with the pseudospectral method. Considerable reduction in computational time compared to the pseudospectral method is also reported in favor of the finite difference schemes. Among the fourth-order schemes, the compact scheme provides better accuracy than the others for fully resolved computations. The fourth-order Arakawa scheme provides more accurate results for under-resolved computations, however, due to its conservation properties. Our results show that, contrary to conventional wisdom, difference methods demonstrate superior performance in terms of accuracy and efficiency for fully resolved DNS computations of the complex flows considered here. For under-resolved simulations, however, the choice of difference method should be made with care.

4.1 Introduction

The physics of two-dimensional turbulence have been elucidated substantially during the past decades by theoretical models, intensive numerical investigations, and dedicated soap film experiments (Bruneau and Fischer, 2009). Two-dimensional turbulence research efforts have applicability in geophysics, astronomy and plasma physics, in which numerical experiments play a large role. One of the most important reasons for studying two-dimensional turbulence is to improve our understanding of geophysical flows in the atmosphere and ocean (Lilly, 1971; Herring et al., 1974; McWilliams, 1984; Maltrud and Vallis, 1991; Lindborg, 1999; Ferziger et al., 2002; San et al., 2011). We may also find two-dimensional flows in a wide variety of situations such as flows in rapidly rotating systems and flows in a fluid film on top of the surface of another fluid or a rigid object (Kolvin et al., 2009).

Two-dimensional turbulence behaves in a profoundly different way from three-dimensional turbulence due to different energy cascade behavior, and follows the Kraichnan-Batchelor-Leith (KBL) theory (Kraichnan, 1967; Batchelor, 1969; Leith, 1971). In three-dimensional turbulence, energy is transferred forward, from large scales to smaller scales, via vortex

stretching. In two dimensions that mechanism is absent, and it turns out that under most forcing and dissipation conditions energy will be transferred from smaller scales to larger scales. This is largely because of another quadratic invariant, the potential enstrophy, defined as the integral of the square of the potential vorticity. Despite the apparent simplicity in dealing with two rather than three spatial dimensions, two-dimensional turbulence is possibly richer in its dynamics than three-dimensional turbulence due to its conservation properties, such as its inverse energy and forward enstrophy cascading mechanisms. Danilov and Gurarie (2000) and Tabeling (2002) reviewed both theoretical and experimental two-dimensional turbulence studies along with extensions into geophysical flow settings. More recent reviews on two-dimensional turbulence are also provided by Clercx and van Heijst (2009) and Boffetta and Ecke (2012). Recent studies in two-dimensional turbulence, both forced (stationary) turbulence (Danilov and Gurarie, 2001a; Boffetta and Musacchio, 2010; Bracco and McWilliams, 2010; Vallgren and Lindborg, 2011) and unforced (decaying) turbulence (Lindborg and Vallgren, 2010; Kuznetsov et al., 2010; Fox and Davidson, 2010) provide high resolution computational confirmation of the KBL theory.

Simulation of turbulent and other convection-dominated unsteady flows using direct numerical simulation (DNS) requires a numerical method that properly resolves all the multiscale flow structures (Orlandi, 2000). Since high accuracy is crucial in numerical simulation of complex flows with multiscale structures, such as the unsteady evolution of a turbulent flow field, most two-dimensional turbulence studies have been performed using pseudospectral methods based on fast Fourier transform (FFT) algorithms (Lindborg and Vallgren, 2010; Boffetta and Ecke, 2012). Simulations performed by the lattice Boltzmann method (LBM) have been also presented for two-dimensional decaying turbulence Házi and Jiménez (2006). Pseudospectral methods are highly accurate but mostly limited to ideal geometries such as rectangular or circular domains. Discretization methods such as finite difference, finite element, or finite volume methods are often preferred in more realistic problems. Finite difference methods offer an attractive alternative to spectral methods in the direct and large eddy simulations (LES) of turbulence providing reasonable accuracy coupled with rel-

ative ease of implementation in simple and complex flow geometries (Tafti, 1996; Jordan and Ragab, 1996a; Ekaterinaris, 2005; Merle et al., 2010). Computational algorithms developed in the past were mainly designed for solving large-scale fluid dynamics problems using second-order spatial accuracy (Harlow and Welch, 1965; Lilly, 1965; Mavriplis, 1997). These algorithms usually have rather significant dispersion errors and if they are not centered schemes they also have large dissipation errors, making it hard to accurately compute fine structures in the flow field using them (Mattsson et al., 2007). There are two ways to improve the resolution of these methods; one is to refine the grid and the other is to construct a high-order accurate scheme. Our approach here is to test and evaluate different high-order formulations for instantaneous and statistical properties of two-dimensional turbulence and compare their accuracy and efficiency with those of the pseudospectral and the second-order schemes. Furthermore, it has been shown by Kravchenko and Moin (1997) that the subgrid-scale models in LES are effective only if central discretization of order higher than two is employed. With this in mind, we will investigate the behavior of four different families of high-order accurate finite difference methods in the decay of two-dimensional isotropic turbulence.

High-order finite difference schemes can be formulated to reduce the truncation errors associated with the difference approximations. A straightforward Taylor series expansion of a pointwise discretization under certain assumptions results in a family of the explicit difference (ED) schemes. The compact difference (CD) schemes feature high-order accuracy with smaller stencils and smaller truncation errors than the ED schemes, and have been employed as an alternative to spectral methods in simulations of turbulence with great flexibility (Lele, 1992). On the other hand, increasing the stencil size allows us to optimize the weight coefficients in the difference equation. This strategy leads to the dispersion-relation-preserving (DRP) schemes (Tam and Webb, 1993), which have been used mostly in acoustics. Another strategy to construct a numerical scheme is based on the conservation properties of the discrete form of the equations. Arakawa (1966) suggested that the conservation of energy, enstrophy, and skew-symmetry is sufficient to avoid computational instabilities

stemming from nonlinear interactions. The conservation and stability properties of the Arakawa scheme were investigated by Lilly (1965) by means of spectral analysis along with several first and second-order time integration methods. In the present work, we test several Runge-Kutta methods for time integration, although the primary goal here is to analyze the accuracy of these high-order accurate spatial differencing methods for the long-term evolution of complex two-dimensional turbulent flows. For finite difference schemes, the combination of differentiation errors and nonlinear truncation and aliasing errors, which usually manifest themselves in the high wavenumbers of the resolved scales, determines the overall error at the small scales. Looking at the accuracy of the whole solution procedure we also investigate the resolution requirements for these finite difference families, the effects of the order of the schemes, and the importance of the global conservation properties.

The paper is organized as follows: the mathematical formulation of the problem is given in Section 4.2. The numerical methods are presented in Section 4.3 with descriptions of high-order accurate spatial discretization schemes, temporal discretization algorithms, and an efficient fast Poisson solver algorithm. These schemes are validated in Section 4.4 by simulating the Taylor-Green decaying vortex benchmark problem for the unsteady incompressible Navier-Stokes equations. The effective accuracies of these methods are also provided in this section, and are confirmed to be the theoretical accuracies of the schemes. Section 4.5 presents a careful numerical investigation of their performance for a challenging benchmark problem which consists of strong shear layers. The results for two-dimensional isotropic homogeneous decaying turbulence are provided in Section 4.6. The behavior of these nine different spatial schemes are tested in terms of accuracy and efficiency. The effects of several explicit Runge-Kutta time advancement techniques on the whole solution procedure are also analyzed. In addition, the Reynolds number (Re) dependency of the turbulence statistics is illustrated in this section. Final conclusions and some comments on the performance of these schemes are drawn in section 4.7.

4.2 Mathematical model

The governing equations for two-dimensional incompressible flows can be written in a dimensionless form of the vorticity-stream function formulation as

$$\frac{\partial \omega}{\partial t} + \frac{\partial \psi}{\partial y}\frac{\partial \omega}{\partial x} - \frac{\partial \psi}{\partial x}\frac{\partial \omega}{\partial y} = \frac{1}{Re}\left(\frac{\partial^2 \omega}{\partial x^2} + \frac{\partial^2 \omega}{\partial y^2}\right) \tag{4.1}$$

along with the kinematic relationship between vorticity and stream function according to a Poisson equation, which is given as

$$\frac{\partial^2 \psi}{\partial x^2} + \frac{\partial^2 \psi}{\partial y^2} = -\omega. \tag{4.2}$$

From a computational point of view, this formulation has several advantages over the primitive variable formulation. It eliminates pressure from the Navier-Stokes equations and hence has no corresponding odd-even decoupling between the pressure and velocity components, as well as projection inaccuracies usually observed in fractional step approaches (Brown et al., 2001). Therefore, the usage of a collocated grid does not produce any spurious modes in the vorticity-stream function formulation. The vorticity-stream function formulation automatically satisfies the divergence-free condition and allows one to reduce the number of equations to be solved.

The main objective of our work is to test and evaluate different frameworks for high-order accurate finite difference schemes and compare them with a spectrally accurate pseudospectral method for two-dimensional isotropic turbulent flows. In fact, to be able to compare the numerical schemes more precisely we restricted ourselves to periodic boundary conditions and a uniform Cartesian grid. Consequently, we eliminated errors coming from the mesh non-uniformities and inconsistent boundary schemes. It should also be noted that using the vorticity-stream function formulation on a collocated grid provides us with an ideal computational setting in which to test the characteristics of the numerical schemes by eliminating

any possible errors coming from projection inaccuracies.

4.3 Numerical methods

The objective of the present work is to test and evaluate different frameworks for high-order accurate finite difference schemes and compare them with a spectrally accurate pseudospectral method for two-dimensional isotropic turbulence flows. We will also compare them with their classical second-order accurate formulations in order to analyze the effects of order of accuracy. In the text that follows, the high-order finite difference approximations for spatial discretization, the pseudospectral method, an efficient procedure for the Poisson equation, and the time integration methods that we utilize for time advancement are given briefly for completeness.

4.3.1 Explicit difference (ED) scheme

For any scalar pointwise value of f the classical centered finite difference schemes for the first derivative up the the sixth order accuracy are given by (Strikwerda, 2004)

$$f'_i = \frac{1}{2h}(-f_{i-1} + f_{i+1}) + O(h^2) \tag{4.3}$$

$$f'_i = \frac{1}{12h}(f_{i-2} - 8f_{i-1} + 8f_{i+1} - f_{i+2}) + O(h^4) \tag{4.4}$$

$$f'_i = \frac{1}{60h}(-f_{i-3} + 9f_{i-2} - 45f_{i-1} + 45f_{i+1} - 9f_{i+2} + f_{i+3}) + O(h^6) \tag{4.5}$$

Similarly, the second derivative approximations become

$$f''_i = \frac{1}{h^2}(f_{i-1} - 2f_i + f_{i+1}) + O(h^2) \tag{4.6}$$

$$f''_i = \frac{1}{12h^2}(-f_{i-2} + 16f_{i-1} - 30f_i + 16f_{i+1} - f_{i+2}) + O(h^4) \tag{4.7}$$

$$f''_i = \frac{1}{180h^2}(2f_{i-3} - 27f_{i-2} + 270f_{i-1} - 490f_i + 270f_{i+1} - 27f_{i+2} + 2f_{i+3}) + O(h^6) \tag{4.8}$$

where h is the step size in the derivative direction.

4.3.2 Compact difference (CD) scheme

Apart from the explicit centered schemes, with the cost of a tridiagonal system solution (i.e., by using the well-known Thomas algorithm), the first derivative can be computed accordingly (Lele, 1992)

$$\alpha f'_{i-1} + f'_i + \alpha f'_{i+1} = a\frac{f_{i+1} - f_{i-1}}{2h} + b\frac{f_{i+2} - f_{i-2}}{4h} \tag{4.9}$$

which gives rise to an α-family of tridiagonal schemes with $a = \frac{2}{3}(\alpha + 2)$, and $b = \frac{1}{3}(4\alpha - 1)$. Here, $\alpha = 0$ leads to the explicit non-compact fourth-order scheme for the first derivative. A classical compact fourth-order scheme, which is also known as the Padé scheme, is obtained by setting $\alpha = 1/4$. The truncation error in the Eq. (4.9) is $\frac{4}{5!}(3\alpha - 1)h^4 f^{(5)}$. Therefore, a sixth-order compact scheme is obtained by choosing $\alpha = 1/3$.

The second derivative compact centered scheme is given by

$$\alpha f''_{i-1} + f''_i + \alpha f''_{i+1} = a\frac{f_{i+1} - 2f_i + f_{i-1}}{h^2} + b\frac{f_{i+2} - 2f_i + f_{i-2}}{4h^2} \tag{4.10}$$

where $a = \frac{4}{3}(1 - \alpha)$, and $b = \frac{1}{3}(10\alpha - 1)$. For $\alpha = 1/10$ the classical fourth-order Padé scheme is obtained. The truncation error in the Eq. (4.10) is $-\frac{4}{6!}(11\alpha - 2)h^4 f^{(6)}$. Therefore, a sixth-order compact scheme is also obtained by choosing $\alpha = 2/11$.

These compact schemes for the first and second derivatives show better spectral accuracy then their explicit counterparts. However, they involve solving tridiagonal matrix equations and are therefore effectively non-local. This requires special care for designing parallel computations. However, in this study, we focus on a single domain without domain decomposition, and so the compact schemes can be adopted easily.

4.3.3 Dispersion-relation-preserving (DRP) scheme

An optimized dispersion-preserving scheme was proposed in Tam and Webb (1993). The scheme increases the stencil size, but improves the resolution in wavespace. The finite difference approximation for the first derivative is

$$f_i' = \frac{1}{h} \sum_{j=-N}^{M} a_j f_{i+j} \tag{4.11}$$

Fourth-order accuracy is obtained for $N = M = 3$ (centered DRP scheme) and the optimized coefficients are $a_0 = 0$, $a_1 = -a_{-1} = 0.79926643$, $a_2 = -a_{-2} = -0.18941314$, and $a_3 = -a_{-3} = 0.02651995$. The viscous terms can be computed by using the explicit difference schemes.

4.3.4 Arakawa scheme

Arakawa (1966) suggested that the conservation of energy, enstrophy and skew symmetry is sufficient to avoid computational instabilities arising from nonlinear interactions. The nonlinear terms in Eq. (4.1) were defined as the Jacobian

$$J(\omega, \psi) = \frac{\partial \psi}{\partial y}\frac{\partial \omega}{\partial x} - \frac{\partial \psi}{\partial x}\frac{\partial \omega}{\partial y} \tag{4.12}$$

The second-order Arakawa scheme for the Jacobian is

$$J_I(\omega, \psi) = \frac{1}{3}(J_1(\omega, \psi) + J_2(\omega, \psi) + J_3(\omega, \psi)) \tag{4.13}$$

where the discrete parts of the Jacobian

$$\begin{aligned} J_1(\omega, \psi) = \frac{1}{4h_x h_y}[&(\omega_{i+1,j} - \omega_{i-1,j})(\psi_{i,j+1} - \psi_{i,j-1}) \\ &-(\omega_{i,j+1} - \omega_{i,j-1})(\psi_{i+1,j} - \psi_{i-1,j})] \end{aligned} \tag{4.14}$$

$$J_2(\omega,\psi)=\frac{1}{4h_xh_y}[\omega_{i+1,j}(\psi_{i+1,j+1}-\psi_{i+1,j-1})-\omega_{i-1,j}(\psi_{i-1,j+1}-\psi_{i-1,j-1}) \\ -\omega_{i,j+1}(\psi_{i+1,j+1}-\psi_{i-1,j+1})+\omega_{i,j-1}(\psi_{i+1,j-1}-\psi_{i-1,j-1})] \tag{4.15}$$

$$J_3(\omega,\psi)=\frac{1}{4h_xh_y}[\omega_{i+1,j+1}(\psi_{i,j+1}-\psi_{i+1,j})-\omega_{i-1,j-1}(\psi_{i-1,j}-\psi_{i,j-1}) \\ -\omega_{i-1,j+1}(\psi_{i,j+1}-\psi_{i-1,j})+\omega_{i+1,j-1}(\psi_{i+1,j}-\psi_{i,j-1})] \tag{4.16}$$

The fourth-order accurate Arakawa discretization of the Jacobian becomes

$$J_{II}(\omega,\psi)=\frac{1}{3}(J_4(\omega,\psi)+J_5(\omega,\psi)+J_6(\omega,\psi)) \tag{4.17}$$

where

$$J_4(\omega,\psi)=\frac{1}{8h_xh_y}[(\omega_{i+1,j+1}-\omega_{i-1,j-1})(\psi_{i-1,j+1}-\psi_{i+1,j-1}) \\ -(\omega_{i-1,j+1}-\omega_{i+1,j-1})(\psi_{i+1,j+1}-\psi_{i-1,j-1})] \tag{4.18}$$

$$J_5(\omega,\psi)=\frac{1}{8h_xh_y}[\omega_{i+1,j+1}(\psi_{i,j+2}-\psi_{i+2,j})-\omega_{i-1,j-1}(\psi_{i-2,j}-\psi_{i,j-2}) \\ -\omega_{i-1,j+1}(\psi_{i,j+2}-\psi_{i-2,j})+\omega_{i+1,j-1}(\psi_{i+2,j}-\psi_{i,j-2})] \tag{4.19}$$

$$J_6(\omega,\psi)=\frac{1}{8h_xh_y}[\omega_{i+2,j}(\psi_{i+1,j+1}-\psi_{i+1,j-1})-\omega_{i-2,j}(\psi_{i-1,j+1}-\psi_{i-1,j-1}) \\ -\omega_{i,j+2}(\psi_{i+1,j+1}-\psi_{i-1,j+1})+\omega_{i,j-2}(\psi_{i+1,j-1}-\psi_{i-1,j-1})] \tag{4.20}$$

Arakawa showed that J_{II} conserves enstrophy and energy and the following Jacobian

$$J(\omega,\psi)=2J_I(\omega,\psi)-J_{II}(\omega,\psi)+O(h^4) \tag{4.21}$$

has fourth-order accuracy. The viscous terms can be discretized with the 4th-order explicit difference scheme given in the previous section. This scheme was used to compute two-

dimensional isotropic turbulence by Orlandi (2000).

4.3.5 Fourier-Galerkin pseudospectral method

Fourier series expansion based methods are often used for solving problems with periodic boundary conditions. One of the most accurate methods for solving the Navier-Stokes equations in periodic domains is the pseudospectral method, which exploits fast Fourier transform (FFT) algorithms, resulting in spectral accuracy (Canuto, 2006). It should be noted that the discrete Fourier transform is $O(N_x^2 N_y^2)$, which becomes very expensive for larger resolutions. On the other hand, the discrete Fourier transform can, in fact, be computed in $O(N_x N_y log(N_x N_y))$ operations with well-known FFT algorithms (Press et al., 1992). Given a set of N_x and N_y uniformly distributed points on the interval $[0,\, L_x]\times\, [0,\, L_y]$, the forward Fourier transformation of any discrete function u is

$$u_{i,j} = \sum_{m=-\frac{N_x}{2}}^{\frac{N_x}{2}-1} \sum_{n=-\frac{N_y}{2}}^{\frac{N_y}{2}-1} \tilde{u}_{m,n} e^{\boldsymbol{i}(\frac{2\pi m}{L_x} x_i + \frac{2\pi n}{L_y} y_j)} \tag{4.22}$$

and its inverse transform to find the Fourier coefficients is

$$\tilde{u}_{m,n} = \frac{1}{N_x \times N_y} \sum_{i=0}^{N_x-1} \sum_{j=0}^{N_y-1} u_{i,j} e^{-\boldsymbol{i}(\frac{2\pi m}{L_x} x_i + \frac{2\pi n}{L_y} y_j)} \tag{4.23}$$

where $\boldsymbol{i} = \sqrt{-1}$ and i, and j represent indices for physical space, and m, and n are the Fourier space indices. The discrete grid coordinates for $i = 0, 1, ..N_x$ and $j = 0, 1, ..N_y$ are given by

$$x_i = \frac{iL_x}{N_x}, \quad y_j = \frac{jL_y}{N_y}. \tag{4.24}$$

Since the domain is periodic, $x_0 = x_{N_x}$ and $y_0 = y_{N_y}$. Defining the wave numbers

$$k_x = \frac{2\pi m}{L_x}, \quad k_y = \frac{2\pi n}{L_y}. \tag{4.25}$$

Now, we can easily perform differentiation in both directions. The first and second order differentiation of any function u in discrete domain becomes

$$\frac{\partial u_{i,j}}{\partial x} = \sum_{m=-\frac{N_x}{2}}^{\frac{N_x}{2}-1} \sum_{n=-\frac{N_y}{2}}^{\frac{N_y}{2}-1} \tilde{u}_{m,n}(\boldsymbol{i}k_x)e^{\boldsymbol{i}(k_x x_i + k_y y_j)} \tag{4.26}$$

$$\frac{\partial^2 u_{i,j}}{\partial x^2} = \sum_{m=-\frac{N_x}{2}}^{\frac{N_x}{2}-1} \sum_{n=-\frac{N_y}{2}}^{\frac{N_y}{2}-1} \tilde{u}_{m,n}(-k_x^2)e^{\boldsymbol{i}(k_x x_i + k_y y_j)} \tag{4.27}$$

and similarly for the y direction derivatives. By transforming Eq. (4.1) and Eq. (4.2) to Fourier space, the governing equations become

$$\frac{\partial \tilde{\omega}_{m,n}}{\partial t} + \tilde{N} = \frac{1}{Re}[(-k_x^2 - k_y^2)\tilde{\omega}_{m,n}] \tag{4.28}$$

$$(-k_x^2 - k_y^2)\tilde{\psi}_{m,n} = -\tilde{\omega}_{m,n} \tag{4.29}$$

where $\tilde{N}$ represents the nonlinear terms (Fourier transform of the Jacobian) and needs to be computed according to the following convolution

$$\tilde{N} = (\boldsymbol{i}k_y\tilde{\psi}_{m,n}) \circ (\boldsymbol{i}k_x\tilde{\omega}_{m,n}) - (\boldsymbol{i}k_x\tilde{\psi}_{m,n}) \circ (\boldsymbol{i}k_y\tilde{\omega}_{m,n}) \tag{4.30}$$

The convolution sum for these nonlinear terms is actually computed in the physical domain, with the help of the convolution theorem. One of the basic techniques for removing the aliasing error for the nonlinear terms is the 3/2-rule which is known as the padding or truncation algorithm. The key to this dealiasing algorithm is the use of the discrete transform of M_x and M_y rather than N_x and N_y points, so that $M_x \geq 3N_x/2$ and $M_y \geq 3N_y/2$. For example, let's denote $\tilde{a}_{m,n}$ and $\tilde{b}_{m,n}$, the Fourier coefficients of two multiplicand terms, as being in $\tilde{N}$, and we would like to compute the Fourier coefficients of the multiplication of these two terms, $\tilde{c}_{m,n} = \tilde{a}_{m,n} \circ \tilde{b}_{m,n}$. In the pseudospectral (PS) method, we can compute this

term as $\tilde{c}_{m,n} = F^{-1}(F(\tilde{a}_{m,n})F(\tilde{b}_{m,n}))$, where F and F^{-1} represent the forward and inverse transforms, respectively. First we need to use the forward transformation using M_x and M_y wavenumbers such that

$$A_{i,j} = \sum_{m=-\frac{M_x}{2}}^{\frac{M_x}{2}-1} \sum_{n=-\frac{M_y}{2}}^{\frac{M_y}{2}-1} \tilde{a}_{m,n} e^{\boldsymbol{i}(k_X X_i + k_Y Y_j)} \tag{4.31}$$

$$B_{i,j} = \sum_{m=-\frac{M_x}{2}}^{\frac{M_x}{2}-1} \sum_{n=-\frac{M_y}{2}}^{\frac{M_y}{2}-1} \tilde{b}_{m,n} e^{\boldsymbol{i}(k_X X_i + k_Y Y_j)} \tag{4.32}$$

where $X_i = \frac{iL_x}{M_x}$, $Y_j = \frac{jL_y}{M_y}$. The Fourier coefficients are padded with zeros for the additional wavenumbers such as

$$\tilde{a}_{m,n} = \begin{cases} \tilde{a}_{m,n} & |m| \leq N_x, \quad |n| \leq N_y \\ 0 & \text{otherwise} \end{cases} \tag{4.33}$$

$$\tilde{b}_{m,n} = \begin{cases} \tilde{b}_{m,n} & |m| \leq N_x, \quad |n| \leq N_y \\ 0 & \text{otherwise} \end{cases} \tag{4.34}$$

Multiplication is performed in physical space but with padded higher wavenumbers in the following way

$$C_{i,j} = A_{i,j} B_{i,j}. \tag{4.35}$$

Then, the inverse transform gives the dealiased Fourier coefficients as

$$\tilde{C}_{m,n} = \frac{1}{N_x \times N_y} \sum_{i=0}^{M_x-1} \sum_{j=0}^{M_y-1} C_{i,j} e^{-\boldsymbol{i}(k_X X_i + k_Y Y_j)} \tag{4.36}$$

in which we are only interested in $\tilde{C}_{m,n}$ for $|m| \leq N_x$, $|n| \leq N_y$ (i.e., $\tilde{c}_{m,n} = \tilde{C}_{m,n}$ for $|m| \leq N_x$, $|n| \leq N_y$). Although in practice dealiasing need only be performed with $M_x \geq 3N_x/2$, we have used $M_x = 2N_x$ here since the FFT solver we are using requires resolutions that are powers of two. In order to make a fair comparison of CPU times, however, we have chosen to

present the dealisased computational CPU times an appropriately interpolated factor of the actual time between N_x and M_x. In this study, the semi-discrete vorticity transport equation in Fourier space, Eq. (4.28), is solved explicitly by third-order or forth-order accurate Runge-Kutta time marching schemes which will be given later.

4.3.6 Poisson solver

In order to obtain the stream function from the vorticity field, Eq. (4.2) needs to be solved. In general, Gauss-Seidel or successive over relaxation (SOR) types of iterative algorithms for solving the Poisson equation are of $O(N^2)$ where N is the total number of grid points (i.e., $N = N_x N_y$ for two-dimensional problems). It is not feasible to use these types of iterative Poisson solvers for high resolution (and therefore high Reynolds number) computations along with long time integration. In order to accelerate these solvers, very successful multi-grid (MG) algorithms have been developed that reduce the computational effort to $O(C_{MG}N)$ where C_{MG} is a proportionality constant (Gupta et al., 1997). On the other hand, for certain ideal problems on equally-spaced grids, fast Fourier transform (FFT)-based fast Poisson solvers (FPS) can be used to solve elliptic problems directly with an $O(C_{FPS}Nlog(N))$ operational cost, and they are presently the fastest available algorithms ($C_{FPS}log(N) < C_{MG}$ in relevant resolutions) for solving Poisson equations (Press et al., 1992; Moin, 2001).

A preliminary study is performed to test the computational efficiencies of different Poisson solvers for a square domain with equidistant grid spacing. The computational time (CPU time) for solving just one Poisson equation is illustrated in Figure 4.1. This preliminary comparison shows that the FPS is the most efficient solver for Cartesian grid problems. We take advantage of the simple rectangular shape of our domain and utilize the FPS for all the simulations in this study. The basic three-step procedure to find ψ from known ω values at any time (also for the inner steps of the Runge-Kutta time stepping algorithms) has the following form.

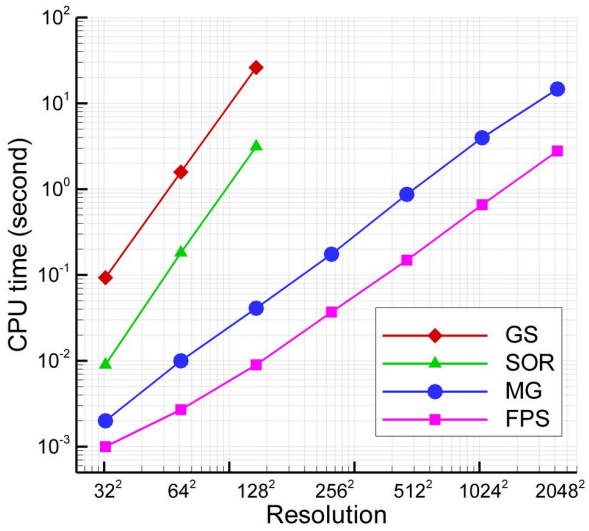

Figure 4.1: Efficiency of Poisson solvers for a two-dimensional square domain.

1. Use forward FFT for ω to find Fourier coefficients according to Eq. (4.22).

2. Compute Fourier coefficients of stream function from Eq. (4.29)

$$\tilde{\psi}_{m,n} = \frac{\tilde{\omega}_{m,n}}{(k_x^2 + k_y^2)}. \tag{4.37}$$

3. Use inverse FFT for ψ values according to Eq. (4.23).

4.3.7 Time integration algorithms

Steady calculations in fluid flows have been mostly handled using implicit time advancement algorithms and corresponding large time steps. It is tempting to adopt a similar practice in computations of turbulent flows. Unfortunately, the requirement of time accuracy over a wide range of scales does not permit very large time steps in such calculations (Moin and Mahesh, 1998). The use of large time steps implies that the small scales can have large errors, which can corrupt the solutions. Therefore, the families of fourth-order (Carpenter et al., 2005) and third-order (Williamson, 1980) Runge-Kutta time integration schemes

have been extensively used in turbulence simulations with their certain numerical stability requirements (Pruett et al., 1995). In fluid dynamics, the numerical stability of such explicit algorithms is usually addressed by using the convective Courant-Friedrichs-Lewy (CFL) or viscous Neumann stability conditions (Chorin, 1968). Usually the fourth-order Runge-Kutta schemes have a greater accuracy for a given time step and a larger allowable stability domain than the third-order Runge-Kutta schemes. To be practical, an explicit algorithm for turbulence computations must provide long-time temporal accuracy while requiring modest temporary storage resulting in the development of a low-storage Runge-Kutta family for demanding computations.

Semi-discrete ordinary differential equations (ODEs) are obtained after spatial discretization of the partial differential equations. To implement the Runge-Kutta schemes, we cast the governing vorticity transport equation in the following form

$$\frac{d\omega}{dt} = \pounds(\omega, \psi) \tag{4.38}$$

where $\pounds(\omega, \psi)$ is the discrete operator of spatial derivatives including nonlinear convective terms and linear diffusive terms, and ψ is obtained from the Poisson equation. A fourth-order Runge-Kutta scheme can be written in the following form (Pike and Roe, 1985)

$$\begin{aligned}
\omega^{(1)} &= \omega^n + \frac{\Delta t}{2}\pounds(\omega^n, \psi^n) \\
\omega^{(2)} &= \omega^n + \frac{\Delta t}{2}\pounds(\omega^1, \psi^1) \\
\omega^{(3)} &= \omega^n + \Delta t\pounds(\omega^2, \psi^2) \\
\omega^{n+1} &= \frac{1}{3}(-\omega^n + \omega^{(1)} + 2\omega^{(2)} + \omega^{(3)}) + \frac{\Delta t}{6}\pounds(\omega^{(3)}, \psi^{(3)})
\end{aligned} \tag{4.39}$$

The optimal third-order accurate TVD Runge-Kutta scheme is given as (Gottlieb and Shu,

1998)

$$\begin{aligned}\omega^{(1)} &= \omega^n + \Delta t \pounds(\omega^n, \psi^n) \\ \omega^{(2)} &= \frac{3}{4}\omega^n + \frac{1}{4}\omega^{(1)} + \frac{1}{4}\Delta t \pounds(\omega^{(1)}, \psi^{(1)}) \\ \omega^{n+1} &= \frac{1}{3}\omega^n + \frac{2}{3}\omega^{(2)} + \frac{2}{3}\Delta t \pounds(\omega^{(2)}, \psi^{(2)}).\end{aligned} \tag{4.40}$$

Alternatively, memory-effective $2N$-storage schemes that require only two sets of variables to be held in memory can be used. The iterative form of the $2N$-storage schemes can be written as

$$\begin{aligned}g^{(i)} &= \alpha_i g^{(i-1)} + \Delta t \pounds(\omega^{(i-1)}, \psi^{(i-1)}) \\ \omega^{(i)} &= \omega^{(i-1)} + \beta_i g^{(i)}.\end{aligned} \tag{4.41}$$

For a third-order accurate three-step scheme, we have indices $i = 1, 2, 3$. In order to advance from ω^n at time t^n to ω^{n+1} at time $t^{n+1} = t^n + \Delta t$ we set in Eq. (4.41) $\omega^{(0)} = \omega^n$ and, after the last step, $\omega^{n+1} = \omega^{(3)}$. In order to be able to calculate the first step, $i = 1$, for which no $g^{(0)}$ exists, we require $\alpha_1 = 0$. The corresponding coefficients for different types of constructed schemes are listed in Table 4.1. In practice all of them are approximately equally good as advocated by Brandenburg (2003). Although our main objective is to evaluate the performance of the various high-order spatial discretization schemes, we will perform a comparative study on these explicit Runge-Kutta schemes presented above to test their long-term characteristics for two-dimensional turbulence.

Table 4.1: Coefficients for various low-storage third-order Runge-Kutta methods.

scheme	α_2	α_3	β_1	β_2	β_3
symmetric	$-\frac{2}{3}$	-1	$\frac{1}{3}$	1	$\frac{1}{2}$
predictor/corrector	$-\frac{1}{4}$	$-\frac{4}{3}$	$\frac{1}{2}$	$\frac{2}{3}$	$\frac{1}{2}$
inhomogeneous	$-\frac{17}{32}$	$-\frac{32}{27}$	$\frac{1}{4}$	$\frac{8}{9}$	$\frac{3}{4}$
Williamson Williamson (1980)	$-\frac{5}{9}$	$-\frac{153}{128}$	$\frac{1}{3}$	$\frac{15}{16}$	$\frac{8}{15}$

4.4 Validation problem: Taylor-Green vortex

In this section, the schemes under consideration are validated on a square domain by solving the Taylor-Green decaying vortex problem. The Taylor-Green vortex problem is the two-dimensional, unsteady flow of a decaying vortex, which is an exact closed form solution to the incompressible Navier-Stokes equations in Cartesian coordinates. The exact solution of this vortex flow in a $[0, 2\pi] \times [0, 2\pi]$ domain with periodic boundary conditions is given by

$$\omega^e(x, y, t) = 2\kappa \cos(\kappa x)\cos(\kappa y)e^{-2\kappa^2 t/Re} \tag{4.42}$$

where κ is an integer which represents the number of vortices in each direction. In order to quantify the effective order of accuracy for each scheme, using the difference between exact and computed solutions, we compute the discrete L_2 norm as

$$\|\omega\|_{L_2} = \sqrt{\frac{1}{N_x N_y} \sum_{i=1}^{N_x} \sum_{j=1}^{N_y} |\omega^e_{i,j} - \omega_{i,j}|^2}. \tag{4.43}$$

In order to test the spatial convergence rate, we first perform numerical simulations for $Re = 1$ and $\kappa = 4$ with all the spatial schemes introduced earlier using the third-order TVD Runge-Kutta scheme with $\Delta t = 10^{-4}$. We choose this small time step (wherein the maximum CFL number is around 0.002 for the 128^2 resolution case) to eliminate possible temporal discretization errors due to the Runge-Kutta time integration schemes. A study

Table 4.2: Discrete L_2 error norms and corresponding convergence rates showing the effective order of the spatial difference schemes for the Taylor-Green vortex problem at $t = 0.1$ for $Re = 1$ and $\kappa = 4$, obtained using the time step $\Delta t = 10^{-4}$. The final column shows the CPU times in seconds for the 128^2 resolution computations.

Scheme	$\|\omega\|_{L_2}^{16^2}$	$n_{32^2}^{16^2}$	$\|\omega\|_{L_2}^{32^2}$	$n_{64^2}^{32^2}$	$\|\omega\|_{L_2}^{64^2}$	$n_{128^2}^{64^2}$	$\|\omega\|_{L_2}^{128^2}$	CPU
PS	0.76E-9		6.63E-9		1.61E-8		2.36E-8	210
ED6	1.04E-2	5.67	2.05E-4	5.92	3.39E-6	6.00	5.28E-8	46
ED4	3.28E-2	3.92	2.16E-3	3.97	1.38E-4	4.00	8.65E-6	44
ED2	1.44E-1	2.29	2.94E-2	2.09	6.91E-3	2.03	1.70E-3	42
CD6	2.90E-3	6.19	3.98E-5	6.06	5.96E-7	6.14	8.47E-9	79
CD4	1.58E-2	4.17	8.74E-4	4.05	5.28E-5	4.02	3.26E-6	76
A4	3.28E-2	3.92	2.16E-3	3.97	1.38E-4	4.00	8.65E-6	52
A2	1.44E-1	2.29	2.94E-2	2.09	6.91E-3	2.03	1.70E-3	45
DRP4	3.28E-2	3.92	2.16E-3	3.97	1.38E-4	4.00	8.65E-6	45

with $\Delta t = 2 \times 10^{-4}$, 10^{-4}, and 5×10^{-5} shows that the predicted flow field is independent of Δt. To further verify whether the simulations are independent of the errors associated with

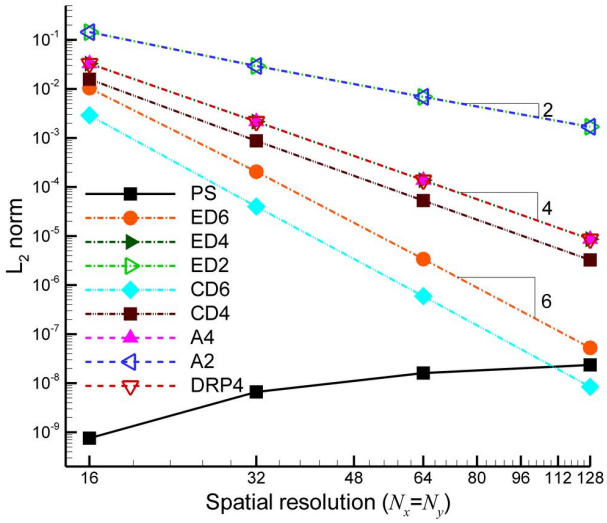

Figure 4.2: Convergence of the discrete L_2 error norms at time $t = 0.1$ for the Taylor-Green vortex decaying problem at $Re = 1$.

temporal discretization, we also run the same computations using the fourth-order Runge Kutta scheme, which yields exactly the same results.

In evaluating the performance of different finite difference formulations, the computed discrete L_2 norms at time $t = 0.1$ (when a 95% decay of the initial field has happened) are tabulated in Table 4.2 and are also plotted in Figure 4.2. Results show that the theoretical order of accuracies for all the schemes are obtained in practice. A linear reduction rate is obtained with the slope of all curves being their theoretical values, verifying the correct spatial convergence rate for each scheme. The most accurate difference scheme is found to be the sixth-order compact difference scheme. We also demonstrate that the errors associated with all the high-order formulations are several order magnitudes lower than the second-order formulations. It can be seen from Figure 4.2 that the predicted result of the 6th-order compact scheme becomes more accurate than the pseudospectral solution for the case with 128^2 resolution. This is mainly due to the accumulation of round off errors in the FFTs of the pseudospectral method. It can also be seen that the associated error increases slightly with increasing resolution for pseudospectral computations, again, due to the round-off errors associated with the FFTs. That is actually why Lele (1992) called these compact schemes "spectral-like schemes." It can also be seen that the compact schemes give more accurate results than the explicit finite difference schemes due to their smaller truncation error. Since the viscous difference formulations are equivalent, it should be noted here that the fourth-order Arakawa, dispersion-relation-preserving, and explicit difference schemes predict almost the same answer because of the inherent dynamics of the Taylor-Green vortex validation problem. This problem does not have a convective flow field, hence, the center of the each vortex stays stationary.

Next, we perform a convergence rate analysis for the temporal schemes. As we can see from the previous analysis, the pseudospectral scheme provides much more accurate results than the finite difference schemes, especially for lower resolutions. In order to be able to test the convergence rate of the temporal schemes properly, we choose our spatial discretization scheme to be the pseudospectral scheme with a resolution of 16^2, for which the temporal

Table 4.3: Discrete L_2 error norms and corresponding convergence rates showing the effective order of the temporal integration schemes for the Taylor-Green vortex problem at $t = 20$ for $Re = 1000$ and $\kappa = 4$, obtained using the pseudospectral scheme with a spatial resolution of 16^2.

Scheme	$\|\omega\|_{L_2}^{\Delta t=0.1}$	rate	$\|\omega\|_{L_2}^{\Delta t=0.2}$	rate	$\|\omega\|_{L_2}^{\Delta t=0.4}$	rate	$\|\omega\|_{L_2}^{\Delta t=0.8}$
RK4	1.23E-12	4.03	2.01E-11	4.01	3.23E-10	4.02	5.23E-09
TVDRK3	1.96E-09	3.00	1.57E-08	3.01	1.26E-07	3.01	1.02E-06
SYMRK3	1.96E-09	3.00	1.57E-08	3.01	1.26E-07	3.01	1.02E-06
P/CRK3	1.96E-09	3.00	1.57E-08	3.01	1.26E-07	3.01	1.02E-06
INHRK3	1.96E-09	3.00	1.57E-08	3.01	1.26E-07	3.01	1.02E-06
WILRK3	1.96E-09	3.00	1.57E-08	3.01	1.26E-07	3.01	1.02E-06

discretization error becomes greater than the spatial discretization error. The computed error norms are shown in Table 4.3 at time $t = 20$ for $Re = 1000$. It can be seen from Figure 4.3 that a linear reduction rate is obtained with the slope of all curves being 3 for all the third-order Runge-Kutta schemes, and 4 for the fourth-order Runge-Kutta scheme. We report that all the third-order Runge-Kutta schemes utilized in this study produce the same result within negligible differences due to round-off error.

The Taylor-Green vortex problem is one of the simplest incompressible flow test problems, having a smoothly decaying field. We solve it to be able to perform an exact error convergence rate analysis by comparing our results to the analytical solution of the problem. In the following sections, the effects of the order of the schemes and their global conservation properties will be analyzed for more challenging convective dominated flow problems. A truly fair comparison might require implementation of the same discretization scheme for the viscous terms. Therefore, in order to do a fair comparison among spatial difference schemes, the viscous diffusion terms are approximated using the six-order accurate compact scheme for all the finite difference schemes being considered for the rest of the paper.

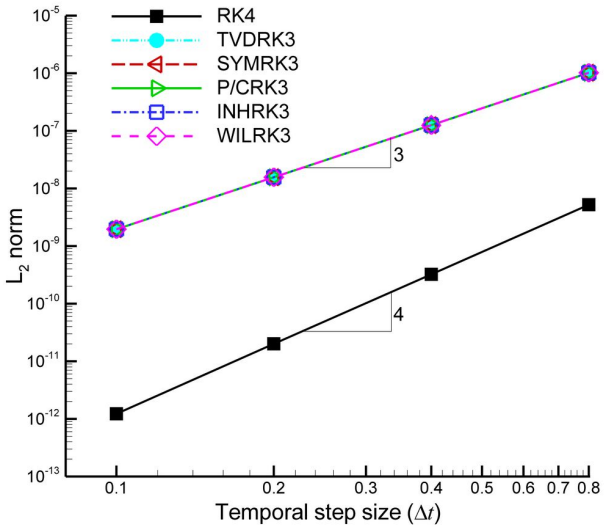

Figure 4.3: Convergence of the discrete L_2 error norms for the temporal schemes at time $t = 20$ for the Taylor-Green vortex decaying vortex problem at $Re = 1000$.

4.5 Double shear layer problem

The double shear layer problem was introduced by Bell et al. (1989) to test the performance of a projection method, and was studied later by Minion and Brown (1997) using various schemes to determine the effects of the grid resolution on solutions of the unsteady, incompressible Navier-Stokes equations. It is a benchmark problem for testing the accuracy and resolution of a time dependent numerical method. The double shear layer problem with periodic boundary conditions in a square domain $[0, 2\pi] \times [0, 2\pi]$ is subjected to the following initial conditions

$$\omega(x, y, 0) = \begin{cases} \delta \cos(x) - \sigma \cosh^{-2}[\sigma(y - \frac{\pi}{2})] & \text{if } y \leq \pi \\ \delta \cos(x) + \sigma \cosh^{-2}[\sigma(\frac{3\pi}{2} - y)] & \text{if } y > \pi \end{cases} \tag{4.44}$$

where the constants σ and δ determine the thickness of the shear layer and the amplitude of the initial perturbation, respectively. In our computations, the thickness parameter is $\sigma = 15/\pi$, the perturbation amplitude is $\delta = 0.05$, the Reynolds number is $Re = 10^4$, and

Table 4.4: Discrete L_2 error norms and computational efficiencies of the spatial schemes for the double shear layer problem at $t = 10$ for $Re = 10^4$. The reference solution for computing the L_2 norm is obtained using the pseudospectral method with a resolution of 1024^2.

Scheme	$\|\omega\|_{L_2}^{256^2}$	CPU_{256^2}(hrs)	$\|\omega\|_{L_2}^{512^2}$	CPU_{512^2}(hrs)	$\|\omega\|_{L_2}^{1024^2}$	CPU_{1024^2}(hrs)
PS	5.91E-3	2.94	3.34E-6	17.65		97.03
ED6	8.10E-2	0.67	6.86E-3	3.08	1.87E-4	19.29
ED4	1.48E-1	0.66	2.53E-2	2.99	2.04E-3	17.84
ED2	3.97E-1	0.64	1.81E-1	2.95	5.86E-2	16.93
CD6	3.36E-2	0.92	1.03E-3	4.10	8.10E-5	23.60
CD4	6.93E-2	0.90	6.47E-3	4.05	3.71E-4	21.73
A4	1.45E-1	0.76	2.52E-2	3.37	2.04E-3	19.32
A2	4.45E-1	0.69	2.01E-1	3.15	6.46E-2	17.92
DRP4	5.69E-2	0.67	8.23E-3	3.05	1.02E-3	18.07

the time step is $\Delta t = 10^{-3}$. We choose this time step (wherein the corresponding maximum CFL number is 0.25 for the case with a resolution of 1024^2) to concentrate on the differences among the spatial discretization schemes by eliminating the temporal integration errors in the simulations. Since the dominant error is due to the spatial difference operator rather than the temporal integration method, we employ the TVD Runge-Kutta scheme for the time advancement. We also perform, but do not report in detail here, a time step refinement study revealing that the temporal discretization error is indeed negligible. Moreover, we use the same discrete approximation, the 6th-order compact difference scheme, for the viscous terms in all the cases. In the following, we investigate the behavior of the spatial discretization schemes for convective terms by solving the double shear layer problem for various resolutions.

The perturbed shear layers roll up into a single vortex and the shear layers become thinner and thinner as the flow evolves over time, as shown in Figure 4.4. The three-dimensional view of the shear layers developed at time $t = 10$ is also illustrated in Figure 4.5, which shows the magnitude of the vorticity as the z-axis. This shear layer problem is particularly important

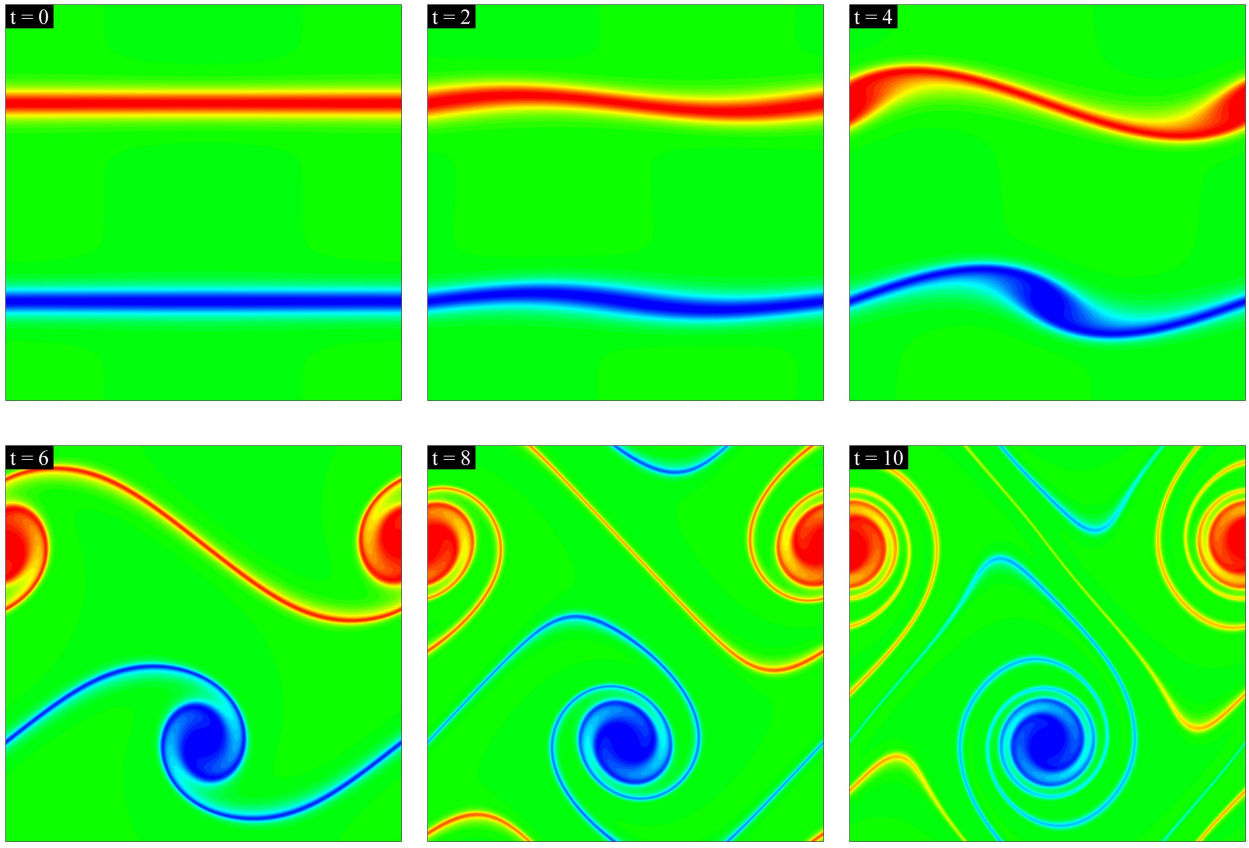

Figure 4.4: Evolution of the double shear layer problem for $Re = 10^4$ with the perturbation and thickness parameters of $\delta = 0.05$ and $\sigma = 15/\pi$ in a doubly periodic domain.

in that the presence of thinner and thinner shear layers as the flow field evolves in time is not captured by low grid resolution representations. The Gibbs phenomenon, numerical oscillations occurring near sharp vorticity gradients, occurs for under-resolved simulations in which the grid size is larger than the shear layer thickness. Since sharp discontinuities are observed in the vorticity field, this benchmark flow problem is very appropriate to test the overall accuracy of the methods presented in this study.

Vorticity contours at $t = 10$ obtained using all the spatial discretization schemes introduced earlier are shown in Figures 4.6-4.8 for different spatial resolutions. To make the distinctions among the schemes more clear, the centerline vorticity distributions along the y-axis at $t = 10$ are also shown in Figure 4.9-4.11 for different resolutions. Our comparison

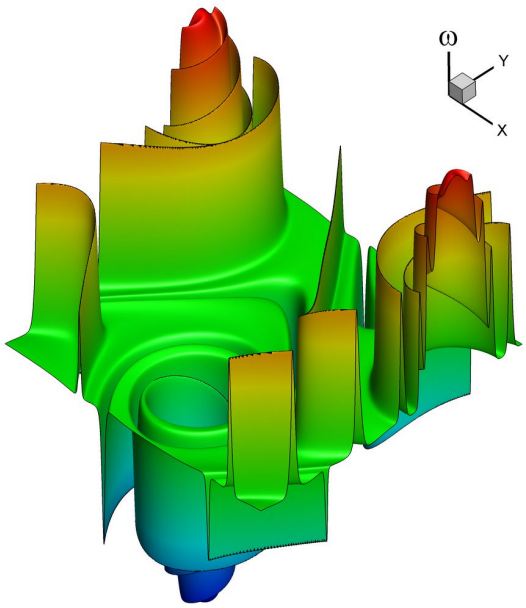

Figure 4.5: The three-dimensional view of the shear layers at time $t = 10$ by plotting the magnitude of the vorticity as the z-axis.

in these figures includes four families of fourth-order difference schemes, two second-order schemes, and two sixth-order difference schemes, as well as the pseudospectral scheme. Figure 4.6 illustrates a comparison of vorticity fields obtained by using 256^2 resolution for these nine different spatial discretization schemes. The corresponding comparison of centerline vorticity distributions is also provided in Figure 4.9. As we can see from these figures, both the sixth-order compact scheme and the pseudospectral scheme yield almost the same accuracy. It can also be seen that all the high-order formulations provide much better accuracy than the second-order schemes. A truly fair comparison among all the finite difference formulations presented in this study is to look at the fourth-order discretization schemes. Results show that there is no significant difference between explicit difference and Arakawa schemes. The discrete conservation properties of the Arakawa scheme do not improve the overall accuracy of the whole solution procedure in this case. On the other hand, the compact difference and dispersion-relation-preserving schemes result in better accuracy than the Arakawa or explicit difference schemes by eliminating numerical oscillations. Increasing the resolution to 512^2, as illustrated in Figure 4.7 and Figure 4.10, we show that it is possible to obtain numerical

oscillation-free results only by using high-order schemes. Second-order schemes, both the explicit difference and the Arakawa scheme, still produce numerical oscillations. Finally, we perform computations by using 1024^2 resolution and results are demonstrated in Figure 4.8 and Figure 4.11 for vorticity contour fields and centerline vorticity distributions, respectively. We can see that all numerical schemes provide an accurate oscillation-free solution to the double shear layer problem with this resolution.

As a result of this study, a rule of thumb is that second-order central difference schemes, whether standard explicit difference or conservative Arakawa scheme, require about twice resolution (in each direction) to achieve the same results obtained by a high-order finite difference or pseudospectral scheme. Therefore, this study demonstrates that the numerical oscillations that occur in under-resolved simulations with strong shear layers can be eliminated efficiently by using the high-order formulations with the same resolution. For example, at a relatively high Reynolds number $Re = 10^4$, it can clearly be seen that a resolution of 512^2 is not high enough to capture the correct physics without numerical oscillations using a low-order finite difference formulation. To be able to obtain all the small-scale physical layers, at least a 1024^2 resolution needs to be used with a spatially second-order accurate scheme for solving underlying equations. On the other hand, we demonstrated that the properly-resolved physical behavior without a Gibbs phenomenon is obtained using a resolution of 512^2 with only a slight increase in the computational price.

In evaluating the efficiency of the different formulations, the CPU times are tabulated in Table 4.4. In this table, we also present the corresponding discrete L_2 norms which show the average root-mean-square deviations of the vorticity field from the data obtained by well-resolved pseudospectral calculation using 1024^2 resolution. These results demonstrate that high fidelity numerical simulations can be obtained using the high-order finite difference methods with a speed-up factor of 5 if we compare them with the pseudospectral computation. More importantly, if we compare them with their second-order counterparts, the additional cost due to high-order formulations becomes quite small. The data presented in Table 4.4 also demonstrates that the computational speed-up increases with increasing

spatial resolution as expected. With this in mind, one of the interesting results is that the errors associated with both the second-order explicit difference (ED2) and the second-order Arakawa (A2) schemes with 1024^2 resolution are greater than the error associated with the sixth-order compact scheme (CD6) with a much smaller 256^2 resolution. This clearly demonstrates that the high-order difference formulations can provide an efficient way of solving flow problems even with strong shear components.

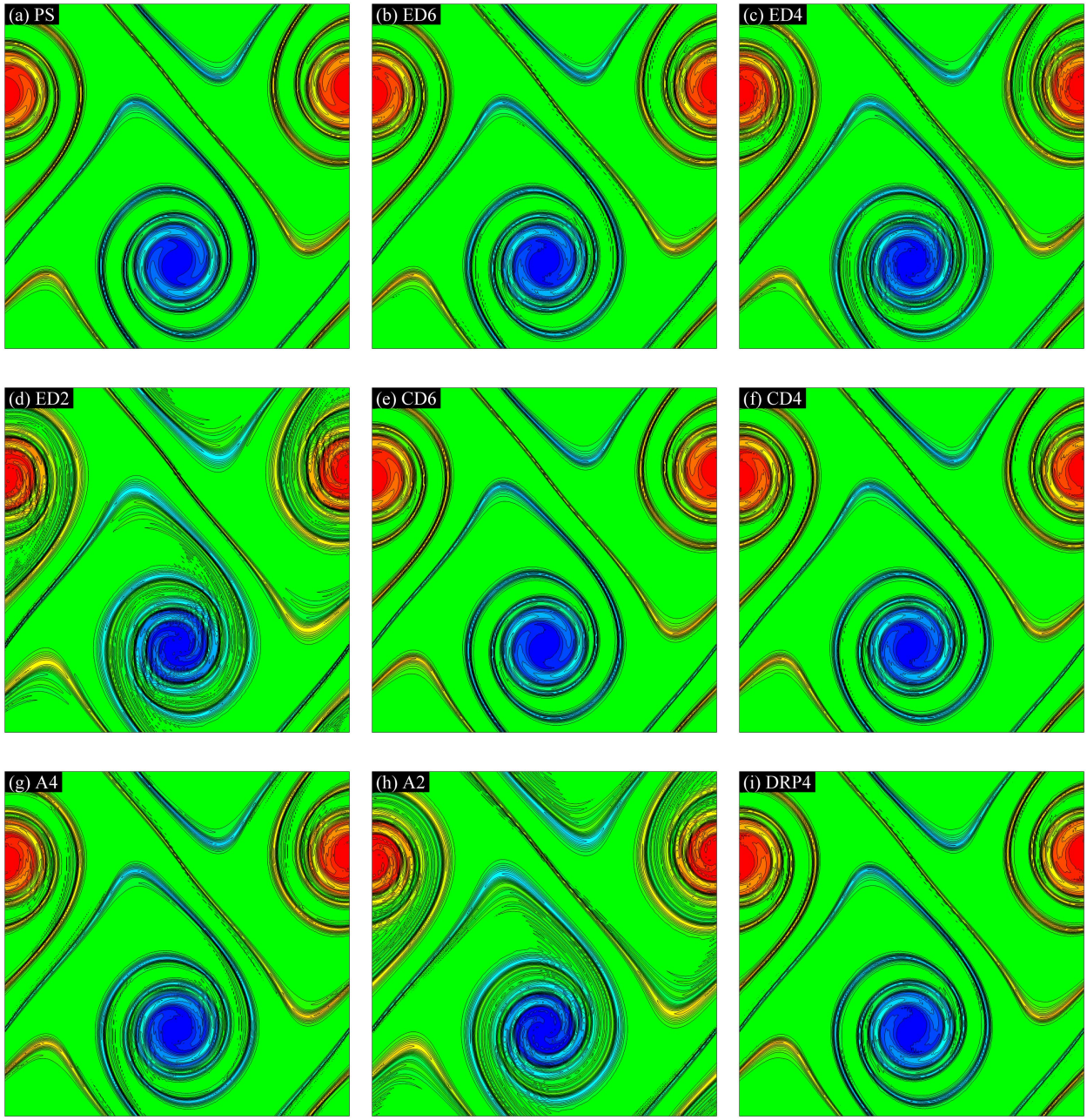

Figure 4.6: Comparison of the numerical schemes for the double shear layer problem at time $t = 10$ with a resolution of 256^2. (a) Pseudospectral (PS) method, (b) sixth-order explicit difference (ED6) method, (c) fourth-order explicit difference (ED4) method, (d) second-order explicit difference (ED2) method, (e) sixth-order compact difference (CD6) method, (f) fourth-order compact difference (CD4) method, (g) fourth-order Arakawa (A4) method, (h) second-order Arakawa (A2) method, and (i) fourth-order dispersion-relation-preserving (DRP4) method. The vorticity contour layouts are identical in all nine cases illustrating 27 equidistant levels in the interval [-4.5, 4.5].

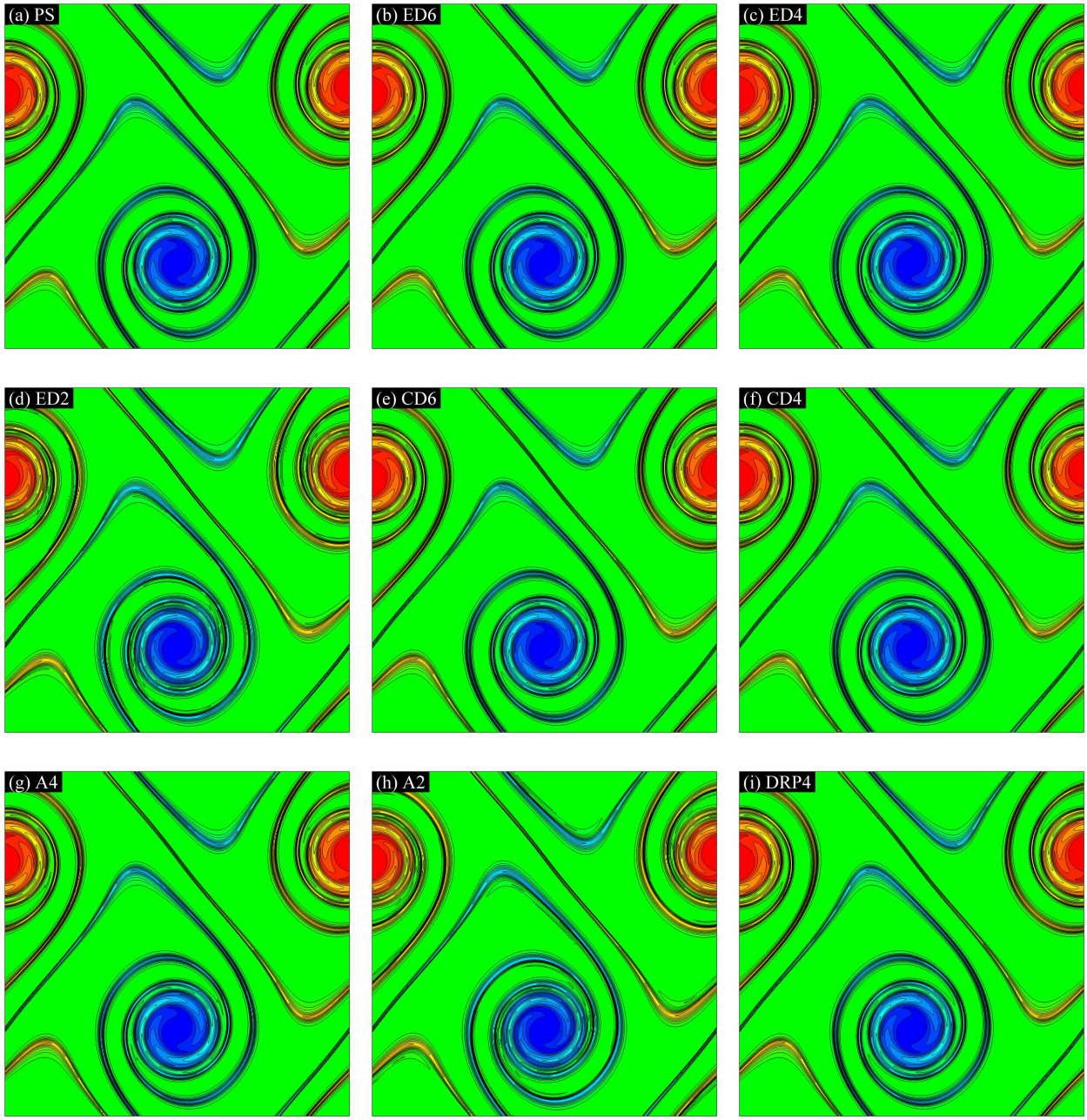

Figure 4.7: Comparison of the numerical schemes for the double shear layer problem at time $t = 10$ with a resolution of 512^2. (a) Pseudospectral (PS) method, (b) sixth-order explicit difference (ED6) method, (c) fourth-order explicit difference (ED4) method, (d) second-order explicit difference (ED2) method, (e) sixth-order compact difference (CD6) method, (f) fourth-order compact difference (CD4) method, (g) fourth-order Arakawa (A4) method, (h) second-order Arakawa (A2) method, and (i) fourth-order dispersion-relation-preserving (DRP4) method. The vorticity contour layouts are identical in all nine cases illustrating 27 equidistant levels in the interval [-4.5, 4.5].

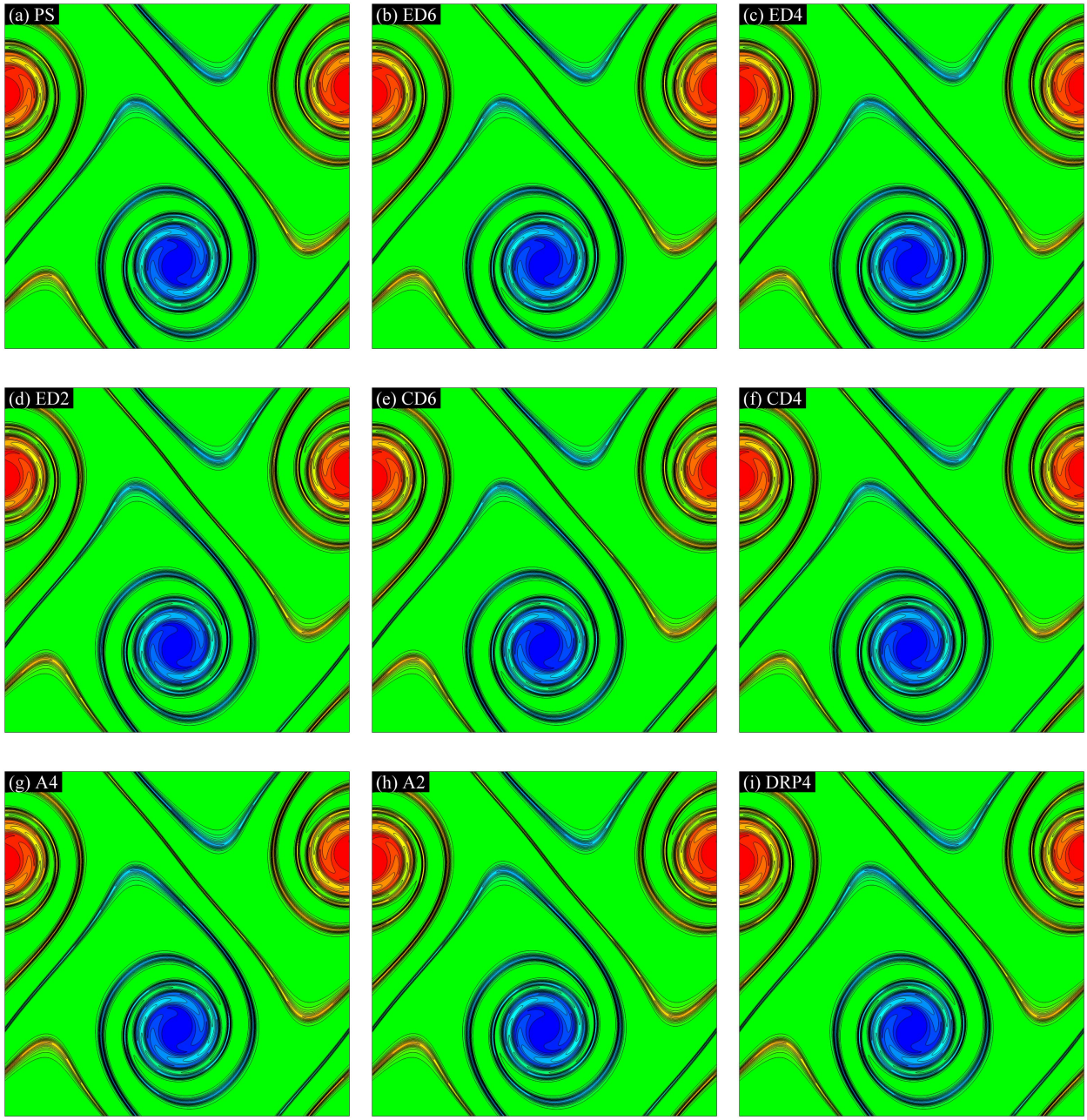

Figure 4.8: Comparison of the numerical schemes for the double shear layer problem at time $t = 10$ with a resolution of 1024^2. (a) Pseudospectral (PS) method, (b) sixth-order explicit difference (ED6) method, (c) fourth-order explicit difference (ED4) method, (d) second-order explicit difference (ED2) method, (e) sixth-order compact difference (CD6) method, (f) fourth-order compact difference (CD4) method, (g) fourth-order Arakawa (A4) method, (h) second-order Arakawa (A2) method, and (i) fourth-order dispersion-relation-preserving (DRP4) method. The vorticity contour layouts are identical in all nine cases illustrating 27 equidistant levels in the interval [-4.5, 4.5].

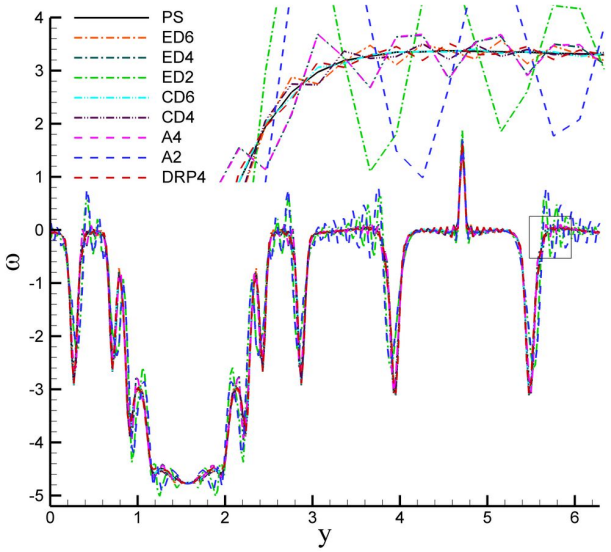

Figure 4.9: The centerline vorticity distributions at $x = \pi$ for the double shear layer problem, plotted for a resolution of 256^2. Comparison of the different numerical schemes at time $t = 10$. Inset: close-up of boxed area.

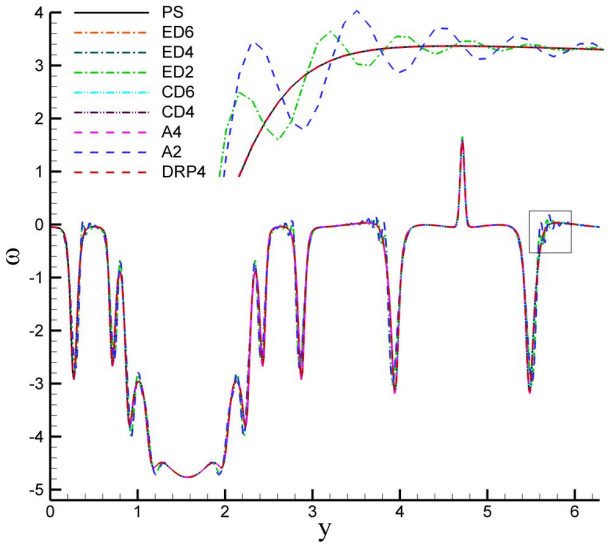

Figure 4.10: The centerline vorticity distributions at $x = \pi$ for the double shear layer problem, plotted for a resolution of 512^2. Comparison of the different numerical schemes at time $t = 10$. Inset: close-up of boxed area.

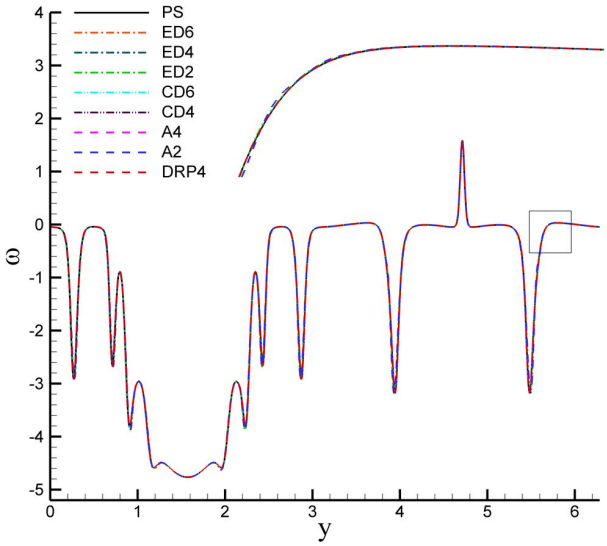

Figure 4.11: The centerline vorticity distributions at $x = \pi$ for the double shear layer problem, plotted for a resolution of 1024^2. Comparison of the different numerical schemes at time $t = 10$. Inset: close-up of boxed area.

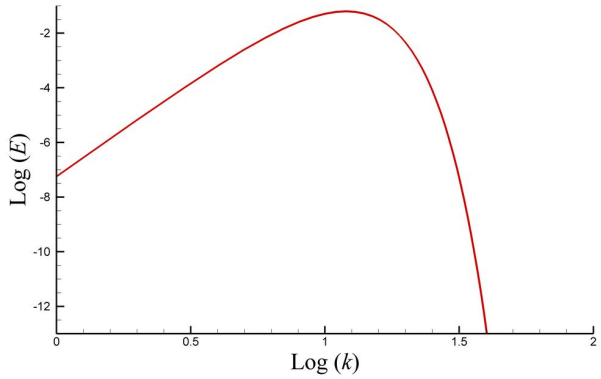

Figure 4.12: Initial energy spectrum for the two-dimensional decaying turbulence problem.

4.6 Two-dimensional decaying turbulence

Two-dimensional homogenous decaying turbulence is an incompressible flow problem in which the kinetic energy decays (McWilliams, 1990). The problem of the free decay of two-dimensional turbulence is to determine how abundant populations of vortices freely evolve with time (Tabeling, 2002). In this study, we solve this problem to examine the accuracy and efficiency of the presented finite difference approximations. The results are compared with those of the pseudospectral method. According to the KBL theory for two-dimensional turbulence this system has an inertial range in the energy spectrum that is proportional to k^{-3} in the inviscid limit.

The computational domain is a square with sides of length 2π. Periodic boundary conditions are applied. The initial energy spectrum in Fourier space is given by

$$E(k) = \frac{a_s}{2}\frac{1}{k_p}\left(\frac{k}{k_p}\right)^{2s+1} \exp\left[-\left(s+\frac{1}{2}\right)\left(\frac{k}{k_p}\right)^2\right] \tag{4.45}$$

where $k = |\mathbf{k}| = \sqrt{k_x^2 + k_y^2}$. The maximum value of initial energy spectrum occurs at wavenumber k_p which is assumed to be $k_p = 12$ in this study. The coefficient a_s normalizes the initial kinetic energy and is given by

$$a_s = \frac{(2s+1)^{s+1}}{2^s s!} \tag{4.46}$$

where s is a shape parameter. In this study, we take $s = 3$. The corresponding energy spectrum given in Eq. (4.45) is illustrated in Figure 4.12. The magnitude of vorticity Fourier coefficients related to the assumed initial energy spectrum becomes

$$|\tilde{\omega}(\mathbf{k})| = \sqrt{\frac{k}{\pi}E(k)} \tag{4.47}$$

The initial vorticity distribution in Fourier space is then obtained by introducing a random

phase

$$\tilde{\omega}(\mathbf{k}) = \sqrt{\frac{k}{\pi}E(k)}\; e^{i\zeta(\mathbf{k})} \tag{4.48}$$

where the phase function is given by $\zeta(\mathbf{k}) = \xi(\mathbf{k}) + \eta(\mathbf{k})$, where $\xi(\mathbf{k})$ and $\eta(\mathbf{k})$ are independent random values chosen in $[0, 2\pi]$ at each coordinate point in the first quadrant of the $k_x - k_y$ plane. The conjugate relations for other quadrants are

$$\begin{aligned}
\xi(-k_x, k_y) &= -\xi(k_x, k_y) \\
\xi(-k_x, -k_y) &= -\xi(k_x, k_y) \\
\xi(k_x, -k_y) &= \xi(k_x, k_y) \\
\eta(-k_x, k_y) &= \eta(k_x, k_y) \\
\eta(-k_x, -k_y) &= -\eta(k_x, k_y) \\
\eta(k_x, -k_y) &= -\eta(k_x, k_y).
\end{aligned} \tag{4.49}$$

After the randomization process described above for the phases, the initial vorticity distribution in the physical space is computed by taking the inverse FFT. However, we use a random phase generator to obtain initial flow field, it should be noted that we will use exactly same initial vorticity field when we compare the numerical schemes for the same resolution. The corresponding initial vorticity distribution is a vortex population which satisfies the divergence free condition and provides the energy spectrum given in Eq. (4.45). In the following text, we first investigate how homogeneous two-dimensional decaying turbulence varies with Re when using the sixth-order compact difference scheme. Then we will focus our attention on the behavior of a selection of numerical methods for computations of two-dimensional turbulence. It should be noted here that the diffusion terms are approximated using the sixth-order compact scheme for all difference formulations in order to provide a fair comparison between them. To make the simulation independent of the errors associated with temporal discretization, a time step of $\Delta t = 2 \times 10^{-4}$ is used in all simulations except when the temporal discretization schemes are evaluated by a time refinement analysis. A

study with $\Delta t = 1 \times 10^{-4}$, 2×10^{-4}, and 4×10^{-4} also show that the predicted flow field is independent of Δt.

4.6.1 Reynolds number dependence

Starting from a divergence free initial vorticity field having the specified energy spectrum, we solve Eq. (4.1) for various Reynolds numbers. Figure 4.13 shows the evolution of the vorticity field for $Re = 1000$. As shown in Figure 4.13, initial flow field at time $t = 0$ consists of many vortices according to the spectrum given by Eq. (4.45). As we can see, a filamentation process occurs, initially randomly distributed vortices start to interact with each other and become bigger vortices with time by a vortex merging mechanism. As also illustrated in Figure 4.13, as time evolves, the exterior strain field from each vortex deforms the vorticity field of the other one so that the vorticity fields wrap around each other.

In order to examine the characteristics of two-dimensional decaying turbulence simulations and their dependencies on Re, we first define two statistical measures. one is the energy spectrum in wave space, and the other is the structure function in physical space. The energy spectrum is defined as

$$\hat{E}(\mathbf{k}, t) = \frac{1}{2} k^2 |\tilde{\psi}(\mathbf{k}, t)|^2 \tag{4.50}$$

and the angle averaged energy spectrum is

$$E(k, t) = \sum_{k \le |\acute{\mathbf{k}}| \le k+1} \hat{E}(\acute{\mathbf{k}}, t). \tag{4.51}$$

It is known from the KBL theory that the energy spectrum in the inertial range approaches the classical k^{-3} scaling in the limit of infinite Reynolds number. On the other hand, the statistics of two-dimensional turbulent flow can be further investigated considering powers of vorticity differences in the physical space. A commonly used statistical quantity in two-

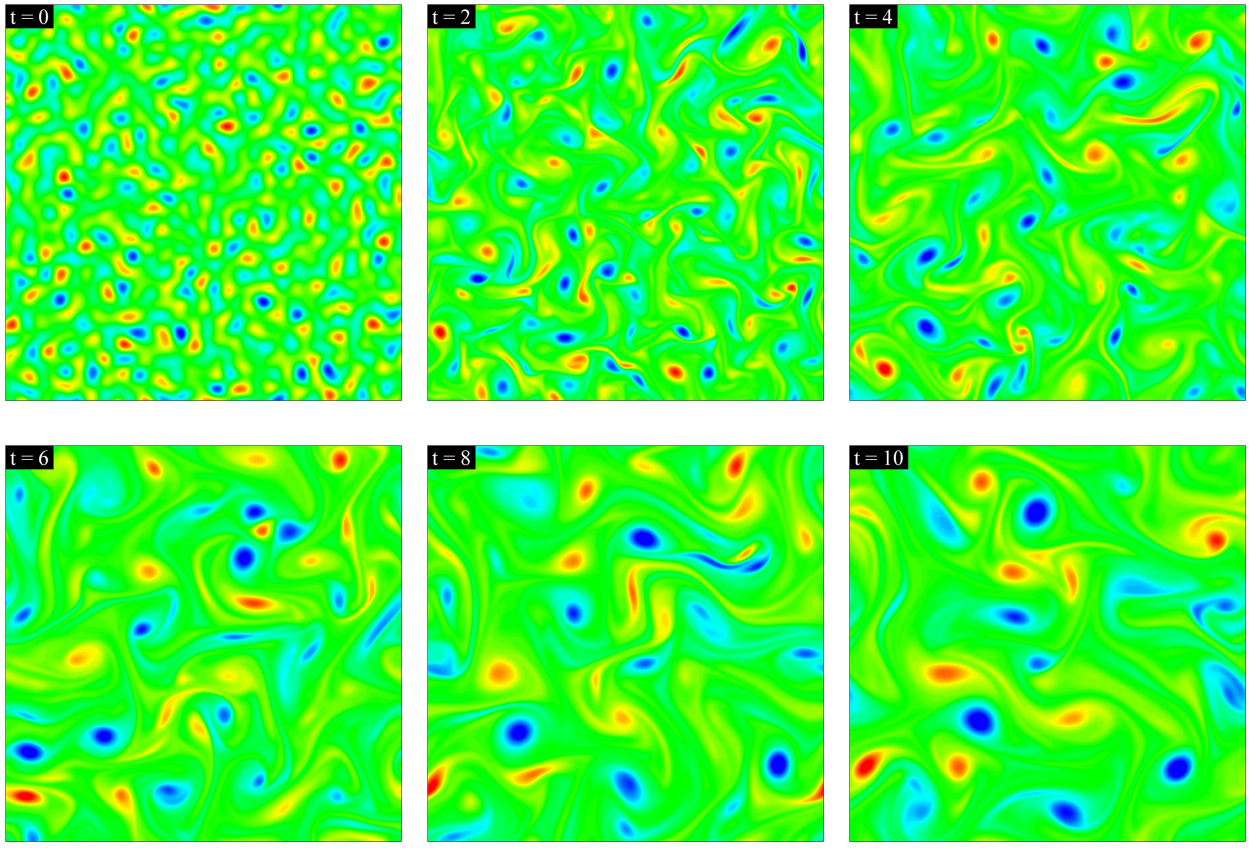

Figure 4.13: Evolution of the vorticity field in decaying turbulence for $Re = 1000$. Initially randomly distributed vortices start to interact with each other and merge to form larger vortices with time.

dimensional turbulence is the second-order vorticity structure function which is defined as

$$\langle \delta\omega(r)^2 \rangle = \langle |\omega(\mathbf{x}+\mathbf{r}) - \omega(\mathbf{x})|^2 \rangle \tag{4.52}$$

with $r = |\mathbf{r}|$ being the spatial separation. Statistical properties of decaying two-dimensional turbulence are investigated here by numerical simulations for different Reynolds numbers.

In this part of our analysis, in order to elucidate the flow field evolution for various Re and how the energy spectra and structure functions depend on Re, we perform a set of numerical experiments for Re = 100, 300, 600, 1000, 3000, and 6000. All numerical simulations are performed using a resolution of 1024^2 and start from the same initial condition. Figure 4.14

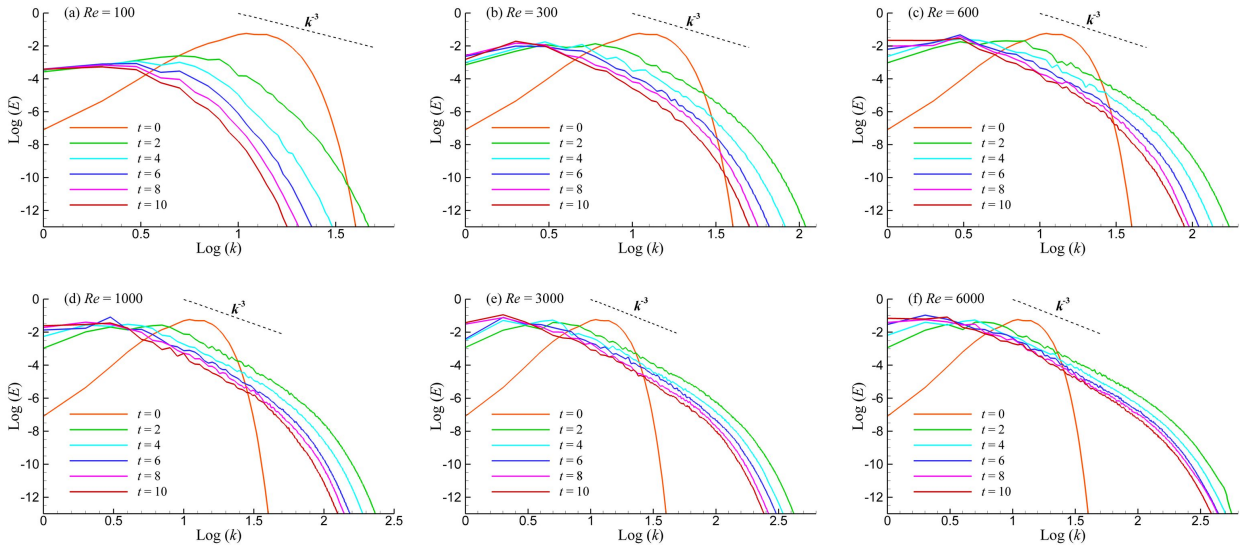

Figure 4.14: Evolution of energy spectra in decaying turbulence for (a) Re=100, (b) Re=300, (c) Re=600, (d) Re=1000, (e) Re=3000, and (f) Re=6000. The energy spectrum in the inertial range flattens towards the classical k^{-3} scaling limit as Re increases, in agreement with the KBL theory of two-dimensional turbulence.

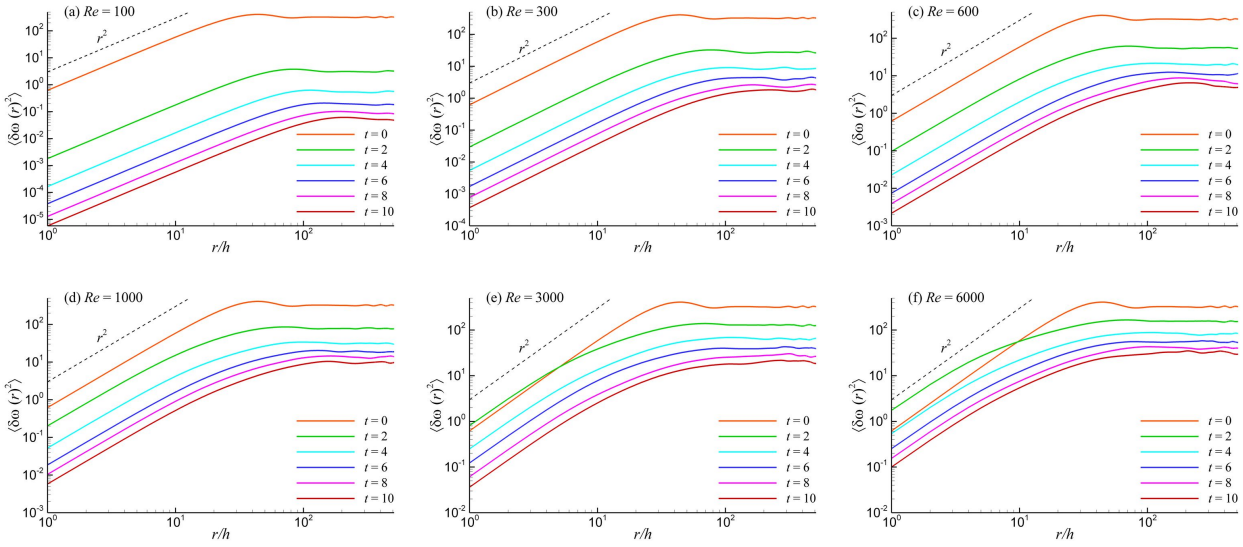

Figure 4.15: Evolution of the second-order vorticity structure functions in decaying turbulence for (a) Re=100, (b) Re=300, (c) Re=600, (d) Re=1000, (e) Re=3000, and (f) Re=6000. The line r^2 is included in each subfigure.

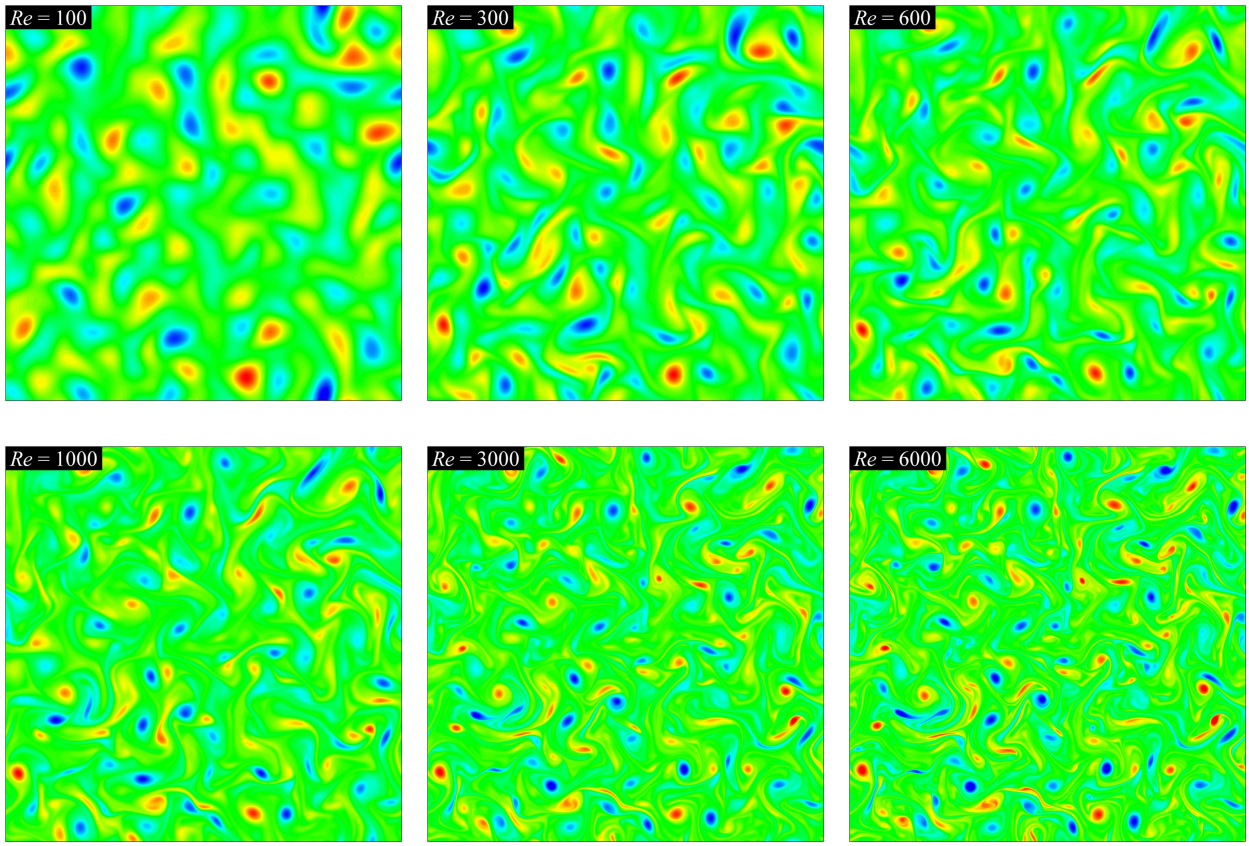

Figure 4.16: Vorticity contour plots at time $t = 2$ for various Reynolds numbers. Stronger filamentation processes occur with increasing Reynolds number.

demonstrates the evolution of the angle averaged energy spectrum for different Reynolds numbers. As we can see, the energy spectrum becomes steeper than k^{-3} for $Re = 100$ due to the smaller filamentation and less interaction among vortices. However, increasing Re, the energy spectrum in the inertial range approaches towards the classical k^{-3} limit, in agreement with KBL theory of two-dimensional turbulence. Similarly, the evolution of the second-order structure functions for various Reynolds numbers is exhibited in Figure 4.15 showing r^2 scaling for small separations in all the cases. They flatten for large separations as predicted by the KBL theory of two-dimensional turbulence in the inviscid limit. Comparisons of the angle averaged energy spectra and the second-order vorticity structure functions at time

$t = 2$ are also shown in Figure 4.17 and Figure 4.18, respectively. As demonstrated by Figure 4.17, the angle averaged energy spectrum defined by Eq. (4.51) asymptotically reaches the k^{-3} spectrum in the inertial range as Re increases. We find that the Reynolds number dependency is more stringent if we look at the turbulence statistics in wave space such the angle averaged energy spectrum. The corresponding instantaneous vorticity fields at time $t = 2$ are compared in Figure 4.16 for the same set of Reynolds numbers. As we can see from Figure 4.16, the amount of filamentation increases for higher Reynolds numbers. Due to the smaller convection in lower Reynolds numbers, the interaction between two vortices is not as strong as that of the higher Reynolds number cases, such that less amount of filamentation occurs and results in bigger vortices with less magnitude of vorticity during the evolution because of faster decay rate.

Noticeably, our results provide numerical proof of the KBL theory for decaying two-dimensional turbulence using the sixth-order compact finite difference scheme for spatial discretization along with the third-order TVD Runge-Kutta scheme for the time advancement. However, we emphasize that our primary goal in this study is to investigate the behavior of different numerical schemes for long time integration of turbulence simulations. In the following, we first test the temporal schemes and their numerical stabilities, and then focus on the evaluation of the behavior of spatial discretization schemes for computations of decaying turbulence.

4.6.2 Comparison of temporal schemes

We devote this section to investigating the characteristics of the temporal integration schemes described in Section 4.3.7. In general, the errors associated with temporal discretization are smaller than the errors associated with the spatial discretization, especially if we use high-order methods. Although time step limitations in an explicit time integration method can be an impediment to efficient solutions, for turbulent flow computations small time steps are indeed desirable to resolve the small turbulent time scales. In fact, a balanced spatio-

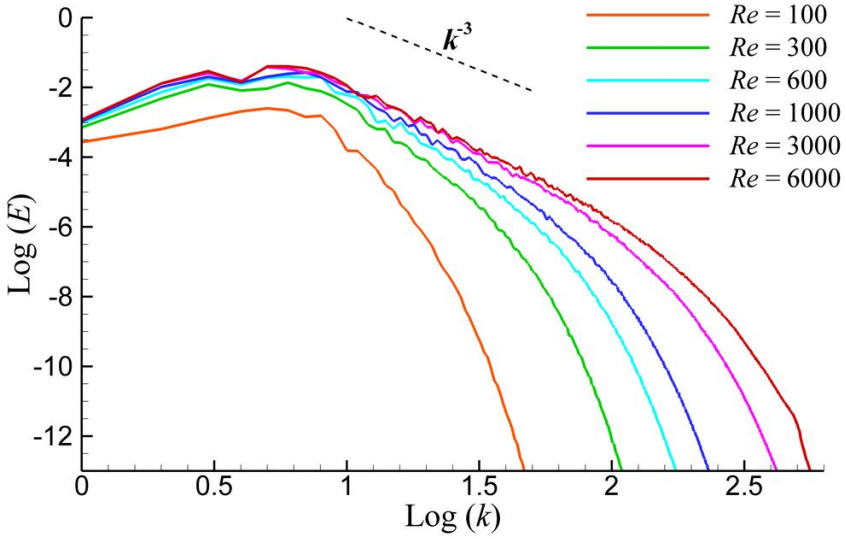

Figure 4.17: Reynolds number dependence of the energy spectrum in wave space. In the inertial range, the angle averaged energy spectrum, defined by Eq. (4.51), asymptotically reaches k^{-3} scaling with increasing Reynolds number.

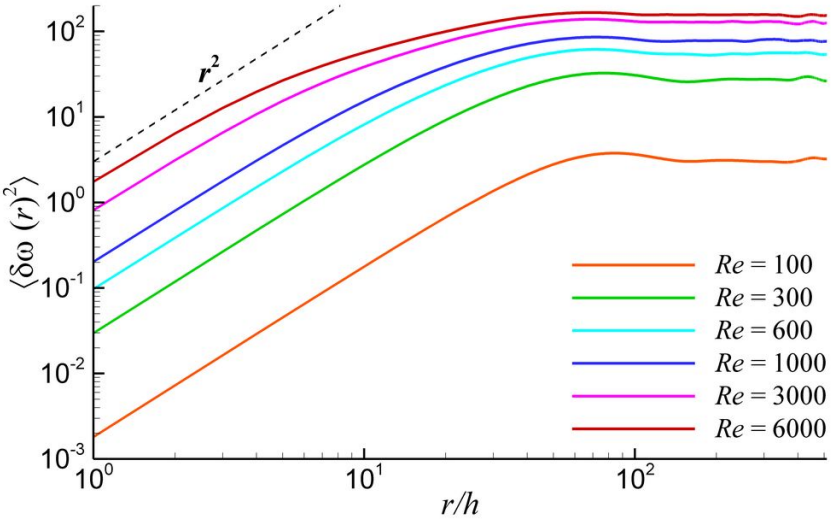

Figure 4.18: Reynolds number dependence of the second-order vorticity structure functions in physical space showing the second-order vorticity structure function, as defined by Eq. (4.52).

temporal discretization dictates a CFL number of $O(1)$ and large time steps can have the same undesirable effect on the solution as a coarse spatial resolution or a low-order dissipative spatial discretization.

In this section, we evaluate the behavior of different explicit Runge-Kutta schemes introduced earlier for time integration procedure by performing a time step refinement study. The domain of absolute stability for the explicit Runge-Kutta schemes for scalar equations can be found in many references including Canuto et al. (1988) and Butcher (2003). What is true for scalar equations is not necessarily true for systems as advocated by Pruett et al. (1995). Our method of estimating stability limits is somewhat heuristic here, but it becomes a useful guideline in practical applications for a wide variety of numerical methods.

For this purpose, we first compare the accuracy and stability of the temporal schemes by performing a time refinement study using the the sixth-order compact difference scheme as a spatial discretization method with 512^2 resolution. Table 4.5 shows the discrete L_2 error norms at $t = 10$ for $Re = 10^3$ obtained by the explicit Runge-Kutta schemes introduced earlier varying the time steps. The corresponding maximum CFL numbers for each computation are also documented in the table. Deviations of ω are computed from the base solution which is obtained by the forth-order Runge-Kutta method with a small time step of $\Delta t = 2 \times 10^{-4}$. In terms of numerical stability, it is demonstrated in the table that the fourth-order Runge-Kutta scheme has a greater stability region than the third-order ones as we expect. Among the third-order Runge-Kutta schemes for the explicit time integration, the optimal TVD Runge-Kutta scheme becomes more accurate than all the low-storage schemes. However, the difference between the Williamson scheme and the TVD Runge-Kutta scheme is negligible. On the other hand, we find that the predictor/corrector type Runge-Kutta scheme exhibit substantially lower accuracy than other third-order methods.

Next, we perform a similar analysis by using the second-order conservative Arakawa schemes for the same parameters. Results are demonstrated in Table 4.6 showing the similar trends as observed in the Table 4.5 for the compact scheme. The interesting outcome is that the second-order scheme can run using almost triple the effective time step if we compare with the sixth-order scheme due to a wider stability region. Although the results are not shown here, we also performed similar studies for the fourth-order Arakawa and the fourth-order compact schemes. Between the second-order scheme and the fourth-order ones, the second-

Table 4.5: Discrete L_2 error norms for the decaying turbulence problem at $t = 10$ for $Re = 10^3$ using the sixth-order compact difference scheme as a spatial discretization method. The reference solution for computing the L_2 norm is obtained using the RK4 method with a time step of $\Delta t = 2 \times 10^{-4}$. A dash indicates the numerical instability.

Scheme	$\|\omega\|_{L_2}^{CFL\approx 0.1}$	$\|\omega\|_{L_2}^{CFL\approx 0.2}$	$\|\omega\|_{L_2}^{CFL\approx 0.4}$	$\|\omega\|_{L_2}^{CFL\approx 0.8}$	$\|\omega\|_{L_2}^{CFL\approx 1.0}$
	$(\Delta t = 4 \times 10^{-4})$	(8×10^{-4})	(16×10^{-4})	(32×10^{-4})	(40×10^{-4})
RK4	7.50E-7	4.01E-6	5.31E-5	7.87E-4	1.84E-3
TVDRK3	3.92E-5	3.11E-4	2.46E-3	1.94E-2	–
SYMRK3	4.65E-4	1.94E-3	8.46E-3	3.98E-2	–
P/CRK3	1.32E-3	5.23E-3	2.06E-2	8.16E-2	–
INHRK3	4.02E-5	3.18E-4	2.51E-3	1.96E-2	–
WILRK3	3.99E-5	3.14E-4	2.49E-3	1.95E-2	–

Table 4.6: Discrete L_2 error norms for the decaying turbulence problem at $t = 10$ for $Re = 10^3$ using the second-order conservative Arakawa scheme as a spatial discretization method. The reference solution for computing the L_2 norm is obtained using the RK4 method with a time step of $\Delta t = 2 \times 10^{-4}$. A dash indicates the numerical instability.

Scheme	$\|\omega\|_{L_2}^{CFL\approx 0.2}$	$\|\omega\|_{L_2}^{CFL\approx 0.4}$	$\|\omega\|_{L_2}^{CFL\approx 1.25}$	$\|\omega\|_{L_2}^{CFL\approx 2.5}$	$\|\omega\|_{L_2}^{CFL\approx 3.0}$
	$(\Delta t = 8 \times 10^{-4})$	(16×10^{-4})	(50×10^{-4})	(100×10^{-4})	(125×10^{-4})
RK4	2.05E-6	1.94E-5	1.76E-3	3.31E-2	9.89E-2
TVDRK3	1.65E-4	1.33E-3	4.34E-2	4.16E-1	–
SYMRK3	2.05E-3	8.61E-3	1.04E-1	5.70E-1	–
P/CRK3	5.78E-3	2.28E-2	2.09E-1	7.18E-1	–
INHRK3	1.77E-4	1.41E-3	4.52E-2	4.20E-1	–
WILRK3	1.75E-4	1.40E-3	4.47E-2	4.16E-1	–

order spatial operator runs at nearly double the effective time step. These results suggest that the second-order scheme becomes more competitive with other high-order accurate spatial schemes by allowing larger time steps. On the other hand, as we will show in the following section, the second-order scheme usually requires double the resolution in each

direction to be able to obtain a similar accuracy. Even if using a low order scheme allows us to use larger time steps, still, the high-order schemes become more effective in terms of the tradeoff between the accuracy and efficiency. We also demonstrate that although we use an optimal fast Poisson solver, the CPU time increases approximately 8 times by doubling the resolution in each direction. In fact, it would be larger if we use other suboptimal Poisson solver. In other worlds, that fraction of CPU time is much bigger in other geometries in which the solution of the elliptic equation dominates the computational time. It should also be noted that the efficiency of the high-order schemes would be more pronounced for three dimensional computations.

4.6.3 Comparison of spatial schemes

Our main objective is to investigate and analyze the behaviors of the spatial numerical schemes presented in Section 4.3 for two-dimensional decaying turbulence simulations. In this section, four different families of high-order accurate finite difference representations are compared with pseudospectral simulations for various Reynolds numbers. We also compare high-order accurate schemes with the second-order accurate schemes. From our previous time refinement study, we conclude that the truncation error produced by Runge-Kutta time integration schemes is much smaller than the discretization schemes when we use a time step within the stability region. The TVD-RK scheme with $\Delta t = 2 \times 10^{-4}$ is used as a time integration algorithm for the following analysis in which the CFL number becomes $O(0.1)$. Therefore, we can compare different spatial schemes without contaminating the solution due to time stepping algorithm. We also highlight that we use the sixth-order compact difference formulation for discretization of viscous terms in all schemes tested here.

First, we present a set of numerical experiments using a resolution of 1024^2 for $Re = 1000$. The vorticity fields obtained by nine different spatial schemes at time $t = 5$ are presented and compared in Figure 4.19. A comparison of the vorticity distributions on the vertical center-line is also illustrated in Figure 4.23 by showing also a close-up figure to make the comparison

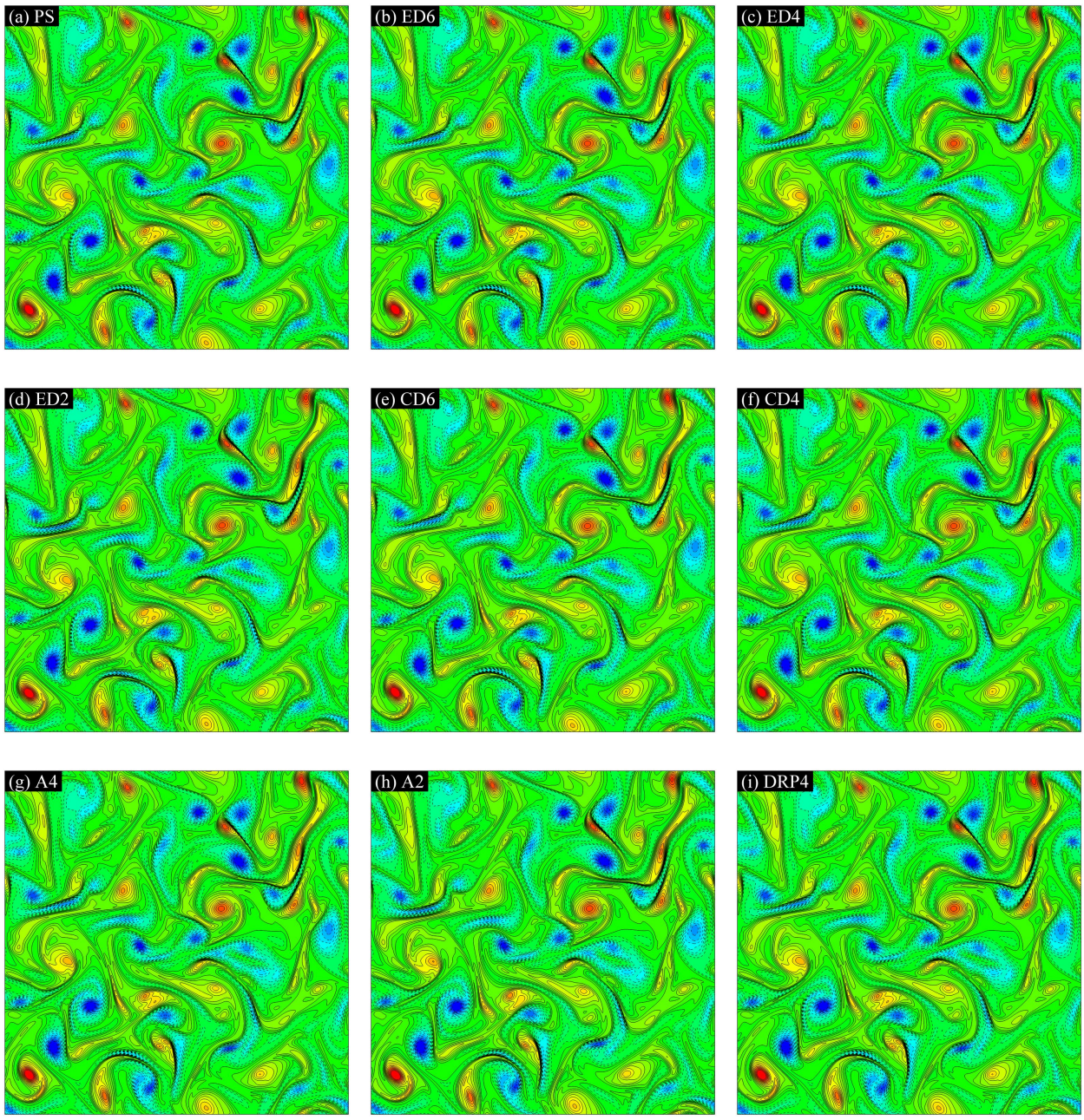

Figure 4.19: Comparison of the numerical schemes at time $t = 5$ for $Re = 1000$ with a resolution of 1024^2 ($Re_c = 6.13$). (a) Pseudospectral (PS) method, (b) sixth-order explicit difference (ED6) method, (c) fourth-order explicit difference (ED4) method, (d) second-order explicit difference (ED2) method, (e) sixth-order compact difference (CD6) method, (f) fourth-order compact difference (CD4) method, (g) fourth-order Arakawa (A4) method, (h) second-order Arakawa (A2) method, and (i) fourth-order dispersion-relation-preserving (DRP4) method. The vorticity contour layouts are identical in all nine cases illustrating 27 equidistant levels in the interval [-13, 13].

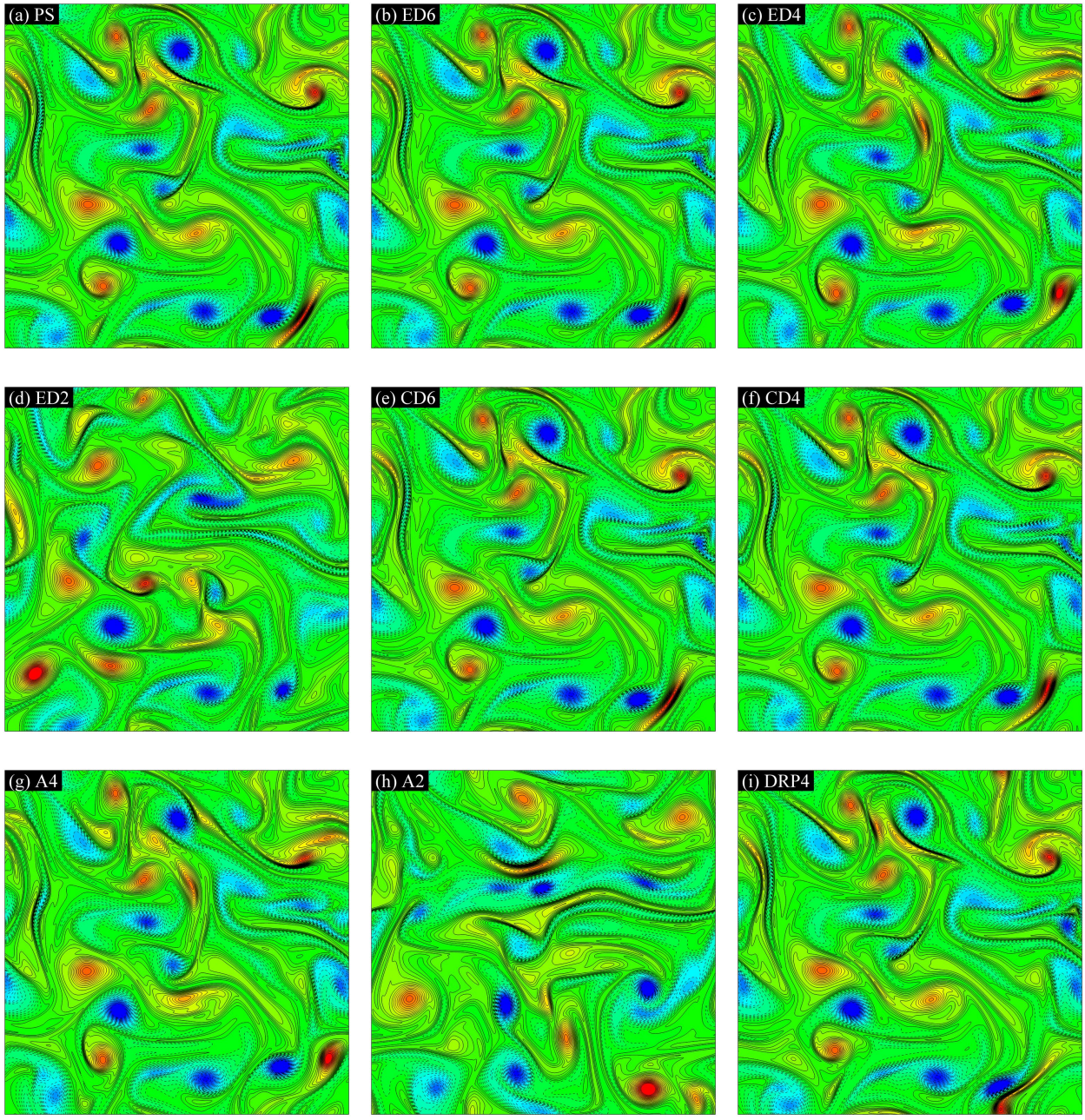

Figure 4.20: Comparison of the numerical schemes at time $t = 10$ for $Re = 1000$ with a resolution of 512^2 ($Re_c = 12.27$). (a) Pseudospectral (PS) method, (b) sixth-order explicit difference (ED6) method, (c) fourth-order explicit difference (ED4) method, (d) second-order explicit difference (ED2) method, (e) sixth-order compact difference (CD6) method, (f) fourth-order compact difference (CD4) method, (g) fourth-order Arakawa (A4) method, (h) second-order Arakawa (A2) method, and (i) fourth-order dispersion-relation-preserving (DRP4) method. The vorticity contour layouts are identical in all nine cases illustrating 41 equidistant levels in the interval [-8, 8].

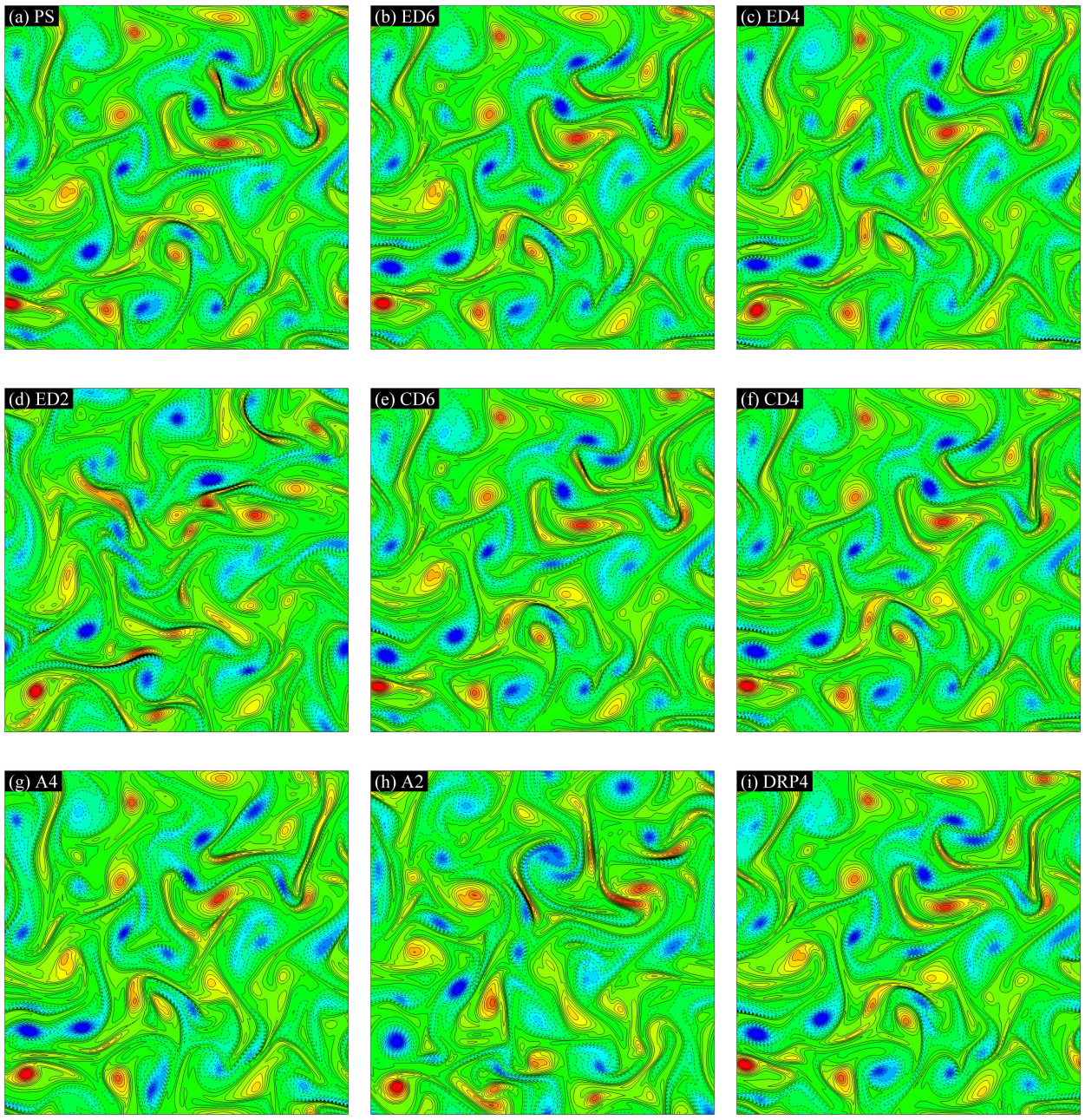

Figure 4.21: Comparison of the numerical schemes at time $t = 6$ for $Re = 1000$ with a resolution of 256^2 ($Re_c = 24.54$). (a) Pseudospectral (PS) method, (b) sixth-order explicit difference (ED6) method, (c) fourth-order explicit difference (ED4) method, (d) second-order explicit difference (ED2) method, (e) sixth-order compact difference (CD6) method, (f) fourth-order compact difference (CD4) method, (g) fourth-order Arakawa (A4) method, (h) second-order Arakawa (A2) method, and (i) fourth-order dispersion-relation-preserving (DRP4) method. The vorticity contour layouts are identical in all nine cases illustrating 23 equidistant levels in the interval [-11, 11].

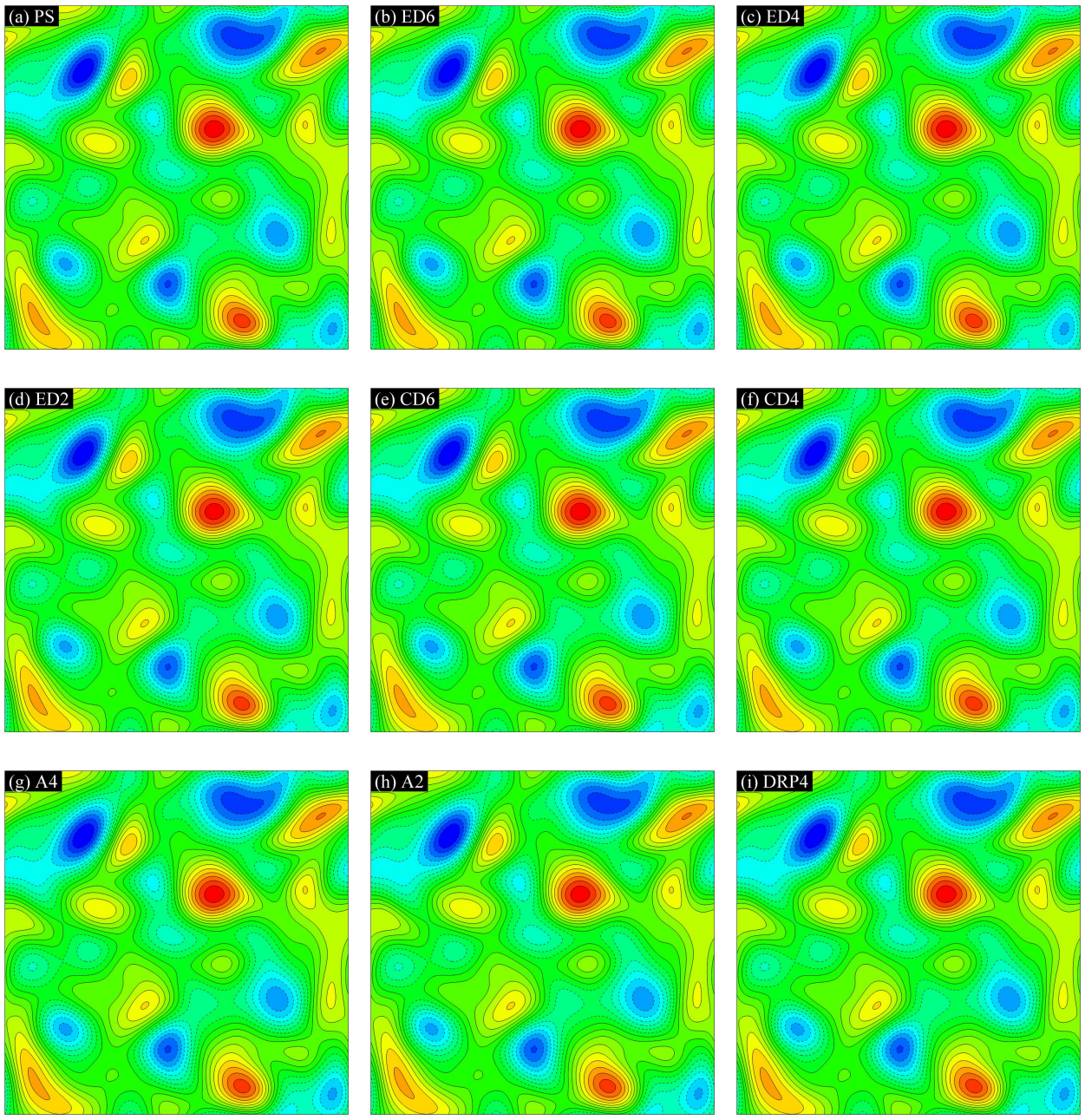

Figure 4.22: Comparison of the numerical schemes at time $t = 10$ for $Re = 100$ with a resolution of 512^2 ($Re_c = 1.23$). (a) Pseudospectral (PS) method, (b) sixth-order explicit difference (ED6) method, (c) fourth-order explicit difference (ED4) method, (d) second-order explicit difference (ED2) method, (e) sixth-order compact difference (CD6) method, (f) fourth-order compact difference (CD4) method, (g) fourth-order Arakawa (A4) method, (h) second-order Arakawa (A2) method, and (i) fourth-order dispersion-relation-preserving (DRP4) method. The vorticity contour layouts are identical in all nine cases illustrating 19 equidistant levels in the interval [-0.45, 0.45].

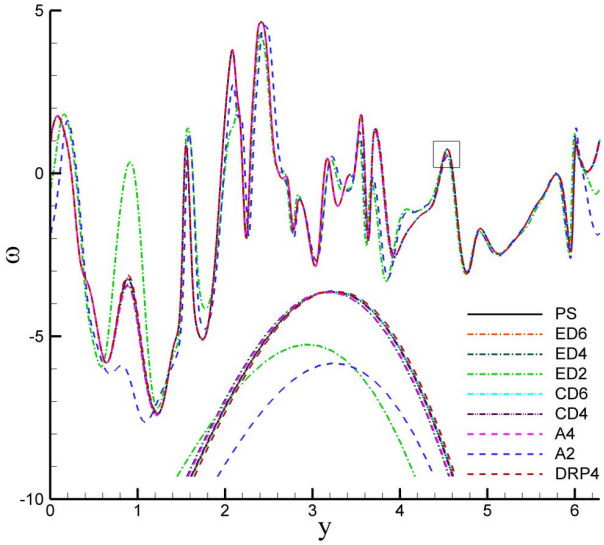

Figure 4.23: Comparison of the numerical schemes for $Re = 1000$ with a resolution of 1024^2 ($Re_c = 6.13$) at time $t = 5$. The centerline vorticity distributions at $x = \pi$ are plotted. Inset: close-up of boxed area.

more clear. Furthermore, a comparison of statistical behavior in terms of the second-order vorticity structure functions is also demonstrated in Figure 4.24. As we can see, the high-order schemes and the pseudospectral schemes yield similar flow fields. The second-order accurate schemes, both the explicit difference and the Arakawa schemes, predict slightly less accurate results. The sixth-order compact scheme exhibits the best prediction capability among the different formulations tested. In evaluating the performance of the different finite difference approximations, the deviation of vorticity field from the spectral solution is calculated by using the definition of discrete L_2 norm given by Eq. (4.49). Table 4.7 shows the L_2 norms, CPU times, and corresponding speed-up ratios for the finite difference formulations. The speed-up ratio is defined here as the ratio of CPU times for the computations performed using the pseudospectral method and those performed using finite difference schemes. First, all the finite difference methods are considerably more efficient than the pseudospectral method. The data in the table exhibits that the high-order schemes provide the same accuracy level as the Fourier-Galerkin pseudospectral method, while significantly decreasing its computational cost with a speed-up factor of 5 over the pseudospectral method. Among the

fourth-order schemes, both the compact and dispersion-relation-preserving schemes show a better performance than the Arakawa and explicit difference schemes. This clearly shows that designing a scheme with reduced truncation error or optimizing the scheme with respect to the dispersion relation could result in a better prediction capability than the designing a scheme with its discrete conservation properties.

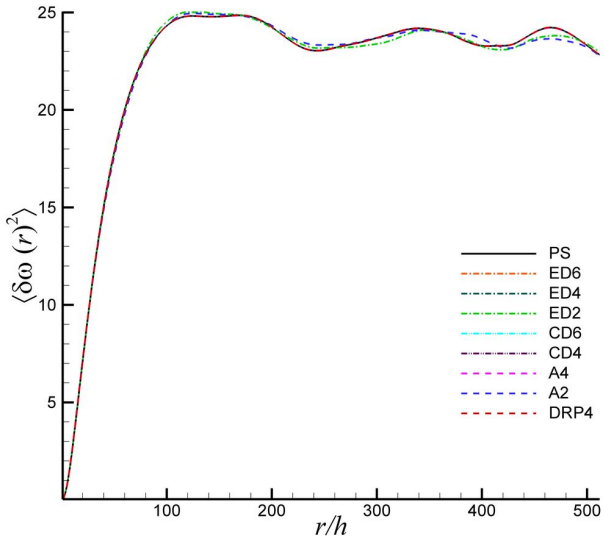

Figure 4.24: Comparison of the second-order vorticity structure functions for $Re = 1000$ with a resolution of 1024^2 ($Re_c = 6.13$) at time $t = 5$.

In order to analyze the effects of the Reynolds number and required resolution to the performance of schemes, it is useful to define a cell Reynolds number in the following form

$$Re_c = Re\frac{2\pi}{N_x} \tag{4.53}$$

Therefore, in our previous experiments having a resolution of 1024^2 at $Re = 1000$, the cell Reynolds number is $Re_c = 6.13$. Next, we perform similar experiments for $Re = 1000$ with 512^2 resolutions with an increasing cell Reynolds number of $Re_c = 12.27$. The vorticity fields at time $t = 10$ obtained by nine different spatial schemes are plotted in Figure 4.20. The corresponding second-order vorticity structure functions are also illustrated in Figure 4.25. We can easily see that the difference between high-order and low-order schemes becomes ampli-

Table 4.7: Accuracy and efficiency of the finite difference approximations for the decaying turbulence problem at $Re = 10^3$ using a resolution of 1024^2. The reference solution for the L_2 norms is obtained by the pseudo-specral method which takes a CPU time of 621.32 hrs. The speed-up ratio is defined as the ratio of CPU times.

Scheme	$\|\omega\|_{L_2}$	CPU (hrs.)	Speed-up
ED6	1.96E-3	128.39	4.84
ED4	3.51E-2	124.12	5.00
ED2	1.07	121.63	5.11
CD6	1.63E-4	149.52	4.16
CD4	6.23E-3	142.79	4.35
A4	3.29E-2	148.75	4.17
A2	1.11	127.29	4.88
DRP4	1.80E-2	126.59	4.90

fied, and there is a substantial difference in the corresponding flow fields. If we decrease the resolution to the 256^2 resulting in a higher cell Reynolds number, $Re_c = 24.54$, as shown in Figure 4.21 and Figure 4.26, low-order accurate numerical schemes produce totally different

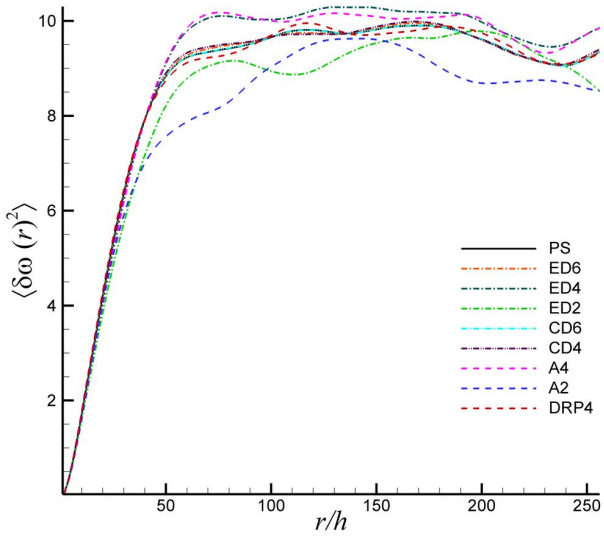

Figure 4.25: Comparison of the second-order vorticity structure functions for $Re = 1000$ with a resolution of 512^2 ($Re_c = 12.27$) at time $t = 10$.

flow fields. As the result of the series of calculations performed in the second and third sets of experiments, we can see that the sixth-order accurate schemes always predict the same accuracy results as the pseudospectral methods. In terms of fourth-order accurate schemes, we can see that the compact difference scheme produces a slightly better accuracy than the dispersion-relation-preserving scheme due to its lower truncation error properties. Between the compact scheme and Arakawa scheme, the compact scheme exhibits better accuracy than the Arakawa scheme. The computational efficiencies in terms of speed-up ratios for these sets of experiments are very similar to the previous high resolution computations given by Table 4.7. Making a comparison between low-order and high-order schemes, we can see that a slight increase in the computational time for a higher-order accurate scheme can result in significantly more accurate results than those obtained by the conventional second-order accurate schemes, and provide the same level of accuracy with the pseudospectral method in much less computational time.

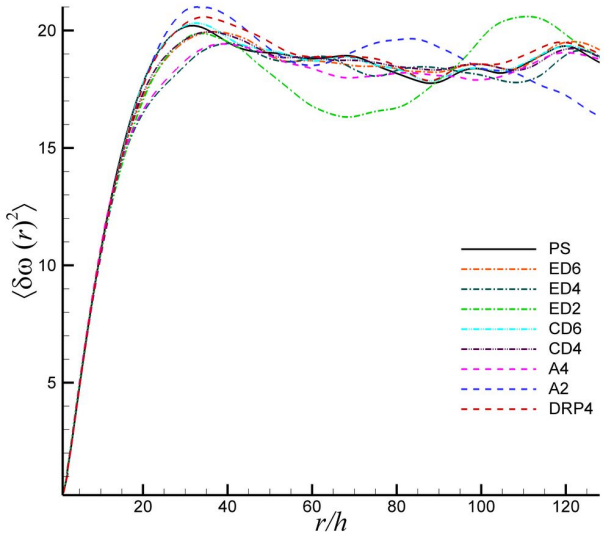

Figure 4.26: Comparison of the second-order vorticity structure functions for $Re = 1000$ with a resolution of 256^2 ($Re_c = 24.54$) at time $t = 6$.

We perform one more set of numerical experiments in order to demonstrate that the results of the various spatial schemes converge the same flow field under well resolved conditions using a resolution of 512^2 at a reduced $Re = 100$ for which $Re_c = 1.23$. The vorticity contour

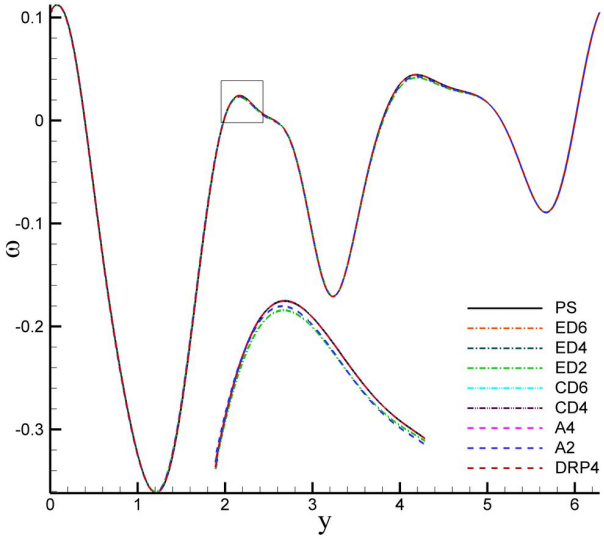

Figure 4.27: Comparison of the numerical schemes for $Re = 100$ with a resolution of 512^2 ($Re_c = 1.23$) at time $t = 10$. The centerline vorticity distributions at $x = \pi$ are plotted. Inset: close-up of boxed area.

plots obtained by these nine schemes are demonstrated in Figure 4.22 which shows that there is negligible difference among them. Both low-order and high-order difference schemes predict the same flow field with the pseudospectral method. This can also be seen clearly from Figure 4.27 showing the centerline vorticity distributions. Since the cell Reynolds number is smaller than 2, both second-order accurate and high-order accurate schemes produce similar results (i.e., well resolved direct numerical simulations). However, we can see that for larger cell Reynolds numbers, higher-order accurate schemes are required.

4.6.4 Pile-up phenomenon for high cell Reynolds number

Finally, we would like to test the performance of the finite difference formulations for extremely high cell Reynolds numbers. Two sets of numerical experiments are performed for a resolution of 256^2 at $Re = 3000$ and $Re = 6000$. The corresponding cell Reynolds numbers in these sets are $Re_c = 73.63$ and $Re_c = 147.26$, respectively. A comparison of the fourth-order difference schemes is shown in Figure 4.28 illustrating the evolution of the energy spectra

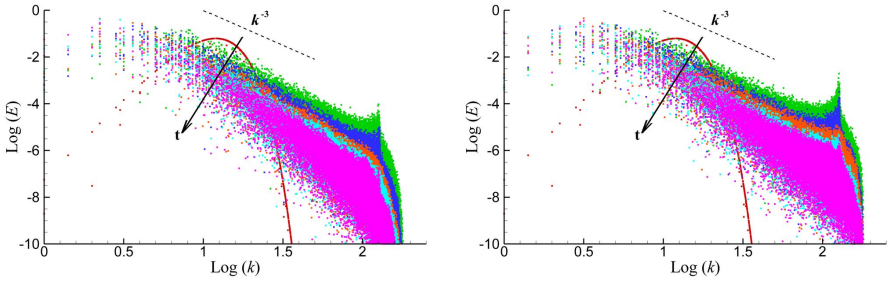

(a) ED4 for $Re = 3000$ (b) ED4 for $Re = 6000$

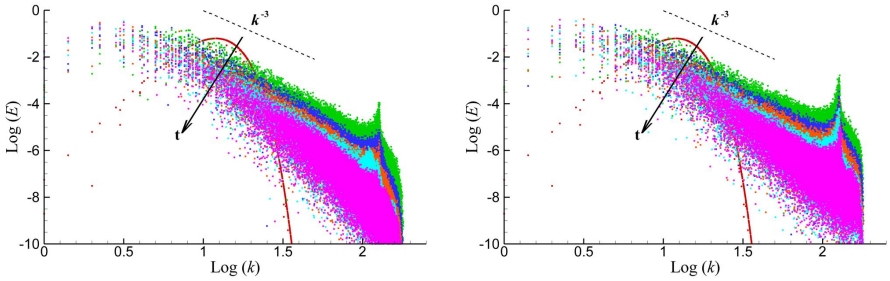

(c) CD4 for $Re = 3000$ (d) CD4 for $Re = 6000$

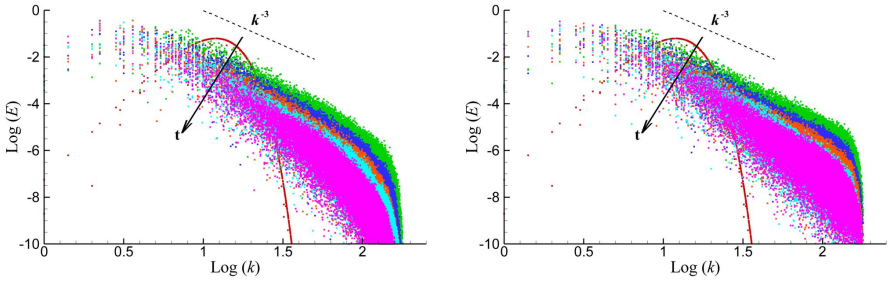

(e) A4 for $Re = 3000$ (f) A4 for $Re = 6000$

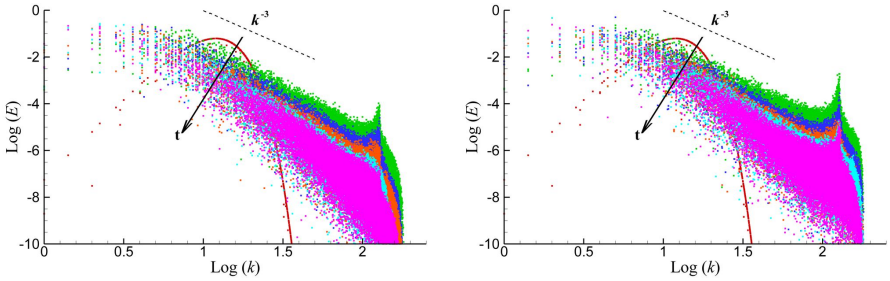

(g) DRP4 for $Re = 3000$ (h) DRP4 for $Re = 6000$

Figure 4.28: Evolution of energy spectra in decaying turbulence for two sets of Reynolds numbers: $Re = 3000$ ($Re_c = 73.63$) in the left column and $Re = 6000$ ($Re_c = 147.26$) in the right column. Comparison of the fourth-order finite difference schemes using a resolution of 256^2: (a-b) explicit difference (ED4), (c-d) compact difference (CD4), (e-f) Arakawa (A4), and (g-h) dispersion-relation-preserving (DRP4) schemes. Energy spectra, defined by Eq. (4.50), are shown for times $t = 0$, 2, 4, 6, 8, and 10.

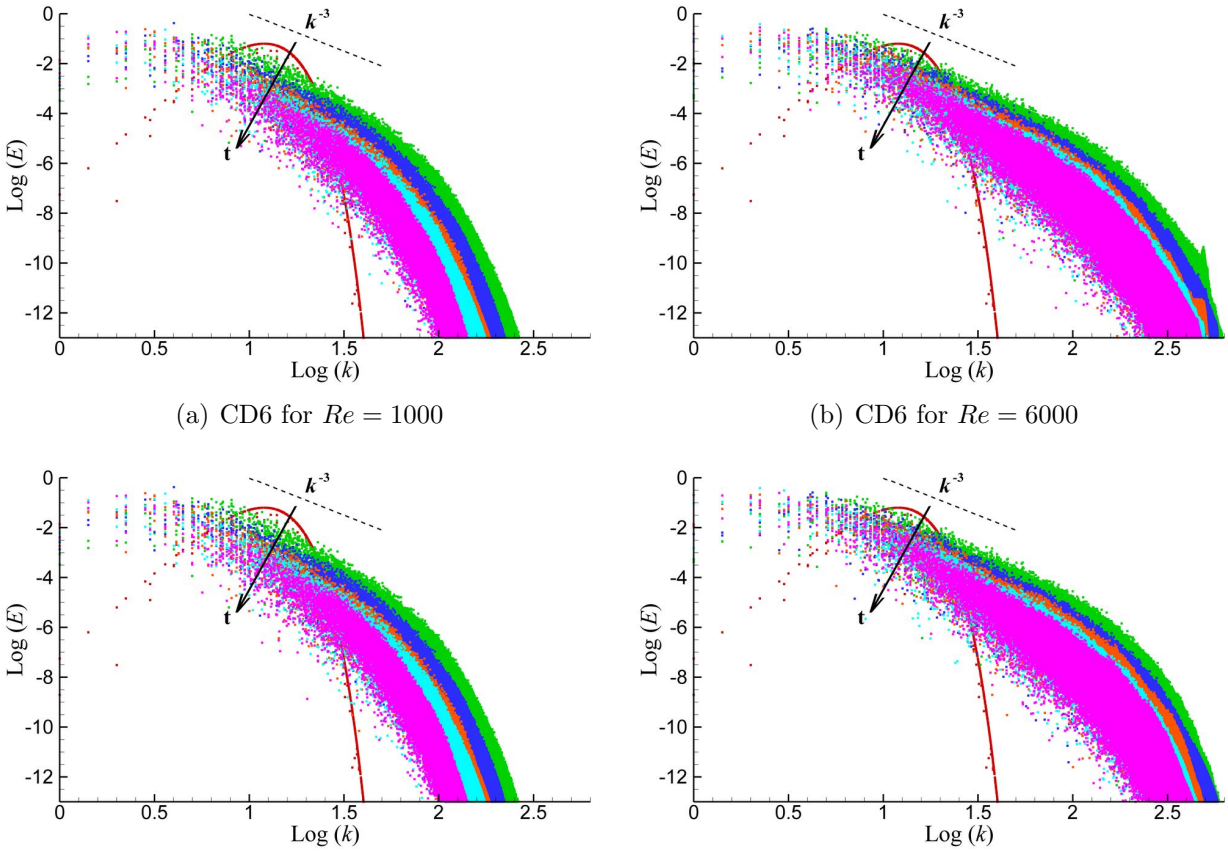

(a) CD6 for $Re = 1000$

(b) CD6 for $Re = 6000$

(c) A4 for $Re = 1000$

(d) A4 for $Re = 6000$

Figure 4.29: Evolution of energy spectra in decaying turbulence using a resolution of 1024^2 obtained by (a) the sixth-order compact difference (CD6) scheme at $Re = 1000$ ($Re_c = 6.13$), (b) the sixth-order compact difference (CD6) scheme at $Re = 6000$ ($Re_c = 36.78$), (c) the forth-order Arakawa (A4) scheme at $Re = 1000$ ($Re_c = 6.13$), and (d) the forth-order Arakawa (A4) scheme at $Re = 6000$ ($Re_c = 36.78$). Energy spectra, defined by Eq. (4.50), are shown for times $t = 0$, 2, 4, 6, 8, and 10.

for these Reynolds number. Instead of presenting the angle averaged energy spectra, we prefer to show the full energy spectra, as defined by Eq. (4.50), for each pair $\mathbf{k} = (k_x, k_y)$ in wave space to make the comparison more visible. This figure clearly illustrates that a higher degree of pile-up phenomenon occurs for all the finite difference schemes except the Arakawa scheme. Some sort of aliasing errors produce the growth of unphysical small scales. We demonstrate that these peaks of energy at small scales can be eliminated using the conservative Arakawa scheme. Although there is no big difference between the Arakawa scheme

and the explicit difference scheme for smaller cell Reynolds numbers as shown in the previous sections, the discrete global conservation properties of the Arakawa schemes prevent the pile-up phenomena for higher cell Reynolds numbers.

Another sets of experiments using a higher resolution of 1024^2 are also performed to demonstrate the limits of the difference schemes by considering the pile-up phenomenon. Evolution of the energy spectra for both sixth-order compact and Arakawa schemes are shown in Figure 4.29. Based on our numerical experiments, it is concluded that the pile-up phenomenon occurs with non fully conservative schemes for higher cell Reynolds numbers ($Re_c > 30$). Therefore, the Arakawa scheme is a better candidate for under-resolved simulations. It is mandatory to conserve energy to have a realistic simulations for higher cell Reynolds number. High-order centered schemes often show spurious wiggles for convective dominated problems when the numerical resolution is insufficient. The cell Reynolds number is restricted in some degree for these schemes. As the cell Reynolds number becomes larger, the nature of the finite difference equation is changed because of the cell size used. The spurious Nyquist signal would be generated almost instantaneously that propagates into the whole domain resulting an instability in the solution. In order to prevent these numerical instabilities for a centered difference scheme without enough resolution, the filtering methodology can be also used for under-resolved flows.

4.7 Summary and conclusions

A systematic comparison of a variety of high-order accurate finite difference schemes has been performed for two-dimensional decaying turbulence simulations by solving the vorticity-stream function formulation of two-dimensional incompressible Navier-Stokes equations. The following schemes were considered: the 6th-, 4th-, and 2nd-order explicit difference schemes, the 6th- and 4th-order compact difference schemes, the 4th- and 2nd-order Arakawa schemes, and the 4th-order dispersion-relation-preserving scheme. The objective of this study was to

determine the accuracy and efficiency of these schemes for long-time integration of decaying turbulence simulations, which serves as an instance of a complex flow. We compared the schemes with the spectrally accurate Fourier-Galerkin pseudospectral method. A brief description of these algorithms is given in Section 4.3. In order to eliminate the errors coming from boundary conditions, we performed our experiments in a doubly periodic domain. This setting provides a suitable framework for testing the spatial discretization schemes.

We first validated the methods by solving the Taylor-Green vortex problem which is one of the available exact solutions for two-dimensional unsteady incompressible flows. We showed that the theoretical orders of accuracies of the schemes were obtained in practice. Then we solved a more challenging double shear layer benchmark problem which has been used to test the grid-independence of many incompressible algorithms, since the presence of thinner and thinner shear layers evolving with time is not captured by low grid resolution representations. We found that the low-order difference schemes require about twice the resolution in each direction to achieve the same results as the high-order difference schemes. We also demonstrated that numerical oscillations near the sharp vorticity gradients can be eliminated using the high-order difference formulations.

We tested the efficiency and accuracy of several variants of third- and fourth-order Runge-Kutta time stepping algorithms for decaying two-dimensional turbulence. The numerical stabilities of the spatio-temporal schemes were addressed by performing a time refinement study. We first showed that the fourth-order Runge-Kutta schemes have greater accuracy for a given time step and have larger allowable stability regions than the third-order Runge-Kutta schemes. We found that the spatially second-order accurate schemes can run using almost triple the effective time step compared with the sixth-order schemes, and can also run using almost double the effective time step compared with the fourth-order schemes, thereby making them more competitive with the high-order finite difference schemes. On the other hand, we showed that the second-order schemes usually require double the resolution in each direction to be able to obtain a similar accuracy. Therefore, we found that higher order schemes become more effective in terms of the tradeoff between the accuracy and efficiency.

We studied the Reynolds number dependence of freely decaying turbulence. We showed that the predicted energy spectrum asymptotically converged to the theoretical k^{-3} scaling as the Reynolds number increased, which is predicted by the KBL theory for forward cascading two-dimensional turbulence in the inviscid limit. We also demonstrated that the analysis was also relatively free from temporal discretization errors. We then tested the spatial finite difference schemes for various Reynolds numbers. We defined a cell Reynolds number $Re_c = Re2\pi/N_x$. We demonstrated that for well resolved simulations, accurate results are obtained for all the schemes if $Re_c < 2$. If we increase the Reynolds number, however, the difference between the high-order accurate and second-order accurate schemes increases dramatically. Compact difference schemes provide more accurate results if $Re_c < 30$. Spurious Nyquist signals have been observed for larger Re_c resulting in a pile-up phenomenon. In this case, the fully conservative Arakawa schemes gives more accurate results.

Our results demonstrate the importance of high-order accurate representations in convection dominated complex flow problems, which, in general, require long time integrations. Although the order of accuracy is less important for well-resolved direct numerical simulations, it becomes significant for $Re_c > 2$. We show that, for fully resolved simulations, high-order accurate schemes do not require spectral-like simulation times. In fact, spectral-like accuracy is obtained with a speed-up factor of 5 over the pseudospectral method using the 6th-order compact scheme. We also demonstrate that the fourth-order Arakawa scheme is a better choice for higher cell Reynolds number computations.

Chapter 5

Stationary Two-Dimensional Turbulence Statistics Using a Markovian Forcing Scheme

In this study we investigate the statistics of two-dimensional stationary turbulence using a Markovian forcing scheme, which correlates the forcing process in the current time step to the previous time step according to a defined memory coefficient. In addition to the Markovian forcing mechanism, the hyperviscous dissipation mechanism for small scales and the Ekman friction type of linear damping mechanism for the large scales are included in the model. We examine the effects of various dissipation and forcing parameters on the turbulence statistics in both wave space and physical space. Our analysis includes the effects of the effective forcing scale, the bandwidth of the forcing, the memory correlation coefficient, and the forcing amplitude, along with the large scale friction and small scale dissipation coefficients. Scaling exponents of structure functions and energy spectra are calculated, and the role of the parameters associated with the Markovian forcing is discussed. We found that the scaling

O. San and A. E. Staples, "Stationary two-dimensional turbulence statistics using a Markovian forcing scheme," submitted to *Computers & Fluids*.

exponents are approximately invariant and show a universal behavior for the various forms of forcing schemes used. We found, however, that the final states strongly depend on the large scale friction mechanism considered. When the large scale friction mechanism is included in the model with a high friction coefficient, we demonstrate that the behavior is no longer universal. Our analysis also shows that the second-order vorticity structure function has an asymptotic scaling exponent for larger dissipation. Additionally, we confirmed that vorticity behaves as a passive scalar when the dissipation mechanism becomes less effective. Finally, although turbulence is not believed to have a separation of time scales in the dynamics of the velocity field, we conjectured that a separation of time scales exists in the dynamics of the energy spectrum.

5.1 Introduction

The phenomenology of turbulence was described by Richardson (1920) and quantified in a scaling theory by Kolmogorov (1941). It is believed that the turbulent flow phenomena are describable through the three-dimensional (3D) Navier-Stokes equations (Kaneda et al., 2003). Two-dimensional (2D) turbulence, to the first approximation, is a reduced dimensional version of 3D turbulence, where the flow is constrained to two dimensions. In reality, 2D turbulence is never realized in nature or in the laboratory, both of which have some degree of three-dimensionality (Boffetta and Ecke, 2012). Nevertheless, many aspects of idealized 2D turbulence appear to be relevant for physical systems in geophysics, astronomy and plasma physics (Rosa et al., 1998). One of the most important reasons for studying two-dimensional turbulence is to improve our understanding of geophysical flows in the atmosphere and ocean (Lilly, 1971; Charney, 1971; Herring et al., 1974; McWilliams, 1984; Maltrud and Vallis, 1991; Lindborg, 1999; Ferziger et al., 2002; San et al., 2011), in which stratification and rotation suppress vertical motions in the thin layers of fluid.

From a theoretical perspective, 2D turbulence is not simply a reduced dimensional version

of 3D turbulence because a completely different phenomenology arises from new conservation laws in two dimensions (Boffetta and Ecke, 2012). In fact, two-dimensional turbulence behaves in a profoundly different way from three-dimensional turbulence due to different energy cascade behavior, and follows the Kraichnan-Batchelor-Leith (KBL) theory (Kraichnan, 1967; Batchelor, 1969; Leith, 1971). In three-dimensional turbulence, energy is transferred forward, from large scales to smaller scales, via the vortex stretching and tilting mechanism. In two dimensions that mechanism is absent, and it turns out that under most forcing and dissipation conditions energy will be transferred from smaller scales to larger scales. This is largely because of another quadratic invariant, the potential enstrophy, defined as the integral of the square of the potential vorticity. Despite the apparent simplicity of dealing with two rather than three spatial dimensions, two-dimensional turbulence is possibly richer in its dynamics due to its conservation properties, such as its inverse energy and forward enstrophy cascading mechanisms, which three-dimensional turbulence do not possess.

The physics of two-dimensional turbulence have been elucidated substantially during the past decades by theoretical models, intensive numerical investigations, and dedicated soap film experiments (Goldburg et al., 1997; Bruneau and Fischer, 2009). Danilov and Gurarie (2000), Kellay and Goldburg (2002), and Tabeling (2002) reviewed both theoretical and experimental two-dimensional turbulence studies. More recent reviews on two-dimensional turbulence are also provided by Clercx and van Heijst (2009) and Boffetta and Ecke (2012). Recent studies in two-dimensional turbulence, both forced (stationary) turbulence (Lindborg and Alvelius, 2000; Danilov and Gurarie, 2001a; Tran and Shepherd, 2002; Boffetta and Musacchio, 2010; Bracco and McWilliams, 2010; Vallgren and Lindborg, 2011) and unforced (decaying) turbulence (Yin et al., 2004; Lindborg and Vallgren, 2010; Kuznetsov et al., 2010; Fox and Davidson, 2010) provide high resolution computational confirmation of the KBL theory. The conjecture in KBL theory is that enstrophy, not energy, cascades to the small scales, and the energy, on the contrary, cascades to the large scales (Weiss, 1991). Therefore, in two-dimensional turbulence there are two inertial ranges, one for the forward cascade of enstrophy and one for the inverse cascade of energy. In this dual cascading phenomenon, the

relative locations of the Kolmogorov and Kraichnan scalings in 2D turbulence energy spectra depend on the forcing scale (Tran and Bowman, 2003). According to Kolmogorov theory, in the energy cascade range, the only parameters of practical importance would be energy injection rate ϵ and wave number k. Dimensional reasoning states that the energy density (i.e., energy spectrum) is $E(k) \sim \epsilon^{2/3} k^{-5/3}$. In KBL theory, a similar argument gives that $E(k) \sim \eta^{2/3} k^{-3}$ in the forward enstrophy cascade range; where η is the enstrophy injection rate (i.e., energy injection rate is related to the enstrophy injection rate by $\epsilon = \eta / k_f^2$ in which k_f is the energy injection scale). These predictions for dual cascade given by KBL theory are illustrated in Figure 5.1.

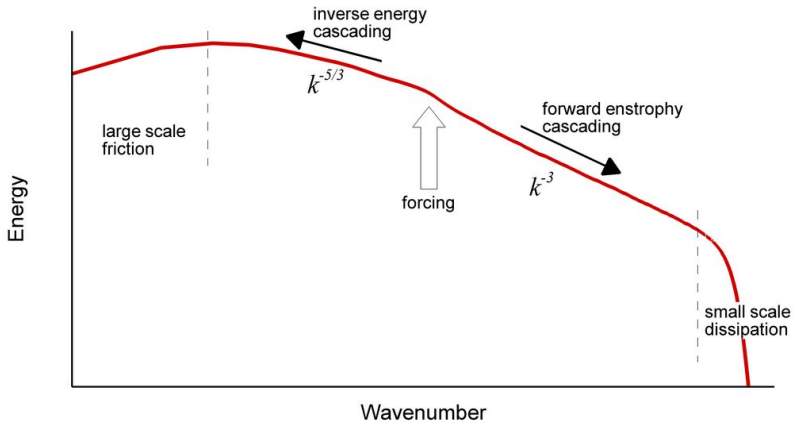

Figure 5.1: A qualitative picture of the energy spectrum which shows double cascade scalings of stationary two-dimensional turbulence.

The dual cascade conjecture, along with the dissipation mechanisms, challenges the universality of the scalings in stationary two-dimensional turbulence. In general, the dissipation mechanism contains an energy sink on large-scales and an enstrophy sink on small-scales (Maltrud and Vallis, 1991; Borue, 1993; Smith and Yakhot, 1993, 1994; Legras et al., 1988; Danilov and Gurarie, 2001a; Haugen and Brandenburg, 2004). The presence of these two sinks is necessary to reach a stationary regime if two different fluxes are assumed to flow in opposite directions from the forcing zone as hypothesized in two-dimensional turbulence. In other words, due to inverse energy cascading in two-dimensional turbulence, the station-

ary final state can only be obtained if there exist a dissipation mechanism in large scales. Therefore, large-scale dissipation mechanisms have been routinely employed in numerical simulations of stationary two-dimensional turbulence to absorb energy at large scales. Blackbourn and Tran (2011) have recently studied the effects of friction on forced two-dimensional Navier-Stokes turbulence.

Two-dimensional turbulence models are useful for understanding large scale motions of forced-dissipative systems occurring in the atmosphere and oceans. The frictional and forcing effects discussed in this study are crucial to understanding the dynamics of these systems. The statistics of such a forced-dissipative two-dimensional turbulence system are investigated here for a wide range of physical considerations. One of our major goals is to analyze the universality of the scaling laws for these statistics in both wave space and physical space by considering the energy or enstrophy spectra and velocity or vorticity structure functions. In order to minimize the effects of dissipation at intermediate scales of the spectrum, following many two-dimensional turbulence studies (e.g., Maltrud and Vallis (1991); Borue (1993); Smith and Yakhot (1993, 1994); Legras et al. (1988); Danilov and Gurarie (2001a); Haugen and Brandenburg (2004)), we use high-order Laplacian for viscosity (sometimes called hyperviscosity) which separates sharply the inertial and dissipative ranges. To model the forcing and energy injection mechanism, we use a Markovian process, which correlates the forcing structure in the current time step to the previous one according to a defined memory coefficient. The effects of the amplitude of the forcing, the effective forcing scale, and the bandwidth of the forcing are considered here in addition to the memory coefficient parameter that measures the stochastic behavior of the forcing mechanism in the system. We integrate the hyperviscous Navier-Stokes equations with a pseudospectral method using the third-order Runge-Kutta scheme for nonlinear terms and the second-order Crank-Nicolson scheme for the linear dissipation terms. We should also note that our hyperviscous model reduces to the classical Navier-Stokes turbulence model in the limiting case.

The paper is organized as follows: the mathematical formulation of the forced-dissipative two-dimensional turbulence is given in Section 5.2. The numerical methods are briefly pre-

sented in Section 5.3. The results for two-dimensional isotropic homogeneous stationary turbulence are provided in Section 5.4. This section also explores the effects of large scale friction and small scale dissipation mechanisms, and systematically analyzes the relevant parameters of the Markovian forcing scheme. The turbulence statistics in the stationary regime and their scaling exponents are shown in this section as well. Final conclusions and comments are drawn in Section 5.5.

5.2 Mathematical model

The governing equation for two-dimensional incompressible flows can be written in its vorticity formulation in the following form (Danilov and Gurarie, 2000)

$$\frac{\partial \omega}{\partial t} + J = D + F \tag{5.1}$$

where ω is the vorticity which is a scalar quantity in two-dimensional flows. Here, J is the nonlinear Jacobian which symbolizes nonlinear interactions, D represents the dissipation mechanism, and F is for forcing. The Jacobian term in Eq. (5.1) is defined as

$$J = \mathbf{u}.\nabla\omega = \frac{\partial \psi}{\partial y}\frac{\partial \omega}{\partial x} - \frac{\partial \psi}{\partial x}\frac{\partial \omega}{\partial y} \tag{5.2}$$

using the definition of the velocity stream function

$$u = \frac{\partial \psi}{\partial y}; \quad v = -\frac{\partial \psi}{\partial x} \tag{5.3}$$

where u and v are components of the two-dimensional velocity vector field $\mathbf{u}$. The dissipation term in classical Navier-Stokes equation is given as $D = \upsilon\nabla^2\omega$, where ∇^2 is the Laplacian. In this study, we use a generalized form of the dissipation $D = \upsilon\nabla^{2p}\omega$ in place of the regular viscosity dissipation. The purpose of using high order Laplacian, which is called as hyperviscosity, is to eliminate as much as possible the effects of viscosity at the intermediate

scales, thus extending turbulence inertial scales. On the other hand, in order to sink energy at the large scales we use Ekman type friction to be able reach a statistically steady state. In the case of periodic boundary conditions the applied forcing mechanism would result in an unbounded growth of the total kinetic energy if we would not include a large scale friction mechanism. The Ekman friction terminology is usually used in the contexts of the rotating flows. We can also interpret this large scale friction term as Rayleigh friction for stratified flows, or Hartman friction for magnetohydrodynamic flows. Finally, the dissipation mechanism in our study is modeled by the following generalized form

$$D = (-1)^{p+1} \upsilon \nabla^{2p} \omega - \lambda \omega \tag{5.4}$$

in which it reduces the classical Ekman-Navier-Stokes equation for $p = 1$. The kinematic relationship between vorticity and stream function according is given as

$$\frac{\partial^2 \psi}{\partial x^2} + \frac{\partial^2 \psi}{\partial y^2} = -\omega. \tag{5.5}$$

From a computational point of view, this formulation has several advantages over the primitive variable formulation. It eliminates pressure from the Navier-Stokes equations and hence has no corresponding odd-even decoupling between the pressure and velocity components, as well as projection inaccuracies usually observed in fractional step approaches (Brown et al., 2001). The vorticity-stream function formulation also automatically satisfies the divergence-free condition and allows one to reduce the number of equations to be solved.

5.3 Numerical methods

Fourier series expansion based methods are often used for solving problems with periodic boundary conditions. One of the most accurate methods for solving the Navier-Stokes equations in periodic domains is the pseudospectral method, which exploits fast Fourier transform

(FFT) algorithms, resulting in spectral accuracy (Press et al., 1992; Moin, 2001). By transforming Eq. (5.1) to Fourier space the governing equation becomes

$$\frac{\partial \hat{\omega}_{\mathbf{k}}}{\partial t} + J_{\mathbf{k}} = D_{\mathbf{k}} + F_{\mathbf{k}} \tag{5.6}$$

where a hat over the variable represents the Fourier coefficients of the corresponding variable in the wave space $\mathbf{k} = (k_x, k_y)$. The relationship between vorticity and stream function in the Fourier space becomes

$$(-k_x^2 - k_y^2)\hat{\psi}_{\mathbf{k}} = -\hat{\omega}_{\mathbf{k}}. \tag{5.7}$$

The nonlinear Jacobian in Fourier space is

$$J_{\mathbf{k}} = (\boldsymbol{i}k_y\hat{\psi}_{\mathbf{k}}) \circ (\boldsymbol{i}k_x\hat{\omega}_{\mathbf{k}}) - (\boldsymbol{i}k_x\hat{\psi}_{\mathbf{k}}) \circ (\boldsymbol{i}k_y\hat{\omega}_{\mathbf{k}}) \tag{5.8}$$

where i is the complex unit number (i.e., $i^2 = -1$). The convolution sum in the nonlinear Jacobian term is computed in the spatial domain using the convolution theorem. In the pseudospectral method, the convolution sum of these nonlinear terms is actually computed in the physical domain and fast Fourier transforms are used to go back and forth between Fourier wave space and physical space. In the present study, we use the standard Fourier-Galerkin pseudospectral method in a periodic square box of a length 2π (Canuto, 2006). The dissipation terms in the Fourier space becomes

$$D_{\mathbf{k}} = -[\upsilon k^{2p} + \lambda]\hat{\omega}_{\mathbf{k}} = -[\nu(\frac{k}{k_d})^{2p} + \lambda]\hat{\omega}_{\mathbf{k}} \tag{5.9}$$

where $k = \sqrt{k_x^2 + k_y^2}$. We redefine the small scale viscosity coefficient by using the expression of $\nu = \upsilon k_d^{2p}$ where k_d is the effective dissipation wave number, which we set in our study as $k_d = 0.96N/2$, where $N^2 = 512^2$ is the resolution of the problem. Note that the power $p = 1$ corresponds the regular constant property Navier-Stokes equations for Reynolds number of $Re = k_d^2/\nu$. In our model, we use a Markovian forcing scheme, which correlates the forcing in the current time step to the previous one according to a defined memory coefficient. The

forcing is localized within narrow spectral range $(k_f-\sigma, k_f+\sigma)$ in the vicinity of the forcing wave number k_f. The bandwidth of the effective forcing is determined by the σ variable. The Markovian forcing process at the current time step becomes

$$F_{\mathbf{k}}^n = f_0(1-\rho^2)^{1/2}e^{i\zeta} + \rho f_k^{n-1} \tag{5.10}$$

where f_0 is the forcing amplitude, ρ is the memory correlation coefficient, and the ζ is the uniformly distributed phase on interval $[0, 2\pi]$. In this study, the semi-discrete vorticity transport equation in Fourier space, Eq. (5.6), is solved by a combination of the third-order Runge-Kutta and second-order Crank-Nicolson schemes in a periodic square. The dissipation terms are treated by an implicit Crank-Nicolson scheme and nonlinear Jacobian and forcing terms are treated by the explicit Runge-Kutta scheme. Therefore, starting with the value of the Fourier coefficients of vorticity, $\hat{\omega}_{\mathbf{k}}^n$, at the current time step, the time marching algorithm for computing the vorticity at the next time step, $\hat{\omega}_{\mathbf{k}}^{n+1}$, consists of the following three substeps:

$$\begin{aligned}
\hat{\omega}_{\mathbf{k}}^{(1)} &= \alpha_1\hat{\omega}_{\mathbf{k}}^n + \beta_1(-J_{\mathbf{k}}^n + F_{\mathbf{k}}^n) \\
\hat{\omega}_{\mathbf{k}}^{(2)} &= \alpha_2\hat{\omega}_{\mathbf{k}}^{(1)} + \beta_2(-J_{\mathbf{k}}^{(1)} + F_{\mathbf{k}}^n) - \gamma_2(-J_{\mathbf{k}}^n + F_{\mathbf{k}}^n) \\
\hat{\omega}_{\mathbf{k}}^{n+1} &= \alpha_3\hat{\omega}_{\mathbf{k}}^{(2)} + \beta_3(-J_{\mathbf{k}}^{(2)} + F_{\mathbf{k}}^n) - \gamma_3(-J_{\mathbf{k}}^{(1)} + F_{\mathbf{k}}^n).
\end{aligned} \tag{5.11}$$

where the coefficients are

$$\begin{aligned}
\alpha_1 &= \frac{1+\frac{4}{15}\alpha\Delta t}{1-\frac{4}{15}\alpha\Delta t}; \quad \beta_1 = \frac{\frac{8}{15}\Delta t}{1-\frac{4}{15}\alpha\Delta t}; \quad \alpha = -[\nu(\frac{k}{k_d})^{2p} + \lambda] \\
\alpha_2 &= \frac{1+\frac{1}{15}\alpha\Delta t}{1-\frac{1}{15}\alpha\Delta t}; \quad \beta_2 = \frac{\frac{5}{12}\Delta t}{1-\frac{1}{15}\alpha\Delta t}; \quad \gamma_2 = \frac{\frac{17}{60}\Delta t}{1-\frac{1}{15}\alpha\Delta t} \\
\alpha_3 &= \frac{1+\frac{1}{6}\alpha\Delta t}{1-\frac{1}{6}\alpha\Delta t}; \quad \beta_3 = \frac{\frac{3}{4}\Delta t}{1-\frac{1}{6}\alpha\Delta t}; \quad \gamma_3 = \frac{\frac{5}{12}\Delta t}{1-\frac{1}{6}\alpha\Delta t}
\end{aligned} \tag{5.12}$$

in which Δt is the time step.

5.4 Results

In this section we present numerical results for homogeneous isotropic stationary turbulence for various physical parameters which determine the forcing and dissipation mechanisms. The spatial resolution is fixed $N^2 = 512^2$ Fourier modes, the time step size is $\Delta t = 0.005$, and the solution is advanced forward in time in Fourier space. For all the simulations we start from a rest state, integrate the model until a statistically steady state is obtained, and continue for enough time to compute turbulence statistics. The boundary conditions are 2π-periodic in both directions. The domain-integrated kinetic energy is tracked for each simulation to measure the energy level of the system, which is quantified by the following integral

$$E(t) = \frac{1}{2} \iint \left(\frac{\partial \psi}{\partial x} \right)^2 + \left(\frac{\partial \psi}{\partial y} \right)^2 dx\, dy, \tag{5.13}$$

in which we can estimate when the system reaches quasi-stationary regime. Averaging over time is not possible unless a statistically steady state is established by a large scale friction mechanism. The mean values are obtained by ensemble averaging the data between time $t = 50$ and $t = 100$ throughout the study.

In order to examine the characteristics of two-dimensional stationary turbulence, we first define two statistical measures; one is the energy spectrum in wave space, and the other is the structure function in physical space. The energy spectrum is defined as

$$\hat{E}(\mathbf{k}, t) = \frac{1}{2} k^2 |\hat{\psi}(\mathbf{k}, t)|^2 \tag{5.14}$$

and the angle averaged energy spectrum is

$$E(k, t) = \sum_{k \le |\acute{\mathbf{k}}| \le k+1} \hat{E}(\acute{\mathbf{k}}, t). \tag{5.15}$$

In the forward enstrophy cascade (i.e., in the inertial scale between the forcing scale and the small scale dissipation), it is known from the KBL theory that the energy spectrum in the

inertial range approaches the classical k^{-3} scaling in the inviscid limit. On the other hand, in the inverse energy cascade (i.e., the inertial scale which includes the scales larger than the forcing scale), the theory predicts that the energy spectrum scales by $k^{-5/3}$, since the scaling arguments leading to this Kolmogorov scaling nowhere assume a specified direction of the cascade.

The statistics of two-dimensional turbulent flow can be further investigated considering powers of velocity or vorticity differences in the physical space. A commonly used statistical quantity in two-dimensional turbulence is the second-order vorticity structure function which is defined as

$$\langle \delta\omega(r)^2 \rangle = \langle |\omega(\mathbf{x}+\mathbf{r}) - \omega(\mathbf{x})|^2 \rangle \tag{5.16}$$

with $r = |\mathbf{r}|$ being the spatial separation. Assuming that the system is homogeneous and isotropic, the structure functions depend on r only. The classical $k^{-5/3}$ scaling of energy spectrum in the inverse energy cascade relates to a $r^{2/3}$ scaling of second-order velocity structure function. In the enstrophy cascade range, where Kraichnan k^{-3} scaling appears, the corresponding r^2 scaling is equal to the upper bound. Hence, steeper energy spectra always results in r^2 scaling (Kramer et al., 2011). Vorticity transport equation in two-dimension is formally identical to passive scalar transport equation that describes the transport of a scalar quantity θ passively advected by velocity field (Benzi et al., 1990; Celani and Seminara, 2005; Falkovich and Fouxon, 2005). In the context of passive scalar, according to the theory (Benzi et al., 1990; Paret et al., 1999; Bracco and McWilliams, 2010), the second-order vorticity structure function in the inviscid limit is proportional with $\langle \delta\omega(r)^2 \rangle \sim r^d$ for a given energy spectrum $E(k) \sim k^{-3-d}$, for $0 < d < 2$.

The scaling exponents of turbulence statistics that deviate from the values predicted by the theory have been observed in the literature (Saffman, 1971; McWilliams, 1984; Legras et al., 1988; Benzi et al., 1990; Maltrud and Vallis, 1991; Danilov and Gurarie, 2000; Ishihara and Kaneda, 2001; Kevlahan et al., 2007). The universality of the statistics of two-dimensional turbulence in both wave space and physical space have also been questioned

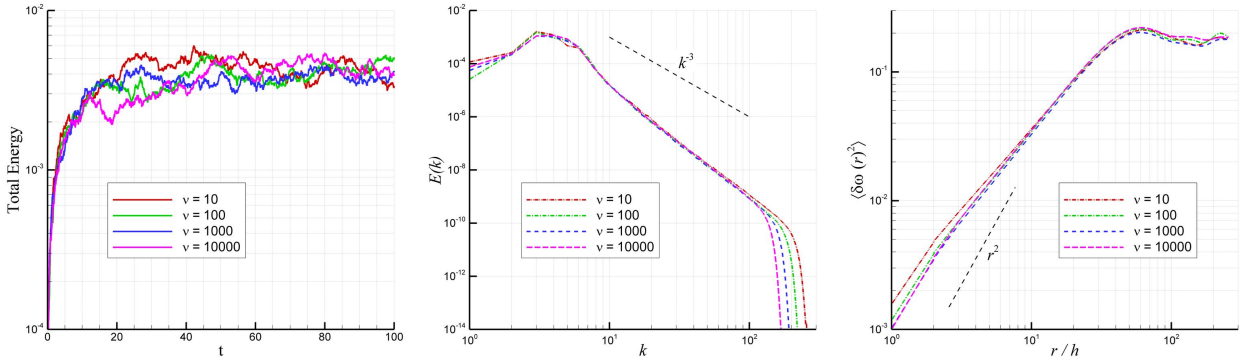

(a) (b) (c)

Figure 5.2: The effects of the small scale dissipation coefficient on the statistics ($\lambda = 0.05$, $p = 8$ and $k_f = 5$); (a) time series of total energy, (b) angle averaged energy spectra, and (c) second-order vorticity structure functions.

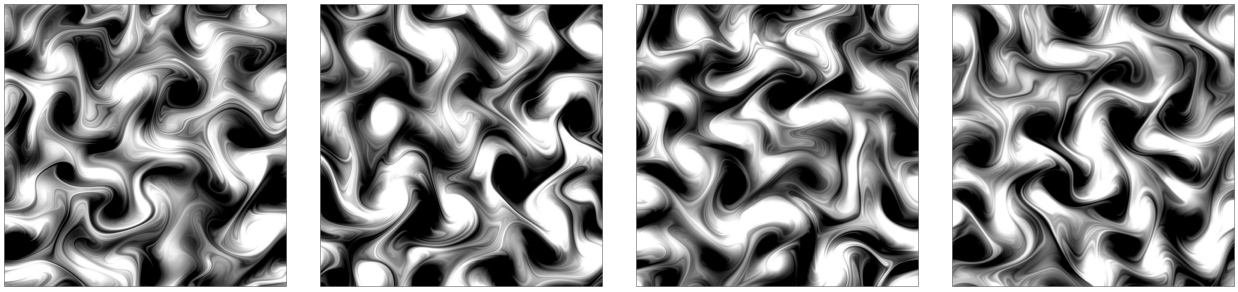

(a) $\nu = 10$ (b) $\nu = 100$ (c) $\nu = 1000$ (d) $\nu = 10000$

Figure 5.3: Instantaneous vorticity fields at time $t = 100$ for varying the small scale dissipation coefficient using the forcing scale $k_f = 5$ and the order of Laplacian $p = 8$.

(Danilov and Gurarie, 2001b). In the following analysis, statistical properties of the forced two-dimensional turbulence are systematically investigated by numerical simulations for different physical parameters. Our primary goal here is to elucidate the effects of the various forcing and dissipation mechanisms on the turbulence statistics.

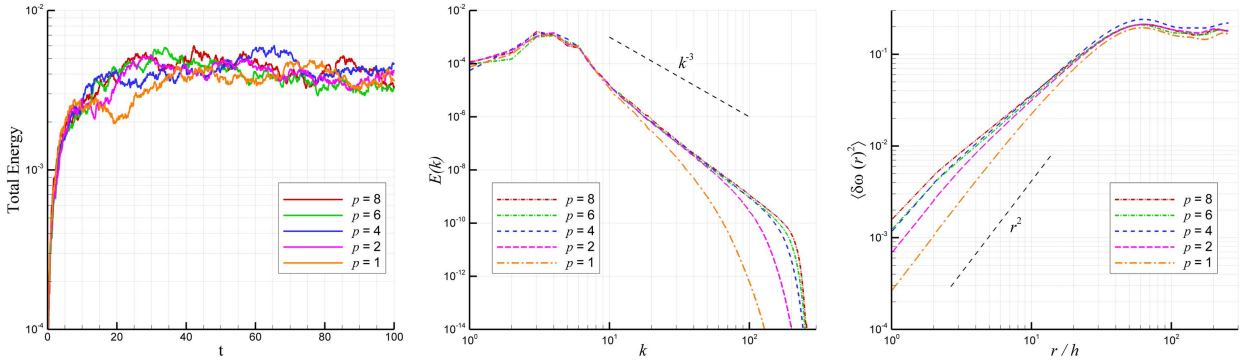

(a) (b) (c)

Figure 5.4: The effects of the order of hyperviscosity on the statistics ($\lambda = 0.05$, $\nu = 10$ and $k_f = 5$); (a) time series of total energy, (b) angle averaged energy spectra, and (c) second-order vorticity structure functions.

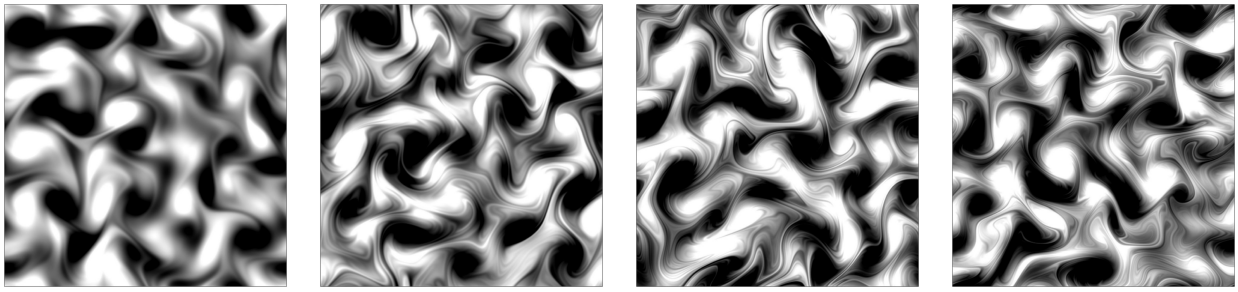

(a) $p = 1$ (b) $p = 2$ (c) $p = 4$ (d) $p = 6$

Figure 5.5: Instantaneous vorticity fields at time $t = 100$ for various order of the hyperviscosity using the forcing scale of $k_f = 5$ and the small scale dissipation coefficient of $\nu = 10$.

5.4.1 Effects of small scale dissipation mechanism

First, we analyze the effects of small scales dissipation mechanism on turbulence statistics. Figure 5.2 shows the statistics for different values of small scale dissipation coefficient ν. The order of the Laplacian, the large scale dissipation coefficient, and all the coefficients for forcing scheme remain fixed ($p = 8$, $\lambda = 0.05$, $k_f = 5$, $\sigma = 2$, and $\rho = 0.5$). As we can see from the figure, an increase in the dissipation coefficient results in a slightly smaller inertial range in the energy spectrum; however, the scalings of the spectra remain the same. This deviation can also be seen from the comparison plot of the vorticity structure function for

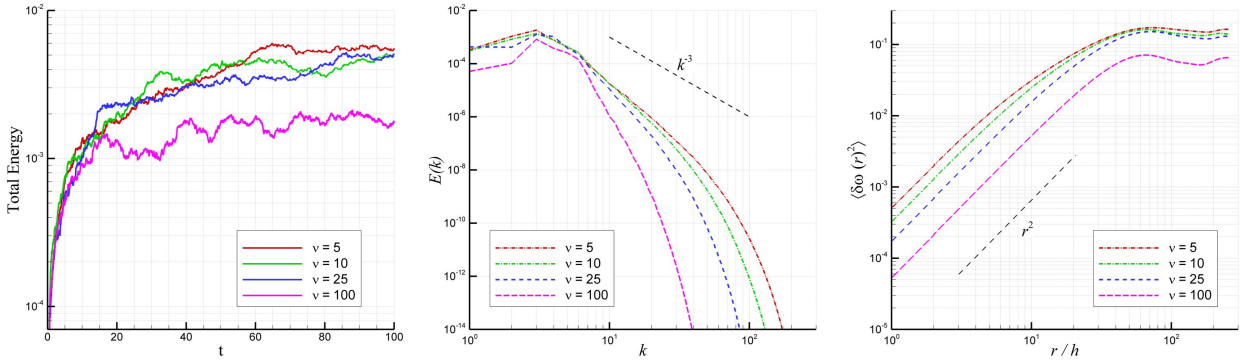

(a) (b) (c)

Figure 5.6: The effects of the small scale dissipation coefficient on the statistics without hyperviscosity ($\lambda = 0.01$, $p = 1$, $\rho = 0$, $\sigma = 2$, $f_0 = 0.1$ and $k_f = 5$); (a) time series of total energy, (b) angle averaged energy spectra, and (c) second-order vorticity structure functions.

smaller scales. The levels of energy of the systems in the stationary regime are close to each other. This comparison clearly shows that the small scale dissipation mechanism has slight effect on the statistics, due to the sharp effect of the high order Laplacian in the dissipation mechanism. The instantaneous vorticity fields are also plotted in Figure 5.3, showing that there are no significant effects on flow field structures as well.

Second, the effects of the order of the Laplacian in the small scale dissipation mechanism are investigated by using the same coefficients given above for other mechanisms ($\lambda = 0.05$, $k_f = 5$, $\sigma = 2$, and $\rho = 0.5$). The case for the order of Laplacian $p = 1$ represents regular quadratic dissipation for Navier-Stokes equations, and all the other cases of $p > 1$ represent the hyperviscous Navier-Stokes equations. As shown in Figure 5.4, increasing the hyperviscosity order p extends the inertial range and results in the small scale dissipation becomes effective in larger wave numbers. Its effect on the flow field is also illustrated in Figure 5.5, showing that the $p = 1$ case has a less amount of filamentation compared to the hyperviscous cases. The comparison of vorticity structure functions in Figure 5.4 also demonstrates that the scaling for the case of $p = 1$ is $\langle \delta\omega(r)^2 \rangle \sim r^2$ for smaller separation distances.

Next, we investigate the Reynolds number dependence of the statistics of stationary

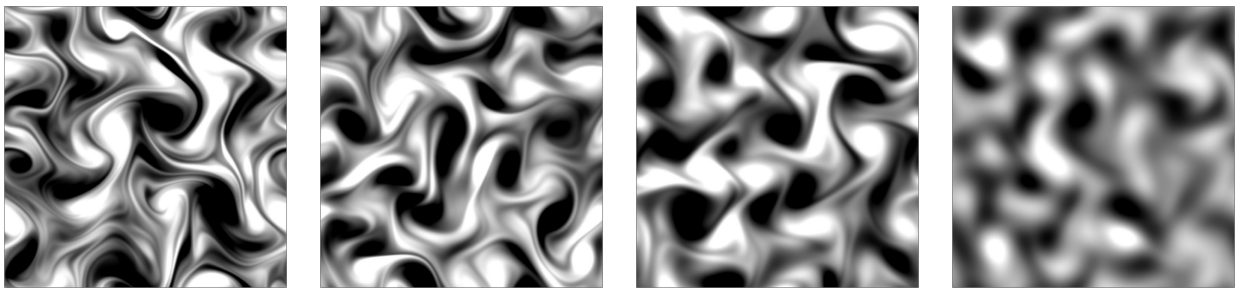

(a) $\nu = 5$ ($Re = 12080$) (b) $\nu = 10$ ($Re = 6040$) (c) $\nu = 25$ ($Re = 2416$) (d) $\nu = 100$ ($Re = 604$)

Figure 5.7: Instantaneous vorticity fields at time $t = 100$ for varying Reynolds number using the forcing scale $k_f = 5$ and the order of Laplacian $p = 1$.

turbulence using the the order of Laplacian $p = 1$ that represents the classical quadratic dissipation mechanism in Navier-Stokes equation without using hyperviscosity. As demonstrated in Figure 5.6, the angle averaged energy spectrum asymptotically reaches the k^{-3} scaling in the inertial range as ν decreases (i.e., Re increases). We find that the Reynolds number dependency is more stringent if we look at the turbulence statistics in wave space using the angle averaged energy spectrum. The structure functions are proportional to r^2 for the smaller separations and flatten for higher separations. The corresponding instantaneous vorticity fields at time $t = 100$ are compared in Figure 5.7 for the same set of Reynolds numbers. As we can see from Figure 5.7, the amount of filamentation increases for higher Reynolds numbers. Due to the smaller convection in lower Reynolds numbers, the interaction between two vortices is not as strong as that of the computations with higher Reynolds numbers.

5.4.2 Effects of large scale dissipation mechanism

In order to investigate the effects of large scale dissipation mechanism in the dynamics of two-dimensional homogeneous turbulence, we perform a similar analysis by varying the large scale friction coefficient, while the other parameters associated with small scale friction and forcing mechanisms are held constant in the model. Figure 5.8 shows the computed

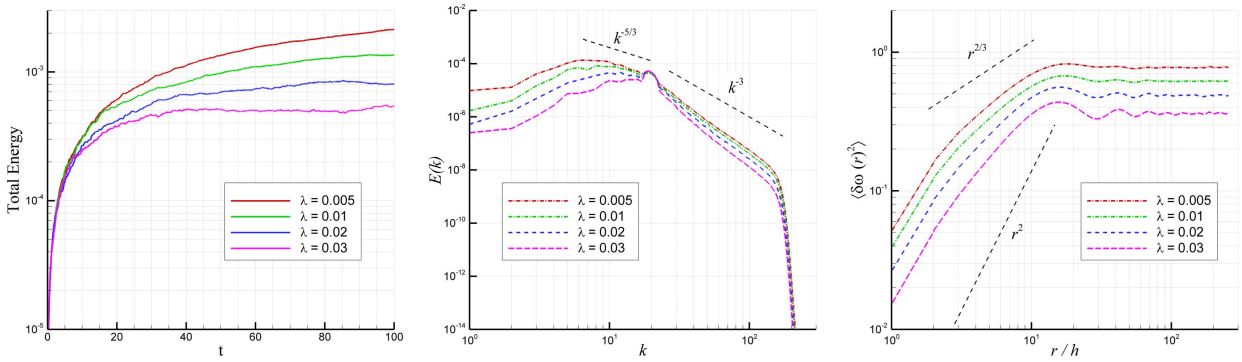

(a) (b) (c)

Figure 5.8: The effects of the large scale dissipation coefficient on the statistics ($k_f = 20$, $f_0 = 0.1$, $\sigma = 2$, $\rho = 0.0$, $\nu = 1000$ and $p = 8$); (a) time series of total energy, (b) angle averaged energy spectra, and (c) second-order vorticity structure functions.

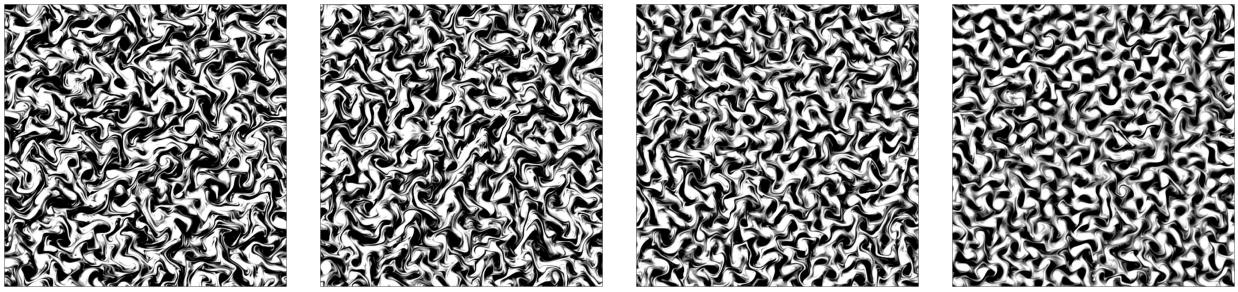

(a) $\lambda = 0.005$ (b) $\lambda = 0.01$ (c) $\lambda = 0.02$ (d) $\lambda = 0.03$

Figure 5.9: Instantaneous vorticity fields at time $t = 100$ for varying large scale friction coefficient λ using the forcing scale is $k_f = 20$ and the small scale dissipation coefficients are $\nu = 1000$ and $p = 8$.

statistics for the effective forcing scale $k_f = 20$ applied in all cases. The statistics on the evolution of the total energy clearly demonstrate that the main mechanism that determines the time scale for stationary regime is the large-scale friction mechanism. Due to the inverse energy cascading in two-dimensional turbulence, a statistically steady state is established by damping mechanism in low-wavenumbers. Increasing the large scale damping coefficient λ provides an earlier statistically steady state with a less amount of energy. It is interesting to note that the structure of the large scale spectrum also depends considerably on the amount of the large scale friction coefficient in which Kolmogorov scaling appears for smaller value

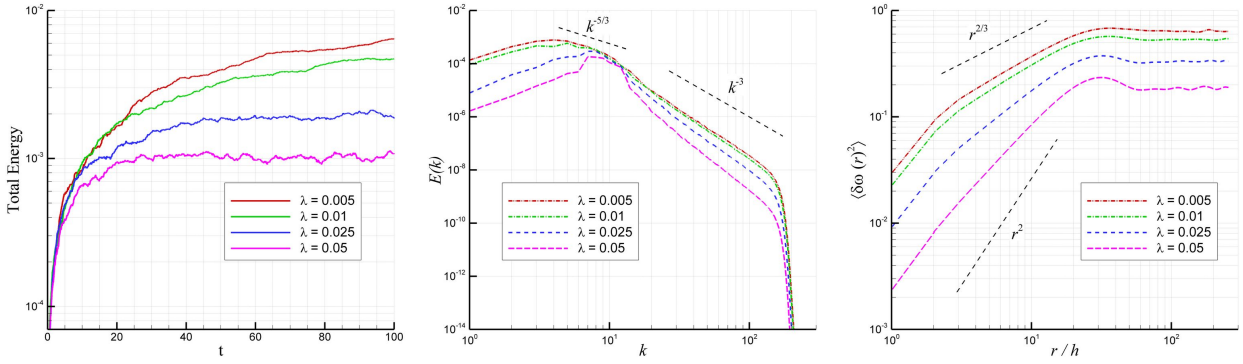

(a) (b) (c)

Figure 5.10: The effects of the large scale dissipation coefficient on the statistics ($k_f = 10$, $f_0 = 0.1$, $\sigma = 3$, $\rho = 0.0$, $\nu = 1000$ and $p = 8$); (a) time series of total energy, (b) angle averaged energy spectra, and (c) second-order vorticity structure functions.

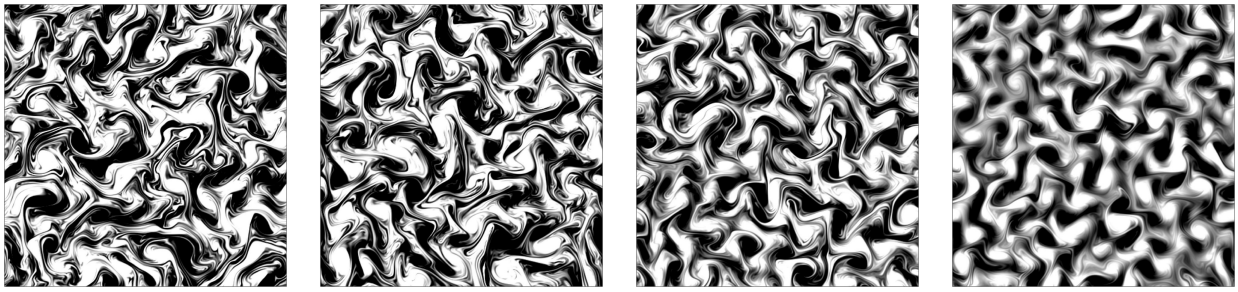

(a) $\lambda = 0.005$ (b) $\lambda = 0.01$ (c) $\lambda = 0.025$ (d) $\lambda = 0.05$

Figure 5.11: Instantaneous vorticity fields at time $t = 100$ for varying the large scale friction coefficient λ using the forcing scale $k_f = 10$ and the small scale dissipation coefficients of $\nu = 1000$ and $p = 8$.

of the λ. It can also be seen from Figure 5.8 that energy spectra in forward enstrophy cascade range appear steeper than k^{-3} with increasing large scale damping coefficients. We found that the vorticity structure functions are independent of the separation length for larger r, as indicated by KBL theory in the inviscid limit, and change gradually from r^2 to $r^{2/3}$ for smaller separations. Thus, we conclude that the scaling exponents of the structure function are considerably influenced by the large scale damping mechanism for the small separation r. The instantaneous vorticity fields compared in Figure 5.9 show another interesting observation that the flow pattern has more vorticity filaments for smaller large

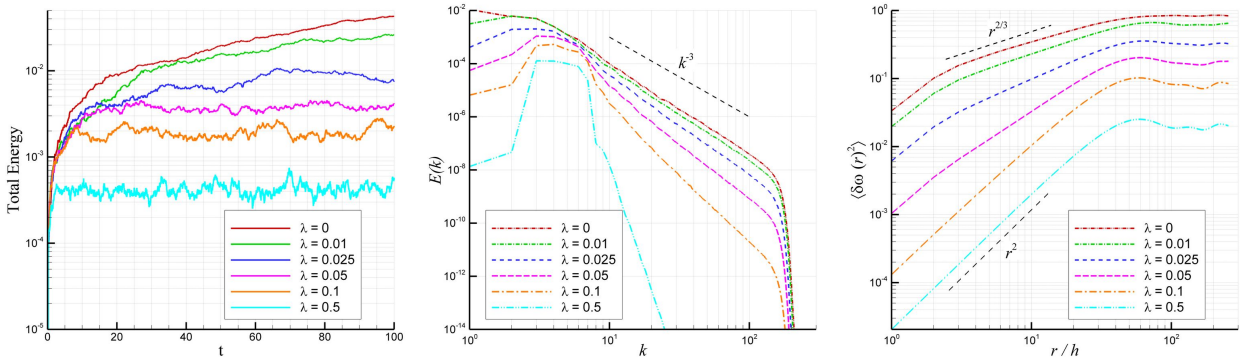

(a) (b) (c)

Figure 5.12: The effects of the large scale dissipation coefficient on the statistics ($k_f = 5$, $f_0 = 0.1$, $\sigma = 2$, $\rho = 0.5$, $\nu = 1000$ and $p = 8$); (a) time series of total energy, (b) angle averaged energy spectra, and (c) second-order vorticity structure functions.

scale friction coefficients, whereas the amount of vortical structures seems equivalent in each case due to the use of the same forcing scale.

Figure 5.10 shows statistics for $k_f = 10$. Similar to the previous comparisons with $k_f = 20$, the dual cascading phenomenon, Kraichnan scaling for the scales smaller than the energy injection scale, and Kolmogorov scaling for the scales greater than the forcing scale, appears in statistics for energy spectra and structure functions. The lines $k^{-5/3}$ and k^{-3} are shown in the plot for energy spectra and lines $r^{2/3}$ and r^2 are included in the plot for structure functions for comparison. The corresponding flow patterns are also shown in Figure 5.11, demonstrating a clear comparison for the effect of the large scale friction coefficient into the flow structure. For larger friction coefficient, flow tends to be concentrated in the centers of corresponding vortices, showing less interactions among them. The grid-like pattern of vortices emerges, corresponding to the accumulation of energy near forcing scales; this pattern is also evident in energy spectra.

In order to further investigate the effects of large scale friction mechanism, we next perform a similar analysis for a larger energy injection scale $k_f = 5$. The results are summarized in Figure 5.12, showing evolution of total kinetic energy, mean energy spectra, and mean second-order vorticity structure functions for a series of runs with varying large scale friction

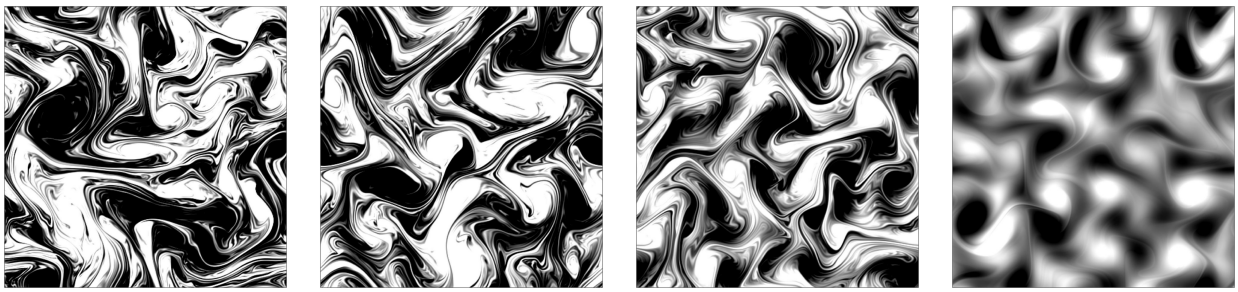

(a) $\lambda = 0.0$ (b) $\lambda = 0.01$ (c) $\lambda = 0.025$ (d) $\lambda = 0.1$

Figure 5.13: Instantaneous vorticity fields at time $t = 100$ for varying the large scale friction coefficient λ using the forcing scale $k_f = 5$ and the small scale dissipation coefficients of $\nu = 1000$ and $p = 8$.

coefficient. For $\lambda = 0$, the flow approaches two-dimensional homogenous turbulence with a forward cascade of enstrophy and an inverse cascade of energy. After an initial period of nonlinear adjustment, the total energy grows linearly in time, $dE/dt \approx t$. Some part of the energy input injected by forcing mechanism at forcing scale $k_f = 5$ is transferred to scales smaller than the forcing scale, and dissipated by viscosity. In this finite system for $\lambda = 0$, however, there is no statistically steady state due to inverse energy cascade in which energy is continuously transferring from the forcing scale to the larger scales. Figure 5.12 also shows that as the large scale friction coefficient is decreased, the growth of energy is decreased, until at a value $\lambda \approx 0.025$, the growth is completely suppressed by the large scale damping, and stationary turbulence is obtained. Comparing energy spectra in Figure 5.12, Kraichnan scaling is obtained for $\lambda \to 0$, though the spectra for larger λ appear steeper than k^{-3}. It is also important to note that the tails of corresponding second-order vorticity structure functions scale as r^2 for larger λ. Therefore, we confirm that the scaling for the structure functions shows an asymptotical limit for flows having energy spectrum is steeper than k^{-3}. Based on these findings, we conjecture that looking for turbulence statistics only in terms of structure functions does not guarantee the proper scaling exponents in energy cascading predictions. Figure 5.12 also shows that the second-order vorticity structure function flattens for larger separation distances r, as predicted by the KBL theory in the inviscid limit. Figure 5.13

illustrates the instantaneous vorticity field at time $t = 100$ for a set of values for λ. Similar to our previous outcomes, we observe more layered flow patterns for smaller λ, while energy is concentrated in the vortical structures associated with the forcing scale for larger λ.

Figure 5.14 shows energy spectra at several times to illustrate the spectral energy density evolution for a series of cases with two values of λ and k_f. The time interval between two adjacent lines is $\delta t = 2$. The damping effect of the large scale friction mechanism in the development of the energy cascade is observable for the $k_f = 5$ cases in the early time evolution. We also observe that a separation of time scales exists in the dynamics of the energy spectrum. This can be seen more clearly for the cases in which $k_f = 15$. Once the forcing of the initially at-rest fluid begins, the entire spectrum immediately fills out with noise and a strong forcing peak appears centered around a wave number commensurate with the forcing length scale. Certain wave number ranges in a typical energy spectrum in a developing turbulent flow are populated immediately, while certain characteristics, the $k^{-5/3}$ scaling in the wave numbers smaller than the forcing scale, for example, evolve slowly over time. The spectrum fills out slowly until, after a long time, the final statistically steady state Kolmogorov spectrum appears if there exist even a small amount of large scale damping. This may be contrasted with the time evolution of a three-dimensional homogeneous isotropic turbulent flow, which develops its structure immediately, and with time transfers this structure to progressively smaller length scales.

5.4.3 Effects of forcing mechanism

Here, we systematically analyze the effects of the parameters associated with Markovian forcing scheme. The underlying settings for the small scale dissipation mechanism are same for all the cases (i.e., $\nu = 1000$ and $p = 8$). The use of hyperviscosity maintains a constant flux of enstrophy in a wider interval $k_f > k > k_d$ by eliminating as much as possible the effects of viscosity at intermediate scales, thus extending the inertial ranges. First, we compute the statistics by varying the corresponding scale for Markovian forcing using a large

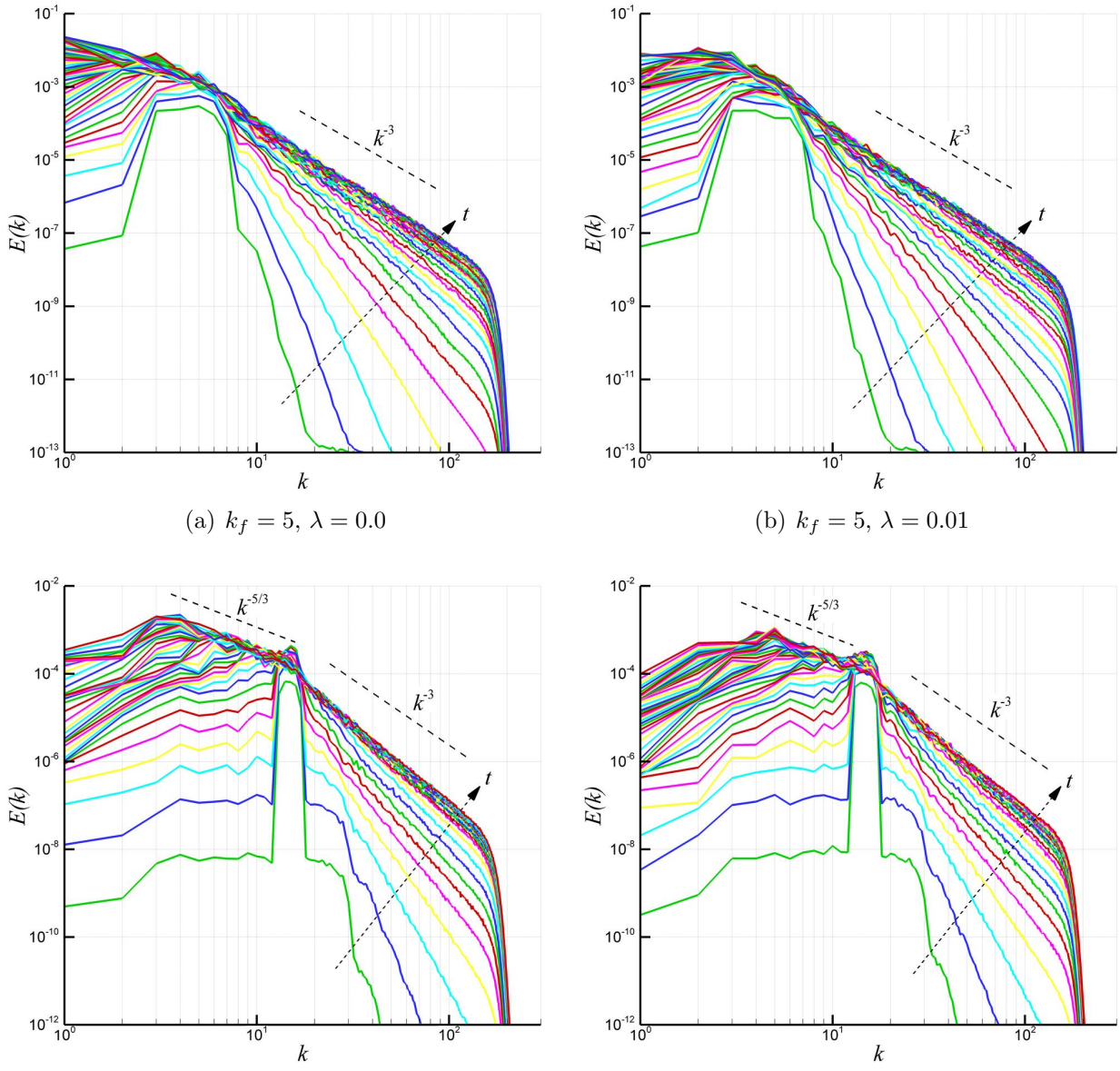

(a) $k_f = 5$, $\lambda = 0.0$

(b) $k_f = 5$, $\lambda = 0.01$

(c) $k_f = 15$, $\lambda = 0.0$

(d) $k_f = 15$, $\lambda = 0.01$

Figure 5.14: Evolution of the angle averaged energy spectrum ($f_0 = 0.1$, $\sigma = 2$, $\rho = 0.5$, $\nu = 1000$ and $p = 8$) for varying the large scale friction coefficient λ and the effective forcing scale k_f.

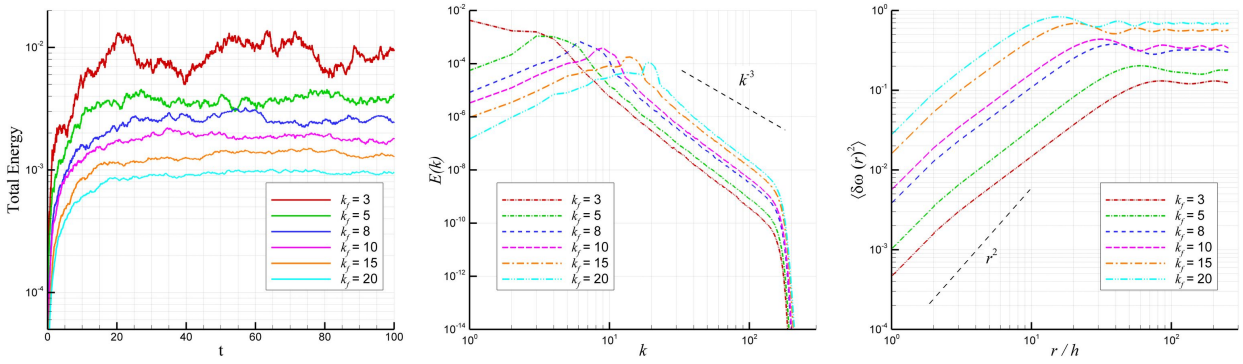

(a) (b) (c)

Figure 5.15: The effects of the forcing scale on the statistics ($\lambda = 0.05$, $\sigma = 2$, $\rho = 0.5$, and $f_0 = 0.1$); (a) time series of total energy, (b) angle averaged energy spectra, and (c) second-order vorticity structure functions.

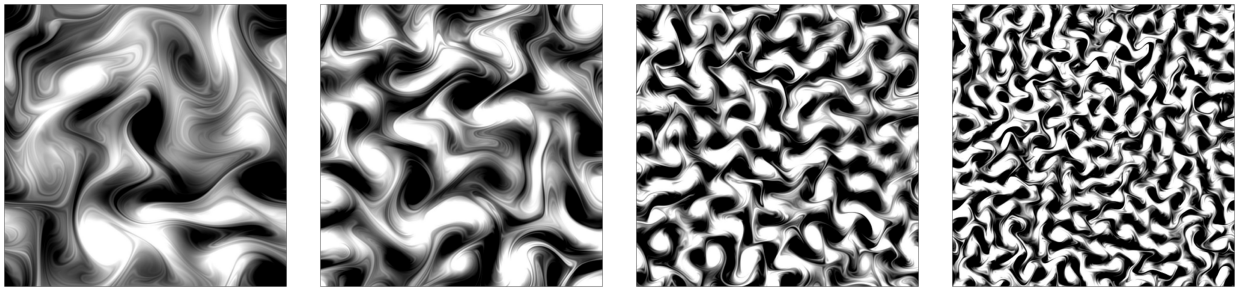

(a) $k_f = 3$ (b) $k_f = 5$ (c) $k_f = 10$ (d) $k_f = 15$

Figure 5.16: Instantaneous vorticity fields at time $t = 100$ for varying the forcing scale k_f using the large scale dissipation coefficient of $\lambda = 0.05$.

scale friction coefficient of $\lambda = 0.05$. Figure 5.15 shows the statistics in terms of evolution of the total energy, mean energy spectrum, and mean second-order vorticity structure function for different forcing scales with the same memory correlation coefficient, forcing amplitude, and forcing bandwidth. The comparison of time series clearly demonstrates that all computations reach quasistationary regime at the same time but having a different level of energy. Increasing the forcing scale result in a decrease in quasistationary energy level. It is also shown that the variability increases by decreasing forcing scale. On the other hand, the scaling exponents in energy spectra and structure functions are invariant of the forcing

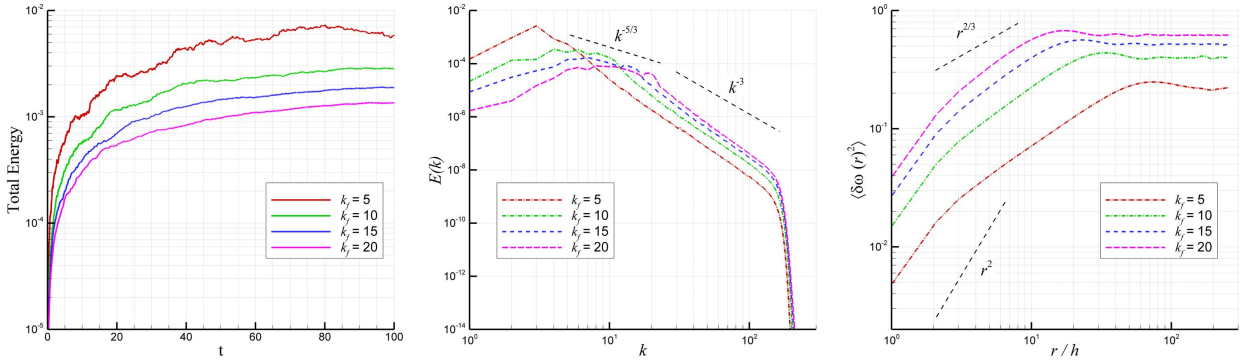

(a) (b) (c)

Figure 5.17: The effects of the forcing scale on the statistics ($\lambda = 0.01$, $\sigma = 2$, $\rho = 0.0$, and $f_0 = 0.1$); (a) time series of total energy, (b) angle averaged energy spectra, and (c) second-order vorticity structure functions.

scale. Instantaneous vorticity fields at time $t = 100$ for varying the forcing scale k_f are also illustrated in Figure 5.16 showing the similar pattern of mixing and filamentation.

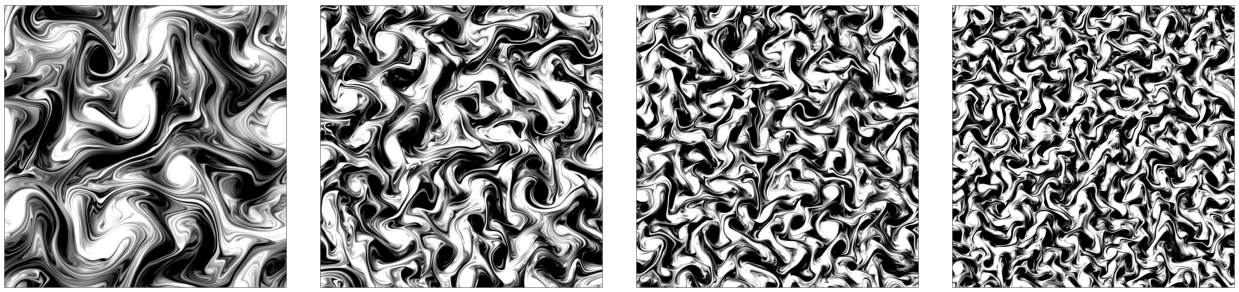

(a) $k_f = 5$ (b) $k_f = 10$ (c) $k_f = 15$ (d) $k_f = 20$

Figure 5.18: Instantaneous vorticity fields at time $t = 100$ for varying the forcing scale k_f using the large scale dissipation coefficient of $\lambda = 0.01$.

Similarly, we compute the statistics by varying the effective scale for Markovian forcing using a smaller large scale friction coefficient of $\lambda = 0.01$. The statistics and flow field patterns are shown in Figure 5.17 and Figure 5.18, respectively. Due to the reduction in damping coefficient we observe more interaction between vortical structures for all the cases with varying k_f. In the inertial range, especially for $k_f = 5$, it is also interesting to see that energy spectrum scales as k^{-3}, while structure functions scales as $r^{2/3}$. The main reason for

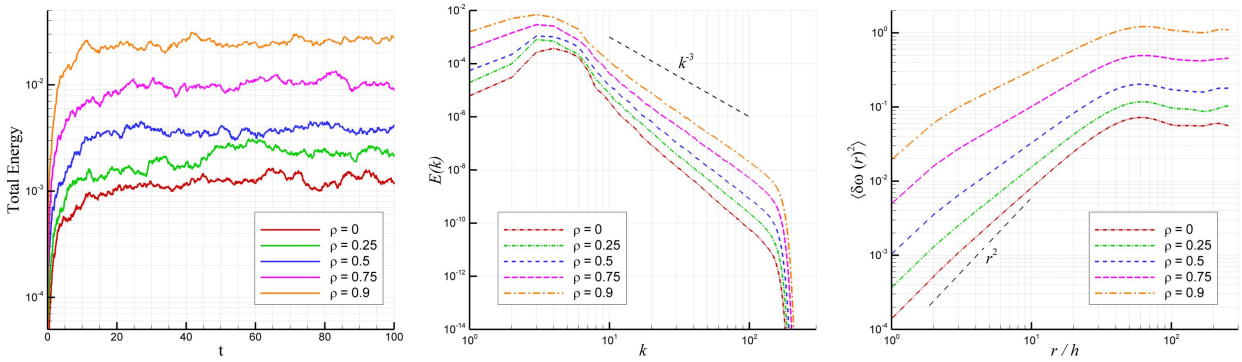

(a) (b) (c)

Figure 5.19: The effects of the memory coefficient on the statistics ($\lambda = 0.05$, $k_f = 5$, $\sigma = 2$, $\nu = 1000$ and $p = 8$); (a) time series of total energy, (b) angle averaged energy spectra, and (c) second-order vorticity structure functions.

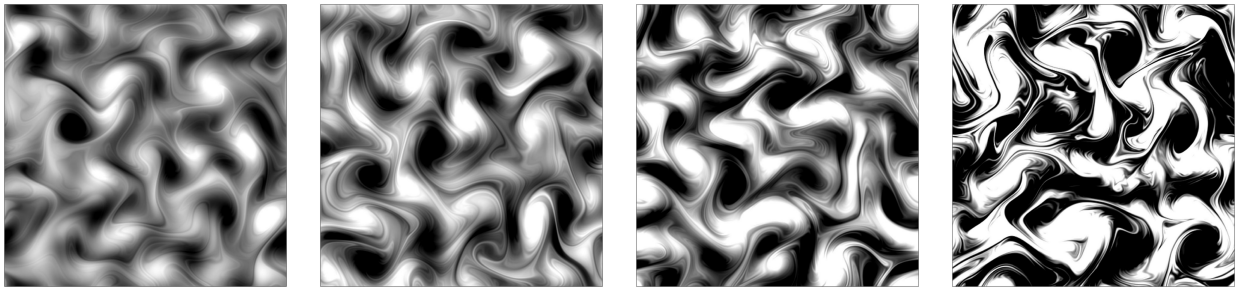

(a) $\rho = 0.0$ (b) $\rho = 0.25$ (c) $\rho = 0.5$ (d) $\rho = 0.9$

Figure 5.20: Instantaneous vorticity fields at time $t = 100$ for varying the memory coefficient using the large scale dissipation coefficient of $\lambda = 0.05$ and the small scale dissipation coefficients of $\nu = 1000$ and $p = 8$.

energy spectrum appearing steeper than k^{-3} for increasing k_f is that the relative importance of the large scale damping coefficient in larger k_f cases is greater. This can also be seen from the energy levels shown in Figure 5.17.

Next, we analyze the effects of the memory coefficient ρ in the Markovian forcing scheme. As shown in Figure 5.19, its main effect on the statistics is the translation of the level of energy. There is no significant effect into the scaling exponents of the energy spectra and structure functions. The vorticity fields are also illustrated in Figure 5.20 showing that

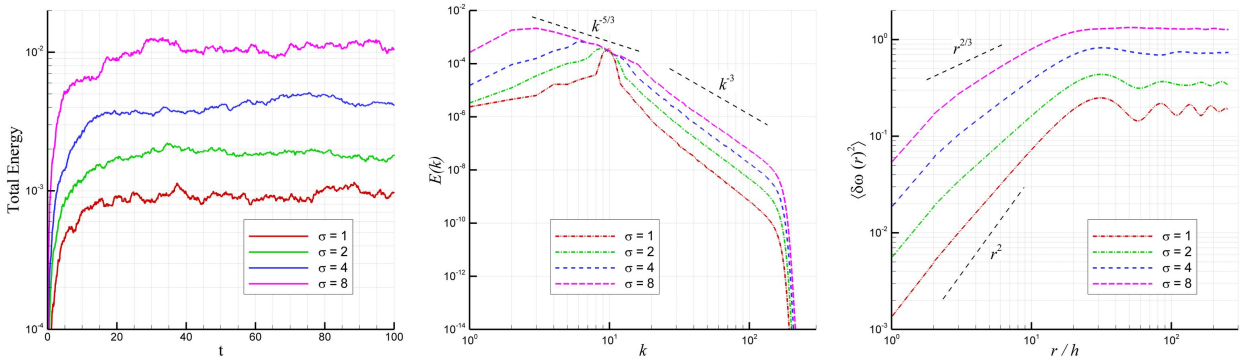

(a) (b) (c)

Figure 5.21: The effects of the forcing bandwidth on the statistics ($\lambda = 0.05$, $k_f = 10$, $\rho = 0.5$, $\nu = 1000$ and $p = 8$); (a) time series of total energy, (b) angle averaged energy spectra, and (c) second-order vorticity structure functions.

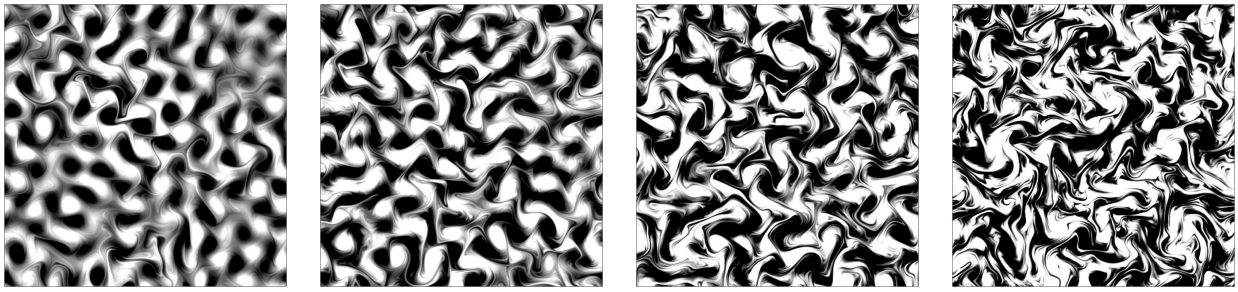

(a) $\sigma = 1$ (b) $\sigma = 2$ (c) $\sigma = 4$ (d) $\sigma = 8$

Figure 5.22: Instantaneous vorticity fields at time $t = 100$ for varying the forcing bandwidth using the large scale dissipation coefficient of $\lambda = 0.05$ and the small scale dissipation coefficients of $\nu = 1000$ and $p = 8$.

the amplitude of vorticity increases with increasing memory coefficient ρ. In this study, we focus on the random forcing mechanism controlled by this coefficient that measures the stochastic process in the system for which the forcing is purely random (i.e., $\rho = 0$). It will be interesting to further investigate the effects of deterministic forcing in the context of generation of coherent vortices. However, we particulary use a random forcing mechanism to concentrate on the statistical deviations from the theoretical scalings which are solely due to viscous effects and eliminate possible situations that coherent vortices might play a role.

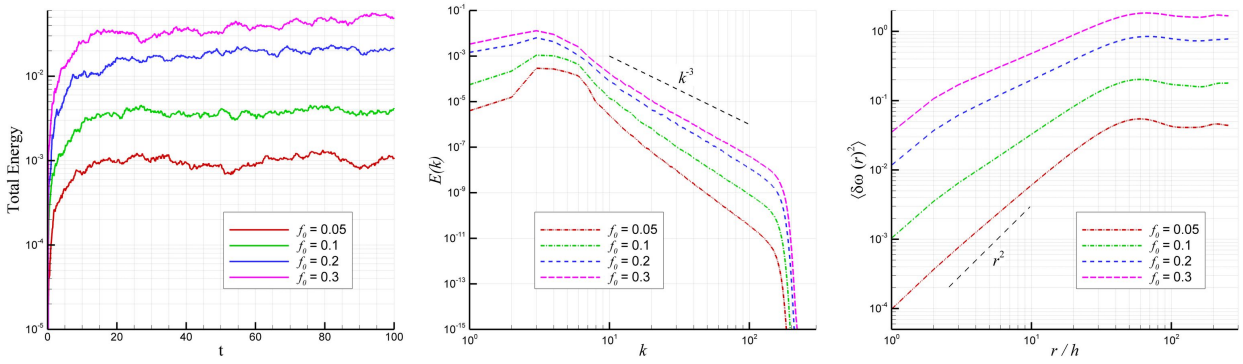

(a) (b) (c)

Figure 5.23: The effects of the forcing amplitude on the statistics ($\lambda = 0.05$, $k_f = 5$, $\rho = 0.5$, $\nu = 1000$ and $p = 8$); (a) time series of total energy, (b) angle averaged energy spectra, and (c) second-order vorticity structure functions.

Figures 5.21 and 5.22 examine the effects of forcing bandwidth σ for the forcing scale $k_f = 10$. The effective energy injection occurs in the scales within the interval ($k_f - \sigma$, $k_f + \sigma$). As shown in Figure 5.21, the level of energy of the system in statistically steady state increases with increasing the σ since we inject more energy due to enhanced forcing zone. In the forward energy range we observe the same scaling for energy spectrum. For $\sigma = 8$, it is also shown that the energy spectrum within the forcing zone scales as $E(k) \sim k^{-5/3}$. Comparing the structure functions, we illustrate that $\langle \delta\omega(r)^2 \rangle$ wiggles more rapidly for smaller values of σ. It is also interesting to see that the flow pattern shows more vortical filaments for increasing forcing bandwidth.

Finally, we show the effects of forcing amplitude f_0 in Figures 5.23 and 5.24. The linear translation of system's energy level in the statistically steady state can be clearly seen from Figure 5.23. Here f_0 represents the energy injection rate of the external forcing. Therefore, increasing f_0 also results in an increase for the amplitude of vorticity which can be seen Figure 5.24. However, the shapes of corresponding energy spectra and structure functions look like similar and there is no significant differences for these statistical quantities.

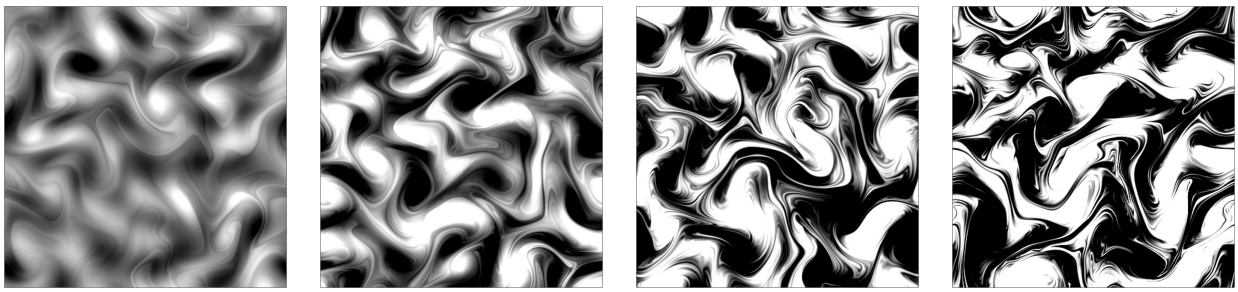

(a) $f_0 = 0.05$ (b) $f_0 = 0.1$ (c) $f_0 = 0.2$ (d) $f_0 = 0.3$

Figure 5.24: Instantaneous vorticity fields at time $t = 100$ for varying the forcing amplitude using the large scale dissipation coefficient of $\lambda = 0.05$ and the small scale dissipation coefficients of $\nu = 1000$ and $p = 8$.

5.5 Summary and conclusions

Numerical simulations of forced two-dimensional turbulence have been performed by solving the Ekman-Navier-Stokes equations using the Fourier-Galerkin pseudospectral method. Large scale friction, high order small scale dissipation, and Markovian forcing mechanisms have been included in the model. The formulation presented here can be reduced to the classical Navier-Stokes model as a special case by setting the Ekman friction coefficient equal to zero and the order of the viscosity equal to unity. Including the large scale friction mechanism in the model is crucial to be able to obtain a stationary turbulent flow regime in the case of periodic boundary conditions due to the inverse energy cascading phenomenon. Otherwise, the applied forcing mechanism would result in the unbounded growth of the total kinetic energy. The objective of this study was to determine the turbulence statistics for the long-time integration of stationary turbulence simulations, and to investigate the scaling exponents for a large range of physical settings. Specifically, we computed the statistics in terms of the evolution of total kinetic energy, angle averaged energy spectrum, and second-order vorticity structure function.

We first concentrated on the effects of the small scale dissipation mechanism using hyperviscosity, which turns on much more abruptly than the gradual increase of normal viscosity

at the small scales. We also studied the Reynolds number dependence when using classical viscosity with the order of Laplacian $p = 1$. We showed that the predicted energy spectrum asymptotically converged to the theoretical k^{-3} scaling as the Reynolds number increased, which is predicted by the KBL theory for forward cascading two-dimensional turbulence. We also showed that hyperviscosity effectively eliminates the effects of viscosity at the intermediate scales, thus extending the turbulence inertial range. We demonstrated the shape of the second-order vorticity structure function that is proportional to r^2 for the smallest separations and flattens when approaching the forcing length scale.

Next, we studied the effects of the large-scale friction mechanism within the turbulence statistics. The linear damping mechanism is utilized in the model, with the friction coefficient λ varying from zero to higher values. These computations revealed that the existence of a statistically steady state is maintained by this mechanism and significantly effects the turbulence statistics. We confirmed the classical dual cascade picture of two-dimensional stationary turbulence for $\lambda \to 0$, which indicates that a direct enstrophy cascade is developed from the forcing range to the dissipation range, and an inverse energy cascade is developed for the scales greater than the effective forcing scale. We found, however, that the large scale damping mechanism is a major source of deviations from the classical k^{-3} scaling in the forward, and $k^{-5/3}$ scaling in the inverse, cascade ranges. We also showed that the tails of corresponding second-order vorticity structure functions scale as r^2 for large λ, and reduce to the $r^{2/3}$ scaling as λ vanishes.

Finally, we performed a detailed study by systematically varying the parameters associated with Markovian forcing mechanism such as the energy injection scale, the forcing bandwidth, the forcing amplitude, and memory correlation coefficient. We found that these parameters exhibit no significant difference on turbulence statistics, except their translational effects on the total levels of energy in the statistically steady state. We demonstrate that the flow patterns show more vortical filaments for increased forcing bandwidth. We also showed that there is a separation of time scales in the dynamics of the energy spectrum, such that energy is transferred quickly in the forward enstrophy cascade range, while the

shape of the spectrum fills out slowly, until, after a long time, the final statistically steady state Kolmogorov spectrum appears in the inverse energy cascade range. This separation of time scales in the energy spectrum might be a useful starting point for developing multiscale computational algorithms for turbulence research, a topic we intend to investigate further in a future study.

Chapter 6

Approximate Deconvolution Large Eddy Simulation of a Barotropic Ocean Circulation Model

A new large eddy simulation closure modeling strategy is put forth for two-dimensional turbulent geophysical flows. This closure modeling approach utilizes *approximate deconvolution*, which is based solely on mathematical approximations and does not employ additional phenomenological arguments in the model. The new approximate deconvolution model is tested in the numerical simulation of the wind-driven circulation in a shallow ocean basin, a standard prototype of more realistic ocean dynamics. The model employs the barotropic vorticity equation driven by a symmetric double-gyre wind forcing, which yields a four-gyre circulation in the time mean. The approximate deconvolution model yields the correct four-gyre circulation structure predicted by a direct numerical simulation, but on a coarser mesh and at a fraction of the computational cost. This first step in the numerical assessment of the new model shows that approximate deconvolution could represent a viable tool for under-

O. San, A. E. Staples, Z. Wang, and T. Iliescu, "Approximate deconvolution large eddy simulation of a barotropic ocean circulation model," *Ocean Modelling*, vol. 40, pp. 120–132, 2011. Reprinted with permission from Ocean Modelling, Elsevier.

resolved computations in the large eddy simulation of more realistic turbulent geophysical flows.

6.1 Introduction

As a first approximation, the mean near-surface currents in the oceans are driven by the mean effects of winds. Wind-driven flows of mid-latitude ocean basins have been studied by modelers using idealized single and double-gyre wind forcing. This type of double-gyre circulation characterizes all mid-latitude ocean basins, including those in the North and South Atlantic, as well as the North and South Pacific. The *barotropic vorticity equation (BVE)* represents one of the most commonly used mathematical models for this type of geostrophic flows with various dissipative and forcing terms (Majda and Wang, 2006). For more details on the physical mechanism and formulations of the BVE, the reader is referred to Holland and Rhines (1980); Munk and Wunsch (1982); Griffa and Salmon (1989); Cummins (1992); Greatbatch and Nadiga (2000); Nadiga and Margolin (2001); Fox-Kemper (2005); Cushman-Roisin (1994).

The main assumptions that go into the BVE model are hydrostatic balance, the β-plane approximation, geostrophic balance, and horizontal eddy viscosity parametrization. Despite the fact that the BVE models are a simplified version of the full-fledged equations of geophysical flows, their numerical simulation is still computationally challenging when long-time integration is required, as is the case in climate modeling. Thus, to further reduce the computational cost of the BVE, *large eddy simulation (LES)* appears to be a natural approach. In LES only the large spatial structures are approximated, whereas the small scales are modeled. This allows for much coarser spatial meshes and thus a computational cost that is significantly lower than that of a *direct numerical simulation (DNS)*. To achieve the same order of physical accuracy as DNS, however, LES needs to correctly treat the *closure problem* (Meneveau and Katz, 2000; Sagaut, 2006; Berselli et al., 2006): the effect

of the small scales on the large ones needs to be modeled. This closure problem represents a significant challenge for quasi-two-dimensional turbulent flows, such as those in the ocean and atmosphere (McWilliams, 1989; Danilov and Gurarie, 2000; Smith et al., 2002; Lesieur, 2008; Salmon, 1998; Majda, 2003; Holton, 2004; McWilliams, 2006; Vallis, 2006).

Two-dimensional turbulence is a fundamental topic for understanding of geophysical flows and behaves in a profoundly different way from the three-dimensional turbulence due to different energy cascade behavior (Kraichnan, 1967; Batchelor, 1969; Leith, 1971), which is described in the Kraichnan-Batchelor-Leith two-dimensional turbulence theory. In three-dimensional turbulence, energy is transferred forward, from large scales to smaller scales, via vortex stretching. In two dimensions that mechanism is absent, and under most forcing and dissipation conditions energy is transferred from small scales to larger scales, largely because of the potential enstrophy, a quadratic invariant defined as the integral of the square of the potential vorticity. The physical mechanism behind the enstrophy cascade is the stretching of small-scale vorticity gradients by the strain arising from larger-scale vortices (Chen et al., 2003). This results in energy being trapped at large scales in forced-dissipative two-dimensional flows. Additionally, enstrophy is transferred to the smaller scales from large scales, and is finally dissipated at large wavenumbers. Danilov and Gurarie (2000) and Tabeling (2002) reviewed both theoretical and experimental two-dimensional turbulence studies and provided extensive insights into the applicability of two-dimensional turbulence theory to geophysical flows. We also refer the reader to the energy-enstrophy conservation arguments provided by Vallis (2006).

Modeling the ocean and atmosphere inspired the first LES models, but most of the subsequent development of LES has taken place in the engineering community (Sagaut, 2006; Berselli et al., 2006). The majority of LES models have been developed for three-dimensional turbulent flows, such as those encountered in engineering applications. These LES models fundamentally rely on the concept of the forward energy cascade and so their extension to geophysical flows is beset with difficulties. The effective viscosity values in oceanic models are much greater than the molecular viscosity of seawater, hence a uniform eddy viscosity

coefficient is generally used to parameterize the unresolved, subfilter-scale effects in most oceanic models (McWilliams, 2006; Vallis, 2006). LES models specifically developed for two-dimensional turbulent flows, such as those in the ocean and atmosphere, are relatively scarce (Fox-Kemper and Menemenlis, 2008; Awad et al., 2009; Özgökmen et al., 2009; Chen et al., 2011), at least when compared to the plethora of LES models developed for three-dimensional turbulent flows. Holm and Nadiga (2003) combine the uniform eddy viscosity parametrization with the alpha regularization LES approach to capture the under-resolved flow where the grid length becomes greater than the specified Munk scale of the problem. In that work the structural alpha parameterization was tested on the BVE in an ocean basin with double-gyre wind forcing, which displays a four-gyre mean ocean circulation pattern. It was found that the alpha models provide a promising approach to LES closure modeling of the barotropic ocean circulation by predicting the correct four-gyre circulation structure for under-resolved flows.

This paper puts forth a new LES closure modeling strategy for two-dimensional turbulent geophysical flows. The new closure modeling approach utilizes *approximate deconvolution (AD)*, which is particularly appealing for geophysical flows because of no additional phenomenological approximations to the BVE. The AD approach can achieve high accuracy by employing repeated filtering, which is computationally efficient and easy to implement. The AD method has been used successfully in LES of three-dimensional turbulent engineering flows (Stolz and Adams, 1999; Stolz et al., 2001a,b, 2004). We emphasize, however, that to the best of our knowledge, this is the *first time* that the AD methodology is used in LES of large scale geophysical flows, such as the barotropic ocean circulation flow we consider in this paper. To assess the new AD closure modeling approach, we test it on the same two-dimensional barotropic flow problem as that employed in Nadiga and Margolin (2001) and in Holm and Nadiga (2003).

The rest of the paper is organized as follows: The BVE, the mathematical model used in this report, is presented in Section 6.2. Section 6.3 presents the AD methodology and introduces the new closure model. The numerical methods used in our simulations are briefly

discussed in Section 6.4. The results for the new AD model are presented in Section 6.5. Finally, the conclusions are summarized in Section 6.6.

6.2 Barotropic vorticity equation

In this section, we present the BVE, the mathematical model used in the numerical investigation of the new AD model. The BVE is one of the most used mathematical models for geostrophic flows with various dissipative and forcing terms (Majda and Wang, 2006). Studies of wind-driven circulation using an idealized double-gyre wind forcing have played an important role in understanding various aspects of ocean dynamics, including the role of mesoscale eddies and their effect on mean circulation. Following Greatbatch and Nadiga (2000), we briefly describe the BVE. For more details on the physical mechanism and various formulations utilized, the reader is referred to Holland and Rhines (1980); Munk and Wunsch (1982); Griffa and Salmon (1989); Cummins (1992); Greatbatch and Nadiga (2000); Nadiga and Margolin (2001); Fox-Kemper (2005).

The governing equations for two-dimensional incompressible barotropic flows can be written in dimensionless form of the potential vorticity formulation in the beta plane as the BVE:

$$\frac{\partial q}{\partial t} + J = D + F. \tag{6.1}$$

In Eq. (6.1), q is the potential vorticity, defined as

$$q = \mathrm{Ro}\,\omega + y, \tag{6.2}$$

where ω is the vorticity and Ro is the Rossby number.

The nonlinear convection term in Eq. (6.1), called the Jacobian, is defined as

$$J = \frac{\partial \psi}{\partial y}\frac{\partial q}{\partial x} - \frac{\partial \psi}{\partial x}\frac{\partial q}{\partial y}, \tag{6.3}$$

where ψ is the stream function. The kinematic relationship between the vorticity and the stream function yields the following Poisson equation:

$$\frac{\partial^2 \psi}{\partial x^2} + \frac{\partial^2 \psi}{\partial y^2} = -\omega. \tag{6.4}$$

The viscous dissipation in Eq. (6.1) has the form

$$D = \left(\frac{\delta_M}{L}\right)^3 \left(\frac{\partial^2 \omega}{\partial x^2} + \frac{\partial^2 \omega}{\partial y^2}\right), \tag{6.5}$$

where δ_M is the Munk scale and L is the basin dimension. The double-gyre wind forcing is given by

$$F = F_0 \sin(\pi y), \tag{6.6}$$

where $F_0 = 1$ due to the Sverdrup velocity scale used for nondimensionalization (Greatbatch and Nadiga, 2000). In this nondimensionalization, the velocity scale is

$$V = \frac{\pi\ \tau_0}{\rho H \beta L}, \tag{6.7}$$

where τ_0 is the maximum amplitude of double-gyre wind stress, ρ is the mean density, H is the mean depth of the basin, and β is the gradient of the Coriolis parameter at the basin center ($y = 0$). The dimensionless variables are then defined as

$$x = \frac{\tilde{x}}{L},\ y = \frac{\tilde{y}}{L},\ t = \frac{\tilde{t}}{L/V},\ q = \frac{\tilde{q}}{\beta L},\ \psi = \frac{\tilde{\psi}}{VL}, \tag{6.8}$$

where the tilde denotes the corresponding dimensional variables. In dimensionless form, there are only two physical parameters, the Rhines scale and the Munk scale, which are related to the physical parameters in the following way:

$$\frac{\delta_I}{L} = \left(\frac{V}{\beta L^2}\right)^{1/2}; \qquad \frac{\delta_M}{L} = \left(\frac{\nu}{\beta L^3}\right)^{1/3}, \tag{6.9}$$

where ν is the uniform eddy viscosity coefficient. The physical parameters in the BVE (i.e., Eq. (6.1)), the Rhines scale δ_I and the Munk scale δ_M, are related to the Reynolds and Rossby numbers through the following formulas:

$$\frac{\delta_I}{L} = (\mathrm{Ro})^{1/2}, \tag{6.10}$$

$$\frac{\delta_M}{L} = (\mathrm{Re}^{-1}\mathrm{Ro})^{1/3}, \tag{6.11}$$

where Re is the Reynolds number based on the basin dimension, L. We note that some authors use a boundary layer Reynolds number, which is written as

$$\mathrm{Re}_B = \mathrm{Re}\frac{\delta_I}{L} = \frac{\delta_I^3}{\delta_M^3}, \tag{6.12}$$

where $\mathrm{Re}_B \sim O(10) - O(10^3)$ for oceanic flows (Fox-Kemper, 2005). Finally, in order to completely specify the mathematical model, boundary and initial conditions need to be prescribed. In many theoretical studies of large scale ocean circulation, slip or no-slip boundary conditions are used. Following these studies (e.g., Greatbatch and Nadiga, 2000; Nadiga and Margolin, 2001; Holm and Nadiga, 2003; Cummins, 1992; Özgökmen and Chassignet, 1998; Munk, 1950; Bryan, 1963), we use slip boundary conditions for the velocity, which translate into homogenous Dirichlet boundary conditions for the vorticity: $\omega|_\Omega = 0$. The impermeability boundary condition is imposed as $\psi|_\Omega = 0$. For the initial condition, we start our computations from a quiescent state ($q = 0$) and integrate Eq. (6.1) until a statistically steady state is obtained in which the wind forcing, dissipation, and Jacobian balance each other.

6.3 Approximate deconvolution model

The AD approach aims to obtain accurate and stable approximations of the original, unfiltered flow variables when approximations of the filtered variables are available (Stolz and Adams, 1999; Germano, 2009). The AD methodology was developed in the image processing community, and has been successfully adapted to the closure problem in turbulence modeling for engineering flows (Stolz et al., 2001a,b; Adams and Stolz, 2002; Stolz et al., 2004). We emphasize that this approach is purely mathematical, with no additional phenomenological arguments being used. This is particularly appealing for LES of geophysical flows in which different energy transfer characteristics are displayed than those in three-dimensional turbulent flows, for which successful phenomenological modeling has been done. Next, we present the mathematical derivation of the new AD model for the BVE given by Eq. (6.1).

To derive the equations for the filtered flow variables, the BVE (Eq. (6.1)) is first filtered with a rapidly decaying spatial filter (to be specified later). Thus, using a bar to denote the filtered quantities, the filtered BVE reads:

$$\frac{\partial \bar{q}}{\partial t} + J(\bar{q}, \bar{\psi}) = \bar{D} + \bar{F} + S, \tag{6.13}$$

where S is the subfilter-scale term, given by

$$S = -\overline{J(q, \psi)} + J(\bar{q}, \bar{\psi}). \tag{6.14}$$

It is precisely at this point in the LES model derivation that the celebrated closure problem must be addressed. In order to close the filtered BVE (i.e., Eq. (6.13)), the subfilter-scale term S in Eq. (6.14) needs to be modeled in terms of the filtered flow variables, $\bar{q}$ and $\bar{\psi}$.

This paper proposes a new LES closure modeling approach for two-dimensional turbulent geophysical flows. The AD approach can achieve high accuracy, is computationally efficient, and is easy to implement. Although the AD methodology has already been successfully used

in LES of three-dimensional turbulent engineering flows (Stolz and Adams, 1999; Stolz et al., 2001a,b, 2004), this is the *first time* that it is used in LES of large scale geophysical flows, such as the barotropic ocean circulation flow considered in this paper.

The goal in AD is to use repeated filtering in order to obtain approximations of the unfiltered flow variables when approximations of the filtered flow variables are available. These approximations of the unfiltered flow variables are then used in the subfilter-scale terms to close the LES system. To derive the new AD model, we start by denoting by G the spatial filtering operator: $Gq = \bar{q}$. Since $G = I - (I - G)$, an inverse to G can be written formally as the non-convergent Neumann series:

$$G^{-1} \sim \sum_{i=1}^{\infty} (I - G)^{i-1}. \tag{6.15}$$

Truncating the series gives the Van Cittert approximate deconvolution operator, Q_N. We truncate the series at N and obtain Q_N as an approximation of G^{-1}:

$$Q_N = \sum_{i=1}^{N} (I - G)^{i-1}, \tag{6.16}$$

where I is the identity operator. The approximations Q_N are not convergent as N goes to infinity, but rather are asymptotic as the filter radius, δ, approaches zero (Berselli et al., 2006). An approximate deconvolution of $\bar{q}$ can now be obtained as follows:

$$q \approx q^* = Q_N \bar{q}. \tag{6.17}$$

For higher values of N we get increasingly more accurate approximations of q:

$$Q_1 = I \tag{6.18}$$

$$Q_2 = 2I - G \tag{6.19}$$

$$Q_3 = 3I - 3G + G^2 \tag{6.20}$$

$$Q_4 = 4I - 6G + 4G^2 - G^3 \tag{6.21}$$

$$Q_5 = 5I - 10G + 10G^2 - 5G^3 + G^4 \tag{6.22}$$

$$\vdots$$

Following the same approach as that used in Dunca and Epshteyn (2006), one can prove that these models are highly accurate ($O(\delta^{2N+2})$ modeling consistency error) and stable. We choose $N = 5$ and find an AD approximation of the variable q as

$$q \approx q^* = 5\bar{q} - 10\bar{\bar{q}} + 10\bar{\bar{\bar{q}}} - 5\bar{\bar{\bar{\bar{q}}}} + \bar{\bar{\bar{\bar{\bar{q}}}}} \tag{6.23}$$

and, similarly, an AD approximation of the variable ψ:

$$\psi \approx \psi^* = 5\bar{\psi} - 10\bar{\bar{\psi}} + 10\bar{\bar{\bar{\psi}}} - 5\bar{\bar{\bar{\bar{\psi}}}} + \bar{\bar{\bar{\bar{\bar{\psi}}}}}. \tag{6.24}$$

Using Eq. (6.23) and Eq. (6.24), we can now approximate the nonlinear Jacobian:

$$\overline{J(q,\psi)} \approx \overline{J(q^*,\psi^*)}. \tag{6.25}$$

Finally, using Eq. (6.25) in Eq. (6.14), closes the filtered BVE given by Eq. (6.13) and yields the new *AD model*:

$$\frac{\partial \bar{q}}{\partial t} + J(\bar{q},\bar{\psi}) = \bar{D} + \bar{F} + S^*, \tag{6.26}$$

where S^* is the subfilter-scale term, given by

$$S^* = -\overline{J(q^*,\psi^*)} + J(\bar{q},\bar{\psi}). \tag{6.27}$$

To completely specify the new AD model given by Eqs. (6.26)-(6.27), we need to choose a computationally efficient filtering operator. Following Stolz and Adams (1999), we use the following second-order accurate filtering operator:

$$\alpha \bar{f}_{i-1} + \bar{f}_i + \alpha \bar{f}_{i+1} = \left(\frac{1}{2} + \alpha\right)\left(f_i + \frac{f_{i-1} + f_{i+1}}{2}\right), \tag{6.28}$$

where the subscript i is the spatial index in the x-direction. This results in a tridiagonal system of equations for each fixed value of y. A generalization of Eq. (6.28), the spectral-type high-order compact filter introduced in Visbal and Gaitonde (2002), is given by

$$\alpha \bar{f}_{i-1} + \bar{f}_i + \alpha \bar{f}_{i+1} = \sum_{n=0}^{M} \frac{a_n}{2}(f_{i+n} + f_{i-n}), \tag{6.29}$$

where f is the computed value, and $\bar{f}$ is the corresponding once filtered value. This filter provides $2M$th-order accurate filtering on a $2M+1$ point stencil (Visbal and Gaitonde, 2002). The free parameter, α, which is in the range $0 \leq |\alpha| \leq 0.5$, determines the filtering properties, with high values of α yielding less dissipative results. The coefficients for different order filters are given in Table 6.1. In our numerical tests, we found that for moderately fine meshes, the range of $0.25 \leq \alpha \leq 0.5$ is appropriate, but for coarser meshes, lower values (e.g., $\alpha = 0.1$) should be used to eliminate spurious oscillations. Most of our numerical simulations use the free parameter $\alpha = 0.25$ (Stolz and Adams, 1999). Since we used a second-order accurate space discretization in this study, the filtered simulations are conducted either by using the second-order accurate filter given in Eq. (6.28) or the fourth-order accurate compact filter given in Eq. (6.29) with different parameter values for α.

The existence and uniqueness of strong solutions of the BVE model using the AD closure was investigated by Stanculescu (2008). According to this work, the transfer function of the filter used in the AD closure should be positive definite. The transfer function of the

Table 6.1: Coefficients of the compact filters of various orders given by Eq. (6.29).

	2nd-order	4th-order	6th-order	8th-order
a_0	$\frac{1}{2}+\alpha$	$\frac{5}{8}+\frac{3\alpha}{4}$	$\frac{11}{16}+\frac{5\alpha}{8}$	$\frac{93}{128}+\frac{70\alpha}{128}$
a_1	$\frac{1}{2}+\alpha$	$\frac{1}{2}+\alpha$	$\frac{15}{32}+\frac{17\alpha}{16}$	$\frac{7}{16}+\frac{18\alpha}{16}$
a_2	0	$-\frac{1}{8}+\frac{\alpha}{4}$	$-\frac{3}{16}+\frac{3\alpha}{8}$	$-\frac{7}{32}+\frac{14\alpha}{32}$
a_3	0	0	$\frac{1}{32}-\frac{\alpha}{16}$	$\frac{1}{16}-\frac{\alpha}{8}$
a_4	0	0	0	$-\frac{1}{128}+\frac{\alpha}{64}$

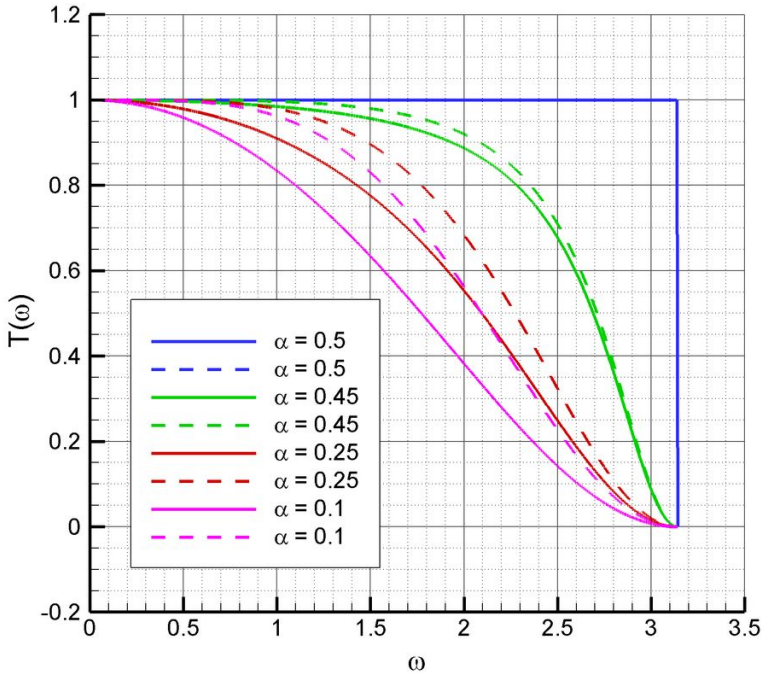

Figure 6.1: Transfer functions of the second-order (solid lines) and fourth-order (dashed lines) tridiagonal filters.

tridiagonal filter given in Eq. (6.28) can be written as

$$T(\omega) = (\frac{1}{2}+\alpha)\frac{1+\cos(\omega)}{1+2\alpha\cos(\omega)}. \tag{6.30}$$

The transfer function of the generalized filter given in Eq. (6.29) can be written as

$$T(\omega) = \frac{\sum_{n=0}^{M} a_n \cos(n\ \omega)}{1 + 2\alpha\cos(\omega)}. \tag{6.31}$$

The transfer functions corresponding to the second- and fourth-order filters are plotted in Figure 6.1 and are positive definite in the interval of $0 \leq |\alpha| \leq 0.5$, where α is a free parameter of the filter. By substituting these transfer functions into the deconvolution operator, it can be easily seen that the transfer functions of the deconvolution operators also become positive definite. With these two conditions verified (the positive definiteness of the transfer functions of the filters and deconvolution operators), the theoretical results in Stanculescu (2008) provide solid mathematical support for our numerical investigations.

6.4 Numerical methods

In this section, we provide a brief description of the numerical methods employed in the investigation of the new AD model. For the time discretization, we employ an optimal third-order total variation diminishing Runge-Kutta (TVDRK3) scheme (Gottlieb and Shu, 1998). For clarity of notation, we rewrite the new AD model in the following form

$$\frac{d\bar{q}}{dt} = R, \tag{6.32}$$

where R denotes the discrete spatial derivative operator, including the nonlinear convective term, the linear diffusive term, the forcing term, and the subfilter-scale term. The TVDRK3 scheme then becomes

$$\begin{aligned}
\bar{q}^{(1)} &= \bar{q}^n + \Delta t R^{(n)} \\
\bar{q}^{(2)} &= \frac{3}{4}\bar{q}^n + \frac{1}{4}\bar{q}^{(1)} + \frac{1}{4}\Delta t R^{(1)} \\
\bar{q}^{n+1} &= \frac{1}{3}\bar{q}^n + \frac{2}{3}\bar{q}^{(2)} + \frac{2}{3}\Delta t R^{(2)},
\end{aligned} \tag{6.33}$$

where Δt is the adaptive time step size which can be computed at the end of each time step by:

$$\Delta t = c\frac{\min(\Delta x, \Delta y)}{\max\left(|\frac{\partial\bar{\psi}}{\partial x}|, |\frac{\partial\bar{\psi}}{\partial y}|\right)}, \tag{6.34}$$

where c is known as Courant-Friedrichs-Lewy (CFL) number. We set $c = 1.0$ for all the simulations reported here.

For the spatial discretization of linear operators, such as the viscous dissipation term and the Poisson equation, we use a second-order finite difference method. For the nonlinear convection term, we utilize Arakawa's conservative scheme (Arakawa, 1966). Finally, a direct Poisson solver based on the fast sine transform is used to solve the kinematic relationship between the vorticity and the stream function in Eq. (6.4). Specifically, we use a fast sine transform in one direction and a tridiagonal system solver in the other direction (Moin, 2001).

For completeness, we summarize the solution algorithm for one time step. We assume that the numerical approximation for time level n is known, and we seek the numerical approximation for time level $n+1$, after the time step Δt. We write the algorithm for the new AD model given in Eqs. (6.26)-(6.27), but we emphasize that it is the same algorithm, with some obvious modifications, that is used for the high resolution well resolved simulation, which is referred to here as DNS. We emphasize that the term DNS in this study is not meant to indicate that a fully detailed solution is being computed, but instead refers to resolving the simulation down to the Munk scale via the specified lateral eddy viscosity parameterization. The solution algorithm has the following form

1. Compute $\bar{\psi}^n$ using the Poisson solver for the following equation:

$$\frac{\partial^2\bar{\psi}^n}{\partial x^2} + \frac{\partial^2\bar{\psi}^n}{\partial y^2} = -\frac{1}{Ro}\left(\bar{q}^n - y\right). \tag{6.35}$$

2. Compute q^{n*} and ψ^{n*} using $\bar{q}^n$ and $\bar{\psi}^n$, the filtering procedure in Eq. (6.29), and the

AD method in Eqs. (6.23) and (6.24).

3. Compute the nonlinear Jacobian terms $\overline{J(q^{n*}, \psi^{n*})}$ and $J(\bar{q}^n, \bar{\psi}^n)$ using the Arakawa scheme.

4. Compute the subfilter-scale term S^* using $\overline{J(q^{n*}, \psi^{n*})}, J(\bar{q}^n, \bar{\psi}^n)$, and Eq. (6.27).

5. Compute the viscous dissipation term $\bar{D}$ using a central difference scheme and calculate the right-hand-side term R in Eq. (6.32).

6. Apply the Runge-Kutta algorithm by repeating steps 1-5 for each stage of Runge-Kutta scheme.

7. Adjust the time step according to the CFL number given in Eq. (6.34).

8. Go to step 1 to begin the next time step.

6.5 Numerical results

The main goal of this section is to test the new AD model given by Eqs. (6.26)-(6.27) in the numerical simulation of the BVE defined in Eq. (6.1). Before testing the new model, however, we first validate the code in Section 6.5.1. The new AD model is then tested in the numerical simulation of a four-gyre barotropic model with double-gyre wind forcing in Section 6.5.2.

6.5.1 Method of manufactured solutions: Code validation

To validate the code, we consider the following exact solution, which corresponds to a steady state Taylor-Green vortex flow:

$$q(x,y,t) = \left(\frac{\delta_I}{L}\right)^2 2\,\pi^2 \sin(\pi x)\sin(\pi y) + y, \tag{6.36}$$

$$\omega(x,y,t) = 2\,\pi^2 \sin(\pi x)\sin(\pi y), \tag{6.37}$$

$$\psi(x,y,t) = \sin(\pi x)\sin(\pi y). \tag{6.38}$$

The forcing function is calculated by plugging Eqs. (6.36)-(6.38) into the BVE (i.e., Eq. (6.1)):

$$F(x,y,t) = -\pi\,\cos(\pi x)\sin(\pi y) + \left(\frac{\delta_M}{L}\right)^3 4\,\pi^4 \sin(\pi x)\sin(\pi y). \tag{6.39}$$

We use $q(x,y,0) = 0$ as the initial condition. The spatial resolution is 64×128 and the time step Δt is computed adaptively as given in Eq. (6.34). We utilize the numerical algorithm in Section 6.4 to integrate the BVE until the steady state solution is obtained. Our numerical results closely match the exact solution. To investigate the individual effects of the nonlinear Jacobian, dissipation, forcing and subfilter-scale terms, we compute the time series of following integral quantities:

$$Q_J(t) = \frac{1}{2}\iint \left(J(\bar{q},\bar{\psi})\right)^2 dx\,dy, \tag{6.40}$$

$$Q_D(t) = \frac{1}{2}\iint \bar{D}^2 dx\,dy, \tag{6.41}$$

$$Q_F(t) = \frac{1}{2}\iint \bar{F}^2 dx\,dy, \tag{6.42}$$

$$Q_S(t) = \frac{1}{2}\iint \left(S^*\right)^2 dx\,dy. \tag{6.43}$$

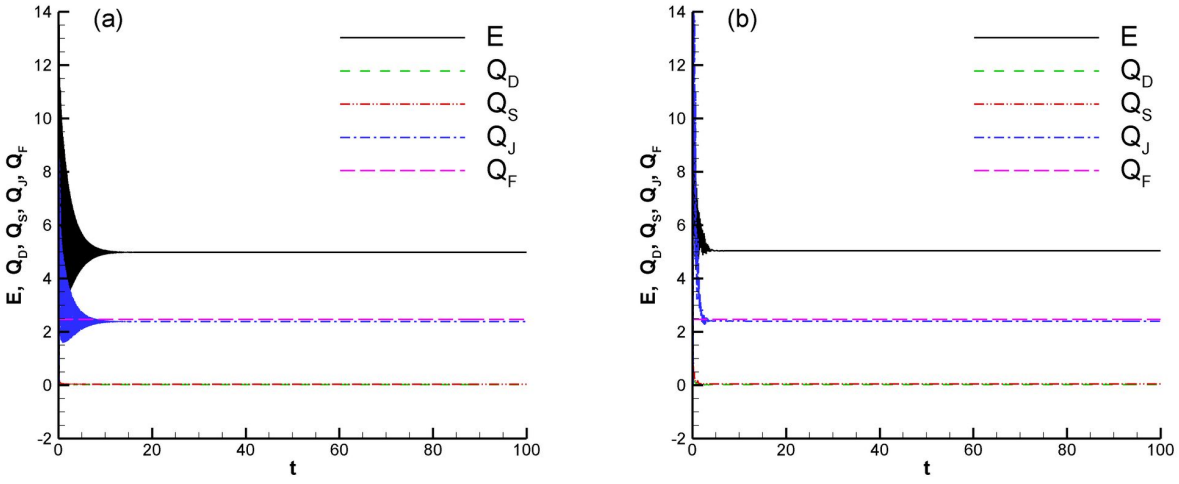

Figure 6.2: Code validation test case. Time history of the total energy, individual dissipation, Jacobian, subfilter-scale and forcing terms: (a) $\delta_I/L = 0.04$ and $\delta_M/L = 0.02$; and (b) $\delta_I/L = 0.06$ and $\delta_M/L = 0.02$. The numerical approximation converges to the correct value after a short transient interval.

We also plot with respect to time the total energy:

$$E(t) = \frac{1}{2} \iint \left(\frac{\partial \psi}{\partial y} \right)^2 + \left(\frac{\partial \psi}{\partial x} \right)^2 dx\, dy, \tag{6.44}$$

Since the exact steady state solution is given in Eqs. (6.36)-(6.38), we can calculate the exact values of the above integral quantities.

In Figure 6.2 we plot the time evolution of the total energy, and contributions of the individual dissipation, subfilter-scale, nonlinear Jacobian, and forcing terms. We plot these time series for two parameter sets: $\delta_I/L = 0.04$ and $\delta_M/L = 0.02$ in Figure 6.2(a), and $\delta_I/L = 0.06$ and $\delta_M/L = 0.02$ in Figure 6.2(b). For both parameter sets, the time evolution of the above integral quantities follows the same pattern: after a short transient interval, they converge to the correct exact values. Thus, we conclude that the numerical algorithm produces accurate results for these validation test cases.

6.5.2 Four-gyre problem with double-gyre forcing

The main goal of this section is to test the new AD model given by Eqs. (6.26)-(6.27) in the numerical simulation of the wind-driven circulation in a shallow ocean basin, a standard prototype of more realistic ocean dynamics. The model employs the BVE driven by a symmetric double-gyre wind forcing, which yields a four-gyre circulation in the time mean. This test problem has been used in numerous studies (e.g., Cummins, 1992; Greatbatch and Nadiga, 2000; Nadiga and Margolin, 2001; Holm and Nadiga, 2003; Fox-Kemper, 2005). This problem represents an ideal test for the new AD model. Indeed, as showed in Greatbatch and Nadiga (2000), although a double gyre wind forcing is used, the long time average yields a four gyre pattern, which is challenging to capture on coarse spatial resolutions. Thus, we will investigate numerically whether the new AD model can reproduce the four gyre time average on a coarse mesh.

The mathematical model used in the four gyre problem is the BVE defined by Eq. (6.1). The double-gyre forcing is given in Eq. (6.6). Following Holm and Nadiga (2003), we utilize two different parameter sets, corresponding to two physical oceanic settings: Experiment (i) with a Rhines scale of $\delta_I/L = 0.04$ and a Munk scale of $\delta_M/L = 0.02$, which corresponds to a Reynolds number of $Re = 200$ (or a boundary layer based Reynolds number of $Re_B = 8$) and a Rossby number of $Ro = 0.0016$; and Experiment (ii) with a Rhines scale of $\delta_I/L = 0.06$ and a Munk scale of $\delta_M/L = 0.02$, which corresponds to a Reynolds number of $Re = 450$ (or a boundary layer based Reynolds number of $Re_B = 27$) and a Rossby number of $Ro = 0.0036$. Since we set the Munk scale to $\delta_M/L = 0.02$ in our study, the uniform eddy viscosity coefficient embedded in the model can be calculated from Eq. (6.9). For example, if we set the mid-latitude ocean basin length to $L = 2000$ km and the gradient of the Coriolis parameter to $\beta = 1.75 \times 10^{-11}$ m^{-1}s^{-1}, then our model uses $\nu = 1120$ m^{2}s^{-1} as its eddy viscosity parametrization. All numerical experiments conducted here are solved for a maximum dimensionless time of $T_{max} = 100$. This value corresponds to the dimensional times of 56.6 and 25.15 years for Experiment (i) and Experiment (ii), respectively, which are

long enough to capture statistically steady states. All computations were carried out using the gfortran compiler on a Linux cluster system.

To assess the new AD model, we employ the standard LES methodology: we first run a DNS computation on a fine mesh. We then run an under-resolved numerical simulation on a much coarser mesh (denoted in what follows as BVE_{coarse}), which does not employ any subfilter-scale model. We expect BVE_{coarse} to produce inaccurate results. Finally, we employ the new AD model on the same coarse mesh utilized in BVE_{coarse}. The AD model should yield results that are significantly better than those obtained with BVE_{coarse} and are close to the DNS results, at a fraction of the computational cost.

We start by performing a DNS computation on a fine mesh (512×256 spatial resolution). After a transient period, a statistically steady state solution is obtained at a time of around $t = 10$. Instantaneous contour plots at time $t = 90$ for the potential vorticity, vorticity, and stream function are shown in Figure 6.3 and Figure 6.4 for Experiment (i) and Experiment (ii), respectively. Two gyres are clearly seen in the stream function contour plots. Next, the time average of the data is taken between time $t = 20$ and $t = 100$ using 8001 snapshots. The results are given in Figure 6.5 and Figure 6.6. We emphasize that, for both parameter sets, *four gyres* are clearly visible in the stream function plots. This is in stark contrast with the instantaneous stream function contour plots in Figure 6.3 and Figure 6.4, in which only two gyres are present. The computational time of each DNS run was longer than 3.5 days.

In addition to the time series of each individual term given by Eqs. (6.40)-(6.43), following Marshall and Pillar (2011), we compute the force functions in order to analyze the contribution of individual terms, including the subfilter-scale term, in the new AD model given by Eqs. (6.26)-(6.27). The defining equations for the force functions corresponding to the dissipation, subfilter-scale, nonlinear Jacobian, and forcing terms are:

$$\nabla^2 \phi_D = \bar{D}, \tag{6.45}$$

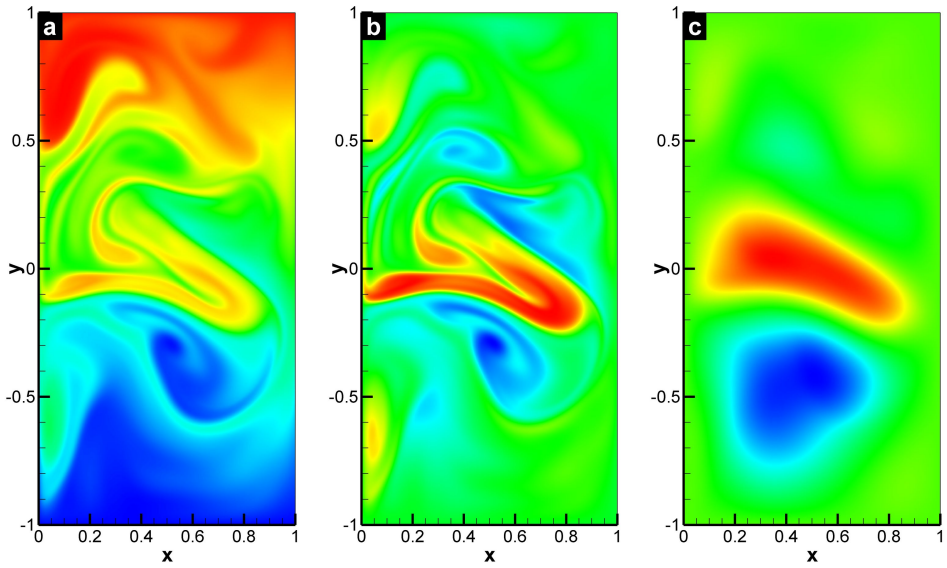

Figure 6.3: Experiment (i): DNS results for $Re = 200, Ro = 0.0016$ and a spatial resolution of 512×256. Instantaneous field data for: (a) potential vorticity; (b) vorticity; and (c) stream function. Note that two gyres appear in the stream function contour plot.

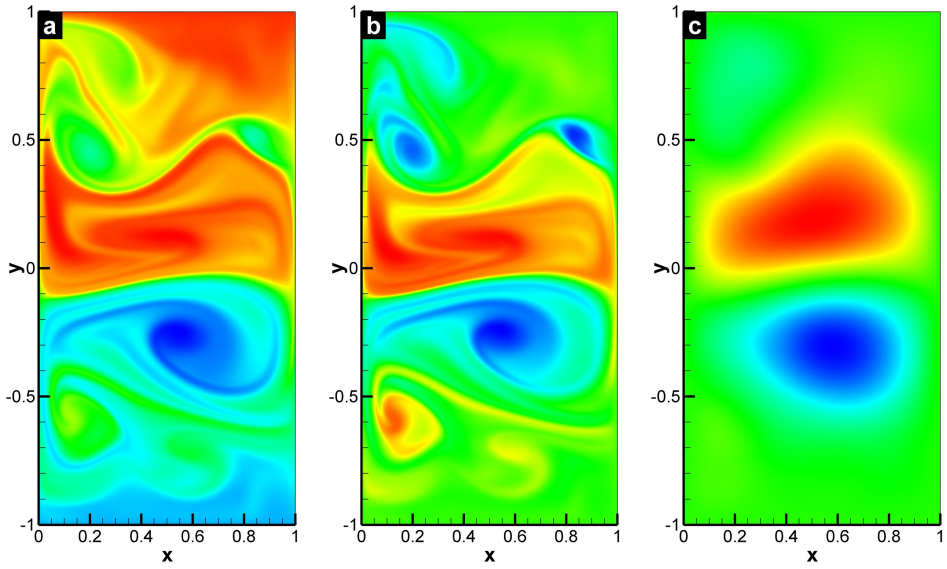

Figure 6.4: Experiment (ii): DNS results for $Re = 450, Ro = 0.0036$ and a spatial resolution of 512×256. Instantaneous field data for: (a) potential vorticity; (b) vorticity; and (c) stream function. Note that two gyres appear in the stream function contour plot.

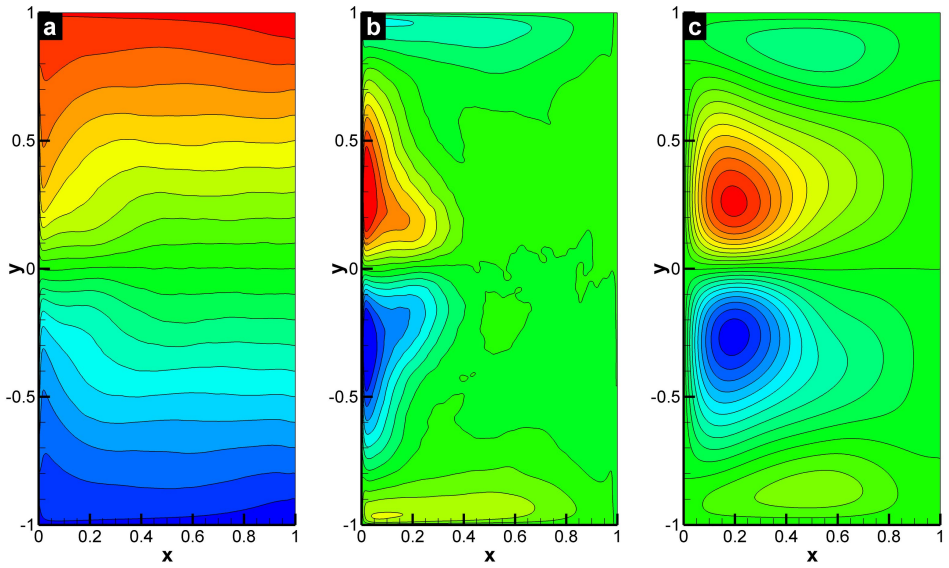

Figure 6.5: Experiment (i): DNS results for $Re = 200, Ro = 0.0016$ and a spatial resolution of 512×256. Time-averaged field data for: (a) potential vorticity; (b) vorticity; and (c) stream function. Note that four gyres appear in the stream function contour plot.

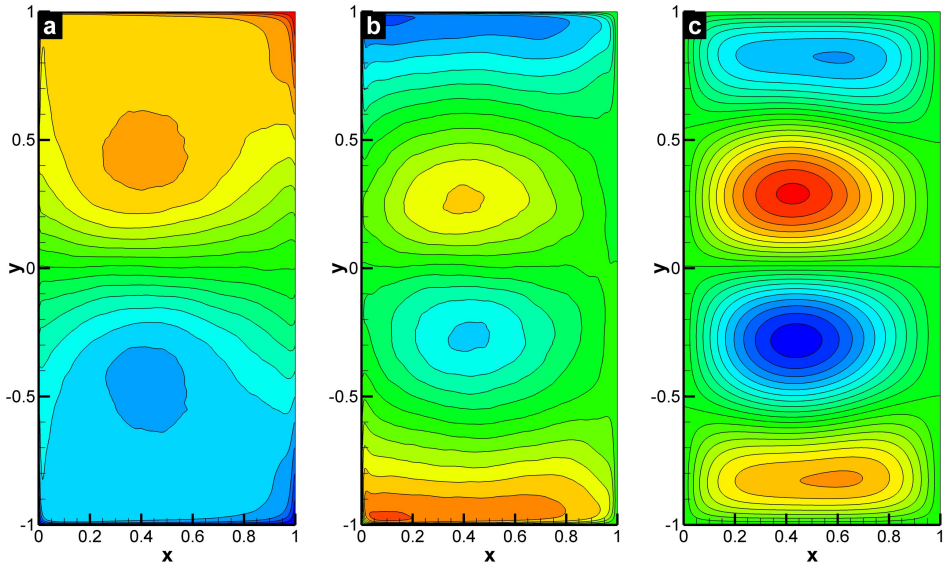

Figure 6.6: Experiment (ii): DNS results for $Re = 450, Ro = 0.0036$ and a spatial resolution of 512×256. Time-averaged field data for: (a) potential vorticity; (b) vorticity; and (c) stream function. Note that four gyres appear in the stream function contour plot.

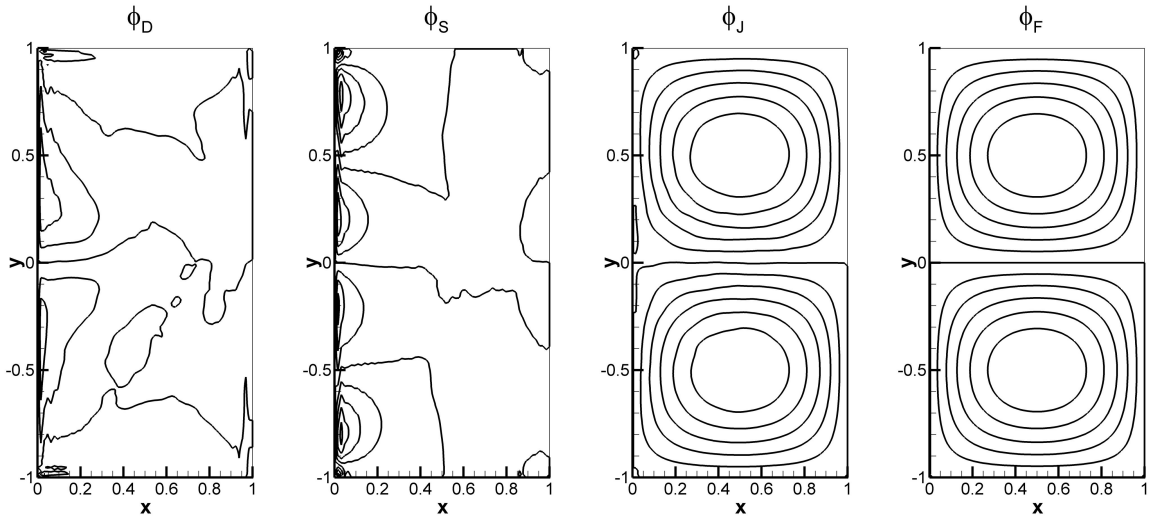

Figure 6.7: Experiment (i): AD results for $Re = 200, Ro = 0.0016$, and a spatial resolution of 128×64. Time-averaged force function contour plots for the dissipation, subfilter-scale, Jacobian, and forcing terms. The contour intervals are between -0.05 and 0.05 for the forcing and Jacobian terms, and -0.002 and 0.002 for the dissipation and subfilter-scale terms.

$$\nabla^2 \phi_S = S^*, \tag{6.46}$$

$$\nabla^2 \phi_J = \bar{J}, \tag{6.47}$$

$$\nabla^2 \phi_F = \bar{F}. \tag{6.48}$$

Solving these Poisson equations for time averaged data (between $t = 20$ and $t = 100$ using $8,001$ snapshots) yields the corresponding force functions. Figure 6.7 and Figure 6.8 illustrate these force function contour plots for Experiment (i) and Experiment (ii) for a spatial resolution of 128×64. The time series of the total energy, dissipation, subfilter-scale, Jacobian and forcing terms are plotted in Figure 6.9. It can be seen that at this spatial resolution the subfilter-scale effects are on the same order as the effects of the dissipation term.

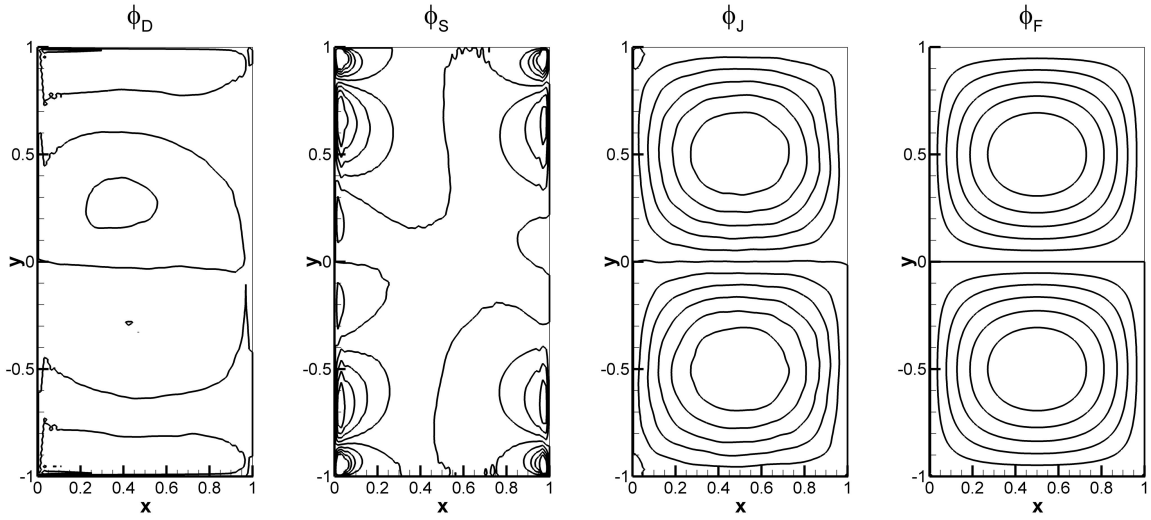

Figure 6.8: Experiment (ii): AD results for $Re = 450$, $Ro = 0.0036$, and a spatial resolution of 128×64. Time-averaged force function contour plots for the dissipation, subfilter-scale, Jacobian, and forcing terms. The contour intervals are between -0.05 and 0.05 for the forcing and Jacobian terms, and -0.002 and 0.002 for the dissipation and subfilter-scale terms.

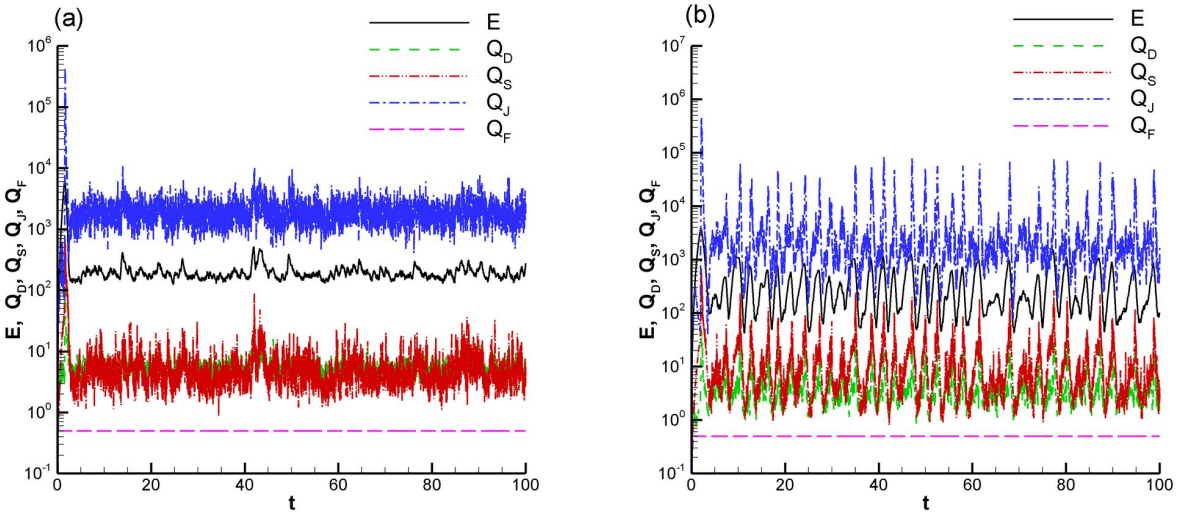

Figure 6.9: Time history of the total energy, dissipation, subfilter-scale, Jacobian, and forcing terms: (a) Experiment (i): $\delta_I/L = 0.04$ and $\delta_M/L = 0.02$; and (b) Experiment (ii): $\delta_I/L = 0.06$ and $\delta_M/L = 0.02$.

Next, we test the new AD model given by Eqs.(6.26)-(6.27) using a coarser mesh with a spatial resolution of 32×16, which is 16 *times coarser* than the DNS mesh with a resolution of 512×256. On this coarse mesh, we test both the new AD model and the under-resolved numerical simulation BVE_{coarse}, which does not employ any subfilter-scale model. To compare the models, we utilize data that is time-averaged between $t = 20$ and $t = 100$. The new AD model is tested with a second-order filtering operation and $N = 5$ (as in Eq. (6.23) and Eq. (6.24)), and with the smoothing parameter $\alpha = 0.25$.

For $Re = 200$ and $Ro = 0.0016$ we plot the time-averaged stream function and potential vorticity contours in Figure 6.10 and Figure 6.11, respectively. We note that the new AD model yields improved results by smoothing out the numerical oscillations present in the under-resolved BVE_{coarse} results. This improvement is more clearly displayed in the potential vorticity contour plot in Figure 6.11. For $Re = 450$ and $Ro = 0.0036$ we plot the time-averaged stream function and potential vorticity contours in Figure 6.12 and Figure 6.13, respectively. The new AD model yields results that are significantly better than those corresponding to the under-resolved BVE_{coarse} run. Indeed, in the stream function plot in Figure 6.12 the new AD model clearly displays the correct four gyre pattern (as in the DNS plot), whereas the under-resolved BVE_{coarse} run incorrectly yields only two gyres, which is nonphysical. We also plot in Figure 6.14 the time history of the total energy. It is clear that the new AD model yields accurate results that are close to the DNS results. The under-resolved BVE_{coarse} run, however, yields totally inaccurate results. The contributions of the individual terms in Experiment (i) and Experiment (ii), obtained using the AD model for under-resolved simulations at a spatial resolution of 32×16, are also shown in Figure 6.15. When we compare this to the higher resolution simulation illustrated in Figure 6.9, it can be seen that the relative contribution of the subfilter-scale terms is more prominent in the under-resolved simulations.

To summarize, the new AD model performs significantly better than the under-resolved BVE_{coarse} simulation in all tests. For the higher Reynolds number case the improvement is more dramatic. Indeed, the AD model correctly yields the four gyre pattern, just like the

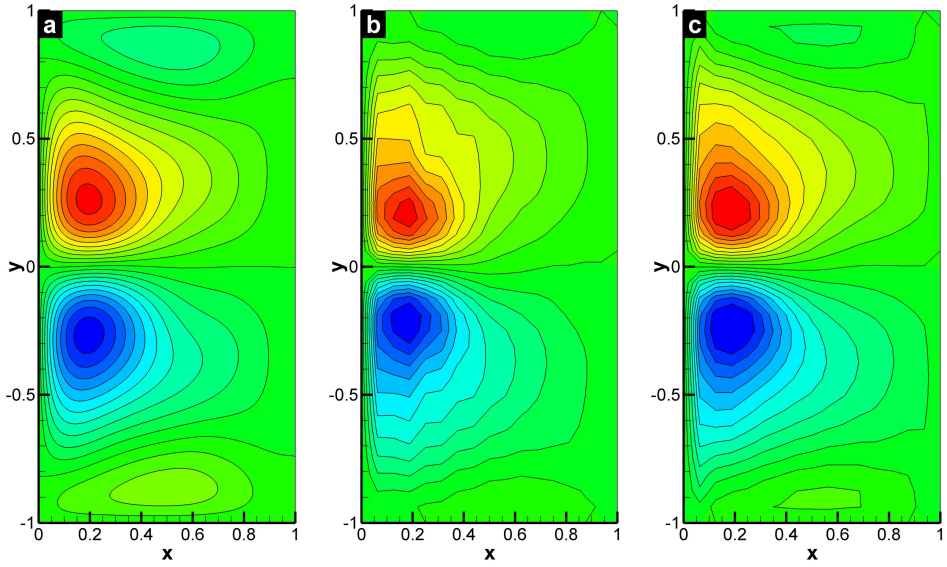

Figure 6.10: Experiment (i): Time-averaged stream function data for $Re = 200$ and $Ro = 0.0016$: (a) DNS results at a resolution of 512×256; (b) under-resolved BVE_{coarse} results at a resolution of 32×16; (c) new AD model results at a resolution of 32×16. Note the smoothing effect of the AD model on contour lines. The contour interval layouts are identical in all three cases.

DNS computation, whereas the under-resolved BVE_{coarse} computation incorrectly predicts just two gyres. We also emphasize that the new AD model (resolution of 32×16) is significantly more efficient than the DNS (resolution of 512×256), yielding a *speed-up factor of more than* $1,000$.

Finally, we perform a sensitivity study with respect to the parameters used in the new AD model: M, the order of the high-order compact filter in Eq. (6.29); N, the order of the AD procedure in Eq. (6.16); and α, the smoothing parameter of the second-order filter in Eq. (6.28). First, we investigate the sensitivity of the AD model with respect to M, the order of the high-order compact filter in Eq. (6.29). Since our tests show no significant differences among the different values of M, we are presenting below only the results obtained with the second-order filter in Eq. (6.28).

Next, we perform a sensitivity study with respect to N, the order of the AD procedure

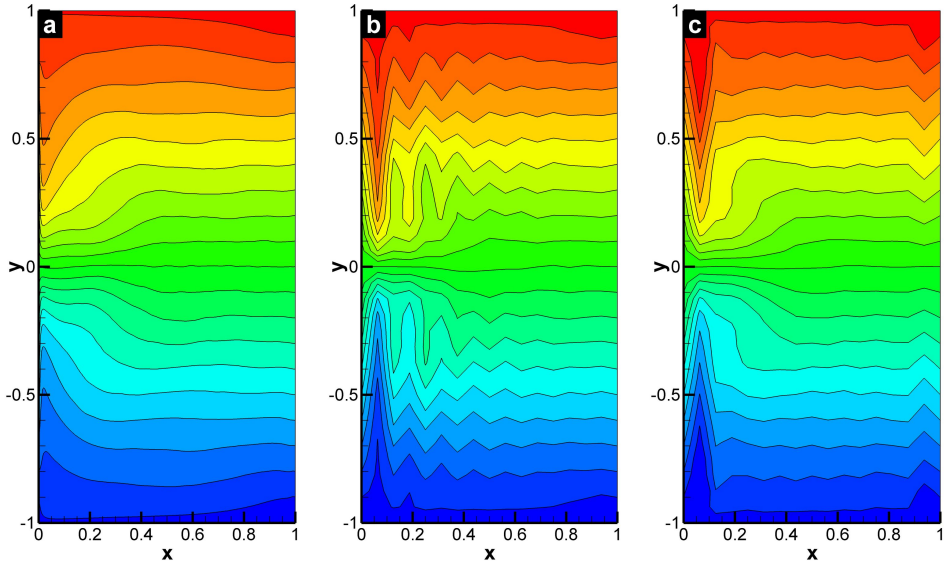

Figure 6.11: Experiment (i): Time-averaged potential vorticity data for $Re = 200$ and $Ro = 0.0016$: (a) DNS results at a resolution of 512×256; (b) under-resolved BVE_{coarse} results at a resolution of 32×16; (c) new AD model results at a resolution of 32×16. Note the smoothing effect of the AD model on contour lines. The contour interval layouts are identical in all three cases.

in Eq. (6.16). For a fixed smoothing parameter $\alpha = 0.25$, the time-averaged stream function contour plots in Figure 6.16 show a low sensitivity with respect to N. The time history of the total energy plotted in Figure 6.17, however, displays a non-negligible sensitivity with respect to N. Indeed, higher values of N yield more accurate results. Of course, the tradeoff is an increase in computational time due to the additional filtering operations needed for higher values of N: The CPU time is 170 s for $N = 5$, 145 s for $N = 3$, and 113 s for $N = 1$. Thus, the two numerical investigations in Figure 6.16 and Figure 6.17 seem to suggest that, in order to balance the numerical accuracy and the computational efficiency, a relative low value for N might be desirable.

Finally, we investigate the sensitivity of the AD model with respect to α, the smoothing parameter of the second-order filter in Eq. (6.28). For a fixed order of the AD procedure $N = 5$, the time-averaged stream function contour plots in Figure 6.18 show a low sensitivity with respect to α. Our numerical experiments, however, suggest an optimal range of $0.1 <$

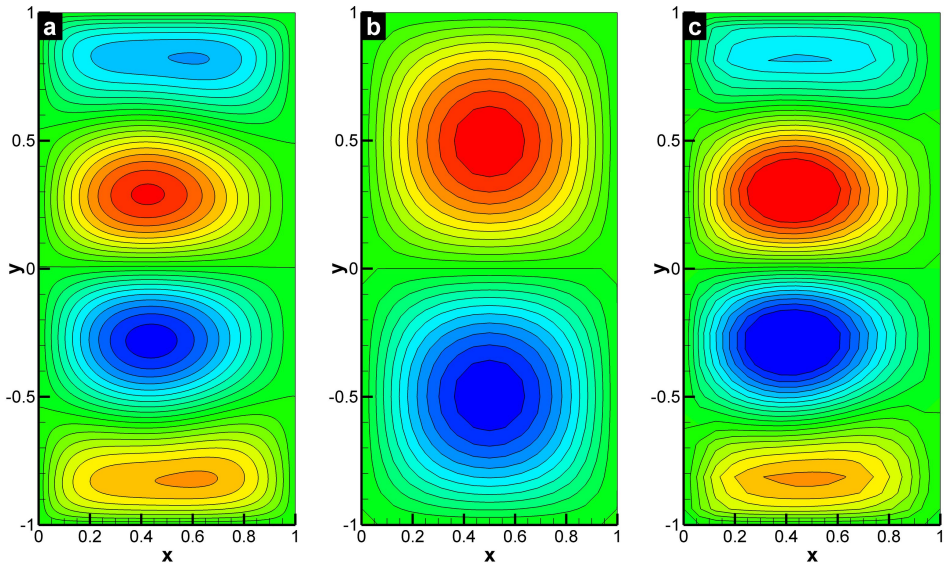

Figure 6.12: Experiment (ii): Time-averaged stream function data for $Re = 450$ and $Ro = 0.0036$: (a) DNS results at a resolution of 512×256; (b) under-resolved BVE_{coarse} results at a resolution of 32×16; (c) new AD model results at a resolution of 32×16. Note that the BVE_{coarse} results are nonphysical, whereas the DNS and AD model results are qualitatively close. The contour interval layouts are identical only for (a) and (c).

$\alpha < 0.3$, since higher values of α do not eliminate numerical oscillations for coarse grids.

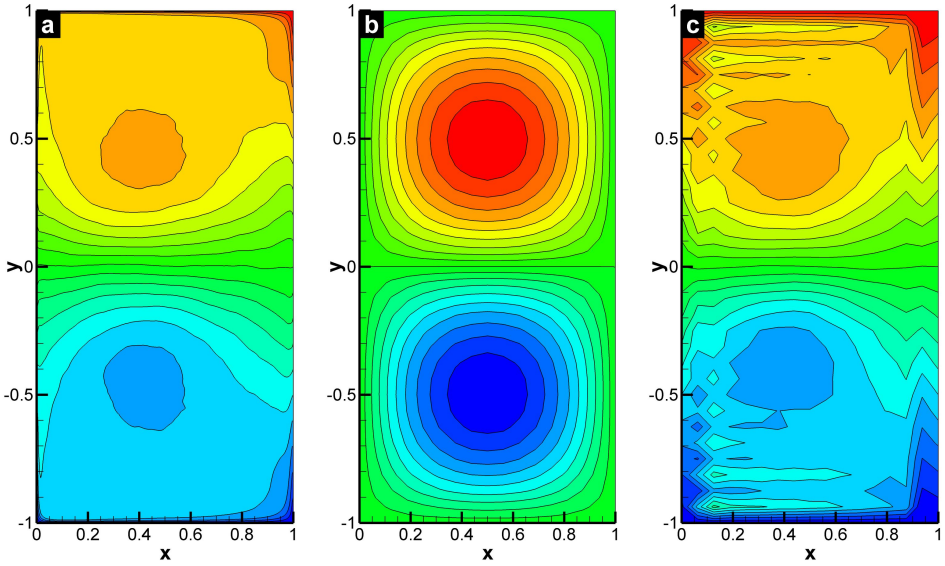

Figure 6.13: Experiment (ii): Time-averaged potential vorticity data for $Re = 450$ and $Ro = 0.0036$: (a) DNS results at a resolution of 512×256; (b) under-resolved BVE_{coarse} results at a resolution of 32×16; (c) new AD model results at a resolution of 32×16. Note that the BVE_{coarse} results are nonphysical, whereas the DNS and AD model results are qualitatively similar. The contour interval layouts are identical only for (a) and (c).

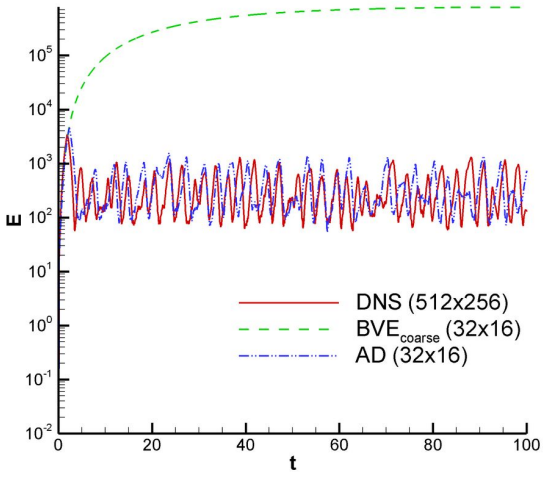

Figure 6.14: Experiment (ii): Time history of the total energy for $Re = 450$ and $Ro = 0.0036$: DNS results at a resolution of 512×256, under-resolved BVE_{coarse} results at a resolution of 32×16, new AD model results at a resolution of 32×16. Note the significant improvement of the new AD model over the results from the under-resolved BVE_{coarse} run.

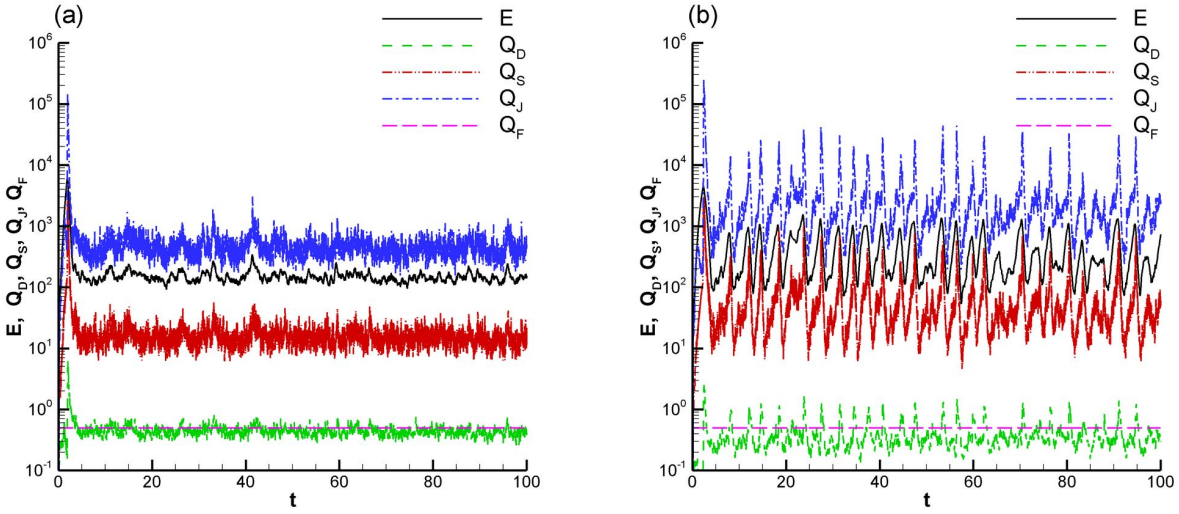

Figure 6.15: Time history of the total energy, dissipation, subfilter-scale, Jacobian, and forcing terms: (a) Experiment (i): $\delta_I/L = 0.04$ and $\delta_M/L = 0.02$; and (b) Experiment (ii): $\delta_I/L = 0.06$ and $\delta_M/L = 0.02$.

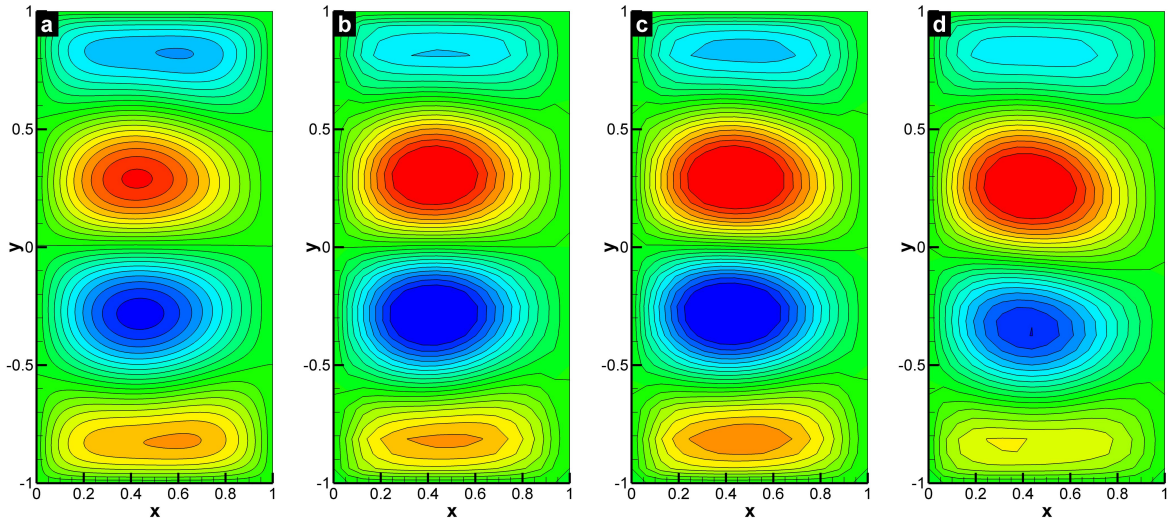

Figure 6.16: Experiment (ii): Time-averaged stream function data for $Re = 450$ and $Ro = 0.0036$. Sensitivity with respect to the AD order N: (a) DNS results at a resolution of 512×256; (b) AD model results at a resolution of 32×16 with $N = 5$, (c) AD model results at a resolution of 32×16 with $N = 3$, (d) AD model results at a resolution of 32×16 with $N = 1$. Note the low sensitivity of the results with respect to N. The contour intervals are identical in all four cases.

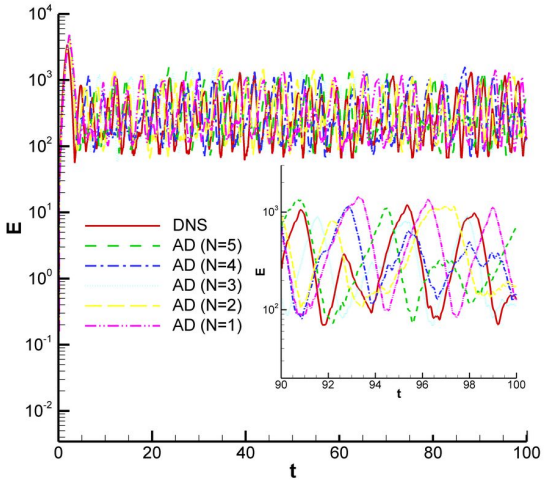

Figure 6.17: Experiment (ii): Time history of the total energy for $Re = 450$ and $Ro = 0.0036$. Sensitivity with respect to the AD order N: DNS results at a resolution of 512×256 and new AD model results at a resolution of 32×16. Note the non-negligible sensitivity with respect to N. The inset figure shows the time series between t=90 and t=100.

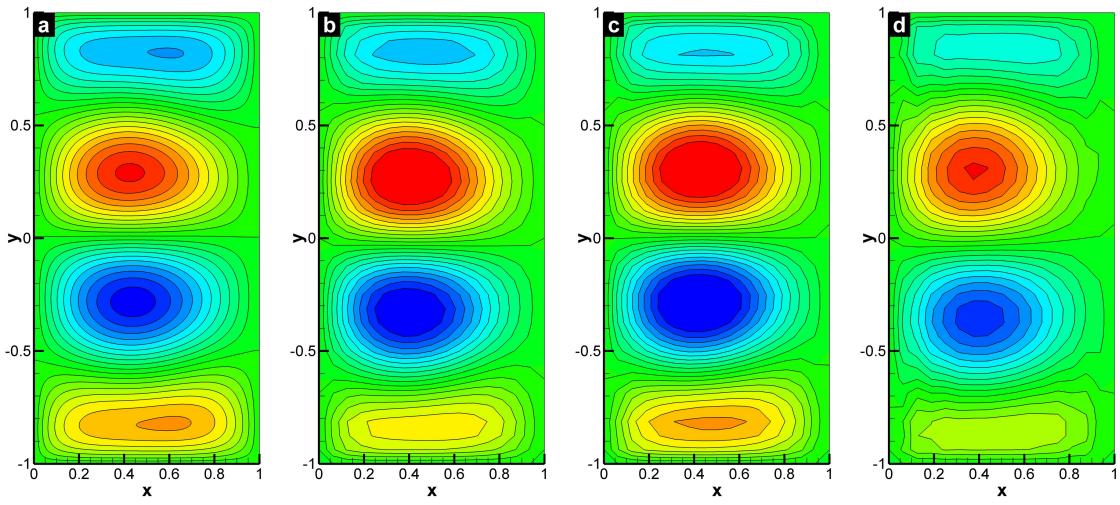

Figure 6.18: Experiment (ii): Time-averaged stream function data for $Re = 450$ and $Ro = 0.0036$. Sensitivity with respect to the smoothing filtering parameter α. (a) DNS results at a resolution of 512×256; (b) AD model results at a resolution of 32×16 with $\alpha = 0.1$, (c) AD model results at a resolution of 32×16 with $\alpha = 0.25$, (d) AD model results at a resolution of 32×16 with $\alpha = 0.45$. Note the low sensitivity of the results with respect to α. The contour intervals are identical in all four cases.

6.6 Conclusions

A new approximate deconvolution (AD) model was introduced for the LES of two-dimensional turbulent geophysical flows. The AD model was tested in the numerical simulation of the wind-driven circulation in a shallow ocean basin, a standard prototype of more realistic ocean dynamics. The mathematical model employed was the barotropic vorticity equation (BVE) driven by a symmetric double-gyre wind forcing, which yielded a four-gyre circulation in the time mean. The AD model was tested on a mesh that was 16 times coarser than that used by the direct numerical simulation (DNS) run. The AD model yielded numerical results that were in close agreement with those of the DNS. In particular, the four gyre structure of the time-averaged stream function contour plots was recovered by the AD model. Moreover, the CPU time of the AD model computations was 1,000 times lower than that of the DNS. We emphasize that this combination of computational efficiency and numerical accuracy achieved by the new AD model was due to the specific subfilter-scale model utilized. Indeed, an under-resolved numerical simulation without any subfilter-scale model on the same coarse mesh as that employed by the AD model produced inaccurate results. We also performed a numerical investigation of the sensitivity of the new AD model with respect to the parameters used and we found that the model is robust. This first step in the numerical assessment of the new model shows that AD could represent a viable tool in the LES of more realistic turbulent geophysical flows.

Chapter 7

Approximate Deconvolution Large Eddy Simulation of a Stratified Two-Layer Quasigeostrophic Ocean Model

We develop and present an approximate deconvolution (AD) large eddy simulation (LES) model for the two-layer quasigeostrophic equations. The AD closure modeling approach is particularly appealing for geophysical flows because of no additional phenomenological approximations to the original set of equations. The AD approach can achieve high accuracy by employing repeated filtering, which is computationally efficient and easy to implement. We applied the new AD-LES model to mid-latitude two-layer square oceanic basins, which are standard prototypes of more realistic stratified ocean dynamics models. Compared with a high-resolution numerical simulation, the AD-LES model yielded accurate numerical results at a significantly lower computational cost. A sensitivity analysis of the AD-LES results

O. San, A. E. Staples, and T. Iliescu "Approximate deconvolution large eddy simulation of a stratified two-layer quasigeostrophic ocean model," submitted to *Ocean Modelling*.

with respect to changes in input parameters was performed. We discovered that, although the AD-LES model was quite robust with respect to changes in parameters, changing the spatial filter made a very significant difference. Two spatial filters were investigated in the AD-LES model: a tridiagonal filter and an elliptic differential filter. It was found that the tridiagonal filter introduced a negligibly small amount of numerical dissipation into the AD-LES model. The differential filter, however, added a significant amount of numerical dissipation to the AD-LES model. In fact, our numerical results show that the new AD-LES model used in conjunction with the differential filter can be employed successfully on meshes that are significantly coarser than the Munk scale and with an eddy viscosity coefficient that is dramatically lower than that used in the original two-layer quasigeostrophic equations. Although this report does not provide a solution to the longstanding quest to find a rigorous derivation of appropriate eddy viscosity coefficients to use in ocean modeling, it puts forth a novel approach to determining them, serendipitously discovered during the course of our numerical investigations. We believe that the main strength of this new approach is that the modeling error can be disentangled from the numerical discretization error and can be studied separately in this new framework. This could lead to more robust and general LES models for large scale geophysical flows.

7.1 Introduction

The investigation of characteristics of forced-dissipative general circulation models is of primary importance in developing our understanding of the large-scale nonlinear motions of geophysical flows. As one of the main circulation sources, winds drive the general circulation associated with the subtropical and subpolar gyres which can be identified with the strong, persistent, sub-tropical and sub-polar western boundary currents in the North Atlantic Ocean (the Gulf Stream and the Labrador Current) and North Pacific Ocean (the Kuroshio and the Oyashio Currents) and sub-tropical counterparts in the southern hemisphere (Stommel, 1972; McWilliams, 2006). One of the major similarities between the various ocean basins

is the asymmetry of the gyres: strong western boundary currents and weaker flow in the interior; weak and shallow eastern boundary currents. The most obvious motivation for being interested in forced-dissipative wind-driven ocean circulation is the connection between ocean currents and climate dynamics (Ghil et al., 2008).

The wind-driven circulation in an enclosed, midlatitude rectangular or square basin is a classical problem, studied extensively by modelers (Allen, 1980; Holland and Rhines, 1980; Griffa and Salmon, 1989; Vallis, 2006; Miller, 2007). Various models are derived from the full-fledged equations of geophysical flows, Boussinesq equations (BEs) or the primitive equations (PEs), to guide the theoretical studies on boundary currents, alternating zonal flows, or jet formations, as well as to identify some key issues related to the robustness of the model dynamics to the changes of parameters that is closely linked to a dynamical system point of view (Speich et al., 1995; Meacham, 2000; Chang et al., 2001; Nauw et al., 2004; Dijkstra, 2005; Dijkstra and Ghil, 2005). The quasigeostrophic (QG) model is a simplification of the primitive equation model that retains many of the essential features of geophysical fluid flows. Details of the mathematical and physical approximations may be found in standard textbooks on geophysical fluid dynamics, such as Pedlosky (1987), Vallis (2006), and McWilliams (2006). The main assumptions that go into the QG models are: the hydrostatic balance, the β-plane approximation, the geostrophic balance, and the eddy viscosity parameterization.

The one-layer QG model, sometimes called the barotropic vorticity equation (BVE), represents one of the most commonly used mathematical models for these types of geostrophic flows with various dissipative and forcing terms (Majda and Wang, 2006; Vallis, 2006; Nadiga and Margolin, 2001). In reality, the ocean is a stratified fluid on a rotating Earth driven from its upper surface by patterns of momentum and buoyancy fluxes (Marshall et al., 1997). While the barotropic model is not stratified, it exhibits many of the features that are observed in the stratified case. To explore some of the effects of the stratification, the one-layer barotropic equation can be extended to the 1.5-layer model, also called the reduced gravity QG model (Özgökmen et al., 2001). There are two layers in this model, but the second

layer is infinitely deep and at rest (passive), and the dynamics are effectively barotropic. The two-layer model takes the next step in increasing the complexity of stratification by adding a second dynamically active layer (Holland, 1978; Özgökmen and Chassignet, 1998; Berloff and McWilliams, 1999; DiBattista and Majda, 2001; Berloff et al., 2009). The dynamics in this model include the first baroclinic modes. The complexity of the models could be increased by adding more active layers, resulting in the N-layer models (Siegel et al., 2001), which, in turn, yield the three dimensional primitive equations when N goes to infinity (McWilliams, 2006). In this study, we use the *two-layer QG (QG2)* model.

Geophysical turbulence is strongly affected by the planetary vorticity, the variation of the Coriolis parameter with latitude, the so-called β effect (Maltrud and Vallis, 1991; Smith et al., 2002; Chen et al., 2003). The inverse cascade typically occurring in pure two-dimensional turbulence, in this case preferentially transfers small-scale energy towards zonal modes; the resulting flow is then anisotropic and characterized by a strong interaction between waves and turbulence, and is known as the arrest of the inverse energy cascade (Rhines, 1975; Sukoriansky et al., 2007; Espa et al., 2008). Rhines (1975) explained the emergence of flow anisotropy and the organization of a banded pattern of alternating zonal currents, or jets, due to Rossby wave dynamics in terms of a competition between nonlinear and β terms in the barotropic vorticity equation. Under the effects of planetary rotation, Rossby waves dominate turbulent motions prohibiting the triad interactions, and arrest the inverse energy cascade when the scale of motions becomes larger than a critical value, later known as the Rhines scale (Tanaka and Akitomo, 2010).

Along with the Rhines scale which is a measure of the strength of nonlinear interactions, another important scale for determining the dynamics of the large scale motions in the ocean is the Munk scale (Munk, 1950), which corresponds to the dissipative behavior of the system and can be linked to the Reynolds number. Although the water molecular viscosity is around $10^{-6}\ m^2 s^{-1}$, the one- and two-layer QG models use viscosities on the order of $10^{2}\ m^2 s^{-1}$. This is called *eddy viscosity (EV)* parameterization, and is used because the horizontal scale of the ocean basin is much larger than the effective scale for molecular

diffusion. An impractically fine resolution would be necessary if the ocean models were to resolve the full spectra of turbulence down to the Kolmogorov scale. Thus, the viscosity coefficients employed in the QG models typically remain much greater than the molecular viscosity (Campin et al., 2011). The eddy viscosities generally used in the oceanic models are summarized in Table 7.1. The eddy viscosity parameterization used in the QG models plays a crucial role in the dynamics of the problem. Indeed, Berloff and McWilliams (1999) studied the wind-driven circulation in a three-layer QG model for varying values of the eddy viscosity coefficient in a square oceanic basin. For $\nu = 1200\ m^2 s^{-1}$ an asymmetric steady state was found. When the eddy viscosity coefficient was decreased, the flow first displayed a variability characterized by the presence of interior Rossby waves. At $\nu = 1000\ m^2 s^{-1}$, the flow regime showed a quasi-periodic variability. At a smaller eddy viscosity coefficient, starting from $\nu = 800\ m^2 s^{-1}$, the flow regime was chaotic and showed a persistent eastward jet penetration by fluctuating between two preferred states, one of which corresponds to a low energy state and a long eastward jet, and the other to a high energy state and a short jet. The study of Berloff and McWilliams (1999) clearly shows that different EV coefficients can result in different dynamics of the QG models. Thus, a natural question is "What EV coefficient should be used in the QG models?" The EV coefficients summarized in Table 7.1 seem to convey, at first glance, a confusing message: they vary by as much as an order of magnitude. At a closer look, however, Table 7.1 clarifies this issue: With the ever increasing computational power, the mesh size used in numerical simulations with the QG models constantly decreases and allows the use of smaller, more realistic EV coefficients. The development of a rigorous, mathematical understanding and subsequent modeling strategy for the eddy viscosity coefficients (see Table 7.1) is the "elephant in the room," one of the major unsolved problems in ocean modeling (Visbeck et al., 1997; Campin et al., 2011; Majda and Wang, 2006; Cushman-Roisin and Beckers, 2011; Vallis, 2006). Although addressing this grand challenge is beyond the scope of this report, we do address the intimate relationship between the EV coefficients and the numerical resolution employed by the QG models.

To capture the under-resolved flow, i.e., the flow in the regions where the grid size becomes

Table 7.1: The eddy viscosity coefficients used in QG models

Study	Range of ν ($m^2 s^{-1}$)	Resolution
Bryan (1963)	500 - 10000	40×80
Gates (1968)	6000 - 10000	74×50
Holland and Lin (1975)	330	50×50
Jiang et al. (1995)	300	50×100
Özgökmen and Chassignet (1998)	50	151×151
Berloff and McWilliams (1999)	400 - 1600	256×256
Sura et al. (2001)	200	120×120
Berloff et al. (2009)	100	512×256
Tanaka and Akitomo (2010)	100	500×500

greater than the specified Munk scale, *large eddy simulation (LES)* appears as a natural choice. Most of the LES models have been developed for three-dimensional turbulent flows, such as those encountered in engineering applications (Sagaut, 2006; Berselli et al., 2006). These LES models fundamentally rely on the concept of the forward energy cascade and so their extension to geophysical flows is beset with difficulties. The effective viscosity values in oceanic models are much greater than the molecular viscosity of seawater, hence a uniform eddy viscosity coefficient is generally used to parameterize the unresolved, subfilter-scale effects in most oceanic models (McWilliams, 2006; Vallis, 2006). LES models specifically developed for two-dimensional turbulent flows, such as those in the ocean and atmosphere, are relatively scarce (Fox-Kemper and Menemenlis, 2008; Awad et al., 2009; Özgökmen et al., 2009; Chen et al., 2011), at least when compared to the plethora of LES models developed for three-dimensional turbulent flows. Holm and Nadiga (2003) combined the uniform eddy viscosity parameterization with the alpha regularization LES approach to capture the under-resolved flow where the grid length becomes greater than the specified Munk scale of the problem. In that work, the structural alpha parameterization was tested on the barotropic vorticity equation (BVE) in an ocean basin with double-gyre wind forcing, which displays a four-gyre mean ocean circulation pattern. It was found that the alpha models provide a

promising approach to LES closure modeling of the barotropic ocean circulation by predicting the correct four-gyre circulation structure for under-resolved flows.

San et al. (2011) put forth a new LES closure modeling strategy for two-dimensional turbulent geophysical flows. The new closure modeling approach utilizes *approximate deconvolution (AD)*, which is particularly appealing for geophysical flows because of no additional phenomenological approximations to the BVE. The AD approach can achieve high accuracy by employing repeated filtering, which is computationally efficient and easy to implement. The AD method has been used successfully in LES of three-dimensional turbulent engineering flows (Stolz and Adams, 1999; Stolz et al., 2001a,b, 2004; Domaradzki and Adams, 2002) and even of small scale geophysical flows, such as the atmospheric boundary layer (Chow et al., 2005; Chow and Street, 2009; Duan et al., 2010; Zhou and Chow, 2011). The AD methodology was also used in LES of large scale geophysical flows, such as the barotropic ocean circulation flow. To assess the new AD closure modeling approach, San et al. (2011) tested it on the same two-dimensional barotropic flow problem as that employed in Nadiga and Margolin (2001) and in Holm and Nadiga (2003). It was shown that the new LES-AD model provides an accurate approximation for under-resolved subfilter-scale effects.

The main goal of this report is to extend the LES-AD approach used for the one-layer QG model (San et al., 2011) to to the two-layer QG model. Along the way, however, a second, equally important goal emerged: We investigated whether the combination of LES-AD modeling and a particular spatial filter can, in fact, account for some of the eddy viscosity parameterization used in practical QG numerical simulations (see Table 7.1). In our numerical investigations, we serendipitously discovered that the AD procedure, combined with one specific spatial filter, can actually decrease the value of these *ad hoc* EV coefficients. The numerical investigation of this approach represents the second major goal of this manuscript.

The initial motivation to investigate the AD-DF model was provided by a sensitivity study of the LES-AD results with respect to changes in various input parameters. We discovered that, although the LES-AD model was quite robust with respect to changes

in parameters, changing the filter made a huge difference: The TF did not introduce a significant amount of EV, whereas the DF did. These results prompted us to find out how much of the usual EV parameterization (see Table 7.1) can the AD-DF combination account for. To our surprise, the numerical investigation indicated that most of the standard EV parameterization can be replaced by the AD-DF.

Two cautionary remarks are in order: First, since the focus of this paper is on LES, the criterion used in assessing the various models is their ability to approximate the *average* behavior of the flow, and not the instantaneous behavior. Thus, we have used the *time-averaged* stream function, potential vorticity and kinetic energy to assess the models, and not their instantaneous counterparts. We emphasize that, in the traditional LES spirit, our models are not intended to represent pointwise (in space or time) quantities.

The second caveat is that our numerical experiments clearly show that the ability of the AD-DF model to replace some of the standard EV is due to using *both* the AD-LES model and the DF. Indeed, just using the AD-LES model would not be enough to replace the AD (since the AD-TF is shown not to work for the molecular viscosity). Furthermore, the DF alone without the AD-LES model does not have the same effect either, as our numerical experiments show. That being said, our study *does not explain* how exactly the AD-DF combination works, i.e., what percentage of the standard AD is accounted for by the AD model, and what percentage is accounted for by the DF. Our numerical experiments show that the DF does add numerical dissipation, but the exact amount and form still need to be determined. We emphasize that this issue is common to LES modeling in general. Indeed, not only is it hard to find the "best" LES model, i.e., the model that produces the most accurate results at the lowest computational cost, but once this model is found, it is often hard to decide whether the success of the model is due to the actual closure model or the numerical discretization used (Berselli et al., 2006; Sagaut, 2006). In an actual LES of turbulent flow there are several ingredients - some are used at a continuum level (e.g., the closure model with its various parameters), some are used at a discrete level (e.g., the temporal and spatial discretization or the linear solver). Often, it is hard to disentangle the modeling effects

from the numerical discretization effects. Our QG setting is no different in this respect. We plan to investigate this complex relationship in a future study, by performing extensive numerical experiments in simplified settings and by developing mathematical support for these numerical results.

Our numerical results represent a clear, first step in showing that AD-DF can account for some of the EV parameterization used in the QG models. We emphasize that this study, however, does not represent a solution to the longstanding quest to find the origin of, and for modeling, the EV coefficients in ocean modeling. Instead, we propose a fresh take on this challenging issue and put forth a novel approach, serendipitously discovered in our numerical investigations. We believe that the main strength of this new approach is that the modeling error can be disentangled from the numerical discretization error and be studied separately in this new framework (Gullbrand and Chow, 2003; Chow et al., 2005; Habisreutinger et al., 2007). This could lead to more robust and general LES models in geophysical fluid dynamics. We plan to investigate this new framework in more complex settings in future studies.

The rest of the paper is organized as follows: Section 7.2 presents the two-layer QG equations for large-scale geophysical flows. The proposed AD methodology, the mathematical model used in this report, is presented in Section 7.3. The numerical methods used in our simulations are briefly discussed in Section 7.4. The results for the new AD model are presented in Section 7.5. Finally, the conclusions are summarized in Section 7.6.

7.2 Mathematical models

7.2.1 The two-layer quasigeostrophic equations

The two-layer quasigeostrophic model used in this study is one of the simplified forced-dissipative oceanic models that considers baroclinic effects. The stratified ocean is partitioned into two isopycnal layers, each of constant depth, density and temperature. The

governing quasigeostrophic potential vorticity equations for the two dynamically active layers are (Pedlosky, 1987; Salmon, 1998; McWilliams, 2006)

$$\frac{\partial q_1}{\partial t} + J(\psi_1, q_1) = D_1 + F_1, \tag{7.1}$$

$$\frac{\partial q_2}{\partial t} + J(\psi_2, q_2) = D_2 + F_2, \tag{7.2}$$

where the layer index starts from top, q_i represents potential vorticities, and ψ_i denotes for stream functions. The Jacobian operator is defined as $J(a,b) = \frac{\partial a}{\partial x}\frac{\partial b}{\partial y} - \frac{\partial a}{\partial y}\frac{\partial b}{\partial x}$. The dissipation and forcing (Ekman pumping) terms are represented by D_i, and F_i, respectively. The potential vorticities for each layer are related to the velocity stream functions through the following elliptic coupled system of equations:

$$q_1 = \nabla^2\psi_1 + \beta y + \frac{f_0^2}{g' H_1}(\psi_2 - \psi_1), \tag{7.3}$$

$$q_2 = \nabla^2\psi_2 + \beta y + \frac{f_0^2}{g' H_2}(\psi_1 - \psi_2). \tag{7.4}$$

The isopycnal flow velocity components can be found from the velocity stream functions:

$$u_i = -\frac{\partial \psi_i}{\partial y}; \quad v_i = \frac{\partial \psi_i}{\partial x}. \tag{7.5}$$

The two symbols β and f_0 are parts of the linearized β-plane approximation to the Coriolis parameter $f = f_0 + \beta y$. Here $f_0 = 2\,\Omega \sin(\phi_0)$ is the local rotation rate at $y = 0$, where Ω is the rotational speed of the earth and ϕ_0 is the latitude at $y = 0$. This is equivalent to approximating the spherical Earth with a tangent plane at $y = 0$. Stratification is represented by two stacked isopycnal layers with thicknesses H_1 and H_2, starting from the top, and $g' = g\frac{\Delta\rho}{\rho_1}$ is reduced gravity associated with the density jump between the two layers in which $\Delta\rho$ is the density difference between the two layers, ρ_1 is the reference (upper layer) density, and g is the gravitational acceleration. The inertial radius of deformation between layers, a measure of stratification strength, is defined as the Rossby deformation

radius $R_d = \sqrt{\frac{g' H_1 H_2}{f_0^2 H}}$, where $H = H_1 + H_2$. In this study, the top and bottom layers of the ocean are forced by an Ekman pumping of the form

$$F_1 = \frac{1}{\rho_1 H_1} \hat{k} \cdot \nabla \times \vec{\tau}, \tag{7.6}$$

$$F_2 = -\gamma \nabla^2 \psi_2, \tag{7.7}$$

where $\vec{\tau} = (\tau^{(x)}, \tau^{(y)})$ is the stress vector for surface wind forcing, and $\hat{k}$ is unit vector in vertical direction. In the present model, we use a double-gyre wind forcing only for zonal direction: $\tau^{(x)} = \tau_0 \cos\left(\frac{2\pi}{L} y\right)$, where L is the meridional length of the ocean basin centered at $y = 0$, and τ_0 is the maximum amplitude of the wind stress. This form of wind stress represents the meridional profile of easterly trade winds, mid-latitude westerlies, and polar easterlies from South to North. The bottom Ekman layer is parameterized by a linear bottom friction with coefficient γ. In the equations above, ∇ and ∇^2 are the gradient and Laplacian operators, respectively. For the dissipation terms, the following EV parameterizations are used:

$$D_1 = \nu \nabla^4 \psi_1, \tag{7.8}$$

$$D_2 = \nu \nabla^4 \psi_2, \tag{7.9}$$

where ν is eddy viscosity coefficient.

7.2.2 Governing equations in dimensionless form

The governing equations can be written in dimensionless form by using the Sverdrup balance to set the velocity scale of the form

$$V = \frac{2\pi \tau_0}{\rho_1 H_1 \beta L}. \tag{7.10}$$

The dimensionless variables (denoted by tilde) are defined as

$$\tilde{x} = \frac{x}{L};\ \tilde{y} = \frac{y}{L};\ \tilde{t} = \frac{t}{L/V};\ \tilde{q} = \frac{q}{\beta L};\ \tilde{\psi} = \frac{\psi}{VL}. \tag{7.11}$$

Then the two-layer quasigeostrophic equations in dimensionless form become

$$\frac{\partial \tilde{q}_1}{\partial \tilde{t}} + J(\tilde{\psi}_1, \tilde{q}_1) = \tilde{D}_1 + \sin(2\pi\tilde{y}), \tag{7.12}$$

$$\frac{\partial \tilde{q}_2}{\partial \tilde{t}} + J(\tilde{\psi}_2, \tilde{q}_2) = \tilde{D}_2 - \sigma\tilde{\nabla}^2\tilde{\psi}_2, \tag{7.13}$$

in which the dissipative terms can be written as

$$\tilde{D}_1 = A\tilde{\nabla}^4\tilde{\psi}_1 \tag{7.14}$$

$$\tilde{D}_2 = A\tilde{\nabla}^4\tilde{\psi}_2. \tag{7.15}$$

In dimensionless form, the kinematic relationships between potential vorticities and stream functions become:

$$\tilde{q}_1 = \mathrm{Ro}\tilde{\nabla}^2\tilde{\psi}_1 + \tilde{y} + \frac{\mathrm{Fr}}{\delta}(\tilde{\psi}_2 - \tilde{\psi}_1), \tag{7.16}$$

$$\tilde{q}_2 = \mathrm{Ro}\tilde{\nabla}^2\tilde{\psi}_2 + \tilde{y} + \frac{\mathrm{Fr}}{1-\delta}(\tilde{\psi}_1 - \tilde{\psi}_2). \tag{7.17}$$

For clarity of exposition, in the remainder of the paper we will drop the tilde symbol used for the dimensionless variables. In the two-layer QG model, $\delta = \frac{H_1}{H}$ is the aspect ratio of vertical layer thicknesses, Ro is the Rossby number, Fr is the Froude number, A is the lateral eddy viscosity coefficient, and σ is the Ekman bottom later friction coefficient. The definitions of these dimensionless parameters are:

$$\mathrm{Ro} = \frac{V}{\beta L^2};\ \mathrm{Fr} = \frac{f_0^2 V}{g'\beta H};\ A = \frac{\nu}{\beta L^3};\ \sigma = \frac{\gamma}{\beta L}. \tag{7.18}$$

The following three length scales are useful for setting the problem parameters: (i) the

Munk scale, $\delta_M = \left(\frac{\nu}{\beta}\right)^{1/3}$, for the viscous boundary layer; this is related to the smaller scale dissipation; (ii) the Stommel scale, $\delta_S = \frac{\gamma}{\beta}$, for the bottom boundary layer thickness; this is accounting for larger scale damping; and (iii) the Rhines scale, $\delta_I = \left(\frac{V}{\beta}\right)^{1/2}$, for the inertial boundary layer; this is measuring the strength of the nonlinearity.

In order to complete the mathematical model, boundary and initial conditions should be prescribed. In many theoretical studies of ocean circulation, the modelers either use free-slip boundary conditions or no-slip boundary conditions. Following Cummins (1992); Özgökmen and Chassignet (1998), we use free-slip boundary conditions for the velocity for both isopycnal layers, which translates into homogenous Dirichlet boundary conditions for the vorticity (Laplacian of stream function): $\nabla^2\psi|_\Omega = 0$. The impermeability boundary condition is imposed as $\psi|_\Omega = 0$. We start from a rest state ($\psi = 0$), integrate the model until a statistically steady state is obtained, and continue for several decades to compute time-averaged results.

7.3 Approximate deconvolution method

The goal in AD is to use repeated filtering in order to obtain approximations of the unfiltered unresolved flow variables when approximations of the filtered resolved flow variables are available. These approximations of the unfiltered flow variables are then used in the subfilter-scale terms to close the LES system. To derive the new AD model, we start by denoting by G the spatial filtering operator: $Gu = \bar{u}$, $G\bar{u} = \bar{\bar{u}}$ and so on, where u represents any flow variable (i.e., potential vorticity and stream function in this study). Since $G = I - (I - G)$, an inverse to G can be written formally as the non-convergent Neumann series:

$$G^{-1} \sim \sum_{i=0}^{\infty} (I - G)^i. \tag{7.19}$$

Truncating the series gives the van Cittert approximate deconvolution operator, Q_N. We truncate the series at N and obtain Q_N as an approximation of G^{-1}:

$$Q_N = \sum_{i=1}^{N} (I - G)^{i-1}, \tag{7.20}$$

where I is the identity operator. The approximations Q_N are not convergent as N goes to infinity, but rather are asymptotic as the filter radius, Δ, approaches zero (Berselli et al., 2006). An approximate deconvolution of any variable u can now be obtained as follows:

$$u^* = Q_N u. \tag{7.21}$$

For higher values of N, we get increasingly more accurate approximations of u:

$$Q_1 = I \tag{7.22}$$

$$Q_2 = 2I - G \tag{7.23}$$

$$Q_3 = 3I - 3G + G^2 \tag{7.24}$$

$$Q_4 = 4I - 6G + 4G^2 - G^3 \tag{7.25}$$

$$Q_5 = 5I - 10G + 10G^2 - 5G^3 + G^4 \tag{7.26}$$

$$\vdots$$

Following the same approach as that used in Dunca and Epshteyn (2006), one can prove that these models are highly accurate ($O(\Delta^{2N+2})$ modeling consistency error) and stable. For example, if we choose $N = 5$, we can find an AD approximation of the resolved variable q as

$$q^* = 5q - 10\bar{q} + 10\bar{\bar{q}} - 5\bar{\bar{\bar{q}}} + \bar{\bar{\bar{\bar{q}}}} \tag{7.27}$$

and, similarly, an AD approximation of the variable ψ as

$$\psi^* = 5\psi - 10\bar{\psi} + 10\bar{\bar{\psi}} - 5\bar{\bar{\bar{\psi}}} + \bar{\bar{\bar{\bar{\psi}}}}, \tag{7.28}$$

where q and ψ are the resolved potential vorticity and stream function variables. We use a bar to denote the application of one filtering operation. Using Eq. (7.27) and Eq. (7.28), we can now approximate the subfilter-scale contribution by applying a filter to the governing equation. This results in the following model:

$$\frac{\partial q_1}{\partial t} + J(\psi_1, q_1) = A\nabla^4\psi_1 + \sin(2\pi y) + S_1^*, \tag{7.29}$$

$$\frac{\partial q_2}{\partial t} + J(\psi_2, q_2) = A\nabla^4\psi_2 - \sigma\nabla^2\psi_2 + S_2^*, \tag{7.30}$$

where S_i^* is the subfilter-scale term for the i^{th} layer, given by

$$S_i^* = -\overline{J(\psi_i^*, q_i^*)} + J(\psi_i, q_i), \tag{7.31}$$

where asterisk represents the approximated value for the unfiltered (unresolved) quantities. To completely specify the new AD model given by Eqs.(7.30)-(7.31), we need to choose a computationally efficient filtering operator. In Section 7.5, we will show that the selection of the filtering operator affects the dissipative behavior of the system.

7.3.1 Tridiagonal filter

Following Stolz and Adams (1999), we use the following second-order *tridiagonal filter (TF)*:

$$\alpha\bar{f}_{i-1} + \bar{f}_i + \alpha\bar{f}_{i+1} = \left(\frac{1}{2} + \alpha\right)\left(f_i + \frac{f_{i-1} + f_{i+1}}{2}\right), \tag{7.32}$$

where $\bar{f}_i$ represents the filtered value of a discrete quantity f_i. The transfer function of the TF given in Eq. (7.32) can be written as

$$T(\omega) = \left(\frac{1}{2} + \alpha\right)\frac{1 + \cos(\omega)}{1 + 2\alpha\cos(\omega)}. \tag{7.33}$$

The free parameter, α, which is in the range $0 \leq |\alpha| \leq 0.5$, determines the filtering properties, with high values of α yielding less dissipative results. If the transfer function of the filter used in the AD closure is positive definite, then the existence and uniqueness of strong solutions of the AD model can be proved (Stanculescu, 2008). The transfer function corresponding to the TF becomes positive definite in the interval of $0 \leq |\alpha| \leq 0.5$. More details can be found in San et al. (2011).

7.3.2 Elliptic differential filter

The second filter used in our numerical investigation is the elliptic *differential filter (DF)* (Germano, 1986a; Sagaut, 2006; Berselli et al., 2006):

$$\bar{f} - \lambda^2 \left(\frac{\partial^2 \bar{f}}{\partial x^2} + \frac{\partial^2 \bar{f}}{\partial y^2} \right) = f \qquad \text{in } \Omega, \tag{7.34}$$

$$\bar{f} = f \qquad \text{on } \partial\Omega, \tag{7.35}$$

where Ω is the computational domain and λ is the Helmholtz length, which determines the effective width of the filter. The filtered value $\bar{f}$ is obtained by applying the inverse Helmholtz operator to the unfiltered flow variable f. This inversion is done efficiently by using the fast Fourier transform (FFT) techniques (Press et al., 1992). The DF given by Eqs. (7.34)-(7.35) was introduced in LES by Germano (1986a). Since then, it has been successfully used in LES of three-dimensional engineering flows (Iliescu and Fischer, 2003) and small scale oceanic flows (Özgökmen et al., 2009). It has also been analyzed mathematically (Dunca and Epshteyn, 2006; Layton and Lewandowski, 2006; Layton and Neda, 2007; Rebholz, 2007; Stanculescu, 2008; Berselli and Lewandowski, 2012). In this study, the DF is used in the LES of large scale oceanic flows.

7.4 Numerical Methods

In many physically relevant situations, where the Munk and Rhines scales being close to each other, the solutions to oceanic models, such as the QG2 models, do not converge to a steady state as time goes to infinity (Medjo, 2000). Rather they remain time dependent by producing statistically steady state with one or multiple equilibria. Therefore, numerical schemes designed for numerical integration of such phenomena should be suited for such behavior of the solutions and for the long-time integration. In this study, the governing equations are solved by a fully conservative finite difference scheme along with a third-order Runge-Kutta adaptive time stepping algorithm. An efficient, linear-cost, fast sine transform method is utilized for solving the linear coupled inversion subproblem.

7.4.1 Arakawa scheme for the Jacobian

Arakawa (1966) suggested that the conservation of energy, enstrophy, and skew-symmetry is sufficient to avoid computational instabilities stemming from nonlinear interactions. The second-order Arakawa scheme for the Jacobian (i.e., the nonlinear term in the governing equations) is

$$J(\psi,q)=\frac{1}{3}\big(J_1(\psi,q)+J_2(\psi,q)+J_3(\psi,q)\big), \tag{7.36}$$

where the discrete Jacobians have the following forms:

$$\begin{aligned} J_1(\psi,q)=\frac{1}{4\,\Delta_x\,\Delta_y}\big[&-(q_{i+1,j}-q_{i-1,j})(\psi_{i,j+1}-\psi_{i,j-1})\\ &+(q_{i,j+1}-q_{i,j-1})(\psi_{i+1,j}-\psi_{i-1,j})\big], \end{aligned} \tag{7.37}$$

$$\begin{aligned} J_2(\psi,q)=\frac{1}{4\,\Delta_x\,\Delta_y}\big[&-q_{i+1,j}(\psi_{i+1,j+1}-\psi_{i+1,j-1})+q_{i-1,j}(\psi_{i-1,j+1}-\psi_{i-1,j-1})\\ &+q_{i,j+1}(\psi_{i+1,j+1}-\psi_{i-1,j+1})-q_{i,j-1}(\psi_{i+1,j-1}-\psi_{i-1,j-1})\big], \end{aligned} \tag{7.38}$$

$$\begin{aligned} J_3(\psi,q)=\frac{1}{4\,\Delta_x\,\Delta_y}\big[&-q_{i+1,j+1}(\psi_{i,j+1}-\psi_{i+1,j})+q_{i-1,j-1}(\psi_{i-1,j}-\psi_{i,j-1})\\ &+q_{i-1,j+1}(\psi_{i,j+1}-\psi_{i-1,j})-q_{i+1,j-1}(\psi_{i+1,j}-\psi_{i,j-1})\big]. \end{aligned} \tag{7.39}$$

Note that J_1, which corresponds to the central second-order difference scheme, is not sufficient for the conservation of energy, enstrophy, and skew-symmetry by the numerical discretization. Arakawa (1966) showed that the judicious combination of J_1, J_2, and J_3 in Eq. (7.36) achieves the above discrete conservation properties.

7.4.2 Time integration scheme

For the time discretization, we employ an optimal third-order total variation diminishing Runge-Kutta (TVDRK3) scheme (Gottlieb and Shu, 1998). For clarity of notation, we rewrite the governing equations in the following form:

$$\frac{dq_i}{dt} = R_i, \tag{7.40}$$

where subscript i represents the layer index and R_i denotes the discrete spatial derivative operator, including the nonlinear Jacobian of the convective term, the linear biharmonic diffusive term, the forcing term, and the subfilter-scale term. For each layer, the TVDRK3 scheme then becomes:

$$\begin{aligned} q_i^{(1)} &= q^n + \Delta t R_i^{(n)}, \\ q_i^{(2)} &= \frac{3}{4} q_i^n + \frac{1}{4} q_i^{(1)} + \frac{1}{4} \Delta t R_i^{(1)}, \\ q_i^{n+1} &= \frac{1}{3} q_i^n + \frac{2}{3} q_i^{(2)} + \frac{2}{3} \Delta t R_i^{(2)}, \end{aligned} \tag{7.41}$$

where Δt is the adaptive time step size, which can be computed at the end of each time step by:

$$\Delta t = c \, \frac{\min(\Delta_x, \Delta_y)}{\max\left\{ |\frac{\partial \psi_i}{\partial x}|, |\frac{\partial \psi_i}{\partial y}| \right\}}, \tag{7.42}$$

where c is known as the Courant-Friedrichs-Lewy (CFL) number. To ensure the numerical stability of the time discretization scheme, we require that $c \leq 1$.

7.4.3 Inversion subproblem

Most of the demand on computing resources posed by QG models comes in the solution of the elliptic inversion subproblem (Miller, 2007). This is also true for our study. However, we take advantage of the simple square shape of our domain and utilize one of the fastest available techniques (Moin, 2001), which is the FFT based direct inversion to solve the subproblem:

$$Q_1 = \mathrm{Ro}\nabla^2\psi_1 + \frac{\mathrm{Fr}}{\delta}(\psi_2 - \psi_1), \tag{7.43}$$

$$Q_2 = \mathrm{Ro}\nabla^2\psi_2 + \frac{\mathrm{Fr}}{1-\delta}(\psi_1 - \psi_2), \tag{7.44}$$

where $Q_1 = q_1 - y$ and $Q_2 = q_2 - y$. The impermeability boundary condition imposed as $\psi|_\Omega = 0$ suggests the use of a fast sine transform (an inverse transform) for each layer:

$$\hat{Q}_{1_{k,l}} = \frac{2}{N_x}\frac{2}{N_y}\sum_{i=1}^{N_x-1}\sum_{j=1}^{N_y-1} Q_{1_{i,j}} \sin\left(\frac{\pi k i}{N_x}\right)\sin\left(\frac{\pi l j}{N_y}\right), \tag{7.45}$$

$$\hat{Q}_{2_{k,l}} = \frac{2}{N_x}\frac{2}{N_y}\sum_{i=1}^{N_x-1}\sum_{j=1}^{N_y-1} Q_{2_{i,j}} \sin\left(\frac{\pi k i}{N_x}\right)\sin\left(\frac{\pi l j}{N_y}\right), \tag{7.46}$$

where N_x and N_y are the total number of grid points in x and y directions. Here the symbol hat is used to represent the corresponding Fourier coefficient of the physical grid data with a subscript pair i, j, where $i = 0, 1, ...N_x$ and $j = 0, 1, ...N_y$. As a second step, we directly solve the subproblem in Fourier space:

$$\hat{\psi}_{1_{k,l}} = \frac{\alpha_{k,l}\hat{Q}_{1_{k,l}} - \frac{\mathrm{Fr}}{1-\delta}\hat{Q}_{1_{k,l}} - \frac{\mathrm{Fr}}{\delta}\hat{Q}_{2_{k,l}}}{\alpha_{k,l}\left(\alpha_{k,l} - \frac{\mathrm{Fr}}{\delta} - \frac{\mathrm{Fr}}{1-\delta}\right)}, \tag{7.47}$$

$$\hat{\psi}_{2_{k,l}} = \frac{\alpha_{k,l}\hat{Q}_{2_{k,l}} - \frac{\mathrm{Fr}}{1-\delta}\hat{Q}_{1_{k,l}} - \frac{\mathrm{Fr}}{\delta}\hat{Q}_{2_{k,l}}}{\alpha_{k,l}\left(\alpha_{k,l} - \frac{\mathrm{Fr}}{\delta} - \frac{\mathrm{Fr}}{1-\delta}\right)}, \tag{7.48}$$

where

$$\alpha_{k,l} = \frac{\mathrm{Ro}}{\Delta_x^2}\left[2\cos\left(\frac{\pi k}{N_x}\right) - 2\right] + \frac{\mathrm{Ro}}{\Delta_y^2}\left[2\cos\left(\frac{\pi l}{N_y}\right) - 2\right]. \tag{7.49}$$

Finally, the stream function arrays for each layer are found by performing a forward sine transform:

$$\psi_{1_{i,j}} = \sum_{k=1}^{N_x-1}\sum_{l=1}^{N_y-1} \hat{\psi}_{1_{k,l}} \sin\left(\frac{\pi k i}{N_x}\right)\sin\left(\frac{\pi l j}{N_y}\right), \tag{7.50}$$

$$\psi_{2_{i,j}} = \sum_{k=1}^{N_x-1}\sum_{l=1}^{N_y-1} \hat{\psi}_{2_{k,l}} \sin\left(\frac{\pi k i}{N_x}\right)\sin\left(\frac{\pi l j}{N_y}\right), \tag{7.51}$$

The computational cost of this elliptic solver is $\mathcal{O}\left(N_x\, N_y\, \log(N_x)\, \log(N_y)\right)$. The FFT algorithm given by Press et al. (1992) is used for forward and inverse sine transforms.

7.5 Results

The main goal of this section is to test the new AD model, Eqs. (7.30)-(7.31), in the numerical simulation of the two-layer QG model. We also investigate the sensitivity of the AD model with respect to the model parameters. It turns out that the most important modeling choice is the spatial filter employed in the AD procedure. We consider two spatial filters in conjunction with the AD model: the tridiagonal filter (Section 7.3.1) and the differential filter (Section 7.3.2). We denote the resulting models AD-TF and AD-DF, respectively. To test the AD-TF and AD-DF models, we utilize two different parameter sets, corresponding to two physical oceanic settings: (i) Experiment 1 represents a large ocean basin with the physical parameters used by Tanaka and Akitomo (2010), (ii) Experiment 2 represents a moderate ocean basin with the physical parameters used by Özgökmen and Chassignet (1998). In terms of the classification given by Berloff and McWilliams (1999), both sets of experiments lie under the chaotic regime. The physical parameters and corresponding dimensionless parameters are summarized in Table 7.2. All computations were carried out using a gfortran compiler on a Linux cluster system. The rest of the section is organized as follows. In

Section 7.5.1, we present results from the *direct numerical simulation (DNS)* for the two settings, Experiment 1 and Experiment 2. Section 7.5.2 presents results with the AD-TF model. Finally, Section 7.5.3 presents results with the AD-DF model.

7.5.1 Direct numerical simulation

We start by performing a DNS on a fine mesh of 512^2 spatial resolution. We emphasize that the term DNS in this study is not meant to indicate that a fully detailed solution is being computed on the molecular viscosity scale, but instead refers to resolving the simulation down to the Munk scale via the specified lateral eddy viscosity parameterization. A statistically steady state solution is obtained after an initial transient spin-up process. Instantaneous contour plots for the potential vorticities in the upper and lower layers are shown in Figure 7.1 and Figure 7.2 for Experiment 1 and Experiment 2, respectively. The length scales in these two experiments are quite different. For example, the ratio of the basin length scale L to the Rossby deformation radius R_d is $L/R_d = 160.5$ for Experiment 1 and $L/R_d = 46.74$ for Experiment 2. Therefore, the structure of the eastward jet formation on the western boundary for Experiment 1 is different from that of Experiment 2. This difference becomes more obvious in the mean flow field. The results for time-averaged mean field data obtained from 2000 snapshots in the statistically steady state are given in Figure 7.3 and Figure 7.4. The results show strong western boundary currents with cyclonic (counter-clockwise rotating) subpolar gyres and anticyclonic (clockwise rotating) subtropical gyres producing a strong eastward jet in both experiments. However, the produced eastward jet formation in Experiment 2 shows swirling structure and almost reaches the eastern boundary of the basin. Compared to Experiment 1, the bottom layer is more active in Experiment 2. Since in Experiment 2 we used the same parameters and boundary conditions as in Özgökmen and Chassignet (1998), the plot in Figure 7.4 is similar to Figure 2 in Özgökmen and Chassignet (1998). Although in Experiment 1 we have used the same parameters as those used in Tanaka and Akitomo (2010), the boundary conditions we used are different

Table 7.2: Physical parameter sets used in the numerical experiments.

Variable (unit)	Experiment 1	Experiment 2
L (km)	5000	2000
H_1 (km)	0.6	1.0
H_2 (km)	3.4	4.0
f_0 (s^{-1})	9.35×10^{-5}	9.35×10^{-5}
β $(m^{-1}s^{-1})$	1.75×10^{-11}	1.75×10^{-11}
ρ_1 (kgm^{-3})	1030	1030
g' (ms^{-2})	0.02	0.02
τ_0 (Nm^{-2})	0.1	0.1
γ (s^{-1})	4×10^{-7}	5×10^{-8}
ν (m^2s^{-1})	100	50
δ_M (km)	17.88	14.19
δ_S (km)	22.86	2.86
δ_I (km)	25.77	31.56
R_d (km)	31.16	42.79
V (ms^{-1})	0.0116	0.0174
L/V $(year)$	13.64	3.64
L/R_d	160.5	46.74
Ro	2.66×10^{-5}	2.49×10^{-4}
Fr	0.073	0.087
σ	4.57×10^{-3}	1.43×10^{-3}
A	4.57×10^{-8}	3.57×10^{-7}
δ	0.15	0.2
Re	580.97	697.16

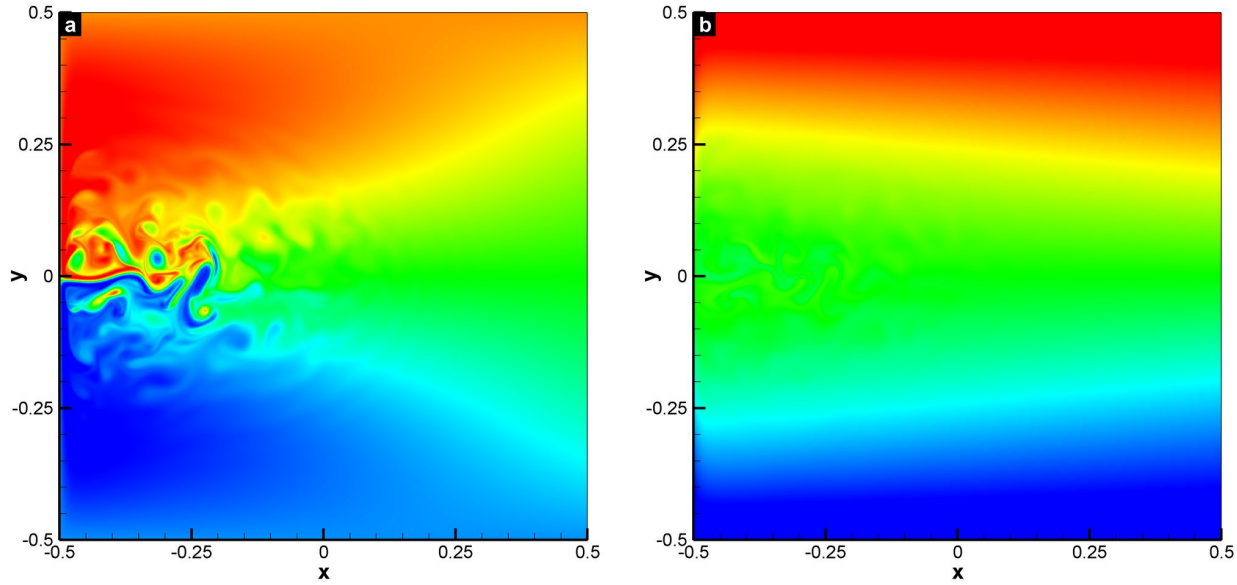

Figure 7.1: Experiment 1: DNS results for (a) instantaneous potential vorticity for the upper layer, and (b) instantaneous potential vorticity for the lower layer.

from their boundary conditions: we used the slip boundary conditions, whereas they used the no-slip boundary conditions. Thus, the plot in Figure 7.3 is different from the corresponding one in Tanaka and Akitomo (2010).

To quantify the effect of the numerical discretization on the numerical results, we vary the grid resolution ($N_x \times N_y$), the time step (Δt), and the eddy viscosity coefficient (ν) in the QG2 model. The following quantities are monitored. The first quantity is the time-averaged L_2 norm of the error of the potential vorticity, denoted as $\|q_i\|$, where the subscript i represents the layer index. The reference solution used in the computation of the error is the numerical approximation obtained at a grid resolution of 512^2. The second quantity is the time-averaged basin-integrated kinetic energy, E_i, which is defined as

$$E_i = \frac{1}{T_2 - T_1} \int_{t=T_1}^{t=T_2} E_i(t)\, dt, \tag{7.52}$$

where, again, the subscript i represents the layer index and $T_1 = 6$ and $T_2 = 8$ are the temporal bounds for the averaging window. The integrand $E_i(t)$ in Eq. (7.52) is the instantaneous

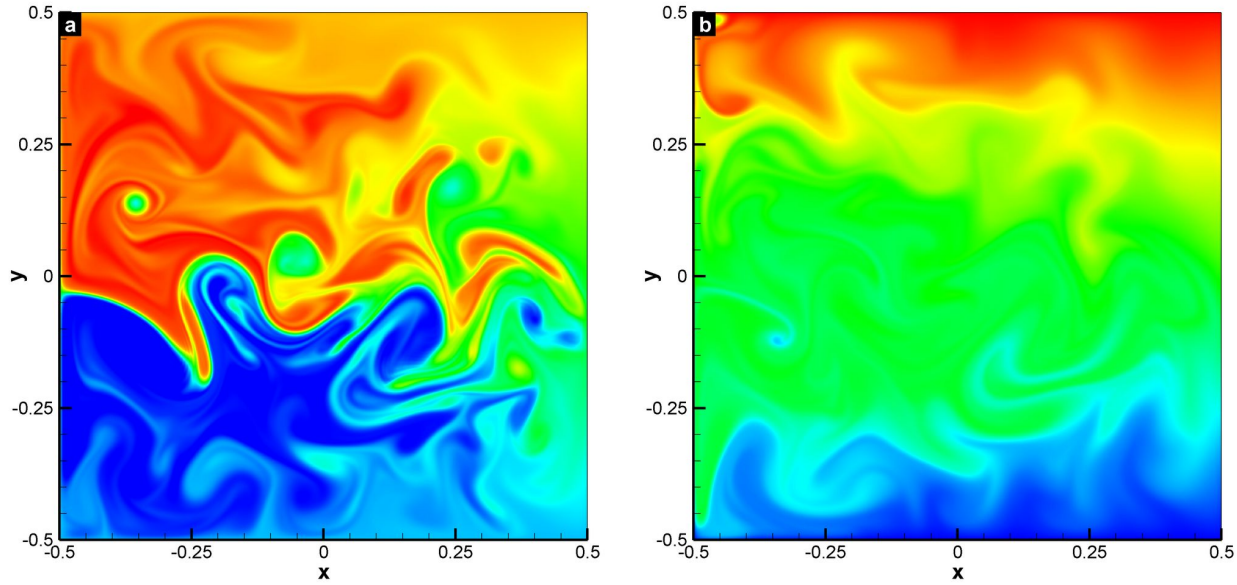

Figure 7.2: Experiment 2: DNS results for (a) instantaneous potential vorticity for the upper layer, and (b) instantaneous potential vorticity for the lower layer.

basin integrated kinetic energy in each layer and is defined as

$$E_i(t) = \frac{1}{2} \iint \left(\frac{\partial \psi_i}{\partial x} \right)^2 + \left(\frac{\partial \psi_i}{\partial y} \right)^2 dx\, dy, \tag{7.53}$$

First, we investigate the effect of the grid resolution on the numerical results. To this end, we fix the time step $\Delta t = 2 \times 10^{-5}$ and vary the grid resolution, $N_x \times N_y$, and the eddy viscosity coefficient in the QG2 model, ν. Table 7.3 presents the time-averaged basin-integrated kinetic energy of the upper layer, E_1, defined in Eq. (7.52). This table shows that, for most grid resolutions, accurate results are obtained for the high values of the eddy viscosity coefficient, ν. For the lowest values of ν, however, the results are inaccurate at the lower grid resolutions, and relatively accurate at the higher grid resolutions. This behavior is natural, since lower values of ν correspond to a more chaotic behavior of the system. Table 7.4 presents the time-averaged L_2 norm of the error of the potential vorticity in the two layers, $\|q_1\|$ and $\|q_2\|$. This table shows that, as expected, the error decreases as the grid resolution increases. We note that this decrease in the error is faster for the high values of ν. This behavior is

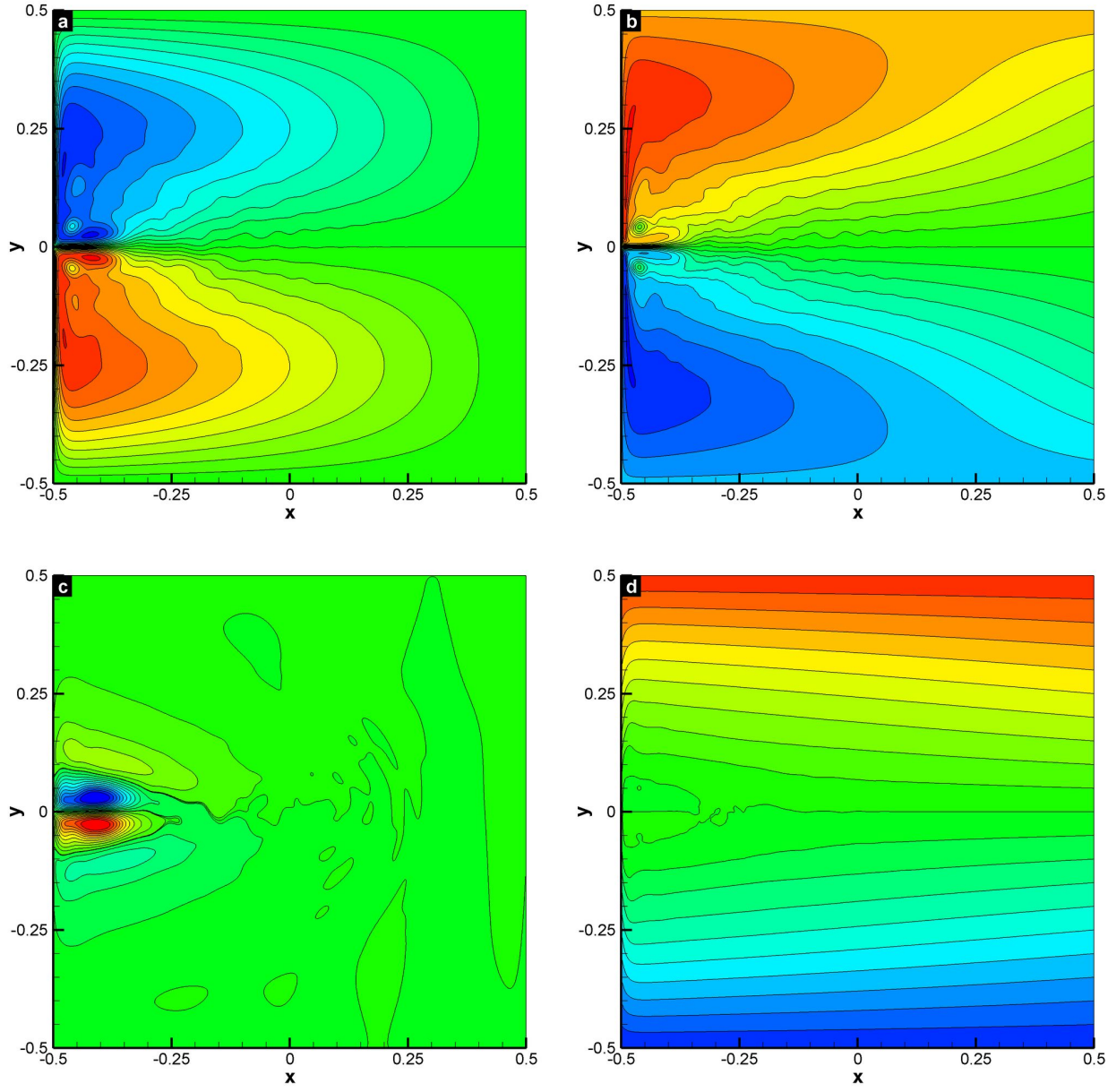

Figure 7.3: Experiment 1: DNS results for (a) mean stream function contours for the upper layer, (b) mean potential vorticity contours for the upper layer, (c) mean stream function contours for the lower layer, and (d) mean potential vorticity contours for the lower layer.

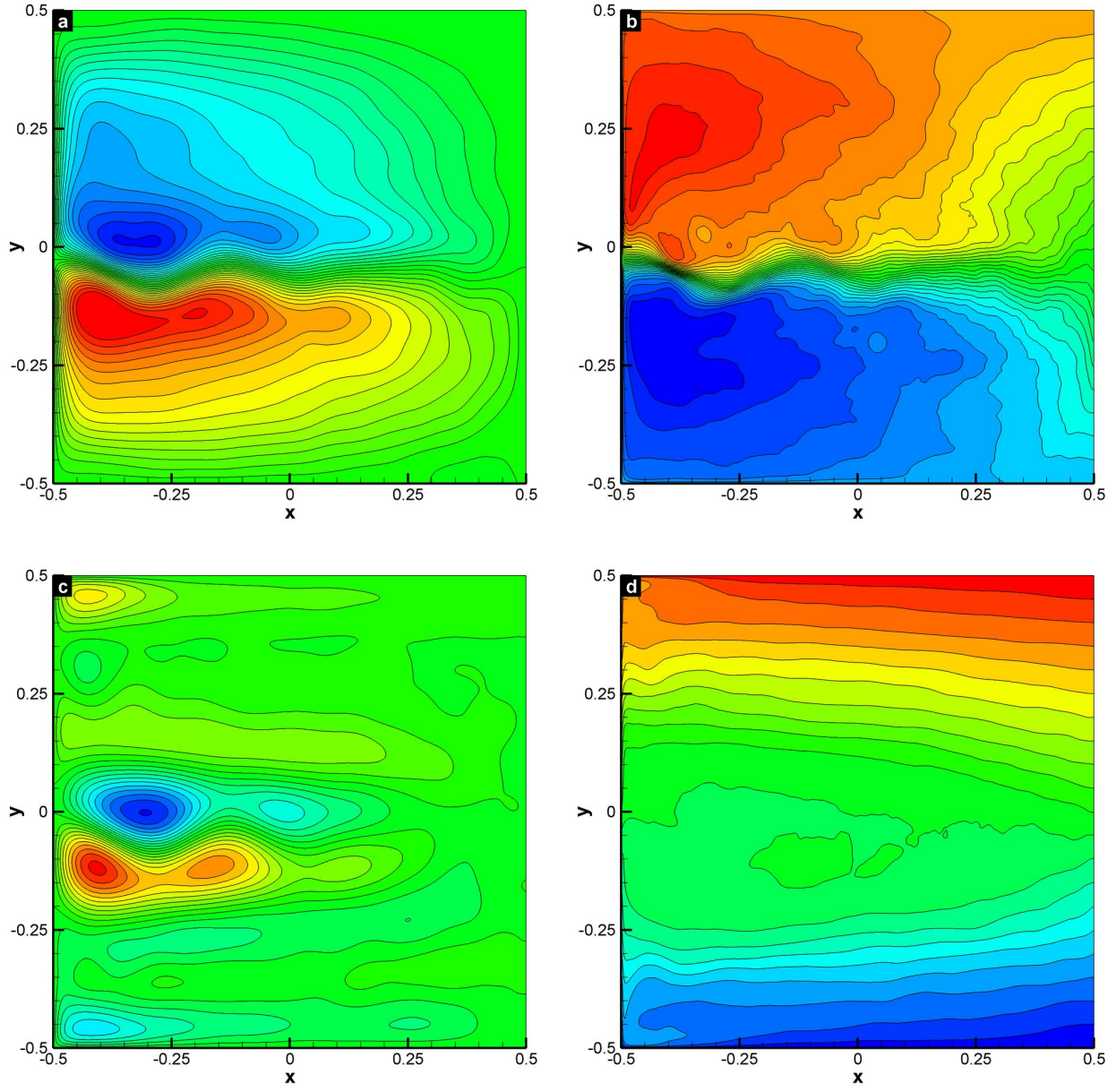

Figure 7.4: Experiment 2: DNS results for (a) mean stream function contours for the upper layer, (b) mean potential vorticity contours for the upper layer, (c) mean stream function contours for the lower layer, and (d) mean potential vorticity contours for the lower layer.

similar to that observed in Table 7.3. Finally, the results in Table 7.4 and are also plotted in Figure 7.5. This figure clearly shows that a second-order spatial accuracy is obtained for the high values of ν, and a first-order spatial accuracy is obtained for the lowest values of ν. Again, the suboptimal spatial accuracy for the smallest values of ν is attributed to the increased chaotic behavior of the system.

Next, we investigate the effect of the time step on the numerical results. To this end, we fix the the eddy viscosity coefficient, $\nu = 100$, and vary the grid resolution, $N_x \times N_y$, and the time step, Δt. Table 7.5 presents the time-averaged basin-integrated kinetic energy of the two layers, E_1 and E_2. This table shows that, for a fixed spatial resolution, varying the time step does not yield a significant change in the numerical results. To investigate the effects of the adaptive time discretization described in Section 7.4.2, we performed the same numerical experiments as those in Table 7.5, this time, however, using the adaptive time-stepping scheme with a fixed CFL number $c = 0.95$. This approach yielded the same qualitative results as those in Table 7.5.

The above numerical studies quantify the effects of the numerical discretization described in Section 7.4. The following general conclusions can be drawn. The spatial discretization is optimal (second-order) for high values of the eddy viscosity coefficient, and is suboptimal (first-order) for the low values that we use in this study. The time discretization error appears to be dominated by the spatial discretization error. Indeed, for a fixed grid resolution, changing the time step had only negligible effects on the numerical results. Although it is hard to decouple the numerical effects from the LES modeling effects, the above numerical studies will serve as a guide in the subsequent interpretation of the LES results. Furthermore, a more detailed presentation of error estimates for the spatial and temporal schemes utilized here can be found in a recent study on two-dimensional decaying turbulence conducted by San and Staples (2012).

Table 7.3: Experiment 1: Time-averaged basin-integrated kinetic energy of the upper layer, E_1, for varying grid resolutions, $N_x \times N_y$, and varying eddy viscosity coefficients, ν.

$N_x \times N_y$	$\nu = 100$	$\nu = 200$	$\nu = 400$	$\nu = 800$	$\nu = 1600$	$\nu = 3200$
32^2	195.028	200.188	151.178	89.139	57.016	36.500
64^2	103.787	77.749	59.083	43.305	33.567	27.878
128^2	77.617	63.618	51.364	42.545	34.003	27.661
256^2	79.478	65.560	52.646	42.208	34.764	27.851
512^2	81.609	66.084	52.787	42.051	35.096	27.921

Table 7.4: Experiment 1: Time-averaged L_2 norm of the error of the potential vorticity in the two layers, $\|q_1\|$ and $\|q_2\|$, for varying grid resolutions, $N_x \times N_y$, and varying eddy viscosity coefficients ν. The reference solution used in the computation of the error is the numerical approximation obtained at a grid resolution of 512^2.

$N_x \times N_y$	$\nu = 100$		$\nu = 400$		$\nu = 3200$	
	$\| q_1 \|$	$\| q_2 \|$	$\| q_1 \|$	$\| q_2 \|$	$\| q_1 \|$	$\| q_2 \|$
32^2	1.2446E-1	1.8075E-2	1.4552E-1	2.0959E-2	4.7177E-2	7.2268E-3
64^2	6.5465E-2	7.7261E-3	4.3220E-2	5.2517E-3	1.6356E-2	2.5420E-3
128^2	2.9121E-2	3.3675E-3	1.3513E-2	1.7138E-3	4.7441E-3	7.4199E-4
256^2	1.2296E-2	1.5355E-3	4.5496E-3	5.4868E-4	1.0002E-3	1.5671E-4

Table 7.5: Experiment 1: Time-averaged basin-integrated kinetic energy of the two layers, E_1 and E_2, for varying grid resolutions, $N_x \times N_y$, and fixed eddy viscosity coefficient, $\nu = 100$.

$N_x \times N_y$	$\Delta t = 1 \times 10^{-5}$		$\Delta t = 2 \times 10^{-5}$		$\Delta t = 4 \times 10^{-5}$	
	E_1	E_2	E_1	E_2	E_1	E_2
32^2	198.862	1.124	195.028	1.086	196.293	1.095
64^2	104.332	0.874	103.787	0.876	104.143	0.875
128^2	78.210	1.195	77.617	1.961	77.768	1.952
256^2	79.194	2.532	79.478	2.523	79.416	2.538
512^2	81.277	2.592	81.609	2.594	80.996	2.601

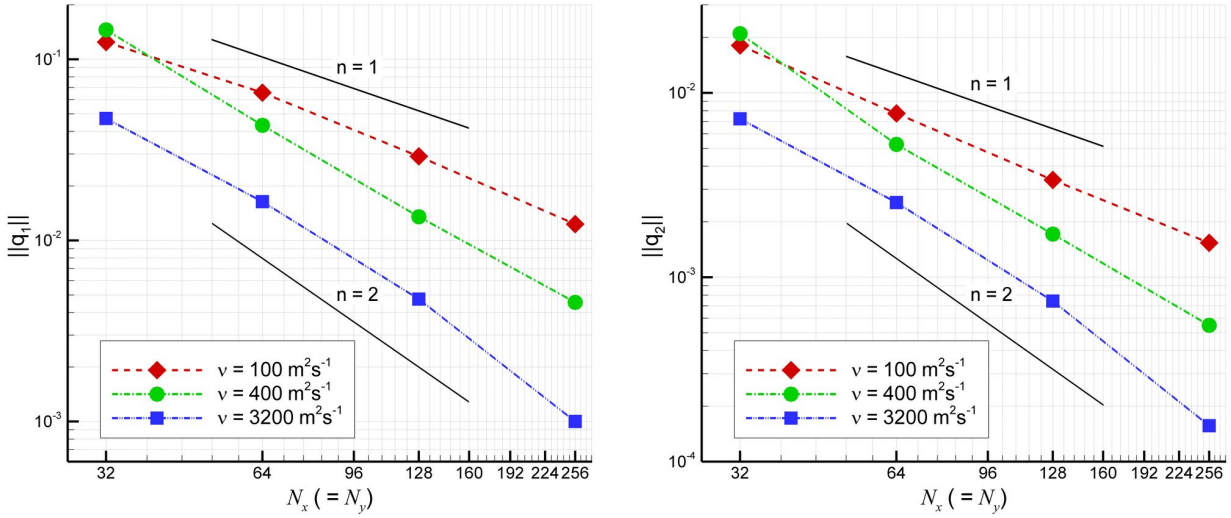

(a) (b)

Figure 7.5: Experiment 1: Log-log plot of the time-averaged L_2 norm of the error of the potential vorticity in the two layers, $\|q_1\|$ and $\|q_2\|$, for varying eddy viscosity coefficients ν. The reference solution used in the computation of the error is the numerical approximation obtained at a grid resolution of 512^2.

7.5.2 Approximate deconvolution model with the tridiagonal filter (AD-TF)

To test the new AD-TF model given by Eqs. (7.30)-(7.31), we employ the standard LES methodology: We first run a DNS on a fine mesh (of 512^2 spatial resolution). We then run on a much coarser mesh (of 32^2 spatial resolution) an under-resolved numerical simulation (denoted in what follows as QG2$_c$). We emphasize that QG2$_c$ does not employ any subfilter-scale model. Finally, we employ the new AD-TF model on the same coarse mesh utilized in QG2$_c$ (of 32^2 spatial resolution). The criterion used in assessing the success of the new AD-TF model is its ability to produce more accurate (i.e., closer to the DNS data) results than those for QG2$_c$, without a significant increase in computational time. Following San et al. (2011), in the AD-TF model, we use the tridiagonal filtering procedure with $N = 5$ and $\alpha = 0.25$. To compare the DNS, the QG2$_c$, and the AD-TF model, we utilize data that

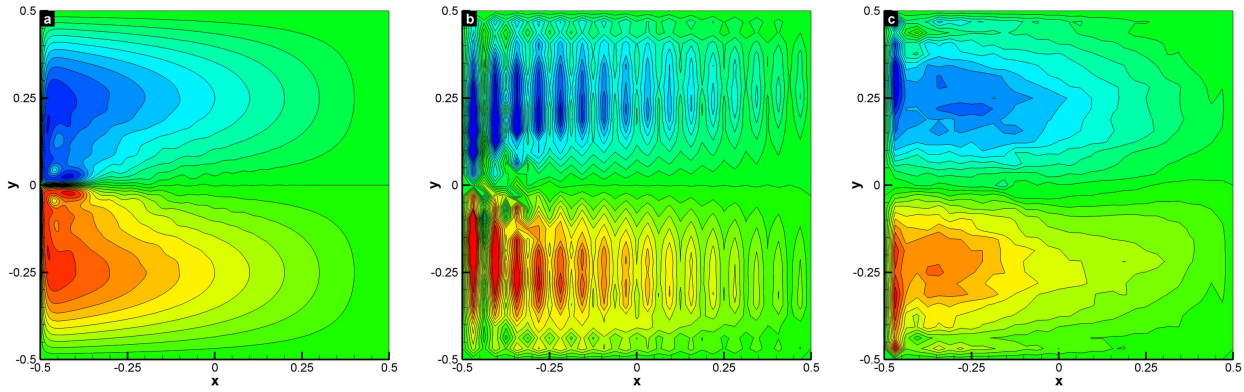

Figure 7.6: Experiment 1: Time-averaged stream function contours for the upper layer: (a) DNS results at a resolution of 512^2; (b) QG2$_c$ (under-resolved numerical simulation without any subfilter-scale model) results at a resolution of 32^2; and (c) AD-TF results at a resolution of 32^2. The contour layouts are identical. Note that the AD-TF results are significantly better than the QG2$_c$ results.

is time-averaged between $t = 6$ and $t = 8$ by using 2000 snapshots of the field. Note that that this averaging period corresponds to 27.28 years for Experiment 1.

For Experiment 1, we plot the mean stream function and potential vorticity contours in Figures 7.6 and 7.7, respectively. The new AD-TF model yields results that are significantly better than those corresponding to the under-resolved QG2$_c$ run. Similarly, we plot the mean stream function and potential vorticity contours in Figures 7.8 and 7.9 for Experiment 2. We note that the proposed AD-TF model yields again improved results by smoothing out the numerical oscillations present in the under-resolved QG2$_c$ simulations. We also note that the computational cost of the new AD-TF model is significantly lower than that of the DNS, and is comparable to the computational cost of the QG2$_c$. Indeed, the CPU time is 119.6 hrs. for the DNS, 141.8 secs. for QG2$_c$, and 174.7 secs. for the AD-TF model. The numerical results for both experiments clearly suggest that the the AD-TF model can provide relatively accurate results for under-resolved geophysical flows at a low computational cost.

Although the AD-TF model performs well given the coarse mesh utilized, a natural question is whether we can increase its accuracy by using a finer mesh. Of course, to preserve

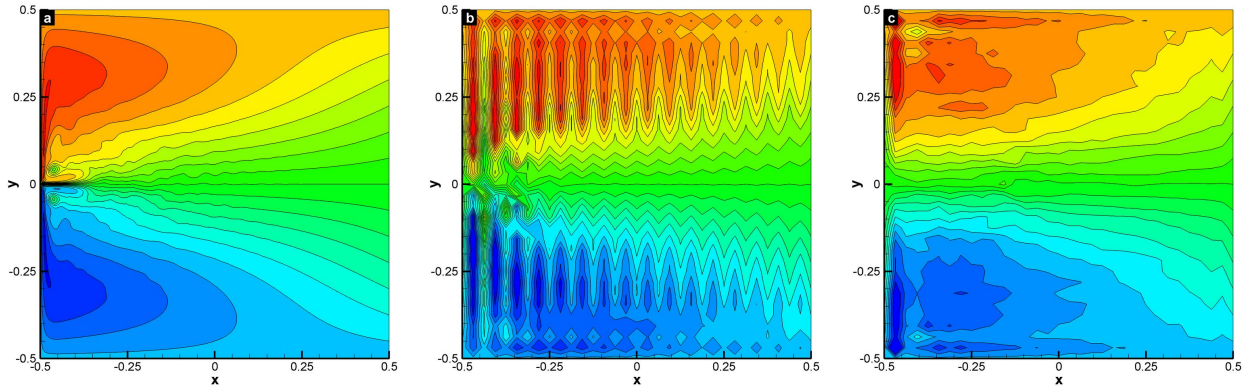

Figure 7.7: Experiment 1: Time-averaged potential vorticity contours for the upper layer: (a) DNS results at a resolution of 512^2; (b) QG2$_c$ (under-resolved numerical simulation without any subfilter-scale model) results at a resolution of 32^2; and (c) AD-TF results at a resolution of 32^2. The contour layouts are identical. Note that the AD-TF results are significantly better than the QG2$_c$ results.

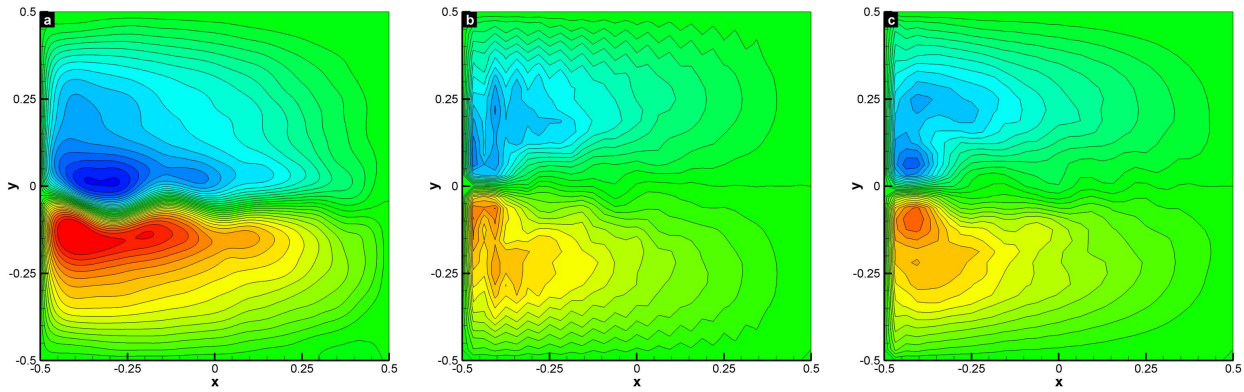

Figure 7.8: Experiment 2: Time-averaged stream function contours for the upper layer: (a) DNS results at a resolution of 512^2; (b) QG2$_c$ (under-resolved numerical simulation without any subfilter-scale model) results at a resolution of 32^2; and (c) AD-TF results at a resolution of 32^2. The contour layouts are identical. Note that the AD-TF results are significantly better than the QG2$_c$ results.

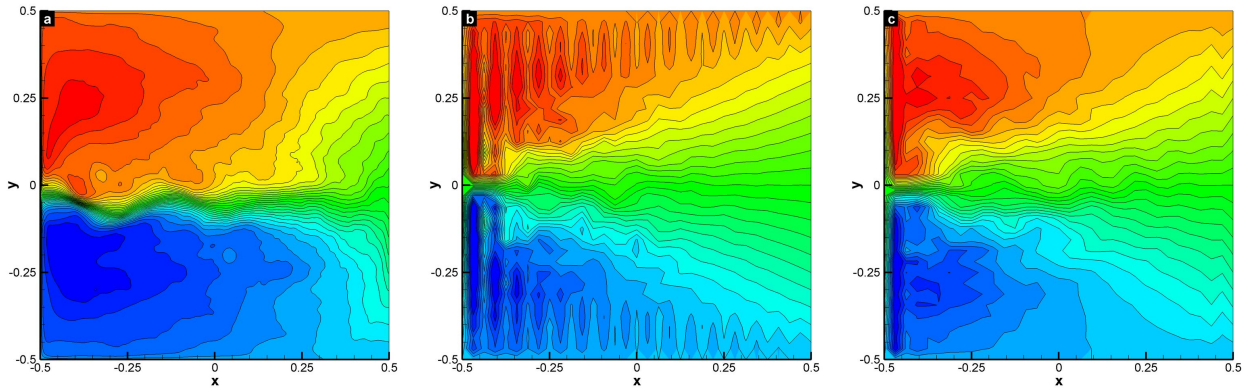

Figure 7.9: Experiment 2: Time-averaged potential vorticity contours for the upper layer: (a) DNS results at a resolution of 512^2; (b) QG2$_c$ (under-resolved numerical simulation without any subfilter-scale model) results at a resolution of 32^2; and (c) AD-TF results at a resolution of 32^2. The contour layouts are identical. Note that the AD-TF results are significantly better than the QG2$_c$ results.

the low computational cost of the AD-TF model, this finer mesh should still be significantly coarser than the DNS mesh. Thus, we investigate the behavior of the AD-TF model for various resolutions: 512^2, 256^2, 128^2, 64^2, and 32^2. Since similar conclusions hold for both experiments, we only discuss the results for Experiment 1. It can be easily computed that Munk scale resolving simulations should be performed at a resolution that is at least 280^2 for Experiment 1. Thus, only the 512^2 resolution corresponds to a resolved numerical simulation - all the other resolutions correspond to under-resolved numerical simulations. The time-averaged stream function and potential vorticity contour plots for the upper layers are shown in Figures 7.10 and (7.11), respectively. In terms of computational efficiency, the CPU time for the DNS results is 296 hrs. The CPU times for the under-resolved simulations are: 48.5 hrs for the 256^2 resolution, 4.1 hrs for the 128^2 resolution, 0.34 hrs for the 64^2 resolution, and 2.9 mins for the 32^2 resolution. The main conclusion that can be drawn from the plots in Figures 7.10 and 7.11 and the computational efficiency study is that, at the 128^2 resolution, the AD-TF model yields very accurate flow fields, while achieving a speed-up factor of 72 with respect to the DNS. A further reduction in resolution results in a loss of accuracy. If, however, the accuracy of a coarser resolution simulation is deemed as acceptable, even more

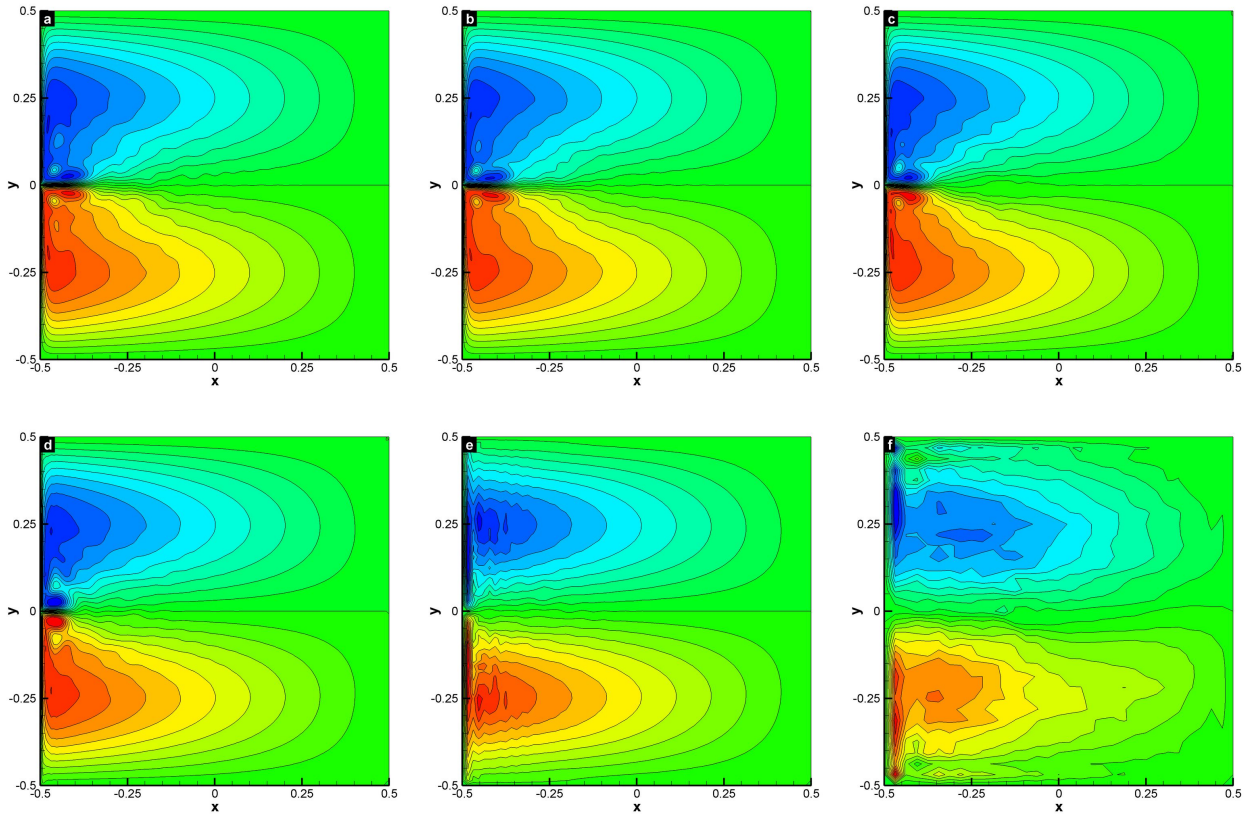

Figure 7.10: Experiment 1: Time-averaged stream function for the upper layer: (a) DNS results at a resolution of 512^2; (b) AD-TF results at a resolution of 512^2; (c) AD-TF results at a resolution of 256^2; (d) AD-TF results at a resolution of 128^2; (e) AD-TF results at a resolution of 64^2; and (f) AD-TF results at a resolution of 32^2. The contour layouts are identical. Note: (i) the accuracy of the AD-TF results at the 128^2 resolution; and (ii) the consistency of the AD-TF results with respect to the mesh size.

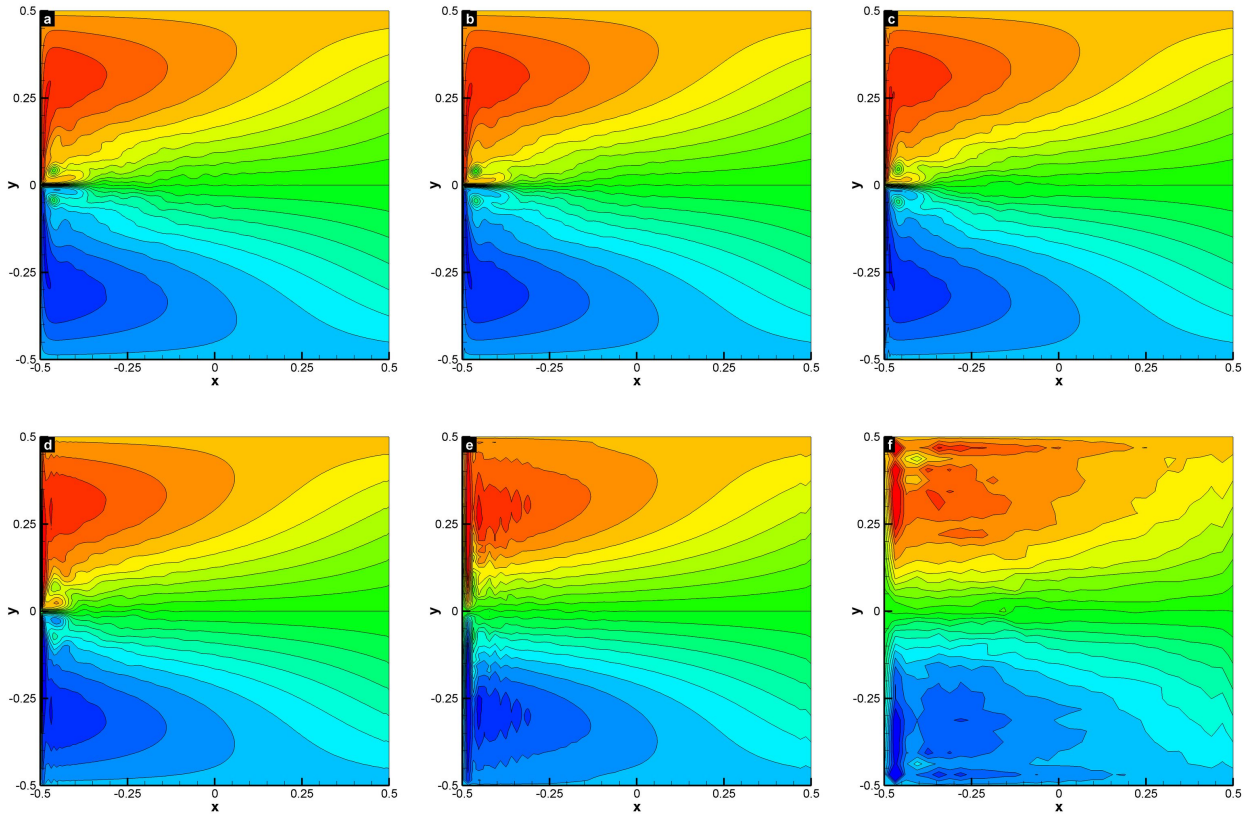

Figure 7.11: Experiment 1: Time-averaged potential vorticity for the upper layer: (a) DNS results at a resolution of 512^2; (b) AD-TF results at a resolution of 512^2; (c) AD-TF results at a resolution of 256^2; (d) AD-TF results at a resolution of 128^2; (e) AD-TF results at a resolution of 64^2; and (f) AD-TF results at a resolution of 32^2. The contour layouts are identical. Note: (i) the accuracy of the AD-TF results at the 128^2 resolution; and (ii) the consistency of the AD-TF results with respect to the mesh size.

dramatic computational savings can be achieved. We emphasize that the AD subfilter-scale model plays an essential role. Indeed, as shown in Figures 7.6 and 7.7, the accuracy of the AD-TF simulation at a resolution of 32^2 is significantly higher than the accuracy of $\mathrm{QG2}_c$ (i.e., the under-resolved numerical simulation without any subfilter-scale model). Thus, the combination of computational efficiency and numerical accuracy displayed by the AD-TF model is the result of using both a coarse mesh and appropriate LES modeling. A second conclusion that can be drawn from the plots in Figures 7.10 and 7.11 is that the AD-TF model is *consistent* with the original set of equations. Indeed, the above mesh refinement study shows that the numerical results obtained with the AD-TF model converge to the DNS results when the mesh size approaches zero.

Finally, we perform a sensitivity study of the free smoothing parameter α and the order N in the AD-TF model. Figure 7.12 shows the time history of the basin integrated kinetic energy for the upper and lower layers for several α values. As shown in this figure, the system reaches the statistically steady state after the dimensionless time $t = 1$. As expected, the total energy of the upper layer is much larger than that in the lower layer. It is important to emphasize that, at the statistically steady state, the AD-TF model has almost the same energy level as the DNS. The time histories plotted in Figure 7.12 also display a relatively small sensitivity to α, the free parameter in the model. Table 7.6 presents the time-averaged L_2 norm of the error of the potential vorticity in the two layers, $\|q_1\|$ and $\|q_2\|$ for varying grid resolutions, $N_x \times N_y$, and varying free parameter α of the AD-TF model. Figure 7.12 and Table 7.6 show that the AD-TF model is robust with respect to changes in α. Table 7.7 presents the time-averaged L_2 norm of the error of the stream functions, $\|\psi_1\|$ and $\|\psi_2\|$, and potential vorticities in the two layers, $\|q_1\|$ and $\|q_2\|$, for a fixed parameter $\alpha = 0.25$, varying grid resolutions, $N_x \times N_y$, and varying orders N in the AD-TF model. This table shows that the AD-TF model displays a relatively low sensitivity with respect to N.

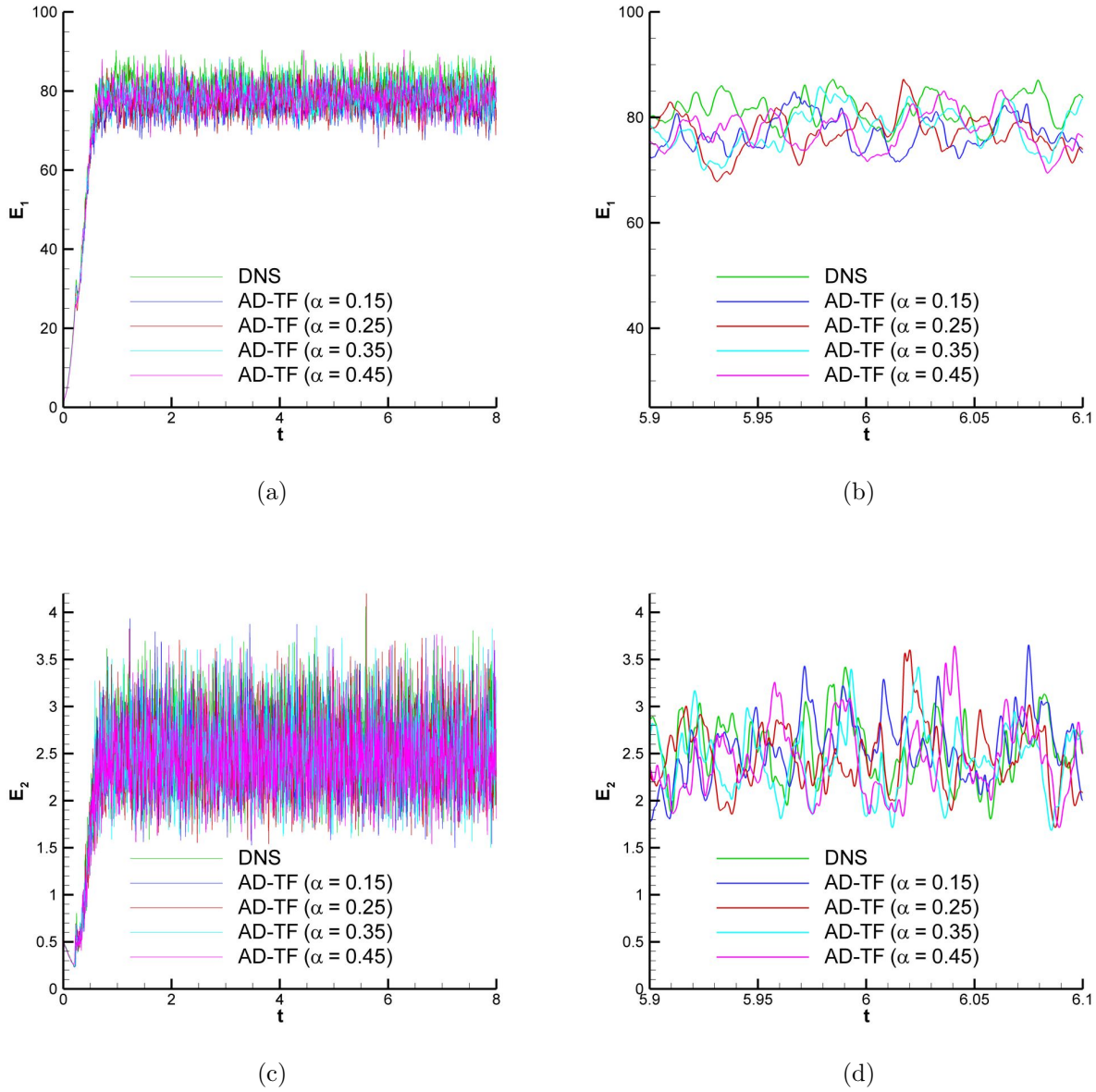

Figure 7.12: Experiment 1: Time history of basin integrated kinetic energy given by Eq. (7.53) for the DNS and the AD-TF model: (a-b) for the upper layer; and (c-d) for the lower layer. Note that the AD-TF model displays a low sensitivity with respect to α.

Table 7.6: Experiment 1: Time-averaged L_2 norm of the error of the potential vorticity in the two layers, $\|q_1\|$ and $\|q_2\|$, for varying grid resolutions, $N_x \times N_y$, and varying free parameters α of the AD-TF model. The reference solution used in the computation of the error is the numerical approximation obtained at a grid resolution of 512^2.

$N_x \times N_y$	$\alpha = 0.15$		$\alpha = 0.25$		$\alpha = 0.35$	
	$\| q_1 \|$	$\| q_2 \|$	$\| q_1 \|$	$\| q_2 \|$	$\| q_1 \|$	$\| q_2 \|$
32^2	6.0693E-2	1.0159E-2	5.9979E-2	9.6823E-3	6.2375E-2	9.4457E-3
64^2	4.3571E-2	6.4168E-3	5.0597E-2	7.5032E-3	5.6905E-2	7.8186E-3
128^2	2.7169E-2	3.3440E-3	2.8909E-2	3.4828E-3	3.1908E-2	3.7337E-3
256^2	1.0672E-2	1.3943E-3	1.1025E-2	1.4169E-3	1.1935E-2	1.4821E-3

7.5.3 Approximate deconvolution model with the differential filter (AD-DF)

Section 7.5.2 clearly showed that, for a fixed value of the EV coefficient ν, the AD-DF model can provide an accurate approximation of the mean flow field on a mesh that is significantly coarser than that used in a DNS. Furthermore, it also showed that the AD-TF model is robust with respect to changes in the smoothing parameter α used in the definition of the tridiagonal filter. A natural question is whether the AD model is sensitive with respect to other choices in the input parameters, such as the spatial filter. Thus, we tested the AD model with a differential filter (Section 7.3.2) instead of the tridiagonal filter used in Section 7.5.2. Our numerical investigation showed that the approximate deconvolution model with the differential filter (AD-DF) yields significantly different results from the AD-TF model considered in Section 7.5.2. Indeed, we discovered that the differential filter introduces a significant amount of numerical dissipation, whereas the tridiagonal filter does not. The rest of the section is devoted to a careful numerical investigation of the amount of numerical dissipation in the AD-DF model.

As mentioned in the introduction, the origin and modeling of the EV coefficient ν in the QG models is a thorny issue (the "elephant in the room"). Indeed, Table 7.1 shows

Table 7.7: Experiment 1: Time-averaged L_2 norm of the error of the stream functions, $\|\psi_1\|$ and $\|\psi_2\|$, and potential vorticities in the two layers, $\|q_1\|$ and $\|q_2\|$, for a fixed parameter $\alpha = 0.25$, and varying orders N in the AD-TF model. The reference solution used in the computation of the error is the numerical approximation obtained at a grid resolution of 512^2.

Method ($N_x \times N_y$)	$\| \psi_1 \|$	$\| \psi_2 \|$	$\| q_1 \|$	$\| q_2 \|$
QG2$_c$ (32^2)	2.2090E-1	2.6845E-2	1.2446E-1	1.8075E-2
AD-TF; $N = 1$ (32^2)	2.0484E-1	1.9669E-2	1.1848E-1	1.6965E-2
AD-TF; $N = 2$ (32^2)	1.4563E-1	3.0302E-2	8.0293E-2	1.3159E-2
AD-TF; $N = 3$ (32^2)	1.1990E-1	2.5521E-2	6.1966E-2	1.0139E-2
AD-TF; $N = 4$ (32^2)	1.1642E-1	2.4431E-2	6.0171E-2	9.7303E-3
AD-TF; $N = 5$ (32^2)	1.1701E-1	2.3525E-2	5.9979E-2	9.6823E-3

the wide range of values used for the EV coefficient ν over the years. It is clear that no unique choice exists for ν. Instead, the value used in numerical simulations is dictated by the available computational resources. To illustrate the importance of the particular value used for ν in practical computations, we carried out several high-resolution 128^2 numerical simulations for various EV coefficients ν. Figure 7.13(a) shows the time series of the basin integrated kinetic energy for Experiment 1 for different values of ν. The corresponding evolution of the maximum speed V_m is also plotted in Figure 7.13(b), in which we convert the dimensionless velocity to its dimensional counterpart to get a better physical insight. As seen from Figure 7.13, after an initial transient spin-up process, the system with $\nu = 100$ $m^2 s^{-1}$ reaches a statistically steady state at an average maximum speed of 1.78 ms^{-1} (having an upper bound of 2.05 ms^{-1} and a lower bound of 1.55 ms^{-1}), which is close to the observed maximum zonal velocities of 2 ms^{-1} at $68°W$ (Dijkstra, 2005). Thus, Figure 7.13 illustrates the procedure used in choosing the EV coefficient ν in practical computations with the QG model: The available computational resources dictate the numerical resolution that can be used; this, in turn, determines the EV coefficient ν that yields physical values for the computed flow fields (i.e., values that match those from observational data). Using higher or lower values for ν can result in unphysical flow field data, as illustrated in Figure 7.13.

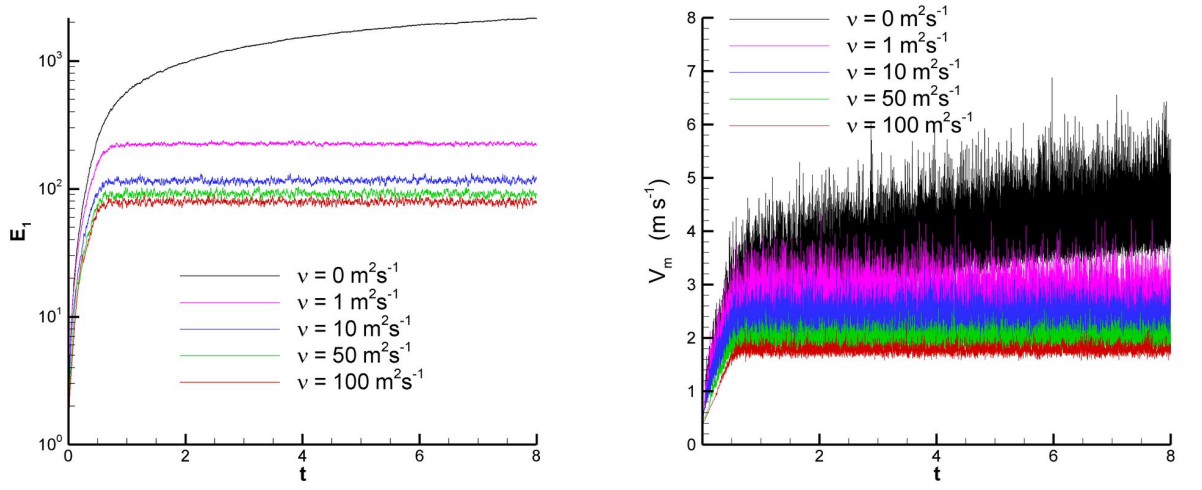

(a) (b)

Figure 7.13: Experiment 1: Numerical simulation at a 128^2 resolution for different values of the EV coefficient ν. (a) Time history of basin integrated kinetic energy given by Eq. (7.53) for the upper layer, and (b) time series of the maximum speed V_m in the field. Note the sensitivity of the results with respect to ν.

In order to measure the amount of numerical dissipation in the AD-DF model, we run this model with EV coefficients that span three orders of magnitude. The results for Re = 580.97 ($\nu = 100\ m^2s^{-1}$), Re = 5809.7 ($\nu = 10\ m^2s^{-1}$), and Re = 58097 ($\nu = 1\ m^2s^{-1}$) obtained with the AD-DF model are presented in Figure 7.14, which shows the time histories of the basin integrated kinetic energy given by Eq. (7.53) for the AD-DF model (for all three Reynolds numbers). Results for the DNS and for the No-SFS run (the under-resolved numerical simulation without any LES model) for Re = 580.97 ($\nu = 100\ m^2s^{-1}$) (i.e., the Reynolds number used in Section 7.5.2) are also included for comparison purposes. As expected, No-SFS does yield a non-physical flow field with an unrealistically increasing energy level. The kinetic energy of the AD-DF model for Re = 580.97 ($\nu = 100\ m^2s^{-1}$), on the other hand, is significantly lower than the kinetic energy of the DNS. Thus, we conclude that the differential filter in the AD-DF model yields too much numerical dissipation. Lowering the value of the eddy viscosity coefficient ν alleviates this problem. Indeed, the AD-DF model

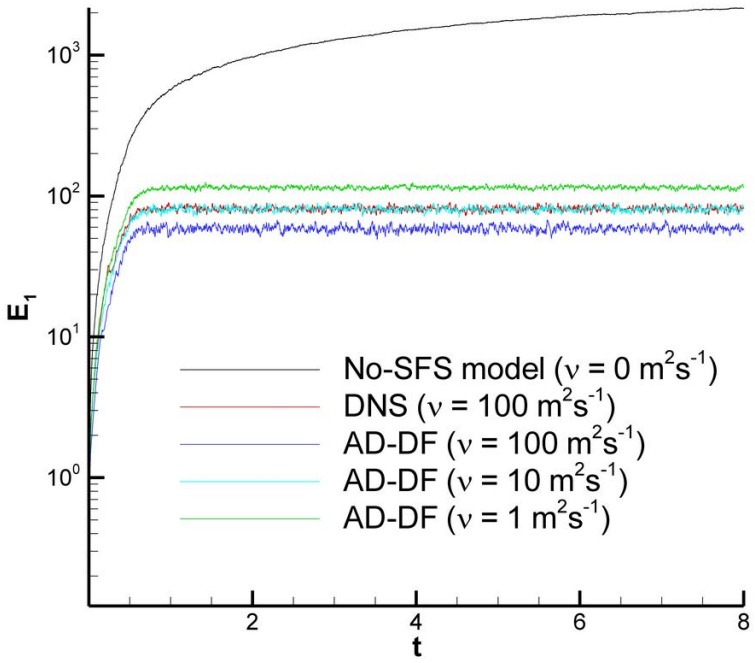

Figure 7.14: Experiment 1: Time histories of basin integrated kinetic energy for the upper layer obtained by the AD-DF model for Re = 580.97 ($\nu = 100\ m^2s^{-1}$), Re = 5809.7 ($\nu = 10\ m^2s^{-1}$), and Re = 58097 ($\nu = 1\ m^2s^{-1}$). Results for the DNS and the No-SFS (under-resolved numerical simulation without any LES model) are also included. Note that the AD-DF introduces numerical dissipation and produces the same mean flow field as the DNS on a coarser mesh *and for a lower, more physical, eddy viscosity coefficient* ν.

with Re = 5809.7 ($\nu = 10\ m^2s^{-1}$) produces the same level of kinetic energy as the DNS for the Re = 580.97 ($\nu = 100\ m^2s^{-1}$). Lowering even further the value of ν results in a kinetic energy level that is unrealistically high. Based on the results in Figure 7.14, we conclude that the differential filter in the AD-DF model introduces numerical dissipation. As a result, the AD-DF model produces the same mean flow field as the DNS on a coarser mesh *and for a lower, more physical, eddy viscosity coefficient* ν.

We've already seen in Figure 7.14 that the AD-DF model can successfully run on coarse meshes at a lower, more realistic, eddy viscosity coefficient ν. The next natural step is to quantify the amount of EV parameterization that the AD-DF model can account for. We

address this issue in Figure 7.15 for Experiment 1 and in Figure 7.16 for Experiment 2 by showing the time series of the total kinetic energy for the upper layers. Starting form rest, long time integrations are performed by using a resolution of 128^2 for all the runs.

For completeness, we start by presenting results for the tridiagonal filter. For the same EV coefficient as that used in Section 7.5.2 (i.e., $\nu = 100\ m^2 s^{-1}$), Figure 7.15(a) shows results for the AD-TF model with various filtering parameters α. We can see that decreasing α adds a low level of numerical dissipation. We emphasize, however, that this does not result in an important qualitative decrease in the kinetic energy level. Therefore, we conclude that the AD-TF is robust with respect to changes in the parameter α. We then turn-off the dissipation in the system (i.e., set $\nu = 0\ m^2 s^{-1}$), and rerun the AD-TF model for the same set of values of α. The resulting data is plotted in Figure 7.15(b). This figure clearly shows that the AD-TF model yields a high, non-physical kinetic energy level. Thus, from Figures 7.15(a) and 7.15(b), we conclude that the AD-TF model adds some numerical dissipation to the system, but cannot replace the entire EV parameterization in the system.

Next, we run the same numerical experiments as above, but now for the AD-DF model. Figure 7.15(c) shows results for the AD-DF model with various filtering parameters λ for $\nu = 100\ m^2 s^{-1}$. As for the AD-TF model, changing the filter radius λ does not change significantly the energy level. Thus, we conclude that the AD-DF model is also robust with respect to changes in λ. As opposed to the AD-TF case, the differential filter does provide a significant amount of numerical dissipation to the AD-DF model and decreases the energy level to a much lower state. The main difference between the AD-DF and the AD-TF models, however, is illustrated in Figure 7.15(d), which presents results for the AD-DF model with the eddy viscosity turned off (i.e., $\nu = 0\ m^2 s^{-1}$). This plot clearly shows that, as opposed to the AD-TF model, the AD-DF model can account for most (although not all) of the EV parameterization in the QG model. Indeed, the kinetic energy level of the AD-DF model for $\nu = 0\ m^2 s^{-1}$ is similar (although not exactly the same as) the kinetic energy level of the DNS for $\nu = 100\ m^2 s^{-1}$.

Of course, a natural question is whether these results should be attributed to the AD procedure, to the differential filter, or to both (i.e., to the AD-DF model). To answer this question, we plot in Figure 7.15(e) results for the under-resolved numerical simulation without any LES model for $\nu = 100\ m^2 s^{-1}$, which we denote by No-SFS. The No-SFS's kinetic energy level is clearly inaccurate. Thus, we conclude that the LES model is, at least in part, responsible for the success of the approach. Next, for different values of λ, we plot in Figure 7.15(f) results for an under-resolved numerical simulation with the EV parameterization turned off (i.e., $\nu = 0\ m^2 s^{-1}$), in which at each time-step we smooth out the potential vorticity and stream function values by using the differential filter. We also include corresponding results for the AD-TF. These results clearly show that using the DF to smooth the approximation in the under-resolved numerical simulation results in a high, unphysical kinetic energy level. From Figure 7.15(e) and Figure 7.15(f), we conclude that *both* the AD procedure *and* the differential filter are *necessary* in order to obtain a physical kinetic energy level.

Figure 7.16 presents the same results as those for Experiment 1 displayed in Figure 7.15, but for Experiment 2. The same qualitative conclusions can be drawn. The only difference is that in Figure 7.16(d), the kinetic energy level is straddled by the kinetic energy levels of the AD-DF model with $\nu = 0\ m^2 s^{-1}$ for $\lambda = 2h$ and $\lambda = 3h$. Thus, it appears that an intermediate value of λ (somewhere between $2h$ and $3h$) could actually allow the AD-DF model with $\nu = 0\ m^2 s^{-1}$ to replace the *entire* EV parameterization.

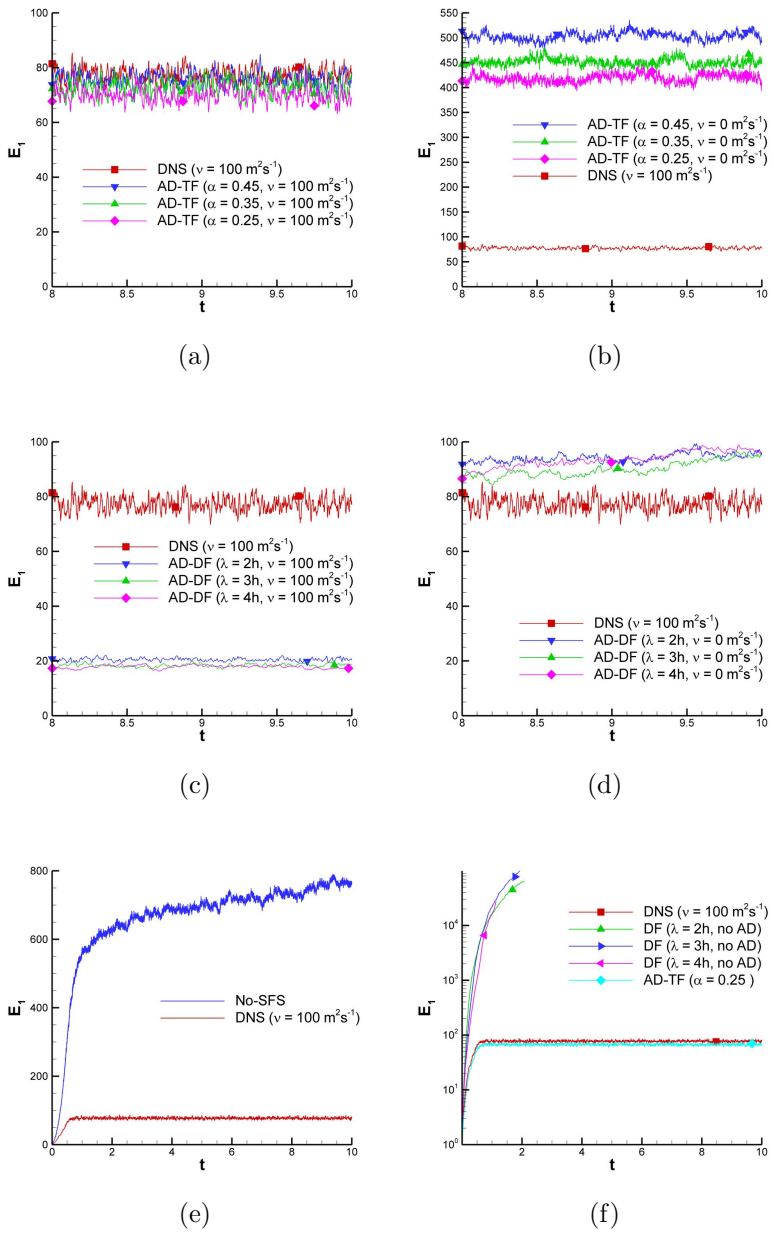

Figure 7.15: Experiment 1: Time histories of basin integrated kinetic energy for the upper layer showing a sensitivity analysis with respect to the model parameters: (a) AD-TF model ($\nu = 100\ m^2s^{-1}$), (b) AD-TF model ($\nu = 0\ m^2s^{-1}$), (c) AD-DF model ($\nu = 100\ m^2s^{-1}$), (d) AD-DF model ($\nu = 0\ m^2s^{-1}$), (e) No-SFS (under-resolved numerical simulation without any subfilter-scale model) ($\nu = 100\ m^2s^{-1}$), and (f) DF (under-resolved numerical simulation smoothed with the DF) ($\nu = 0\ m^2s^{-1}$). Results for the DNS ($\nu = 100\ m^2s^{-1}$) are also included for all plots for comparison purposes. Note that the AD-DF model can replace most of the EV parameterization in the QG2 model. For this, both the AD model and the DF are needed.

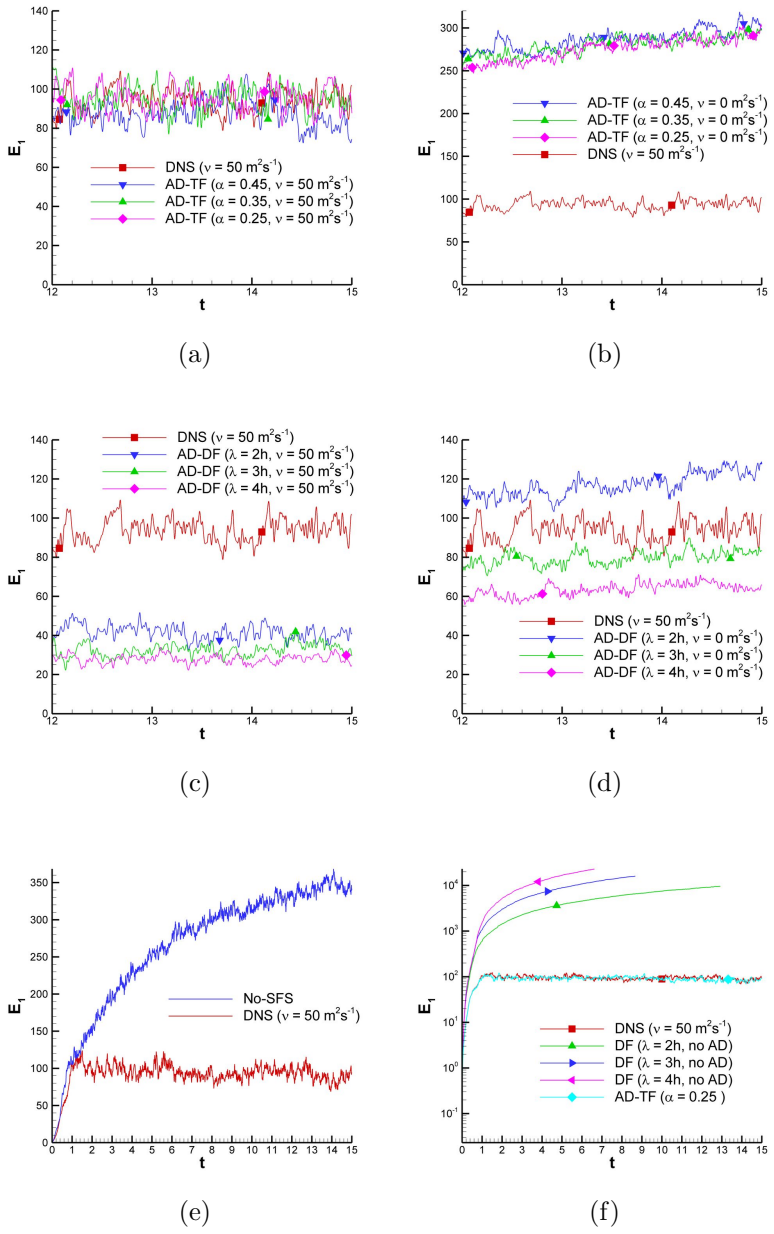

Figure 7.16: Experiment 2: Time histories of basin integrated kinetic energy for the upper layer showing a sensitivity analysis with respect to the model parameters: (a) AD-TF model ($\nu = 50\ m^2s^{-1}$), (b) AD-TF model ($\nu = 0\ m^2s^{-1}$), (c) AD-DF model ($\nu = 50\ m^2s^{-1}$), (d) AD-DF model ($\nu = 0\ m^2s^{-1}$), (e) No-SFS (under-resolved numerical simulation without any subfilter-scale model) ($\nu = 50\ m^2s^{-1}$), and (f) DF (under-resolved numerical simulation smoothed with the DF) ($\nu = 0\ m^2s^{-1}$). Results for the DNS ($\nu = 50\ m^2s^{-1}$) are also included for all plots for comparison purposes. Note that the AD-DF model can replace most of the EV parameterization in the QG2 model. For this, both the AD model and the DF are needed.

7.6 Conclusions

A new AD-LES model for the two-layer quasigeostrophic equations, a standard prototype of more realistic wind-driven ocean circulation, was introduced. Two different ocean settings with eastward jet formations of different strengths were considered. Two variants of the AD-LES model were proposed: one with a tridiagonal filter (AD-TF), and the other with a differential filter (AD-DF). Both the AD-TF and the AD-DF models yielded accurate solutions, with physically relevant energy levels and realistic mean stream function and potential vorticity contour plots. The two models also dramatically decreased the computational cost of the corresponding high-resolution numerical simulation, by using a mesh significantly coarser than the Munk scale. We emphasize that the AD procedure plays an essential role in the success of the AD-LES modeling strategy. Indeed, the under-resolved numerical simulations without AD modeling on the same coarse mesh as that employed by the AD-LES models produced inaccurate results. The AD-TF and AD-DF models, however, had completely different behaviors in terms of numerical dissipation added to the system. Indeed, the numerical results showed that the AD-TF introduced a practically negligible amount of numerical dissipation. The AD-DF model, on the other hand, introduced a significant amount of numerical dissipation. In fact, our numerical results showed that the AD-DF model can be employed successfully on meshes that are significantly coarser than the Munk scale *and* with an eddy viscosity coefficient that is dramatically lower and more physically realistic than that used in the original two-layer quasigeostrophic equations. We emphasize that the differential filter must be used in conjunction with the AD procedure to guarantee the success of the under-resolved numerical simulation. Indeed, our tests showed that an under-resolved numerical simulation in which the approximate flow fields are smoothed by convolution with the differential filter after each time-step yields an unphysically high energy level.

Although our report does not provide a solution to the longstanding quest to find the origin of and for modeling the eddy viscosity coefficients in ocean modeling, it puts forth a

novel approach to finding them, serendipitously discovered during the course of our numerical investigations. We feel that the main strength of this new approach is the ability to disentangle the modeling error from the numerical discretization error and to study it separately in this new framework (Gullbrand and Chow, 2003; Chow et al., 2005; Habisreutinger et al., 2007). This new development could lead to more robust and general LES models for large scale geophysical flows.

Chapter 8

A Posteriori Analysis of Spatial Filters for Approximate Deconvolution Large Eddy Simulations of Homogeneous Incompressible Flows

The goal of this paper is twofold: first, it investigates the effect of low-pass spatial filters for approximate deconvolution large eddy simulation (AD-LES) of turbulent incompressible flows. Second, it proposes the hyper-differential filter as a means of increasing the accuracy of the AD-LES model without increasing the computational cost. Box filters, Padé filters, and differential filters with a wide range of parameters are studied in the AD-LES framework. The AD-LES model, in conjunction with these spatial filters, is tested in the numerical simulation of the three-dimensional Taylor-Green vortex problem. The numerical results are

O. San, A. E. Staples, and T. Iliescu "A posteriori analysis of spatial filters for approximate deconvolution large eddy simulations of homogeneous incompressible flows," submitted to *Journal of Computational Physics*.

benchmarked against direct numerical simulation (DNS) data. An under-resolved numerical simulation is also used for comparison purposes. Four criteria are used to investigate the AD-LES model equipped with these spatial filters: (i) the time series of the volume-averaged enstrophy; (ii) the volume-averaged third-order structure function; (iii) the L_2 norm of the velocity and vorticity errors; and (iv) the volume-averaged velocity and vorticity correlation coefficients. According to these criteria, the numerical results yield the following two conclusions: first, the AD-LES model equipped with any of these spatial filters yields accurate results at a fraction of the computational cost of DNS. Second, the most accurate results are obtained with the hyper-differential filter, followed by the differential filter.

8.1 Introduction

Large eddy simulation (LES) is a widespread approach to performing accurate, relatively low cost computations of complex turbulent flows (Lesieur and Metais, 1996; Meneveau and Katz, 2000; Bouffanais, 2010). In this approach, a low pass filter is applied to the governing equations, separating the large, resolved scales from the unresolved, subfilter level scales. One of the main challenges in LES is the celebrated closure problem, which aims at modeling the subfilter-scale (SFS) stress tensor. This tensor appears in LES as a result of the nonlinearity in the Navier-Stokes equations (NSE). The SFS stress tensor depends on both the filtered and unfiltered flow variables. Thus, to derive a practical LES model, one needs to address the closure problem, i.e., to approximate the SFS stress tensor in terms of the filtered flow variables only.

One of the recent closure modeling strategies used in LES is the approximate deconvolution (AD). The AD closure model was introduced in LES by Stolz and Adams (1999). The AD model uses repeated filtering on the available filtered flow variables to derive computable models for the SFS stress tensor. The mathematical approach used in the derivation of the AD model distinguishes it from the standard closure modeling strategies em-

ployed in LES, such as eddy viscosity, which rely on phenomenological arguments. The AD model has been used successfully in LES of three-dimensional turbulent engineering flows (Stolz and Adams, 1999; Stolz et al., 2001a,b, 2004; Schlatter et al., 2004; Domaradzki and Adams, 2002; Habisreutinger et al., 2007; Adams et al., 2007), small scale geophysical flows, such as the atmospheric boundary layer (Chow et al., 2005; Chow and Street, 2009; Duan et al., 2010; Zhou and Chow, 2011), and large scale ocean circulation problems (San et al., 2011). The mathematical nature of the AD closure model has allowed the development of a strong mathematical support for the AD-LES model, including both well-posedness results and error analysis for the numerical discretization (Dunca and Epshteyn, 2006; Layton and Lewandowski, 2006; Layton and Neda, 2007; Rebholz, 2007; Stanculescu, 2008; Dunca, 2011; Berselli and Lewandowski, 2012; Layton and Rebholz, 2012). The applicability of AD method for computing the SFS stress tensor has been recently highlighted by Germano (2009) as well.

The need for low-pass filters arises in the numerical solution of partial differential equations. The ability to control the high-frequency content is an essential ingredient for many applications in computational fluid dynamics (Aldama, 1990; Raymond, 1994; Mullen and Fischer, 1999). Low pass filters play a central role in LES, where they are used to define the large scales. The most popular spatial filters used are the sharp cut-off, the Gaussian, and the box (or top-hat) filters. The sharp cut-off filters operate in the spectral domain, whereas the box and the Gaussian filters are applied in the physical space. The majority of LES calculations have employed sharp cut-off filters and Fourier spectral discretizations. The remaining LES calculations have generally utilized box filters and finite difference discretizations. A natural question is whether the particular spatial filter used has any effect on the LES results (Jordan and Ragab, 1996b). A comparison of various discrete test filters within a finite difference discretization has been performed by Najjar and Tafti (1996) using the dynamic subgrid-stress scale model. Similar studies were performed using several other classes of filters for large eddy simulations of turbulent flows (Schumann, 1975; Vasilyev et al., 1998; Sagaut and Grohens, 1999; Brandt, 2006).

In the AD-LES framework, the role of the spatial filter is central, since the SFS tensor is computed by the repeated use of the spatial filter. The main goal of this study is to investigate the effect of the low-pass spatial filters in the AD-LES of turbulent incompressible flows. Three classes of spatial filters are studied in conjunction with the AD-LES model. The first class of filters consists of discrete representations (Schumann, 1975; Jordan and Ragab, 1996b; Najjar and Tafti, 1996) based on the box filters with trapezoidal and Simpson's integration rules, and high-order constructions. These filters are local and computationally efficient. The second class of spatial filters that we examine comprises the Padé-type low pass filters (Pruett and Adams, 2000; Lele, 1992; Visbal and Gaitonde, 2002) with various orders of accuracy. The third class of spatial filter that we investigate consists of the Helmholtz-type elliptic differential filters (Germano, 1986a,b; Mullen and Fischer, 1999). To our knowledge, this represents the first numerical investigation of the role of spatial filtering in AD-LES. The second goal of this report is to propose the use of the hyper-differential filter as a means of increasing the physical accuracy of the AD-LES model without increasing its computational cost.

The AD-LES model, equipped with these spatial filters, is tested in the numerical simulation of the three-dimensional Taylor-Green vortex problem. The Taylor-Green vortex problem is one of the simplest systems for the study of turbulent flows and has been extensively used to investigate the behavior of LES models for homogeneous flows (Berselli, 2005; Drikakis et al., 2007; Adams et al., 2007). The numerical discretization employed throughout the paper is based on a vorticity-velocity formulation of the NSE (Fasel, 1976; Dennis et al., 1979; Fasel et al., 1990; Quartapelle, 1993; Fasel, 2002). This formulation is discretized in space using a finite difference discretization and in time using the total variation diminishing Runge-Kutta scheme. The numerical results are benchmarked against a direct numerical simulation (DNS). An under-resolved numerical simulation, denoted No-AD in the rest of the paper, is also used for comparison purposes. The following four criteria are used to investigate the AD-LES model equipped with the spatial filters described above: (i) the time series of the volume-averaged enstrophy; (ii) the volume-averaged third-order structure

function; (iii) the L_2 norm of the velocity and vorticity errors; and (iv) the volume-averaged velocity and vorticity correlation coefficients.

This paper is organized as follows. Section 8.2 presents the governing equations for the incompressible flows. Section 8.3 describes the AD methodology, and various low pass spatial filters and their transfer functions are given in Section 8.4. The temporal and spatial discretizations are briefly discussed in Section 8.5. The Taylor-Green vortex problem, a benchmark test case for homogeneous isotropic flows, is introduced in Section 8.6. The results of the AD-LES method are presented in Section 8.7. Finally, the conclusions are summarized in Section 8.8.

8.2 Governing Equations

The dimensionless form of the NSE, which govern the incompressible viscous flows, is written as:

$$\frac{\partial \boldsymbol{u}}{\partial t} + \boldsymbol{u} \cdot \nabla \boldsymbol{u} = -\nabla \boldsymbol{p} + \frac{1}{Re} \nabla^2 \boldsymbol{u} \tag{8.1}$$

$$\nabla \cdot \boldsymbol{u} = 0, \tag{8.2}$$

where Re is the Reynolds number, $\boldsymbol{u} = (u, v, w)$ is the velocity vector, and p is the pressure. The NSE given by Eqs. (8.1)-(8.2) have to be supplemented with appropriate boundary conditions and initial conditions. In this study, we exclusively consider periodic boundary conditions. This choice allows us to focus on the effect of the spatial filter on the SFS tensor, eliminating the potential complications introduced by the boundary conditions. The initial conditions for the NSE, Eqs. (8.1)-(8.2), are specified in Section 8.6. In addition to the standard primitive variable formulation of the NSE given in Eqs. (8.1)-(8.2), several alternative formulations are used in practice. For an overview of these alternative formulations, the reader is referred to the exquisite presentation given by Quartapelle (1993). In this study, we employ the vorticity-velocity formulation of the NSE (Fasel, 1976; Dennis et al., 1979;

Fasel et al., 1990; Quartapelle, 1993; Fasel, 2002). Next, we briefly describe this formulation; more details are given in Chapter 4 in Quartapelle (1993).

Taking the curl of Eq. (8.1), one obtains the vorticity equation

$$\frac{\partial \boldsymbol{\omega}}{\partial t} + \boldsymbol{u} \cdot \nabla \boldsymbol{\omega} = \boldsymbol{\omega} \cdot \nabla \boldsymbol{u} + \frac{1}{Re} \nabla^2 \boldsymbol{\omega}, \tag{8.3}$$

where the vorticity field is defined as the curl of velocity field, $\boldsymbol{\omega} = \nabla \times \boldsymbol{u}$. Next, taking the curl of the equation $\boldsymbol{\omega} = \nabla \times \boldsymbol{u}$ and using Eq. (8.2) yields the following Poisson equation for the velocity:

$$-\nabla^2 \boldsymbol{u} = \nabla \times \boldsymbol{\omega}. \tag{8.4}$$

Componentwise, the Eq. (8.4) can also be written as (Fasel, 2002)

$$\frac{\partial^2 v}{\partial x^2} + \frac{\partial^2 v}{\partial y^2} + \frac{\partial^2 v}{\partial z^2} = \frac{\partial \omega_z}{\partial x} - \frac{\partial \omega_x}{\partial z} \tag{8.5}$$

$$\frac{\partial^2 u}{\partial x^2} + \frac{\partial^2 u}{\partial z^2} = \frac{\partial \omega_y}{\partial z} - \frac{\partial^2 v}{\partial x \partial y} \tag{8.6}$$

$$\frac{\partial^2 w}{\partial x^2} + \frac{\partial^2 w}{\partial z^2} = -\frac{\partial \omega_y}{\partial x} - \frac{\partial^2 v}{\partial y \partial z}. \tag{8.7}$$

Eqs. (8.3) and (8.4) represent the vorticity-velocity formulation of the NSE. In Theorem 4.2 in Quartapelle (1993) it is shown that the primitive formulation of the NSE given in Eqs. (8.1) and (8.2) and the vorticity-velocity formulation of the NSE given in Eqs. (8.3) and (8.4) are equivalent. Both the advantages and disadvantages of the vorticity-velocity formulation over other formulations of the NSE are carefully discussed in Chapter 4 in Quartapelle (1993). All the theoretical and computational developments in this report are presented for the vorticity-velocity formulation given by Eqs. (8.3) and (8.4), which has been also used in LES for three-dimensional incompressible flows (Mansfield et al., 1998; Tenaud et al., 2005; Cocle et al., 2009). We emphasize, however, that all these developments could equally well be presented for any other NSE formulation, such as the primitive variable one

in Eqs. (8.1) and (8.2).

8.3 Approximate Deconvolution Method

To derive the equations for the filtered flow variables, Eqs. (8.3) and (8.4) are first filtered with a low pass filter (to be specified later). Thus, using a bar to denote the filtered quantities, the filtered equations read:

$$\frac{\partial \overline{\boldsymbol{\omega}}}{\partial t} + \overline{\boldsymbol{u} \cdot \nabla \boldsymbol{\omega}} = \overline{\boldsymbol{\omega} \cdot \nabla \boldsymbol{u}} + \frac{1}{Re} \nabla^2 \overline{\boldsymbol{\omega}} \tag{8.8}$$

$$-\nabla^2 \overline{\boldsymbol{u}} = \nabla \times \overline{\boldsymbol{\omega}}. \tag{8.9}$$

The nonlinear Eq. (8.8) can also be written as

$$\frac{\partial \overline{\boldsymbol{\omega}}}{\partial t} + \overline{\boldsymbol{u}} \cdot \nabla \overline{\boldsymbol{\omega}} = \overline{\boldsymbol{\omega}} \cdot \nabla \overline{\boldsymbol{u}} + \frac{1}{Re} \nabla^2 \overline{\boldsymbol{\omega}} + \mathbf{S}, \tag{8.10}$$

where $\mathbf{S}$ is the subfilter-scale term, given by

$$\mathbf{S} = \overline{\boldsymbol{u}} \cdot \nabla \overline{\boldsymbol{\omega}} - \overline{\boldsymbol{u} \cdot \nabla \boldsymbol{\omega}} - \overline{\boldsymbol{\omega}} \cdot \nabla \overline{\boldsymbol{u}} - \overline{\boldsymbol{\omega} \cdot \nabla \boldsymbol{u}}. \tag{8.11}$$

It is precisely at this point in the LES model derivation that the celebrated closure problem must be addressed. In order to close the filtered Eq. (8.10), the subfilter-scale term $\mathbf{S}$ in Eq. (8.11) needs to be modeled in terms of the filtered flow variables, $\overline{\boldsymbol{\omega}}$ and $\overline{\boldsymbol{u}}$.

The goal in AD is to use repeated filtering in order to obtain approximations of the unfiltered unresolved flow variables when approximations of the filtered resolved flow variables are available. These approximations of the unfiltered flow variables are then used in the SFS tensor to close the LES system. To derive the new AD model, we start by denoting by G the spatial filtering operator: $Gf = \bar{f}$, $G\bar{f} = \bar{\bar{f}}$ and so on, where f represents any flow variable (i.e., vorticity or velocity components in this study) and a bar denotes the application of one

filtering operation. Since $G = I - (I - G)$, an inverse to G can be written formally as the non-convergent Neumann series:

$$G^{-1} \sim \sum_{i=0}^{\infty} (I - G)^i. \tag{8.12}$$

Truncating the series gives the Van Cittert approximate deconvolution operator, Q_N (Bertero and Boccacci, 1998; Layton and Rebholz, 2012). We truncate the series at N and obtain Q_N as an approximation of G^{-1}:

$$Q_N = \sum_{i=1}^{N} (I - G)^{i-1}, \tag{8.13}$$

where I is the identity operator. The approximations Q_N are not convergent as N goes to infinity, but rather are asymptotic as the filter radius, Δ, approaches zero (Berselli et al., 2006). An approximate deconvolution of any variable f can now be obtained as follows:

$$f^* = Q_N f, \tag{8.14}$$

where an asterisk represents the approximated value for the unfiltered (unresolved) quantities. For higher values of N, we get increasingly more accurate approximations of f:

$$Q_1 = I \tag{8.15}$$

$$Q_2 = 2I - G \tag{8.16}$$

$$Q_3 = 3I - 3G + G^2 \tag{8.17}$$

$$Q_4 = 4I - 6G + 4G^2 - G^3 \tag{8.18}$$

$$Q_5 = 5I - 10G + 10G^2 - 5G^3 + G^4 \tag{8.19}$$

$$\vdots$$

For example, if we choose $N = 5$, we can find an AD approximation of the resolved variable f as

$$f \approx f^* = 5\bar{f} - 10\bar{\bar{f}} + 10\bar{\bar{\bar{f}}} - 5\bar{\bar{\bar{\bar{f}}}} + \bar{\bar{\bar{\bar{\bar{f}}}}}\,. \tag{8.20}$$

Using Eq. (8.20), we can now approximate the SFS tensor given in Eq. (8.11) by applying a filter to each flow variable:

$$\mathbf{S} = \overline{\boldsymbol{u}} \cdot \nabla \overline{\boldsymbol{\omega}} - \overline{\boldsymbol{\omega}} \cdot \nabla \overline{\boldsymbol{u}} - \overline{\boldsymbol{u}^* \cdot \nabla \boldsymbol{\omega}^*} - \overline{\boldsymbol{\omega}^* \cdot \nabla \boldsymbol{u}^*} \tag{8.21}$$

The *AD-LES model* that we investigate in this study consists of Eqs. (8.8), (8.9), and (8.21). To completely specify the AD-LES model, we need to choose a computationally efficient filtering operator.

8.4 Spatial Filters

In this section, we describe the three classes of spatial filters that we use in our LES investigation: box filters (Section 8.4.1), Padé-type filters (Section 8.4.2), and differential filters (Section 8.4.3). For each type of filter, we study its transfer function in the wavenumber space and compare it to the transfer function of the Fourier cut-off filter. A particular emphasis is placed on how much each filter attenuates the high and low wavenumber components of the function being filtered. For each class of filters, a wide range of parameters is considered.

8.4.1 Box filters

The box filter, which is also known as the top-hat filter, is commonly used in finite difference discretizations of LES models (see, e.g., Balaras et al. (1995), Jordan and Ragab (1996b), and Najjar and Tafti (1996)).

Formally, any filter operation in the three-dimensional physical space is defined by the convolution integral:

$$\bar{f}(\mathbf{x}) = \int f(\acute{\mathbf{x}}) G(\mathbf{x}, \acute{\mathbf{x}}) d\acute{\mathbf{x}}, \tag{8.22}$$

where $G(\mathbf{x}, \acute{\mathbf{x}})$ is the filter kernel. For the box filter, the filter kernel is given by the following

formula:

$$G(\mathbf{x}, \acute{\mathbf{x}}) = \begin{cases} 1/\Delta & \text{if} \quad |\mathbf{x}_i - \acute{\mathbf{x}}| < \Delta/2 \\ 0 & \text{otherwise.} \end{cases} \tag{8.23}$$

Next, we briefly sketch the derivation of the discrete form of the box filter (for details, see Sagaut (2006) and Garnier et al. (2009)). We start with the one-dimensional case. Using grid point averaging in Eq. (8.22), we get

$$\bar{f}(x) = \frac{1}{2\Delta} \int_{-\Delta}^{\Delta} f(\acute{x}) d\acute{x}. \tag{8.24}$$

Using numerical integration to approximate the integral in Eq. (8.24) yields the following discrete box filters: The trapezoidal rule yields the *trapezoidal filter (TF)*

$$\bar{f}_j = \frac{1}{4}(f_{j+1} + 2f_j + f_{j-1}) \tag{8.25}$$

and using Simpson's rule yields the *Simpson's filter (SF)*

$$\bar{f}_j = \frac{1}{6}(f_{j+1} + 4f_j + f_{j-1}), \tag{8.26}$$

where $\bar{f}_j$ is the filtered quantity at discrete point j. Extending this procedure to a three-dimensional grid is straightforward. For example, in the three-dimensional physical space, the TF (i.e., Eq. (8.25)) and the SF (i.e., Eq. (8.26)) result in a 27-point operator

$$\begin{aligned} \bar{f}_{i,j,k} = f_{i,j,k} &+ c_1(f_{i\pm1,j,k} + f_{i,j\pm1,k} + f_{i,j,k\pm1}) \\ &+ c_2(f_{i\pm1,j\pm1,k} + f_{i\pm1,j,k\pm1} + f_{i,j\pm1,k\pm1}) + c_3(f_{i\pm1,j\pm1,k\pm1}), \end{aligned} \tag{8.27}$$

where $c_1 = \frac{1}{16}$, $c_2 = \frac{1}{32}$, and $c_3 = \frac{1}{64}$ for the TF, and $c_1 = \frac{2}{27}$, $c_2 = \frac{1}{54}$, and $c_3 = \frac{1}{216}$ for the SF. The box filters can also be constructed by using high-order numerical integration schemes that include more neighboring points. For example, in the one-dimensional physical space,

a *seven-point filter (7PF)* is given by Najjar and Tafti (1996):

$$\bar{f}_j = \frac{1}{256}(f_{j+3} - 18f_{j+2} + 63f_{j+1} + 164f_j + 63f_{j-1} - 18f_{j-2} + f_{j-3}). \tag{8.28}$$

The 7PF given in Eq. (8.28) can easily be extended to the three-dimensional grid (Najjar and Tafti, 1996).

Since the box filters have been constructed in the physical space, a Fourier analysis is applied to study their characteristics in the wavenumber space. This analysis leads to the transfer function, $G(k)$, that correlates the Fourier coefficients of the filtered variable to those of the unfiltered variable as follows:

$$\hat{\bar{f}} = G(k)\hat{f}, \tag{8.29}$$

where $\hat{\bar{f}}$ and $\hat{f}$ are the corresponding Fourier coefficients of the filtered and unfiltered variables, respectively. The transfer function of the TF is

$$G^{(TF)}(k) = \frac{1}{2}\big(1 + \cos(k\Delta)\big), \tag{8.30}$$

where $\Delta = 2\pi/N$ and N is the number of grid points in the corresponding direction. Similarly, the transfer function of the SF is

$$G^{(SF)}(k) = \frac{1}{3}\big(2 + \cos(k\Delta)\big), \tag{8.31}$$

and the transfer function of the 7PF is

$$G^{(7PF)}(k) = \frac{1}{128}\big(82 + 63\cos(k\Delta) - 18\cos(2k\Delta) + \cos(3k\Delta)\big). \tag{8.32}$$

Figure 8.1 illustrates the transfer functions for the three box filters that we consider: the TF, SF, and 7PF. The transfer functions of the Fourier cut-off filter is also shown for comparison purposes. It is known that the Fourier cut-off filter removes the small scales with wavenum-

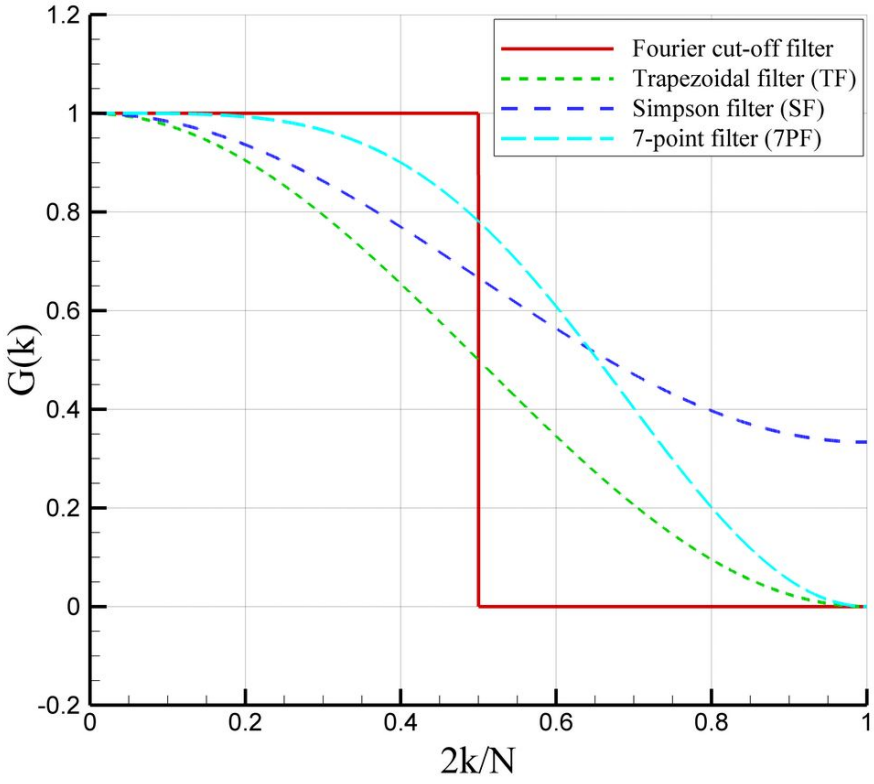

Figure 8.1: Transfer functions for the TF, the SF, and the 7PF. The transfer function of the Fourier cut-off filter is also included for comparison purposes.

bers $2k/N > 1/2$, while retaining the larger scales with wavenumbers $2k/N < 1/2$. The box filters, however, attenuate the wavenumber components differently, as shown in Figure 8.1. Ranking the three box filters in the decreasing order of wavenumber attenuation, the TF is consistently the first. For low wavenumbers ($2k/N < 1/2$), the SF is the second and the 7PF is the third. For high wavenumbers ($2k/N > 1/2$), the ranking starts to change: the 7PF increasingly attenuates more than the SF.

8.4.2 Padé-type filters

The implicit Padé-type discrete filters, which have been introduced by Lele (1992), have been successfully used in LES (see, e.g., Stolz and Adams (1999), Stolz et al. (2001a), Pruett and

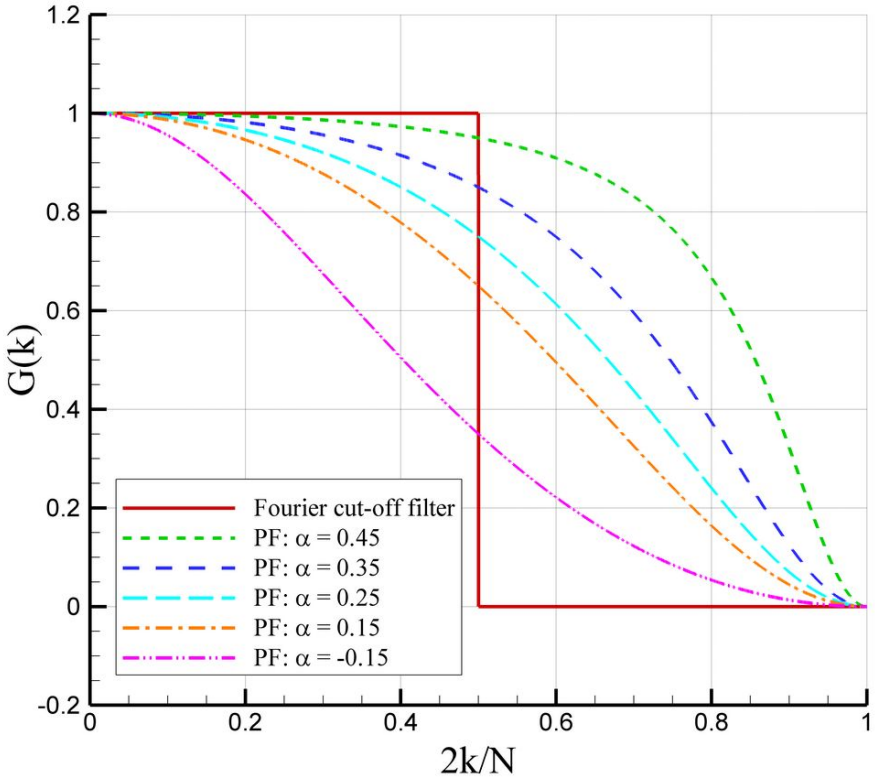

Figure 8.2: Transfer functions for the PF for different values of the parameter α. The transfer function of the Fourier cut-off filter is also included for comparison purposes.

Adams (2000) and San et al. (2011)). In this study, we consider the following one-parameter second-order *Padé-type filter (PF)*, proposed by Stolz and Adams (1999):

$$\alpha \bar{f}_{j-1} + \bar{f}_j + \alpha \bar{f}_{j+1} = \left(\frac{1}{2} + \alpha\right)\left(f_j + \frac{f_{j-1} + f_{j+1}}{2}\right), \tag{8.33}$$

where $\bar{f}_j$ represents the filtered value of a discrete quantity f_j. This results in a tridiagonal system of equations, which can be solved efficiently by using, e.g., the well-known Thomas-algorithm. The transfer function of the PF given in Eq. (8.33) can be written as

$$G^{(PF)}(k) = \left(\frac{1}{2} + \alpha\right) \frac{1 + \cos(k\Delta)}{1 + 2\alpha\cos(k\Delta)}. \tag{8.34}$$

The free parameter, α, determines the filtering properties of the PF, with high values of α yielding less dissipative results. The transfer function $G^{(PF)}$ is positive when the parameter lies in the interval of $0 \leq |\alpha| \leq 0.5$. This, in turn, ensures the well-posedness of the AD-LES model, as shown in literature (Stanculescu, 2008; Layton and Rebholz, 2012). Thus, in this report, we follow Lele (1992) and Pruett and Adams (2000), and use parameter values in the interval $0 \leq |\alpha| \leq 0.5$. More details on the PF can be found in Pruett and Adams (2000).

To study the characteristics of the PF given by Eq. (8.33), we plot in Figure 8.2 its transfer function $G^{(PF)}$ (which is given by Eq. (8.34)) for different values of the parameter α. As pointed out in Pruett and Adams (2000) (see also Lele (1992)), rewriting the filter parameter as $\alpha = -\cos(\beta_c)/2$ allows an easier interpretation of the transfer function $G^{(PF)}$ in terms of the new cut-off parameter β_c, which lies in the range $0 \leq \beta_c \leq \pi$. It is clear from Figure 8.2 that β_c plays the role of a cut-off number for the PF: $\beta_c = \pi$ turns off the filter, whereas low β_c values result in extreme dissipation (i.e., high attenuation of all the wavenumber components). Increasing the value of the cut-off parameter results in a corresponding increase in the dissipation levels over the entire range of wavenumbers. Similar conclusions were drawn by Pruett and Adams (2000) (see Figure 2 in Pruett and Adams (2000)).

8.4.3 Elliptic differential filters

The concept of differential filters was introduced in LES by Germano (1986a). Since then, it has been successfully used in LES of both engineering and geophysical flows (Iliescu and Fischer, 2003; Özgökmen et al., 2009). Solid mathematical foundations were also developed (Dunca and Epshteyn, 2006; Layton and Lewandowski, 2006; Layton and Neda, 2007; Rebholz, 2007; Stanculescu, 2008; Layton and Rebholz, 2012).

The elliptic *differential filter (DF)*, also called Helmholtz filter, can be written as:

$$\bar{f} - \lambda^2 \left(\frac{\partial^2 \bar{f}}{\partial x^2} + \frac{\partial^2 \bar{f}}{\partial y^2} + \frac{\partial^2 \bar{f}}{\partial z^2} \right) = f, \tag{8.35}$$

where λ determines the effective width of the filter. The filtered value $\bar{f}$ is obtained by applying the inverse Helmholtz operator to the unfiltered flow variable f. This inversion is done efficiently by using the *fast Fourier transform (FFT)* techniques (Press et al., 1992). The transfer function of the DF is:

$$G^{(DF)}(k) = \frac{1}{1 + \lambda^2 k^2}. \tag{8.36}$$

It is obvious that the transfer function $G^{(DF)}$ in Eq. (8.36) is positive, which ensures the well-posedness of the AD-LES model (Stanculescu, 2008; Layton and Rebholz, 2012). To study the characteristics of the DF, we plot in Figure 8.3 its transfer function, $G^{(DF)}$, for different values of the parameter γ. This parameter is defined as $\gamma = \lambda/\Delta$, where Δ is the grid spacing. That is, the filter parameter γ represents the ratio of the filter width λ to the grid spacing Δ. Thus, increasing the value of γ in Figure 8.3 amounts to increasing the filter width while keeping the grid spacing fixed. Figure 8.3 clearly shows that increasing γ (i.e., increasing the filter radius) results in a significant increase of the dissipation of the DF (i.e., the attenuation of the wavenumber components of the filtered variable).

In order to provide a more rapid decay of the high wavenumber components of the filtered variables, a generalized form of the Helmholtz filter has been suggested by Mullen and Fischer (1999). This filter, which we call in this report the *hyper-differential elliptic filter (HDF)*, is defined as follows:

$$\bar{f} - \lambda^{2m} \left(\frac{\partial^{2m} \bar{f}}{\partial x^{2m}} + \frac{\partial^{2m} \bar{f}}{\partial y^{2m}} + \frac{\partial^{2m} \bar{f}}{\partial z^{2m}} \right) = f, \tag{8.37}$$

where m is any positive integer. Note that we recover the DF when we let $m = 1$ in the HDF given by Eq. (8.37). We emphasize that, to the best of our knowledge, this study represents

the first use of the HDF in an AD-LES framework. The transfer function of the HDF is

$$G^{(HDF)}(k) = \frac{1}{1 + \lambda^{2m} k^{2m}}. \tag{8.38}$$

The transfer functions of the HDF for $m = 4$, $m = 8$, $m = 16$, and for different values of $\gamma = \lambda/\Delta$ are plotted in Figures 8.4, 8.5, and 8.6, respectively. These figures yield the following general conclusions. First, increasing the parameter γ results in a significant increase of the dissipation of the HDF, just like it did for the DF in Figure 8.3. Compared with the transfer function of the DF, however, the transfer function of the HDF has a much sharper transition between small and large wavenumbers. Indeed, for all values of m, the HDF with $0.5 \leq \gamma \leq 1.0$ satisfactorily captures the contribution of the scales with wavenumbers $2K/N < 1/2$ and attenuates the contribution of the scales with wavenumbers $2K/N > 1/2$, just like the Fourier cut-off filter. Figures 8.4-8.6 also show that increasing the parameter m in the HDF makes the transition region between small and large wavenumbers if the corresponding transfer functions even sharper. We also note that, since we utilize FFT techniques to invert the elliptic subproblems, the computational overhead of the HDF is negligible.

8.4.4 Summary

In this section, we presented the following classes of spatial filters: the box filters (Section 8.4.1), the Padé-type filters (Section 8.4.2), and the differential filters (Section 8.4.3). For each class of filters, we considered several model parameters. The characteristics of these filters were illustrated by plotting their corresponding transfer functions. The effect of the parameters on the transfer functions was discussed for each class of filters. Comparing the three classes of spatial filters among them, it seems that no general conclusion that is valid for all parameters can be drawn. The one exception, however, is the HDF given by Eq. (8.37), whose transfer function resembles that of a Fourier cut-off for all parameter values.

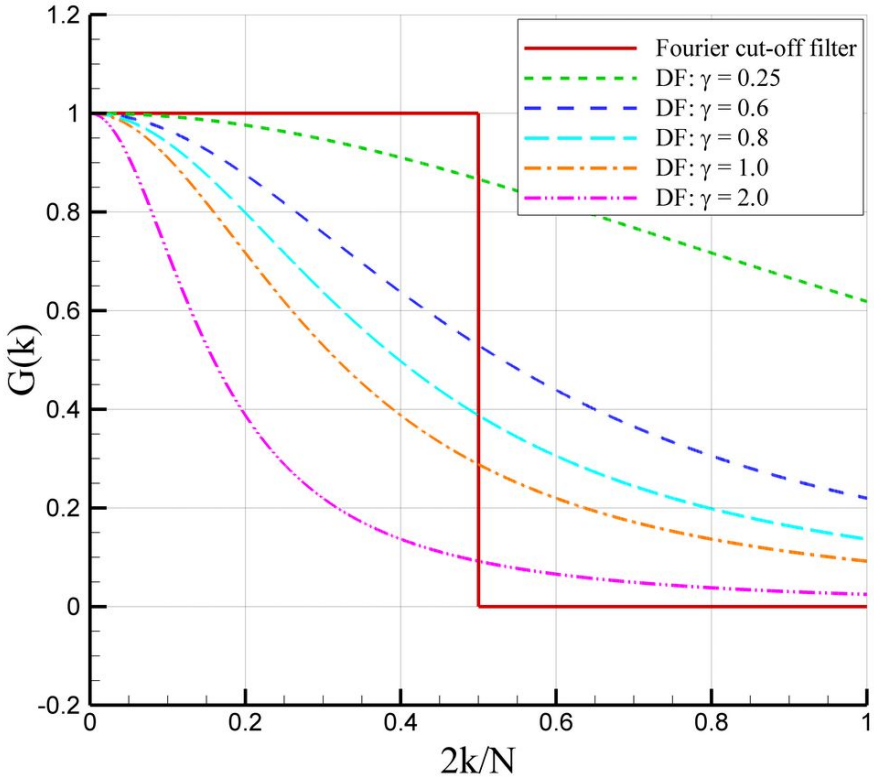

Figure 8.3: Transfer functions for the DF for different values of the parameter γ. The transfer function of the Fourier cut-off filter is also included for comparison purposes.

Since the main goal of this study is to investigate the effect of the spatial filters on the AD-LES model, the following natural question arises: "Which spatial filter is the most appropriate for AD-LES?" Based on the discussion in this section, the answer to this question is not clear. Indeed, *a priori* one cannot decide whether the spatial filter used in the AD-LES model should resemble the Fourier cut-off filter (like the HDF), or, e.g., be more like the Padé-type filters. Thus, to answer the question above, in Section 8.7 we carry out an *a posteriori* testing of the AD-LES model given by Eqs. (8.10)-(8.11) equipped with each type of spatial filter that we considered in this section.

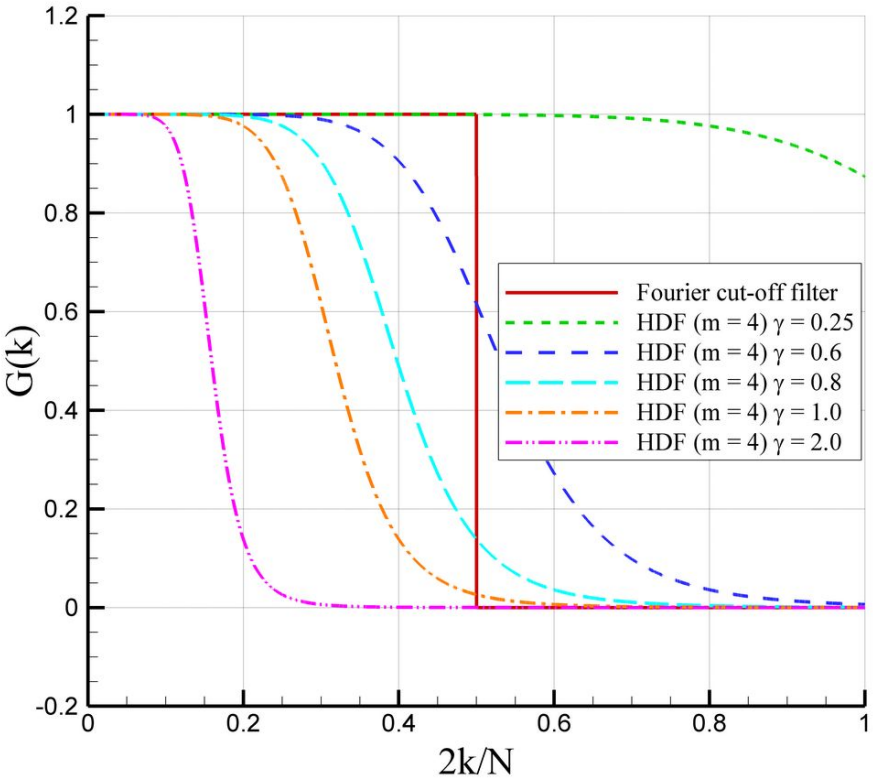

Figure 8.4: Transfer functions for the HDF for $m = 4$ and different values of the parameter γ. The transfer function of the Fourier cut-off filter is also included for comparison purposes.

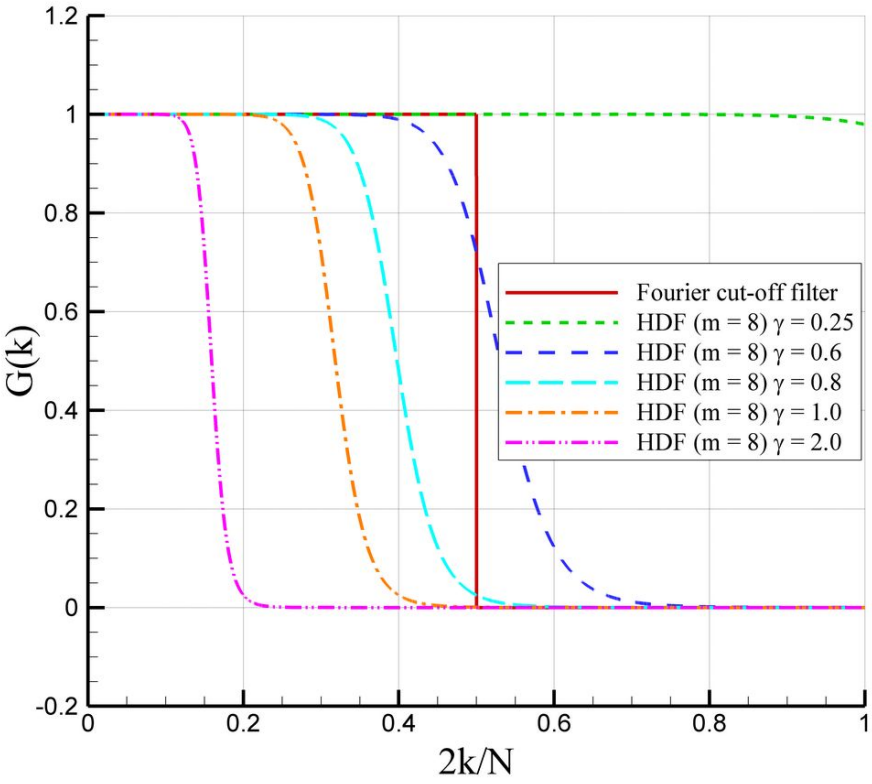

Figure 8.5: Transfer functions for the HDF for $m = 8$ and different values of the parameter γ. The transfer function of the Fourier cut-off filter is also included for comparison purposes.

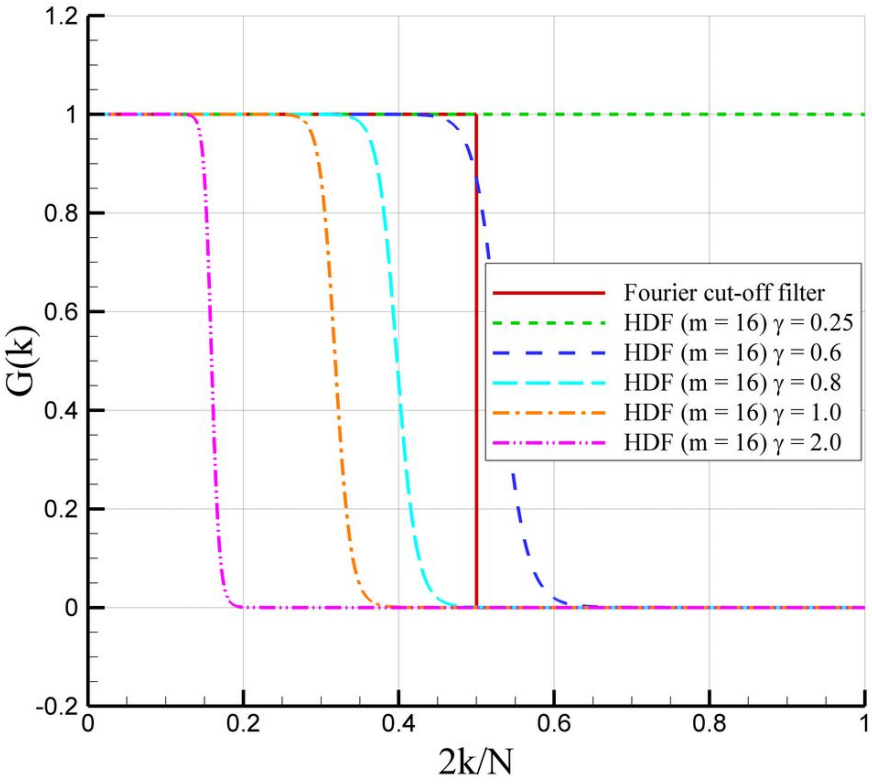

Figure 8.6: Transfer functions for the HDF for $m = 16$ and different values of the parameter γ. The transfer function of the Fourier cut-off filter is also included for comparison purposes.

8.5 Numerical Methods

In this section, we briefly describe the numerical discretization used for all the tests in Section 8.7. To describe the time discretization, we rewrite the AD-LES model (i.e., Eqs. (8.10)-(8.11)) as follows:

$$\frac{d\overline{\boldsymbol{\omega}}}{dt} = \pounds(\overline{\boldsymbol{\omega}}, \overline{\boldsymbol{u}}), \tag{8.39}$$

where $\pounds(\overline{\boldsymbol{\omega}}, \overline{\boldsymbol{u}})$ is the discrete operator of spatial derivatives for the nonlinear convective terms, linear diffusive terms, and SFS term:

$$\pounds(\overline{\boldsymbol{\omega}}, \overline{\boldsymbol{u}}) = -\overline{\boldsymbol{u}} \cdot \nabla\overline{\boldsymbol{\omega}} + \overline{\boldsymbol{\omega}} \cdot \nabla\overline{\boldsymbol{u}} + \frac{1}{Re}\nabla^2\overline{\boldsymbol{\omega}} + \mathbf{S}. \tag{8.40}$$

All the spatial derivatives in Eq. (8.40) are computed by using standard second-order finite difference approximations. To discretize the resulting system of ordinary differential equations, we assume that the numerical approximation for time level n is known, and we seek the numerical approximation for time level $n+1$, after the time step Δt. To this end, we utilize the third-order accurate total variation diminishing Runge-Kutta scheme (Gottlieb and Shu, 1998):

$$\begin{aligned}
\overline{\boldsymbol{\omega}}^{(1)} &= \overline{\boldsymbol{\omega}}^{n} + \Delta t \pounds(\overline{\boldsymbol{\omega}}^{n}, \overline{\boldsymbol{u}}^{n}) \\
\overline{\boldsymbol{\omega}}^{(2)} &= \frac{3}{4}\overline{\boldsymbol{\omega}}^{n} + \frac{1}{4}\overline{\boldsymbol{\omega}}^{(1)} + \frac{1}{4}\Delta t \pounds(\overline{\boldsymbol{\omega}}^{(1)}, \overline{\boldsymbol{u}}^{(1)}) \\
\overline{\boldsymbol{\omega}}^{n+1} &= \frac{1}{3}\overline{\boldsymbol{\omega}}^{n} + \frac{2}{3}\overline{\boldsymbol{\omega}}^{(2)} + \frac{2}{3}\Delta t \pounds(\overline{\boldsymbol{\omega}}^{(2)}, \overline{\boldsymbol{u}}^{(2)}).
\end{aligned} \tag{8.41}$$

Finally, to recover the velocity field $\overline{\boldsymbol{u}}^{n+1}$ from the vorticity field $\overline{\boldsymbol{\omega}}^{n+1}$ at time level $n+1$, a direct solver based on the FFT is used to solve the elliptic subproblems given in (8.5)-(8.7). The FFT based direct elliptic solvers are also utilized for computing the filtered variables used in the definition of the SFS tensor $\mathbf{S}$ in Eq. (8.40). More details on the FFT based direct elliptic solvers can be found in Press et al. (1992) and Moin (2001).

8.6 Test Case

The fundamental mechanism involved in isotropic, homogeneous three-dimensional turbulent flows is the enhancement of vorticity by vortex stretching and consequent production of small eddies. Energy is transferred forward in the spectral space, from low wavenumbers (large scales) to high wavenumbers (smaller scales). This process controls the turbulent energy dynamics and hence the global structure of the evolution of the turbulent flow. A prototype of this process is given by the generalized Taylor-Green vortex problem (Taylor and Green, 1937; Brachet et al., 1983; Brachet, 1991; Brachet et al., 1992; Shu et al., 2005; Adams et al., 2007), which models the decay of isotropic, homogeneous, turbulent incompressible flow that develops from the single mode initial condition:

$$u(x,y,z,t=0) = \frac{2}{\sqrt{3}}\sin\left(\theta + \frac{2\pi}{3}\right)\sin(x)\cos(y)\cos(z) \tag{8.42}$$

$$v(x,y,z,t=0) = \frac{2}{\sqrt{3}}\sin\left(\theta - \frac{2\pi}{3}\right)\cos(x)\sin(y)\cos(z) \tag{8.43}$$

$$w(x,y,z,t=0) = \frac{2}{\sqrt{3}}\sin\left(\theta\right)\cos(x)\cos(y)\sin(z). \tag{8.44}$$

All the numerical tests conducted in this study are for the Taylor-Green vortex flow problem. The computational domain used in all the numerical tests is a cubic box whose edge has a length of 2π. Periodic boundary conditions are used in all directions. We set $\theta = 0$ in Eqs. (8.42)-(8.44). In this case, the initial flow has two-dimensional streamlines, but the flow is three-dimensional for all $t > 0$. The Reynolds number used in all the numerical tests was $Re = 200$. The same Reynolds number was used by Brachet et al. (1983) and Adams et al. (2007). The time evolution of the x-component of vorticity field, ω_x, is shown in Figure 8.7. The instantaneous vorticity isosurfaces for $\omega_x = \pm 0.5$ at six time instances are plotted in Figure 8.7. These isosurfaces clearly display the generation of small scale structures.

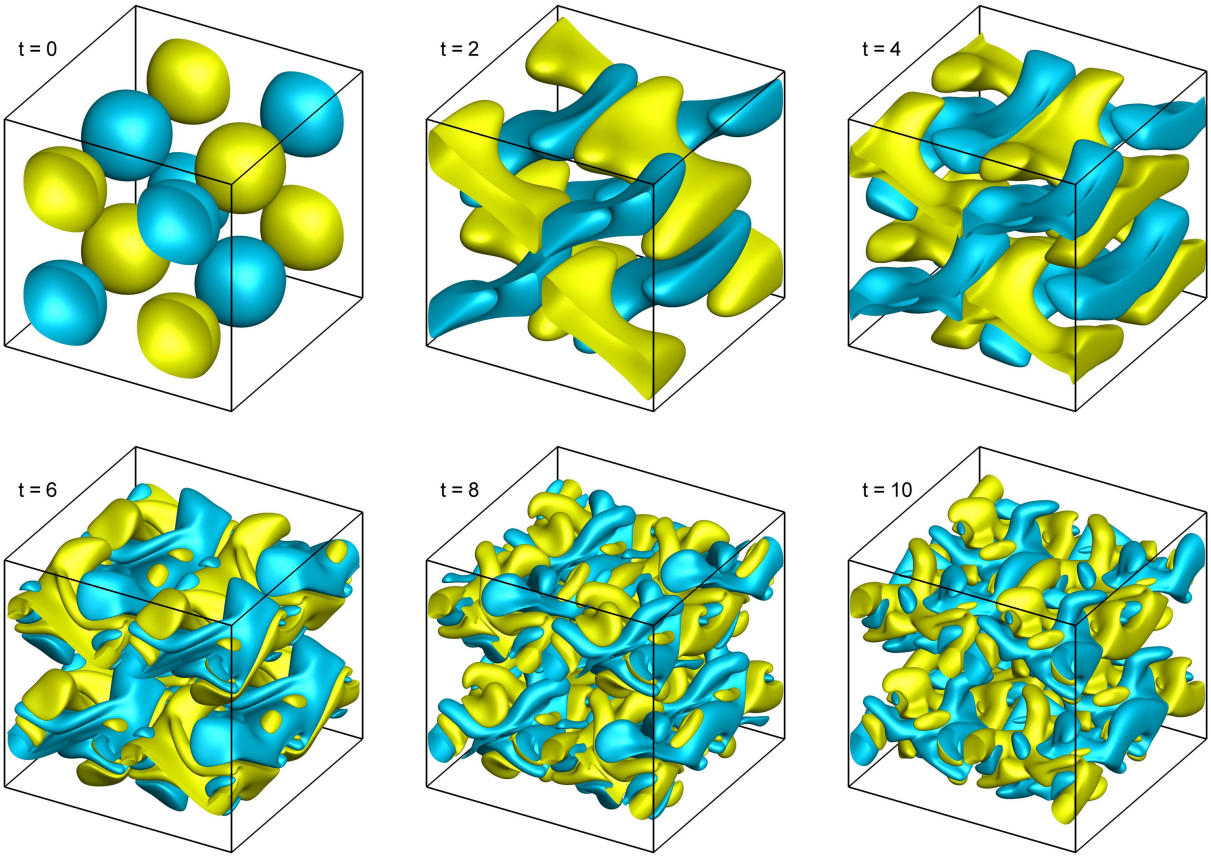

Figure 8.7: Evolution of the x-component of the vorticity on a 256^3 resolution grid for $Re = 200$. Isosurfaces of $\omega_x = \pm\ 0.5$ are shown.

8.7 Numerical Results

The goal of this section is twofold: First, we numerically investigate the effect of the spatial filters described in Section 8.4 on the AD-LES model given by Eqs. (8.10)-(8.11). As mentioned in Section 8.4, a simple visual inspection of the corresponding transfer functions would not allow us to decide which spatial filter is the most appropriate for the AD-LES model. The second goal of this section is to test the AD-LES model with the HDF given in Eq. (8.37).

There are several model parameters that need to be monitored in this numerical investigation. First, the order of the AD filter, N, should be considered. In this study, we use

two values: $N = 2$ and $N = 5$. Furthermore, for each fixed N, each filter introduces new parameter choices, e.g., α for the PF and γ for the DF and the HDF.

For clarity, we use the following approach in presenting the numerical results. In this section, we investigate the sensitivity of the AD-LES model with respect to parameters for each class of filters separately. In Section 8.8, we compare the results for all the spatial filters and draw some general conclusions.

All the numerical tests are carried out on the Taylor-Green vortex decay problem described in Section 8.6 and employ the numerical discretization outlined in Section 8.5 with a time-step $\Delta t = 5 \times 10^{-3}$. In our numerical investigation, we employ the standard LES methodology: We first run a DNS computation on a fine mesh with a resolution of 256^3. A mesh refinement study clearly shows that the DNS resolution has been achieved. We note that the same DNS spatial resolution was used by Brachet et al. (1983) and Adams et al. (2007). Furthermore, our DNS results are qualitatively similar to the DNS results of Brachet et al. (1983) and Adams et al. (2007): All three numerical datasets display a fairly consistent dissipation peak at $t \approx 6$. Next, we run an under-resolved numerical simulation on a much coarser mesh with a resolution of 64^3 (denoted in what follows as No-AD), which does not employ any SFS model. Finally, we employ the AD-LES model on the same coarse mesh utilized in No-AD (i.e., with a resolution of 64^3). We expect that the AD-LES model should yield results that are significantly better than those obtained with No-AD and are close to the DNS results, at a fraction of the computational cost.

Four criteria are used in evaluating the numerical results. The first criterion is the time series of integrated enstrophy, which is defined as follows:

$$Q(t) = \frac{1}{2} \iiint \left(\omega_x^2 + \omega_y^2 + \omega_z^2\right) dx\, dy\, dz. \tag{8.45}$$

The second criterion is the correlation coefficient between the DNS and the LES data. For any two fields f and g, which in our case will be velocity or vorticity components, the standard correlation coefficient is given by the following formula (Pruett and Adams, 2000):

$$C(f,g) = \frac{\langle fg\rangle - \langle f\rangle\langle g\rangle}{[(\langle f^2\rangle - \langle f\rangle^2)(\langle g^2\rangle - \langle g\rangle^2)]^{1/2}} \tag{8.46}$$

where the angle brackets denote the volume averages over the entire domain (e.g., $\langle f\rangle = \int f dV/V$, where $dV = dxdydz$). The third criterion is the L_2 norms of the flow variables. The reference solution for computing the L_2 norms is the DNS, which is obtained at a resolution of 256^3, while all other LES computations are performed on a coarser resolution of 64^3. The same coarse resolution results without the AD procedure are also included for comparison purposes. The fourth criterion is the third-order structure function, which is defined as

$$\langle \delta \boldsymbol{u}(r)^3\rangle = \langle |\boldsymbol{u}(\mathbf{x}+\mathbf{r}) - \boldsymbol{u}(\mathbf{x})|^3\rangle \tag{8.47}$$

with $r = |\mathbf{r}|$ being the spatial separation. Note that, since the turbulence is assumed isotropic, the velocity increment depends only on the modulus of the vector $\mathbf{r}$. According to the Kolmogorov theory of turbulence (Frisch, 1995; Davidson, 2004), the nth-order structure function scales as $\langle \delta \boldsymbol{u}(r)^n\rangle \sim r^{n/3}$ in the inertial range ($\eta \ll r \ll L$).

8.7.1 The AD-LES model with box filters

In this section, we numerically investigate the AD-LES model in conjunction with the three box filters discussed in Section 8.4.1: the TP (Eq. (8.25)), the SF (Eq. (8.26)), and the 7PF (Eq. (8.28)). The resulting LES models are denoted as AD-TF, AD-SF, and AD-7PF, respectively.

Figure 8.8 presents the time series of the integrated enstrophy $Q(t)$ defined in Eq. (8.45) for the AD-TF, AD-SF and AD-7PF with $N = 2$ and $N = 5$. Results for the DNS and No-AD are also included for comparison purposes. For $N = 2$, the AD-7PF performs the best, and AD-TF and AD-SF perform badly. For $N = 5$, the AD-SF performs the best. Comparing the $N = 2$ plot with the $N = 5$ plot, the AD-SF with $N = 5$ performs the best. As expected, the No-AD performs the worst for both $N = 2$ and $N = 5$. In fact, the

numerical simulation with the No-AD blows up around $t = 12$.

Figure 8.9 presents the third-order structure function defined in Eq. (8.47) for the AD-TF, AD-SF and AD-7PF with $N = 2$ and $N = 5$ at $t = 10$. Results for the DNS and No-AD are also included for comparison purposes. For $N = 2$, the AD-TF and AD-SF perform the best. For $N = 5$, the AD-TF and AD-SF again perform the best, with a plus for the former. Comparing the $N = 2$ plot with the $N = 5$ plot, the AD-TF and AD-SF with $N = 2$ perform the best for the small values of the ratio r/h, and the AD-TF with $N = 5$ performs the best for the large values of the ratio r/h. As expected, the No-AD performs the worst for both $N = 2$ and $N = 5$.

Table 8.1 presents the L_2 norm of the error of the AD-TF, AD-SF, and AD-7PF for $N = 2$ and $N = 5$. Results for the No-AD are also included for comparison purposes. The errors are averaged over the time interval $8 \leq t \leq 12$. For $N = 2$, the AD-SF performs the best. For $N = 5$, the AD-SF again performs the best. Comparing the $N = 2$ results with the $N = 5$ results, the AD-SF with $N = 5$ consistently performs the best. As expected, the No-AD performs the worst. Table 8.1 also shows that there is a significant sensitivity of the numerical results with respect to N. For the AD-TF, increasing N does not yield a consistent qualitative change - for some flow variables the error increases, for others it decreases. For the AD-SF, increasing N yields a consistent dramatic decrease in the error. Finally, for the AD-7PF, increasing N results in a consistent significant increase in the error. We also note that in general the velocity components have lower errors than the vorticity components. This is true for the No-AD run, for the AD-LES models, and for both $N = 2$ and $N = 5$. We attribute this behavior to the fact that the vorticity requires first order derivatives of the velocity components and, thus, is less accurately approximated than the velocity.

Table 8.2 presents the correlation coefficients for the AD-TF, AD-SF, and AD-7PF for $N = 2$ and $N = 5$. The correlation coefficients are averaged over the time interval $8 \leq t \leq 12$. Results for the No-AD are also included for comparison purposes. For $N = 2$, the AD-SF

and the AD-7PF perform the best. For $N = 5$, the AD-SF performs the best. Comparing the $N = 2$ results with the $N = 5$ results, the AD-SF with $N = 5$ consistently performs the best. As expected, the No-AD performs the worst. Increasing N has the following effect on the correlation coefficients: no consistent trend for the AD-TF, a consistent dramatic increase for the AD-SF, and a consistent significant decrease for the AD-7PF. In general, the correlation coefficients of the velocity components are higher than those of the vorticity components.

Based on the results in Figures 8.8 and 8.9 and Tables 8.1 and 8.2, we conclude that the AD-SF with $N = 5$ yields the best overall results.

8.7.2 The AD-LES model with Padé-type filters

In this section, we numerically investigate the AD-LES model in conjunction with the Padé-type filter given in Eq. (8.33) and discussed in Section 8.4.2. The resulting LES model is denoted as AD-PF. The following values for the parameter α are considered: $\alpha = 0.25$, $\alpha = 0.15$, and $\alpha = -0.15$.

Figure 8.10 presents the time series of the integrated enstrophy $Q(t)$ defined in Eq. (8.45) for the AD-PF with $N = 2$ and $N = 5$. Results for the DNS and No-AD are also included for comparison purposes. For $N = 2$, $\alpha = -0.15$ yields the best results. For $N = 5$, $\alpha = -0.15$ yields again the best results. Comparing the $N = 2$ plot with the $N = 5$ plot, $\alpha = -0.15$ yields similar (good) results for both cases. As expected, the No-AD performs the worst for both $N = 2$ and $N = 5$.

Figure 8.11 presents the third-order structure function defined in Eq. (8.47) for the AD-PF with $N = 2$ and $N = 5$ at $t = 10$. Results for the DNS and No-AD are also included for comparison purposes. For $N = 2$, $\alpha = -0.15$ yields the best results, just as it did in Figure 8.10. For $N = 5$, $\alpha = -0.15$ yields again the best results.. Comparing the $N = 2$ plot with the $N = 5$ plot, $\alpha = -0.15$ with $N = 2$ consistently performs the best. As expected,

the No-AD performs the worst for both $N = 2$ and $N = 5$.

Table 8.3 presents the L_2 norm of the error of the AD-PF for $N = 2$ and $N = 5$. Results for the No-AD are also included for comparison purposes. The errors are averaged over the time interval $8 \leq t \leq 12$. For $N = 2$, $\alpha = -0.15$ yields the best results. For $N = 5$, $\alpha = -0.15$ yields again the best results. Comparing the $N = 2$ results with the $N = 5$ results, $\alpha = -0.15$ with $N = 2$ consistently performs the best. As expected, the No-AD performs the worst. Increasing N results in a consistent significant increase for all values of the parameter α. In general, the errors of the velocity components are lower than those of the vorticity components.

Table 8.4 presents the correlation coefficients for the AD-PF for $N = 2$ and $N = 5$. Results for the No-AD are also included for comparison purposes. The correlation coefficients are averaged over the time interval $8 \leq t \leq 12$. For $N = 2$, $\alpha = -0.15$ yields the best results. For $N = 5$, $\alpha = -0.15$ yields again the best results. Comparing the $N = 2$ results with the $N = 5$ results, $\alpha = -0.15$ with $N = 2$ consistently performs the best. As expected, the No-AD performs the worst for both $N = 2$ and $N = 5$. Increasing N results in a consistent significant decrease for all values of the parameter α. In general, the correlation coefficients of the velocity components are higher than those of the vorticity components.

Based on the results in Figures 8.10 and 8.11 and Tables 8.3 and 8.4, we conclude that the AD-PF with $\alpha = -0.15$ and $N = 2$ yields the best overall results.

8.7.3 The AD-LES model with differential filters

In this section, we numerically investigate the AD-LES model in conjunction with the differential filter given in Eq. (8.35) and discussed in Section 8.4.3. The resulting LES model is denoted as AD-DF. The following values for the parameter α are considered: $\gamma = 0.6$, $\gamma = 0.8$, and $\gamma = 1.0$.

Figure 8.12 presents the time series of the integrated enstrophy $Q(t)$ defined in Eq. (8.45)

for the AD-DF with $N = 2$ and $N = 5$. Results for the DNS and No-AD are also included for comparison purposes. For $N = 2$, $\gamma = 0.6$ yields the best results. For $N = 5$, $\gamma = 0.8$ yields the best results. Comparing the $N = 2$ plot with the $N = 5$ plot, the combination $\gamma = 0.6$ and $N = 2$ yields the best results. As expected, the No-AD performs the worst for both $N = 2$ and $N = 5$.

Figure 8.13 presents the third-order structure function defined in Eq. (8.47) for the AD-DF with $N = 2$ and $N = 5$ at $t = 10$. Results for the DNS and No-AD are also included for comparison purposes. For $N = 2$, $\gamma = 0.8$ yields the best results. For $N = 5$, $\gamma = 1.0$ yields the best results.. Comparing the $N = 2$ plot with the $N = 5$ plot, the combination $\gamma = 0.8$ and $N = 2$ yields the best results. As expected, the No-AD performs the worst for both $N = 2$ and $N = 5$.

Table 8.5 presents the L_2 norm of the error of the AD-DF for $N = 2$ and $N = 5$. Results for the No-AD are also included for comparison purposes. The errors are averaged over the time interval $8 \leq t \leq 12$. For $N = 2$, $\gamma = 1.0$ yields the best results. For $N = 5$, $\gamma = 1.0$ yields again the best results. Comparing the $N = 2$ results with the $N = 5$ results, the combination $\gamma = 1.0$ and $N = 2$ yields the best results. As expected, the No-AD performs the worst. Increasing N results in a consistent significant increase of the error for all values of the parameter γ. In general, the errors of the velocity components are lower than those of the vorticity components.

Table 8.6 presents the correlation coefficients for the AD-DF for $N = 2$ and $N = 5$. Results for the No-AD are also included for comparison purposes. The correlation coefficients are averaged over the time interval $8 \leq t \leq 12$. For $N = 2$, $\gamma = 1.0$ yields the best results. For $N = 5$, $\gamma = 1.0$ yields again the best results. Comparing the $N = 2$ results with the $N = 5$ results, the combination $\gamma = 1.0$ and $N = 2$ yields the best results. As expected, the No-AD performs the worst for both $N = 2$ and $N = 5$. Increasing N results in a consistent significant decrease of the correlation coefficients for all values of the parameter γ. In general, the correlation coefficients of the velocity components are higher than those of the vorticity

components.

Based on the results in Figures 8.12 and 8.13 and Tables 8.5 and 8.6, we conclude that the AD-DF with $\gamma = 1.0$ and $N = 2$ yields the best overall results.

8.7.4 The AD-LES model with hyper-differential filters ($m = 4$)

In this section, we numerically investigate the AD-LES model in conjunction with the hyper-differential filter given in Eq. (8.37) and discussed in Section 8.4.3, with $m = 4$. The resulting LES model is denoted as AD-HDF-4. The following values for the parameter α are considered: $\gamma = 0.6$, $\gamma = 0.8$, and $\gamma = 1.0$.

Figure 8.14 presents the time series of the integrated enstrophy $Q(t)$ defined in Eq. (8.45) for the AD-HDF-4 with $N = 2$ and $N = 5$. Results for the DNS and No-AD are also included for comparison purposes. For $N = 2$, $\gamma = 0.8$ yields the best results. For $N = 5$, $\gamma = 0.8$ yields again the best results. Comparing the $N = 2$ plot with the $N = 5$ plot, the combination $\gamma = 0.8$ and $N = 2$ yields the best results. As expected, the No-AD performs the worst for both $N = 2$ and $N = 5$.

Figure 8.15 presents the third-order structure function defined in Eq. (8.47) for the AD-HDF-4 with $N = 2$ and $N = 5$ at $t = 10$. Results for the DNS and No-AD are also included for comparison purposes. For $N = 2$, $\gamma = 1.0$ yields the best results. For $N = 5$, $\gamma = 1.0$ yields again the best results.. Comparing the $N = 2$ plot with the $N = 5$ plot, $\gamma = 1.0$ together with $N = 2$ or $N = 5$ yields the best results. As expected, the No-AD performs the worst for both $N = 2$ and $N = 5$.

Table 8.7 presents the L_2 norm of the error of the AD-HDF-4 for $N = 2$ and $N = 5$. Results for the No-AD are also included for comparison purposes. The errors are averaged over the time interval $8 \leq t \leq 12$. For $N = 2$, $\gamma = 1.0$ yields the best results. For $N = 5$, $\gamma = 1.0$ yields again the best results. Comparing the $N = 2$ results with the $N = 5$ results, $\gamma = 1.0$ together with $N = 2$ or $N = 5$ yields the best results. As expected, the No-AD

performs the worst. Increasing N results in a consistent significant increase of the error for $\gamma = 0.6$ and $\gamma = 0.8$, but no clear trend is observed for $\gamma = 1.0$. In general, the errors of the velocity components are lower than those of the vorticity components.

Table 8.8 presents the correlation coefficients for the AD-HDF-4 for $N = 2$ and $N = 5$. Results for the No-AD are also included for comparison purposes. The correlation coefficients are averaged over the time interval $8 \leq t \leq 12$. For $N = 2$, $\gamma = 0.8$ and $\gamma = 1.0$ yield the best results. For $N = 5$, $\gamma = 1.0$ yields the best results. Comparing the $N = 2$ results with the $N = 5$ results, the combination $\gamma = 1.0$ and $N = 5$ yields the best results. As expected, the No-AD performs the worst for both $N = 2$ and $N = 5$. Increasing N results in a consistent significant decrease of the correlation coefficients for $\gamma = 0.6$ and $\gamma = 0.8$, but no clear trend is observed for $\gamma = 1.0$. In general, the correlation coefficients of the velocity components are higher than those of the vorticity components.

Based on the results in Figures 8.14 and 8.15 and Tables 8.7 and 8.8, we conclude that the AD-HDF-4 with $\gamma = 1.0$ and $N = 2$ or $N = 5$ yields the best overall results.

8.7.5 The AD-LES model with hyper-differential filters ($m = 8$)

In this section, we numerically investigate the AD-LES model in conjunction with the hyper-differential filter given in Eq. (8.37) and discussed in Section 8.4.3, with $m = 8$. The resulting LES model is denoted as AD-HDF-8. The following values for the parameter α are considered: $\gamma = 0.6$, $\gamma = 0.8$, and $\gamma = 1.0$.

Figure 8.16 presents the time series of the integrated enstrophy $Q(t)$ defined in Eq. (8.45) for the AD-HDF-8 with $N = 2$ and $N = 5$. Results for the DNS and No-AD are also included for comparison purposes. For $N = 2$, $\gamma = 0.8$ yields the best results. For $N = 5$, $\gamma = 0.8$ yields again the best results. Comparing the $N = 2$ plot with the $N = 5$ plot, the combination $\gamma = 0.8$ and $N = 2$ yields the best results. As expected, the No-AD performs the worst for both $N = 2$ and $N = 5$.

Figure 8.17 presents the third-order structure function defined in Eq. (8.47) for the AD-HDF-8 with $N = 2$ and $N = 5$ at $t = 10$. Results for the DNS and No-AD are also included for comparison purposes. For $N = 2$, $\gamma = 1.0$ yields the best results. For $N = 5$, $\gamma = 1.0$ yields again the best results.. Comparing the $N = 2$ plot with the $N = 5$ plot, $\gamma = 1.0$ together with $N = 2$ yields the best results. As expected, the No-AD performs the worst for both $N = 2$ and $N = 5$.

Table 8.9 presents the L_2 norm of the error of the AD-HDF-8 for $N = 2$ and $N = 5$. Results for the No-AD are also included for comparison purposes. The errors are averaged over the time interval $8 \leq t \leq 12$. For $N = 2$, $\gamma = 0.8$ yields the best results. For $N = 5$, $\gamma = 1.0$ yields the best results. Comparing the $N = 2$ results with the $N = 5$ results, $\gamma = 1.0$ together with $N = 5$ yields the best results. As expected, the No-AD performs the worst. Increasing N results in a consistent significant increase of the error for $\gamma = 0.6$, no trend for $\gamma = 0.8$, and a consistent decrease for $\gamma = 1.0$. In general, the errors of the velocity components are lower than those of the vorticity components.

Table 8.10 presents the correlation coefficients for the AD-HDF-8 for $N = 2$ and $N = 5$. Results for the No-AD are also included for comparison purposes. The correlation coefficients are averaged over the time interval $8 \leq t \leq 12$. For $N = 2$, $\gamma = 0.8$ yields the best results. For $N = 5$, $\gamma = 1.0$ and $\gamma = 0.8$ yield the best results. Comparing the $N = 2$ results with the $N = 5$ results, the combination $\gamma = 1.0$ and $N = 5$ yields the best results. As expected, the No-AD performs the worst for both $N = 2$ and $N = 5$. Increasing N results in a consistent significant decrease of the correlation coefficients for $\gamma = 0.6$, no trend for $\gamma = 0.8$, and a consistent significant increase for $\gamma = 1.0$. In general, the correlation coefficients of the velocity components are higher than those of the vorticity components.

Based on the results in Figures 8.16 and 8.17 and Tables 8.9 and 8.10, we conclude that the AD-HDF-8 with $\gamma = 1.0$ and $N = 2$ or $N = 5$ yields the best overall results.

8.7.6 The AD-LES model with hyper-differential filters ($m = 16$)

In this section, we numerically investigate the AD-LES model in conjunction with the hyper-differential filter given in Eq. (8.37) and discussed in Section 8.4.3, with $m = 16$. The resulting LES model is denoted as AD-HDF-16. The following values for the parameter α are considered: $\gamma = 0.6$, $\gamma = 0.8$, and $\gamma = 1.0$.

Figure 8.18 presents the time series of the integrated enstrophy $Q(t)$ defined in Eq. (8.45) for the AD-HDF-16 with $N = 2$ and $N = 5$. Results for the DNS and No-AD are also included for comparison purposes. For $N = 2$, $\gamma = 1.0$ yields the best results. For $N = 5$, $\gamma = 1.0$ yields again the best results. Comparing the $N = 2$ plot with the $N = 5$ plot, the combination $\gamma = 1.0$ and $N = 2$ or $N = 5$ yields the best results. As expected, the No-AD performs the worst for both $N = 2$ and $N = 5$.

Figure 8.19 presents the third-order structure function defined in Eq. (8.47) for the AD-HDF-16 with $N = 2$ and $N = 5$ at $t = 10$. Results for the DNS and No-AD are also included for comparison purposes. For $N = 2$, $\gamma = 1.0$ yields the best results. For $N = 5$, $\gamma = 1.0$ yields again the best results. Comparing the $N = 2$ plot with the $N = 5$ plot, $\gamma = 1.0$ together with $N = 5$ yields the best results. As expected, the No-AD performs the worst for both $N = 2$ and $N = 5$.

Table 8.11 presents the L_2 norm of the error of the AD-HDF-16 for $N = 2$ and $N = 5$. Results for the No-AD are also included for comparison purposes. The errors are averaged over the time interval $8 \leq t \leq 12$. For $N = 2$, $\gamma = 0.8$ yields the best results. For $N = 5$, $\gamma = 0.8$ yields again the best results. Comparing the $N = 2$ results with the $N = 5$ results, $\gamma = 0.8$ together with $N = 2$ or $N = 5$ yields the best results. As expected, the No-AD performs the worst. Increasing N results in a consistent increase of the error for $\gamma = 0.6$, no trend for $\gamma = 0.8$, and a consistent decrease for $\gamma = 1.0$. In general, the errors of the velocity components are lower than those of the vorticity components.

Table 8.12 presents the correlation coefficients for the AD-HDF-16 for $N = 2$ and $N = 5$.

Results for the No-AD are also included for comparison purposes. The correlation coefficients are averaged over the time interval $8 \leq t \leq 12$. For $N = 2$, $\gamma = 0.8$ yields the best results. For $N = 5$, $\gamma = 0.8$ yields again the best results. Comparing the $N = 2$ results with the $N = 5$ results, the combination $\gamma = 1.0$ and $N = 2$ or $N = 5$ yields the best results. As expected, the No-AD performs the worst for both $N = 2$ and $N = 5$. Increasing N results in a consistent decrease of the correlation coefficients for $\gamma = 0.6$, no trend for $\gamma = 0.8$, and a consistent increase for $\gamma = 1.0$. In general, the correlation coefficients of the velocity components are higher than those of the vorticity components.

Based on the results in Figures 8.18 and 8.19 and Tables 8.11 and 8.12, we conclude that the AD-HDF-16 with $\gamma = 0.8$ and $N = 2$ or $N = 5$ yields the best overall results.

8.7.7 Computational efficiency

This section presents the computational efficiencies of the various methods for the AD-LES model. The CPU times for the AD-LES model with the box filters (TF, SF, 7PF), Padé-type filter (PF), differential filter (DF), and hyper-differential filter (HDF) are listed in Table 8.13. The CPU times for the DNS and No-AD models are also included. The following conclusions can be drawn. The CPU times of all the AD-LES runs are significantly lower than that of the DNS, and higher than the CPU time of the No-AD. We note here that the DNS data are obtained using a computation with a resolution of 256^3, which requires a CPU time of 171 hours, while all other computations are performed using a resolution of 64^3, which require much lower CPU times, on the order of 3-10 hours. We also note that increasing the AD order N from 2 to 5 results in an increase by a factor of 2-3 of the CPU time for the PF, DF, and HDF. The increase for the box filters is lower (about 40%). Among all the filters, the box filters are the most efficient, followed by the PF, and then the DF and HDF. The HDF is as efficient as the DF due to the FFT-based inversion method for solving the elliptic system.

8.8 Summary and Conclusions

A selection of discrete low pass spatial filters has been evaluated for the approximate deconvolution large eddy simulation (AD-LES) of homogeneous incompressible three-dimensional flows. Four families of filters were considered: (i) box filters, (ii) Padé-type filters, (iii) differential filters, and (iv) hyper-differential filters. Fourier analyses have been performed to compute the filter transfer functions, which relate the resolved quantities to unresolved quantities. The AD-LES model equipped with these four classes of spatial filters was tested on the three-dimensional Taylor-Green vortex problem, and the results were compared with direct numerical simulation (DNS) data for the same problem. An under-resolved numerical simulation (No-AD) was also used for comparison purposes. Detailed sensitivity analyses of the filter parameters have been presented. Four criteria were used to assess the numerical results: (i) the time series of the volume-averaged enstrophy; (ii) the volume-averaged third-order structure function; (iii) the L_2 norm of the velocity and vorticity errors; and (iv) the volume-averaged velocity and vorticity correlation coefficients.

The numerical results yielded the following conclusions. For all cases, the AD-LES model produced more accurate results than No-AD and had a computational cost that is significantly lower than the DNS cost. The numerical results with the AD-LES model displayed a significant sensitivity with respect to the spatial filter employed, the filter parameters, and the order of the AD procedure, N. Besides these conclusions, it is hard to draw any other general conclusions that cover all cases. Thus, we first discuss each type of filter separately. Among the box filters, the SF with a high AD order ($N = 5$) consistently performs the best. For the Padé filters, a negative value of the parameter ($\alpha = -0.15$) and a low AD order ($N = 2$) consistently yield the best results. For the differential filters, a high value of the parameter ($\gamma = 1.0$) and a low AD order ($N = 2$) consistently yield the best results. For the HDF, a low HDF order ($m = 4$), a high value of the parameter ($\gamma = 1.0$), and a low AD order ($N = 2$) yield the best results.

Among the filters considered, the HDF yields the most accurate results, although the

DF also produces accurate results. This can been seen in Fig. 8.20, which presents results for the instantaneous isosurfaces of the x-component of the vorticity, ω_x. All the AD-LES models are more accurate than the No-AD run, yielding results that are relatively close to the DNS data. Fig. 8.20 clearly shows that the most accurate results are obtained with the AD-HDF model. All the other models are either inaccurate (e.g., AD-7PF and AD-PF), or overly-dissipative (e.g., AD-SF and AD-DF). Given that both the the AD-HDF and AD-DF have a computational cost that is much lower than that of a DNS, the HDF and the DF appear as appropriate choices in the AD-LES framework. We note that there is no surprise that the DF's performance is close to that of the HDF, since the latter in fact reduces to the former when $m = 1$. The numerical results also yield the following general conclusion: Although a careful parameter choice makes each class of filters competitive, it seems that filters whose transfer function resembles that of the Fourier cut-off filter (such as the HDF) tend to perform best.

Finally, we emphasize that the entire numerical study was centered around a second-order finite difference discretization used in both the DNS and the AD-LES model. Although this type of discretizations can be encountered in numerous practical applications, we emphasize that higher-order discretizations could (and probably should) be used in the AD-LES framework (see, e.g., Drikakis et al. (2009) and Habisreutinger et al. (2010) for first steps in this direction). Thus, a natural question is whether the qualitative conclusions drawn from this numerical study extend to the higher-order numerical discretization case, and if they do, to what extent these conclusions carry over. We plan to investigate these issues in a follow-up study.

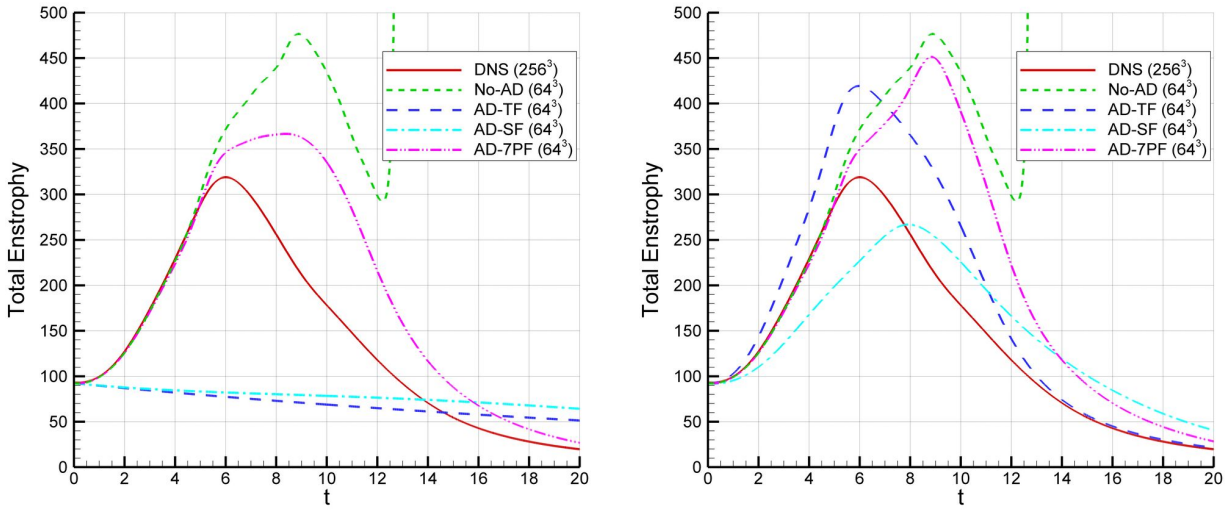

(a) $N = 2$ (b) $N = 5$

Figure 8.8: Time series of total enstrophy for the box filters.

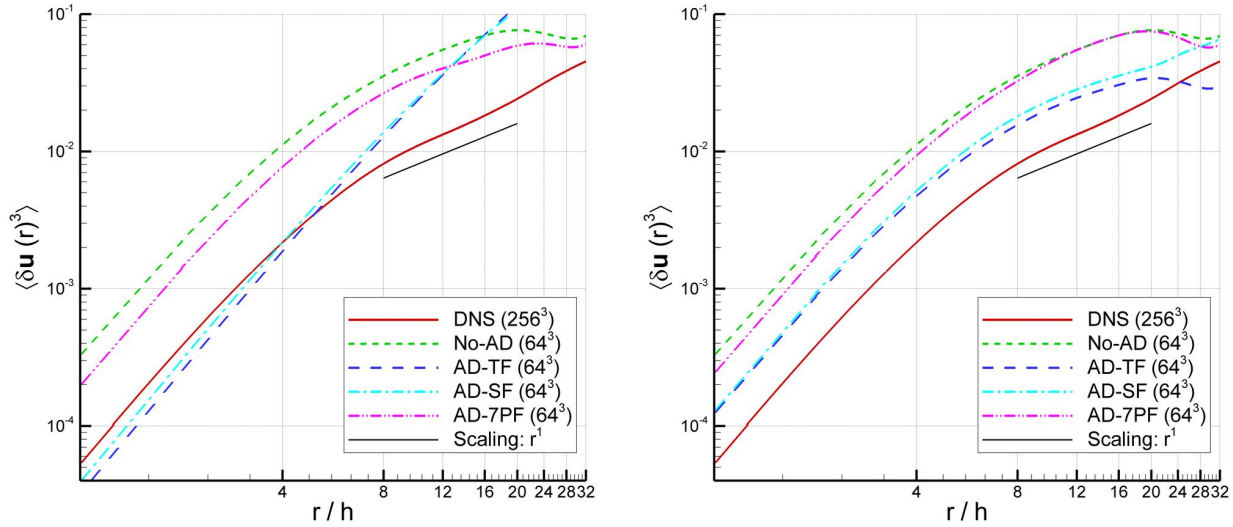

(a) $N = 2$ (b) $N = 5$

Figure 8.9: The third-order structure functions at $t = 10$ for the box filters.

Table 8.1: Discrete L_2 norms using the explicit box filters (with resolutions of 64^3) for ensemble averaging the data on a time interval between $t = 8$ and $t = 12$. The reference solution for computing the L_2 norm is the DNS data obtained with a resolution of 256^3.

Field	No-AD	Trapezoidal filter		Simpson filter		7-point filter	
		$N = 2$	$N = 5$	$N = 2$	$N = 5$	$N = 2$	$N = 5$
u	0.151	0.214	0.132	0.199	0.083	0.131	0.152
v	0.169	0.216	0.144	0.200	0.083	0.139	0.169
w	0.166	0.124	0.134	0.125	0.094	0.146	0.170
ω_x	1.233	0.739	0.844	0.727	0.586	0.875	0.995
ω_y	1.001	0.730	0.840	0.721	0.623	0.810	0.898
ω_z	1.307	0.639	0.801	0.611	0.468	0.806	0.937

Table 8.2: Correlation coefficient between the DNS data (with a resolution of 256^3) and AD results with explicit box filters (with resolutions of 64^3) for ensemble averaging on a time interval between $t = 8$ and $t = 12$. Correlation coefficients between the DNS and No-AD model (with a resolution of 64^3) are also listed for comparison purposes.

Field	C(DNS, No-AD)	C(DNS, TF)		C(DNS, SF)		C(DNS, 7PF)	
		$N = 2$	$N = 5$	$N = 2$	$N = 5$	$N = 2$	$N = 5$
u	0.692	0.732	0.700	0.760	0.922	0.751	0.664
v	0.528	0.730	0.570	0.761	0.899	0.615	0.500
w	0.552	0.305	0.577	0.392	0.825	0.661	0.565
ω_x	0.342	0.190	0.440	0.280	0.751	0.493	0.378
ω_y	0.410	0.206	0.405	0.287	0.696	0.503	0.440
ω_z	0.277	0.433	0.378	0.461	0.703	0.442	0.350

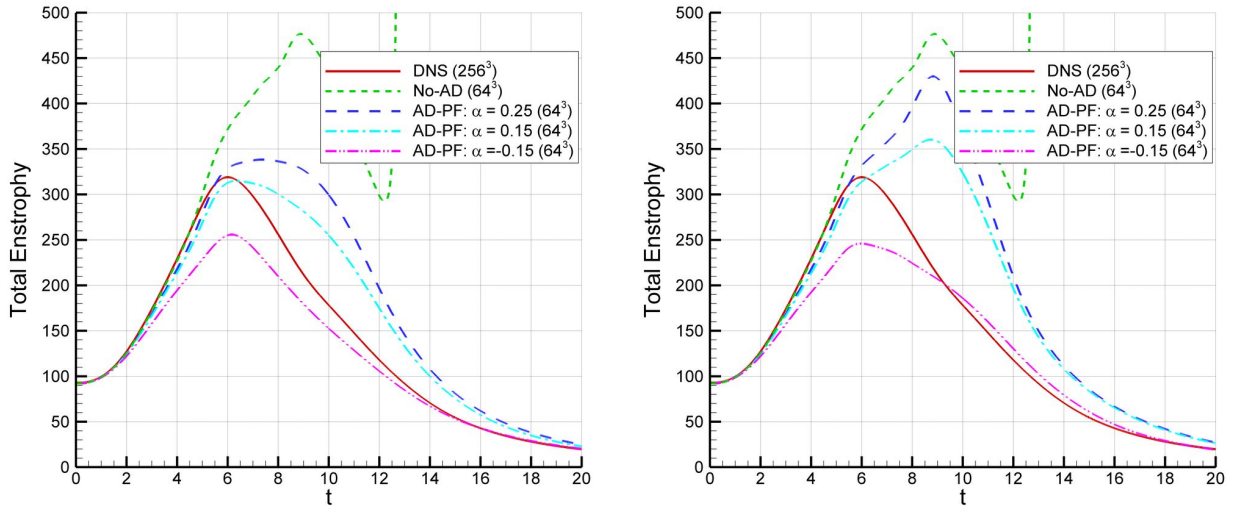

(a) $N = 2$ (b) $N = 5$

Figure 8.10: Time series of total enstrophy for the second-order Padé-type filters.

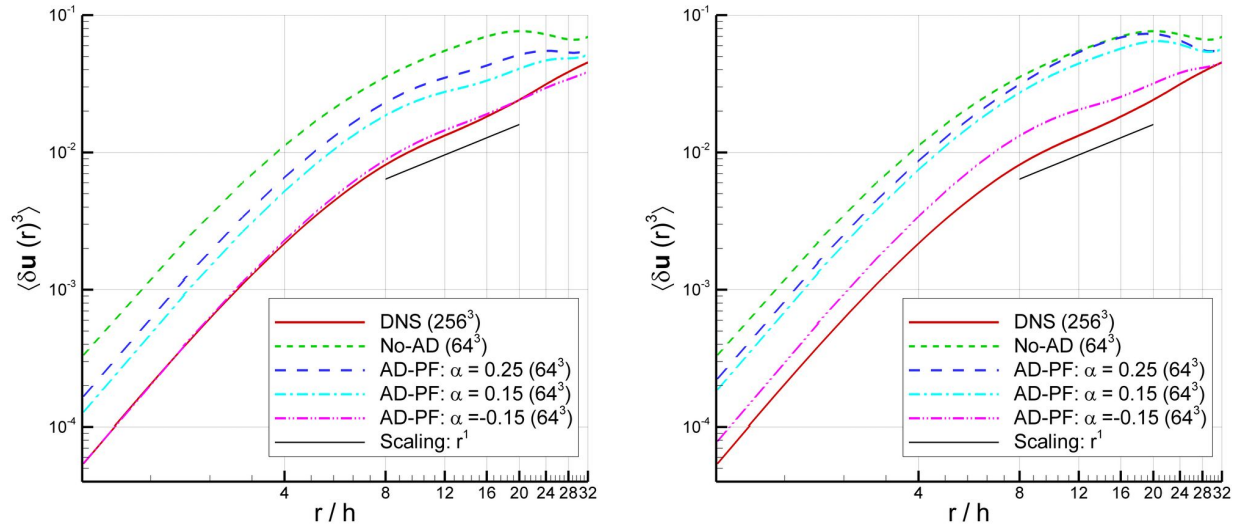

(a) $N = 2$ (b) $N = 5$

Figure 8.11: The third-order structure functions at $t = 10$ for the second-order Padé-type filters.

Table 8.3: Discrete L_2 norms using the second-order Padé filters (with resolutions of 64^3) for ensemble averaging the data on a time interval between $t = 8$ and $t = 12$. The reference solution for computing the L_2 norm is the DNS data obtained with a resolution of 256^3.

Field	No-AD	PF($\alpha = 0.25$)		PF($\alpha = 0.15$)		PF($\alpha = -0.15$)	
		$N = 2$	$N = 5$	$N = 2$	$N = 5$	$N = 2$	$N = 5$
u	0.151	0.124	0.152	0.107	0.141	0.065	0.096
v	0.169	0.130	0.170	0.113	0.153	0.073	0.101
w	0.166	0.137	0.170	0.118	0.157	0.075	0.106
ω_x	1.233	0.820	0.980	0.722	0.895	0.478	0.615
ω_y	1.001	0.762	0.873	0.682	0.796	0.493	0.581
ω_z	1.307	0.747	0.915	0.639	0.810	0.398	0.518

Table 8.4: Correlation coefficient between the DNS data (with a resolution of 256^3) and AD results with the second-order Padé filters (with resolutions of 64^3) for ensemble averaging on a time interval between $t = 8$ and $t = 12$. Correlation coefficients between the DNS and No-AD model (with a resolution of 64^3) are also listed for comparison purposes.

Field	C(DNS, No-AD)	C(DNS, $\alpha = 0.25$)		C(DNS, $\alpha = 0.15$)		C(DNS, $\alpha = -0.15$)	
		$N = 2$	$N = 5$	$N = 2$	$N = 5$	$N = 2$	$N = 5$
u	0.692	0.771	0.657	0.821	0.705	0.924	0.848
v	0.528	0.648	0.492	0.721	0.556	0.887	0.768
w	0.552	0.678	0.554	0.723	0.606	0.816	0.725
ω_x	0.342	0.521	0.368	0.590	0.434	0.756	0.627
ω_y	0.410	0.521	0.439	0.571	0.480	0.717	0.608
ω_z	0.277	0.465	0.348	0.535	0.404	0.729	0.589

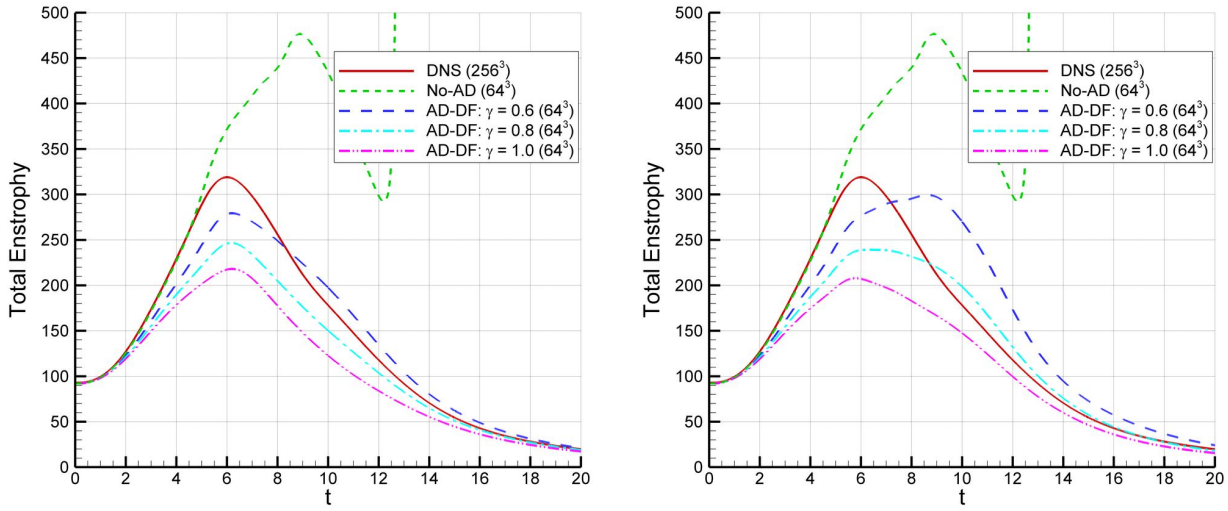

(a) $N = 2$ (b) $N = 5$

Figure 8.12: Time series of total enstrophy for the differential filters.

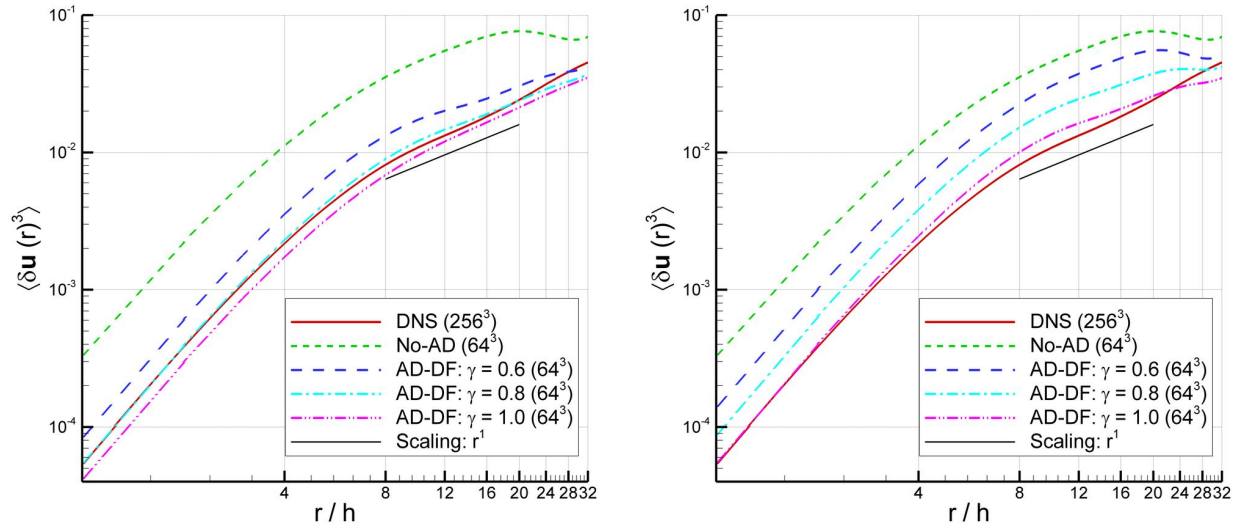

(a) $N = 2$ (b) $N = 5$

Figure 8.13: The third-order structure functions at $t = 10$ for the differential filters.

Table 8.5: Discrete L_2 norms using the differential filters (with resolutions of 64^3) for ensemble averaging the data on a time interval between $t = 8$ and $t = 12$. The reference solution for computing the L_2 norm is the DNS data obtained with a resolution of 256^3.

Field	No-AD	HF($\gamma = 0.6$)		HF($\gamma = 0.8$)		HF($\gamma = 1.0$)	
		$N = 2$	$N = 5$	$N = 2$	$N = 5$	$N = 2$	$N = 5$
u	0.151	0.089	0.135	0.070	0.115	0.060	0.098
v	0.169	0.097	0.147	0.078	0.123	0.067	0.106
w	0.166	0.098	0.149	0.079	0.125	0.070	0.104
ω_x	1.233	0.608	0.843	0.490	0.705	0.426	0.606
ω_y	1.001	0.591	0.731	0.508	0.637	0.464	0.573
ω_z	1.307	0.532	0.752	0.421	0.607	0.367	0.516

Table 8.6: Correlation coefficient between the DNS data (with a resolution of 256^3) and AD results with the differential filters (with resolutions of 64^3) for ensemble averaging on a time interval between $t = 8$ and $t = 12$. Correlation coefficients between the DNS and No-AD model (with a resolution of 64^3) are also listed for comparison purposes.

Field	C(DNS, No-AD)	C(DNS, $\gamma = 0.6$)		C(DNS, $\gamma = 0.8$)		C(DNS, $\gamma = 1.0$)	
		$N = 2$	$N = 5$	$N = 2$	$N = 5$	$N = 2$	$N = 5$
u	0.692	0.862	0.715	0.911	0.779	0.936	0.832
v	0.528	0.786	0.572	0.867	0.670	0.913	0.747
w	0.552	0.757	0.607	0.798	0.665	0.817	0.700
ω_x	0.342	0.650	0.440	0.737	0.530	0.794	0.595
ω_y	0.410	0.625	0.491	0.694	0.541	0.743	0.585
ω_z	0.277	0.598	0.414	0.701	0.493	0.758	0.558

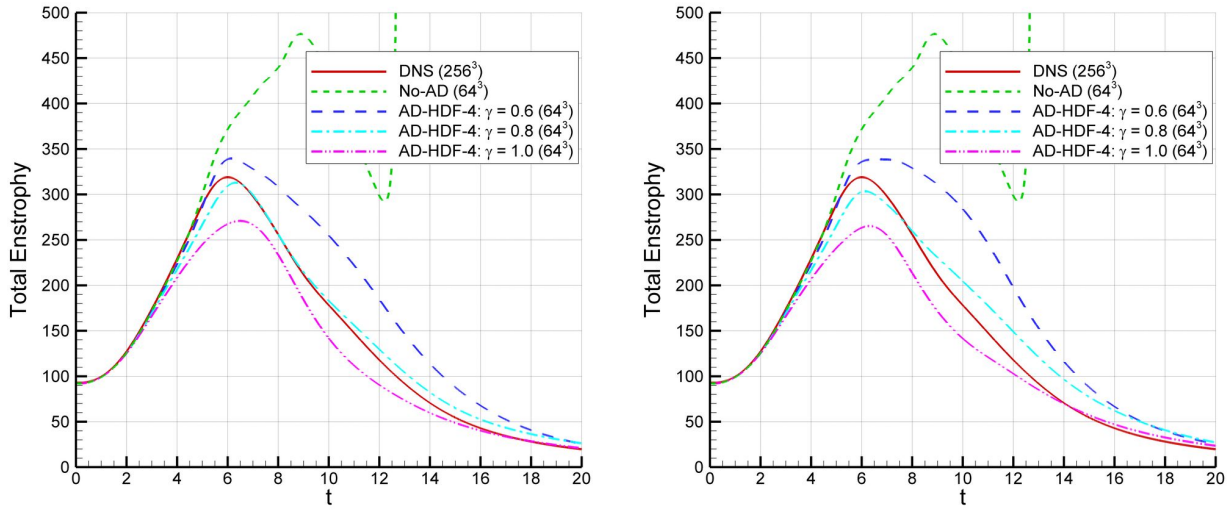

(a) $N = 2$ (b) $N = 5$

Figure 8.14: Time series of total enstrophy for the hyper-differential filters ($m = 4$).

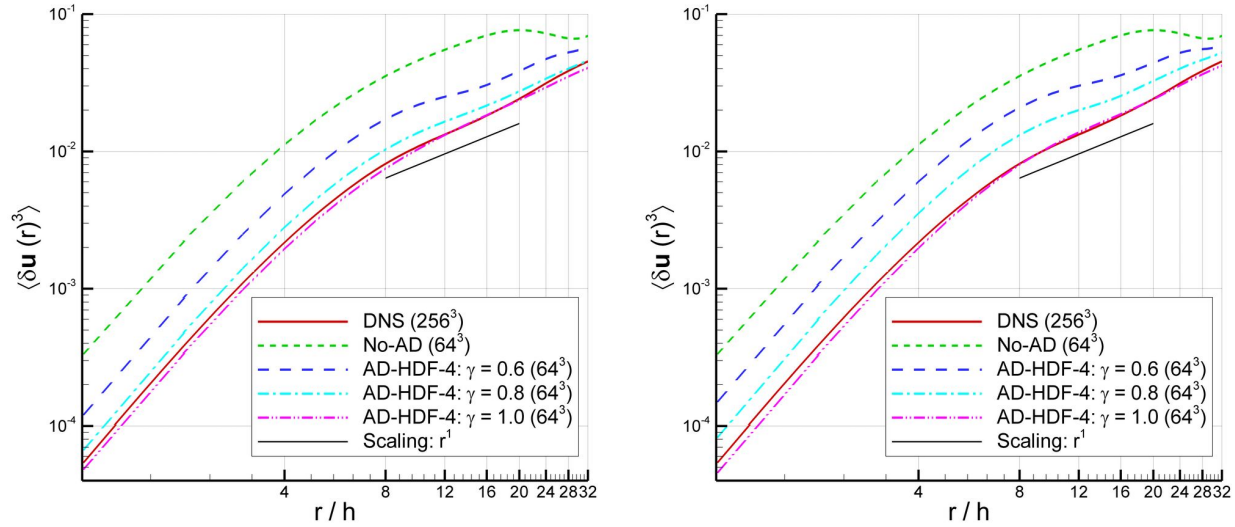

(a) $N = 2$ (b) $N = 5$

Figure 8.15: The third-order structure functions at $t = 10$ for the hyper-differential filters ($m = 4$).

Table 8.7: Discrete L_2 norms using the hyper-differential filters for $m = 4$ (with resolutions of 64^3) for ensemble averaging the data on a time interval between $t = 8$ and $t = 12$. The reference solution for computing the L_2 norm is the DNS data obtained with a resolution of 256^3.

Field	No-AD	HDF($m = 4$, $\gamma = 0.6$)		HDF($m = 4$, $\gamma = 0.8$)		HDF($m = 4$, $\gamma = 1.0$)	
		$N = 2$	$N = 5$	$N = 2$	$N = 5$	$N = 2$	$N = 5$
u	0.151	0.092	0.107	0.062	0.073	0.055	0.059
v	0.169	0.093	0.110	0.066	0.075	0.061	0.063
w	0.166	0.103	0.121	0.074	0.084	0.075	0.070
ω_x	1.233	0.659	0.738	0.496	0.538	0.481	0.463
ω_y	1.001	0.636	0.697	0.509	0.516	0.506	0.468
ω_z	1.307	0.553	0.637	0.401	0.414	0.373	0.385

Table 8.8: Correlation coefficient between the DNS data (with a resolution of 256^3) and AD results with the hyper-differential filters (with resolutions of 64^3) for the power $m = 4$ for ensemble averaging on a time interval between $t = 8$ and $t = 12$. Correlation coefficients between the DNS and No-AD model (with a resolution of 64^3) are also listed for comparison purposes.

Field	C(DNS, No-AD)	C(DNS, $\gamma = 0.6$)		C(DNS, $\gamma = 0.8$)		C(DNS, $\gamma = 1.0$)	
		$N = 2$	$N = 5$	$N = 2$	$N = 5$	$N = 2$	$N = 5$
u	0.692	0.877	0.831	0.937	0.923	0.950	0.940
v	0.528	0.806	0.739	0.909	0.877	0.932	0.921
w	0.552	0.776	0.731	0.836	0.822	0.805	0.827
ω_x	0.342	0.671	0.609	0.775	0.747	0.771	0.778
ω_y	0.410	0.639	0.582	0.732	0.729	0.727	0.750
ω_z	0.277	0.630	0.561	0.744	0.726	0.767	0.749

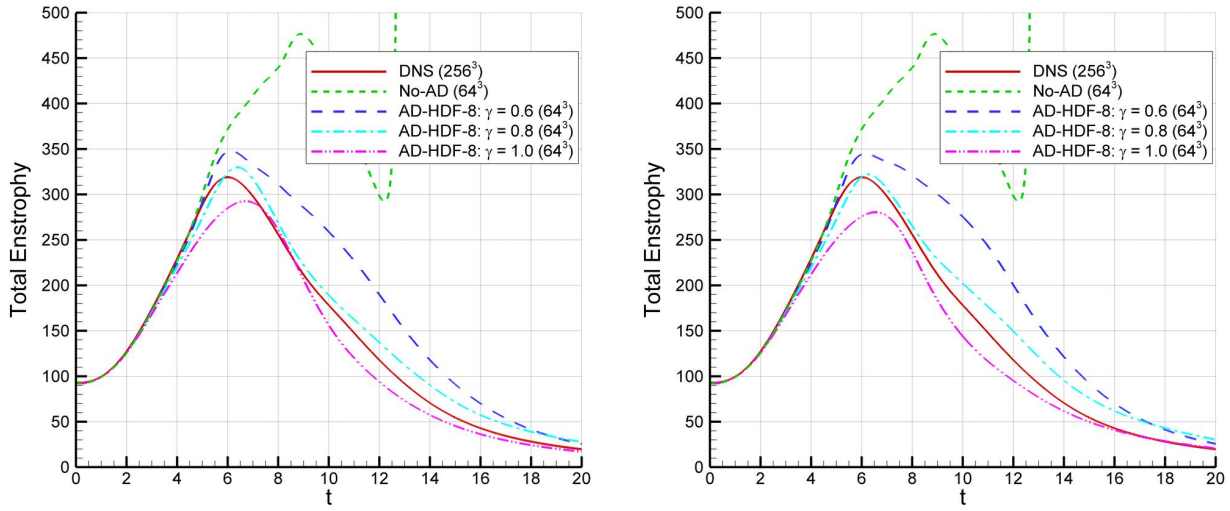

(a) $N = 2$ (b) $N = 5$

Figure 8.16: Time series of total enstrophy for the hyper-differential filters ($m = 8$).

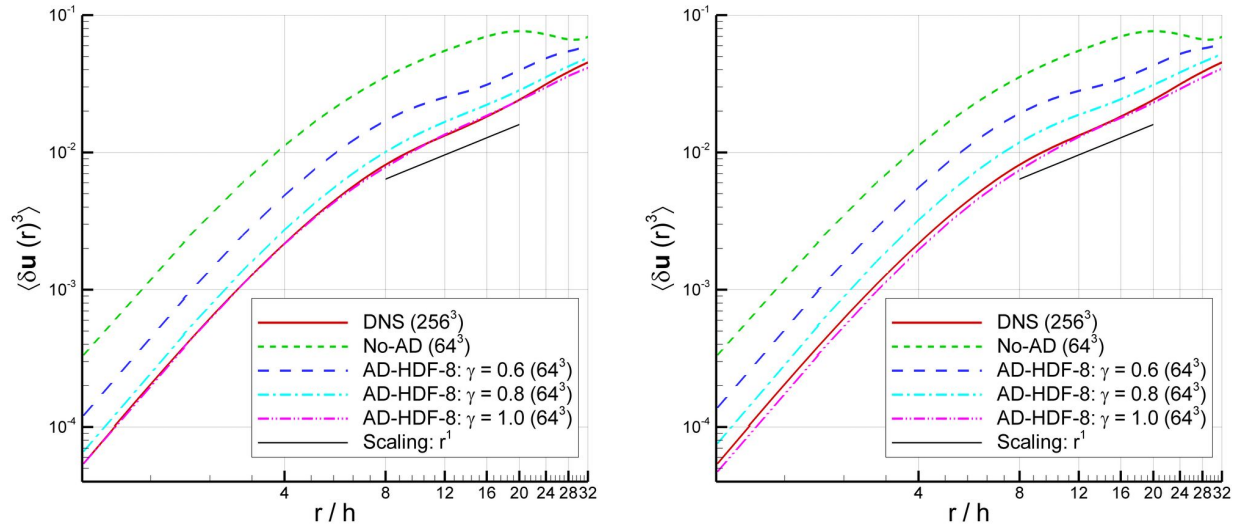

(a) $N = 2$ (b) $N = 5$

Figure 8.17: The third-order structure functions at $t = 10$ for the hyper-differential filters ($m = 8$).

Table 8.9: Discrete L_2 norms using the hyper-differential filters for $m = 8$ (with resolutions of 64^3) for ensemble averaging the data on a time interval between $t = 8$ and $t = 12$. The reference solution for computing the L_2 norm is the DNS data obtained with a resolution of 256^3.

Field	No-AD	HDF($m = 8$, $\gamma = 0.6$)		HDF($m = 8$, $\gamma = 0.8$)		HDF($m = 8$, $\gamma = 1.0$)	
		$N = 2$	$N = 5$	$N = 2$	$N = 5$	$N = 2$	$N = 5$
u	0.151	0.091	0.100	0.063	0.065	0.062	0.058
v	0.169	0.091	0.101	0.064	0.067	0.065	0.061
w	0.166	0.101	0.110	0.074	0.078	0.085	0.072
ω_x	1.233	0.658	0.699	0.518	0.532	0.535	0.490
ω_y	1.001	0.640	0.668	0.540	0.521	0.586	0.509
ω_z	1.307	0.557	0.600	0.417	0.405	0.412	0.397

Table 8.10: Correlation coefficient between the DNS data (with a resolution of 256^3) and AD results with the hyper-differential filters (with resolutions of 64^3) for the power $m = 8$ for ensemble averaging on a time interval between $t = 8$ and $t = 12$. Correlation coefficients between the DNS and No-AD model (with a resolution of 64^3) are also listed for comparison purposes.

Field	C(DNS, No-AD)	C(DNS, $\gamma = 0.6$)		C(DNS, $\gamma = 0.8$)		C(DNS, $\gamma = 1.0$)	
		$N = 2$	$N = 5$	$N = 2$	$N = 5$	$N = 2$	$N = 5$
u	0.692	0.883	0.858	0.938	0.939	0.939	0.943
v	0.528	0.815	0.774	0.918	0.906	0.925	0.933
w	0.552	0.784	0.761	0.828	0.831	0.755	0.822
ω_x	0.342	0.680	0.646	0.765	0.760	0.727	0.761
ω_y	0.410	0.644	0.620	0.714	0.736	0.663	0.732
ω_z	0.277	0.634	0.603	0.735	0.743	0.726	0.745

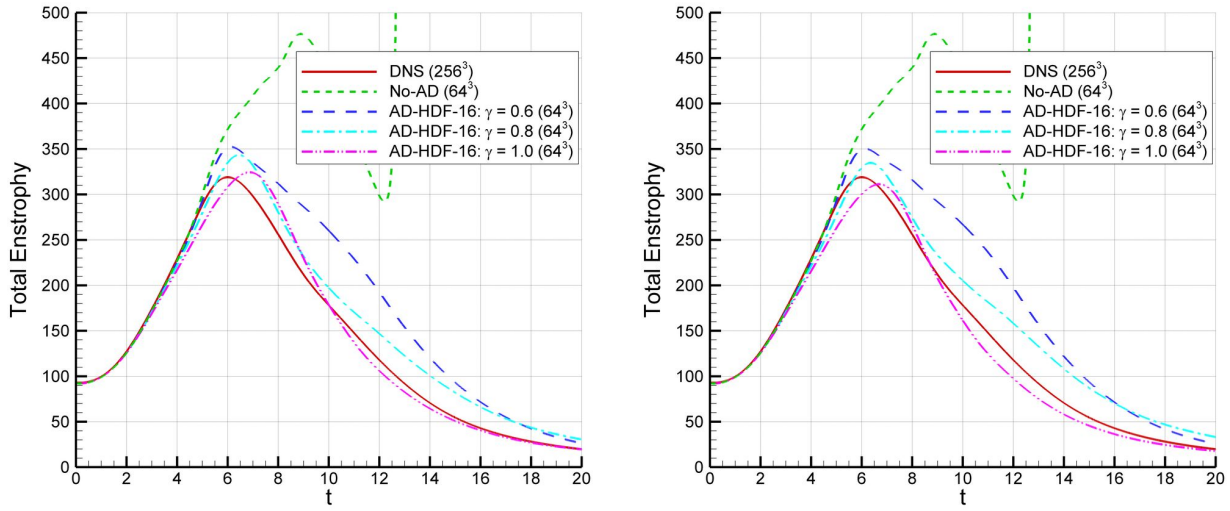

(a) $N = 2$ (b) $N = 5$

Figure 8.18: Time series of total enstrophy for the hyper-differential filters ($m = 16$).

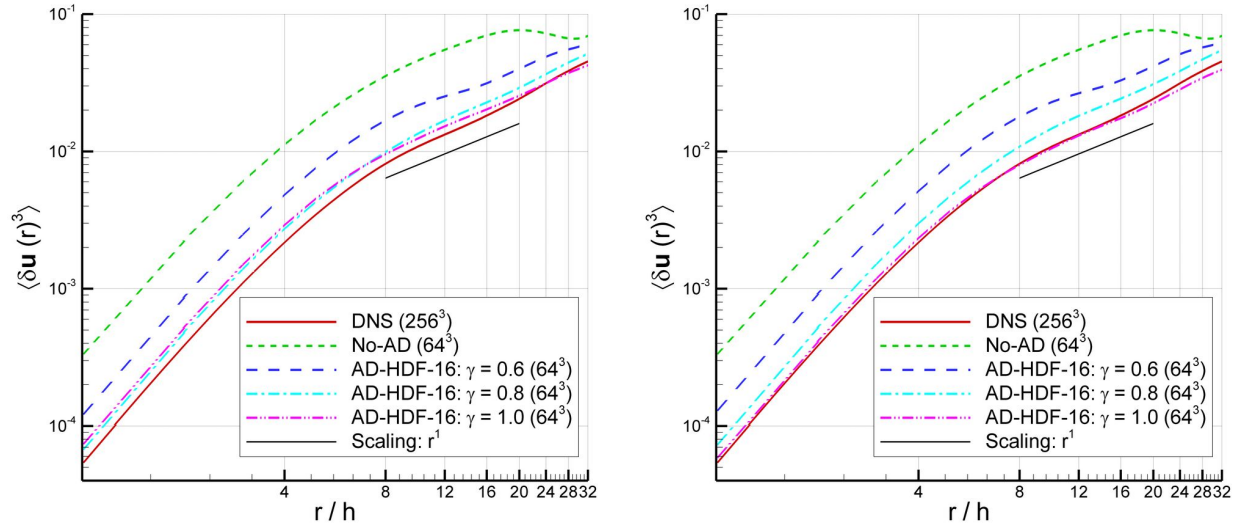

(a) $N = 2$ (b) $N = 5$

Figure 8.19: The third-order structure functions at $t = 10$ for the hyper-differential filters ($m = 16$).

Table 8.11: Discrete L_2 norms using the hyper-differential filters for $m = 16$ (with resolutions of 64^3) for ensemble averaging the data on a time interval between $t = 8$ and $t = 12$. The reference solution for computing the L_2 norm is the DNS data obtained with a resolution of 256^3.

Field	No-AD	HDF($m = 16$, $\gamma = 0.6$)		HDF($m = 16$, $\gamma = 0.8$)		HDF($m = 16$, $\gamma = 1.0$)	
		$N = 2$	$N = 5$	$N = 2$	$N = 5$	$N = 2$	$N = 5$
u	0.151	0.092	0.096	0.065	0.066	0.073	0.072
v	0.169	0.090	0.094	0.063	0.065	0.078	0.073
w	0.166	0.100	0.103	0.077	0.079	0.093	0.092
ω_x	1.233	0.656	0.669	0.549	0.560	0.620	0.597
ω_y	1.001	0.652	0.656	0.594	0.582	0.639	0.602
ω_z	1.307	0.569	0.585	0.437	0.434	0.465	0.459

Table 8.12: Correlation coefficient between the DNS data (with a resolution of 256^3) and AD results with the hyper-differential filters (with resolutions of 64^3) for the power $m = 16$ for ensemble averaging on a time interval between $t = 8$ and $t = 12$. Correlation coefficients between the DNS and No-AD model (with a resolution of 64^3) are also listed for comparison purposes.

Field	C(DNS, No-AD)	C(DNS, $\gamma = 0.6$)		C(DNS, $\gamma = 0.8$)		C(DNS, $\gamma = 1.0$)	
		$N = 2$	$N = 5$	$N = 2$	$N = 5$	$N = 2$	$N = 5$
u	0.692	0.885	0.874	0.938	0.939	0.907	0.909
v	0.528	0.823	0.805	0.927	0.921	0.892	0.908
w	0.552	0.786	0.780	0.819	0.809	0.733	0.729
ω_x	0.342	0.685	0.674	0.744	0.732	0.657	0.668
ω_y	0.410	0.639	0.636	0.685	0.696	0.624	0.650
ω_z	0.277	0.627	0.617	0.729	0.729	0.656	0.663

Table 8.13: Computational efficiencies of the DNS, No-AD, and AD-LES models.

Method	CPU time
DNS (256^3)	171.5 hrs
No-AD (64^3)	1.8 hrs
AD-TF (64^3)	2.0 hrs ($N = 2$); 2.8 hrs ($N = 5$)
AD-SF (64^3)	2.0 hrs ($N = 2$); 2.8 hrs ($N = 5$)
AD-7PF (64^3)	2.1 hrs ($N = 2$); 2.9 hrs ($N = 5$)
AD-PF (64^3) ($\alpha = 0.25$)	3.1 hrs ($N = 2$); 9.1 hrs ($N = 5$)
AD-DF (64^3) ($\gamma = 0.8$)	4.0 hrs ($N = 2$); 9.5 hrs ($N = 5$)
AD-HDF (64^3) ($\gamma = 0.8$, $m = 8$)	4.0 hrs ($N = 2$); 9.5 hrs ($N = 5$)

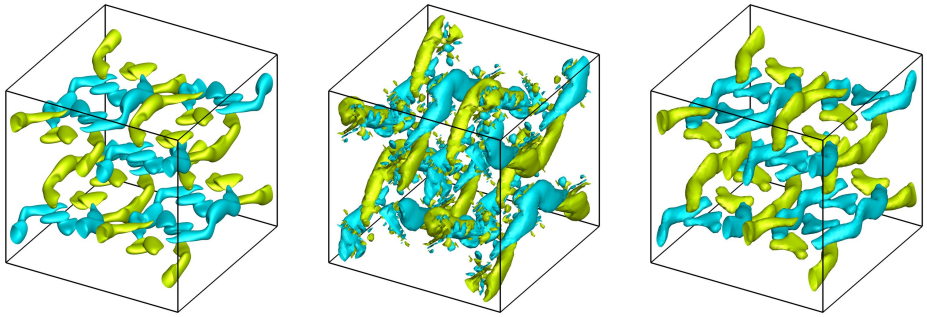

(a) DNS (b) No-AD (c) AD-HDF-8 ($\gamma = 0.8$)

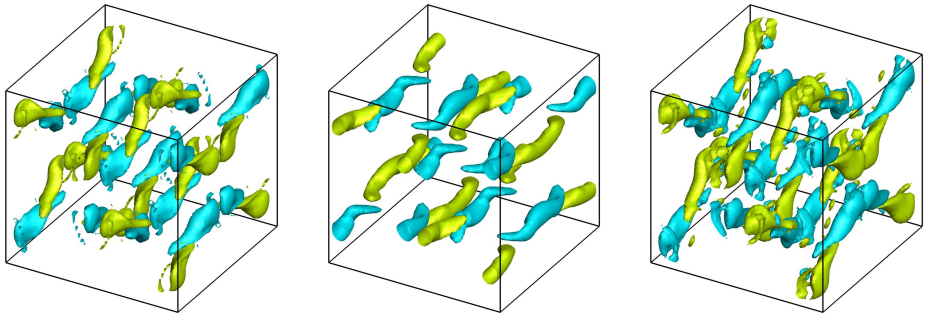

(d) AD-TF (e) AD-SF (f) AD-7PF

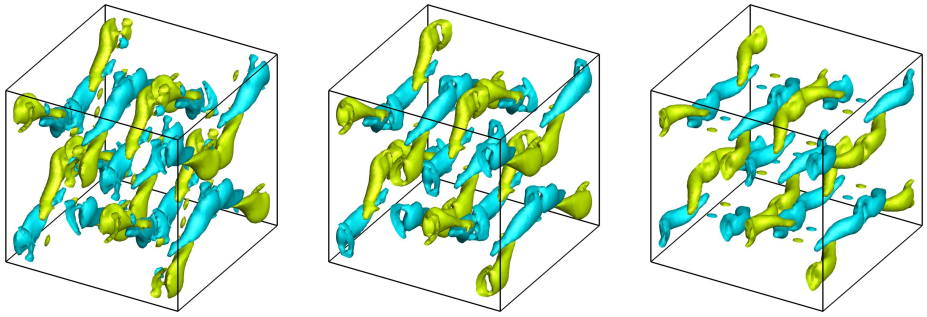

(g) AD-PF ($\alpha = 0.25$) (h) AD-PF ($\alpha = 0.15$) (i) AD-PF ($\alpha = -0.15$)

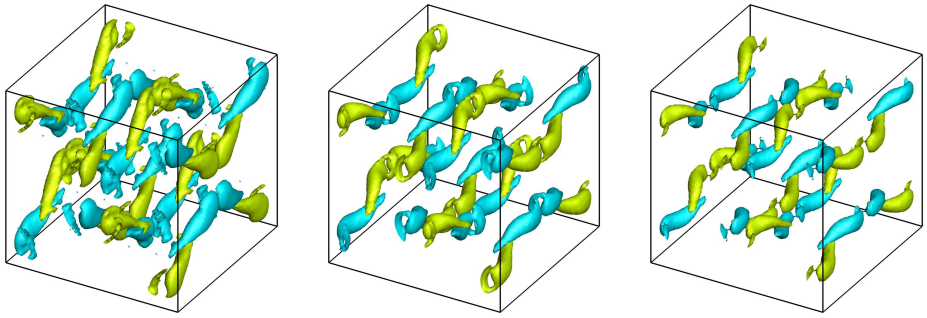

(j) AD-DF ($\gamma = 0.5$) (k) AD-DF ($\gamma = 0.8$) (l) AD-DF ($\gamma = 1.0$)

Figure 8.20: Isosurfaces of $\omega_x = \pm 2.0$ at time $t = 10$ using $N = 5$ for the AD-LES models.

Chapter 9

Conclusions and Future Work

I am an old man now, and when I die and go to Heaven there are two matters on which I hope enlightenment. One is quantum electro-dynamics and the other is turbulence. About the former, I am really rather optimistic.

H. Lamb (1932)

Quite consistently, it has also been said that turbulence is the invention of the Devil, put on Earth to torment us.

G. K. Vallis (2006)

9.1 Summary and concluding remarks

Geophysical flows displays an enormous range of temporal and spatial scales, from seconds to decades, and from centimeters to thousands of kilometers. Therefore, a model incorporating all the relevant physics of the ocean and atmosphere would be impractical for numerical simulations. During the past decades, significant achievements were made in developing simplified mathematical models for geophysical fluid dynamics, such as the *Boussinesq equations*, the

primitive equations, the *quasigeostrophic equations*, and the *shallow water equations*, which have been instrumental in providing relatively accurate numerical results at a reasonable computational price. These models form the basis of highly successful applications and research at numerous weather and climate centers. Consequently, developing accurate and efficient numerical methods for geophysical flows is of paramount importance in numerical weather prediction and long-term climate modeling. To decrease the computational cost for accurate representations of the numerous computationally intensive problems of geophysical fluid dynamics (GFD), in this thesis, we performed a dedicated investigation of the development and testing of several types of modern multiscale modeling and simulation (MMS) methods. The main effort in our research consisted of new applications of interpolation based approaches in the context of the multigrid/multiresolution framework and approximate deconvolution based structural models in the context of the large eddy simulation framework.

First, we presented a coarse-grid projection (CGP) method: an acceleration technique for reducing the computational time for incompressible flow solvers involving an elliptic Poisson equation. The underpinning idea behind the CGP is to use a smaller number of grid points for solving this elliptic constraint equation. One of the important aspects of the CGP approach proposed in this thesis is the modularity of the method. The CGP method is independent of the Poisson solver that is used. It doesn't require changing anything in the existing black-box Poisson solver. The same is true for the algorithm for the advection-diffusion part of governing equations. Here, we developed a particular CGP method, CGPRK3, that uses the full weighting operation for mapping from fine to coarse grids, the third-order Runge-Kutta method for time stepping, and finite differences for the spatial discretization. After solving the Poisson equation on a coarsened grid, bilinear interpolation is used to obtain the fine data for consequent time stepping on the full grid. We add the costs of the restriction and prolongation operations to the solver, but we save much more computational time in solving the elliptic system because the Poisson equation is solved on a coarser grid. In our study, we intentionally used optimal Poisson solvers with linear computational cost, either a FFT-

based fast Poisson solver or a V-cycle multigrid Poisson solver, as our black-box solver. We also showed that the speed-up of the CGP method increases dramatically for versions of the method that use other, suboptimal, Poisson solvers (which are generally $O(N^2)$).

The success of applying this interpolation based multiscale method relies on the different levels of complexity for different parts of the mathematical formulations. The computational cost per time step of the pressure-based methods is that of solving a vector-valued parabolic-type advection-diffusion equation and a scalar-valued elliptic-type Poisson equation. The number of Poisson equations that must be solved at each time step varies with the formulations and the problem dimensions, but for all the pressure-based methods, solving the Poisson equation usually takes considerably more computational resources than solving the advection-diffusion type equation, especially for large scale problems and high Reynolds number flows. In our study, CGP was applied to three different formulations of the Navier-Stokes equations: the primitive variable fractional step formulation, the vorticity-stream function formulation, and the vorticity-velocity formulations. In the context of the present study, all these formulations have in common a Poisson equation needs to be solved at every time step that takes most of the computational effort within that step.

Several carefully chosen two- and three-dimensional test problems were solved using the coarse-grid projection method in order to demonstrate its robustness and efficacy. We demonstrated that, for one-level of coarsening, it is possible to accelerate simulations without a loss of accuracy by utilizing simple averaging and interpolations between the advection-diffusion part of the solver and the elliptic Poisson part. For two further levels of grid coarsening (reducing the number of grid points in each direction by factors of 4 and 8, respectively), increased reductions in computational time were found, but the accuracy of the fine resolution field data was reduced at each level of coarsening. Speed-up factors between 2 and 42 were documented using the CGP method, and the speedup obtained was found to increase with increasing resolution of the fine-level field data, as was expected. We also found that the acceleration rate of the computations due to CGP increases with the grid distortion ratio in curvilinear grid settings. The results of these computations demonstrated that the CGP

approach is well suited for accelerating incompressible flow solvers that require the solution of a Poisson equation as a constraint to produce a divergence-free field.

Next, the CGP method was applied to large scale ocean circulation problems solving one-layer and two-layer quaisgeostropic (QG) equations for mid-latitude oceanic basins in the beta plane, which are standard prototypes of more realistic ocean dynamics. Most of the demand on computational resources of these quasigeostrophic models comes in the solution of the elliptic inversion of the sub-problem. The natural advantages of quasigeostrophic models may well lead to increased application when efficient methods available for solving the elliptic sub-problem. The idea in the CGP method is straightforward: since solving elliptic inversion sub-problem (i.e., kinematic relationships between the stream functions and the potential vorticity in fluid layers) is the most computationally intensive, this is solved on a coarse mesh in the new algorithm, the potential vorticity transport equations are solved on the fine mesh. The CGP method was tested on meshes that were coarser than those used for the direct numerical simulation (DNS) computations. The CGP method yielded numerical results that were in close agreement with those of the DNS for both barotropic and stratified ocean circulation models. The method was found to accelerate these computations while retaining the same level of accuracy in the fine-resolution field. In particular, we demonstrated that the new CGP models with both one-level and multiple-level coarsening yield improved results by smoothing out the numerical oscillations present in the results obtained by under-resolved standard computations without the CGP procedure. This first step in the numerical assessment of the proposed ocean circulation models showed that CGP methodology could represent a viable tool for QG models of more realistic turbulent geophysical flows.

To further analyze truncation errors, both the temporal and spatial discretization errors, the performance of several high-order accurate numerical schemes was investigated for the DNS of homogeneous isotropic two-dimensional decaying turbulent flows. Numerical schemes used for the integration of complex flow simulations should provide accurate solutions for the long time integrations these flows require. To this end, four different finite difference formu-

lations (i.e., compact difference, explicit central difference, Arakawa, and dispersion-relation-preserving schemes) were analyzed and compared with the Fourier-Galerkin pseudospectral scheme. We also tested the efficiency, accuracy and numerical stability of several variants of third- and fourth-order Runge-Kutta time stepping algorithms for decaying two-dimensional turbulence. We serendipitously found during the course of our numerical investigations that the spatially second-order accurate schemes can run using almost triple the effective time step compared with the sixth-order schemes, and can also run using almost double the effective time step compared with the fourth-order schemes, thereby making them more competitive with the high-order finite difference schemes. On the other hand, we showed that the second-order schemes usually require double the resolution in each direction to be able to obtain a similar accuracy. Therefore, we demonstrated that higher order schemes become more effective in terms of the tradeoff between the accuracy and efficiency. We also pointed out that the centered schemes suffer from spurious Nyquist signals that are generated almost instantaneously and propagate into much of the field when the numerical resolution is insufficient. We further showed that the order of the scheme becomes increasingly important for increasing cell Reynolds number. Our results also demonstrated that, contrary to conventional wisdom, difference methods demonstrate superior performance in terms of accuracy and efficiency for fully resolved DNS computations of the complex flows considered here. Although the order of accuracy is less important for well-resolved DNS computations, we numerically demonstrated that it becomes significant for under-resolved simulations having the critical cell Reynolds number $Re_c > 2$.

Two-dimensional forced-dissipative turbulence models are inevitably useful for understanding large scale motions of geophysical flows occurring in the atmosphere and oceans. The scale specific characteristics of both the frictional and forcing effects are also crucial to understanding the dynamics of these systems. In contrast to freely evolving turbulence, the motion in stationary turbulence is continuously stimulated by energy which is injected into the flow at some scale through the action of some prescribed body force. The statistics of such a forced-dissipative two-dimensional turbulence system were investigated here for a

wide range of physical considerations. Specifically, we computed the statistics in terms of the evolution of total kinetic energy, angle averaged energy spectrum, and second-order vorticity structure function. One of our major goals was to analyze the universality of the scaling laws for these statistics in both wave space and physical space. To this end, a Markovian forcing scheme, which correlates the forcing process in the current time step to the previous time step according to a defined memory coefficient, was developed using a Fourier-Galerkin pseodospectral method. To characterize the damping effects, the hyperviscous dissipation mechanism for small scales and the Ekman friction type of linear damping mechanism for the large scales were also included in the model. We demonstrated that the scaling exponents are approximately invariant and show a universal behavior for the various forms of forcing schemes used. We found, however, that the final states strongly depend on the large scale friction mechanism considered. Finally, although turbulence is not believed to have a separation of time scales in the dynamics of the velocity field, we observed that a separation of time scales exists in the dynamics of the energy spectrum.

Next, we present a structural large eddy simulation (LES) technique for large scale ocean circulation problems. The idea of spatial filtering is central in LES: the large spatially filtered flow variables are approximated, whereas the effect if small scales are modeled. The use of techniques of LES allows one to reduce the computational cost by computing the problem using smaller number of grid points with a closure model which accounts for the subgrid scale effects. The most popular LES modeling strategy is based on increasing the effective viscosity of the system which, in practice, results in higher damping for the undesired numerical oscillations. This eddy viscosity approach, although very successful in engineering flows, would be arguable for turbulent geophysical flows, which usually display different characteristics such as the inverse energy cascade mechanism, Ekman pumping, rotational beta effects, and density stratification. In this thesis, we were the first to propose the use of approximate deconvolution (AD) closure modeling strategies, which employ repeated filtering of the filtered variables to obtain an approximation of unfiltered variables, to large scale geostrophic flows. As one of the important features of the proposed method, the AD

is based on only mathematical approximations of a truncated series of repeated filtering operations and does not employ any phenomenological arguments to the model. The AD model was applied to the barotropic double gyre circulation problem, a benchmark oceanic flow problem whose behavior is difficult to capture correctly for under-resolved computations. It was found that the well-resolved DNS computation with a resolution of 512×256 displayed four gyres. However, on a significantly coarser mesh (32×16), the AD model correctly captured these four gyres, whereas the no-model simulation with the same coarse mesh displayed unphysical results.

After the success of the AD method for the barotropic vorticity equation for a one-layer ocean model, we extended our analysis by developing the AD subgrid-scale modeling framework for two-layer quasigeostrophic (QG2) wind-driven oceanic flows. We highlight that the AD approach requires a consistent filtering operator to obtain approximations for the unfiltered subgrid-scale contribution when the resolved flow variables are available. Two variants of the AD method were proposed: one with the tridiagonal filter (AD-TF); and the other with the differential filter (AD-DF). We applied these procedures to mid-latitude two-layer square oceanic basins which are standard prototypes of more realistic stratified ocean dynamics models. A detailed sensitivity analysis of the AD parameters was also performed in a systematic way.

By comparing it to high-resolution direct numerical simulation, it was found that the AD-TF method yields good approximations for under-resolved flow simulations where the Munk layer is smaller than the grid size. It was also shown that the AD-TF procedure does not add extra dissipation to the system due to the repeating pointwise tridiagonal filtering operations to obtain a better non-oscillatory flow fields for a reduced resolution computations. We demonstrated that the AD-TF method is quite robust, eliminates numerical oscillations and provides more accurate results for under-resolved simulations by considering the subgrid-scale effects. Indeed, the under-resolved numerical simulations without AD-TF modeling on the same coarse mesh as that employed by the AD-TF model produced inaccurate results. Moreover, the CPU time of the AD-TF models was much more lower than that of the fully

resolved simulations.

The differential filter, however, adds a significant amount of numerical dissipation to the AD-LES model. Therefore, AD-DF method yields the physically relevant statically steady state level for a higher Reynolds number. To further investigate this behavior, we performed a systematic study of AD-DF by varying the amount of eddy viscosity coefficient. This study showed that the AD-DF procedure does provide an extra dissipation to system by regularizing subgrid-scale effects. This lead us to simulate higher Reynolds number flows with smaller viscosity coefficients. We also showed that the amount of ad-hoc eddy viscosity coefficient in the model can be quantified by the AD-DF procedure which is based on solely mathematical approximations using a repeated Helmholtz operations. This analysis provides a purely mathematical foundation to the eddy viscosity concept. The amount of eddy viscosity coefficient is somehow arbitrarily chosen in the ocean models. Our analysis puts forth a first connection to the appropriate amount of viscosity by using a solely mathematical subgrid-scale LES approach.

We emphasize that two forms of the approximate deconvolution method, both the AD-TF method and the AD-DF method, yielded solutions within the physically relevant energy levels, but with different dissipative characteristics. With this in mind, we finally performed an error analysis study for various low-pass spatial filters for approximate deconvolution large eddy simulation (AD-LES) of turbulent incompressible flows. Box filters, Pade filters and differential filters within a wide range of parameters were studied in the AD-LES framework. The AD-LES model, in conjunction with these spatial filters, was tested in the numerical simulation of the three-dimensional Taylor-Green vortex problem, which is perhaps the simplest system in which to study the generation of increasingly smaller scale motions and the resulting turbulence. The numerical results were benchmarked against DNS data. An under-resolved numerical simulation was also used for comparison purposes. First, the AD-LES model equipped with any of these spatial filters yielded accurate results at a fraction of the computational cost of the DNS. Second, the most accurate results were obtained with the hyper-differential filter, followed by the differential filter. Although a careful parameter

choice makes each class of filters competitive, it was found that filters whose transfer function resembles that of the Fourier cut-off filter (such as the hyper-differential filter) performed best.

9.2 Recommendations for future research

The development and testing of several modern multiscale methods for geophysical flows were presented and very promising results were obtained in this study. There are, however, a few promising directions for future study. First, this dissertation is centered around the quasigeostrophic equations, which models a rich variety of systems in physical oceanography. In continuing studies, the proposed methodologies can be extended to other mathematical models in the hierarchy of geophysical fluid dynamics such as the Boussinesq equations, the primitive equations, or the shallow water equations. Second, an extension of the present methodologies to atmospheric flows (e.g., density gravity flow problems) is a highly logical next step.

Almost all large-scale ocean circulation problems use some sort of ad-hoc eddy viscosity coefficient. The development of a rigorous, mathematical understanding and subsequent modeling strategy for eddy viscosity coefficients is one of the major unsolved problems in ocean modeling. Although this dissertation does not provide a rigorous mathematical basis to the longstanding quest to find the origin of and for modeling the eddy viscosity coefficients, it puts forth a novel approach to finding them, serendipitously discovered during the course of our numerical investigations. We feel that the main strength of this new approach is its ability to disentangle the modeling error from the numerical discretization error and to study it separately in this new approximate deconvolution large eddy simulation (AD-LES) framework. In any continuation of this project, further applications of different filters should be incorporated into the AD-LES method. Another interesting direction for future work is in monitoring the modelling error due to the relevant filtering parameters in the

approximate deconvolution method. Having a quantitative measure of the error would allow one to automate the method completely.

The current study yielded promising results for structured Cartesian and curvilinear grids using the coarse-grid projection (CGP) methodology. Three-dimensional computations also suggested that the CGP method can be used to accelerate the direct numerical simulations (DNS) of turbulence by coarsening the number of grid points for the Poisson solver without affecting the well resolved DNS data. The investigation of the behavior of the CGP framework for high Reynolds number turbulent flows could be an interesting followup study, possibly including results for inhomogeneous wall-bounded turbulent channel flow problems. It would be a worthwhile study to now simulate several high Reynolds number unsteady flow problems, and understand how different prolongation and restriction mapping operators influence the accuracy of the CGP method. The mapping procedures used in this study could potentially be improved by introducing higher-order spline formulas, or more advanced methods for deriving interpolations. This could be extremely useful for designing high-order accurate CGP algorithms. In addition to the finite difference framework, it is also quite natural to seek other approximation schemes for applications of the CGP methodology.

Our two-dimensional turbulence computations showed that there is a separation of time scales in the dynamics of the energy spectrum, such that energy is transferred quickly in the forward enstrophy cascade range, while the shape of the spectrum fills out slowly, until, after a long time, the final statistically steady state Kolmogorov spectrum appears in the inverse energy cascade range. This separation of time scales in the energy spectrum might be a useful starting point for developing multiscale computational algorithms for turbulence research, a topic that could be very worthwhile to investigate further in a future study. Another important area for future work is the investigation of the turbulence statistics of two-dimensional turbulence and their universality for confined flows with finite boundaries.

Finally, we emphasize that a large part of the dissertation is devoted to the understanding the behavior of the AD method. In testing the AD methodology, the numerical approach was

centered around a second-order finite difference discretization for the governing equations. Although this type of discretization can be encountered in numerous practical applications, we emphasize that higher-order discretizations could be used in the AD-LES framework. Thus, a natural question is whether the qualitative conclusions drawn from the second-order numerical discretization case extend to the higher-order numerical discretization case, and if they do, to what extent these conclusions carry over. Therefore, the development of high-order accurate AD-LES method is highly recommended. In order to better understand the AD-LES method, equipped with various filters, it should be further developed for non-homogeneous flows applications such as the three-dimensional cavity and channel flow problems. Extensions of the AD-LES model to more complex engineering or geophysical flow problems such as these may further highlight its advantages and robustness. It would also be of interest to design a comparative study on the performances of the AD-LES and the standard eddy viscosity models for geophysical flows.

Bibliography

N. A. Adams and S. Stolz, "A subgrid-scale deconvolution approach for shock capturing," *Journal of Computational Physics*, vol. 178, pp. 391–426, 2002.

N. A. Adams, S. Hickel, and J. A. Domaradzki, "Approximate deconvolution," in *Implicit large eddy simulation: computing turbulent fluid dynamics*, F. F. Grinstein, L. G. Margolin, and W. Rider, Eds. Cambridge University Press, New York, 2007, pp. 222–242.

J. M. Alam, "Towards a multiscale approach for computational atmospheric modelling," *Monthly Weather Review*, vol. 139, pp. 3906–3922, 2011.

A. A. Aldama, *Filtering techniques for turbulent flow simulation.* Springer-Verlag, Berlin, 1990.

J. S. Allen, "Models of wind-driven currents on the continental shelf," *Annual Review of Fluid Mechanics*, vol. 12, pp. 389–433, 1980.

A. Arakawa, "Computational design for long-term numerical integration of the equations of fluid motion: Two-dimensional incompressible flow. Part I," *Journal of Computational Physics*, vol. 1, pp. 119–143, 1966.

E. Awad, E. Toorman, and C. Lacor, "Large eddy simulations for quasi-2D turbulence in shallow flows: A comparison between different subgrid scale models," *Journal of Marine Systems*, vol. 77, pp. 511–528, 2009.

E. Balaras, C. Benocci, and U. Piomelli, "Finite-difference computations of high Reynolds number flows using the dynamic subgrid-scale model," *Theoretical and Computational Fluid Dynamics*, vol. 7, no. 3, pp. 207–216, 1995.

T. J. Barth, T. F. Chan, and R. Haimes, *Multiscale and multiresolution methods: Theory and applications*. Springer-Verlag, Berlin, 2002.

G. K. Batchelor, "Computation of the energy spectrum in homogeneous two-dimensional turbulence," *Physics of Fluids*, vol. 12, pp. 233–239, 1969.

J. B. Bell, P. Colella, and H. M. Glaz, "A second-order projection method for the incompressible Navier-Stokes equations," *Journal of Computational Physics*, vol. 85, pp. 257–283, 1989.

R. Benzi, G. Paladin, and A. Vulpiani, "Power spectra in two-dimensional turbulence," *Physical Review A*, vol. 42, no. 6, pp. 3654–3656, 1990.

P. S. Berloff and J. C. McWilliams, "Large-scale, low-frequency variability in wind-driven ocean gyres," *Journal of Physical Oceanography*, vol. 29, pp. 1925–1949, 1999.

P. S. Berloff, I. Kamenkovich, and J. Pedlosky, "A mechanism of formation of multiple zonal jets in the oceans," *Journal of Fluid Mechanics*, vol. 628, pp. 395–425, 2009.

L. C. Berselli, "On the large eddy simulation of the Taylor–Green vortex," *Journal of Mathematical Fluid Mechanics*, vol. 7, pp. 164–191, 2005.

L. C. Berselli and R. Lewandowski, "Convergence of approximate deconvolution models to the mean Navier–Stokes equations," *Annales de l'Institut Henri Poincare (C) Non Linear Analysis*, vol. 29, no. 2, pp. 171–198, 2012.

L. C. Berselli, T. Iliescu, and W. J. Layton, *Mathematics of large eddy simulation of turbulent flows*. Springer-Verlag, Berlin, 2006.

M. Bertero and P. Boccacci, *Introduction to inverse problems in imaging.* Institute of Physics Publishing, Bristol, 1998.

L. A. K. Blackbourn and C. V. Tran, "Effects of friction on forced two-dimensional Navier-Stokes turbulence," *Physical Review E*, vol. 84, no. 4, pp. 046 322 (1–6), 2011.

J. Blasco, R. Codina, and A. Huerta, "A fractional-step method for the incompressible Navier-Stokes equations related to a predictor-multicorrector algorithm," *International Journal for Numerical Methods in Fluids*, vol. 28, pp. 1391–1419, 1998.

G. J. Boer and T. G. Shepherd, "Large-scale two-dimensional turbulence in the atmosphere," *Journal of Atmospheric Sciences*, vol. 40, pp. 164–184, 1983.

G. Boffetta and R. E. Ecke, "Two-dimensional turbulence," *Annual Review of Fluid Mechanics*, vol. 44, pp. 427–451, 2012.

G. Boffetta and S. Musacchio, "Evidence for the double cascade scenario in two-dimensional turbulence," *Physical Review E*, vol. 82, pp. 016 307 (1–5), 2010.

V. Borue, "Spectral exponents of enstrophy cascade in stationary two-dimensional homogeneous turbulence," *Physical Review Letters*, vol. 71, no. 24, pp. 3967–3970, 1993.

R. Bouffanais, "Advances and challenges of applied large-eddy simulation," *Computers & Fluids*, vol. 39, no. 5, pp. 735–738, 2010.

A. Bracco and J. C. McWilliams, "Reynolds-number dependency in homogeneous, stationary two-dimensional turbulence," *Journal of Fluid Mechanics*, vol. 646, pp. 517–526, 2010.

M. E. Brachet, "Direct simulation of three-dimensional turbulence in the Taylor-Green vortex," *Fluid Dynamics Research*, vol. 8, no. 1, pp. 1–8, 1991.

M. E. Brachet, D. I. Meiron, S. A. Orszag, B. G. Nickel, R. H. Morf, and U. Frisch, "Small-scale structure of the Taylor-Green vortex," *Journal of Fluid Mechanics*, vol. 130, pp. 411–452, 1983.

M. E. Brachet, M. Meneguzzi, H. Politano, and P. L. Sulem, "The dynamics of freely decaying two-dimensional turbulence," *Journal of Fluid Mechanics*, vol. 194, pp. 333–349, 1988.

M. E. Brachet, M. Meneguzzi, A. Vincent, H. Politano, and P. L. Sulem, "Numerical evidence of smooth self-similar dynamics and possibility of subsequent collapse for three-dimensional ideal flows," *Physics of Fluids*, vol. 4, pp. 2845–2854, 1992.

A. Brandenburg, "Computational aspects of astrophysical MHD and turbulence," in *Advances in Nonlinear Dynamos, The Fluid Mechanics of Astrophysics and Geophysics*, A. Ferriz-Mas and M. Núnez, Eds., vol. 9. Taylor & Francis, New York, 2003, pp. 269–344.

A. Brandt, "Multi-level adaptive solutions to boundary value problems," *Mathematics of Computation*, vol. 31, pp. 333–390, 1977.

——, "Multiscale scientific computation: Review 2001," in *Lecture Notes in Computational Science and Engineering*, T. J. Barth, T. Chan, and R. Haimes, Eds., vol. 20. Springer-Verlag, Heidelberg, 2002, pp. 3–96.

——, "Multiscale solvers and systematic upscaling in computational physics," *Computer Physics Communications*, vol. 169, pp. 438–441, 2005.

——, "Principles of systematic upscaling," in *Multiscale methods: Bridging the scales in science and engineering*, J. Fish, Ed. Oxford University Press, New York, 2010, pp. 193–215.

T. Brandt, "A priori tests on numerical errors in large eddy simulation using finite differences and explicit filtering," *International Journal for Numerical Methods in Fluids*, vol. 51, no. 6, pp. 635–657, 2006.

M. Brezina, R. Falgout, S. MacLachlan, T. Manteuffel, S. F. McCormick, and J. Ruge, "Adaptive smoothed aggregation (αSA) multigrid," *SIAM Review*, pp. 317–346, 2005.

W. L. Briggs, V. E. Henson, and S. F. McCormick, *A multigrid tutorial*. Society for Industrial and Applied Mathematics, Pennsylvania, 2000.

D. L. Brown, R. Cortez, and M. L. Minion, "Accurate projection methods for the incompressible Navier-Stokes equations," *Journal of Computational Physics*, vol. 168, pp. 464–499, 2001.

C. H. Bruneau and P. Fischer, "Influence of the filtering tools on the analysis of two-dimensional turbulent flows," *Computers & Fluids*, vol. 38, no. 7, pp. 1324–1337, 2009.

F. Bryan, "Parameter sensitivity of primitive equation ocean general circulation models," *Journal of Physical Oceanography*, vol. 17, no. 7, pp. 970–985, 1987.

K. Bryan, "A numerical investigation of a nonlinear model of a wind-driven ocean," *Journal of Atmospheric Sciences*, vol. 20, pp. 594–606, 1963.

J. D. Buntine and D. I. Pullin, "Merger and cancellation of strained vortices," *Journal of Fluid Mechanics*, vol. 205, pp. 263–295, 1989.

J. C. Butcher, *Numerical methods for ordinary differential equations*. John Wiley & Sons, England, 2003.

J. M. Campin, C. Hill, H. Jones, and J. Marshall, "Super-parameterization in ocean modeling: Application to deep convection," *Ocean Modelling*, vol. 36, pp. 90–101, 2011.

C. Canuto, *Spectral methods: Fundamentals in single domains*. Springer-Verlag, New York, 2006.

C. Canuto, M. Y. Hussaini, A. Quarteroni, and T. A. Zang, *Spectral methods in fluid dynamics*. Springer-Verlag, New York, 1988.

M. H. Carpenter, C. A. Kennedy, H. Bijl, S. A. Viken, and V. N. Vatsa, "Fourth-order Runge-Kutta schemes for fluid mechanics applications," *Journal of Scientific Computing*, vol. 25, no. 1, pp. 157–194, 2005.

A. Celani and A. Seminara, "Large-scale structure of passive scalar turbulence," *Physical Review Letters*, vol. 94, no. 21, pp. 214 503 (1–4), 2005.

K. I. Chang, M. Ghil, K. Ide, and C. C. A. Lai, "Transition to aperiodic variability in a wind-driven double-gyre circulation model," *Journal of Physical Oceanography*, vol. 31, pp. 1260–1286, 2001.

J. G. Charney, "Geostrophic turbulence," *Journal of Atmospheric Sciences*, vol. 28, pp. 1087–1094, 1971.

Q. Chen, M. Gunzburger, and T. Ringler, "A scale-invariant formulation of the anticipated potential vorticity method," *Monthly Weather Review*, vol. 139, pp. 2614–2629, 2011.

S. Chen, R. E. Ecke, G. L. Eyink, X. Wang, and Z. Xiao, "Physical mechanism of the two-dimensional enstrophy cascade," *Physical Review Letters*, vol. 91, pp. 214 501 (1–4), 2003.

D. Choi and C. L. Merkle, "Application of time-iterative schemes to incompressible flow," *AIAA Journal*, vol. 23, pp. 1518–1524, 1985.

H. Choi and P. Moin, "Effects of the computational time step on numerical solutions of turbulent flow," *Journal of Computational Physics*, vol. 113, pp. 1–4, 1994.

J. I. Choi, R. C. Oberoi, J. R. Edwards, and J. A. Rosati, "An immersed boundary method for complex incompressible flows," *Journal of Computational Physics*, vol. 224, pp. 757–784, 2007.

A. J. Chorin, "A numerical method for solving incompressible viscous flow problems," *Journal of Computational Physics*, vol. 2, pp. 12–26, 1967.

——, "Numerical solution of the Navier-Stokes equations," *Mathematics of Computation*, vol. 22, pp. 745–762, 1968.

F. K. Chow and R. L. Street, "Evaluation of turbulence closure models for large-eddy simulation over complex terrain: Flow over Askervein Hill," *Journal of Applied Meteorology and Climatology*, vol. 48, pp. 1050–1065, 2009.

F. K. Chow, R. L. Street, M. Xue, and J. H. Ferziger, "Explicit filtering and reconstruction turbulence modeling for large-eddy simulation of neutral boundary layer flow," *Journal of Atmospheric Sciences*, vol. 62, pp. 2058–2077, 2005.

H. J. H. Clercx and G. J. F. van Heijst, "Two-dimensional Navier-Stokes turbulence in bounded domains," *Applied Mechanics Reviews*, vol. 62, no. 2, pp. 020 802 (1–25), 2009.

R. Cocle, L. Bricteux, and G. Winckelmans, "Scale dependence and asymptotic very high Reynolds number spectral behavior of multiscale subgrid models," *Physics of Fluids*, vol. 21, pp. 085 101 (1–12), 2009.

M. Coutanceau and R. Bouard, "Experimental determination of the main features of the viscous flow in the wake of a circular cylinder in uniform translation. Part 1. Steady flow," *Journal of Fluid Mechanics*, vol. 79, pp. 231–256, 1977.

P. F. Cummins, "Inertial gyres in decaying and forced geostrophic turbulence," *Journal of Marine Research*, vol. 50, pp. 545–566, 1992.

B. Cushman-Roisin, *Introduction to geophysical fluid dynamics*. Prentice-Hall, New Jersey, 1994.

B. Cushman-Roisin and J. M. Beckers, *Introduction to geophysical fluid dynamics: Physical and numerical aspects*. Academic Press, New York, 2011.

S. D. Danilov and D. Gurarie, "Quasi-two-dimensional turbulence," *Physics-Uspekhi*, vol. 43, pp. 863–900, 2000.

——, "Forced two-dimensional turbulence in spectral and physical space," *Physical Review E*, vol. 63, no. 6, pp. 061 208 (1–12), 2001.

——, "Nonuniversal features of forced two-dimensional turbulence in the energy range," *Physical Review E*, vol. 63, no. 2, pp. 020 203 (1–4), 2001.

P. A. Davidson, *Turbulence: An introduction for scientists and engineers.* Oxford University Press, New York, 2004.

S. C. R. Dennis and G. Z. Chang, "Numerical solutions for steady flow past a circular cylinder at Reynolds numbers up to 100," *Journal of Fluid Mechanics*, vol. 42, pp. 471–489, 1970.

S. C. R. Dennis, D. B. Ingham, and R. N. Cook, "Finite-difference methods for calculating steady incompressible flows in three dimensions," *Journal of Computational Physics*, vol. 33, no. 3, pp. 325–339, 1979.

M. T. DiBattista and A. J. Majda, "Equilibrium statistical predictions for baroclinic vortices: The role of angular momentum," *Theoretical and Computational Fluid Dynamics*, vol. 14, pp. 293–322, 2001.

H. A. Dijkstra, *Nonlinear physical oceanography.* Springer-Verlag, New York, 2005.

H. A. Dijkstra and M. Ghil, "Low-frequency variability of the large-scale ocean circulation: A dynamical systems approach," *Reviews of Geophysics*, vol. 43, pp. 122–59, 2005.

J. A. Domaradzki and N. A. Adams, "Direct modelling of subgrid scales of turbulence in large eddy simulations," *Journal of Turbulence*, vol. 3, pp. 1–19, 2002.

D. Drikakis, C. Fureby, F. F. Grinstein, and D. Youngs, "Simulation of transition and turbulence decay in the Taylor–Green vortex," *Journal of Turbulence*, vol. 8, no. 20, pp. 1–12, 2007.

D. Drikakis, M. Hahn, A. Mosedale, and B. Thornber, "Large eddy simulation using high-resolution and high-order methods," *Philosophical Transactions of the Royal Society A: Mathematical, Physical and Engineering Sciences*, vol. 367, no. 1899, pp. 2985–2997, 2009.

J. Duan, P. Fischer, T. Iliescu, and T. M. Özgökmen, "Bridging the Boussinesq and primitive equations through spatio-temporal filtering," *Applied Mathematics Letters*, vol. 23, pp. 453–456, 2010.

A. Dunca and Y. Epshteyn, "On the Stolz–Adams deconvolution model for the large-eddy simulation of turbulent flows," *SIAM Journal on Mathematical Analysis*, vol. 37, pp. 1890–1902, 2006.

A. A. Dunca, "On the existence of global attractors of the approximate deconvolution models of turbulence," *Journal of Mathematical Analysis and Applications*, vol. 389, no. 2, pp. 1128–1138, 2011.

D. R. Durran, *Numerical methods for fluid dynamics: With applications to geophysics*. Springer Verlag, 2010.

W. E, *Principles of multiscale modeling*. Cambridge University Press, New York, 2011.

W. E, B. Engquist, X. Li, W. Ren, and E. Vanden-Eijnden, "The heterogeneous multiscale method: A review," *Communications in Computational Physics*, vol. 2, pp. 367–450, 2007.

J. A. Ekaterinaris, "High-order accurate, low numerical diffusion methods for aerodynamics," *Progress in Aerospace Sciences*, vol. 41, pp. 192–300, 2005.

S. Espa, G. F. Carnevale, A. Cenedese, and M. Mariani, "Quasi-two-dimensional decaying turbulence subject to the β effect," *Journal of Turbulence*, vol. 9, pp. 1–18, 2008.

G. Falkovich and A. Fouxon, "Anomalous scaling of a passive scalar in turbulence and in equilibrium," *Physical Review Letters*, vol. 94, no. 21, p. 214502, 2005.

H. Fasel, "Investigation of the stability of boundary layers by a finite-difference model of the Navier-Stokes equations," *Journal of Fluid Mechanics*, vol. 78, pp. 355–383, 1976.

H. F. Fasel, "Numerical investigation of the interaction of the Klebanoff-mode with a Tollmien-Schlichting wave," *Journal of Fluid Mechanics*, vol. 450, pp. 1–34, 2002.

H. F. Fasel, U. Rist, and U. Konzelmann, "Numerical investigation of the three-dimensional development in boundary-layer transition," *AIAA Journal*, vol. 28, pp. 29–37, 1990.

J. H. Ferziger, M. Peric, and K. W. Morton, *Computational methods for fluid dynamics*. Springer-Verlag, Berlin, 1999.

J. H. Ferziger, J. R. Koseff, and S. G. Monismith, "Numerical simulation of geophysical turbulence," *Computers & Fluids*, vol. 31, pp. 557–568, 2002.

J. Fish, *Multiscale methods: Bridging the scales in science and engineering*. Oxford University Press, New York, 2009.

J. Fish and W. Chen, "Discrete-to-continuum bridging based on multigrid principles," *Computer Methods in Applied Mechanics and Engineering*, vol. 193, pp. 1693–1711, 2004.

S. Fox and P. A. Davidson, "Freely decaying two-dimensional turbulence," *Journal of Fluid Mechanics*, vol. 659, pp. 351–364, 2010.

B. Fox-Kemper, "Reevaluating the roles of eddies in multiple barotropic wind-driven gyres," *Journal of Physical Oceanography*, vol. 35, pp. 1263–1278, 2005.

B. Fox-Kemper and D. Menemenlis, "Can large eddy simulation techniques improve mesoscale rich ocean models?" in *Ocean Modeling in an Eddying Regime, Geophysical Monograph Series*, M. Hecht and H. Hasumi, Eds., vol. 177. American Geophysical Union, Washington, DC, 2008, pp. 319–338.

U. Frisch, *Turbulence*. Cambridge University Press, Cambridge, UK, 1995.

M. C. Galbraith and S. Abdallah, "Implicit solutions of incompressible Navier-Stokes equations using the pressure gradient method," *AIAA Journal*, vol. 49, pp. 2491–2501, 2011.

E. Garnier, P. Sagaut, and N. A. Adams, *Large eddy simulation for compressible flows*. Springer-Verlag, New York, 2009.

W. L. Gates, "A numerical study of transient Rossby waves in a wind-driven homogeneous ocean," *Journal of Atmospheric Sciences*, vol. 25, pp. 3–22, 1968.

M. Germano, "Differential filters of elliptic type," *Physics of Fluids*, vol. 29, pp. 1757–1758, 1986.

——, "Differential filters for the large eddy numerical simulation of turbulent flows," *Physics of Fluids*, vol. 29, pp. 1755–1757, 1986.

——, "A new deconvolution method for large eddy simulation," *Physics of Fluids*, vol. 21, pp. 045 107 (1–3), 2009.

M. Ghil, M. D. Chekroun, and E. Simonnet, "Climate dynamics and fluid mechanics: Natural variability and related uncertainties," *Physica D: Nonlinear Phenomena*, vol. 237, pp. 2111–2126, 2008.

A. E. Gill, *Atmosphere-ocean dynamics*. Academic Press, New York, 1982.

W. I. Goldburg, M. A. Rutgers, and X. L. Wu, "Experiments on turbulence in soap films," *Physica A: Statistical Mechanics and its Applications*, vol. 239, no. 1, pp. 340–349, 1997.

S. Gottlieb and C. W. Shu, "Total variation diminishing Runge-Kutta schemes," *Mathematics of Computation*, vol. 67, pp. 73–85, 1998.

R. J. Greatbatch and B. T. Nadiga, "Four-gyre circulation in a barotropic model with double-gyre wind forcing," *Journal of Physical Oceanography*, vol. 30, pp. 1461–1471, 2000.

A. Griffa and R. Salmon, "Wind-driven ocean circulation and equilibrium statistical mechanics," *Journal of Marine Research*, vol. 47, pp. 457–492, 1989.

J. L. Guermond, P. Minev, and J. Shen, "An overview of projection methods for incompressible flows," *Computer Methods in Applied Mechanics and Engineering*, vol. 195, pp. 6011–6045, 2006.

J. Gullbrand and F. K. Chow, "The effect of numerical errors and turbulence models in large-eddy simulations of channel flow, with and without explicit filtering," *Journal of Fluid Mechanics*, vol. 495, pp. 323–341, 2003.

M. M. Gupta, J. Kouatchou, and J. Zhang, "Comparison of second-and fourth-order discretizations for multigrid Poisson solvers," *Journal of Computational Physics*, vol. 132, pp. 226–232, 1997.

M. Habisreutinger, R. Bouffanais, and M. O. Deville, "Grid filter modeling for large-eddy simulation," in *Turbulence and Interactions*, M. O. Deville, T. H. Lê, and P. Sagaut, Eds., vol. 110. Springer-Verlag, Berlin, 2010, pp. 159–165.

M. A. Habisreutinger, R. Bouffanais, E. Leriche, and M. O. Deville, "A coupled approximate deconvolution and dynamic mixed scale model for large-eddy simulation," *Journal of Computational Physics*, vol. 224, pp. 241–266, 2007.

W. Hackbusch, *Multi-grid methods and applications*. Springer-Verlag, Berlin, 1985.

M. M. Hafez and D. Kwak, *Numerical simulations of incompressible flows*. World Scientific, Singapore, 2003.

F. H. Harlow and J. E. Welch, "Numerical calculation of time-dependent viscous incompressible flow of fluid with free surface," *Physics of Fluids*, vol. 8, pp. 2182–2189, 1965.

N. E. L. Haugen and A. Brandenburg, "Inertial range scaling in numerical turbulence with hyperviscosity," *Physical Review E*, vol. 70, no. 2, pp. 026 405 (1–7), 2004.

G. Házi and C. Jiménez, "Simulation of two-dimensional decaying turbulence using the "incompressible" extensions of the lattice Boltzmann method," *Computers & Fluids*, vol. 35, no. 3, pp. 280–303, 2006.

J. R. Herring, S. A. Orszag, R. H. Kraichnan, and D. G. Fox, "Decay of two-dimensional homogeneous turbulence," *Journal of Fluid Mechanics*, vol. 66, pp. 417–444, 1974.

J. O. Hinze, *Turbulence*. McGraw-Hill, New York, 1975.

K. A. Hoffmann and S. T. Chiang, *Computational fluid dynamics, Vol. 1*. Engineering Education System, Kansas, 2000.

W. R. Holland, "The role of mesoscale eddies in the general circulation of the ocean-numerical experiments using a wind-driven quasi-geostrophic model," *Journal of Physical Oceanography*, vol. 8, pp. 363–392, 1978.

W. R. Holland and L. B. Lin, "On the generation of mesoscale eddies and their contribution to the oceanic general circulation. I. A preliminary numerical experiment," *Journal of Physical Oceanography*, vol. 5, pp. 642–657, 1975.

W. R. Holland and P. B. Rhines, "An example of eddy-induced ocean circulation," *Journal of Physical Oceanography*, vol. 10, pp. 1010–1031, 1980.

K. Höllig, U. Reif, and J. Wipper, "Multigrid methods with web-splines," *Numerische Mathematik*, vol. 91, pp. 237–256, 2002.

D. D. Holm and B. T. Nadiga, "Modeling mesoscale turbulence in the barotropic double-gyre circulation," *Journal of Physical Oceanography*, vol. 33, pp. 2355–2365, 2003.

J. R. Holton, *An introduction to dynamic meteorology*. Academic Press, London, 2004.

F. Hourdin and A. Armengaud, "The use of finite-volume methods for atmospheric advection of trace species. Part I: Test of various formulations in a general circulation model," *Monthly Weather Review*, vol. 127, no. 5, pp. 822–837, 1999.

J. Hurrell, G. A. Meehl, D. Bader, T. L. Delworth, B. Kirtman, and B. Wielicki, "A unified modeling approach to climate system prediction," *Bulletin of the American Meteorological Society*, vol. 90, no. 12, pp. 1819–1832, 2009.

T. Iliescu and P. F. Fischer, "Large eddy simulation of turbulent channel flows by the rational large eddy simulation model," *Physics of Fluids*, vol. 15, no. 10, pp. 3036–3047, 2003.

T. Ishihara and Y. Kaneda, "Energy spectrum in the enstrophy transfer range of two-dimensional forced turbulence," *Physics of Fluids*, vol. 13, no. 2, pp. 544–547, 2001.

K. Ishiko, N. Ohnishi, K. Ueno, and K. Sawada, "Implicit large eddy simulation of two-dimensional homogeneous turbulence using weighted compact nonlinear scheme," *Journal of Fluids Engineering*, vol. 131, pp. 061 401 (1–14), 2009.

M. Iskandarani, D. B. Haidvogel, J. C. Levin, E. Curchitser, and C. A. Edwards, "Multi-scale geophysical modeling using the spectral element method," *Computing in Science and Engineering*, vol. 4, pp. 42–48, 2002.

S. Jiang, F. Jin, and M. Ghil, "Multiple equilibria, periodic, and aperiodic solutions in a wind-driven, double-gyre, shallow-water model," *Journal of Physical Oceanography*, vol. 25, pp. 764–786, 1995.

S. A. Jordan and S. A. Ragab, "An efficient fractional-step technique for unsteady incompressible flows using a semi-staggered grid strategy," *Journal of Computational Physics*, vol. 127, pp. 218–225, 1996.

——, "A large-eddy simulation of the shear-driven cavity flow using dynamic modeling," *International Journal of Computational Fluid Dynamics*, vol. 6, no. 4, pp. 321–335, 1996.

Y. Kaneda, T. Ishihara, M. Yokokawa, K. Itakura, and A. Uno, "Energy dissipation rate and energy spectrum in high resolution direct numerical simulations of turbulence in a periodic box," *Physics of Fluids*, vol. 15, no. 2, pp. L21–L24, 2003.

H. Kellay and W. I. Goldburg, "Two-dimensional turbulence: A review of some recent experiments," *Reports on Progress in Physics*, vol. 65, pp. 845–894, 2002.

K. A. Kelly, R. J. Small, R. M. Samelson, B. Qiu, T. M. Joyce, Y. O. Kwon, and M. F. Cronin, "Western boundary currents and frontal air-sea interaction: Gulf Stream and Kuroshio Extension," *Journal of Climate*, vol. 23, pp. 5644–5667, 2010.

N. K. R. Kevlahan, J. Alam, and O. V. Vasilyev, "Scaling of space-time modes with Reynolds number in two-dimensional turbulence," *Journal of Fluid Mechanics*, vol. 570, pp. 217–226, 2007.

I. G. Kevrekidis and G. Samaey, "Equation-free multiscale computation: Algorithms and applications," *Annual Review of Physical Chemistry*, vol. 60, pp. 321–344, 2009.

M. Khairoutdinov, C. DeMott, and D. Randall, "Evaluation of the simulated interannual and subseasonal variability in an AMIP-style simulation using the CSU Multiscale Modeling Framework," *Journal of Climate*, vol. 21, no. 3, pp. 413–431, 2008.

J. Kim and P. Moin, "Application of a fractional-step method to incompressible Navier-Stokes equations," *Journal of Computational Physics*, vol. 59, pp. 308–323, 1985.

C. Kiris and D. Kwak, "Numerical solution of incompressible Navier-Stokes equations using a fractional-step approach," *Computers & Fluids*, vol. 30, pp. 829–851, 2001.

R. Klein, "Scale-dependent models for atmospheric flows," *Annual Review of Fluid Mechanics*, vol. 42, pp. 249–274, 2010.

A. N. Kolmogorov, "Dissipation of energy in locally isotropic turbulence," *Doklady Akademii Nauk SSSR*, vol. 32, pp. 15–18, 1941.

I. Kolvin, K. Cohen, Y. Vardi, and E. Sharon, "Energy transfer by inertial waves during the buildup of turbulence in a rotating system," *Physical Review Letters*, vol. 102, no. 1, pp. 014 503 (1–4), 2009.

R. H. Kraichnan, "Inertial ranges in two-dimensional turbulence," *Physics of Fluids*, vol. 10, pp. 1417–1423, 1967.

W. Kramer, G. H. Keetels, H. J. H. Clercx, and G. J. F. van Heijst, "Structure-function scaling of bounded two-dimensional turbulence," *Physical Review E*, vol. 84, no. 2, pp. 026 310 (1–10), 2011.

A. G. Kravchenko and P. Moin, "On the effect of numerical errors in large eddy simulations of turbulent flows," *Journal of Computational Physics*, vol. 131, no. 2, pp. 310–322, 1997.

E. A. Kuznetsov, V. Naulin, A. H. Nielsen, and J. Juul Rasmussen, "Sharp vorticity gradients in two-dimensional turbulence and the energy spectrum," *Theoretical and Computational Fluid Dynamics*, vol. 24, pp. 253–258, 2010.

D. Kwak and C. C. Kiris, *Computation of viscous incompressible flows.* Springer-Verlag, Berlin, 2010.

D. Kwak, C. Kiris, and C. S. Kim, "Computational challenges of viscous incompressible flows," *Computers & Fluids*, vol. 34, pp. 283–299, 2005.

P. Lauritzen, C. Jablonowski, M. A. Taylor, and R. D. Nair, *Numerical Techniques for Global Atmospheric Models.* Springer-Verlag, Berlin, 2011.

W. Layton and R. Lewandowski, "Residual stress of approximate deconvolution models of turbulence," *Journal of Turbulence*, vol. 7, pp. 1–21, 2006.

W. Layton and M. Neda, "A similarity theory of approximate deconvolution models of turbulence," *Journal of Mathematical Analysis and Applications*, vol. 333, pp. 416–429, 2007.

W. J. Layton and L. Rebholz, *Approximate deconvolution models of turbulence: Analysis, phenomenology and numerical analysis.* Springer-Verlag, Berlin, 2012.

S. Lee, G. Wolberg, and S. Y. Shin, "Scattered data interpolation with multilevel B-splines," *IEEE Transactions on Visualization and Computer Graphics*, vol. 3, pp. 228–244, 1997.

B. Legras, P. Santangelo, and R. Benzi, "High-resolution numerical experiments for forced two-dimensional turbulence," *Europhysics Letters*, vol. 5, no. 1, pp. 37–42, 1988.

C. E. Leith, "Atmospheric predictability and two-dimensional turbulence," *Journal of Atmospheric Sciences*, vol. 28, pp. 145–161, 1971.

S. K. Lele, "Compact finite difference schemes with spectral-like resolution," *Journal of Computational Physics*, vol. 103, no. 1, pp. 16–42, 1992.

M. Lentine, W. Zheng, and R. Fedkiw, "A novel algorithm for incompressible flow using only a coarse grid projection," *ACM Transactions on Graphics*, vol. 29, pp. 114 (1–9), 2010.

M. Lesieur, *Turbulence in fluids*. Springer-Verlag, Berlin, 2008.

M. Lesieur and O. Metais, "New trends in large-eddy simulations of turbulence," *Annual Review of Fluid Mechanics*, vol. 28, pp. 45–82, 1996.

D. K. Lilly, "On the computational stability of numerical solutions of time-dependent non-linear geophysical fluid dynamics problems," *Monthly Weather Review*, vol. 93, no. 1, pp. 11–25, 1965.

——, "Numerical simulation of developing and decaying two-dimensional turbulence," *Journal of Fluid Mechanics*, vol. 45, no. 2, pp. 395–415, 1971.

E. Lindborg, "Can the atmospheric kinetic energy spectrum be explained by two-dimensional turbulence?" *Journal of Fluid Mechanics*, vol. 388, pp. 259–288, 1999.

E. Lindborg and K. Alvelius, "The kinetic energy spectrum of the two-dimensional enstrophy turbulence cascade," *Physics of Fluids*, vol. 12, no. 5, pp. 945–947, 2000.

E. Lindborg and A. Vallgren, "Testing Batchelor's similarity hypotheses for decaying two-dimensional turbulence," *Physics of Fluids*, vol. 22, pp. 091 704 (1–4), 2010.

M. N. Linnick and H. F. Fasel, "A high-order immersed interface method for simulating unsteady incompressible flows on irregular domains," *Journal of Computational Physics*, vol. 204, pp. 157–192, 2005.

J. G. Liu, "Gauge method for viscous incompressible flows," *Communications in Mathematical Sciences*, vol. 1, pp. 317–332, 2001.

P. Lynch, "The origins of computer weather prediction and climate modeling," *Journal of Computational Physics*, vol. 227, no. 7, pp. 3431–3444, 2008.

A. Majda, *Introduction to PDEs and waves for the atmosphere and ocean.* American Mathematical Society, Rhode Island, 2003.

A. Majda and A. L. Bertozzi, *Vorticity and incompressible flow.* Cambridge University Press, New York, 2002.

A. Majda and X. Wang, *Non-linear dynamics and statistical theories for basic geophysical flows.* Cambridge University Press, New York, 2006.

A. J. Majda and R. Klein, "Systematic multiscale models for the tropics," *Journal of Atmospheric Science*, vol. 60, pp. 393–408, 2003.

M. E. Maltrud and G. K. Vallis, "Energy spectra and coherent structures in forced two-dimensional and beta-plane turbulence," *Journal of Fluid Mechanics*, vol. 228, pp. 321–342, 1991.

J. R. Mansfield, O. M. Knio, and C. Meneveau, "A dynamic LES scheme for the vorticity transport equation: Formulation and apriori tests," *Journal of Computational Physics*, vol. 145, no. 2, pp. 693–730, 1998.

D. P. Marshall and H. R. Pillar, "Momentum balance of the wind-driven and meridional overturning circulation," *Journal of Physical Oceanography*, vol. 41, pp. 960–978, 2011.

J. Marshall, C. Hill, L. Perelman, and A. Adcroft, "Hydrostatic, quasi-hydrostatic, and nonhydrostatic ocean modeling," *Journal of Geophysical Research*, vol. 102, pp. 5733–5752, 1997.

D. Mateescu, M. P. Paidoussis, and F. Belanger, "A time-integration method using artificial compressibility for unsteady viscous flows," *Journal of Sound and Vibration*, vol. 177, pp. 197–205, 1994.

J. Matsumoto, "A fractional step method for incompressible viscous flow based on bubble function element stabilization method," *International Journal of Computational Fluid Dynamics*, vol. 20, pp. 145–155, 2006.

K. Mattsson, M. Svärd, M. Carpenter, and J. Nordström, "High-order accurate computations for unsteady aerodynamics," *Computers & Fluids*, vol. 36, no. 3, pp. 636–649, 2007.

D. J. Mavriplis, "Unstructured grid techniques," *Annual Review of Fluid Mechanics*, vol. 29, pp. 473–514, 1997.

J. C. McWilliams, "Emergence of isolated coherent vortices in turbulent flow," *Journal of Fluid Mechanics*, vol. 146, pp. 21–43, 1984.

——, "Statistical properties of decaying geostrophic turbulence," *Journal of Fluid Mechanics*, vol. 198, pp. 199–230, 1989.

——, "The vortices of two-dimensional turbulence," *Journal of Fluid Mechanics*, vol. 219, pp. 361–385, 1990.

——, "Modeling the oceanic general circulation," *Annual Review of Fluid Mechanics*, vol. 28, pp. 215–248, 1996.

——, *Fundamentals of geophysical fluid dynamics.* Cambridge University Press, New York, 2006.

S. P. Meacham, "Low-frequency variability in the wind-driven circulation," *Journal of Physical Oceanography*, vol. 30, pp. 269–293, 2000.

T. T. Medjo, "Numerical simulations of a two-layer quasi-geostrophic equation of the ocean," *SIAM Journal on Numerical Analysis*, vol. 37, pp. 2005–2022, 2000.

C. Meneveau and J. Katz, "Scale-invariance and turbulence models for large-eddy simulation," *Annual Review of Fluid Mechanics*, vol. 32, pp. 1–32, 2000.

X. Merle, F. Alizard, and J. C. Robinet, "Finite difference methods for viscous incompressible global stability analysis," *Computers & Fluids*, vol. 39, no. 6, pp. 911–925, 2010.

R. N. Miller, *Numerical modeling of ocean circulation.* Cambridge University Press, New York, 2007.

M. L. Minion and D. L. Brown, "Performance of under-resolved two-dimensional incompressible flow simulations, II," *Journal of Computational Physics*, vol. 138, pp. 734–765, 1997.

P. Moin, *Fundamentals of engineering numerical analysis.* Cambridge University Press, New York, 2001.

P. Moin and K. Mahesh, "Direct numerical simulation: A tool in turbulence research," *Annual Review of Fluid Mechanics*, vol. 30, pp. 539–578, 1998.

J. S. Mullen and P. F. Fischer, "Filtering techniques for complex geometry fluid flows," *Communications in Numerical Methods in Engineering*, vol. 15, no. 1, pp. 9–18, 1999.

W. Munk and C. Wunsch, "Observing the ocean in the 1990s," *Philosophical Transactions of the Royal Society A: Mathematical, Physical and Engineering Sciences*, vol. 307, pp. 439–464, 1982.

W. H. Munk, "On the wind-driven ocean circulation," *Journal of Meteorology*, vol. 7, pp. 80–93, 1950.

B. T. Nadiga and L. G. Margolin, "Dispersive-dissipative eddy parameterization in a barotropic model," *Journal of Physical Oceanography*, vol. 31, pp. 2525–2531, 2001.

F. M. Najjar and D. K. Tafti, "Study of discrete test filters and finite difference approximations for the dynamic subgrid-scale stress model," *Physics of Fluids*, vol. 8, pp. 1076–1088, 1996.

J. J. Nauw, H. A. Dijkstra, and E. Simonnet, "Regimes of low-frequency variability in a three-layer quasi-geostrophic ocean model," *Journal of Marine Research*, vol. 62, pp. 684–719, 2004.

P. Orlandi, *Fluid flow phenomena: A numerical toolkit.* Kluwer Academic Publishers, Netherlands, 2000.

S. A. Orszag, "Analytical theories of turbulence," *Journal of Fluid Mechanics*, vol. 41, no. 2, pp. 363–386, 1970.

T. M. Özgökmen and E. P. Chassignet, "Emergence of inertial gyres in a two-layer quasi-geostrophic ocean model," *Journal of Physical Oceanography*, vol. 28, no. 3, pp. 461–484, 1998.

T. M. Özgökmen, E. P. Chassignet, and C. G. H. Rooth, "On the connection between the Mediterranean outflow and the Azores Current," *Journal of Physical Oceanography*, vol. 31, pp. 461–480, 2001.

T. M. Özgökmen, T. Iliescu, and P. F. Fischer, "Large eddy simulation of stratified mixing in a three-dimensional lock-exchange system," *Ocean Modelling*, vol. 26, pp. 134–155, 2009.

J. Paret, M. C. Jullien, and P. Tabeling, "Vorticity statistics in the two-dimensional enstrophy cascade," *Physical Review Letters*, vol. 83, no. 17, pp. 3418–3421, 1999.

J. Pedlosky, *Geophysical fluid dynamics.* Springer-Verlag, New York, 1987.

J. Pike and P. L. Roe, "Accelerated convergence of Jameson's finite-volume Euler scheme using van der Houwen integrators," *Computers & Fluids*, vol. 13, no. 2, pp. 223–236, 1985.

W. H. Press, S. A. Teukolsky, W. T. Vetterling, and B. P. Flannery, *Numerical recipes in FORTRAN.* Cambridge University Press, New York, 1992.

C. D. Pruett and N. A. Adams, "A priori analyses of three subgrid-scale models for one-parameter families of filters," *Physics of Fluids*, vol. 12, pp. 1133–1142, 2000.

C. D. Pruett, T. A. Zang, C. L. Chang, and M. H. Carpenter, "Spatial direct numerical simulation of high-speed boundary-layer flows Part I: Algorithmic considerations and validation," *Theoretical and Computational Fluid Dynamics*, vol. 7, no. 1, pp. 49–76, 1995.

L. Quartapelle, *Numerical solution of the incompressible Navier-Stokes equations*. Birkhäuser, Switzerland, 1993.

W. H. Raymond, "Diffusion and numerical filters," *Monthly Weather Review*, vol. 122, no. 4, pp. 757–761, 1994.

L. G. Rebholz, "Conservation laws of turbulence models," *Journal of Mathematical Analysis and Applications*, vol. 326, pp. 33–45, 2007.

P. B. Rhines, "Waves and turbulence on a beta-plane," *Journal of Fluid Mechanics*, vol. 69, pp. 417–443, 1975.

L. F. Richardson, "The supply of energy from and to atmospheric eddies," *Proceedings of the Royal Society of London. Series A, Mathematical and Physical Science*, vol. 97, pp. 354–373, 1920.

T. Ringler, D. Jacobsen, M. Gunzburger, L. Ju, M. Duda, and W. Skamarock, "Exploring a multi-resolution modeling approach within the shallow-water equations," *Monthly Weather Review*, vol. 139, pp. 3348–3368, 2011.

S. E. Rogers and D. Kwak, "An upwind differencing scheme for the incompressible Navier-Strokes equations," *Applied Numerical Mathematics*, vol. 8, pp. 43–64, 1991.

R. R. Rosa, A. S. Sharma, and J. A. Valdivia, "Characterization of localized turbulence in plasma extended systems," *Physica A: Statistical Mechanics and its Applications*, vol. 257, no. 1, pp. 509–514, 1998.

D. Russell and Z. J. Wang, "A cartesian grid method for modeling multiple moving objects in 2D incompressible viscous flow," *Journal of Computational Physics*, vol. 191, pp. 177–205, 2003.

Y. Saad, *Iterative methods for sparse linear systems*. Society for Industrial and Applied Mathematics, Pennsylvania, 2003.

P. G. Saffman, "On the spectrum and decay of random two-dimensional vorticity distributions at large Reynolds number," *Studies in Applied Mathematics*, vol. 50, pp. 377–383, 1971.

P. Sagaut, *Large eddy simulation for incompressible flows: An introduction*. Springer-Verlag, Berlin, 2006.

P. Sagaut and R. Grohens, "Discrete filters for large eddy simulation," *International Journal for Numerical Methods in Fluids*, vol. 31, no. 8, pp. 1195–1220, 1999.

R. Salmon, *Lectures on geophysical fluid dynamics*. Oxford University Press, New York, 1998.

O. San and A. E. Staples, "High-order methods for decaying two-dimensional homogeneous isotropic turbulence," *Computers & Fluids*, vol. 63, pp. 105–127, 2012.

O. San, A. E. Staples, Z. Wang, and T. Iliescu, "Approximate deconvolution large eddy simulation of a barotropic ocean circulation model," *Ocean Modelling*, vol. 40, pp. 120–132, 2011.

M. Satoh, *Atmospheric circulation dynamics and general circulation models*. Springer-Verlag, Berlin, 2004.

M. Schäfer, *Computational engineering: Introduction to numerical methods*. Springer-Verlag, Berlin, 2006.

P. Schlatter, S. Stolz, and L. Kleiser, "LES of transitional flows using the approximate deconvolution model," *International Journal of Heat and Fluid Flow*, vol. 25, no. 3, pp. 549–558, 2004.

U. Schumann, "Subgrid scale model for finite difference simulations of turbulent flows in plane channels and annuli," *Journal of Computational Physics*, vol. 18, no. 4, pp. 376–404, 1975.

C. W. Shu, "High-order finite difference and finite volume WENO schemes and discontinuous Galerkin methods for CFD," *International Journal of Computational Fluid Dynamics*, vol. 17, pp. 107–118, 2003.

C. W. Shu, W. S. Don, D. Gottlieb, O. Schilling, and L. Jameson, "Numerical convergence study of nearly incompressible, inviscid Taylor-Green vortex flow," *Journal of Scientific Computing*, vol. 24, no. 1, pp. 1–27, 2005.

F. G. Shuman, "Numerical methods in weather prediction: II. Smoothing and filtering," *Monthly Weather Review*, vol. 85, no. 11, pp. 357–361, 1957.

A. Siegel, J. B. Weiss, J. Toomre, J. C. McWilliams, P. S. Berloff, and I. Yavneh, "Eddies and vortices in ocean basin dynamics," *Geophysical Research Letters*, vol. 28, pp. 3183–3186, 2001.

J. Smagorinsky, "General circulation experiments with the primitive equations," *Monthly Weather Review*, vol. 91, no. 3, pp. 99–164, 1963.

K. S. Smith, G. Boccaletti, C. C. Henning, I. Marinov, C. Y. Tam, I. M. Held, and G. K. Vallis, "Turbulent diffusion in the geostrophic inverse cascade," *Journal of Fluid Mechanics*, vol. 469, pp. 13–48, 2002.

L. M. Smith and V. Yakhot, "Bose condensation and small-scale structure generation in a random force driven 2D turbulence," *Physical Review Letters*, vol. 71, no. 3, pp. 352–355, 1993.

——, "Finite-size effects in forced two-dimensional turbulence," *Journal of Fluid Mechanics*, vol. 274, pp. 115–138, 1994.

W. Y. Soh and J. W. Goodrich, "Unsteady solution of incompressible Navier-Stokes equations," *Journal of Computational Physics*, vol. 79, pp. 113–134, 1988.

S. Speich, H. Dijkstra, and M. Ghil, "Successive bifurcations in a shallow-water model applied to the wind-driven ocean circulation," *Nonlinear Processes in Geophysics*, vol. 2, pp. 241–268, 1995.

I. Stanculescu, "Existence theory of abstract approximate deconvolution models of turbulence," *Annali dell'Università di Ferrara*, vol. 54, pp. 145–168, 2008.

A. Staniforth and N. Wood, "Aspects of the dynamical core of a nonhydrostatic, deep-atmosphere, unified weather and climate-prediction model," *Journal of Computational Physics*, vol. 227, no. 7, pp. 3445–3464, 2008.

J. Steppeler, R. Hess, U. Schättler, and L. Bonaventura, "Review of numerical methods for nonhydrostatic weather prediction models," *Meteorology and Atmospheric Physics*, vol. 82, no. 1, pp. 287–301, 2003.

T. Stocker, *Introduction to climate modelling*. Springer-Verlag, Heidelberg, 2011.

S. Stolz and N. A. Adams, "An approximate deconvolution procedure for large-eddy simulation," *Physics of Fluids*, vol. 11, pp. 1699–1701, 1999.

S. Stolz, N. A. Adams, and L. Kleiser, "An approximate deconvolution model for large-eddy simulation with application to incompressible wall-bounded flows," *Physics of Fluids*, vol. 13, pp. 997–1015, 2001.

——, "The approximate deconvolution model for large-eddy simulations of compressible flows and its application to shock-turbulent-boundary-layer interaction," *Physics of Fluids*, vol. 13, pp. 2985–3001, 2001.

——, "The approximate deconvolution model for compressible flows: Isotropic turbulence and shock-boundary-layer interaction," in *Advances in LES of Complex Flows, Fluid Me-*

chanics and its Applications, R. Friedrich and W. Rodi, Eds., vol. 65. Kluwer Academic Publishers, New York, 2004, pp. 33–47.

H. Stommel, *The Gulf Stream: A physical and dynamical description.* University of California Press, California, 1972.

J. C. Strikwerda, *Finite difference schemes and partial differential equations.* Society for Industrial Mathematics, Pennsylvania, 2004.

J. C. Strikwerda and Y. S. Lee, "The accuracy of the fractional step method," *SIAM Journal on Numerical Analysis*, vol. 37, pp. 37–47, 1999.

S. Sukoriansky, N. Dikovskaya, and B. Galperin, "On the arrest of inverse energy cascade and the Rhines scale," *Journal of Atmospheric Sciences*, vol. 64, pp. 3312–3327, 2007.

P. Sura, K. Fraedrich, and F. Lunkeit, "Regime transitions in a stochastically forced double-gyre model," *Journal of Physical Oceanography*, vol. 31, pp. 411–426, 2001.

P. Tabeling, "Two-dimensional turbulence: A physicist approach," *Physics Reports*, vol. 362, pp. 1–62, 2002.

D. Tafti, "Comparison of some upwind-biased high-order formulations with a second-order central-difference scheme for time integration of the incompressible Navier-Stokes equations," *Computers & Fluids*, vol. 25, no. 7, pp. 647–665, 1996.

C. K. W. Tam and J. C. Webb, "Dispersion-relation-preserving finite difference schemes for computational acoustics," *Journal of Computational Physics*, vol. 107, no. 2, pp. 262–281, 1993.

Y. Tanaka and K. Akitomo, "Alternating zonal flows in a two-layer wind-driven ocean," *Journal of Oceanography*, vol. 66, pp. 475–487, 2010.

H. S. Tang and F. Sotiropoulos, "Fractional step artificial compressibility schemes for the unsteady incompressible Navier-Stokes equations," *Computers & Fluids*, vol. 36, pp. 974–986, 2007.

J. C. Tannehill, D. A. Anderson, and R. H. Pletcher, *Computational fluid mechanics and heat transfer*. Taylor & Francis, Pennsylvania, 1997.

G. I. Taylor and A. E. Green, "Mechanism of the production of small eddies from large ones," *Proceedings of the Royal Society of London. Series A, Mathematical and Physical Science*, vol. 158, pp. 499–521, 1937.

R. Temam, *Navier-Stokes equations: Theory and numerical analysis*. American Mathematical Society, Rhode Island, 2001.

C. Tenaud, S. Pellerin, A. Dulieu, and L. Ta Phuoc, "Large eddy simulations of a spatially developing incompressible 3D mixing layer using the v–ω formulation," *Computers & Fluids*, vol. 34, no. 1, pp. 67–96, 2005.

T. E. Tezduyar, J. Liou, D. K. Ganjoo, and M. Behr, "Solution techniques for the vorticity-stream function formulation of two-dimensional unsteady incompressible flows," *International Journal for Numerical Methods in Fluids*, vol. 11, pp. 515–539, 1990.

C. V. Tran and J. C. Bowman, "On the dual cascade in two-dimensional turbulence," *Physica D: Nonlinear Phenomena*, vol. 176, pp. 242–255, 2003.

C. V. Tran and T. G. Shepherd, "Constraints on the spectral distribution of energy and enstrophy dissipation in forced two-dimensional turbulence," *Physica D: Nonlinear Phenomena*, vol. 165, pp. 199–212, 2002.

U. Trottenberg, C. W. Oosterlee, and A. Schüller, *Multigrid*. Academic Press, London, 2001.

A. Vallgren and E. Lindborg, "The enstrophy cascade in forced two-dimensional turbulence," *Journal of Fluid Mechanics*, vol. 671, no. 1, pp. 168–183, 2011.

G. K. Vallis, *Atmospheric and oceanic fluid dynamics: Fundamentals and large-scale circulation*. Cambridge University Press, New York, 2006.

O. V. Vasilyev, T. S. Lund, and P. Moin, "A general class of commutative filters for LES in complex geometries," *Journal of Computational Physics*, vol. 146, no. 1, pp. 82–104, 1998.

M. R. Visbal and D. V. Gaitonde, "On the use of higher-order finite-difference schemes on curvilinear and deforming meshes," *Journal of Computational Physics*, vol. 181, pp. 155–185, 2002.

M. Visbeck, J. Marshall, T. Haine, and M. Spall, "Specification of eddy transfer coefficients in coarse-resolution ocean circulation models," *Journal of Physical Oceanography*, vol. 27, pp. 381–402, 1997.

J. Von Hardenberg, J. C. McWilliams, A. Provenzale, A. Shchepetkin, and J. B. Weiss, "Vortex merging in quasi-geostrophic flows," *Journal of Fluid Mechanics*, vol. 412, pp. 331–353, 2000.

G. J. Wagner, X. Zhou, and S. J. Plimpton, "Equation-free accelerated simulations of the morphological relaxation of crystal surfaces," *International Journal for Multiscale Computational Engineering*, vol. 8, pp. 423–439, 2010.

W. M. Washington, L. Buja, and A. Craig, "The computational future for climate and Earth system models: On the path to petaflop and beyond," *Philosophical Transactions of the Royal Society A: Mathematical, Physical and Engineering Sciences*, vol. 367, pp. 833–846, 2009.

J. Weiss, "The dynamics of enstrophy transfer in two-dimensional hydrodynamics," *Physica D: Nonlinear Phenomena*, vol. 48, no. 2, pp. 273–294, 1991.

P. Wesseling, *Introduction to multigrid methods*. R. T. Edwards, Pennsylvania, 2004.

J. H. Williamson, "Low-storage Runge-Kutta schemes," *Journal of Computational Physics*, vol. 35, no. 1, pp. 48–56, 1980.

M. Yanwen, F. Dexun, T. Kobayashi, and N. Taniguchi, "Numerical solution of the incompressible Navier-Stokes equations with an upwind compact difference scheme," *International Journal for Numerical Methods in Fluids*, vol. 30, pp. 509–521, 1999.

Z. Yin, H. J. H. Clercx, and D. C. Montgomery, "An easily implemented task-based parallel scheme for the Fourier pseudospectral solver applied to 2D Navier-Stokes turbulence," *Computers & Fluids*, vol. 33, no. 4, pp. 509–520, 2004.

Y. Zang, R. L. Street, and J. R. Koseff, "A non-staggered grid, fractional step method for time-dependent incompressible Navier-Stokes equations in curvilinear coordinates," *Journal of Computational Physics*, vol. 114, pp. 18–33, 1994.

J. Zhang, "Fast and high accuracy multigrid solution of the three dimensional Poisson equation," *Journal of Computational Physics*, vol. 143, pp. 449–461, 1998.

B. Zhou and F. K. Chow, "Large-eddy simulation of the stable boundary layer with explicit filtering and reconstruction turbulence modeling," *Journal of Atmospheric Sciences*, vol. 68, pp. 2142–2155, 2011.